NANOCELLULOSE: A MULTIPURPOSE ADVANCED FUNCTIONAL MATERIAL

EDITED BY: Guang Yang, Muhammad Wajid Ullah, Orlando Rojas and
Ronan McCarthy
PUBLISHED IN: Frontiers in Bioengineering and Biotechnology

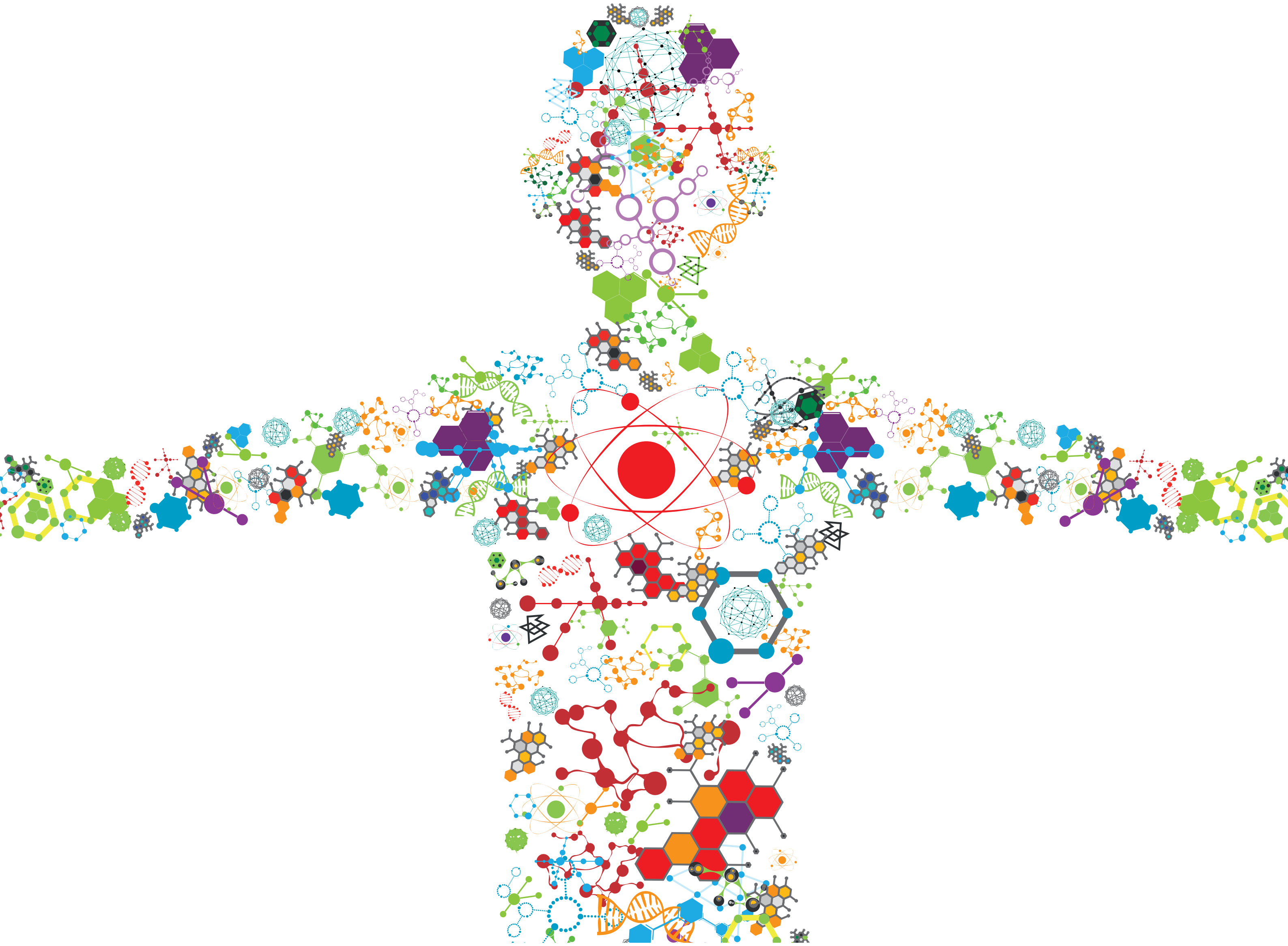

frontiers Research Topics

ISSN 1664-8714
ISBN 978-2-88971-276-2
DOI 10.3389/978-2-88971-276-2

About Frontiers

Frontiers is more than just an open-access publisher of scholarly articles: it is a pioneering approach to the world of academia, radically improving the way scholarly research is managed. The grand vision of Frontiers is a world where all people have an equal opportunity to seek, share and generate knowledge. Frontiers provides immediate and permanent online open access to all its publications, but this alone is not enough to realize our grand goals.

Frontiers Journal Series

The Frontiers Journal Series is a multi-tier and interdisciplinary set of open-access, online journals, promising a paradigm shift from the current review, selection and dissemination processes in academic publishing. All Frontiers journals are driven by researchers for researchers; therefore, they constitute a service to the scholarly community. At the same time, the Frontiers Journal Series operates on a revolutionary invention, the tiered publishing system, initially addressing specific communities of scholars, and gradually climbing up to broader public understanding, thus serving the interests of the lay society, too.

Dedication to Quality

Each Frontiers article is a landmark of the highest quality, thanks to genuinely collaborative interactions between authors and review editors, who include some of the world's best academicians. Research must be certified by peers before entering a stream of knowledge that may eventually reach the public - and shape society; therefore, Frontiers only applies the most rigorous and unbiased reviews.
Frontiers revolutionizes research publishing by freely delivering the most outstanding research, evaluated with no bias from both the academic and social point of view. By applying the most advanced information technologies, Frontiers is catapulting scholarly publishing into a new generation.

What are Frontiers Research Topics?

Frontiers Research Topics are very popular trademarks of the Frontiers Journals Series: they are collections of at least ten articles, all centered on a particular subject. With their unique mix of varied contributions from Original Research to Review Articles, Frontiers Research Topics unify the most influential researchers, the latest key findings and historical advances in a hot research area! Find out more on how to host your own Frontiers Research Topic or contribute to one as an author by contacting the Frontiers Editorial Office: frontiersin.org/about/contact

NANOCELLULOSE: A MULTIPURPOSE ADVANCED FUNCTIONAL MATERIAL

Topic Editors:
Guang Yang, Huazhong University of Science and Technology, China
Muhammad Wajid Ullah, Huazhong University of Science and Technology, China
Orlando Rojas, University of British Columbia, Canada
Ronan McCarthy, Brunel University London, United Kingdom

Image: Guang Yang, Muhammad Wajid Ullah,
Orlando J. Rojas, and Ronan R. McCarthy

Drs. Ullah and Yang hold patents related to cellulose material. All other Topic Editors declare no competing interests with regard to the Research Topic subject.

This Research Topic is dedicated to Prof. Lina Zhang on the occasion of her 80th Birthday, in gratitude, esteem, and affection.

Citation: Yang, G., Ullah, M. W., Rojas, O., McCarthy, R., eds. (2021).
Nanocellulose: A Multipurpose Advanced Functional Material.
Lausanne: Frontiers Media SA. doi: 10.3389/978-2-88971-276-2

Table of Contents

frontiers
in Bioengineering and Biotechnology

EDITORIAL
published: 22 July 2021
doi: 10.3389/fbioe.2021.738779

Editorial: Nanocellulose: A Multipurpose Advanced Functional Material

Muhammad Wajid Ullah[1], Orlando J. Rojas[2], Ronan R. McCarthy[3] and Guang Yang[1]*

[1]Department of Biomedical Engineering, Huazhong University of Science and Technology, Wuhan, China, [2]Bioproducts Institute, Departments of Chemical and Biological Engineering, Chemistry and Wood Science, The University of British Columbia, Vancouver, BC, Canada, [3]Division of Biosciences, Department of Life Sciences, College of Health and Life Sciences, Brunel University London, Uxbridge, United Kingdom

Keywords: nanocellulose, synthesis, characterization, functionalization, tissue engineering, additive manufacturing, textile, environment

Editorial on the Research Topic

Nanocellulose: A Multipurpose Advanced Functional Material

Nanocellulose refers to the cellulosic materials having at least one dimension at the nanoscale. It is the most abundant natural polymer on Earth, extracted from plants termed plant cellulose (Yadav et al., 2021), produced by microbial cells called bacterial cellulose (BC) or bacterial nanocellulose (BNC) (Ul-Islam et al., 2021), and synthesized enzymatically such as by the cell-free enzyme systems, named as bio-cellulose (Ullah et al., 2015; Kim et al., 2019). Over the past few decades, the different forms of nanocellulose, including cellulose nanocrystals (CNCs), cellulose nanofibers (CNF), and BNC have received tremendous attention for the development of innovative materials owing due to their abundance, renewability, and remarkable structural and physical properties such as high surface area and special surface chemistry, high crystallinity and mechanical strength, hydrophilicity, moldability, polyfunctionality, and excellent biological features (biocompatibility, biodegradability, and non-toxicity). These properties could be tuned through the addition of other natural and synthetic polymers, nanomaterials, clays, and other materials, as well as through the incorporation of additional functional groups such as peptides (Malheiros et al., 2018). Unlike CNCs and CNF, the structural features of BC could be tuned by varying the growth and culture conditions of the cellulose-producing microbial cells (Ullah et al., 2016). The surface chemistry, porosity, fiber orientation, and physical structure of nanocellulose can be controlled at macro-, micro-, and even nanoscales. Different types of nanocellulose in the form of gels, sheets, films, membrane, pellets, filaments, fibers, papers, tubes, capsules, sponges, laminates, and coatings find novel and emerging applications in food (Cazón and Vázquez, 2021; Haghighi et al., 2021), tissue engineering (Du et al., 2019), wound dressing (Mao et al., 2021; Wang et al., 2021), drug delivery (Li et al., 2018; Raghav et al., 2021), bioinks for 3D printing (McCarthy et al., 2019; Fourmann et al., 2021), biosensors (Farooq et al., 2020), energy storage devices (Sheng et al., 2019), membrane filters (Yuan et al., 2020), textiles (Salah, 2013), flexible displays (Fernandes et al., 2009), facial masks (Bianchet et al., 2020), and several others.

The global environmental degradation issue, the depletion of natural energy resources, the health-related problems, and other human needs are greatly pushing the material-related research towards the use of various polymeric materials from renewable resources like plants (i.e., cellulose, hemicellulose, lignin) and microorganisms (i.e., BNC) for fabrication of functional materials for different applications. Although nanocellulose obtained from such sources possesses unique features, it does not possess features like antimicrobial activity, antioxidant activity, electromagnetic properties, and catalytic activity, which are required for its specialized applications. Furthermore, nanocellulose also possesses limited biocompatibility and optical transparency. The plant cellulose, although a cheap source, requires complex extraction procedures and post-synthesis processing as it

OPEN ACCESS

Edited and reviewed by:
Hasan Uludag,
University of Alberta, Canada

****Correspondence:***
Guang Yang
yang_sunny@yahoo.com

Specialty section:
This article was submitted to Biomaterials,
a section of the journal Frontiers in Bioengineering and Biotechnology

Received: *09 July 2021*
Accepted: *14 July 2021*
Published: *22 July 2021*

Citation:
Ullah MW, Rojas OJ, McCarthy RR and Yang G (2021) Editorial: Nanocellulose: A Multipurpose Advanced Functional Material.
Front. Bioeng. Biotechnol. 9:738779.
doi: 10.3389/fbioe.2021.738779

contains hemicellulose, lignin, and some minerals. In contrast, the BC, although pure, is expensive and produced at a low yield by the microbial cells. Altogether, all types of nanocellulose require complicated functionalization procedures for tuning their features to meet the demands of desired applications. To date, various studies have been conducted for cost-effective synthesis, processing, and structural modifications of nanocellulose; there is still much to be explored about its facile and low-cost synthesis, tuning its properties and establish structure-function relationship, and explore its innovative and emerging applications.

Taking the advantages of unique surface chemistry and physical structure of nanocellulose, this Research Topic in Frontiers in Bioengineering and Biotechnology, Sections “Biomaterials” and “Nanobiotechnology” entitled “Nanocellulose: A Multipurpose Advanced Functional Material” is aimed to discuss the pilot-scale production, unveil the structure-function relationship, and identify the innovative and emerging applications of different types of nanocellulose. This Research Topic features a total of 20 articles, including fourteen original research articles, a brief research report, four reviews, and one systematic review, contributed by the experts in the field. These articles are mainly focused on the synthesis, characterization, and applications of various forms of nanocellulose in different fields like biomedical (antibacterial, wound dressing, bone tissue engineering, drug delivery, nerve tissue engineering), pharmaceutics, additive manufacturing, food, environment, textile, and optoelectronics.

It has been recognized that the ‘production cost’ and ‘prices of BC-based products’ are two indispensable aspects hindering the commercialization of nanocellulose. To this end, the review by Zhong from Hainan Yeguo Foods Co. Ltd., Hainan, China, rationally demonstrated the feasibility of industrial-scale production by elaborating the industrial setup and discussing the production cost of BC. The article took a case-by-case approach and discussed the market value of various BC-based products for their use in the food, personal care, biomedical, and textile industries. Wang et al. also took on industrial-scale production of nanocellulose, with a focus on producing cellulose nanowhiskers (CNWs), having similar morphology to CNCs, through acid hydrolysis by using low-cost equipment made of common stainless steel, where the used acid was effectively recovered at the end of the process. These CNWs could serve as the effective rheology modifier for their use in the preparation of inks for 3D printing. The emerging 3D printing technology, in contrast to the widely used fabrication techniques of developing nanocellulose-based composites, is providing new avenues based on ‘polymer printing’ for obtaining biological scaffolds. A systematic review by Tarassoli et al. identified the potential of different biomaterials used in extrusion printing and identified that alginate, poly (ε-caprolactone) (PCL), gelatin, and methacrylated gelatin are the most commonly used natural polymer. They realized a shift from synthetic to natural bioinks for biological applications, although the qualitative analysis did not show any link between the type of bioink, the extrusion printing technique, and the target tissue, thus indicating the infancy of this fabrication approach. Although at an early stage of development, the potential merits of 3D printing technology are quite clear, and further requires the formulation of tissue-specific bioinks with balanced printing materials, viable cells, growth factors, and finally the selection of an appropriate bioprinting technique for printing of tissue constructs for targeted applications, which would ultimately lead to maturation of 3D printing technology. As the future of printing technology mainly relies on the selection of unique and novel biomaterials, this systematic overview of different natural and synthetic polymers will provide solid grounds in the pursuit of choosing a suitable polymeric system for targeted applications. Moreover, the clogging caused by the cellulose fibers during the extrusion printing needs to be resolved while keeping in view that the fibrous morphology of biological scaffolds is advantageous for adhesion and proliferation of cells and have a similarity with the biological tissues such as collagen.

As indicated in the title of this Research Topic, nanocellulose is a multipurpose functional material that finds applications in different areas; a large portion of papers in this Research Topic covers different application areas. As nanocellulose serves as a matrix for a range of materials, Wang et al., Khattak et al., and Revin et al. took on developing nanocellulose-based composites with different antimicrobial materials, including gold nanoclusters, silver sulfadiazine, and sodium fusidate by developing films, hydrogels, and aerogels, respectively. These nanocomposites showed antibacterial activity against different clinically relevant microorganisms, such as *Escherichia coli*, *Streptococcus mutans*, *Staphylococcus aureus*, and *Pseudomonas aeruginosa*, which are generally responsible for pathogen burdens at the wound site. Thus such nanocellulose-based antimicrobial nanocomposites could be useful for the development of wound dressing materials. Continuing with the broad-spectrum biomedical applications of BC owing to its non-toxic nature and ability to allow the reinforcement of a variety of materials, Sajjad et al. also took on developing BC-based antimicrobial wound dressings for treating partial thickness skin burns by using a natural product, curcumin, as the reinforcement material having antimicrobial, antioxidant, antineoplastic, and wound healing capabilities and a long history of medical use. In addition to these, several other materials of different sizes, shapes, physiology (liquid and solid), and origin, having antimicrobial activities, have been successfully impregnated into cellulose matrix with the aim to develop antimicrobial materials for biomedical applications. A review by Zheng et al. summarized several wound dressings of nanocellulose with organic antimicrobials (natural polymers, bioactive materials, synthetic materials), inorganic nanomaterials (metal/metal oxides, carbon-based nanomaterials, nanosilicates), and antibiotics. All these studies indicate the usefulness of different types of nanocellulose to serve as a matrix for the impregnation of antimicrobials, thus could be used as a platform for the local and controlled delivery of therapeutics against multidrug-resistant bacteria, a major threat to health care systems globally due to extensive overuse of antibiotics.

Despite the high crystallinity and mechanical strength of nanocellulose, it does not possess the desired strength of a natural bone; nevertheless, this limitation can be effectively overcome by making its composite with other materials, thanks to its unique matrix, to induce the formation of calcium phosphate for bone tissue engineering. Hong et al. reinforced the surface-oxidized CNCs with PCL to induce the formation of calcium phosphate. The 3D printed CNC/PCL nanocomposite demonstrated enhanced mechanical strength, crystallinity, and thermal stability. Furthermore, the scaffold supported the growth of MC3T3 preosteoblasts, thus indicating its biocompatible nature. Altogether, the 3D CNC/PCL scaffolds could be a suitable candidate for bone tissue engineering applications. The mechanical, thermal, and biological features of nanocellulose could also be tuned by making its composites with different materials. A perspective review by Khan et al. discussed that, in addition to serving as a matrix for doping of minerals and bioceramics for developing bone and cartilage substitutes, nanocellulose could also be used as a drug carrier for treating bone-related diseases. The review explicitly described the structure-function relationship of nanocellulose with bone tissues. While there is no doubt about the biocompatible and non-toxic nature of nanocellulose, there is still much to be investigated about its *in-vivo* degradation and unveiling the associated complications. Moreover, nanocellulose as a drug carrier has some limitations due to its hydrophilic nature and only serves as a carrier for hydrophilic drugs especially when used in the form of a hydrogel, following the solubility principle 'like-dissolve-like'. Badshah et al. developed a nanocellulose-based drug delivery system for oral administration. Considering the insolubility of nanocellulose in common organic solvents, BC was dissolved in ionic solvent *N*-methyl-morpholine-oxide and loaded with model drugs, famotidine or tizanidine, which was abruptly released. Although this system could be useful for oral administration of the drug, a sustained and prolonged drug release is desired in some situations. A controlled drug release from nanocellulose could be achieved through its chemical modification, such as with pH-sensitive and electrically conductive materials, which would allow a sustained drug release under the influence of external pH and electrical stimuli, respectively. Nerve tissue engineering is another important application area of nanocellulose-based biomaterials. The development of nanocellulose-based biomaterials capable of stimulating neural tissue repair is in demand owing to the limited regenerative capacity of neural tissues, with neurons as the most noticeable. Towards this goal, Xu et al. developed a spongy electrical conduit of hydroxyethyl cellulose with soy protein and polyaniline and evaluated its regeneration potential of peripheral nerve for treating sciatic nerve injury in a rat model. In addition to the direct use of nanocellulose in tissue engineering or as a carrier for drugs, bioactive materials, and nanomaterials, the nanocellulose-based scaffolds are also used as useful tools in the diagnosis of cancer models (Ul-Islam et al., 2019). Kim et al. developed a bioink comprised of gastric tissue-derived decellularized extracellular matrix (g-dECM) with cellulose nanoparticles and used it as a 3D cell printing-based gastric cancer model. The high mechanical strength of the cellulose nanoparticles imparted stability to the 3D printed scaffold, which in turn better supported the progression of gastric cancer.

The use of nanocellulose in optoelectronics is another exciting area of research. Considering the renewable nature of nanocellulose, it is highly demanding to study its optical behavior and conductive properties to explore its applications in this area. For instance, the portable and wearable electronics requiring highly thermo-conductive but electrically insulating film, the development of nanocellulose-based films with conductive materials could be a good choice considering the innate non-conductive nature of nanocellulose. In contrast to the conventional sustainable approach of combining boron nitrate sheets with regenerated cellulose, which usually produces brittle structures of low toughness, Xu et al. developed a dual crosslinked and anisotropic regenerated cellulose and boron nitrate nanosheets, where the partial chemical bonding interactions enabled the interfiber slippage and prevented the mechanical fracture while the non-covalent hydrogen bonding interactions served as the sacrifice bonds and dissipated the stress energy, and thus led to the development of high mechanical strength and tough nanocellulose-based sheets. Santos et al. also focused on the optoelectronics applications of nanocellulose by developing freestanding CNCs film with silica through the chiral nematic organization. Considering the transparent or semitransparent nature of different forms of nanocellulose, the optical properties of films were tuned by varying the ratio of CNCs and silica. The incorporation of light-emitting Rhodamine 6G allowed the complimentary control of the optical properties of the films. These freestanding luminescent and iridescent CNCs-based films could be useful materials for applications in the development of optical devices like lasers, filters, and sensors. The optical transparency of cellulose can be enhanced in various ways such as acetylation (Gonçalves et al., 2016) and making its composite with transparent materials like poly (2-hydroxyethyl methacrylate) (Di et al., 2017). Likewise, Kim et al. enhanced the optical transparency of CNCs films through reinforcement of polyurethane. The change in optical transparency was determined by measuring the change in the refractive index, which was mainly associated with the alignment of CNCs by dielectrophoresis. Unlike the above-mentioned studies of developing transparent nanocellulose films for wound dressing applications, the developed transparent CNCs films by tuning the refractive index in the presence of polling electric field could be used as a tunable optical lens. Moreover, a study by Tao et al. showed that the self-assembly of CNCs in a tilted cuvette demonstrated simultaneous reflection of left-handed and right-handed circularly polarized light and formed rainbow color CNCs-based films. This phenomenon could be employed in the synthetic development of one-dimensional chiral photonic materials with patterned and ambidextrous reflection for photonic applications.

Nanocellulose also finds useful applications in the textile industry and environment sector. It serves as a matrix for immobilization of catalysts, enzymes, and other sensing materials not only to sense environmental pollutants but also degrade different wastes, for example, wastes from the textile industry, which could be further used as the carbon source and biotransformed into value-added products (Zhang et al., 2021). A review by Felgueiras et al. discussed the various technologies in practice or in the phase of development for the production of nanocellulose-based textiles. Huang et al. synthesized biocompatible fluorescent carbon dots from cellulose, which detected mercury at a small detection level and with high specificity. Ul-Islam et al. developed BC-based multipurpose green nanomaterials with *Aloe vera* hydrogels for biomedical (adhesion and proliferation of osteoblast cells) and environment (adsorption of metal ions) applications.

In conclusion, this Research Topic not only discusses the fundamental knowledge of nanocellulose synthesis, its unique properties, and multipurpose applications in different fields but also provides the base for the production of nanocellulose-based innovative materials for novel and emerging applications and discusses the pilot-scale production and commercialization of nanocellulose-based products.

AUTHOR CONTRIBUTIONS

MWU drafted the manuscript. OR, RM, and GY edited and proofread the manuscript.

REFERENCES

Bianchet, R. T., Vieira Cubas, A. L., Machado, M. M., and Siegel Moecke, E. H. (2020). Applicability of Bacterial Cellulose in Cosmetics - Bibliometric Review. *Biotechnol. Rep.* 27, e00502. doi:10.1016/j.btre.2020.e00502

Cazón, P., and Vázquez, M. (2021). Bacterial Cellulose as a Biodegradable Food Packaging Material: A Review. *Food Hydrocolloids* 113, 106530. doi:10.1016/j.foodhyd.2020.106530

Di, Z., Shi, Z., Ullah, M. W., Li, S., and Yang, G. (2017). A Transparent Wound Dressing Based on Bacterial Cellulose Whisker and Poly(2-Hydroxyethyl Methacrylate). *Int. J. Biol. Macromolecules* 105, 638–644. doi:10.1016/j.ijbiomac.2017.07.075

Du, H., Liu, W., Zhang, M., Si, C., Zhang, X., and Li, B. (2019). Cellulose Nanocrystals and Cellulose Nanofibrils Based Hydrogels for Biomedical Applications. *Carbohydr. Polym.* 209, 130–144. doi:10.1016/j.carbpol.2019.01.020

Farooq, U., Ullah, M. W., Yang, Q., Aziz, A., Xu, J., Zhou, L., et al. (2020). High-density Phage Particles Immobilization in Surface-Modified Bacterial Cellulose for Ultra-sensitive and Selective Electrochemical Detection of *Staphylococcus aureus*. *Biosens. Bioelectron.* 157, 112163. doi:10.1016/j.bios.2020.112163

Fernandes, S. C. M., Oliveira, L., Freire, C. S. R., Silvestre, A. J. D., Neto, C. P., Gandini, A., et al. (2009). Novel Transparent Nanocomposite Films Based on Chitosan and Bacterial Cellulose. *Green. Chem.* 11, 2023. doi:10.1039/b919112g

Fourmann, O., Hausmann, M. K., Neels, A., Schubert, M., Nyström, G., Zimmermann, T., et al. (2021). 3D Printing of Shape-Morphing and Antibacterial Anisotropic Nanocellulose Hydrogels. *Carbohydr. Polym.* 259, 117716. doi:10.1016/j.carbpol.2021.117716

Gonçalves, S., Rodrigues, I. P., Padrão, J., Silva, J. P., Sencadas, V., Lanceros-Mendez, S., et al. (2016). Acetylated Bacterial Cellulose Coated with Urinary Bladder Matrix as a Substrate for Retinal Pigment Epithelium. *Colloids Surf. B: Biointerfaces* 139, 1–9. doi:10.1016/j.colsurfb.2015.11.051

Haghighi, H., Gullo, M., La China, S., Pfeifer, F., Siesler, H. W., Licciardello, F., et al. (2021). Characterization of Bio-Nanocomposite Films Based on Gelatin/polyvinyl Alcohol Blend Reinforced with Bacterial Cellulose Nanowhiskers for Food Packaging Applications. *Food Hydrocolloids* 113, 106454. doi:10.1016/j.foodhyd.2020.106454

Kim, Y., Ullah, M. W., Ul-Islam, M., Khan, S., Jang, J. H., and Park, J. K. (2019). Self-assembly of Bio-Cellulose Nanofibrils through Intermediate Phase in a Cell-free Enzyme System. *Biochem. Eng. J.* 142, 135–144. doi:10.1016/j.bej.2018.11.017

Li, S., Jasim, A., Zhao, W., Fu, L., Ullah, M. W., Shi, Z., et al. (2018). Fabrication of pH-Electroactive Bacterial Cellulose/Polyaniline Hydrogel for the Development of a Controlled Drug Release System. *ES Mater. Manuf.* 1, 41–49. doi:10.30919/esmm5f120

Malheiros, P. S., Jozala, A. F., Pessoa-Jr., A., Jr., Vila, M. M. D. C., Balcão, V. M., and Franco, B. D. G. M. (2018). Immobilization of Antimicrobial Peptides from Lactobacillus Sakei Subsp. Sakei 2a in Bacterial Cellulose: Structural and Functional Stabilization. *Food Packaging and Shelf Life* 17, 25–29. doi:10.1016/j.fpsl.2018.05.001

Mao, L., Wang, L., Zhang, M., Ullah, M. W., Liu, L., Zhao, W., et al. (2021). *In Situ* Synthesized Selenium Nanoparticles-Decorated Bacterial Cellulose/Gelatin Hydrogel with Enhanced Antibacterial, Antioxidant, and Anti-Inflammatory Capabilities for Facilitating Skin Wound Healing. *Adv. Healthc. Mater.*, 2100402. doi:10.1002/adhm.202100402

McCarthy, R. R., Ullah, M. W., Booth, P., Pei, E., and Yang, G. (2019). The Use of Bacterial Polysaccharides in Bioprinting. *Biotechnol. Adv.* 37, 107448. doi:10.1016/j.biotechadv.2019.107448

Raghav, N., Sharma, M. R., and Kennedy, J. F. (2021). Nanocellulose: A Mini-Review on Types and Use in Drug Delivery Systems. *Carbohydr. Polym. Tech. Appl.* 2, 100031. doi:10.1016/j.carpta.2020.100031

Salah, S. M. (2013). Application of Nano-Cellulose in Textile. *J. Textile Sci. Eng.* 03. doi:10.4172/2165-8064.1000142

Sheng, N., Chen, S., Yao, J., Guan, F., Zhang, M., Wang, B., et al. (2019). Polypyrrole@TEMPO-oxidized Bacterial Cellulose/reduced Graphene Oxide Macrofibers for Flexible All-Solid-State Supercapacitors. *Chem. Eng. J.* 368, 1022–1032. doi:10.1016/j.cej.2019.02.173

Ul-Islam, M., Subhan, F., Islam, S. U., Khan, S., Shah, N., Manan, S., et al. (2019). Development of Three-Dimensional Bacterial Cellulose/chitosan Scaffolds: Analysis of Cell-Scaffold Interaction for Potential Application in the Diagnosis of Ovarian Cancer. *Int. J. Biol. Macromolecules* 137, 1050–1059. doi:10.1016/j.ijbiomac.2019.07.050

Ul-Islam, M., Ullah, M. W., Khan, T., and Park, J. K. (2021). "Bacterial Cellulose: Trends in Synthesis, Characterization, and Applications," in *"Bacterial Cellulose: Trends in Synthesis, Characterization, and Applications," in* Handbook Of Hydrocolloids. Editors G. O. Phillips and P. A. Williams (Elsevier), 923–974. doi:10.1016/B978-0-12-820104-6.00010-3

Ullah, M. W., Ul-Islam, M., Khan, S., Kim, Y., and Park, J. K. (2015). Innovative Production of Bio-Cellulose Using a Cell-free System Derived from a Single Cell Line. *Carbohydr. Polym.* 132, 286–294. doi:10.1016/j.carbpol.2015.06.037

Ullah, M. W., Ul-Islam, M., Khan, S., Kim, Y., and Park, J. K. (2016). Structural and Physico-Mechanical Characterization of Bio-Cellulose Produced by a Cell-free System. *Carbohydr. Polym.* 136, 908–916. doi:10.1016/j.carbpol.2015.10.010

Wang, L., Mao, L., Qi, F., Li, X., Wajid Ullah, M., Zhao, M., et al. (2021). Synergistic Effect of Highly Aligned Bacterial Cellulose/gelatin Membranes and Electrical Stimulation on Directional Cell Migration for Accelerated Wound Healing. *Chem. Eng. J.* 424, 130563. doi:10.1016/j.cej.2021.130563

Yadav, C., Saini, A., Zhang, W., You, X., Chauhan, I., Mohanty, P., et al. (2021). Plant-based Nanocellulose: A Review of Routine and Recent Preparation Methods with Current Progress in its Applications as Rheology Modifier and 3D Bioprinting. *Int. J. Biol. Macromolecules* 166, 1586–1616. doi:10.1016/j.ijbiomac.2020.11.038

Yuan, B., Li, L., Li, L., Murugadoss, V., Vupputuri, S., Wang, J., et al. (2020). Nanocellulose-based Composite Materials for Wastewater Treatment and Waste-Oil Remediation. *ES Food Agrofor.* doi:10.30919/esfaf0004

Zhang, Y., Chen, Y., Cao, G., Ma, X., Zhou, J., and Xu, W. (2021). Bacterial Cellulose Production from Terylene Ammonia Hydrolysate by Taonella Mepensis WT-6. *Int. J. Biol. Macromolecules* 166, 251–258. doi:10.1016/j.ijbiomac.2020.10.172

Conflict of Interest: MWU and GY hold patents related to cellulose material.

The remaining authors declare that the research was conducted in the absence of any commercial or financial relationships that could be construed as a potential conflict of interest.

frontiers
in Bioengineering and Biotechnology

ORIGINAL RESEARCH
published: 03 July 2020
doi: 10.3389/fbioe.2020.00709

Conductive Hydroxyethyl Cellulose/Soy Protein Isolate/Polyaniline Conduits for Enhancing Peripheral Nerve Regeneration via Electrical Stimulation

Ping Wu[1,2†], Yanan Zhao[1,2,3†], Feixiang Chen[1,2], Ao Xiao[1,2], Qiaoyue Du[1,2], Qi Dong[1,2], Meifang Ke[1,2], Xiao Liang[1,2], Qing Zhou[4*] and Yun Chen[1,2,5*]

[1] Department of Biomedical Engineering, School of Basic Medical Sciences, Wuhan University, Wuhan, China, [2] Hubei Province Key Laboratory of Allergy and Immune Related Diseases, School of Basic Medical Sciences, Wuhan University, Wuhan, China, [3] Department of Interventional Radiology, The First Affiliated Hospital of Zhengzhou University, Zhengzhou, China, [4] Department of Ultrasound Imaging, Renmin Hospital of Wuhan University, Wuhan, China, [5] Hubei Engineering Center of Natural Polymers-Based Medical Materials, Wuhan University, Wuhan, China

Edited by:
Guang Yang,
Huazhong University of Science and Technology, China

Reviewed by:
Sing Yian Chew,
Nanyang Technological University, Singapore
Mazhar Ul-Islam,
Dhofar University, Oman

***Correspondence:**
Qing Zhou
qingzhou128@163.com
Yun Chen
yunchen@whu.edu.cn

† These authors have contributed equally to this work

Specialty section:
This article was submitted to Biomaterials, a section of the journal Frontiers in Bioengineering and Biotechnology

Received: 23 April 2020
Accepted: 08 June 2020
Published: 03 July 2020

Citation:
Wu P, Zhao Y, Chen F, Xiao A, Du Q, Dong Q, Ke M, Liang X, Zhou Q and Chen Y (2020) Conductive Hydroxyethyl Cellulose/Soy Protein Isolate/Polyaniline Conduits for Enhancing Peripheral Nerve Regeneration via Electrical Stimulation. Front. Bioeng. Biotechnol. 8:709. doi: 10.3389/fbioe.2020.00709

Nerve regeneration remains a challenge to the treatment of peripheral nerve injury. Electrical stimulation (ES) is an assistant treatment to enhance recovery from peripheral nerve injury. A conductive nerve guide conduit was prepared from hydroxyethyl cellulose (HEC)/soy protein isolate (SPI)/PANI sponge (HSPS) and then the HSPS conduits were used to repair 10 mm sciatic nerve injury in rat model with or without ES, using HSPS+brain-derived neurotrophic factor (BDNF) and autografts as controls. The nerve repairing capacities were evaluated by animal experiments of behavioristics, electrophysiology, toluidine blue staining, and transmission electron microscopy (TEM) in the regenerated nerves. The results revealed that the nerve regeneration efficiency of HSPS conduits with ES (HSPS+ES) group was the best among the conduit groups but slightly lower than that of autografts group. HSPS+ES group even exhibited notably increased in the BDNF expression of regenerated nerve tissues, which was also confirmed through *in vitro* experiments that exogenous BDNF could promote Schwann cells proliferation and MBP protein expression. As a result, this work provided a strategy to repair nerve defect using conductive HSPS as nerve guide conduit and using ES as an extrinsic physical cue to promote the expression of endogenous BDNF.

Keywords: hydroxyethyl cellulose, soy protein isolate, polyaniline, peripheral nerve injury, electrical stimulation

INTRODUCTION

In clinical practice, electrical stimulation (ES) has been used to treat many diseases (Gunter et al., 2019). In the treatment of epilepsy, ES can reduce the frequency of seizures by increasing the seizure threshold (Charthad et al., 2018). In patients with myasthenia gravis, appropriate electrical muscle stimulation can promote recovery of muscle function (Gordon et al., 2010). ES can also be used to stimulate the heart after cardiac arrest. In the traditional Chinese acupuncture treatment, ES is also introduced to enhance the effect of acupuncture, which makes the modern improvement of traditional Chinese medicine (Chen et al., 2018; Fei et al., 2019). It suggests that ES has a great application prospect in clinical medicine.

In peripheral nerve injury, the treatment of ES has been getting more and more attention. Huang et al. (2012) demonstrated that an electrical environment with ES localized at the conductive scaffold is capable of accelerating nerve regeneration and promoting functional recovery in rats. Michael and coworkers reported that electrical muscle stimulation immediately following nerve transection enhances electrophysiological and behavioral recovery (Willand et al., 2014). Qi et al. (2013) highlighted the possibility of increasing the neurotrophins secretion in olfactory ensheathing cells (OECs) by combining the conductive scaffolds and ES. In addition, the current of ES was applicated to promote the neurite outgrowth *in vitro* (Durgam et al., 2010), and accelerate the recovery of facial nerve crush injury *in vivo* (Jang et al., 2018). Compared with the current of ES, the voltage of ES not only could promote neurite outgrowth, it also mediate the neuron and multiple stem cells differentiation without the addition of growth factors (Zhu et al., 2019), neuronal cell adhesion and viability (Arteshi et al., 2018; Hu et al., 2019), and motor function restoring (Gunter et al., 2019).

In recent years, it has reported that ES can enhance the expression of brain-derived neurotrophic factor (BDNF) by activating the Ca^{2+} and Erk signaling pathways (Wenjin et al., 2011). Specifically, levels of specific nerve growth factors or neurotrophic factors are downregulated in animal models of sciatic nerve injury, and the application of exogenous nerve growth factors or neurotrophic factors have a positive effect on the repair of nerve defects (Tajdaran et al., 2018; Liu et al., 2020). It is a common method to directly introduce exogenous neurotrophic factors into tissue engineered-nerve guide conduits (Labroo et al., 2018). The common methods used to mobilize growth factor in scaffolds are adsorption, encapsulation, entrapment, and covalent binding, in which adsorption of growth factor on prefabricated scaffold is a convenient, straightforward method (Yu et al., 2018). However, these exogenous neurotrophic factors in the nerve conduits are easy to be lost or be inactive (Hobson et al., 2000). The effects of these two methods on nerve repair induced by the secretion of endogenous nutrient factors via ES and the directly binding of exogenous factors to nerve guide conduits have not been reported in detail (Carvalho et al., 2019).

Many literatures reported that exogenous addition of growth factor could not promote nerve regeneration well, and growth factors were often limited by their high cost and the short half-life (Pan et al., 2013). For this reason, it is of great significance to activate and promote the secretion of endogenous neurotrophic factors instead of using exogenous neurotrophic factors. With the development of life science, many genetic modification techniques have been applied to tissue engineering, but they often raise the risk of tumorigenesis (Lu et al., 2013; Fatemeh et al., 2017). However, ES, a relatively safe method, gradually attracts people's attention and is proved to promote the secretion of BDNF. BDNF is a polypeptide secreted by neurons, glial cells, and their innervating tissues (Xiao et al., 2009). BDNF maintains and promotes the development, differentiation, growth, and regeneration of various neurons (Lopes et al., 2017; Liu et al., 2020). It has been reported that the BDNF is synthesized in neurons and released from the surface of axon, the polarity of Schwann cells can be initiated by p75NTR which activated by BDNF, eventually led to the formation of myelin sheath by Schwann cells surrounding axon (Jonah et al., 2006). Therefore, BDNF plays an important role in the myelinization and the repair of nerve defects.

In order to achieve the goal of ES for nerve repair, the corresponding conductive conduits should be developed and used (Nezakati et al., 2018; Chen et al., 2019). In this work, we constructed a new functional composite conduit using conductive material and natural polymer materials. The basic nerve guide conduits are fabricated from hydroxyethyl cellulose (HEC) and soy protein isolate (SPI), the conductive material polyaniline (PANI) was *in situ* polymerization onto HEC/SPI conduits. And then the HEC/SPI/polyaniline sponge (HSPS) conduits were used to repair 10 mm sciatic nerve injury in rat model with or without ES. The effects of the ES and conductive conduit on the endogenous BNDF express and nerve repair, as well as the effects of exogenous BDNF on the growth of Schwann cells were investigated. This work attempted to provide a new cheap and environmentally friendly conduit combining *in vivo* ES method for the field of nerve regeneration and preliminary reveal the mechanism of ES and HSPS conduits to promote nerve regeneration.

MATERIALS AND METHODS

Materials

Hydroxyethyl cellulose (viscosity, 30,000 mPa) was supplied by Shandong Head Reagent Co., Ltd. (Shandong, China). SPI with weight-average molecular weight (Mw) of 2.05×10^5 was supplied by DuPont Protein Technology (Luohe, China). HEC and SPI were vacuum-dried for 24 h at 60°C before use. Aniline (purity 99.98%), epichlorohydrin (ECH, analytical grade, liquid, 1.18 g/mL), ammonium persulfate (APS), hydrochloric acid (HCl), and acetic acid were supplied by Sinopharm Chemical Reagent Co., Ltd. (Shanghai, China). Other chemicals were of analytical grade agents and used without further treatment.

Preparation of HEC/SPI/Polyaniline Conduits

The HEC/SPI (HEC: SPI = 30: 70, w: w) conduits were prepared as our laboratory previous work (Zhao et al., 2017). The aniline monomer was dissolved in 1 M HCl solution, and the operating concentration of aniline is 0.2 M. Then the HEC/SPI conduits were dipped in aniline/HCl mixture and stirred for 30 min. The same volume of APS solution (0.2 M) was dropped into the aniline/HCl solution to induce the aniline *in situ* polymerization reaction for 2 h, which is the best polymerization time for conductivity according to our previous work (Wu et al., 2019). Then the HEC/SPI/polyaniline sponge (HSPS) conduits were rinsed with running water overnight to remove the acid, salt, and unpolymerized aniline for the animal experiments. The morphology of the HSPS conduits was observed on a scanning electron microscope (SEM, VEGA3, TESCAN, Czechia) with 20 kV as the accelerating voltage.

In vitro Cell Experiments

Schwann Cells Isolation and Culture

The sciatic nerve of six neonatal rats (1–3 days) was harvested according to our previous protocol (Luo et al., 2015). Then the nerves were washed three times by PBS and cut into pieces, digested with 0.04% collagenase II and 0.25% trypsin in the shaker for 40 min, and then terminated and mechanically dispersed the digested nerve tissue. The crude suspension was centrifuged at room temperature for 15 min at 1500 r/min, abandoned the upper solution, added complete DMEM to disperse the collected cells. The cell suspension was seeded on T25 cell culture flasks and incubated at 37°C with 5% CO_2. In order to deplete rapidly proliferating fibroblasts, the non-adherent cells were put into new cell culture flasks to continue culturing after 30 min. Then the Schwann cells were treated with cytosine arabinoside for another 48 h to increase the purity of Schwann cells. The medium was exchanged every other day. Schwann cells were marked by S100 immunofluorescence staining. Schwann cells were fixed with 4% paraformaldehyde for 20 min and incubated with the anti-S100 antibodies (GB11359, Servicebio) overnight at 4°C, washed three times with PBS, and then incubated with secondary antibody [GB21303, Cy3 conjugated Goat Anti-rabbit IgG (H+L), 1:100] at 25°C for 60–120 min.

Evaluation of Proliferation of Schwann Cells by MTT Assay

Schwann cells suspension were seeded in 96-well cell culture plates with 1×10^3 cells/well and cultured at 37°C with 5% CO_2 for 24 h. And then the culture mediums were replaced with fresh complete mediums containing different concentrations of BDNF (0, 10, 50, 100, 250, and 500 ng/mL). After incubating for 1, 2, and 3 days, the Schwann cells were treated with 20 μL 3-(4, 5-dimethylthiazol-2-yl) 2, 5-diphenyltetrazolium bromide solution (MTT, 5 mg/mL) and incubated for another 4 h. Then the MTT was removed from the 96-well cell culture plates. 200 μL dimethyl sulfoxide (DMSO) was added into the plates to dissolve the formazan crystals at 37°C for 15 min. The absorbance values were exam at 490 nm wavelength on a multi-well microplate reader (Multiskanfc, Thermo Scientific).

Western Blot

The Schwann cells were co-cultured with BDNF for 3 days and then the cells were harvested for western blot analysis. And then the Schwann cells protein extracts were prepared by Total Protein Extraction Kit (BestBio, China). All the cell proteins were mixed with sodium dodecyl sulfate–polyacrylamide gel electrophoresis (SDS–PAGE) loading buffer (P0015, Beyotime) and heated at 100°C for 5 min. Protein samples (80 μg/well) were loaded on SDS–PAGE (10–12%) and electroplated onto polyvinylidene fluoride (PVDF) films (Millipore, United States). The PVDF films were blocked with 5% non-fat milk (BD, United States) for 60 min at room temperature and subsequently incubated overnight at 4°C with the primary antibodies: anti-PCNA antibody (GB11010, Servicebio), anti-MBP antibody (GB11226, Servicebio), and rabbit β-actin Rabbit antibody (GB11001, Servicebio). After incubating the PVDF films with horseradish peroxidase (HRP)-labeled secondary antibodies (GB23303, Servicebio) for 60 min at 25°C, the signal was collected by Image Studio Digits Ver 4.0. Density values were normalized to β-actin. The quantification of Western blot data was performed using Image-J software.

In vivo Animal Experiments

Surgical Procedures

All animal experiments were performed according to the "Guidelines and Regulations for the use and care of Animals of the Review Board of Hubei Medical Laboratory Animal Center," based on the Experimental Animal Management Ordinance (National Science and Technology Committee of the People's Republic of China, 1998). The animal study was reviewed and approved by the Animal Care and Welfare Committee of the Wuhan University. Sprague–Dawley (SD) rats (180–220 g, female) supplied by the Beijing Vital River Laboratory Animal Technology Co., Ltd., and acclimatized in the animal care facility for 1 week prior to surgery. The rats were anesthetized by intraperitoneal administration of 10% urethane sodium at a dose of 1 mL per 100 g body weight. After the anesthesia, the hair on the lateral thigh of the rats was shaven and the skin was treated with 75% alcohol solution. The incision extended from the lateral femoral oblique and the muscle tissue was split. Then the sciatic nerve was exposed in visual field. The nerve was cut with a sterile blade and the distance of defects about 8.0–10.0 mm. The animal experiments were divided into five groups (10 rats in each group), including Autograft, HSPS, HSPS+BDNF, HSPS-ES, and HSPS+ES. The detail information of the groups is listed in **Table 1**. HSPS conduits adsorbed 50 ng/mL BDNF polypeptide solution were labeled as HSPS+BDNF conduits. HSPS conduits with electrodes attached to conduit's two ends but without subsequent ES were labeled as HSPS-ES. HSPS conduits with electrodes at conduit's two ends and subsequent with ES was labeled as HSPS+ES. After the nerve were sutured with the HSPS conduits containing two electrodes, 1 h ES (3 V) was administered every 2 days, for a total of seven times. The four kinds of conduits with 12 mm length were used to bridge the nerve gap by 8-0 nylon sutures, respectively. The control group was the Autograft, in which the severed nerve stump was rotated

TABLE 1 | Animal groups and HSPS conduits codes.

Group	HSPS conduit (12 mm)	BDNF	Electrodes	ES (3V)
HSPS	+	–	–	–
HSPS+BDNF	+	50 ng/mL	–	–
HSPS-ES	+	–	+	–
HSPS+ES	+	–	+	+
Autograft	–	–	–	–

The "+" implies that the action element was included, and the "–" implies that the action element is not included.

180° to bridge the nerve defect. Muscle and skin were closed with interrupted absorbable sutures. Post-operative animals were conventional breeding.

Effects of ES on the Expression of Endogenous BDNF *in vivo*

To investigate the effect of ES on endogenous BDNF expression, BDNF immunofluorescence was detected. After the nerve was sutured with the HSPS conduits containing two electrodes (**Figures 1E,F**), ES was administered every 2 days for 60 min. After 2 weeks' ES, the proximal nerve tissues from HSPS-ES and HSPS+ES groups' rats (with and without ES) were fixed with 4% paraformaldehyde, paraffin-embedded to prepare immunofluorescence staining sections. The paraffin sections were deparaffinized and subjected to a heat-mediated antigen retrieval step using citrate buffer (pH 6.0). Then the samples were washed with PBS for three times, blocked with 5% BSA for 60 min, and incubated with the anti-BDNF primary antibody (A1307, Abclonal) at 4℃ overnight. After washing with PBS for three times, the nerve tissue sections were incubated with HRP-labeled secondary antibodies (GB21303, Servicebio) for 60 min, and the cell nuclei were counterstained with DAPI. Finally, the immunofluorescence samples were observed by fluorescence microscope to evaluate the effects of ES to the BDNF endogenous secretion.

Evaluation of Motor Function

Walking track analysis was carried out for the assessment of never functional recovery. Three parameters were derived from the paw prints: print length (PL), toe spread (TS; distance from toe 1 to toe 5), and intermediate TS (IT; distance from toe 2 to toe 4). "N" and "E" represent the non-operated and operated hind limbs, respectively. The SFI value near to "−100" implies totally loss of function, while neared to "0" implies normal nerve function. The SFI was calculated with Eq. (1):

$$\begin{aligned} \mathrm{SFI} = {} & -38.3 \times (\mathrm{EPL} - \mathrm{NPL})/\mathrm{NPL} + 109.5 \times (\mathrm{ETS} - \mathrm{NTS}) \\ & /\mathrm{NTS} + 13.3 \times (\mathrm{EIT} - \mathrm{NIT})/\mathrm{NIT} - 8.8. \end{aligned} \tag{1}$$

Electrophysiological Examination

Three months after surgery, the sciatic nerve on the operated side was re-exposed under anesthesia. The electromyography was evaluated by an electrophysiology system (RM6240, China). The 10 mV electrical stimuli were applied to the nerve trunk at the proximal ends and the compound muscle action potentials (CMAPs) for the gastrocnemius belly on the ipsilateral side were recorded. Normal CMAPs were measured on the contralateral unoperated side.

H&E Staining

Three months after the operation, the regenerated nerve tissue or heart, liver, spleen, lung, and kidney tissue were harvested. The tissues were washed with normal saline and fixed in 4% paraformaldehyde solution for 24 h at 4℃. After tissues were dehydrated, paraffin, embedded, sectioned, and other steps, sections with thickness of 5 μm were obtained, and then H&E staining was performed. Finally, nerve or other tissue microstructures were observed under an optical microscope (BX51, OLYMPUS, Japan).

Myelin Analysis

At 3 months after surgery, the regenerated nerves that formed in place of conduits or autografts were quickly harvested after electrophysiological examination and fixed in cold 2.5% glutaraldehyde solution. The regenerated nerves were washed in PBS and sections were taken from the middle regions of the regenerated sciatic nerve. The samples were post-fixed with 1% osmium tetraoxide solution, dehydrated, and embedded in Epon 812 epoxy resin. Transverse semithin 1 μm sections were stained with toluidine blue and observed under a light microscope (BX51, OLYMPUS, Japan). The total area and the total number of myelinated nerve fibers were measured using Image-Pro Plus software. Transverse ultrathin 50 nm sections were stained with lead citrate and uranyl acetate, followed by examination under a transmission electron microscopy (TEM, HT7700, Hitachi, Japan). Image-Pro Plus 6.0 software was used to measure axon diameter and myelin sheath thickness from the TEM images.

Statistical Analysis

All quantitative data were expressed as mean ± SEM. One-way ANOVA or *t*-test was used for statistics Analysis. The difference ($P < 0.05$) was considered to be statistically significant.

RESULTS

Construction of HSPS Conduits

In aniline/HCl solution, yellow HEC/SPI conduits turn black after *in situ* polymerization of aniline induced by APS (**Figures 1A,B**). **Figures 1C,D** show the longitudinal section and cross-section of the HSPS conduit (Inner diameter = 1.8 mm, outer diameter = 2.0 mm, length = 12 mm) using SEM. The images show that the conduit also has a porous three-dimensional structure. In our previous work, the preparation method and conductive parameters of HSPS have been reported. The conductivity of HSPS was 1.7 S m^{-1}, which was detected was by four-probe method. The mean resistance of the HSPS sponge was 20.6 kΩ detected in our previous work (Wu et al., 2019). Since both the sponge and the conduits are made from the same materials and used the same chemical reaction system, we can assume that the mean resistance of both the conduits and the sponge are 20.6 kΩ. In this research, the conductive HSPS was only prepared as conduit and applied with ES for peripheral nerve repair.

Figure 1E is the picture that the copper wires attached to both ends of the conduits, while **Figure 1F** is the schematic diagram of the *in vivo* ES. As shown in **Figure 1F**, the conductive HSPS and the electrodes form a circuit loop, and the external alternating current (3 V) is connected for ES.

Effects of BDNF on Schwann Cell Proliferation and Myelination *in vitro*

Many literatures have reported that the BDNF secretion can be promoted by ES and the polarity of Schwann cells can be initiated

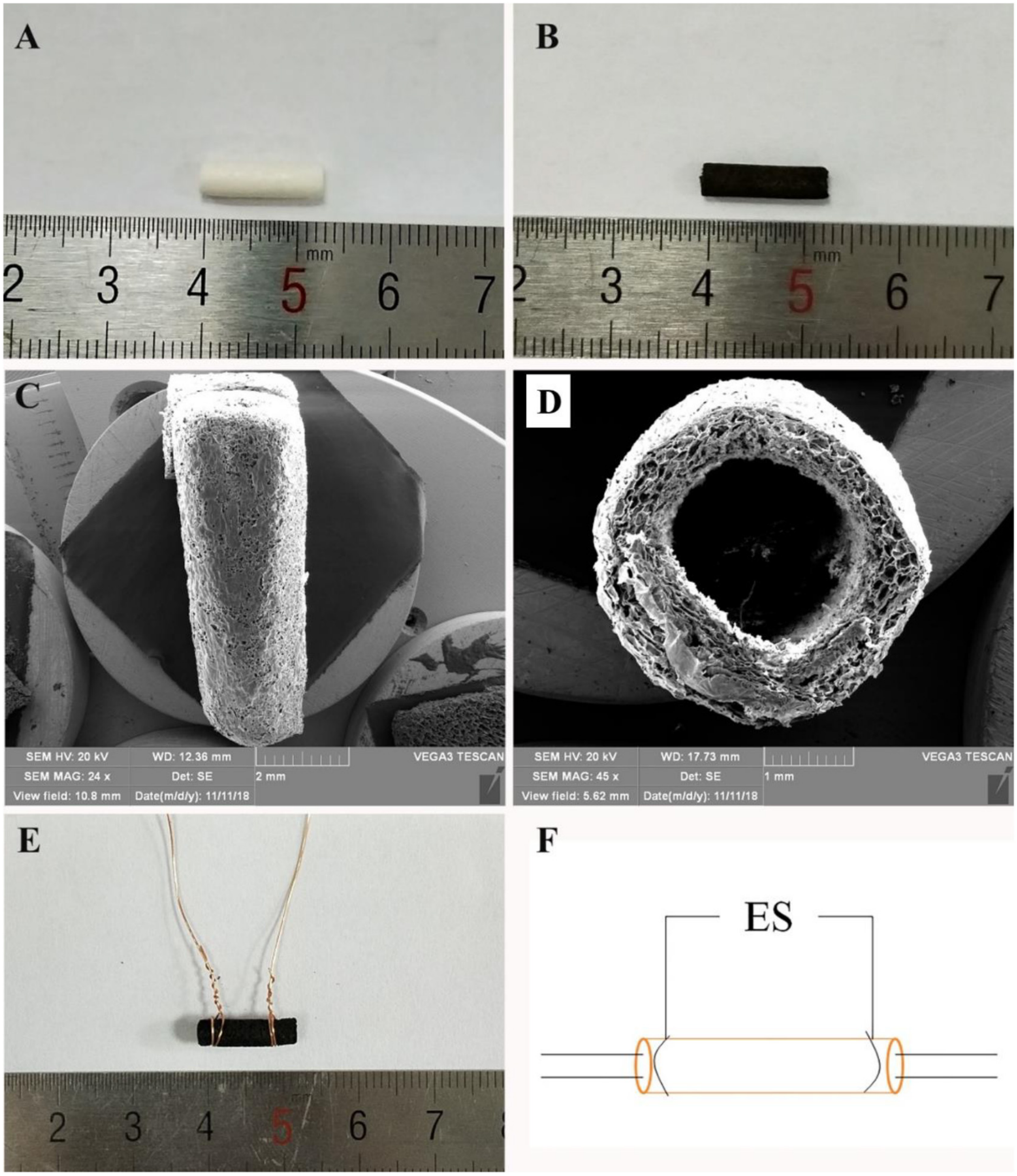

FIGURE 1 | (A) General observation images of HEC/SPI conduit. **(B)** General observation images of HSPS conduit. **(C)** Longitudinal view SEM images of the HSPS conduit. **(D)** Transverse cross-section view SEM images of the HSPS conduit. **(E)** General observation images of HSPS-ES conduit with electrodes. **(F)** Schematic diagram of HSPS+ES electrical stimulation in animals.

by p75NTR that activated by BDNF, which eventually led to the myelination by Schwann cells surrounding axon (Jonah et al., 2006). In order to study the BDNF mechanism on Schwann cell proliferation and myelination, the Schwann cells were extracted from 1–3 days neonatal rats. The purity of Schwann cells is always calculated by the ratio of S100 positive cell number to that of DAPI (Luo et al., 2015). As shown in **Figure 2A**, the purity of Schwann cells was over 95% in the present study. MTT experiments were used to verify the effect of BDNF on Schwann cell proliferation and results are shown in **Figure 2B**. On day 1, there were no significant differences among the groups. On day 2, 50 ng/mL BDNF group had a certain promotion effect on Schwann cells proliferation, while 500 ng/mL BDNF group had a certain inhibition effect. The MTT result of day 3 was consistent with that of day 2.

In order to verify the effects of BDNF on Schwann cell proliferation and myelination, western blot experiments were conducted. In eukaryotes, three DNA polymerases (alpha, delta, and epsilon) have been identified. DNA primase forms a permanent complex with DNA polymerase alpha. PCNA and

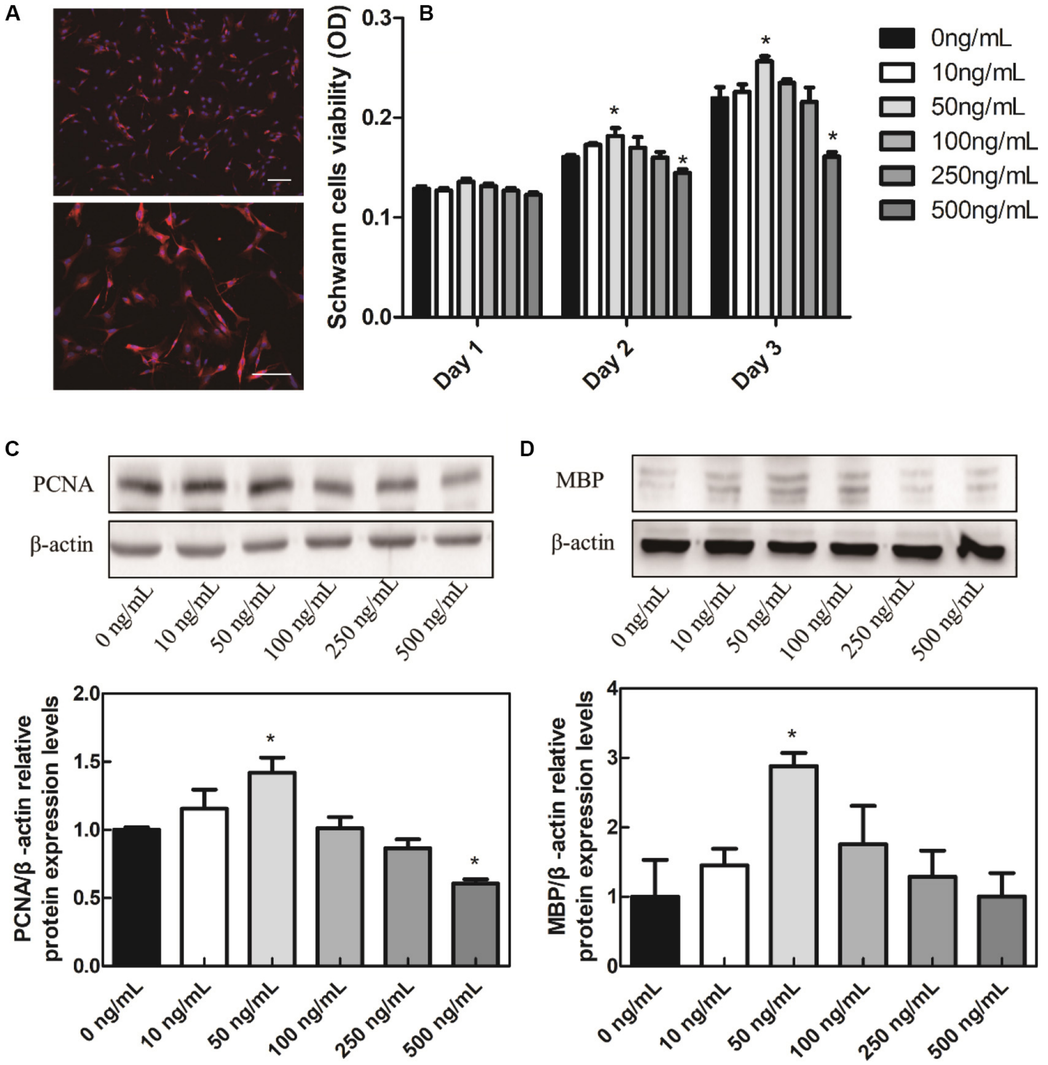

FIGURE 2 | *In vitro* cell experiments. **(A)** Schwann cells S100 IF identification, scale bar = 100 μm. **(B)** BDNF promotes the Schwann cells proliferation. **(C)** BDNF promotes the Schwann cells PCNA. **(D)** MBP protein relative expression levels. $^*P < 0.05$ compared with the 0 ng/mL group.

RFC work as a clamp and a clamp loader. Therefore, in the process of Schwann cells proliferation, PCNA is a biomarker protein for cell proliferation, commonly used to identify cell proliferation (Yang et al., 2019). In addition, myelin basic proteins (MBPs) are a group of seven proteins produced from a single gene mapped to chromosome 18q22–q23 by alternate splicing, and found in the central and peripheral nervous system myelin. MBPs in Schwann cells are common participants in all myelinization, even in the most primitive vertebrates (Tuinstra et al., 2012). Different concentrations of BDNF were added into Schwann cells cultures to verify the effect of BDNF on the proliferation and myelinization of Schwann cells. We applied different concentrations of BDNF to Schwann cells, then detecting the PCNA and MBP expression. In the culture medium containing 50 ng/mL BDNF protein, the PCNA and MBP proteins expression in Schwann cells were significantly upregulated (**Figures 2C,D**). Hence, it can promote the Schwann cells proliferation and myelinization by controlling the exogenous addition of BDNF. In addition, many literatures reported that the BDNF secretion can be enhanced by ES (Wenjin et al., 2011). Therefore, either direct addition of BDNF or ES can improve Schwann cell proliferation and myelinization.

On the contrary, the PCNA protein decreased under the 500 ng/mL BDNF protein levels, so the appropriate BDNF protein concentration would promote Schwann cells proliferation while the excessive BDNF would inhibit their proliferation, which was consistent with the MTT results. In addition, adsorption of growth factor on prefabricated scaffold is a convenient and straightforward strategy to mobilize growth factors in tissue engineering scaffolds (Singh et al., 2012). It could circumvent exposure to harsh conditions, which is especially suitable for the HSPS scaffold fabrication. Therefore, HSPS conduits adsorbed 50 ng/mL BDNF polypeptide were used as the exogenous BDNF nerve conduits group (HSPS+BDNF group) in our follow-up study.

In vivo Evaluation

Effects of ES on BDNF Expression *in vivo*

After 2 weeks of ES, the immunofluorescence images of BDNF secreted from the proximal injured nerve ends in HSPS-ES and HSPS+ES groups are shown in **Figure 3**. Rats in HSPS-ES group were not given ES, but the rats in HSPS+ES group received 3 V ES. Since the success of nerve regeneration is closely related to the secretion of early growth factors, we performed BDNF immunofluorescence analysis on the injured proximal nerve after 2 weeks of ES. The BDNF expression in HSPS+ES group is significantly higher than that of HSPS-ES group. This result is consistent with Huang's result, the BDNF and NGF expression level would elevate under ES *in vivo* (Huang et al., 2010).

Sciatic Nerve Function Index (SFI) Evaluation

The sciatic nerve function index (SFI) is used to evaluate the target muscle motor function of the sciatic nerve. At 3 months after surgery, the mean SFI values of Autograft, HSPS, HSPS+BDNF, HSPS-ES, and HSPS+ES groups were −53.5, −61.1, −62.5, −61.5, and −55.9, respectively. The mean SFI values of HSPS, HSPS+BDNF, and HSPS-ES groups were all lower than that of the Autograft and HSPS+ES group, while the mean SFI values of HSPS+ES and Autograft groups were similar (**Figure 4**). It can be seen that HSPS, HSPS+BDNF, and HSPS-ES conduits can support the recovery of sciatic nerve function of 10 mm nerve defects. Since two extra electrodes were needed for the ES, the HSPS-ES group was set, but the experimental results showed that the addition of the electrodes did not inhibit the function of the sciatic nerve. After the ES, the mean SFI value of the HSPS+ES group was higher than that of the other three conduit groups, so it illustrated that the effect of ES on the recovery of SFI was higher than that of the other conduits.

Electrophysiological Evaluation

Three months after the operation, the peak amplitude of CMAPs was further recorded by the biological signal acquisition and analysis system. **Figure 2C** is representative CMAPs records of the surgical sides of each group. The CMAPs signals could be detected in each group, but the waveforms of signals were quite different among the five groups. The mean peak amplitudes of CMAPs in Autograft, HSPS, HSPS+BDNF, HSPS-ES, and HSPS+ES groups were 18.5, 9.6, 9.62, 10.5, and 15.6 mV, respectively (**Figure 5**). The mean peak amplitudes of CMAPs in HSPS+ES groups were significantly higher than those in HSPS, HSPS+BDNF, and HSPS-ES group, while the mean peak amplitudes of CMAPs in HSPS+ES groups were lower than that in Autograft group. The mean peak amplitudes of CMAPs in HSPS+ES group was significantly higher comparing with other conduits group, demonstrating that ES can promote the recovery of electrophysiological functions comparing with other conduit groups.

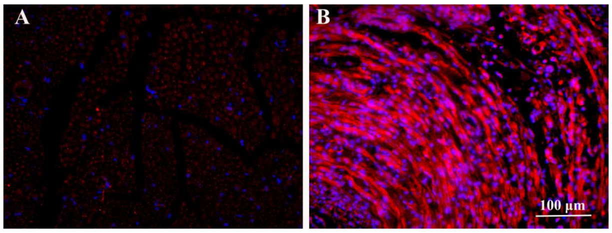

FIGURE 3 | Immunofluorescence image of BDNF proteins in the nerve of HSPS-ES group **(A)** and HSPS+ES group **(B)**.

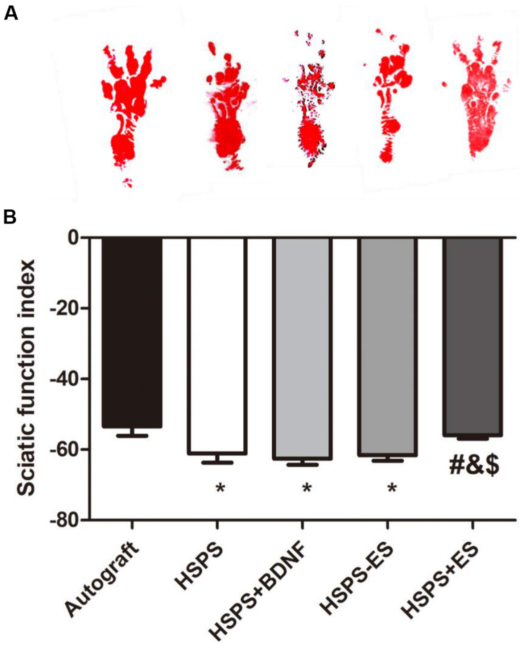

FIGURE 4 | The sciatic functional index (SFI) in each group. **(A)** Images of footprints the SD rats and **(B)** statistical results of SFI values in each group at 3 months after surgery. $^{*}P < 0.05$ compared with the Autograft group, $^{\#}P < 0.05$ compared with the HSPS group, $^{\&}P < 0.05$ compared with the HSPS+BDNF group, $^{\$}P < 0.05$ compared with the HSPS-ES group.

H&E Staining Analysis

Three months after the operation, H&E staining was performed on the longitudinal sections of regenerated complete nerves in the Autograft group, HSPS group, HSPS+BDNF group, HSPS-ES group, and HSPS+ES group, and the results are shown in **Figure 6**. After the 10 mm defect was truncated in the Autograft group, the 10 mm nerve truncated would shrink to 6–8 mm. The HSPS, HSPS+BDNF, HSPS-ES, and HSPS+ES group were all able to grow 10 mm nerve after 12 mm conduits were used to bridge. The mean diameters of regenerated nerve in Autograft, HSPS, HSPS+BDNF, HSPS-ES, and HSPS+ES groups were 1.485, 0.84, 0.807, 0.817, and 1.49 μm, respectively. The diameters of regenerated nerve in HSPS, HSPS+BDNF, and HSPS-ES groups were thinner than that in Autograft group and HSPS+ES group. The results of H&E staining showed that HSPS conduits combined with ES could increase the diameter of the regenerated nerve.

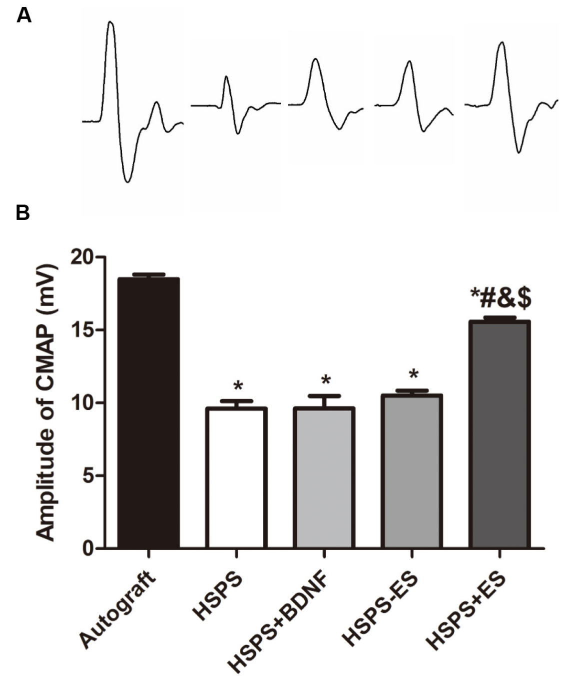

FIGURE 5 | The results of electrophysiological test. **(A)** Representative CMAPs recordings on the injured side for each group. **(B)** The statistical results of peak amplitude of CMAPs. $^{*}P < 0.05$ compared with the Autograft group, $^{\#}P < 0.05$ compared with the HSPS group, $^{\&}P < 0.05$ compared with the HSPS+BDNF group, $^{\$}P < 0.05$ compared with the HSPS-ES group.

Moreover, in the enlarged illustration of HSPS, HSPS+BDNF, HSPS-ES, and HSPS+ES, it can be found that there are many black particles distributed in the regenerated nerve tissues. We speculate that these black particles are polyaniline particles from the degraded HSPS conduits.

Regenerated Myelin Analysis

Toluidine blue staining of regenerated nerve tissues were investigated to evaluate myelin fiber density of different conduits. The results of toluidine blue staining on the cross-section of the middle segment of the regenerated nerve are illustrated in **Figure 7**. The Autograft, HSPS, HSPS+BDNF, HSPS-ES, and HSPS+ES groups all showed different sizes and densities of nerve fibers. The mean density of myelinated nerve fibers in Autograft, HSPS, HSPS+BDNF, HSPS-ES, and HSPS+ES groups were 1.64×10^4, 0.94×10^4, 0.93×10^4, 0.91×10^4, and 1.36×10^4 number/mm^2, respectively. The mean myelin fiber density of HSPS, HSPS+BDNF, and HSPS-ES groups was all lower than that of Autograft and HSPS+ES groups, while the mean myelin fiber density of HSPS+ES group was slightly lower than that of Autograft group.

Transmission electron microscopy observation of the middle segments of regenerated nerve tissues from each group is demonstrated in **Figure 8**. Different axon diameters and thicknesses of myelin sheaths are shown in Autograft, HSPS, HSPS+BDNF, HSPS-ES, and HSPS+ES groups. The axon diameters of HSPS, HSPS+BDNF, and HSPS-ES were smaller than that of Autograft and HSPS+ES, while the axon diameters of HSPS+ES group were lower than that of Autograft group. Second, the trend of myelin thickness is consistent with the trend of myelin diameter. Finally, the G-ratio is the ratio of the inner diameter of axon to the diameter of axon. The higher the G-ratio, the worse the effect of myelin repair effect. The G-ratio values of the three groups of HSPS, HSPS+BDNF, and HSPS-ES were greater than that of the Autograft and HSPS+ES groups, while G-ratio value of the Autograft group was lower than that of HSPS+ES group. After ES, the density of myelin fibers, axon diameters, and thicknesses of myelin sheaths in HSPS+ES group was higher than that in the other three conduit groups, so it can be said that ES can promote the remyelination. In addition, the density of myelin fibers, axon diameters, and thicknesses of myelin sheaths in the HSPS+ES group was slightly lower than that in the Autograft group, indicating that the remyelination could be increased to a large extent by electric stimulation, but the effect was not as high as that of Autograft group.

The Toxicity Assessment of the HSPS Conduits

In order to evaluate the toxic effect of polyaniline in HSPS conduits *in vivo*, H&E staining the heart, liver, spleen, lung, and kidney of rats in Autograft and HSPS conduit group 3 months after nerve repair surgery were harvested, sliced, and stained. **Figure 9** shows that there was no obvious immune response in heart, liver, spleen, lung, and kidney tissues of rats in the Autograft group and the HSPS sponge nerve group, and the degraded polyaniline particles did not invade the organs, indicating that HSPS had no toxic effect *in vivo*.

DISCUSSION

In this study, an efficient strategy for peripheral nerve repair is developed by the combination of ES and conductive HSPS conduits. ES combining with conductive HSPS conduits can effectively promote the recovery of injured nerve motor function, electrophysiology, and morphology. All the indexes of nerve regeneration in HSPS+ES group were better than that of other conduits groups. In addition, the secretion of BDNF can be significantly promoted by ES *in vivo*. Many literatures have also proved that *in vitro* ES can promote the secretion of BDNF (Huang et al., 2012). In our *in vitro* cell experiments, it was also found that the appropriate concentration of BDNF can promote the proliferation and myelination of Schwann cells.

As stated by Du et al. (2018), the polycaprolactone nanofiber nerve conduits were used to repair the sciatic nerve defect in rats, but the ES did not play a positive role in the functional recovery of rats, which may be related to the non-conductive polycaprolactone conduits. When polypyrrole/chitosan conduits were applied to repair sciatic nerve defect in rats, ES group could promote the improvement of SFI value, peak amplitude of CMAPs, myelin fiber density, axon diameters, and thicknesses of myelin sheaths (Huang et al., 2012). In conclusion, ES on the basis of conductive conduit can promote the recovery of sciatic nerve function, while non-conductive conduits cannot

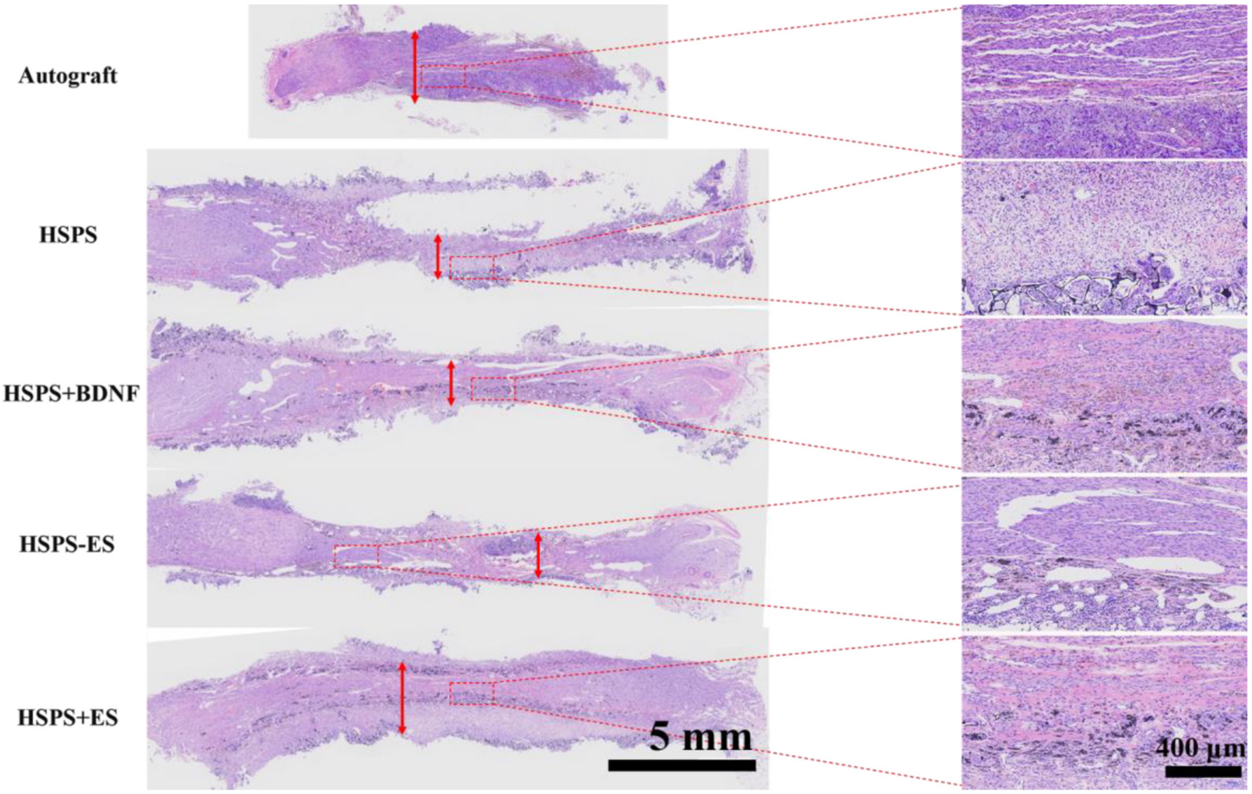

FIGURE 6 | Images of HE-stained longitudinal sections of the regenerated nerve in each group at 3 months after surgery, the red arrows represented the diameter of the regenerated nerves.

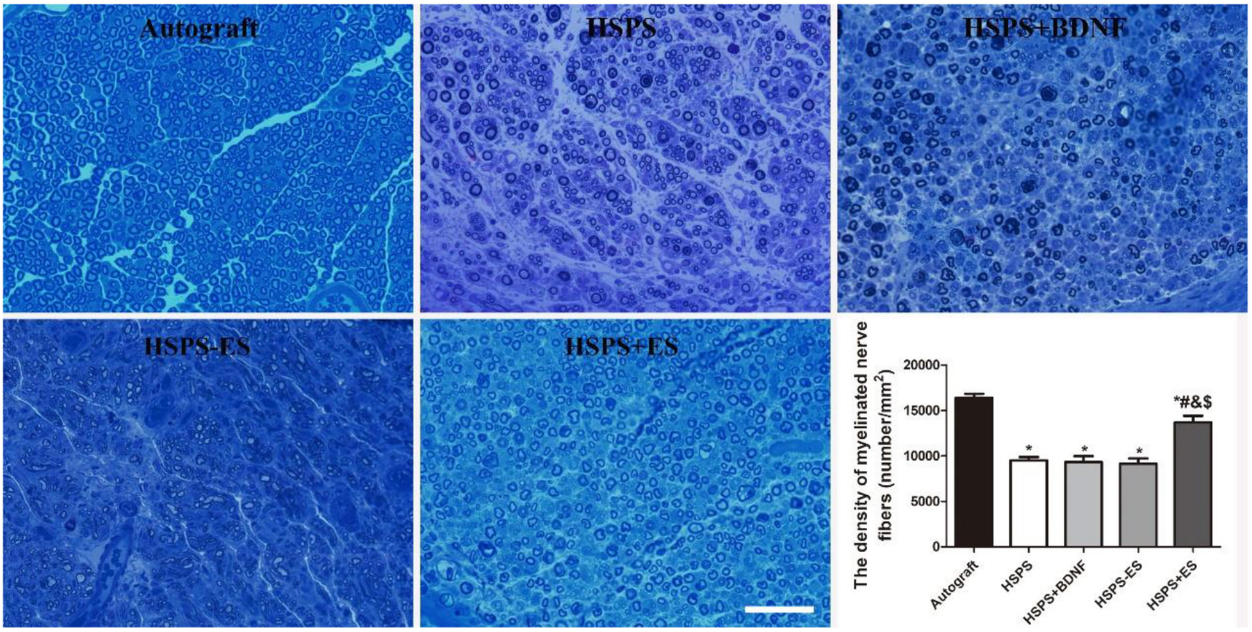

FIGURE 7 | Images of toluidine blue stained regenerated nerve cross sections and the statistical density of myelinated nerve fibers in regenerated nerves for each group, scale bar = 20 µm. $^{*}P < 0.05$ compared with the Autograft group, $^{\#}P < 0.05$ compared with the HSPS group, $^{\&}P < 0.05$ compared with the HSPS+BDNF group, $^{\$}P < 0.05$ compared with the HSPS-ES group.

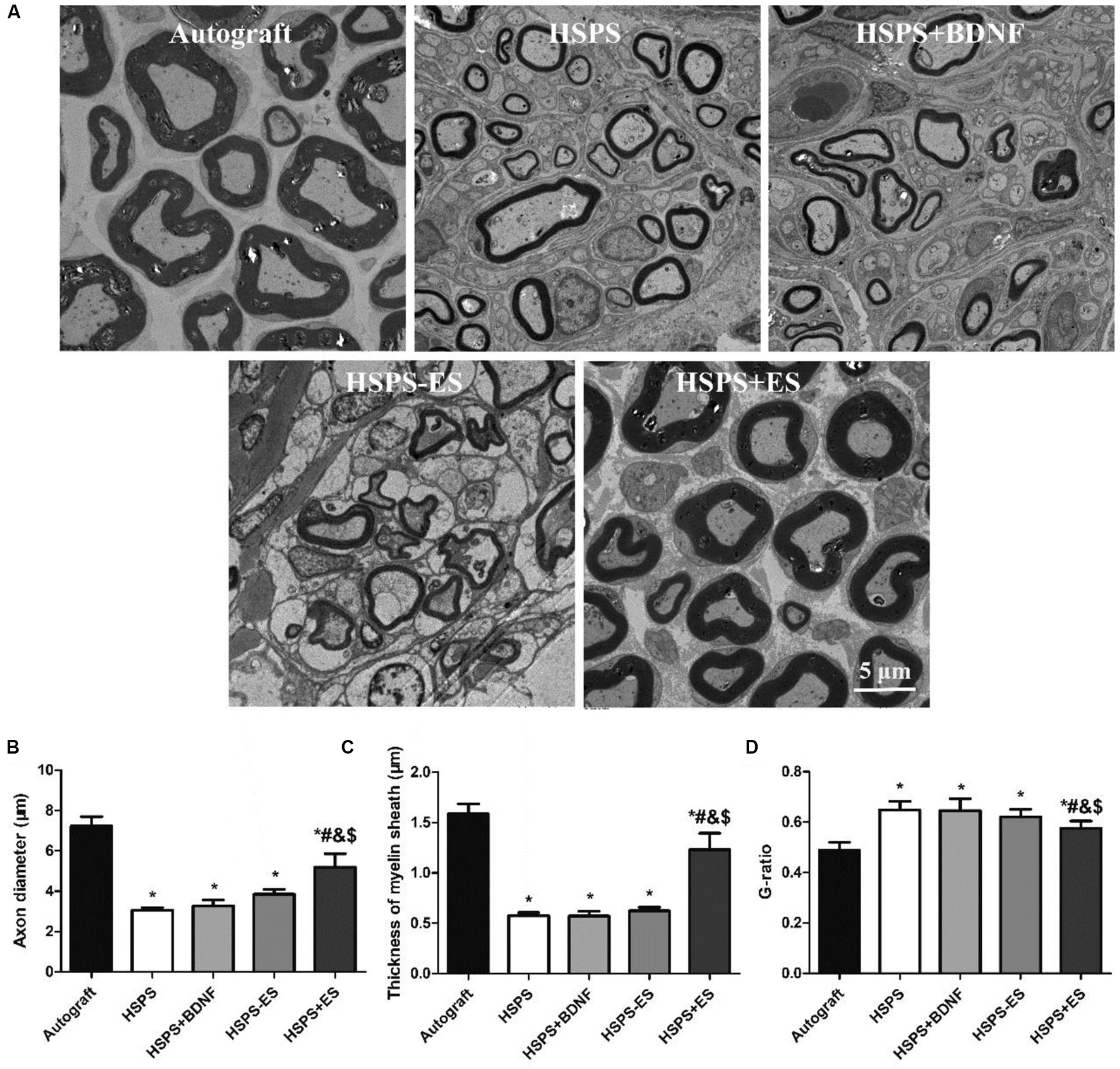

FIGURE 8 | Images of toluidine blue stained regenerated nerve cross sections and the statistical density of myelinated nerve fibers in regenerated nerves for each group. **(A)** TEM images of the middle portion of regenerated nerve and statistical analysis of **(B)** axon diameter, **(C)** thickness of myelin sheath, and **(D)** G-ratio. $^{*}P < 0.05$ compared with the Autograft group, $^{\#}P < 0.05$ compared with the HSPS group, $^{\&}P < 0.05$ compared with the HSPS+BDNF group, $^{\$}P < 0.05$ compared with the HSPS-ES group.

support the corresponding recovery. There are several factors in this ES process. The first one is the electrode, the second one is the ES, and the third one is the conductivity of the conduits (Vijayavenkataraman et al., 2019). Our experiments showed that the electrode had no effect to nerve regeneration in ES. However, the literature has proven that conductive materials are necessary (Du et al., 2018). If non-conductive materials are used, the impact of ES is limited, because it can only directly act on the cells and cannot provide a large area of ES. According to the literature and our this work, it has been demonstrated that the improvement in SFI values, peak amplitude of CMAPs, myelin fiber density, axon diameters, and thicknesses of myelin sheaths are mainly due to the action of ES, which is carried out through the conductive conduits (Huang et al., 2012).

The SFI, electrophysiological, HE staining, myelin analysis results all illustrate that the exogenous BDNF could not significantly promote the nerve function recovery compared with the HSPS group. There are several possible reasons for exogenous BDNF failure of promoting nerve regeneration: The BDNF absorbed by HSPS conduits suffers from a short half-life due to its sensitivity to enzymes and chemical molecules *in vivo*; the sudden release of BDNF has inhibitory effects

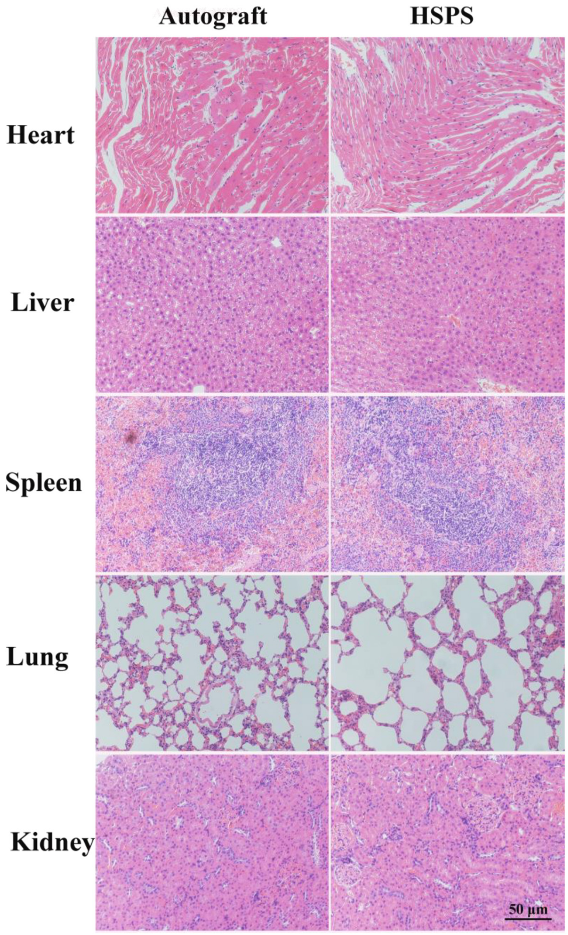

FIGURE 9 | The toxicity assessment of the HSPS conduits *in vivo*.

on nerve regeneration. Unlike exogenous BDNF groups, the continuous secretion of BDNF in HSPS+ES group was thought to protect motor and sensory neurons and stimulate the Schwann cells proliferation and myelination. Durgam et al. reported that PPy–PCL film significantly increased the number of PC12 cells bearing neurites compared to unstimulated PPy–PCL with ES. And the conductive PPy–PCL NGCs which were implanted in a 10 mm defect made in the sciatic nerve could support neurons proliferation and growth *in vivo* without ES (Durgam et al., 2010). Compared with Durgam's work, we have set up a conductive nerve conduit plus ES group *in vivo* animal experiments, so we have demonstrated the effectiveness of ES *in vivo*. Jang et al. (2018) used ES to promote the recovery of facial nerve, but only the control group and the ES group were set up in the animal experiments. Comparing with Jang's work, we not only set up the electrode group, but also set up the exogenous BDNF group, which fully demonstrated that endogenous BDNF had a better effect on promoting nerve repair than that of exogenous BDNF.

Finally, a small quantity of polyaniline particles was found in the regenerated nerve, it is different from our previous results of HSPS sponge subcutaneous implantation *in vivo* (Wu et al., 2019). When the HSPS sponges were implanted subcutaneous after 3 weeks, polyaniline particles had been cleared by the body tissues (Wu et al., 2019). Since the HSPS conduit is a lumen structure but the sponge embedded under the skin is a lumpy structure, macrophages cannot easily enter the conduits and can't clear the polyaniline very quickly. So the polyaniline particles cannot be cleared within 12 weeks. It has also been reported that the size of polyaniline particles formed by the degradation of PLLA/polyaniline/TSA fiber scaffolds *in vivo* ranged from 2.5 to 3.1 nm, while macrophages were able to devour foreign particles of 10 nm size (Yao et al., 2019). Moreover, the polyaniline nanoparticles could be swallowed by macrophages, and foreign particles were mainly dispersed in vesicles and mitochondria of macrophages (Wang et al., 2019). In contrast to our results, the polyaniline nanoparticles produced after HSPS degradation did not cause inflammation in the heart, liver, spleen, lung, and kidney organs, and our results showed that polyaniline particles did not move to the organs. Therefore, HSPS conduits are safe when they are used *in vivo*.

CONCLUSION

In this work, a kind of conductive HSPS sponge conduit was developed as conductive neural tissue engineering scaffold, and it was used to repair nerve defects with or without ES subsequently. The HSPS conduit under ES could facilitate animal nerve function and structure recovery, and upregulate the BDNF expression. Furthermore, the BDNF protein can promote Schwann cells proliferation and MBP expression. Therefore, the combination of HSPS conduit and ES in this work may have potential application in nerve tissue engineering field.

DATA AVAILABILITY STATEMENT

The raw data supporting the conclusions of this article will be made available by the authors, without undue reservation.

ETHICS STATEMENT

The animal study was reviewed and approved by the Review Board of Hubei Medical Laboratory Animal Center.

AUTHOR CONTRIBUTIONS

PW and YZ conceived the initial idea and designed the experiments. PW, FC, AX, QDu, QDo, MK, and XL performed the experiments. PW, YZ, and FC analyzed the data and wrote the manuscript. QZ and YC guided the work and revised the manuscript. YC worked on funding acquisition. All authors have read and approved the final manuscript.

FUNDING

Thanks for the support from the National Natural Science Foundation of China (Grant No. NSFC 81871493) and the Medical Science Advancement Program (Clinical Medicine) of Wuhan University (Grant No. TFLC2018002 and 2018003).

ACKNOWLEDGMENTS

This research topic is dedicated to Prof. Lina Zhang on the occasion of her 80th birthday, in gratitude, esteem, and affection. Thanks for the technical support from the Experimental Teaching Center of Basic Medical Sciences, Wuhan University.

REFERENCES

Arteshi, Y., Aghanejad, A., Davaran, S., and Omidi, Y. (2018). Biocompatible and electroconductive polyaniline-based biomaterials for electrical stimulation. *Eur. Polymer J.* 108, 150–170. doi: 10.1016/j.eurpolymj.2018.08.036

Carvalho, C. R., Oliveira, J. M., and Reis, R. L. (2019). Modern trends for peripheral nerve repair and regeneration: beyond the hollow nerve guidance conduit. *Front. Bioeng. Biotechnol.* 7:337. doi: 10.3389/fbioe.2019.00337

Charthad, J., Chang, T. C., Liu, Z., Sawaby, A., Weber, M. J., Baker, S., et al. (2018). A mm-sized wireless implantable device for electrical stimulation of peripheral nerves. *IEEE Trans. Biomed. Circ. Syst.* 12, 257–270. doi: 10.1109/TBCAS.2018.2799623

Chen, S., Zhao, Y., Yan, X., Zhang, L., Li, G., and Yang, Y. (2019). PAM/GO/gel/SA composite hydrogel conduit with bioactivity for repairing peripheral nerve injury. *J. Biomed. Mater. Res. A* 107, 1273–1283. doi: 10.1002/jbm.a.36637

Chen, Y., Ke, C., Chen, C., and Lin, J. (2018). "Effects of acupuncture on peripheral nerve regeneration," in *Experimental Acupuncturology*, ed. J. G. Lin (Singapore: Springer), 81–94. doi: 10.1007/978-981-13-0971-7_6

Du, J., Zhen, G., Chen, H., Zhang, S., Qing, L., Yang, X., et al. (2018). Optimal electrical stimulation boosts stem cell therapy in nerve regeneration. *Biomaterials* 181, 347–359. doi: 10.1016/j.biomaterials.2018.07.015

Durgam, H., Sapp, S., Deister, C., Khaing, Z., Chang, E., Luebben, S., et al. (2010). Novel degradable co-polymers of polypyrrole support cell proliferation and enhance neurite out-growth with electrical stimulation. *J. Biomater. Sci. Polym. Ed.* 21, 1265–1282. doi: 10.1163/092050609X12481751806330

Fatemeh, M., Ali, R., Mehdi, F., Rassoul, D., Hossein, H., Keng-Liang, O., et al. (2017). Prospects of siRNA applications in regenerative medicine. *Int. J. Pharm.* 524, 312–329. doi: 10.1016/j.ijpharm.2017.03.092

Fei, J., Gao, L., Li, H. H., Yuan, Q. L., and Li, L. J. (2019). Electroacupuncture promotes peripheral nerve regeneration after facial nerve crush injury and upregulates the expression of glial cell-derived neurotrophic factor. *Neural Regen. Res.* 14, 673–682. doi: 10.4103/1673-5374.247471

Gordon, T., Amirjani, N., Edwards, D. C., and Chan, K. M. (2010). Brief post-surgical electrical stimulation accelerates axon regeneration and muscle reinnervation without affecting the functional measures in carpal tunnel syndrome patients. *Exp. Neurol.* 223, 192–202. doi: 10.1016/j.expneurol.2009.09.020

Gunter, C., Delbeke, J., and Ortiz-Catalan, M. (2019). Safety of long-term electrical peripheral nerve stimulation: review of the state of the art. *J. Neuroeng. Rehabil.* 16, 1–16. doi: 10.1186/s12984-018-0474-8

Hobson, M. I., Colin, J. G., and Terenghi, G. (2000). VEGF enhances intraneural angiogenesis and improves nerve regeneration after axotomy. *J. Anat.* 197, 591–605. doi: 10.1046/j.1469-7580.2000.19740591.x

Hu, M., Hong, L., Liu, C., Hong, S., He, S., Zhou, M., et al. (2019). Electrical stimulation enhances neuronal cell activity mediated by Schwann cell derived exosomes. *Sci. Rep.* 9:4206. doi: 10.1038/s41598-019-41007-5

Huang, J., Hu, X., Lu, L., Ye, Z., Zhang, Q., and Luo, Z. (2010). Electrical regulation of Schwann cells using conductive polypyrrole/chitosan polymers. *J. Biomed. Mater. Res. A* 93, 164–174. doi: 10.1002/jbm.a.32511

Huang, J., Lu, L., Zhang, J., Hu, X., Zhang, Y., Liang, W., et al. (2012). Electrical stimulation to conductive scaffold promotes axonal regeneration and remyelination in a rat model of large nerve defect. *PLoS One* 7:e39526. doi: 10.1371/journal.pone.0039526

Jang, C. H., Lee, J. U., and Kim, G. H. (2018). Effect of direct current electrical stimulation on the recovery of facial nerve crush injury. *J. Ind. Eng. Chem.* 64, 143–150. doi: 10.1016/j.jiec.2018.03.011

Jonah, R. C., Junji, Y., Jimmy, E., James, P., Fawcett, B. K., and Ng, M. C. (2006). The polarity protein Par-3 directly interacts with p75NTR to regulate myelination. *Science* 314, 832–836. doi: 10.1126/science.1134069

Labroo, P., Hilgart, D., Davis, B., Lambert, C., Sant, H., Gale, B., et al. (2018). Drug-delivering nerve conduit improves regeneration in a critical sized gap. *Biotechnol. Bioeng.* 116, 143–154. doi: 10.1002/bit.26837

Liu, H., Xu, X., Tu, Y., Chen, K., Song, L., Zhai, J., et al. (2020). Engineering microenvironment for endogenous neural regeneration after spinal cord injury by reassembling extracellular matrix. *ACS Appl. Mater. Interfaces* 12, 17207–17219. doi: 10.1021/acsami.9b19638

Lopes, C. D. F., Goncalves, N. P., Gomes, C. P., Saraiva, M. J., and Pego, A. P. (2017). BDNF gene delivery mediated by neuron-targeted nanoparticles is neuroprotective in peripheral nerve injury. *Biomaterials* 121, 83–96. doi: 10.1016/j.biomaterials.2016.12.025

Lu, C. H., Chang, Y. H., Lin, S. Y., Li, K. C., and Hu, Y. C. (2013). Recent progresses in gene delivery-based bone tissue engineering. *Biotechnol. Adv.* 31, 1695–1706. doi: 10.1016/j.biotechadv.2013.08.015

Luo, L., Gan, L., Liu, Y., Tian, W., Tong, Z., Wang, X., et al. (2015). Construction of nerve guide conduits from cellulose/soy protein composite membranes combined with Schwann cells and pyrroloquinoline quinone for the repair of peripheral nerve defect. *Biochem. Biophys. Res. Commun.* 457, 507–513. doi: 10.1016/j.bbrc.2014.12.121

Nezakati, T., Seifalian, A., Tan, A., and Seifalian, A. M. (2018). Conductive polymers: opportunities and challenges in biomedical applications. *Chem. Rev.* 118, 6766–6843. doi: 10.1021/acs.chemrev.6b00275

Pan, Z., Fukuoka, S., Karagianni, N., Guaiquil, V. H., and Rosenblatt, M. I. (2013). Vascular endothelial growth factor promotes anatomical and functional recovery of injured peripheral nerves in the avascular cornea. *FASEB J.* 27, 2756–2767. doi: 10.1096/fj.12-225185

Qi, F., Wang, Y., Ma, T., Zhu, S., Zeng, W., Hu, X., et al. (2013). Electrical regulation of olfactory ensheathing cells using conductive polypyrrole/chitosan polymers. *Biomaterials* 34, 1799–1809. doi: 10.1016/j.biomaterials.2012.11.042

Singh, S., Wu, B. M., and Dunn, J. C. (2012). Delivery of VEGF using collagen-coated polycaprolactone scaffolds stimulates angiogenesis. *J. Biomed. Mater. Res. A* 100, 720–727. doi: 10.1002/jbm.a.34010

Tajdaran, K., Chan, K., Gordon, T., and Borschel, G. H. (2018). Matrices, scaffolds, and carriers for protein and molecule delivery in peripheral nerve regeneration. *Exp. Neurol.* 319:112817. doi: 10.1016/j.expneurol.2018.08.014

Tuinstra, H. M., Aviles, M. O., Shin, S., Holland, S. J., Zelivyanskaya, M. L., Fast, A. G., et al. (2012). Multifunctional, multichannel bridges that deliver neurotrophin encoding lentivirus for regeneration following spinal cord injury. *Biomaterials* 33, 1618–1626. doi: 10.1016/j.biomaterials.2011.11.002

Vijayavenkataraman, S., Kannan, S., Cao, T., Fuh, J. Y. H., Sriram, G., and Lu, W. F. (2019). 3D-Printed PCL/PPy conductive scaffolds as three-dimensional porous nerve guide conduits (ngcs) for peripheral nerve injury repair. *Front. Bioeng. Biotechnol.* 7:266. doi: 10.3389/fbioe.2019.00266

Wang, G., Wu, W., Yang, H., Zhang, P., and Wang, J. Y. (2019). Intact polyaniline coating as a conductive guidance is beneficial to repairing sciatic nerve injury. *J. Biomed. Mater. Res. B Appl. Biomater.* 108, 128–142. doi: 10.1002/jbm.b.34372

Wenjin, W. W. L., Hao, Z., Feng, L., Yan, W., Wodong, S., Xianqun, F., et al. (2011). Electrical stimulation promotes BDNF expression in spinal cord neurons through Ca(2+)- and Erk-dependent signaling pathways. *Cell. Mol. Neurobiol.* 31, 459–467. doi: 10.1007/s10571-010-9639-0

Willand, M. P., Chiang, C. D., Zhang, J. J., Kemp, S. W. P., Borschel, G. H., and Gordon, T. (2014). Daily electrical muscle stimulation enhances functional recovery following nerve transection and repair in rats. *Neurorehabil. Neural Repair* 29, 690–700. doi: 10.1177/1545968314562117

Wu, P., Xiao, A., Zhao, Y., Chen, F., Ke, M., Zhang, Q., et al. (2019). An implantable and versatile piezoresistive sensor for the monitoring of human–machine interface interactions and the dynamical process of nerve repair. *Nanoscale* 11, 21103–21108. doi: 10.1039/c9nr03925b

Xiao, J., Wong, A. W., Willingham, M. M., Kaasinen, S. K., Hendry, I. A., Howitt, J., et al. (2009). BDNF exerts contrasting effects on peripheral myelination of NGF-dependent and BDNF-dependent DRG neurons. *J. Neurosci.* 29, 4016–4022. doi: 10.1523/JNEUROSCI.3811-08.2009

Yang, G., Chen, Q., Wen, D., Chen, Z., Wang, J., Chen, G., et al. (2019). A therapeutic microneedle patch made from hair-derived keratin for promoting hair regrowth. *ACS Nano* 13, 4354–4360. doi: 10.1021/acsnano.8b09573

Yao, J., Chen, Y., Li, W., Chen, X., and Fan, X. (2019). Fabrication and characterization of electrospun PLLA/PANI/TSA fibers. *RSC Adv.* 9, 5610–5619. doi: 10.1039/c8ra10495f

Yu, Y., Chen, R., Sun, Y., Pan, Y., Tang, W., Zhang, S., et al. (2018). Manipulation of VEGF-induced angiogenesis by 2-N, 6-O-sulfated chitosan. *Acta Biomater.* 71, 510–521. doi: 10.1016/j.actbio.2018.02.031

Zhao, Y., Zhang, Q., Zhao, L., Gan, L., Yi, L., Zhao, Y., et al. (2017). Enhanced peripheral nerve regeneration by a high surface area to volume ratio of nerve conduits fabricated from hydroxyethyl cellulose/soy protein composite sponges. *ACS Omega* 2, 7471–7481. doi: 10.1021/acsomega.7b01003

Zhu, R., Sun, Z., Li, C., Ramakrishna, S., Chiu, K., and He, L. (2019). Electrical stimulation affects neural stem cell fate and function *in vitro*. *Exp. Neurol.* 319:112963. doi: 10.1016/j.expneurol.2019.112963

Conflict of Interest: The authors declare that the research was conducted in the absence of any commercial or financial relationships that could be construed as a potential conflict of interest.

frontiers
in Bioengineering and Biotechnology

ORIGINAL RESEARCH
published: 18 August 2020
doi: 10.3389/fbioe.2020.00986

Coupling Biocompatible Au Nanoclusters and Cellulose Nanofibrils to Prepare the Antibacterial Nanocomposite Films

Peng Wang[1,4†], Baishuang Yin[3†], Huiling Dong[2], Yibo Zhang[1], Yangheng Zhang[5], Rixin Chen[5], Zukun Yang[6], Caoxing Huang[2*] and Qing Jiang[1,4*]

[1] State Key Laboratory of Pharmaceutical Biotechnology, Department of Sports Medicine and Adult Reconstructive Surgery, Nanjing Drum Tower Hospital, The Affiliated Hospital of Nanjing University Medical School, Nanjing, China, [2] College of Chemical Engineering, Nanjing Forestry University, Nanjing, China, [3] College of Animal Science and Technology, Jilin Agricultural Science and Technology University, Jilin, China, [4] Jiangsu Engineering Research Center for 3D Bioprinting, Jiangsu, China, [5] Department of Periodontology, Nanjing Stomatological Hospital, Medical School of Nanjing University, Nanjing, China, [6] Jiangsu Key Laboratory of Oral Diseases, Nanjing Medical University, Nanjing, China

Edited by:
Ronan McCarthy,
Brunel University London,
United Kingdom

Reviewed by:
Xin Zhao,
The Hong Kong Polytechnic
University, Hong Kong
Elisa Mele,
Loughborough University,
United Kingdom

***Correspondence:**
Caoxing Huang
hcx@njfu.edu.cn
Qing Jiang
qingj@nju.edu.cn

† These authors have contributed equally to this work

Specialty section:
This article was submitted to
Nanobiotechnology,
a section of the journal
Frontiers in Bioengineering and
Biotechnology

Received: 02 April 2020
Accepted: 29 July 2020
Published: 18 August 2020

Citation:
Wang P, Yin B, Dong H, Zhang Y, Zhang Y, Chen R, Yang Z, Huang C and Jiang Q (2020) Coupling Biocompatible Au Nanoclusters and Cellulose Nanofibrils to Prepare the Antibacterial Nanocomposite Films.
Front. Bioeng. Biotechnol. 8:986.
doi: 10.3389/fbioe.2020.00986

Cellulose nanofibrils (CNF) is considered as an inexhaustible precursor to produce antibacterial materials, such as antibacterial hydrogel, antibacterial paper, and antibacterial film. However, the poor antimicrobial property of neat CNF required it should be coupled with an antibacterial ingredient. Herein, biocompatible Au nanoclusters (AuNCs) were synthesized and added into the CNF dispersion to prepare a novel antibacterial film (AuNCs@CNF film). The effects of addition of AuNCs with different amount on the morphology and physicochemical properties of AuNCs@CNF films were characterized using atomic force microscopy (AFM), scanning electron microscopy (SEM), X-ray diffraction (XRD), FTIR (Fourier-transform infrared), light transmittance spectra, and thermogravimetric analysis (TGA). The results showed that AuNCs did not affect the nano-structural features of the CNF film and its basic structures, but could greatly increase the hydrophilicity, the flexibility and the thermal stability of CNF film, which might improve its application in antimicrobial wound-healing dressing. The prepared AuNCs@CNF films demonstrated high antibacterial properties toward *Escherichia coli* (*E. coli*) and *Streptococcus mutans* (*S. mutans*) both *in vitro* and *in vivo*, which can prohibit their growths and promote the healing of bacteria-infected wound, respectively. Thus, the prepared AuNCs@CNF film with great antibacterial properties could be applicable in biomedical field.

Keywords: cellulose nanofibrils, Au nanoclusters, antimicrobial property, wound-healing dressing, multipurpose films

INTRODUCTION

Cellulose is the most abundant polysaccharide on earth and has been considered as an inexhaustible source to produce the environmental-friendly and biocompatible materials (Bian et al., 2019; Wu et al., 2019a; Lin et al., 2020; Liu et al., 2020). Recently, procuring cellulose nanofibrils (CNF) from cellulose has gained attention to produce nanofiber-reinforced composites, including microelectronic and electro-optical films, gas-barrier films, cosmetics, and food packing films (Rojo et al., 2015; Li et al., 2017; Zhang et al., 2019). The desired CNF possesses superior properties than the conventional cellulose derivatives, such as high specific surface area, ease of processing, good mechanical properties, biodegradability, and high transparency (Du et al., 2019; Bian et al., 2020). Thus, CNF is considered as the precursor to produce antimicrobial materials, such as antibacterial hydrogel, antibacterial paper, and antibacterial film, which can be used as the food packing films, drug carriers, infected wound-healing formulation and multifunctional antibacterial films (Li et al., 2018; Han et al., 2019). Since the neat CNF lacks the antimicrobial properties, it has limited application in biomedical fields. Hence, various technologies have been applied to improve the antibacterial properties of CNF-based materials, such as surface modification, antibiotic addition, combination with nanomaterials, and combination with antibacterial polymers (Jia et al., 2012; Li et al., 2018; Bagde and Nadanathangam, 2019).

Among the technologies for constructing the antibacterial CNF materials, adding antibiotics in CNF dispersion is the facile method to obtain the antibacterial CNF film for preparing the wound dressing materials (Kaplan et al., 2014). The CNF-based dressings have nanofiber structures with high capability to absorb and retain water, which enhances its ability to absorb wound exudate and control the environment for wound healing (Li et al., 2018). On the other hand, the used antibiotics can inevitably cause the emergence of multidrug-resistant bacterial strains, which is currently a major public health concern globally (Wright, 2011). To overcome this limitation, the biosecurity nanostructures, including metal, metal oxides, and carbon-based nanomaterials, are considered as promising platforms for antibacterial applications, such as infected wound-healing formulation and multifunctional antibacterial films (Han and Wang, 2017; Fardioui et al., 2018; Wahid et al., 2019). The antibacterial property of the engineered nanomaterials facilitates their usage as potential antibacterial alternatives to overcome the superbug and drug resistance infections (Zou et al., 2016; Fang et al., 2018). Elemental nanoparticles (NPs), such as Ag or Cu NPs with intrinsic antimicrobial capacity, have been extensively utilized to produce of antibacterial films (Chen et al., 2019). These NPs can react with the cell membrane protein by thiol groups, then induce the production of intracellular reactive oxygen species (ROS) or affect bacterial transport of substances through the cell membrane (Percival et al., 2005; Dizaj et al., 2014; Yuan et al., 2018). However, the inherent cytotoxicity for human cells restricts their biomedical application (Holt and Bard, 2005; El Badawy et al., 2011). Therefore, finding alternate nanoscale antibacterial candidates with good biosecurity for potentially clinical application is rather challenging.

Au nanostructures with excellent biocompatibility have been attracted considerable attention in biomedical applications. Such materials can exhibit high antibacterial property against a wide spectrum of bacteria and could be functional with high-density antimicrobial peptides or small molecule antibiotics (Rai et al., 2016; Yang et al., 2017). In addition, the size-dependent effects of biological activity indicate novel physicochemical properties at the nanoclusters (NCs) scale. Zhang' group (Zhang et al., 2019) reported the excellent antibacterial efficiency of AuNCs against *S. aureus*, *S. epidermidis*, and *P. aeruginosa* by producing intracellular ROS, and the antibacterial activity could be controllably regulated via the surface properties. Zheng's group synthesized the 6-mercaptohexanoic acid (MHA)-modified sub-2 nm AuNCs with high antibacterial against both Gram-positive and Gram-negative bacteria, which showed a great advantage over that of large-size gold NPs (Zheng et al., 2017). As the surface properties of AuNCs play the major role in their antibacterial activity, AuNCs functionalized with a series of surface ligands have been investigated to obtain high antibacterial activity. Thus, 4, 6-diamino-2-mercaptopyrimidine (DAMP), an analog of 2-mercaptopyrimidine in the tRNA of *E. coli*, has been employed as the surface ligand to functionalize AuNCs. The DAMP-capped AuNCs show a robust capacity to eliminate bacteria through DNA destruction, membrane damage, and ROS production (Zheng et al., 2018). Importantly, the AuNCs have great biocompatibility and antibacterial efficiency, indicating that they are suitable for clinical infection therapy. However, AuNCs can be easily aggregated due to their high specific surface area. Various materials including graphene, silica, metal oxide, and polymers, have been used as the substrate materials to load the AuNCs in order to prevent their aggregation (Ji et al., 2013). Presently, only a few studies considered AuNCs as the precursor to construct the antibacterial CNF film (Lin and Alain, 2014; Guo et al., 2016). Hence, we hypothesized that coupling the AuNCs with CNF can vest the antibacterial property to the CNF film and provide a remarkable substrate material for AuNCs.

In this study, the AuNCs were synthesized as antibacterial ingredient for CNF film and their structural features were characterized. Various amount of AuNCs were added into CNF dispersion to obtain the antibacterial CNF films that were termed as AuNCs@CNF films. The effects of different additions of AuNCs on the morphology, crystallinity, mechanical, thermal, and surface wettability were investigated. The *in vitro* and *in vivo* antibacterial properties of AuNCs@CNF films were evaluated by prohibiting the growth of bacteria (*E. coli* and *S. mutans*) and the skin regeneration of rats by infecting with the bacteria, respectively. Thus, we speculated that the AuNCs@CNF film with great antibacterial activity both *in vitro* and *in vivo* could promote the biomedical application of CNF film.

MATERIALS AND METHODS

Materials and Reagents

$HAuCl_4{\cdot}3H_2O$ and mercaptopyrimidine were purchased from Sigma-Aldrich Co., Ltd. Ultrapure water was obtained from Millipore Autopure system. The bleached hardwood kraft pulp that used as the raw material to prepare the CNF film was provided by Asia Symbol Pulp and Paper Co., Ltd (Shandong, China). The used 2, 2, 6, 6-tetramethylpiperidine-1-oxyl radical (TEMPO), sodium bromide (NaBr), and sodium hypochlorite (NaClO) were analytical grade without purification.

Synthesis and Characterization of AuNCs

The mercaptopyrimidine-modified AuNCs were prepared as described previously (Zheng et al., 2018). Briefly, 254 mg of mercaptopyrimidine was solubilized in 2 mL of 50% ethanol solution. It was mixed with 1 mL of 10 mM chloroauric acid trihydrate solution in 7 mL ultrapure water and heated to 70°C, followed by continuous stirring at 300 rpm for 12 h before cooling to room temperature. The synthesized AuNCs were purified by centrifuging at 10000 rpm for 10 min to remove bulk gold and dialyzed in membrane tubing (MWCO = 5000) against ultrapure water to remove the excess mercaptopyrimidine molecules. Finally, the as-prepared AuNCs were stored at 4°C until further use. The morphology of AuNCs was characterized by transmission electron microscopy (TEM, JEM-2100, Japan) and field-emission scanning electron microscope (FE-SEM, Zeiss Supra 40 Gemini, Germany). The hydrodynamic size of AuNCs was measured by dynamic light scattering (Malvern Zetasizer Nano ZS90, United Kingdom).

Preparation of CNF Dispersion, CNF Film, and AuNCs@CNF Films

The bleached kraft pulp was treated by the NaClO/NaBr/TEMPO system to obtain the TEMPO-oxidized CNF, as described in the work of Yu et al. (2019). The oxidized CNF solution was diluted by distilled water to 0.5% (w/w) concentration and homogenized by the pressured homogenizer at room temperature and 500 bar for 3 cycles to obtain the CNF dispersion. To active the carboxyl group in the TEMPO-oxidized CNF, 0.4 g of EDC and 0.2 g of NHS were dissolved in 200 mL of CNF dispersion and stirred at room temperature for 6 h. The residual EDC and NHS in the CNF dispersion were removed by dialysis (molecular weight cutoff of the membrane was 10000 g/mol). AuNCs solution with the final concentrations of 0.05, 0.1, and 0.2 mM in the CNF dispersion were mixed with active CNF dispersion (0.5%, w/w), respectively, and stirred overnight to obtain the uniform AuNCs@CNF dispersion. The CNF and AuNCs@CNF dispersion were cast into polystyrene Petri dish and dried at 30°C until the films were formed.

Characterization of the Prepared Films

The morphologies of the prepared films were analyzed by atomic force microscopy (AFM, Signal Hill, CA, United States) and SEM (Carl Zeiss NTS, Hitachi Ltd, Tokyo, Japan) at accelerating voltages of 200 and 15 kV, respectively. The spectra of molecular vibrations of the prepared films were obtained by an ATR-FTIR spectrophotometer (Nicolet iS10, Thermo, Waltham, MA, United States). All the spectra were recorded from 400 to 4000 cm^{-1} with 32 scans at a resolution of 4 cm^{-1}. X-ray diffraction (XRD) was performed to evaluate the crystallinity (CrI) properties of the prepared films. The spectra were recorded from 5 to 50° with 4°/min scanning rate at a voltage of 40 kV and a current of 40 mA. The Crl of the prepared films was calculated according to the equation described by Sunghyun work (Sunghyun et al., 2016). The light transmittance spectra of the films were recorded in the range of 300–800 nm using a UV-vis spectrophotometer (Ultraspec 2100, Amersham Bioscience). The transmittance percentages of the films were calculated according to Beer–Lambert Law at the normalized wavelength (400 nm) for the film with similar thickness. The thermogravimetric analysis (TGA) of the prepared films was carried out by a thermogravimetric analyzer (PerkinElmer, Inc., Waltham, MA, United States). The film samples were heated from 30 to 600°C with a heating rate of 10°C/min under nitrogen atmosphere with a gas flow of 20 mL/min. The mechanical properties (tensile strength, tensile strain, and Young's modulus) of the prepared films were measured using a universal material testing machine (Shimadzu Co., Japan). The films were cut into rectangular specimens (length 50 mm, width 5 mm, thickness 0.02–0.04 mm) for tensile testing. The span length and testing speed were 30 mm and 1 mm/min, respectively.

Antibacterial Activity Analysis

The antibacterial activity of the CNF and AuNCs@CNF dispersion were tested using broth dilution method. *Escherichia coli* (*E. coli*, ATCC-25922) and *Streptococcus mutans* (*S. mutans*, ATCC-21059) were cultured at a density of 1.0×10^6 CFU/mL in 1 mL dispersions. The as-prepared bacterial solutions were inoculated at 37°C for 24 h. The reduction in the number of bacteria in the medium were calculated to evaluate the antibacterial activity. The antibacterial activity of the CNF and AuNCs@CNF films were tested using the inhibition zone method. A volume of 200 μL (10^6 spores/mL) of *E. coli* and *S. mutans* were homogeneously swabbed on the surface of the agar media. Then, the prepared films were cut into circles of 0.6 cm in diameter and placed on the agarose gel and incubated at 37°C for 24 h. The images of the plates were recorded to measure the inhibition zone for the bacteria.

The morphological properties of the bacteria treated with CNF and AuNCs@CNF dispersion were observed by FE-SEM. Specifically, the bacterial solutions cultured with the dispersions were harvested by centrifugation at 8000 rpm for 5 min and washed three times with PBS after culturing with AuNCs dispersion, followed by the addition of 2.5% glutaraldehyde at 4°C for 12 h to allow complete immobilization. Subsequently, the bacteria were dehydrated with graded ethanol and resuspended by absolute ethyl alcohol. Finally, the immobilized bacterial solutions were dropped on a silicon wafer (10 mm × 10 mm) and dried in a vacuum drier for FE-SEM analysis.

Animal Experiment

Twenty-four Male Sprague–Dawley rats (weight ∼250 g) were obtained from the Laboratory Animal Center of Drum Tower Hospital Affiliated to the Medical School of Nanjing University (China). All experimental protocols in this study were approved by the Committee of Drum Tower Hospital Affiliated to Medical School of Nanjing University. To establish SD rat skin infection model, two skin defects (10 mm × 10 mm) were made on the back of the animals, followed by the inoculation of 200 μL *E. coli* or *S. mutans* (1×10^9 CFU/mL). Then, the neat CNF and AuNCs@CNF size-matched films were attached to the corresponding skin defects in the experiment and the blank control groups (without any control). After 4 or 8 days post-treatment, the area of the wounds and the histological sections were observed for the *in vivo* evaluation of the antibacterial activities of the CNF and Au NCs@CNF films.

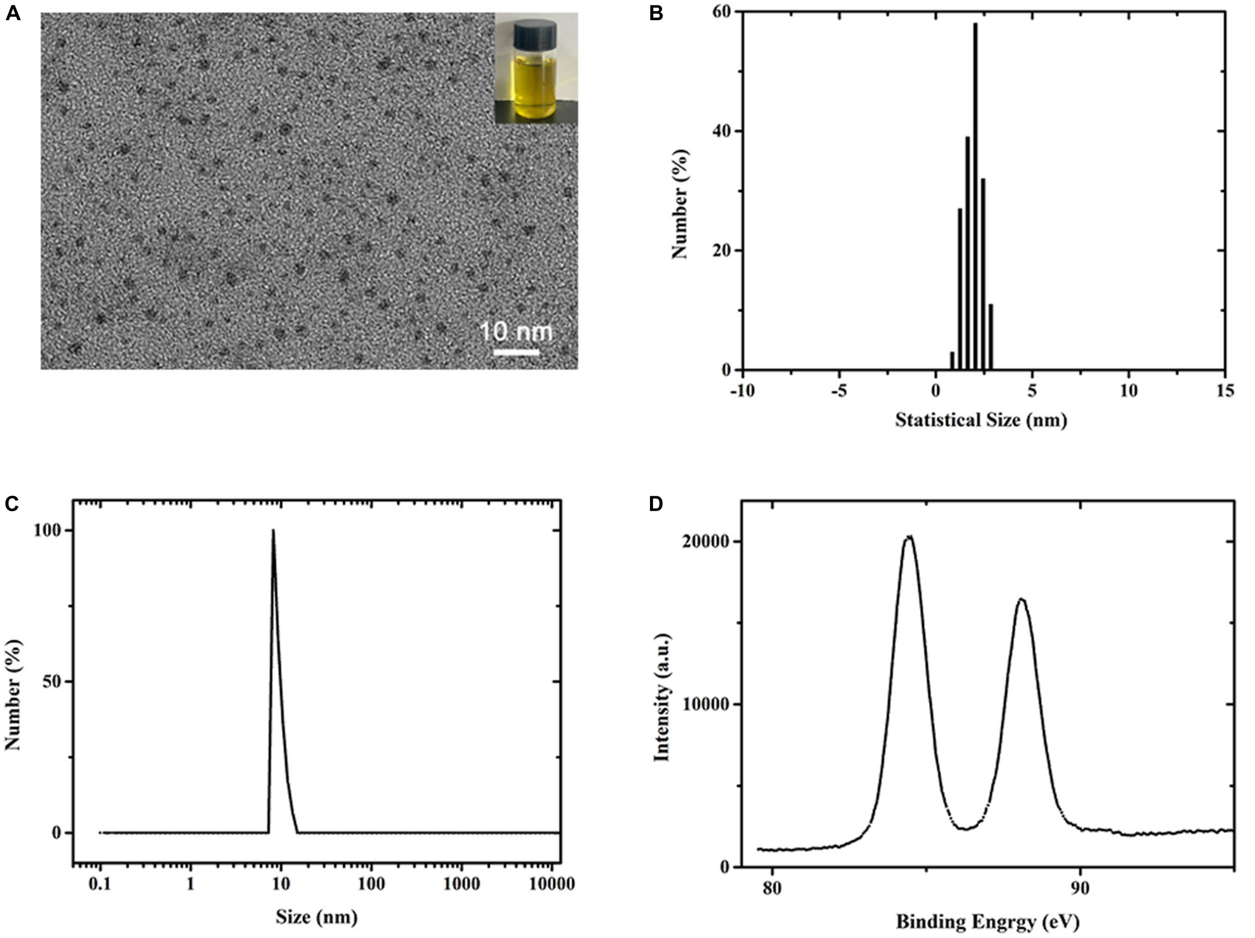

FIGURE 1 | (A–C) TEM image of DAMP modified AuNCs. The inset presents the photograph of the Au NCs solution **(B)** Statistical size distribution of AuNCs in **(A)**. **(C,D)** DLS and XPS spectra measurement of synthesized AuNCs.

Statistical Analysis

All experiments for the antibacterial analysis were performed with three replicates. All the results were expressed as mean ± standard deviation. Statistical analysis was performed using Origin software (8.5 version). Asterisks in the statistical analysis indicate the statistically significant differences between control and experience groups ($^{*}p < 0.05$; $^{**}p < 0.01$; $^{***}p < 0.005$;$^{****}p < 0.001$).

RESULTS

Synthesis and Characterization of AuNCs

The mercaptopyrimidine-modified AuNCs were synthesized by reducing chloroauric acid in the presence of mercaptopyrimidine ligands in 50% ethanol solution. The morphology of the prepared AuNCs was characterized by TEM as shown in **Figure 1A**. Photograph of as-prepared AuNCs solution was shown in **Figure 1A** (inset), which showed fluorescent yellow under visible light. The as-synthesized AuNCs were ultrasmall spherical clusters showing a good monodispersity. According to the TEM image, it can be found that the average size of AuNCs was 1.93 ± 0.21 nm (**Figure 1B**). These results suggested that the obtained AuNCs was present in nanostructure state (Zheng et al., 2019). The data from dynamic light scattering (**Figure 1C**) demonstrated that the average hydrodynamic size of AuNCs was about 10 nm with a polydispersity index of 0.153, indicating their great dispersibility. Also, the AuNCs solution was highly stable and could be stored at 4°C without visible precipitation and flocculation. To further investigate the valence states of Au in AuNCs, X-ray photoelectron spectroscopy (XPS) measurement was performed for the AuNCs aqueous solution. The spectrum (**Figure 1D**) showed that the binding energy (EB) for Au ($4f_{5/2}$) and Au ($4f_{7/2}$) were 88.1 and 84.4 eV, respectively, indicating that the Au occurred in both zerovalent and monovalent state. In addition, biocompatibility of the as-prepared AuNCs was tested in human bone marrow-derived mesenchymal stem cells (hBMSCs) and rat bone marrow mesenchymal stem cells (rBMSCs). After treated with AuNCs for 72 h, almost no obvious morphology changes were observed in rBMSCs and hBMSCs

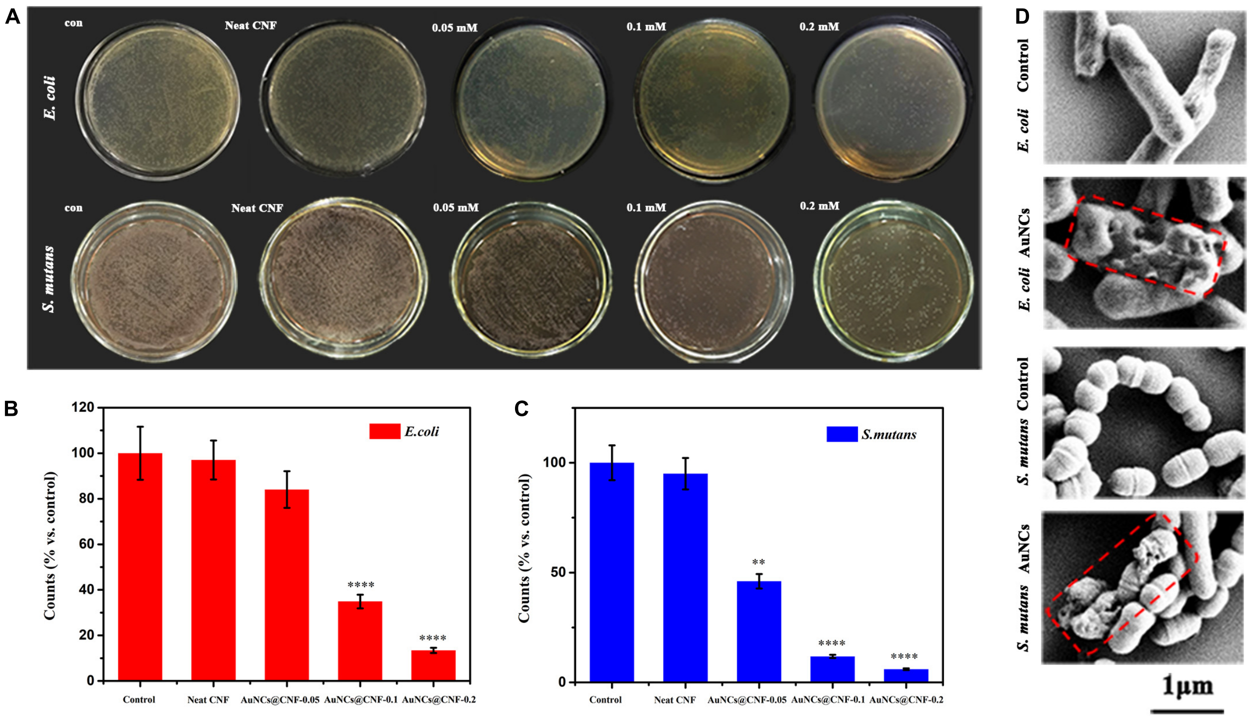

FIGURE 2 | (A) Photographs and **(B,C)** corresponding statistics of bacterial colonies (*E. coli* or *S. mutans*) formed on LB-agar plates after cultivating with AuNCs@CNF dispersion solutions. **(D)** SEM micrographs of *E. coli and S. mutans* when treated or untreated with AuNCs. Asterisk indicates statistically significant differences between control and experience group (**$p < 0.01$; ****$p < 0.001$).

(**Supplementary Figure S1**). Cell Counting Kit-8 (CCK-8) was performed for testing the potential cytotoxicity of cells after treatment with AuNCs for 1, 3, and 5 days. The results for rBMSCs and hBMSCs (**Supplementary Figure S2**) unarguably confirmed that AuNCs showed almost no cytotoxicity, with a good cell viability over 95% even at a concentration up to 0.2 mM. Overall, the aforementioned results indicated the as-prepared DAMP-modified AuNCs were the expectant substance that can be used as the ingredient to fabricate the antibacterial nanocomposite films.

Antibacterial Activity of As-Prepared AuNCs@CNF Dispersion

The present study aimed to add the AuNCs in the CNF film to enhance its antibacterial activity. The effects of the AuNCs@CNF dispersion solutions on the growth of bacteria were shown in **Figure 2A**. Compared with the positive control group, almost no decrease of bacterial colonies formation was observed in the group with neat CNF dispersion, indicating that neat CNF almost had no antibacterial property. On the contrary, it can be seen that a number of bacterial colonies formed on LB-agar plates decreased when they were treated by AuNCs@CNF dispersion. Specifically, the accrued bacterial counts (**Figures 2B,C**) demonstrated that *E. coli* or *S. mutans* treated with AuNCs@CNF dispersion solutions had a dose-dependent increase in antibacterial efficiency with the respective decrement degree of 15.96 ± 1.53% or 53.92 ± 3.85% at 0.05 mM AuNCs, 65.12 ± 5.61% or 88.17 ± 5.67% at 0.1 mM AuNCs, 86.58 ± 7.4% or 94.0 ± 5.94% at 0.2 mM AuNCs, as compared to the control group. In order to further investigate the antibacterial mechanism of AuNCs, the morphological properties of the bacteria treated by AuNCs were observed by FE-SEM (**Figure 2D**). The morphology of the bacterial cells appeared intact and smooth in the control group (without treatment by AuNCs). When treated by 0.2 mM AuNCs at 37°C for 12 h, the bacterial cells showed obvious damage with the wizened membranes.

Morphological Analysis of the Films

Photographs of as-prepared neat CNF film, AuNCs@CNF-0.05, AuNCs@CNF-0.1, and AuNCs@CNF-0.2 were shown in **Supplementary Figure S3**, where it can be seen that the neat CNF film was colorless and transparent and became a little primrose yellow after coupling with Au NCs. The surface morphologies were elucidated by SEM (**Figure 3**). The cellulose nanofibrils (**Figure 3a**) were homogeneously dispersed in the CNF films without the appearance of the individual fibrils on the surface of the film. For AuNCs@CNF films contained 0.05 mM (**Figure 3b**), 0.1 mM (**Figure 3c**), and 0.2 mM (**Figure 3d**) AuNCs, the introduced nano clusters were homogeneously distributed in the films, as indicated by the SEM-mapping images of the Au element (top right pictures). In addition, the cross-section morphologies of the prepared films were also investigated by SEM. The layered structure of the nanofibrils could be observed in the neat

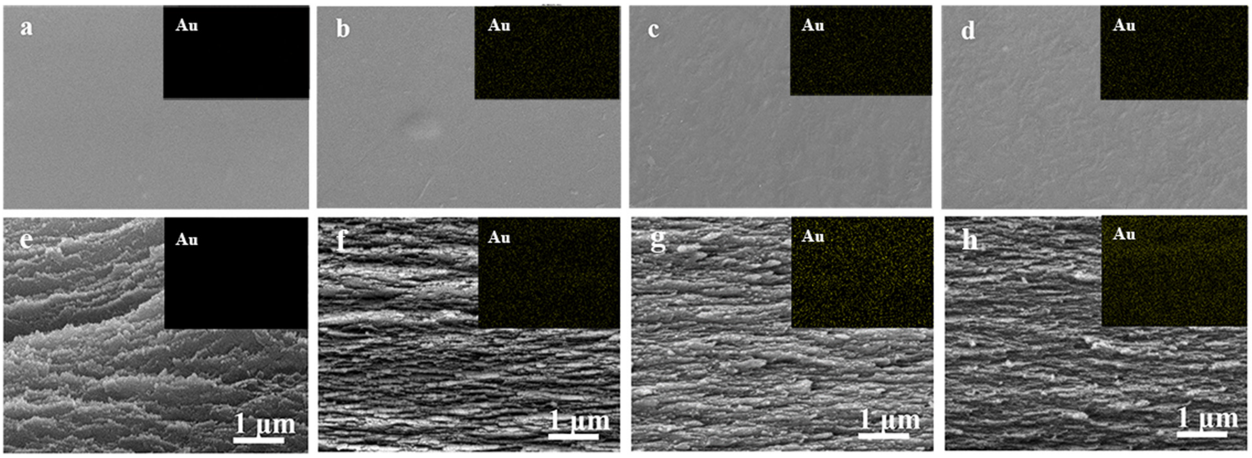

FIGURE 3 | SEM images of surface morphologies of the prepared CNF **(a)** and AuNCs@CNF films with 0.05 mM AuNCs **(b)**, 0.1 mM AuNCs **(c)**, 0.02 mM AuNCs **(d)**, respectively; Cross-sections of prepared CNF **(e)** and AuNCs@CNF films with 0.05 mM AuNCs **(f)**, 0.1 mM AuNCs **(g)**, 0.02 mM AuNCs **(h)**, respectively.

CNF film (**Figure 3e**) and AuNCs@CNF films (**Figures 3f–h**). As proved by the cross-section SEM-mapping images of the Au element distributions (top right pictures), the introduced AuNCs were homogeneously distributed in the matrix of cross-section films.

In order to understand the effect of AuNCs' addition on the surface properties of the CNF film, the plane view and 3D images of the surface structure of the prepared films were evaluated by AFM (**Figures 4a–h**). Specifically, the roughness (RMS) value was 26.4 nm for neat CNF film (**Figure 4e**), while the values for AuNCs@CNF films with increased concentration of AuNCs 0.05–0.2 (**Figures 4f–h**) increased from 26.9 to 32.7 nm. The increased roughness of the prepared AuNCs@CNF films might be due to the degree of consolidation on the surface during drying process for the film forming (Rojo et al., 2015), which was in agreement with the observation of the SEM images (**Figure 3**).

Basic Characterization of CNF and AuNCs@CNF Films

Transparency is the optical property for the CNF film (Mehta and Kumar, 2019; Yu et al., 2019). Hence, the light transmittances of prepared CNF and AuNCs@CNF films were measured (**Figure 5A**). The transparency in visible light spectra of AuNCs@CNF films showed a decline with the increased AuNCs concentration. In order to quantitatively understand the effect of AuNCs on the visible light transmittance of CNF, the light absorption of the normalized films with similar thickness (10 nm) was calculated according to the Beer–Lambert Law at 400 nm (**Table 1**). It can be seen that the transmittance of normalized light of AuNCs@CNF-0.05, AuNCs@CNF-0.1, and AuNCs@CNF-0.2 films were 69.6, 70.1, and 63.4%, respectively, which was lower than that of neat CNF film (73.8%).

To further understand the effects of AuNCs on structural changes of CNF film, the crystal structures of the prepared films with and without AuNCs were investigated by XRD analysis (**Figure 5B**). Consequently, two sharp signals were detected at 15 and 22.5°, which are the diffraction planes of typical cellulose I (Jia et al., 2017). The diffraction patterns of AuNCs@CNF films were similar to that of neat CNF film, indicating that the addition of AuNCs did not change the crystal type of cellulose. **Table 1** shows that the addition of AuNCs from 0.05 to 0.2 mM reduced the crystalline structure of neat CNF film from 63.1 to 63.0–59.3%.

Water mobility plays a critical role in the antibacterial film when it is used as wound healing (Farooq et al., 2019). Hence, the surface wettability of the prepared films were evaluated by water contact angles (**Figure 5C**). The contact angle of CNF films was 57°. When the added AuNCs in AuNCs@CNF films increased from 0.05 to 0.2 mM, the contact angle was gradually decreased from 48 to 44°, which was attributed to fact that the added AuNCs have abundant mercapto groups that can improve the hydrophilic property of the resultant films.

Thermal Property of the Prepared Films

Thermal stability of the prepared films is a critical property for considering its applicability in different areas (Bian et al., 2019; Wu et al., 2019b). Hence, the thermal properties of CNF and AuNCs@CNF films were analyzed by TGA. The obtained weight loss curves and derivative thermogravimetry (DTG) curves of the films were shown in **Figures 6A,B**, respectively. The onset decomposition temperature (Tonset) and maximum decomposition temperature (Tmax) were used as indicators to evaluate the thermal stability of the prepared films (**Table 1**). According to **Figure 6A**, the weight loss curves of the films can be divided into three stages. The first stage at 50–150°C was attributed to the evaporation of the absorbed moisture in the films. The second stage at 200–350°C was mainly caused by the decomposition of cellulose in the films. The third stage at 350–600°C was due to the cracks in the thermal degradation intermediates generated in the second stage (Bian et al., 2019; Abral et al., 2020). In this stage, the thermal degradation of the films were relatively stable, and the residual weights were

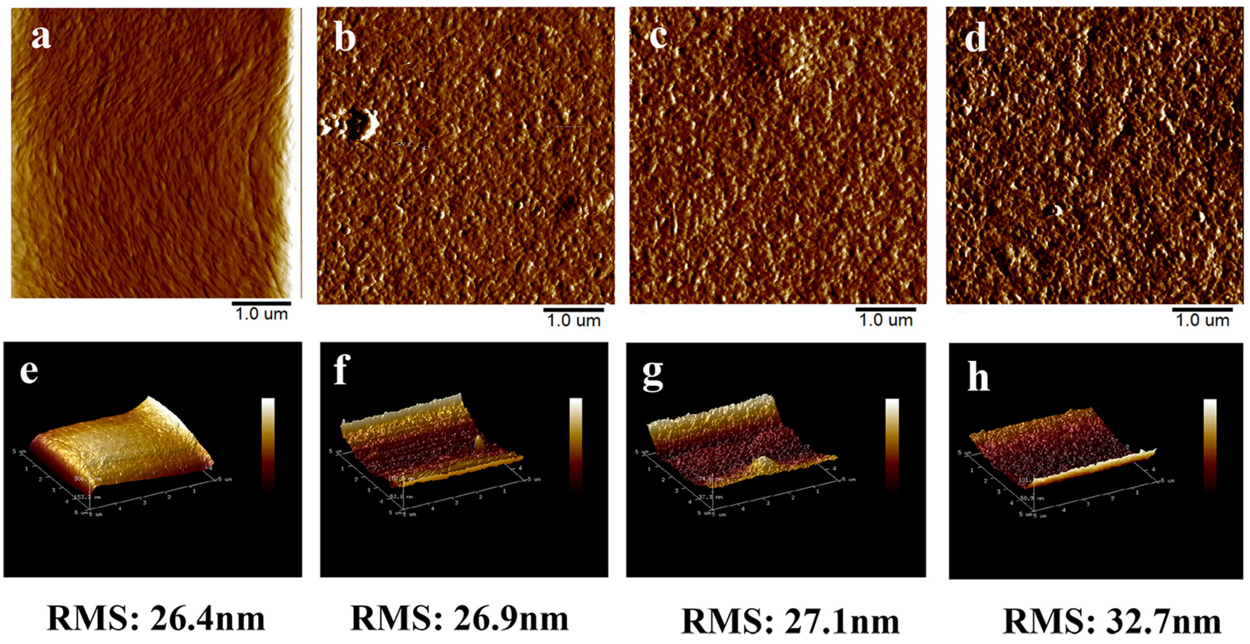

FIGURE 4 | The AFM surface images and 3D images of CNF film **(a,e)** and AuNCs@CNF films with 0.05 mM AuNCs **(b,f)**, 0.1 mM AuNCs **(c,g)**, 0.02 mM AuNCs **(d,h)**.

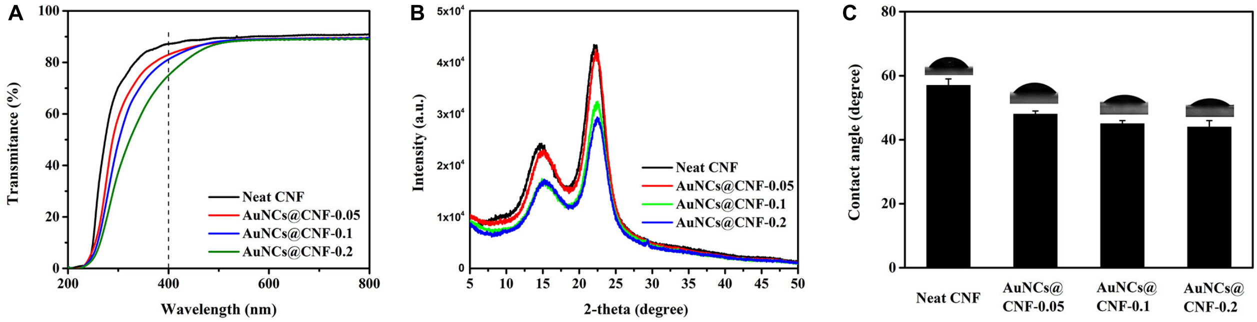

FIGURE 5 | The light transmittance **(A)**, XRD patterns **(B)** and water contact angles **(C)** of the prepared films.

TABLE 1 | Properties of transmittance, crystallinity, and thermal stability of the prepared films.

Film abbreviation	Transmittance (%, at 400 nm)	Crystallinity (%)	Thermal property		
			Tonset (°C)	Tmax (°C)	Residual weights (%)
Neat CNF	73.8	63.1	187	242	23.7
AuNCs@CNF-0.05	69.6	63.0	187	254	25.8
AuNCs@CNF-0.1	70.1	62.4	199	256	26.8
AuNCs@CNF-0.2	63.4	59.3	188	261	31.7

generated. **Table 1** also demonstrated the residual weights of CNF film, AuNCs@CNF-0.05, AuNCs@CNF-0.1, and AuNCs@CNF-0.2 films were 23.7, 25.8, 26.8, and 31.7% at 600°C, respectively. Among the four samples, the CNF film displayed the lowest onset temperature (187°C) and the lowest weight loss temperature (242°C). For the AuNCs@CNF film, the increased concentration from 0.05 to 0.2 mM resulted in the prepared film with higher values of Tonset and Tmax, which were 188–199°C and 254–261°C, respectively.

Mechanical Properties of the Prepared Films

The mechanical properties of cellulose film are the crucial index for its applications (Rojo et al., 2015; Yu et al., 2019;

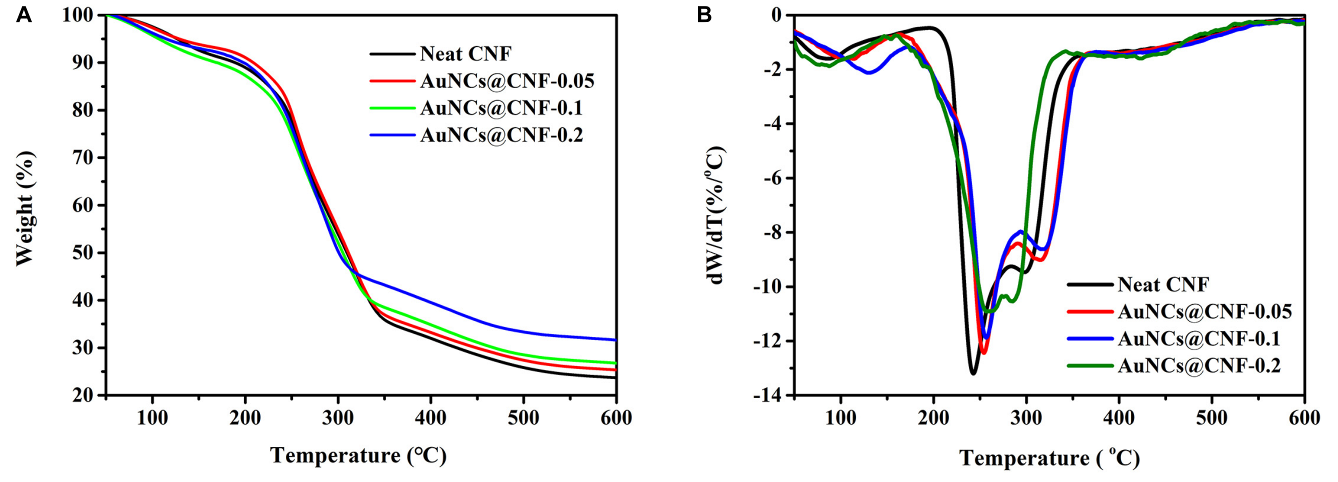

FIGURE 6 | The weight loss curves **(A)** and derivative thermogravimetry curves **(B)** of the prepared films.

TABLE 2 | Mechanical properties of CNF film and AuNCs@CNF films.

Film abbreviation	Tensile strength (MPa)	Elongation at break (%)	Young's modulus (GPa)
CNF	108.5 ± 11.3	5.0 ± 0.6	5.9 ± 1.7
AuNCs@CNF-0.05	54.3 ± 3.1	4.7 ± 0.1	4.7 ± 0.4
AuNCs@CNF-0.1	47.3 ± 2.8	4.2 ± 0.2	4.1 ± 0.3
AuNCs@CNF-0.2	43.2 ± 8.2	4.1 ± 1.2	2.1 ± 0.8

Pei et al., 2020). Hence, the stress-strain curves of the prepared films were evaluated and shown in **Supplementary Figure S4**. The tensile strength, breaking strain, and elastic modulus of the films were calculated from the curves and shown in **Table 2**. The neat CNF film had a tensile strength of 108.5 MPa at break, a tensile strain of 5.0%, and Young's modulus of 5.9 GPa. While, the mechanical properties of CNF film were remarkably influenced by the addition of AuNCs. All AuNCs@CNF films showed the decreased tensile strength and tensile strain of 43.2–54.1 MPa and 4.1–4.7%, respectively. Typically, the tensile properties of the cellulose film are related to single fibrils and interfibrillar bonding, which are linked to the chemical composition, aspect ratio, and the added ingredient (Wang et al., 2018; Imani et al., 2019). Moreover, the CNF films consisted of AuNCs at the concentration of 0.05–0.1 mM had the lower Young's modulus (4.7–2.1 GPa) than that of neat CNF film (5.9 GPa).

In vitro and *in vivo* Antibacterial Behavior of AuNCs@CNF Film

In order to understand the antibacterial effectiveness of as-prepared AuNCs@CNF films, the *in vitro* and *in vivo* assays were performed using bacteria (*E. coli* and *S. mutans*) models and Sprague-Dawley (SD) rats skin infection model, respectively. In **Figures 7A,B**, the AuNCs@CNF film showed remarkable antibacterial activity for prohibiting the growths of bacteria, as deduced by the formation of inhibitory zones of 6–11.2 mm for *E. coli* and 6–9.2 mm for *S. mutans*. The corresponding statistical data (**Figure 7C**) demonstrated that AuNCs@CNF-0.2 film displayed relatively larger zones than that of AuNCs@CNF-0.05 and AuNCs@CNF-0.1. To further investigate their antibacterial mechanism, AuNCs release from AuNCs@CNF film were measured by incubating with PBS buffer at 37°C for 24 and 48 h, the results indicated that the AuNCs@CNF had a dose- and time-dependent increase of AuNCs release (**Supplementary Figure S5**), which play an important role in antibacterial efficiency of AuNCs@CNF films through membrane damage of bacteria (**Figure 2D**). Surprisingly, the AuNCs@CNF films showed great stability even incubated with PBS buffer up to 48 h as shown in **Supplementary Figure S6**, which could be used for infected-wound dressing materials.

In addition, *in vivo* antibacterial efficiency of AuNCs@CNF film was investigated via the SD rat skin infection model, in which the healing degree of the bacteria-tainted wound was evaluated by pasting the film on it. In order to facilitate the assessment, SD rats with two dorsal skin defects (10 mm × 10 mm) were randomly divided into three groups (*E. coli* infected group, *S. mutans* infected group, and the blank control group), wherein the upper dorsal skin defect was employed for the antibacterial evaluation of the AuNCs@CNF film and the lower for neat CNF film (**Figure 7D**). The treatment effect was evaluated by measuring the area of the skin wound every 4 days and the visual images are shown in **Figure 7E**. The healing process of the wound in the AuNCs@CNF film group was faster than that of the neat CNF film and control group. The corresponding statistics (**Figure 7F**) showed that the area of wounds in the AuNCs@CNF film group after 8 days of treatment was 12.3 ± 1.7 and 11.3 ± 2.1 mm^2 for *E. coli* and *S. mutans*, respectively, which were significantly smaller than that of the control group (28.2 ± 2.9 and 34.5 ± 3.2 mm^2, respectively). In order to further validate the effects of AuNCs@CNF films on wound healing, histological examinations were performed by H&E staining on regenerated skin tissue in the wounds treated with neat CNF films and AuNCs@CNF films 14 days post operation, respectively. As shown in **Figure 7G**,

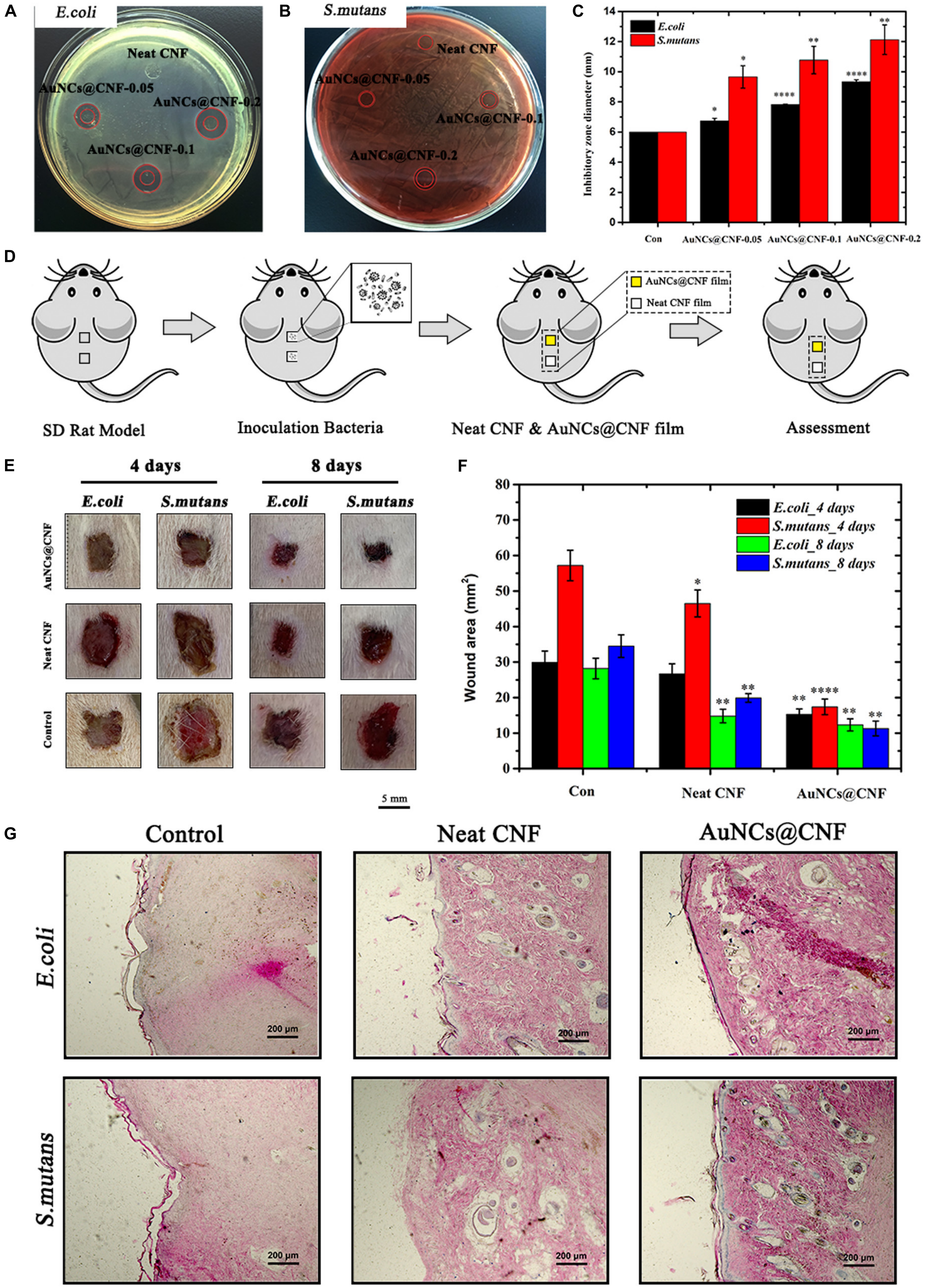

FIGURE 7 | Inhibition zones on the agar plates inoculated with **(A)** *E. coli* and **(B)** *S. mutans* and **(C)** corresponding statistics their diameter. **(D)** Schematic of *in vivo* evaluation process of antibacterial property using skin infected wound model. **(E)** Representative photographs and **(F)** corresponding statistics area of the *E. coli* and *S. mutans* infected wound untreated and treated with AuNCs@CNF films as antibacterial dressings, respectively. **(G)** Histological analysis by H&E staining images of infected wounds covered with neat CNF and AuNCs@CNF films on days 14, respectively. Asterisk indicates statistically significant differences between control and experience group (*$p < 0.05$; **$p < 0.01$; ****$p < 0.001$).

a well-developed vascular network and new hair follicle were observed in AuNCs@CNF film treated group, whereas it was absent in control group.

DISCUSSION

CNF-based materials with great antibacterial properties are considered to be very promising platforms for biomedical applications such as food packing films, infected wound-healing formulation and multifunctional antibacterial films (Li et al., 2018; Han et al., 2019). There are several emerging approaches have been carried out to endow CNF-based materials with antibacterial property (Yuan et al., 2018; Chen et al., 2019). In this work, the biocompatible AuNCs were synthesized and used as intermediate to prepare the AuNCs@CNF dispersion for manufacturing film. The prepared dispersions with different concentration showed the antibacterial ability to inhibit the growth of infectious bacteria of *E. coli* and *S. mutans*. Through the bacterial morphologies observed from SEM images, it can be seen that AuNCs could interact with membranes of bacterial cell and destroy its integrity, which might be one of the attributions for the antibacterial property of AuNCs. Based on these results, it is speculated that the dispersions containing AuNCs are promising to prepare the antibacterial films.

Morphological analysis by SEM indicated that the introduced AuNCs with groups of NH_3 and COOH can form hydrogen bonds with OH group among nanofibers in CNF, resulting in a slick surface for the obtained AuNCs@CNF films. Moreover, the increased amount of AuNCs made the surface of the prepared films rather uneven, which could be attributed to the presence of the surface-active functional groups in the AuNCs particles that can be linked to nanofibrils in the CNF composites (Bian et al., 2019). This can be explained that the AuNCs can cause the flocculation of nanofibrils and disrupt the interfibrillar hydrogen bonding during the dried process for AuNCs@CNF film forming, leading to the uneven surface of the prepared films (Imani et al., 2019). In addition, AuNCs can facilitate to form a relatively compact structure of AuNCs@CNF films, which can be indicated by more compact and flat structures appeared in the AuNCs@CNF films with the increased amount of introduced AuNCs particles. In addition, the AFM surface images of CNF film showed that the neat CNF film contained the nanometer scale cellulose fibrils, which were interconnected to form the fibrous network. This result was in accordance with the work in Yu et al. (2019). When the AuNCs were introduced to the CNF film, the cellulose fibrils in the AuNCs@CNF films were still presented as the fibrous network structure. Overall, the morphology analysis indicated that the addition of AuNCs did not significantly affect the nanostructural features of CNF film.

We further evaluated the basic properties of AuNCs@CNF films, such as transparency, crystal structure, water mobility, thermal stability and mechanical properties. The decreased light transmittance of AuNCs@CNF film was attributed to the surface mercapto group of AuNCs, which is a chromophore that can absorb light and reduce the transmittance of neat CNF film. In addition, the decreased transparency of the AuNCs@CNF film can also be attributed to its enhanced surface roughness (Nogi et al., 2009). Based on the Crl values of prepared films, it can be speculated that the addition of AuNC increased the proportion of amorphous regions of nanofibers in the CNF films (Bian et al., 2019). Even the added AuNCs in CNF films could slightly decrease its contact angle from 57 to 48–44°, the prepared AuNCs@CNF films could be still used as the antibacterial film in the wound field. As pointed out by Kaygusuz et al. (2017), the moderately wettable surface of film with contact angle of 35–50° is benefit for bacteria to adhere, which can improve the contact opportunity between bacteria and antibacterial film. Yang et al. (2016) showed that the enhanced hydrophilic properties of modified cellulose could make contribution to its antimicrobial activity.

From the results of mechanical property analysis, it is found that the added AuNCs in CNF film could slightly reduce its tensile strength, which can be attributed to the weakened interactions between interfibrils in CNF films. Meanwhile, the decreased Crl of the AuNCs@CNF film is another reason for the reduced tensile strength of the CNF film (Bian et al., 2019). In a reported work, the wound dressings from chitosan-cellulose nanocrystals with tensile strength of 34.9–58.0 MPa (Naseri et al., 2015), bacterial cellulose-chitosan membranes with tensile strength of 10.26 MPa (Lin et al., 2013) and 22.48 MPa (Savitskaya et al., 2017), and cellulose-polymer-Ag nanocomposite with 25.1–39.8 (Raghavendra et al., 2013) were successfully prepared and used as antibacterial wound dressing. Hence, it can be speculated that the prepared AuNCs@CNF films with tensile strength of 43.2–54.1 MPa can also perform the comparative mechanical properties than the other wound dressing materials. According to the Young's modulus results, the flexibility of the CNF film could be enhanced by the addition of AuNCs. Generally, the excellent mechanical properties of high strength and flexibility of the films are required for the most advanced material design. However, the enhancement of strength and flexibility for the cellulose films are usually conflicted (Wang et al., 2018). The Young's modulus can be regarded as the indicator to evaluate the stiffness and resistance of a material for deforming (Azevedo et al., 2013). The Young's modulus of wound healing with high value might make it against for skin applications. Comparing to a reported work, it can be found that the Young's modulus of AuNCs@CNF films had the comparative values than that of wound healing from various bacterial cellulose-based composites, which had the Young's modulus of 4.2–6.1 GPa (Ul-Islam et al., 2012) and 7.0 GPa (Kim et al., 2011). In the present study, although the tensile strength of the AuNCs@CNF film was reduced with the increasing addition of AuNCs, the enhanced flexibility indicated that the AuNCs@CNF film possessed high folding strength, making it resistant to fracture (deformability) when used as the antibacterial film for application as the dressing over wound surface (Li et al., 2018; Wang et al., 2018).

In vitro and *in vivo* antibacterial activity of AuNCs@CNF films were further investigated. The reduced inhibitory zones indicated that the added AuNCs in the CNF film ascribed it possessing significantly inhibiting ability for the growth of both *E. coli* and *S. mutans*. These results were in accordance with the antibacterial activity of their dispersion solutions. In the work of Raghavendra et al., 2013, they found that the cellulose-Ag nanocomposite showed antimicrobial efficacy with inhibition zone of 1.7 mm for *E. coli*. Di et al. (2017) prepared bacterial cellulose/Ag and found it could produce a clear inhibition zones of 25 mm for *E. coli*. The comparative values of inhibitory zones achieved from AuNCs@CNF films indicated that they had the considerably antibacterial behavior as Ag-based cellulose films. The wound healing results revealed that the prepared AuNCs@CNF films showed the abilities to facilitate the healing degree of the bacteria-tainted wound (*in vivo*), which might be due to its antibacterial activity. Generally, the wound healing can be impede by various factors, such as the population of microorganisms, existence of multidrug-resistant microorganisms and formation of bacterial microcolonies (Simoes et al., 2018). Hence, it can be speculated that the prepared AuNCs@CNF film with high antibacterial property has great potential in traumatic infection therapy and promoting bacteria-tainted skin healing.

SUMMARY

In this study, the synthesized biocompatible Au nanoclusters showed great antibacterial properties for the prohibition of *E. coli* and *S. mutans* when it was in CNF dispersion solution. When the AuNCs were coupled with CNF film, the obtained the AuNCs@CNF films had improved hydrophilicity, flexibility, and thermal stability than that of neat CNF film. The prepared AuNCs@CNF films could prohibit the growth of bacteria (*E. coli* and *S. mutans*) *in vitro*. In addition, the AuNCs@CNF film showed the ability to heal the bacteria-tainted wound of rat skin *in vivo*. The AuNCs@CNF film with great antibacterial activity indicated it possessed the potential application in biomedical field.

DATA AVAILABILITY STATEMENT

The raw data supporting the conclusions of this article will be made available by the authors, without undue reservation.

ETHICS STATEMENT

The animal study was reviewed and approved by the Ethics Committee of Drum Tower Hospital affiliated to the Medical School of Nanjing University.

AUTHOR CONTRIBUTIONS

CH and QJ proposed the idea. PW and BY did the experiments. HD helped the property evaluation of CNF film. YiZ helped the skin repair experiment. YaZ, RC, and ZY helped the antibacterial evaluation of AuNCs and AuNCs@CNF films. All authors contributed to the article and approved the submitted version.

FUNDING

This work was supported by the Natural Science Foundation of Jiangsu Province (BK20180772 and BK20190133), National Natural Science Foundation of China (81802135), the International Cooperation and Exchange of National Natural Science Foundation (NSFC 81420108021), Key Program of NSFC (81730067).

SUPPLEMENTARY MATERIAL

The Supplementary Material for this article can be found online at: https://www.frontiersin.org/articles/10.3389/fbioe.2020.00986/full#supplementary-material

REFERENCES

Abral, H., Ariksa, J., Mahardika, M., Handayani, D., Aminah, I., Neny, S., et al. (2020). Transparent and antimicrobial cellulose film from ginger nanofiber. *Food Hydrocoll.* 98:105266. doi: 10.1016/j.foodhyd.2019.105266

Azevedo, E. P., Retarekar, R., Raghavan, M. L., and Kumar, V. (2013). Mechanical properties of cellulose: chitosan blends for potential use as a coronary artery bypass graft. *J. Biomater. Sci. Polym. Edn.* 24, 239–252. doi: 10.1080/09205063.2012.690273

Bagde, P., and Nadanathangam, V. (2019). Mechanical, antibacterial and biodegradable properties of starch film containing bacteriocin immobilized crystalline nanocellulose. *Carbohydr. Polym.* 222:115021. doi: 10.1016/j.carbpol.2019.115021

Bian, H., Dong, M., Chen, L., Zhou, X., Wang, R., Jiao, L., et al. (2020). On-demand regulation of lignocellulosic nanofibrils based on rapid fractionation using acid hydrotrope: kinetic study and characterization. *ACS Sustain. Chem. Eng.* 8, 9569–9577. doi: 10.1021/acssuschemeng.0c02968

Bian, H., Luo, J., Wang, R., Zhou, X., Ni, S., Rui, S., et al. (2019). Recyclable and reusable maleic acid for efficient production of cellulose nanofibrils with stable performance. *ACS Sustain. Chem. Eng.* 7, 20022–20031. doi: 10.1021/acssuschemeng.9b05766

Chen, H., Cheng, R., Zhao, X., Yuhui, Z., Allison, T., Yufei, Y., et al. (2019). An injectable self-healing coordinative hydrogel with antibacterial and angiogenic properties for diabetic skin wound repair. *NPG Asia Mater.* 11:3. doi: 10.1038/s41427-018-0103-9

Di, Z., Shi, Z., Ullah, M. W., Li, S., and Yang, G. (2017). A transparent wound dressing based on bacterial cellulose whisker and poly (2-hydroxyethyl methacrylate. *Int. J. Biol. Macromol.* 105, 638–644. doi: 10.1016/j.ijbiomac.2017.07.075

Dizaj, S. M., Lotfipour, F., Barzegar-Jalali, M., Zarrintan, M. H., and Adibkia, K. (2014). Antimicrobial activity of the metals and metal oxide nanoparticles. *Mater. Sci. Eng. C Mater. Biol. Appl.* 44, 278–284. doi: 10.1016/j.msec.2014.08.031

Du, H., Liu, W., Zhang, M., Si, C., Zhang, X., and Li, B. (2019). Cellulose nanocrystals and cellulose nanofibrils based hydrogels for biomedical applications. *Carbohyd. Polym.* 209, 130–144. doi: 10.1016/j.carbpol.2019.01.020

El Badawy, A. M., Silva, R. G., Morris, B., Scheckel, K. G., Suidan, M. T., and Thabet, M. T. (2011). Surface charge-dependent toxicity of silver nanoparticles. *Environ. Sci. Technol.* 45, 283–287. doi: 10.1021/es1034188

Fang, G., Li, W., Shen, X., Perez-Aguilar, J. M., Chong, Y., Gao, X., et al. (2018). Differential Pd-nanocrystal facets demonstrate distinct antibacterial activity against Gram-positive and Gram-negative bacteria. *Nat. Commun.* 9:129. doi: 10.1038/s41467-017-02502-3

Fardioui, M., Meftah Kadmiri, I., Qaiss, A. E. K., and Bouhfid, R. (2018). Bio-active nanocomposite films based on nanocrystalline cellulose reinforced styrylquinoxalin-grafted-chitosan: antibacterial and mechanical properties. *Int. J. Biol. Macromol.* 114, 733–740. doi: 10.1016/j.ijbiomac.2018.03.114

Farooq, M., Zou, T., Riviere, G., Sipponen, M. H., and Osterberg, M. (2019). Strong, ductile, and waterproof cellulose nanofibril composite films with colloidal lignin particles. *Biomacromolecules* 20, 693–704. doi: 10.1021/acs.biomac.8b01364

Guo, J., Filpponen, I., Su, P., Laine, J., and Rojas, O. J. (2016). Attachment of gold nanoparticles on cellulose nanofibrils via click reactions and electrostatic interactions. *Cellulose* 23, 3065–3075. doi: 10.1007/s10570-016-1042-7

Han, J., Wang, S., Zhu, S., Huang, C., Yue, Y., Mei, C., et al. (2019). Electrospun core-shell nanofibrous membranes with nanocellulose-stabilized carbon nanotubes for use as high-performance flexible supercapacitor electrodes with enhanced water resistance, thermal stability and mechanical toughness. *ACS Appl. Mater. Interf.* 11, 44624–44635. doi: 10.1021/acsami.9b16458

Han, Y., and Wang, L. (2017). Sodium alginate/carboxymethyl cellulose films containing pyrogallic acid: physical and antibacterial properties. *J. Sci. Food Agric.* 97, 1295–1301. doi: 10.1002/jsfa.7863

Holt, K. B., and Bard, A. J. (2005). Interaction of silver (I) ions with the respiratory chain of *Escherichia coli*: an electrochemical and scanning electrochemical microscopy study of the antimicrobial mechanism of micromolar Ag+. *Biochemistry* 44, 13214–13223. doi: 10.1021/bi0508542

Imani, M., Ghasemian, A., Dehghani, M. R., Afra, E., and Rojas, O. J. (2019). Coupling nanofibril lateral size and residual lignin to tailor the properties of lignocellulose films. *Adv. Mater. Interf.* 19:1900770. doi: 10.1002/admi.201900770

Ji, Q., Hill, J. P., and Ariga, K. (2013). Shell-adjustable hollow 'soft' silica spheres as a support for gold nanoparticles. *J. Mater. Chem. A* 1, 3600–3606. doi: 10.1039/c3ta01572f

Jia, B., Mei, Y., Cheng, L., Zhou, J., and Zhang, L. (2012). Preparation of copper nanoparticles coated cellulose films with antibacterial properties through one-step reduction. *ACS Appl. Mater. Interf.* 4, 2897–2902. doi: 10.1021/am3007609

Jia, C., Chen, L., Shao, Z., Agarwal, U. P., Hu, L., and Zhu, J. Y. (2017). Using a fully recyclable dicarboxylic acid for producing dispersible and thermally stable cellulose nanomaterials from different cellulosic sources. *Cellulose* 24, 2483–2498. doi: 10.1007/s10570-017-1277-y

Kaplan, E., Ince, T., Yorulmaz, E., Yener, F., Harputlu, E., and Laçin, N. T. (2014). Controlled delivery of ampicillin and gentamycin from cellulose hydrogels and their antibacterial efficiency. *J. Biomater. Tissue Eng.* 7, 543–549. doi: 10.1166/jbt.2014.1198

Kaygusuz, H., Torlak, E., Akn-Evingur, G., Ilhan, Ö, Regine, V. K., and Bedia, F. E. (2017). Antimicrobial cerium ion-chitosan crosslinked alginate biopolymer films: a novel and potential wound dressing. *Int. J. Biol. Macromol.* 105, 1161–1165. doi: 10.1016/j.ijbiomac.2017.07.144

Kim, J., Cai, Z., Lee, H. S., Choi, G. S., Lee, D. H., and Jo, C. (2011). Preparation and characterization of a bacterial cellulose/chitosan composite for potential biomedical application. *J. Polym. Res.* 18, 739–744. doi: 10.1007/s10965-010-9470-9

Li, J. J., Cha, R., Mou, K., Zhao, X. H., Long, K. Y., Luo, H., et al. (2018). Nanocellulose-based antibacterial materials. *Adv. Healthc. Mater.* 20:1800334. doi: 10.1002/adhm.201800334

Li, Z., Ahadi, K., Jiang, K., Ahvazi, B., Peng, L., Anyia, A. O., et al. (2017). Freestanding hierarchical porous carbon film derived from hybrid nanocellulose for high-power supercapacitors. *Adv. Healthc. Mater.* 10, 1847–1860. doi: 10.1007/s12274-017-1573-8

Lin, N., and Alain, D. (2014). Nanocellulose in biomedicine: current status and future prospect. *Eur. Polym. J.* 59, 302–325. doi: 10.1016/j.eurpolymj.2014.07.025

Lin, W., Xing, S., Jin, Y., Lu, X., Huang, C., and Yong, Q. (2020). Insight into understanding the performance of deep eutectic solvent pretreatment on improving enzymatic digestibility of bamboo residues. *Bioresour. Technol.* 306:123163. doi: 10.1016/j.biortech.2020.123163

Lin, W. C., Lien, C. C., Yeh, H. J., Yu, C. M., and Hsu, S. H. (2013). Bacterial cellulose and bacterial cellulose-chitosan membranes for wound dressing applications. *Carbohyd. Polym.* 94, 603–611. doi: 10.1016/j.carbpol.2013.01.076

Liu, W., Du, H., Zhang, M., Liu, K., Liu, H., Xie, H., et al. (2020). bacterial cellulose-based composite scaffolds for biomedical applications: a review. *ACS Sustain. Chem. Eng.* 8, 7536–7562. doi: 10.1021/acssuschemeng.0c00125

Mehta, M. J., and Kumar, A. (2019). Ionic liquid assisted gelatin films: green, UV shielding, antioxidant, and antibacterial food packaging materials. *ACS Sustain. Chem. Eng.* 7, 8631–8636. doi: 10.1021/acssuschemeng.9b00423

Naseri, N., Mathew, A. P., Girandon, L., Fröhlich, M., and Oksman, K. (2015). Porous electrospun nanocomposite mats based on chitosan-cellulose nanocrystals for wound dressing: effect of surface characteristics of nanocrystals. *Cellulose* 22, 521–534. doi: 10.1007/s10570-014-0493-y

Nogi, M., Iwamoto, S., Nakagaito, A. N., and Yano, H. (2009). Optically transparent nanofiber paper. *Adv. Mater.* 21, 1595–1598. doi: 10.1002/adma.200803174

Pei, W., Shang, W., Liang, C., Jiang, X., Huang, C., and Yong, Q. (2020). Using lignin as the precursor to synthesize Fe3O4@lignin composite for preparing electromagnetic wave absorbing lignin-phenol-formaldehyde adhesive. *Industr. Crops Products* 154:112638. doi: 10.1016/j.indcrop.2020.112638

Percival, S. L., Bowler, P. G., and Russell, D. (2005). Bacterial resistance to silver in wound care. *J. Hosp. Infect.* 60, 1–7. doi: 10.1016/j.jhin.2004.11.014

Raghavendra, G. M., Jayaramudu, T., Varaprasad, K., Sadiku, R., Ray, S. S., and Raju, K. M. (2013). Cellulose-polymer-Ag nanocomposite fibers for antibacterial fabrics/skin scaffolds. *Carbohyd. Polym.* 93, 553–560. doi: 10.1016/j.carbpol.2012.12.035

Rai, A., Pinto, S., Velho, T. R., Ferreira, A. F., Moita, C., Pedro, N. S., et al. (2016). One-step synthesis of high-density peptide-conjugated gold nanoparticles with antimicrobial efficacy in a systemic infection model. *Biomaterials* 85, 99–110. doi: 10.1016/j.biomaterials.2016.01.051

Rojo, E., Peresin, M. S., Sampson, W. W., Hoeger, I. C., Vartiainen, J., Janne, L., et al. (2015). Comprehensive elucidation of the effect of residual lignin on the physical, barrier, mechanical and surface properties of nanocellulose films. *Green Chem.* 17, 1853–1866. doi: 10.1039/C4GC02398F

Savitskaya, I. S., Kistaubayeva, A. S., Digel, I. E., and Shokatayeva, D. H. (2017). Physicochemical and antibacterial properties of composite films based on bacterial cellulose and chitosan for wound dressing materials. *Euras. Chem. Technol. J.* 3, 255–264. doi: 10.18321/ectj670

Simoes, D., Miguel, S. P., Ribeiro, M. J., Coutinho, P., Mendonca, A. G., and Correia, I. J. (2018). Recent advances on antimicrobial wound dressing: a review. *Eur. J. Pharm. Biopharm.* 107, 130–141. doi: 10.1016/j.ejpb.2018.02.022

Sunghyun, N., Alfred, D. F., Condon, B. D., and Monica, C. (2016). Segal crystallinity index revisited by the simulation of X-ray diffraction patterns of cotton cellulose I beta and cellulose II. *Carbohyd. Ploym.* 135, 1–9. doi: 10.1016/j.carbpol.2015.08.035

Ul-Islam, M., Khan, T., and Park, J. K. (2012). Nanoreinforced bacterial cellulose-montmorillonite composites for biomedical applications. *Carbohyd. Polym.* 89, 1189–1197. doi: 10.1016/j.carbpol.2012.03.093

Wahid, F., Duan, Y. X., Hu, X. H., Chu, L. Q., Jia, S. R., Cui, J. D., et al. (2019). A facile construction of bacterial cellulose/ZnO nanocomposite films and their photocatalytic and antibacterial properties. *Int. J. Biol. Macromol.* 132, 692–700. doi: 10.1016/j.ijbiomac.2019.03.240

Wang, Q., Du, H., Zhang, F., Zhang, Y., Wu, M., Yu, G., et al. (2018). Flexible cellulose nanopaper with high wet tensile strength, high toughness and tunable ultraviolet blocking ability fabricated from tobacco stalk via a sustainable method. *J. Mater. Chem. A* 27, 13021–13030. doi: 10.1039/c8ta01986j

Wright, D. G. (2011). Molecular mechanisms of antibiotic resistance. *Chem. Commun.* 47:4055. doi: 10.1039/c0cc05111j

Wu, Y., Sun, M., Wu, X., Shi, T., Chen, H., and Wang, H. (2019a). Preparation of nanocellulose aerogel from the poplar (*Populus tomentosa*) catkin fiber. *Forests* 9:749. doi: 10.3390/f10090749

Wu, Y., Tang, Q., Yang, F., Xu, L., Wang, X., and Zhang, J. (2019b). Mechanical and thermal properties of rice straw cellulose nanofibrils-enhanced polyvinyl alcohol films using freezing-and-thawing cycle method. *Cellulose* 26, 3193–3204. doi: 10.1007/s10570-019-02310-6

Yang, X., Yang, J., Wang, L., Ran, B., Jia, Y., Zhang, L., et al. (2017). Pharmaceutical intermediate-modified gold nanoparticles: against multidrug-resistant bacteria and wound-healing application via an electrospun scaffold. *ACS Nano* 11, 5737–5745. doi: 10.1021/acsnano.7b01240

Yang, X. N., Zhong, C., Xue, D. D., Wahid, F., Li, J. Y., and Zhang, Y. M. (2016). Improvement of antimicrobial activity of graphene oxide/bacterial cellulose nanocomposites through the electrostatic modification. *Carbohyd. Polym.* 136, 1152–1160. doi: 10.1016/j.carbpol.2015.10.020

Yu, J., Zhu, Y., Ma, H., Liu, L., Hu, Y., Xu, J., et al. (2019). Contribution of hemicellulose to cellulose nanofiber-based nanocomposite films with enhanced strength, flexibility and UV-blocking properties. *Cellulose* 26, 6023–6034. doi: 10.1007/s10570-019-02518-6

Yuan, P., Ding, X., Yang, Y. Y., and Xu, Q. H. (2018). Metal nanoparticles for diagnosis and therapy of bacterial infection. *Adv. Healthc. Mater.* 7:1701392. doi: 10.1002/adhm.201701392

Zhang, N., Tao, P., Lu, Y., and Nie, S. (2019). Effect of lignin on the thermal stability of cellulose nanofibrils produced from bagasse pulp. *Cellulose* 26, 7823–7835. doi: 10.1007/s10570-019-02657-w

Zheng, K., Setyawati, M. I., Leong, D. T., and Xie, J. (2017). Antimicrobial gold nanoclusters. *ACS Nano* 11, 6904–6910. doi: 10.1021/acsnano.7b02035

Zheng, Y., Liu, W., Chen, Y., Li, C., Jiang, H., and Wang, X. (2019). Conjugating gold nanoclusters and antimicrobial peptides: from aggregation-induced emission to antibacterial synergy. *J. Colloid Interf. Sci.* 546, 1–10. doi: 10.1016/j.jcis.2019.03.052

Zheng, Y. K., Liu, W. W., Qin, Z. J., Chen, Y., Jiang, H., and Wang, X. (2018). Mercaptopyrimidine-conjugated gold nanoclusters as nanoantibiotics for combating multidrug-resistant superbugs. *Bioconjug. Chem.* 29, 3094–3103. doi: 10.1021/acs.bioconjchem.8b00452

Zou, X., Zhang, L., Wang, Z., and Luo, Y. (2016). Mechanisms of the antimicrobial activities of graphene materials. *J. Am. Chem. Soc.* 138, 2064–2077. doi: 10.1021/jacs.5b11411

Conflict of Interest: The authors declare that the research was conducted in the absence of any commercial or financial relationships that could be construed as a potential conflict of interest.

frontiers in Bioengineering and Biotechnology

ORIGINAL RESEARCH
published: 04 September 2020
doi: 10.3389/fbioe.2020.565084

Pilot-Scale Production of Cellulosic Nanowhiskers With Similar Morphology to Cellulose Nanocrystals

Huihui Wang[1,2], Jonathan J. Zhu[3], Qianli Ma[4], Umesh P. Agarwal[2], Roland Gleisner[2], Richard Reiner[2], Carlos Baez[2] and J. Y. Zhu[2]*

[1] State Key Laboratory of Pulp and Paper Engineering, South China University of Technology, Guangzhou, China, [2] USDA Forest Service, Forest Products Laboratory, Madison, WI, United States, [3] Department of Biochemistry, University of Wisconsin-Madison, Madison, WI, United States, [4] International Center for Bamboo and Rattan, Beijing, China

Edited by:
Muhammad Wajid Ullah,
Huazhong University of Science
and Technology, China

Reviewed by:
Rajendra Kumar Singh,
Institute of Tissue Regeneration
Engineering (ITREN), South Korea
PaYaM ZarrinTaj,
Oklahoma State University,
United States

***Correspondence:**
J. Y. Zhu
junyong.zhu@usda.gov

Specialty section:
This article was submitted to
Biomaterials,
a section of the journal
Frontiers in Bioengineering and
Biotechnology

Received: 23 May 2020
Accepted: 20 August 2020
Published: 04 September 2020

Citation:
Wang H, Zhu JJ, Ma Q,
Agarwal UP, Gleisner R, Reiner R,
Baez C and Zhu JY (2020) Pilot-Scale
Production of Cellulosic
Nanowhiskers With Similar
Morphology to Cellulose
Nanocrystals.
Front. Bioeng. Biotechnol. 8:565084.
doi: 10.3389/fbioe.2020.565084

This study describes a class of cellulosic nanomaterials, cellulosic nanowhiskers (CNWs), and demonstrates scaled-up production with acid recovery using less expensive equipment made of common stainless steel rather than glass-lined steel. CNWs produced using concentrated maleic acid (MA) hydrolysis followed by mechanical fibrillation have morphology similar to MA-produced cellulose nanocrystals (CNCs) and sulfuric-acid-produced CNCs (S-CNCs) but differ in crystallinity. Applications of CNWs as a substitute for CNCs for which morphology and surface charge, rather than crystallinity, are the pertinent characteristics are presented. The tested CNW suspensions have a wider viscosity range of 0.001 to 1000 Pa.s over a variety of shear rates of 0.01 to 1000 1/s compared to S-CNCs of 0.001 to 0.1 Pa.s and are better suited for applications such as rheology modification and 3D printing. This study proposes CNWs as a less expensive and sustainable replacement for CNCs in applications that do not require crystalline properties.

Keywords: cellulose nanocrystals (CNCs), cellulose nanowhiskers (CNWs), cellulose nanofibrils (CNFs), mechanical fibrillation, suspension rheology, carboxylation, dispersion, acid hydrotrope

INTRODUCTION

Cellulosic nanomaterials (CNMs) have attracted great interest for a variety of applications due to the renewability of cellulosic raw materials and their unique mechanical and optical properties (Mark, 1967; Revol et al., 1992; Šturcová et al., 2005). To the general scientific community, the term CNMs usually refers to two types of materials: (1) cellulose nanocrystals (CNCs), mainly sulfuric acid CNCs (S-CNCs) produced by concentrated sulfuric acid hydrolysis and dialysis for separation; and (2) cellulose nanofibrils (CNFs), produced by mechanical fibrillation with or without chemical/enzymatic pretreatment of cellulosic fibers. CNCs are highly crystalline, as implied by the name, generally with length of 50–500 nm, or degree of polymerization (DP) of 100–300 (Battista, 1950; Battista et al., 1956; Nishiyama et al., 2003), and diameter of 3–10 nm. However, the range of crystallinity for a material to be classified as CNCs has not been established in literature.

Difficulties in accurately measuring CNC crystallinity using traditional x-ray diffraction technique (Segal et al., 1959; Park et al., 2010) have added more ambiguity to the definition of CNCs. Further compounding the problem is the fact that existing crystallinity measurement techniques, including x-ray diffraction (Segal et al., 1959), NMR (Larsson et al., 1997) and Raman (Agarwal et al., 2010), are ensemble measurements over a volume of cellulose sample and therefore spatially averaged rather than resolved to the cellulose nanofibrils/nanocrystals level. This has led to erroneous references to morphologically CNC-like cellulosic whiskers without high crystallinity as being CNCs (Montanari et al., 2005; Hirota et al., 2010; Leung et al., 2011; Anderson et al., 2014).

We suggest that differentiating morphological dimensions from crystallinity is highly important. CNCs have been used for many applications where high crystallinity is not important, such as rheology modifiers (Ojala et al., 2016; Grishkewich et al., 2017; Molnes et al., 2018), hydrogels (Hou et al., 2017; Kim et al., 2017; De France et al., 2019) and 3D printing (Jia et al., 2017; Palaganas et al., 2017; Hausmann et al., 2018; Sultan and Mathew, 2018; Wang et al., 2018; Li et al., 2019) for which dispersibility and proper morphology, not crystallinity, are the keys to performance. This has significant commercial implications because the cost of producing CNCs is often higher than for other CNMs. Furthermore, difficulties in economic recovery of mineral acids (mainly sulfuric acid) and the need for salt disposal pose significant challenges. Current utilization of the expensive S-CNCs for applications that do not require crystallinity is primarily due to (1) ready market availability, because several S-CNC pilot facilities and a commercial facility have been established, and (2) lack of recognition of the diversity of CNMs, as reflected by the generalization of CNMs as either CNCs (individually separated crystalline particles) or CNFs.

Here we discuss an "in-between," that is, individually separated, charged, and dispersible CNMs with morphology similar to CNCs but without the specification of crystallinity, which allows flexibility in processing to achieve sustainable and economic production. We call this class of CNMs cellulosic nanowhiskers (CNWs), because the term, though not clearly defined, has been previously used (Braun and Dorgan, 2009; Wang et al., 2012a). Individually separated nanoscale cellulosic whiskers were observed in TEM images of substantially fibrillated cellulose fibers (Wang et al., 2012a). Nanoscale cellulosic whiskers were also obtained from mechanical fibrillation of the cellulosic solid residue (CSR) after concentrated sulfuric acid hydrolysis of bleached fibers (Wang et al., 2012b). They have a similar morphology to CNCs but with low crystallinity due to mechanical fibrillation as measured by x-ray diffraction (Wang et al., 2013). Therefore, they are not CNCs.

Previously, we demonstrated integrated production of both CNCs and CNFs at lab-scale (i.e., gram scale) with desired morphologies using dicarboxylic acids (Chen et al., 2016; Wang et al., 2017). Dicarboxylic acids are weak acids resulting in low CNC yields, but the hydrolyzed CSR can be fibrillated into CNMs for substantially higher overall solids (or CNM) yield. Moreover, as weak solid acids with low solubility dicarboxylic acids have substantial advantages over conventional strong mineral acids in terms of acid recovery (Cai et al., 2020a,b) and lower corrosiveness. Furthermore, maleic acid is a U.S. Food and Drug Administration (FDA)-approved indirect food additive per Code of Federal Regulations 21CFR175-177, and therefore with no environmental impact.

The novelty of the present work is to demonstrate pilot-scale production and characterization of alternative CNMs, i.e., CNWs, as a viable substitute for the crystalline but expensive CNCs, with the objective of sustainable processing at higher yields, better use, and broader commercialization of CNMs. Two different acids were chosen to investigate the scalability of each, as well as different starting materials to produce both lignin free CNWs and lignin-containing CNMs (LCNMs).

MATERIALS AND METHODS

Materials

Bleached kraft eucalyptus dry lap pulp (BEP) from Fibria (Aracruz, Brazil) was used for producing lignin-free CNMs. As described elsewhere (Chen et al., 2016; Zhou et al., 2019), BEP was first soaked in distilled water for 24 h and then disintegrated at 10% solid consistency in a lab disintegrator (TMI, Ronkonkoma, NY, United States) at room temperature for 10,000 revolutions at 312 rpm. Disintegrated pulp was collected after vacuum filtration.

Medium density fiberboard (MDF) fibers were used to produce lignin-containing CNMs. MDF fibers were produced by disk-refining birch (*B. papyrifera*) wood chips in a 30.5-cm pressurized disk refiner (Sprout-Bauer, model 1210P, Muncy, PA, United States), as described previously (Bian et al., 2017b). Birch wood logs were from a tree that was approximately 35 years old harvested from the Rhinelander Experimental Forest, USDA Forest Service Northern Research Station, Rhinelander, WI, United States. After hand debarking and chipping at the USDA Forest Products Laboratory, Madison, WI, United States, wood chips were pre-steamed at 165°C for 10 min with a steam pressure of 0.72 MPa before being fed to the disk refiner at approximately 1 kg (OD weight)/min. Resulting pulp fibers were stored in a plastic bag in a refrigerator for further processing.

Anhydrous maleic acid (MA) and *p*-toluenesulfonic acid (*p*-TsOH), both ACS reagent grade, were purchased from Sigma-Aldrich (St. Louis, MO, United States). A commercial endoglucanase, FiberCare®, was complimentarily provided by Novozymes North America (Franklinton, NC, United States). Protein content of FiberCare® was assayed at 7.53 mg/mL.

Scaled-Up Production of CNMs

Preliminary small-scale fractionations using 10 g MDF and *p*-TsOH were conducted under a wide range of conditions to obtain predictive delignification information for process scale-up. In the present study, 750 g batches of BEP and MDF fibers were hydrolyzed using concentrated aqueous MA and *p*-TsOH, respectively, following a scheme depicted in **Figure 1**. MA was applied to BEP fibers and the stronger acid *p*-TsOH was chosen for the MDF fibers. The different hydrolysis conditions were represented by M*xx*T*yy*t*zz* for BEP and P*xx*T*yy*t*zz* for MDF, where M*xx* or P*xx* denote MA or *p*-TsOH acid concentration in *xx* wt%, T*yy* and t*zz* denote hydrolysis temperature in *yy* degree Celsius and reaction duration in *zz* min. All hydrolysis reactions were carried out in a 21-L rotating wood pulping

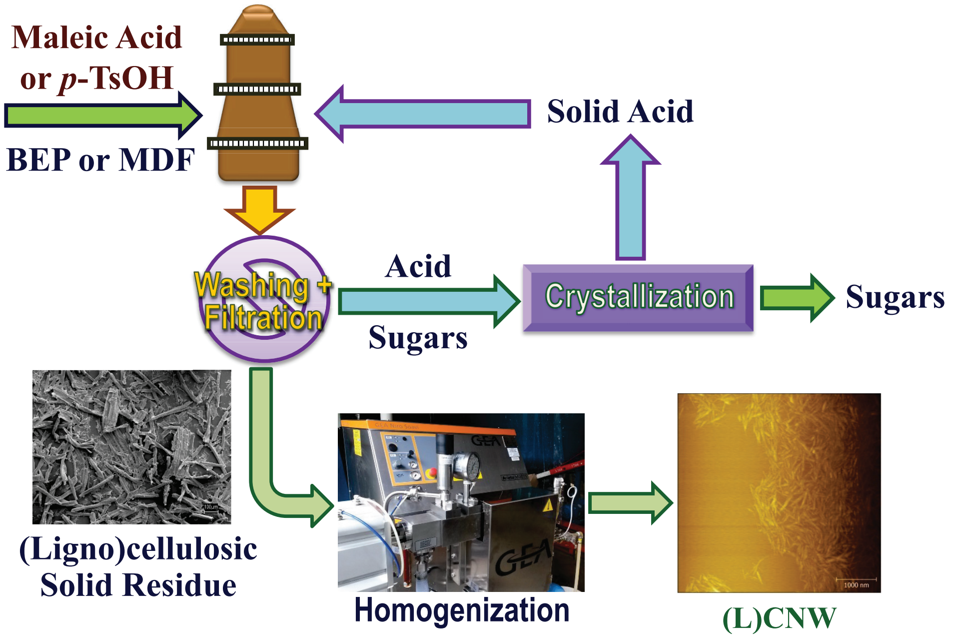

FIGURE 1 | Schematic process flow diagram for pilot-scale production of (ligno)cellulosic nanowhiskers (L)CNWs without separating CNCs (integrated process).

digester at a solid-to-liquor mass ratio of 1:10. Heat-up to the target hydrolysis temperature was only a few minutes. At the end of the reaction period, solids were separated by screen filtration, thoroughly washed, and then fed into a pilot-scale homogenizer (GEA Noro Soavi Ariete NS3015, GEA) for nanoscale fibrillation. The number of passes was varied so as to vary the degree of fibrillation.

Analytical Methods

Chemical composition of untreated and pretreated BEP fibers was analyzed as described previously (Luo et al., 2010) using the standard two-step acid hydrolysis procedure, with resultant hydrolyzates analyzed by ion chromatography using pulsed amperometric detection (ICS-5000, Dionex, Sunnyvale, CA, United States).

Characterizations of CNMs

Crystallinity: For cellulose crystallinity estimation by Raman spectroscopy, the 380-Raman method (Agarwal et al., 2010, 2013) was used. The method determines the crystallinity of a cellulosic sample based on the ratio of Raman scattering intensity at 380 cm^{-1} over the intensity at 1096 cm^{-1} through calibration using the crystallinity data from wide angle x-ray scattering (WAXS) measurements of a set of well-defined cellulosic samples. CNM samples were analyzed in triplicate using a Bruker MultiRam spectrometer (Bruker Instruments Inc., Billerica, MA, United States) equipped with a 1064-nm 1000-mW continuous wave (CW) diode-pumped Nd:YAG laser operated at 600 mW for sample excitation. Sample pellets were made from ~0.1 g, and 2048 scans were co-added. Bruker OPUS 7.2 software was used to determine peak positions and process the spectral data. Some samples produced too much fluorescence, so their 380-Raman crystallinity could not be determined. Wide-angle X-ray diffraction measurements of crystallinity were carried out using a Bruker D8 Discover system with Cu-Kα radiation (Bruker Corp., Billerica, MA, United States) at the Material Science Center, University of Wisconsin (Madison, WI, United States). As described previously (Chen et al., 2015), CNM suspensions were first freeze-dried to avoid film formation and to minimize the potential for preferred orientation in the samples. The freeze-dried samples were pressed into 100-mg, 8-mm-diameter pellets using hydraulic compression (180 MPa). A spot size of 0.5 mm was used. Scattering signals were collected in a 2-min period for every specimen. CrI was calculated according to the Segal method (Segal et al., 1959): $CrI = 100 \times (I_{200} - I_{am})/I_{200}$ with I_{am} the intensity at $2\theta = 18°$.

Atomic Force Microscopy (AFM)

The morphology of CNM samples was characterized by AFM (AFM Workshop, Signal Hill, CA, United States) using a tip curvature radius and vibration frequency of 10–15 nm and 160–225 kHz, respectively. Approximately 0.1wt% suspensions were dispersed with sonication, then a drop of each suspension was placed onto a clean mica surface and air-dried overnight at room temperature prior to characterization.

Thermogravimetric Analyses (TGA)

The thermal stability of CNM samples was analyzed using a Pyris 1 TGA (Perkin-Elmer, Inc., Waltham, MA, United States). Samples were dried overnight at 105°C. Aliquots of approximately 8–10 mg were heated from ambient temperature to 700°C at a rate of 20°C/min, with a highly purified nitrogen stream at 20 mL/min continuously passing into the furnace during pyrolysis.

Surface Properties

The carboxyl group content of CNM samples was determined by the back-titration method (Jeon et al., 1999; Stojanović et al., 2005). Briefly, 50 mg of CNF suspension (0.2 wt%) was carefully added to 10 mL of 0.1 M NaOH maintained at 50°C and stirred for 30 min. The excess NaOH was back-titrated with standard 0.025 M HCl using phenolphthalein as the indicator. Surface charge was measured using a zeta potential analyzer (Nanobrook Omni, Brookhaven Instruments, Holtsville, NY, United States) based on monitoring electrophoretic mobility using phase analysis light scattering (PALS). The same instrument was used for DLS particle sizing. Each sample was circulated five times for a total of 10 min to obtain averaged size. These two methods were developed for spherical particles but were used as an approximation for CNWs in this study.

Suspension Rheology

Rheological analyses of CNC, CNW, and CNF suspensions were performed using a rotational rheometer (MCR 302 Anton Paar Physica) with 43-mm-diameter steel plates in parallel plate geometry. Steady-state shear viscosity curves were generated for all samples in a shear rate range of 0.01 to 1000 s^{-1}. The time required to reach steady state at 0.01 s^{-1} was determined by a transient test, and the sampling time used to generate the flow curves was decreased with increasing shear rate. The average of duplicate measurements is reported.

RESULTS AND DISCUSSION

Process Scale-up

The combined cellulose hydrolysis factor (CHF_G, where G denotes glucan or cellulose) and combined delignification factor (CDF) [Eqs. (S1a) and (S2a)] developed in our earlier studies (Zhu et al., 2012, 2019; Wang et al., 2017) were used to scale-up (750 g OD weight) experiments, rather than using the individual hydrolysis process parameters such as acid concentration, temperature, and time. This is because cellulose depolymerization, predicted by CHF_G (Eq. S1b; **Supplementary Table S1** and **Supplementary Figure S1**), and delignification, predicted by CDF (Eq. S2b; **Supplementary Table S1** and **Supplementary Figure S2**), are considered critical variables in nanoscale fibrillation of bleached chemicals pulps (Qin et al., 2016; Wang et al., 2017) and raw lignocelluloses (Bian et al., 2017b), respectively. Specifically, we used similar reaction severity (i.e., CHF_G, for BEP or CDF for MDF) in the scale-up as was found in the lab scale experiments to produce the desired CNM morphology. For example, our earlier lab-scale study (Wang et al., 2017) indicated that cellulose DP of approximately 250 or lower is required to obtain short, individually separated CNWs from MA-hydrolyzed BEP through mechanical fibrillation. Therefore, pilot-scale runs M1 and M2 as listed in **Table 1** were targeted for CNWs with cellulose DP between 200 and 250; runs M3 and M4 were for producing long fibril-network CNFs. For producing lignin-containing CNWs (LCNWs) using *p*-TsOH hydrolysis of MDF, Run P1 (**Table 1**) was targeted for 50% delignification; P2 with a lower severity was to explore a lower limit for producing LCNWs. P3 and P4 were for lignin-containing CNFs (LCNFs) with high lignin content and varied morphologies (**Supplementary Figure S3**).

We observed that increasing reaction temperature from 100°C (M2) to 120°C (M1), or CHF_G from 3.6 (M2) to 37 (M1) (an order of magnitude), resulted in only a small reduction in DP from 223 (M2) to 200 (M1) due to the asymptotic nature of reaching LODP; however, xylan retained on the hydrolyzed solids was reduced from 57% to 27% which should facilitate fibrillation.

It is important to note that either *p*-TsOH or MA can be used on bleached fibers for producing CNMs (Chen et al., 2016) or

TABLE 1 | Reaction severity of scale-up runs, predicted final cellulose DP (BEP), residual xylan X_R (BEP and MDF) and residual lignin L_R (MDF).

				Predicted					Measured[5]			
Run	**Condition[1]**	**Acid**	**Products**	**CHF_G; CDF**	**CHF_X**	**DP[2]**	**X_R[3] (%)**	**L_R[4] (%)**	**Glucan (%)**	**Xylan (%)**	**Lignin (%)**	**Solids yield (%)**
BEP						1027			; 78.1 ± 1.0	; 15.5 ± 0.6	; 0.9 ± 0.5	100
M1	M70T120t120	MA	CNW	37.4;	233	200	1		; 75.5 ± 2.9	27; 7.1 ± 0.4	; 0.9 ± 0.01	58.2
M2	M70T100t120	MA	CNW;CNC	3.58;	22.3	223	45		; 77.7 ± 2.4	57; 10.7 ± 0.7		82.8
M3	M50T90t60	MA	CNF	0.28;	0.8	819	81		; 74.6 ± 4.4	90; 14.6 ± 0.5		95.2
M4	M40T80t60	MA	CNF	0.05;	0.1	976	97		; 63.9 ± 3.1	97; 15.2 ± 1.2	; 0.8 ± 0.02	98.5
MDF									; 34.6 ± 1.0	; 20.8 ± 0.5	; 23.8 ± 0.1	100
P1	P60T80t60	p-TsOH	LCNW	; 616	171		26	34	; 56.6 ± 0.1	36; 12.7 ± 0.2	24; 9.6 ± 1.1	58.4
P2	P50T81t27	p-TsOH	LCNW	; 105	34.6		40	49	; 58.2 ± 0.3	34; 10.8 ± 0.1	23; 8.5 ± 0.7	65.4
P3	P40T80t60	p-TsOH	LCNF	; 73.5	30.1		33	54	; 52.3 ± 3.5	37; 10.9 ± 0.01	55; 18.8 ± 0.5	70.0
P4	P50T73t34	p-TsOH	LCNF	; 62.2	25.2		45	58	; 57.7 ± 1.3	44; 14.7 ± 0.5	56; 21.1 ± 0.4	62.8

[1] Sample labeling: M and P denote MA and p-toluenesulfonic acid, respectively; xx is acid concentration in wt%; Tyy denotes reaction temperature in yy degree C; tzz denotes reaction duration in zz min. [2] Eq. S1b; [3] Eq. S1d; [4] Eq. S2b. [5] The numbers before the semi-columns are percent of xylan or lignin retained in water insoluble solids (WISs) calculated from measured yields and compositional analysis of the WISs; numbers after semi-columns are measured component content in the fractionated water insoluble solids.

on unbleached fibers for producing LCNMs (Bian et al., 2017a); however, MA cannot delignify the unbleached fibers probably due to extensive lignin condensation, though it is highly effective in solubilizing lignin in untreated wood for producing LCNMs, as recently demonstrated (Cai et al., 2020a,b).

CNM Morphologies

Morphology of CNMs from scaled-up runs (750 g) was evaluated by comparing AFM images to those from our earlier published lab-scale (5 g) runs (Wang et al., 2017). Pilot-scale MA-CNCs using severity CHF_G = 3.58 (run M2) were similar to, lab-scale severity CHF_G = 4.08 demonstrating a successful scale-up, as shown in **Figure 2A** where I and II designate lab- and pilot-scale, respectively.

CNF production was accomplished by mechanical fibrillation of water-insoluble cellulosic solids from MA hydrolysis of BEP fibers. Fibrillation was carried out using a homogenizer for the pilot-scale and a microfluidizer for the lab-scale run for varied passes or extent of fibrillation. Pilot-scale CNFs from severity CHF_G = 0.28 (run M3) were also morphologically similar to lab-scale CNFs from severity CHF_G = 0.29 despite differences in their individual hydrolysis conditions, i.e., acid concentration, temperature and reaction time, for example, comparing I.CNF-5P with II.CNF-5P shown in **Figure 2A** (5P stands for 5 passes in fibrillation).

LCNFs from *p*-TsOH fractionation of MDF were also compared. The higher severity CDF = 105 of the pilot-scale run (P2) than the lab-scale run CDF = 70.8 was due to a slight overshoot in temperature (**Supplementary Figure S4**) and a delay in quenching the pilot-scale reaction. As a result, pilot-scale LCNFs had a lignin content of 8.5% compared with 16% from the lab-scale run (Bian et al., 2017b). However, morphological similarity between these two runs was achieved simply by applying fewer passes in the homogenizer for the pilot-scale sample, as shown by the AFM images and AFM-measured height distributions (**Figure 2B**).

After accomplishing scale-up of CNCs, CNFs, and LCNFs, we targeted the primary interest of the present study: CNWs – for higher yields with similar morphology to the more crystalline but lower yield CNCs. **Figure 3** shows AFM images of (L)CNWs from three high-severity runs: M1, M2, and P1. MA hydrolysis of BEP with subsequent mechanical fibrillation produced individually separated, short whiskers, i.e., CNWs, ranging from 100 to 800 nm in length, with only a single pass through homogenization. Continued fibrillation further reduced aggregations and diameters of the whiskers, resulting in more uniform dimensions. Short and individually separated, lignin-containing LCNWs were obtained after one pass homogenization of the fractionated MDF under P1. However, a sample aliquot after three passes showed significantly longer fibrils, which strongly suggests that P1 condition is not severe enough, or lacking sufficient cellulose depolymerization, to reduce all the fibrils into LCNWs, which will be the topic of future study.

The morphology of pilot-scale CNWs was compared to S-CNCs and CNCs from MA hydrolysis as shown in **Figure 3**. CNWs from the most severe condition (M1-3P) resembled the

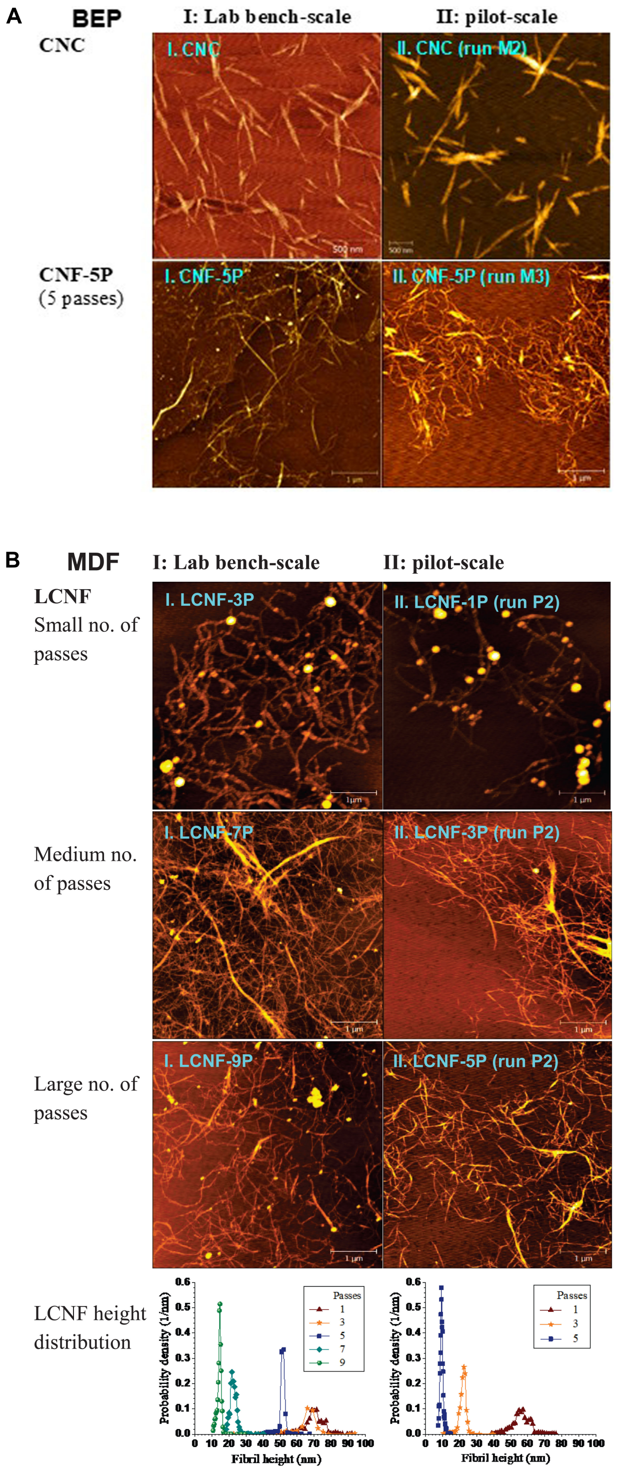

FIGURE 2 | Morphological comparisons of CNMs between samples from lab bench-scale (5 g oven dry weight) runs (I, left panel) and corresponding pilot-scale (750 g) runs (II, right panel). **(A)**: CNC and CNF from BEP using MA; I.CNC: CHF_G = 4.08, I.CNF: CHF_G = 0.29, 5 passes; II.CNC: CHF_G = 3.58, II.CNF: CHF_G = 0.28, 5 passes. **(B)**: LCNF from MDF using p-TsOH with varying numbers of passes through fibrillation. I.LCNF: CDF = 70.8, 3–9 passes, II.LCNF: CDF = 105, 1–5 passes. Detailed reaction conditions are listed in **Table 1**.

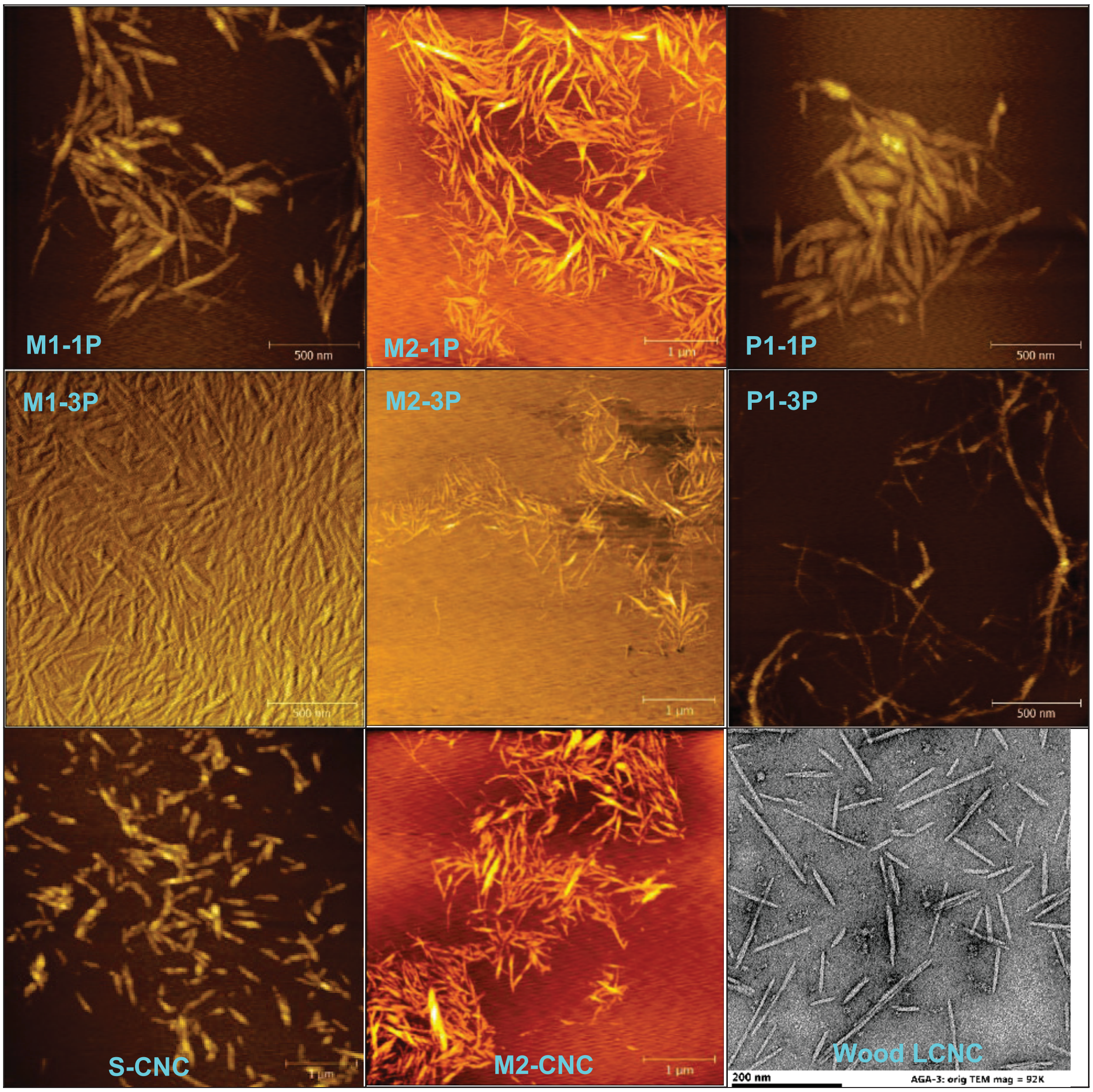

FIGURE 3 | AFM images of CNWs from three high severity pilot-scale runs (M1, M2, and P1) with varied passes (-xP) of homogenization (top and middle rows), S-CNCs (bottom left), CNCs from maleic acid hydrolysis (bottom middle) and LCNCs from sulfuric acid hydrolysis of poplar wood (bottom right).

S-CNCs except longer, i.e., 365 vs.185 nm and aspect ratio 12.2 vs. 7.7 (**Supplementary Table S2**), respectively; CNWs from less severe conditions (M2-1P) were very similar to the MA-CNCs separated from this run by dialysis, i.e., 325 vs. 240 nm and aspect ratio 11.6 vs. 9.2 nm (**Supplementary Table S2**). The pilot-scale LCNWs (P1-1P) were both longer and thicker than LCNCs obtained from direct concentrated sulfuric acid hydrolysis of Wiley-milled poplar wood (Agarwal et al., 2018), i.e., 430 vs. 125 nm and 40 vs. 9 nm (**Supplementary Table S2**).

Post-fibrillation Enzymatic Treatment

Post-fibrillation enzymatic treatment can be an effective way to reduce fibril aggregations for producing CNWs with low environmental impact. Two fibrillated CNM samples (M2-3P and M3-5P) were enzymatically treated using a commercial endoglucanase, FiberCare®, at very low loadings of 0.2 and 0.4 mg protein/g CNFs, respectively. The results (**Figure 4**) clearly indicate the effectiveness of endoglucanase treatments to reduce aggregation, diameter, entanglement and length of CNMs. At a lower endoglucanase loading of 0.2 mg/g, M2-3P became much more uniform in diameter with only 4 h of enzymatic treatment (based on AFM measured topographic height distribution, comparing M2-3P with M2-3P-E4h). The average AFM measured fibril height was also reduced from approximately 16 nm to 13 nm. Extended treatment to 48 h (M2-3P-E48h) did not substantially impact the morphology, suggesting potential accessible sites, such as dislocations and disorder regions, have been effectively digested during the shorter period treatment which left fairly uniform and ordered CNW.

Similar effectiveness was also observed for M3-5P with a fibril network morphology but with a similar height of approximately

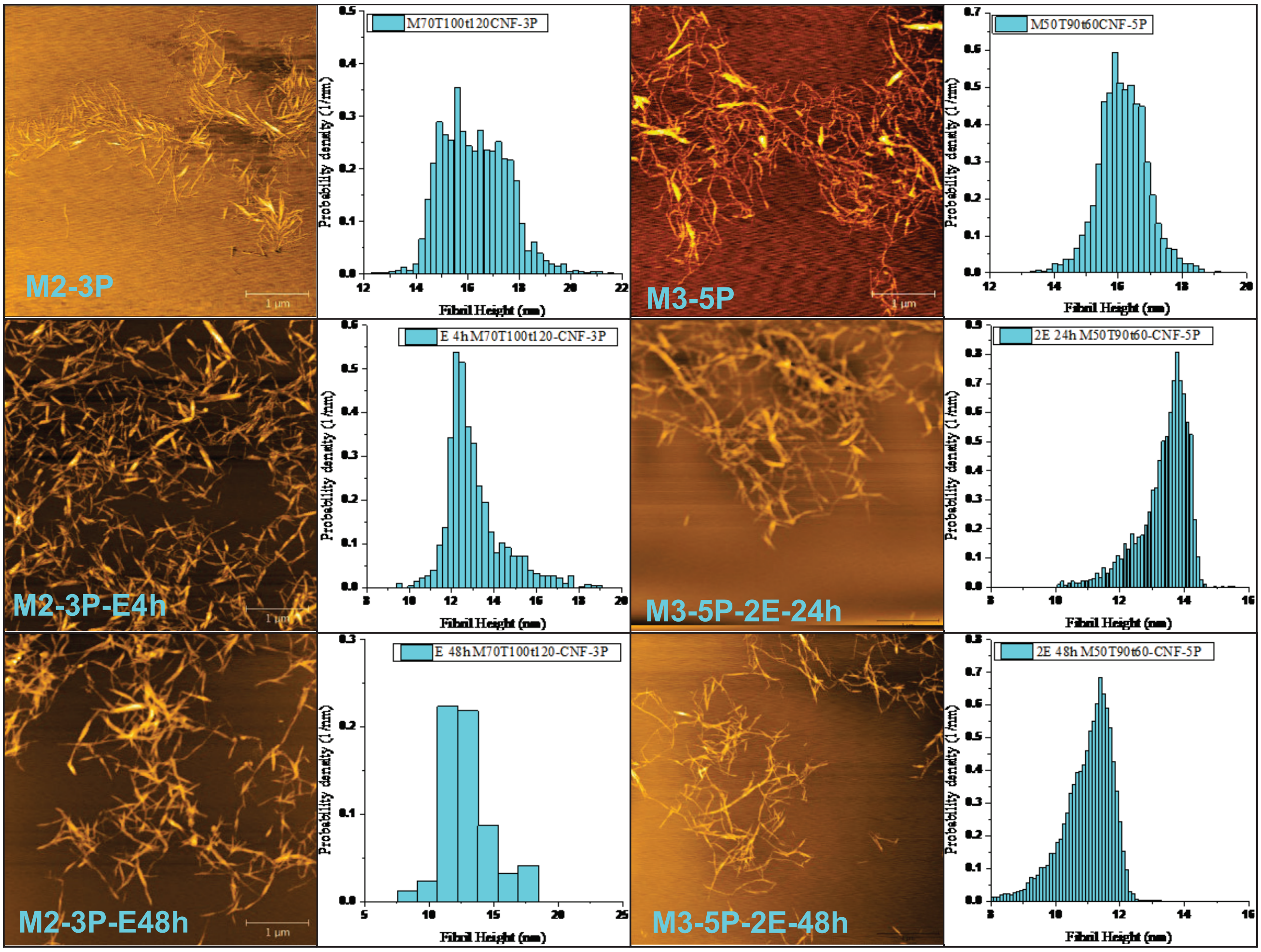

FIGURE 4 | CNM morphological changes through post-fibrillation endoglucanase treatments. FiberCare loading in mg protein/g CNMs: E = 0.2 and 2E = 0.4 for sample M2-3P and M3-5P, respectively. Treatment time: 4 – 48 h.

TABLE 2 | Effect of mechanical fibrillation levels on CrI of CNMs.

		Segal-I		Segal-II		380-Raman	
Run #	**Hydrolysis condition**	**1P**	**3P**	**1P**	**3P**	**1P**	**3P**
M1	M70T120t120	89.1	85.1	77.6	74.0	51.7 ± 2.0	42.5 ± 1.0
M4	M40T80t60	85.0	84.3	72.9	72.3	47.6 ± 1.4	42.1 ± 1.0
P1	P60T80t60	82.0	81.6	68.1	67.0	NA*	NA*
P3	P40T80t60	81.8	77.8	67.5	64.2	NA*	NA*

**Not available; could not be estimated due to fluorescence signal in the Raman spectra.*

16 nm (3rd and 4th columns in **Figure 4**). With a double endoglucanase loading of 0.4 mg/g, the sample network was effectively broken down after 48 h treatment (M3-5P-2E48h). The CNM average height was reduced to approximately 13 and 11 nm after 24 and 48 h treatment, respectively. These results suggest that post-fibrillation enzymatic treatment can be an effective tool to modify CNM morphologies for producing individually separated CNWs, or substantially less entangled CNFs, in agreement with literature (Henriksson et al., 2007; Pääkko et al., 2007; Zhu et al., 2011; Wang et al., 2015, 2016; Yarbrough et al., 2017).

Crystallinity

Crystallinity index (CrI) of selected samples was measured by both Raman spectroscopy (380-Raman) and X-ray diffraction (Segal methods I and II, with and without background subtraction, respectively) as listed in **Table 2**. Segal II CrI for M1-1P (77.6%) and M1-3P (74.0%) are lower than that reported for CNCs (81%) produced from concentrated oxalic acid hydrolysis of the same BEP (Chen et al., 2016), but equivalent to that reported for S-CNCs from the same BEP (Chen et al., 2015). In this sense, the high-severity (M1) product could be called CNCs, though not a product of strong acid hydrolysis and dialysis. In contrast to the insensitivity of the Segal method to changes in crystallinity, the 380-Raman method indicated a much larger reduction in CrI (18% vs. 5%) upon homogenization, thereby suggesting these materials should be called CNWs rather than CNCs.

The reduction of crystallinity by extensive mechanical fibrillation was also confirmed from Raman measurements. Raman CH_2 bands at 1481 and 1462 cm^{-1} have been attributed to crystalline and disordered celluloses, respectively (Schenzel et al., 2005). As shown in **Figure 5**, the CH_2 band shifted from 1472 to 1468 cm^{-1} in M1 going from 1 to 3 pass homogenization (i.e., M1-1P to M1-3P). A similar but smaller shift (1469 to 1467 cm^{-1}) was observed in samples from less severe hydrolysis (i.e., M4-1P to M4-3P).

Another confounding factor with CNM classification via crystallinity measurement is illustrated with the less severity samples P1 and P3, where unlike the M1 sample with low xylan and near-zero lignin content (**Table 1**), the presence of hemicelluloses and/or lignin obscures the reduction of CrI after more homogenization, as shown in **Table 2**.

Thermal Stability Analyses

Thermogravimetric analyses (TGA) indicate CNWs M1-1P and M1-3P have good thermal stability. The onset of degradation, as defined as $dW/dT \geq -1$, was at approximately 247°C and 252°C, respectively, as shown in **Figure 6**. These values are lower than 301°C for MA-CNCs produced at M60T100t45 reported previously, but notably higher than 218°C for S-CNCs (Chen et al., 2016).

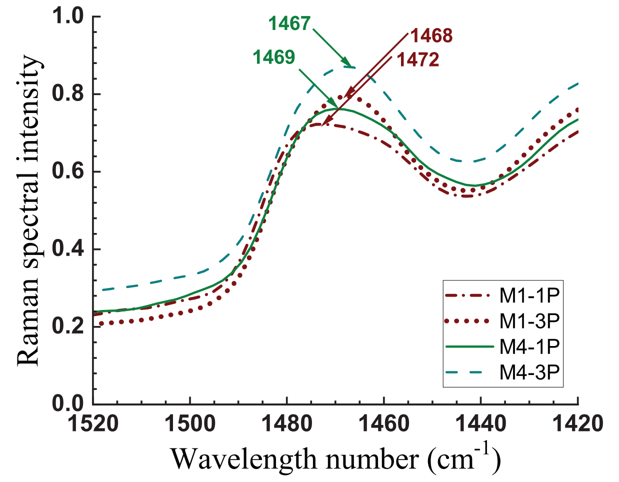

FIGURE 5 | Raman spectra of two sets of CNMs showing the CH_2 band shifts with increased mechanical fibrillation (1 pass to 3 passes homogenization).

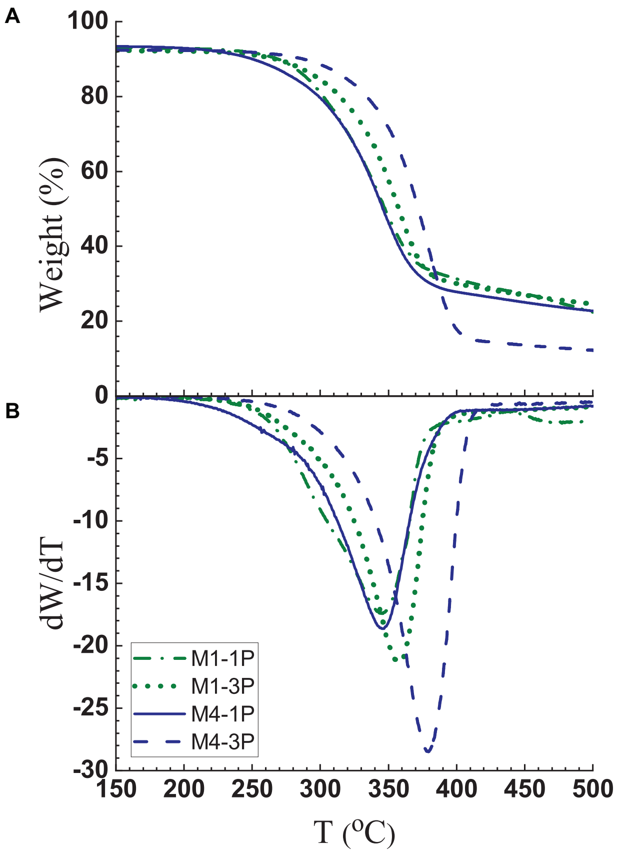

FIGURE 6 | Thermogravimetric analyses of CNW samples from M1 and M4 after 1 and 3 passes. **(A)** Weight loss; **(B)** Derivative weight loss.

It is interesting to notice that increasing fibrillation from one pass to three passes through homogenization increased thermal stability for both M1 CNWs and M4 CNFs. This is perhaps due to the increased exposure of hydroxyl groups with more fibrillation. Homogenization is primarily a shearing action that fibrillates, rather than cuts, cellulose fibrils resulting in minimal cellulose depolymerization. This can be seen from the DP data listed in **Table 3**, as well as from the sample morphologies shown in AFM images in **Figure 3** and **Supplementary Figure S3**. The temperature shift at maximal weight loss is due to increased fibrillation and, as shown in **Figure 6B**, was obvious for both CNMs from M1 and M4. Therefore, we confidently demonstrate that reduction in thermal stability due to depolymerization is low.

Surface Properties

Surface functionalization and charge are important properties to dispersion. M2-CNCs had more than double the carboxyl group content than the corresponding CNWs M2-1P and M2-3P (0.25, 0.11 and 0.13 mmol/g, respectively), as shown in **Table 3** and in agreement with our earlier lab-scale study (Chen et al., 2016); and the higher-severity M1-CNWs had a greater carboxyl group content ($\geq$ 0.25 mmol/g) than the M2-CNWs, as expected.

TABLE 3 | Surface charge and carboxyl group content along with dynamic light scattering (DLS) measured size and degree of polymerization of CNM samples listed in **Table 1**.

CNM Label	Zeta-potential (mV)	DLS size (nm)	Carboxyl content (mmol/g)	DP
M1-1P	−33.5 ± 1.1	693 ± 42	0.250	203 ± 0
M1-3P	−44.5 ± 1.6	649 ± 33	0.270	178 ± 1
M2-CNC	−37.5 ± 0.5	629 ± 25	0.252	N/A *
M2-1P	−34.1 ± 1.6	712 ± 52	0.113	N/A *
M2-3P	−56.6 ± 0.6	678 ± 46	0.129	177 ± 3
M3-1P	−32.5 ± 1.0		0.011	372 ± 1
M3-3P	−48.4 ± 2.8		0.016	331 ± 2
M4-1P	−30.6 ± 3.6			683 ± 8
M4-3P	−30.0 ± 1.8			629 ± 7
P1-1P	−30.7 ± 3.6			
P1-3P	−31.8 ± 2.9			
P3-1P	−27.4 ± 2.2			
P3-3P	−31.7 ± 2.6			

**Not analyzed due to limited sample available.*

M1-1P and M2-1P had surface charge similar level to M2-CNC (−33.5, −34.1, and −37.5 mV, respectively). Increasing mechanical fibrillation increased surface charge for both M1-3P and M2-3P to approximately −45 mV or higher. These numbers suggest that CNWs from M1 and M2 through mechanical fibrillation are just as easily dispersible as M2-CNC.

Further reduction of hydrolysis severity decreased carboxylation as expected (Chen et al., 2016), as can be seen from M3 and M4 samples. Notably, however, despite the very low carboxyl content of only approximately 0.01 mmol/g, surface charge exceeds −30 mV, which is sufficient for dispersion. This suggests that surface charge is affected not only by carboxyl groups but also by hydroxyl groups. With three passes through homogenization, surface charge was increased to over −45 mV for both M2-3P and M3-3P.

Similarly, LCNF samples are also charged, but lower than the MA-produced CNM samples (**Table 3**). This is because p-TsOH does not functionalize fibers. Surface charges of LCNFs from P1 and P3 treatments were below −30 mV. As was the case before, surface charge increased with more fibrillation.

Aqueous Suspension Rheology

As shown in **Figures 7A–C**, the S-CNC suspensions have typical semi-diluted CNC suspension rheology behavior up to 3 wt%, as also indicated in literature (Orts et al., 1998; de Souza Lima and Borsali, 2004; Oguzlu et al., 2017), i.e., shear thinning at low shear rates, a plateau region at moderate shear rates, then shear thinning again at high shear rates. CNW M1-3P at 0.5 wt% concentration (**Figure 7A**) also shows semi-diluted suspension behavior. As a matter of fact, its viscosity vs. shear rate curve almost overlaps with the curve for S-CNCs. However, at 1.5 wt%, M1-3P behaves similar to concentrated S-CNC suspension, as reported in the literature (Bercea and Navard, 2000; Shafiei-Sabet et al., 2012, 2014), i.e., viscosities decreased linearly with increased shear rate.

Compared with the S-CNCs with a mean aspect ratio of 7.7, CNW M1-3P has a greater aspect ratio of 12.2 (**Supplementary Table S3**). As a result, M1-3P has a greater range of viscosity within a very narrow concentration range under the same shear rate. For example, M1-3P viscosity increased over three orders of magnitude at a low shear rate of 0.1 1/s when suspension concentration was increased from 0.5 wt% to 1.5 wt% as shown in **Figure 7D**. There is essentially no change in viscosity for S-CNCs. At a moderate shear rate of 10 1/s, M1-3P viscosity increased approximately three orders of magnitude, much greater than the increase for S-CNCs when concentration was increased from 0.5 wt% to 1.5 wt% (**Figure 7E**). Even at a high shear rate of 1000 1/s, M1-3P viscosity increased approximately one order of magnitude but S-CNCs viscosity had negligible increase when concentration was increased from 0.5 wt% to 3 wt% (**Figure 7F**). This indicates that CNW M1-3P can be a much more effective rheology modifier than S-CNCs.

The two lignin-containing LCNMs showed some interesting rheological behavior. First, CNF P3-3P, which has a higher lignin content of 18.8% than the 9.6% of P1-3P (**Table 1**), has a lower viscosity under the same shear rate at the same suspension concentration, despite having much more entangled fibril networks (**Supplementary Figure S3**) than P1-3P (**Figure 3**). This indicates that lignin as a hydrophobic molecule plays a significant role in the rheological properties of aqueous lignin-containing CNF suspension, primarily due to limiting interactions with water. Second, it appears that both suspensions have a plateau region at suspension concentration below 1.5 wt% (**Figures 7A,B**). At 3 wt%, this plateau disappears (**Figure 7C**) and viscosity decreased linearly with shear rate, similar to concentrated CNC suspension. Due to their fibril network morphology (**Figure 3** and **Supplementary Figure S3**), these two LCNM suspensions have relatively large viscosity ranges, as shown in **Figures 7D–F**. However, their ranges are smaller to the viscosity range of M1-3P except at very high shear rates (**Figure 7F**). Overall, the rheology properties of these two suspensions were very similar.

Applications of CNWs and Final Thoughts

The CNWs from M2-3P (**Figure 3**) were used for producing unsaturated polyester resin (UPR) nanocomposite, though incorrectly labeled in the study (DiLoreto et al., 2019). It was demonstrated that freeze-dried M2-3P can be directly used to reinforce UPR and resulted in 61% and 48% increase in glassy and rubbery modulus, respectively, over the UPR baseline; and glass transition temperature was increased by 12°C. Using S-CNCs decreased UPR nanocomposite tensile strength. Equivalent gains in glassy and rubbery modulus were achieved only after modifying S-CNCs using methyl(triphenyl) phosphonium; however, this resulted in only a 4.5°C gain in glass transition temperature.

Based on the rheology data presented here, we see CNWs being particularly suitable for rheology modification and 3D printing. In this study, we demonstrated scale-up production

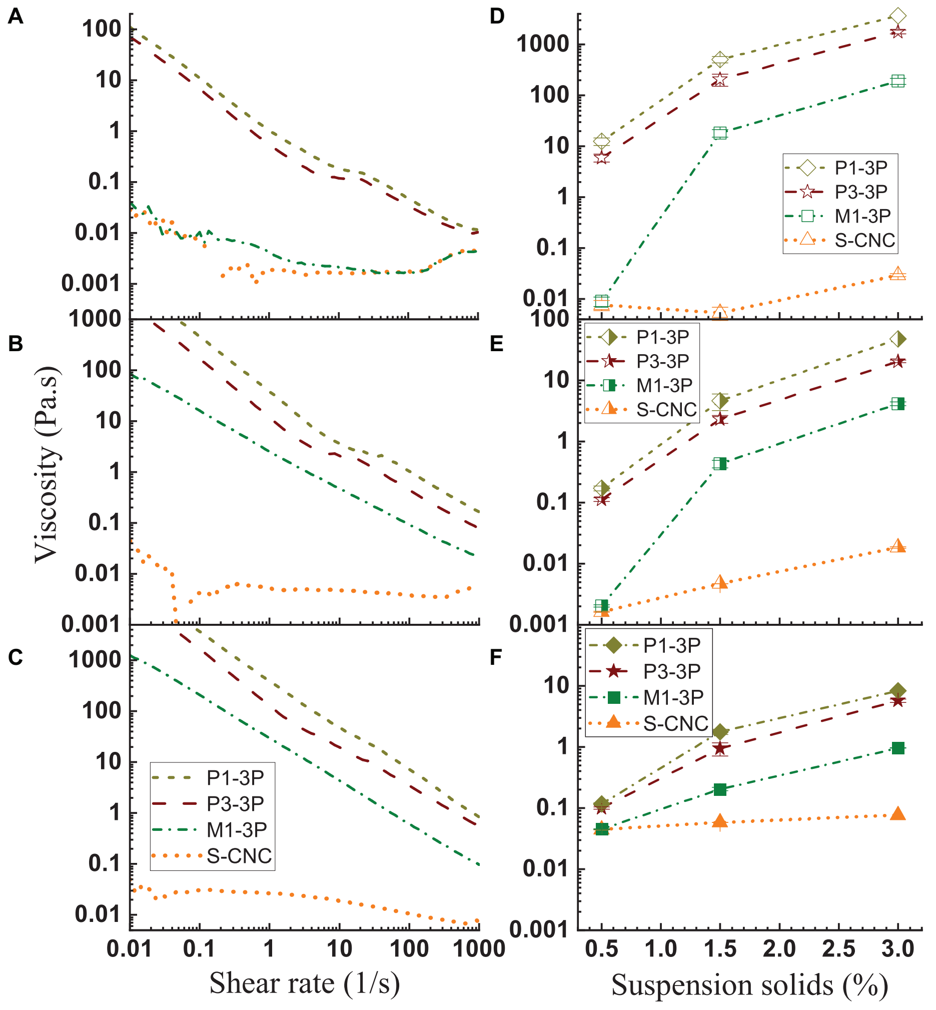

FIGURE 7 | Effects of shear rate and CNM solids loading on CNM suspension viscosity. Left column: Solids loadings = 0.5 wt% **(A)**; 1.5 wt% **(B)**; 3.0 wt% **(C)**. Right column: Shear rate = 0.1 1/s **(D)**; 10 1/s **(E)**; 1000 1/s **(F)**.

with good control of sample morphology. Because MA is a solid acid with a relatively low solubility at room temperature, solidification to partially recover acid can be readily achieved (Chen et al., 2016; Cai et al., 2020a). Using mature technology, the remaining acid can be used to dehydrate the dissolved xylose to furfural at elevated temperatures (Cai et al., 2020a). When commercial bleached pulp fibers are used, the spent liquor is fairly clean after furfural dehydration and distillation and can be simply reused (Cai et al., 2020a). By producing CNWs with morphological and surface charge properties similar to those of CNCs but without dialysis, we can substantially reduce water usage to achieve sustainable production with favorable yields.

CONCLUSION

This study describes a class of cellulosic nanomaterials produced at pilot-scale using maleic acid, an easily recyclable solid dicarboxylic acid and FDA approved indirect food additive per code of federal regulation 21CFR175-177, hydrolysis with subsequent mechanical nanoscale fibrillation, which we call cellulosic nanowhiskers (CNWs). Although crystallinity is not required in classifying CNWs, we characterized crystallinity, along with morphology, surface properties, and suspension rheology. We demonstrated some applications in which CNWs outperform the more expensive crystalline S-CNCs. We clarified why CNCs should not be used for applications that do not require crystalline property, such as rheology modifiers and 3D printings. By both Raman spectroscopy and X-Ray diffraction measurements, we demonstrated the reduction in crystallinity of CNMs with mechanical fibrillation. We therefore put forth the argument that CNWs should not be termed CNCs, although CNWs such as those from MA hydrolysis, can be crystalline with very similar morphology and surface charge to CNCs. Furthermore, we demonstrated that the surface carboxylated CNWs produced from maleic acid hydrolysis have good surface charge of −35 mV or higher that facilitated dispersion suitable for a variety of applications to substitute CNCs. Both CNW and lignin-containing LCNW suspensions, within a very narrow concentration range, exhibit a wide range of viscosity 0.001 to 1000 Pa.s under a range of shear rates for better performance as a rheological modifier compared to the viscosity of 0.001 – 0.1 Pa.s of traditional sulfuric acid S-CNCs. Finally, the scale-up showed good control of product morphology.

DATA AVAILABILITY STATEMENT

All datasets presented in this study are included in the article/**Supplementary Material**.

AUTHOR CONTRIBUTIONS

HW conducted CNM characterization including AFM, carboxyl group and surface charge, and CNM suspension rheology. JJZ conducted post-fibrillation enzymatic treatment and AFM of the treated samples. QM conducted fractionation studies to develop scale-up factors. UA conducted Raman scattering characterization and crystallinity analyses. RG and RR conducted pilot-scale CNMs and S-CNC production. CB conducted x-ray crystallinity measurements. JYZ initiated the research and wrote most of the manuscript. All authors contributed to the article and approved the submitted version.

FUNDING

This work was conducted at the USDA Forest Products Lab (FPL) while HW was a visiting scientist under the sponsorship of Guangzhou Elite Project of China and a China Science Foundation Postdoctoral Fellowship (2019TQ0102).

ACKNOWLEDGMENTS

We acknowledge Dr. Ronald Zalesny, Jr. of Institute for Applied Ecosystem Studies of the USDA Forest Service, Northern Research Station for providing birch wood logs for the study. We also acknowledge Kolby Hirth of FPL for many helpful discussions and suggestions.

SUPPLEMENTARY MATERIAL

The Supplementary Material for this article can be found online at: https://www.frontiersin.org/articles/10.3389/fbioe.2020.565084/full#supplementary-material

REFERENCES

Agarwal, U. P., Ralph, S. A., Reiner, R. S., Hunt, C. G., Baez, C., Ibach, R., et al. (2018). Production of high lignin-containing and lignin-free cellulose nanocrystals from wood. *Cellulose* 25, 5791–5805. doi: 10.1007/s10570-018-1984-z

Agarwal, U. P., Reiner, R. S., and Ralph, S. A. (2010). Celulose I crystallinity determination using FT-Raman spectroscopy: univariate and multivariate methods. *Cellulose* 17, 721–733. doi: 10.1007/s10570-010-9420-z

Agarwal, U. P., Zhu, J. Y., and Ralph, S. A. (2013). Enzymatic hydrolysis of loblolly pine: effects of cellulose crystallinity and delignification. *Holzforschung* 67, 371–377. doi: 10.1515/hf-2012-0116

Anderson, S. R., Esposito, D., Gillette, W., Zhu, J. Y., Baxa, U., and McNeil, S. E. (2014). Enzymatic preparation of nanocrystalline and microcrystalline cellulose. *TAPPI J.* 13, 35–41. doi: 10.32964/tj13.5.35

Battista, O. A. (1950). Hydrolysis and crystallization of cellulose. *Industry Eng. Chem.* 42, 502–507. doi: 10.1021/ie50483a029

Battista, O. A., Coppicic, S., Howsmon, J. A., Morehead, F. F., and Sisson, W. A. (1956). Level-off degree of polymerization: relation to polyphase structure of cellulose fibers. *Ind. Eng. Chem.* 48, 333–335.

Bercea, M., and Navard, P. (2000). Shear dynamics of aqueous suspensions of cellulose whiskers. *Macromolecules* 33, 6011–6016. doi: 10.1021/ma000417p

Bian, H., Chen, L., Dai, H., and Zhu, J. Y. (2017a). Integrated production of lignin containing cellulose nanocrystals (LCNC) and nanofibrils (LCNF) using an easily recyclable di-carboxylic acid. *Carbohyd. Polym.* 167, 167–176. doi: 10.1016/j.carbpol.2017.03.050

Bian, H., Chen, L., Gleisner, R., Dai, H., and Zhu, J. Y. (2017b). Producing wood-based nanomaterials by rapid fractionation of wood at 80°C using a recyclable acid hydrotrope. *Green Chem.* 19, 3370–3379. doi: 10.1039/c7gc00669a

Braun, B., and Dorgan, J. R. (2009). Single-step method for the isolation and surface functionalization of cellulosic nanowhiskers. *Biomacromolecules* 10, 334–341. doi: 10.1021/bm8011117

Cai, C., Hirth, K., Gleisner, R., Lou, H., Qiu, X., and Zhu, J. Y. (2020a). Maleic acid as a dicarboxylic acid hydrotrope for sustainable fractionation of wood at atmospheric pressure and $\leq$ 100°C: mode and utility of lignin esterification. *Green Chem.* 22, 1605–1617. doi: 10.1039/C9GC04267A

Cai, C., Li, J., Hirth, K., Huber, G. W., Lou, H., and Zhu, J. Y. (2020b). Comparison of two acid hydrotropes for sustainabl fractionation of birch wood. *Chemsuschem* 13. doi: 10.1002/cssc.202001120

Chen, L., Wang, Q., Hirth, K., Baez, C., Agarwal, U. P., and Zhu, J. Y. (2015). Tailoring the yield and characteristics of wood cellulose nanocrystals (CNC) using concentrated acid hydrolysis. *Cellulose* 22, 1753–1762. doi: 10.1007/s10570-015-0615-1

Chen, L., Zhu, J. Y., Baez, C., Kitin, P., and Elder, T. (2016). Highly thermal-stable and functional cellulose nanocrystals and nanofibrils produced using fully recyclable organic acids. *Green Chem.* 18, 3835–3843. doi: 10.1039/c6gc00687f

De France, K. J., Badv, M., Dorogin, J., Siebers, E., Panchal, V., Babi, M., et al. (2019). Tissue response and biodistribution of injectable cellulose nanocrystal composite hydrogels. *ACS Biomater. Sci. Eng.* 5, 2235–2246. doi: 10.1021/acsbiomaterials.9b00522

de Souza Lima, M. M., and Borsali, R. (2004). Rodlike cellulose microcrystals: structure, properties, and applications. *Macromol. Rapid Commun.* 25, 771–787. doi: 10.1002/marc.200300268

DiLoreto, E., Haque, E., Berman, A., Moon, R. J., and Kalaitzidou, K. (2019). Freeze dried cellulose nanocrystal reinforced unsaturated polyester composites: challenges and potential. *Cellulose* 26, 4391–4403. doi: 10.1007/s10570-019-02377-1

Grishkewich, N., Mohammed, N., Tang, J., and Tam, K. C. (2017). Recent advances in the application of cellulose nanocrystals. *Curr. Opin. Coll. Interf. Sci.* 29, 32–45. doi: 10.1016/j.cocis.2017.01.005

Hausmann, M. K., Rühs, P. A., Siqueira, G., Läuger, J., Libanori, R., Zimmermann, T., et al. (2018). Dynamics of cellulose nanocrystal alignment during 3D printing. *ACS Nano* 12, 6926–6937. doi: 10.1021/acsnano.8b02366

Henriksson, M., Henriksson, G., Berglund, L. A., and Lindström, T. (2007). An environmentally friendly method for enzyme-assisted preparation of microfibrillated cellulose (MFC) nanofibers. *Eur. Polym. J.* 43, 3434–3441. doi: 10.1016/j.eurpolymj.2007.05.038

Hirota, M., Furihata, K., Saito, T., Kawada, T., and Isogai, A. (2010). Glucose/glucuronic acid alternating co-polysaccharides prepared from TEMPO-oxidized native celluloses by surface peeling. *Angew. Chem. Intern. Edn.* 49, 7670–7672. doi: 10.1002/anie.201003848

Hou, K., Li, Y., Liu, Y., Zhang, R., Hsiao, B. S., and Zhu, M. (2017). Continuous fabrication of cellulose nanocrystal/poly(ethylene glycol) diacrylate hydrogel fiber from nanocomposite dispersion: rheology, preparation and characterization. *Polymer* 123, 55–64. doi: 10.1016/j.polymer.2017.06.034

Jeon, C. H., Makhaeva, E. E., and Khokhlov, A. R. (1999). Complexes of polyelectrolyte hydrogels with organic dyes: effect of charge density on the complex stability and intragel dye aggregation. *J. Polym. Sci. Part B Polym. Phys.* 37, 1209–1217. doi: 10.1002/(sici)1099-0488(19990615)37:12<1209::aid-polb2>3.0.co;2-x

Jia, C., Bian, H., Gao, T., Jiang, F., Kierzewski, I. M., Wang, Y., et al. (2017). Thermally stable cellulose nanocrystals toward high-performance 2D and 3D nanostructures. *ACS Appl. Mater. Interf.* 9, 28922–28929. doi: 10.1021/acsami.7b08760

Kim, D., Park, S., Jo, I., Kim, S. M., Kang, D. H., Cho, S. P., et al. (2017). Multiscale modulation of nanocrystalline cellulose hydrogel via nanocarbon hybridization for 3D neuronal bilayer formation. *Small* 13:1700331. doi: 10.1002/smll.201700331

Larsson, P. T., Wickholm, K., and Iversen, T. (1997). A CP/MAS 13 C NMR investigation of molecular ordering in celluloses. *Carbohyd. Res.* 302, 19–25. doi: 10.1016/s0008-6215(97)00130-4

Leung, A. C. W., Hrapovic, S., Lam, E., Liu, Y., Male, K. B., Mahmoud, K. A., et al. (2011). Characteristics and properties of carboxylated cellulose nanocrystals prepared from a novel one-step procedure. *Small* 7, 302–305. doi: 10.1002/smll.201001715

Li, V. C. F., Kuang, X., Mulyadi, A., Hamel, C. M., Deng, Y., and Qi, H. J. (2019). 3D printed cellulose nanocrystal composites through digital light processing. *Cellulose* 26, 3973–3985. doi: 10.1007/s10570-019-02353-9

Luo, X., Gleisner, R., Tian, S., Negron, J., Horn, E., Pan, X. J., et al. (2010). Evaluation of mountain beetle infested lodgepole pine for cellulosic ethanol production by SPORL pretreatment. *Ind. Eng. Chem. Res.* 49, 8258–8266. doi: 10.1021/ie1003202

Mark, R. E. (1967). *Cell Wall Mechanics and Tracheids*. London: Yale University Press.

Molnes, S. N., Mamonov, A., Paso, K. G., Strand, S., and Syverud, K. (2018). Investigation of a new application for cellulose nanocrystals: a study of the enhanced oil recovery potential by use of a green additive. *Cellulose* 25, 2289–2301. doi: 10.1007/s10570-018-1715-5

Montanari, S., Roumani, M., Heux, L., and Vignon, M. R. (2005). Topochemistry of carboxylated cellulose nanocrystals resulting from TEMPO-mediated oxidation. *Macromolecules* 38, 1665–1671. doi: 10.1021/ma048396c

Nishiyama, Y., Kim, U. J., Kim, D. Y., Katsumata, K. S., May, R. P., and Langan, P. (2003). Periodic disorder along ramie cellulose microfibrils. *Biomacromolecules* 4, 1013–1017. doi: 10.1021/bm025772x

Oguzlu, H., Danumah, C., and Boluk, Y. (2017). Colloidal behavior of aqueous cellulose nanocrystal suspensions. *Curr. Opin. Coll. Interf. Sci.* 29, 46–56. doi: 10.1016/j.cocis.2017.02.002

Ojala, J., Sirviö, J. A., and Liimatainen, H. (2016). Nanoparticle emulsifiers based on bifunctionalized cellulose nanocrystals as marine diesel oil-water emulsion stabilizers. *Chem. Eng. J.* 288, 312–320. doi: 10.1016/j.cej.2015.10.113

Orts, W. J., Godbout, L., Marchessault, R. H., and Revol, J. F. (1998). Enhanced ordering of liquid crystalline suspensions of cellulose microfibrils: a small angle neutron scattering study. *Macromolecules* 31, 5717–5725. doi: 10.1021/ma9711452

Pääkko, M., Ankerfors, M., Kosonen, H., Nykänen, A., Ahola, S., Österberg, M., et al. (2007). Enzymatic hydrolysis combined with mechanical shearing and high-pressure homogenization for nanoscale cellulose fibrils and strong gels. *Biomacromolecules* 8, 1934–1941. doi: 10.1021/bm061215p

Palaganas, N. B., Mangadlao, J. D., De Leon, A. C. C., Palaganas, J. O., Pangilinan, K. D., Lee, Y. J., et al. (2017). 3D printing of photocurable cellulose nanocrystal composite for fabrication of complex architectures via stereolithography. *ACS Appl. Mater. Interf.* 9, 34314–34324. doi: 10.1021/acsami.7b09223

Park, S., Baker, J. O., Himmel, M. E., Parilla, P. A., and Johnson, D. K. (2010). Cellulose crystallinity index: measurement techniques and their impact on interpreting cellulase performance. *Biotechnol. Biofuels* 3:10. doi: 10.1186/1754-6834-3-10

Qin, Y., Qiu, X., and Zhu, J. Y. (2016). Understanding longitudinal wood fiber ultra-structure for producing cellulose nanofibrils using disk milling with dilute acid prehydrolysis. *Sci. Rep.* 6:35602.

Revol, J.-F., Bradford, H., Giasson, J., Marchessault, R. H., and Gray, D. G. (1992). Helicoidal self-ordering of cellulose microfibrils in squeous suspension. *Int. J. Biol. Macromol.* 14, 170–172. doi: 10.1016/s0141-8130(05)80008-x

Schenzel, K., Fischer, S., and Brendler, E. (2005). New method for determining the degree of cellulose I crystallinity by means of FT Raman spectroscopy. *Cellulose* 12, 223–231. doi: 10.1007/s10570-004-3885-6

Segal, L., Creely, J. J., Martin, A. E., and Conrad, C. M. (1959). An empirical method for estimating the degree of crystallinity of native cellulose using the X-ray diffractometer. *Text. Res. J.* 29, 786–794. doi: 10.1177/004051755902901003

Shafiei-Sabet, S., Hamad, W. Y., and Hatzikiriakos, S. G. (2012). Rheology of nanocrystalline cellulose aqueous suspensions. *Langmuir* 28, 17124–17133. doi: 10.1021/la303380v

Shafiei-Sabet, S., Hamad, W. Y., and Hatzikiriakos, S. G. (2014). Ionic strength effects on the microstructure and shear rheology of cellulose nanocrystal suspensions. *Cellulose* 21, 3347–3359. doi: 10.1007/s10570-014-0407-z

Stojanović, Ž, Jeremić, K., Jovanović, S., and Lechner, M. D. (2005). A comparison of some methods for the determination of the degree of substitution of carboxymethyl starch. *Starch* 57, 79–83. doi: 10.1002/star.200400342

Šturcová, A., Davies, G. R., and Eichhorn, S. J. (2005). Elastic modulus and stress-transfer properties of tunicate cellulose whiskers. *Biomacromolecules* 6, 1055–1061. doi: 10.1021/bm049291k

Sultan, S., and Mathew, A. P. (2018). 3D printed scaffolds with gradient porosity based on a cellulose nanocrystal hydrogel. *Nanoscale* 10, 4421–4431. doi: 10.1039/c7nr08966j

Wang, J., Chiappone, A., Roppolo, I., Shao, F., Fantino, E., Lorusso, M., et al. (2018). All-in-one cellulose nanocrystals for 3D printing of nanocomposite hydrogels. *Angew. Chem. Intern. Edn.* 57, 2353–2356. doi: 10.1002/anie.201710951

Wang, Q. Q., Zhu, J. Y., and Considine, J. M. (2013). Strong and optically transparent films prepared using cellulosic solid residue (CSR) recovered from cellulose nanocrystals (CNC) production waste stream. *ACS Appl. Mater. Interf.* 5, 2527–2534. doi: 10.1021/am302967m

Wang, Q. Q., Zhu, J. Y., Gleisner, R., Kuster, T. A., Baxa, U., and McNeil, S. E. (2012a). Morphological development of cellulose fibrils of a bleached eucalyptus pulp by mechanical fibrillation. *Cellulose* 19, 1631–1643. doi: 10.1007/s10570-012-9745-x

Wang, Q. Q., Zhu, J. Y., Reiner, R. S., Verrill, S. P., Baxa, U., and McNeil, S. E. (2012b). Approaching zero cellulose loss in cellulose nanocrystal (CNC) production: recovery and characterization of cellulosic solid residues (CSR) and CNC. *Cellulose* 19, 2033–2047. doi: 10.1007/s10570-012-9765-6

Wang, R., Chen, L., Zhu, J. Y., and Yang, R. (2017). Tailored and integrated production of carboxylated cellulose nanocrystals (CNC) with nanofibrils (CNF) through maleic acid hydrolysis. *Chemnanomat* 3, 328–335. doi: 10.1002/cnma.201700015

Wang, W., Mozuch, M. D., Sabo, R. C., Kersten, P., Zhu, J. Y., and Jin, Y. (2015). Production of cellulose nanofibrils from bleached eucalyptus fibers by hyperthermostable endoglucanase treatment and subsequent microfluidization. *Cellulose* 22, 351–361. doi: 10.1007/s10570-014-0465-2

Wang, W., Mozuch, M. D., Sabo, R. C., Kersten, P., Zhu, J. Y., and Jin, Y. (2016). Endoglucanase post-milling treatment for producing cellulose nanofibers from bleached eucalyptus fibers by a supermasscolloider. *Cellulose* 23, 1859–1870. doi: 10.1007/s10570-016-0946-6

Yarbrough, J. M., Zhang, R., Mittal, A., Vander Wall, T., Bomble, Y. J., Decker, S. R., et al. (2017). Multifunctional cellulolytic enzymes outperform processive fungal cellulases for coproduction of nanocellulose and biofuels. *ACS Nano* 11, 3101–3109. doi: 10.1021/acsnano.7b00086

Zhou, H., St. John, F., and Zhu, J. Y. (2019). Xylanase pretreatment of wood fibers for producing cellulose nanofibrils: a comparison of different enzyme preparations. *Cellulose* 26, 543–555. doi: 10.1007/s10570-019-02250-1

Zhu, J., Chen, L., Gleisner, R., and Zhu, J. Y. (2019). Co-production of bioethanol and furfural from poplar wood via low temperature (≤90°C) acid hydrotropic fractionation (AHF). *Fuel* 254:115572. doi: 10.1016/j.fuel.2019.05.155

Zhu, J. Y., Sabo, R., and Luo, X. (2011). Integrated production of nano-fibrillated cellulose and cellulosic biofuel (ethanol) by enzymatic fractionation of wood fibers. *Green Chem.* 13, 1339–1344. doi: 10.1039/c1gc15103g

Zhu, W., Houtman, C. J., Zhu, J. Y., Gleisner, R., and Chen, K. F. (2012). Quantitative predictions of bioconversion of aspen by dilute acid and SPORL pretreatments using a unified combined hydrolysis factor (CHF). *Process Biochem.* 47, 785–791. doi: 10.1016/j.procbio.2012.02.012

Conflict of Interest: Zhu and RG are co-inventors of the dicarboxylic acid hydrolysis process for producing CNMs.

The remaining authors declare that the research was conducted in the absence of any commercial or financial relationships that could be construed as a potential conflict of interest.

frontiers
in Bioengineering and Biotechnology

ORIGINAL RESEARCH
published: 15 September 2020
doi: 10.3389/fbioe.2020.553037

Fabrication of Bacterial Cellulose-Curcumin Nanocomposite as a Novel Dressing for Partial Thickness Skin Burn

Wasim Sajjad[1], Feng He[2]*, Muhammad Wajid Ullah[3], Muhammad Ikram[4], Shahid Masood Shah[5], Romana Khan[6], Taous Khan[4], Ayesha Khalid[5], Guang Yang[3] and Fazli Wahid[1]*

[1] Department of Biomedical Sciences, Pak-Austria Fachhochschule Institute of Applied Sciences and Technology, Haripur, Pakistan, [2] Hubei Key Laboratory of Economic Forest Germplasm Improvement and Resources Comprehensive Utilization, Huanggang Normal University, Huanggang, China, [3] Department of Biomedical Engineering, Huazhong University of Science and Technology, Wuhan, China, [4] Department of Pharmacy, COMSATS University Islamabad, Abbottabad, Pakistan, [5] Department of Biotechnology, COMSATS University Islamabad, Abbottabad, Pakistan, [6] Department of Environmental Sciences, COMSATS University Islamabad, Abbottabad, Pakistan

OPEN ACCESS

Edited by:
Malcolm Xing,
University of Manitoba, Canada

Reviewed by:
Naing Tun Thet,
University of Bath, United Kingdom
Adil Denizli,
Hacettepe University, Turkey

****Correspondence:***
Feng He
hfeng@hust.edu.cn
Fazli Wahid
fazliwahid@cuiatd.edu.pk

Specialty section:
This article was submitted to Biomaterials,
a section of the journal Frontiers in Bioengineering and Biotechnology

Received: *17 April 2020*
Accepted: *25 August 2020*
Published: *15 September 2020*

Citation:
Sajjad W, He F, Ullah MW, Ikram M, Shah SM, Khan R, Khan T, Khalid A, Yang G and Wahid F (2020) Fabrication of Bacterial Cellulose-Curcumin Nanocomposite as a Novel Dressing for Partial Thickness Skin Burn. Front. Bioeng. Biotechnol. 8:553037. doi: 10.3389/fbioe.2020.553037

The current study aimed to fabricate curcumin-loaded bacterial cellulose (BC-Cur) nanocomposite as a potential wound dressing for partial thickness burns by utilizing the therapeutic features of curcumin and unique structural, physico-chemical, and biological features of bacterial cellulose (BC). Characterization analyses confirmed the successful impregnation of curcumin into the BC matrix. Biocompatibility studies showed the better attachment and proliferation of fibroblast cells on the BC-Cur nanocomposite. The antibacterial potential of curcumin was tested against *Escherichia coli* (*E. coli*), *Pseudomonas aeruginosa* (*P. aeruginosa*), *Salmonella typhimurium* (*S. typhimurium*), and *Staphylococcus aureus* (*S. aureus*). Wound healing analysis of partial-thickness burns in Balb^{C} mice showed an accelerated wound closure up to 64.25% after 15 days in the BC-Cur nanocomposite treated group. Histological studies showed healthy granulation tissues, fine re-epithelialization, vascularization, and resurfacing of wound bed in the BC-Cur nanocomposite group. These results indicate that combining BC with curcumin significantly improved the healing pattern. Thus, it can be concluded that the fabricated biomaterial could provide a base for the development of promising alternatives for the conventional dressing system in treating burns.

Keywords: bacterial cellulose, biocompatibility, burns, curcumin, tissue regeneration, wound healing

INTRODUCTION

Skin, as a vital organ, prevents the water loss from the body and keeps the internal environment moist. It encounters acute or chronic injuries in case of burns, accidents, injuries, or microbial contamination, which cause wounds that subsequently require healing. Wound healing is a complex process, involving different events such as coagulation, inflammation, cell division and migration, the formation of connective tissues and blood vessels, development of extracellular matrix (ECM), and maturation of epithelium (Mohanty and Sahoo, 2017). The healing process is typically comprised of four highly arranged phases, including homeostasis, inflammation, proliferation, and remodeling (Azuma et al., 2015; Ho et al., 2017).

The conventional wound dressings such as cotton and impregnated gauzes are painful, less efficient, causing damage to the newly formed epithelial lining skin, and unable to maintain ideal conditions for tissue repair (Di et al., 2017). In addition, severe burn injuries left a lifetime social and psychological impacts on the victim due to post burns scars, physical disfigurement, and contractures. To date, extensive efforts have been made in burn therapeutics to improve the survival of victims; however, burn-related morbidity and mortality are still alarming issues (Coban, 2012). Therefore, further efforts are required to develop advanced biomaterials-based wound dressings and potential alternatives to traditional counterparts by using tissue engineering strategies which focus on synthesis or regeneration of tissues and amplifying it *in vivo* by using active biofactors and a three-dimensional biocompatible, biodegradable, and porous scaffolds (Duan and Wang, 2010; Aljohani et al., 2018; Torgbo and Sukyai, 2018; McCarthy et al., 2019a,b). An ideal 3D scaffold supports the cellular activities for easy adhesion, penetration, growth, proliferation, and differentiation, in addition to being non-toxic, biodegradable, mechanically stable, and permeable to diffusion of nutrients and oxygen flow (Hu et al., 2014; Douglass et al., 2018). These features bring forward three basic requirements for a wound dressing material: scaffold, bioactive entity, and active cells, in order to mimic the 3D architecture of ECM of native tissues (Oliveira Barud et al., 2015). A variety of dressing systems have been designed in the past decades for efficient healing of dermal wounds, which are mainly comprised of different polymers and a variety of natural products.

Curcumin, a turmeric derivative of the ginger family, is extracted from the dried rhizome (Shehzad et al., 2013). It contains different bioactive ingredients like demethoxycurcumin (curcumin II), bisdemethoxycurcumin (curcumin III), and a newly discovered cyclocurcumin, collectively known as curcuminoids. It possesses wound-healing capabilities, antioxidant, and antineoplastic and can effectively inhibit the growth of various infectious antibiotic-resistant pathogens (Krausz et al., 2015). However, its systematic administration in the therapeutic application has been limited by its low aqueous solubility, rapid metabolism, poor tissue absorption, and limited plasma (Mohanty and Sahoo, 2017). To date, different topical formulations of curcumin like hydrogels, films, emulsions, and nano-formulations have been prepared for its control and targeted delivery to the wounded area (Mohanty and Sahoo, 2017). These formulations are able to deliver the drug to the target site owing to their small size, which can effectively cross the skin (Flora et al., 2013).

Recently, biopolymers have received immense consideration for biomedical applications. To this end, the use of bacterial cellulose (BC), produced by microbial cells (Ullah et al., 2017) and cell-free systems (Ullah et al., 2015; Kim et al., 2019), has received a growing interest as a biomaterial in various biomedical applications (Klemm et al., 2001; Czaja et al., 2006; Khan et al., 2015a,b; Hussain et al., 2019), specialty membrane (Rajwade et al., 2015), biosensors (Jasim et al., 2017; Farooq et al., 2020), and drug release (Numata et al., 2015; Li et al., 2018). These applications utilize both pure BC and its composites with other materials, such as biopolymers including collagen (Takeda et al., 2016), silk-sericin (Lamboni et al., 2016), gelatin (Khan et al., 2018), alginate (Kirdponpattara et al., 2015), and chitosan (Ul-Islam et al., 2019), and nanoparticles such as silver (Maneerung et al., 2008), zinc (Ul-Islam et al., 2014; Khalid et al., 2017a), titanium dioxide (Khan et al., 2015a,b; Ullah et al., 2016a; Khalid et al., 2017b), and gold (Khan et al., 2018), as well as clay materials such as pristine and modified montmorillonite (Ul-Islam et al., 2013b). The unique features of BC include high purity, better mechanical properties, high water holding capacity (WHC) and slow water release rate (WRR), active surface area, moderate biocompatibility, biodegradability, three-dimensional (3D) reticulate fibrous structure, micro-porosity, optical transparency, and non-toxicity, and moldability into different shapes (Czaja et al., 2006; Ul-Islam et al., 2013a; Ullah et al., 2016b; Di et al., 2017). However, pristine BC lacks innate antibacterial and antioxidant properties (Ul-islam et al., 2020); therefore, fabrication or modification of BC with antimicrobial agents like nanoparticles could synergize its wound healing properties, thus obtaining a smart antimicrobial wound dressing system (Khalid et al., 2017a,b). The use of curcumin is quite well-known in traditional medicines for various skin wounds, particularly burns, cuts, and eczema (Khamrai et al., 2017). Several studies have demonstrated the potential of BC and curcumin for different biomedical applications: such as the use of modified BC-curcumin self-healing polyelectrolytic film (Khamrai et al., 2017), curcumin-loaded BC films for treating skin cancer (Subtaweesin et al., 2018), cellulose/curcumin composite films with antibacterial activity for food packaging applications (Luo et al., 2012), curcumin-loaded cellulose-halloysite nanotube composite hydrogel for anticancer and wound dressing applications (Huang et al., 2017), and cellulose/turmeric powder green composite films (Li et al., 2014). However, no such comprehensive study was conducted where the healing activity of these BC-curcumin nanocomposites was investigated for the partial-thickness burns.

The current study was aimed to fabricate curcumin-loaded bacterial cellulose (BC-Cur) nanocomposite as a potential wound dressing, with improved tissue regeneration and wound healing properties, for partial thickness skin burns by utilizing the inherent structural and biocompatible features of BC and therapeutic potential of curcumin. The fabricated BC-Cur nanomaterial was characterized for its structural and physico-chemical properties by different characterization techniques, while its potential wound healing activity was assessed in the burn animal model. The antibacterial activity of curcumin was tested against various burn wound pathogens. The curcumin showed remarkable antibacterial activity against the tested pathogens. The developed nanomaterial showed excellent wound healing and tissue regeneration potential, thus can be used as an efficient curcumin delivery system to the wounded area.

MATERIALS AND METHODS

Materials

Glucose, sodium hydroxide (NaOH), and phosphate buffer saline (PBS) were purchased from Sigma Aldrich (St Louis, MO, United States). Nutrient agar and bacteriological peptone, citric acid, and yeast extract were supplied by the Oxoid Ltd., while dextrose by Daejung, South Korea. Curcumin and sodium dihydrogen phosphate (NaH_2PO_4) purchased from Merck & Company, Inc. (Darmstadt, Germany).

Production and Processing of BC Sheets

Bacterial cellulose sheets were produced by *Gluconacetobacter xylinus* (*G. xylinus*: KCCM 40407) in Hestrin–Schramm (HS) medium following a previously reported protocol (Sajjad et al., 2019). First, the HS medium was prepared by dissolving the respective medium components in distilled water, and its pH was adjusted to 5.0 by using 0.1 M NaOH. Thereafter, the medium was sterilized by autoclaving at 121°C for 15 min at 15 psi. For the preparation of the pre-culture of *G. xylinus*, few bacterial colonies were picked from the culture plate and inoculated into 50 mL HS medium and incubated at 30°C in shaking incubator at 150 rpm for 20 h. For BC production, a 5% pre-culture was inoculated into the liquid HS medium and incubated at 30°C under static cultivation for 7 to 10 days. BC sheets, a hydrogel produced at the air-medium interface, were harvested and washed in running water to remove residual medium components. Thereafter, the washed BC sheets were treated in 0.3 M NaOH solution and sterilized by autoclave to kill any live cells and cell debris (Shah et al., 2010). The washed and sterilized BC sheets were preserved in distilled water at 4°C for further use.

Preparation of BC-Curcumin Nanocomposite

The BC-Cur nanocomposite was prepared by the *ex situ* method. Briefly, 1 wt.% (w/v) homogeneous aqueous suspension of curcumin was prepared through continuous stirring for 1 h. For the preparation of BC-Cur nanocomposite, 3 × 3 cm BC sheets were immersed in 100 mL of 1 wt.% curcumin suspension and placed in shaking incubator at 150 rpm for 24 h. The as-prepared nanocomposite was freeze-dried at −50°C for 10 h to obtain the BC-Cur nanocomposite membrane and stored in air-tight bags for characterization and further analysis.

Characterization of BC and BC-Cur Nanocomposite

The freeze-dried pristine BC and BC-Cur nanocomposite membranes were characterized for their structural and physico-chemical properties by using different techniques. The surface morphologies of both samples were determined by field emission scanning electron microscopy (FE-SEM) by fixing the samples on a brass holder followed by their coating with gold on a Cu SEM before analyzing it through FE-SEM (Nova NanoSEM450, FEI, Holland). Chemical structures of both samples were analyzed through Fourier-transform infrared (FTIR) spectroscopy by recording their spectra between 4000-500 cm^{-1} using an FTIR spectrophotometer (VERTEX 70, Germany). The polymorphic structures of samples were determined at the scanning angle between 0 and 40° using an X-ray diffractometer (X'Pert-APD PHILIPS, Netherlands), operated at X-ray generator tension and current values of was 40 kV and 30 mA, respectively. Further, the effect of curcumin impregnation on the crystallinity of BC was determined using below Eq. (1) (Ul-Islam et al., 2011):

$$CrI = \left[\left\{I\ (200) - I\frac{am}{I}\,(200)\right\} \times 100\right] \tag{1}$$

where CrI is the crystallinity index, while I (200) and I (am) represent the intensities of (200) plane and amorphous peaks, respectively.

Biocompatibility Assay

The biocompatibility assay was performed according to the established protocol by Khan et al. (2015a) with some modifications (Khan et al., 2015b). Briefly, the pristine BC and BC-Cur nanocomposite were briefly dipped in 70% ethanol followed by UV radiation in a clean bench for 1–2 h and finally washed 3 times with the Dulbecco's phosphate-buffered saline (DPBS) for 5 min. Thereafter, both samples were incubated overnight at 37°C in Dulbecco's Modified Eagle's Medium (DMEM). Mouse fibroblast NIH 3T3 cells were detached from a previously cultured 100 mm plate through trypsin EDTA and seeded on BC and BC-Cur samples at a density of 3×10^5 cells/mL and incubated for 1–5 days. The cell growth and spreading on the scaffold were monitored *via* a phase-contrast microscope. The cells were imaged at 1360 × 1024-pixel resolution on the scaffold at the respective time period by using a microscope (Olympus BX50, United States) equipped with a digital camera (Olympus DP70, United States).

Antibacterial Activity

The antibacterial activity of curcumin was examined *in vitro* against most common burn wound pathogens through well diffusion method (Sajjad et al., 2019). Three species of Gram-negative bacteria *Escherichia coli* (*E. coli*), *Pseudomonas aeruginosa* (*P. aeruginosa*), and *Salmonella typhimurium* (*S. typhimurium*) and one strain of Gram-positive *Staphylococcus aureus* (*S. aureus*) were selected for the current study. Silver sulfadiazine (SD) was used as a reference drug (positive control). The selected bacterial strains were grown on the nutrient agar growth medium. The wells of 6 mm diameter were made in the agar medium plates for curcumin suspension. A volume of 80 μl of an aqueous suspension of curcumin was added to each well. The inoculated dishes were incubated at 37°C for 24 h, and the zone of inhibition was measured to determine the antibacterial potential of the curcumin. The experiment was performed in triplicate for each strain. The percent inhibition was determined by using the below Eq. (2):

$$Percent\ inhibition = \left(\frac{Zone\ of\ inhibition\ test\ samples}{Zone\ of\ inhibition\ of\ standard}\right) \times 100 \tag{2}$$

Wound Healing Studies in Burn Mice Model

$BALB^c$ mice were kindly provided by the National Institute of Health, Islamabad, Pakistan, and used as an animal model. The mice were housed in polypropylene cages and had free access to a balanced diet and water. All animal experiments were performed in accordance with the regulation and recommendations of NIH 1985, 1996, and 2011 and the experimental procedures were approved by the "Research Ethics Committee" COMSATS (Commission on Science and Technology for Sustainable Development in the South) University Islamabad, Abbottabad Campus, Pakistan. For experimental analysis, mice were divided into four groups, including BC, BC-Cur nanocomposite, positive control, and negative control. A total of 20 animals were used in the experiment, with five animals in each group. The partial-thickness burns were inflicted according to the established protocol, established in our earlier studies (Khalid et al., 2017a; Sajjad et al., 2019). Before the induction of skin burn wounds, the mice were sedated through intraperitoneal injection of 100 $mg.kg^{-1}$ ketamine and 10 $mg.kg^{-1}$ xylazine. Hairs were removed from the selected area by using a disposable hair removing the blade, and partial thickness skin burns wounds were induced in the shaved area by perpendicularly applying a pre-flame heated metal bar (17 × 17 mm) with gravitational pressure for 7 s. Thereafter, 3 × 3 cm pieces of BC and BC-Cur nanocomposite were used to cover the skin burn wound area and stapled with disposable skin staplers (Ningbo Advan Electrical Co., Ltd., China) (Khalid et al., 2017a; Sajjad et al., 2019). As a positive control, 1 wt.% silver sulfadiazine was applied to burn wounds along with negative control (untreated mice). The healing process by BC-Cur nanocomposite was allowed continued for 15 days, while the bandage was changed on day 5 and 10 of treatment. The wound healing potential of BC-Cur nanocomposite was assessed by measuring the wounded area on day 0, 5, 10, and 15, and the healing percentage was determined in different mice groups by the below Eq. (3):

$$\text{Percent healing} = 1 - \frac{\text{Wound area on corresponding day}}{\text{Wound area on day 0}} \times 100 \tag{3}$$

Histological Studies

For histological studies, mice from all four groups were sacrificed on day 15 by using a cervical dislocation and tissues were surgically removed and stored in 10% formalin. For analysis, the tissues were first fixed in 15% formalin, followed by 15% alcoholic formaldehyde. Thereafter, tissues were dehydrated by treating with 70%, 80%, and absolute alcohol for 2, 3, and 6 h, respectively. For microscopic analysis, slides were prepared by clearing the tissues with xylene, embedding in paraffin wax, and finally cutting with a microtome before staining with hematoxylin and eosin (H&E) dye. The slides were observed under the microscope and imaged.

Statistical Analysis

All data in the present study are expressed as mean and standard deviation. Statistical analysis was performed by using Student's t-test using Sigma Plot. $p \leq 0.05$ was considered statistically significant; asterisk (*) represents significant statistical difference where $^{***}p \leq 0.001$, $^{**}p \leq 0.01$, and $^{*}p \leq 0.05$.

RESULTS AND DISCUSSION

Production and Morphological Analysis of BC and BC-Cur Nanocomposite

Bacterial cellulose is aerobically produced as a hydrogel membrane at the air-medium interface in static cultivation, whose thickness increases downward when new fibrils are added, and this process continues until all bacterial cells entrapped in the hydrogel membrane become inactive or die due to oxygen deficit (Shah et al., 2013). Being highly hydrophilic and porous in nature, the BC hydrogel effectively allowed the dispersion and impregnation of curcumin particles on the surface as well as into its matrix when immersed in 1 wt.% aqueous curcumin suspension as shown by the morphological analysis of BC-Cur nanocomposite through FE-SEM (indicated through arrows in **Figure 1**). The presence of OH functional groups vows BC with highly hydrophilic behavior, which results in the expansion of pore size when rehydrated, which facilitates the impregnation of other molecules such as polymer solution and micro- and nano-sized particles; curcumin powder in this case. The SEM micrograph showed a nearly uniform distribution of curcumin in the BC matrix (**Figure 1**).

Structural Analysis of BC and BC-Cur Nanocomposite

Fourier-transform infrared spectroscopy is used as an investigative tool to verify the presence of different functional groups and the nature of chemical interactions between such groups in the material under investigation. In the present study, FTIR spectroscopy of pristine BC and BC-Cur nanocomposite was carried out, and both spectra were comparatively analyzed to confirm the purity of BC and its possible interaction with curcumin. The combined spectra of pristine BC and BC-Cur nanocomposite is shown in **Figure 2**. FTIR spectrum of pure BC showed all characteristic peaks of pure cellulose, confirming the purity of synthesized BC by *G. xylinus* and the effectiveness of post-synthesis processing (i.e., NaOH treatment and washing with H_2O). Specifically, the FTIR spectrum of pristine BC demonstrated characteristic peaks for − OH and − CH stretching at 3347 cm^{-1} and 2987 cm^{-1}, respectively, while the presence of − CH group was further supported by the appearance of several small peaks between 1450–1200 cm^{-1}.

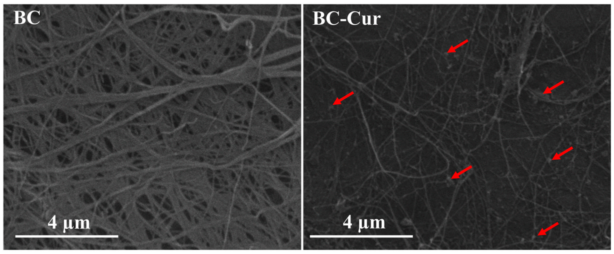

FIGURE 1 | Field-emission scanning electron microscopic micrographs of BC and BC-Cur nanocomposite. The arrows indicate the presence of curcumin.

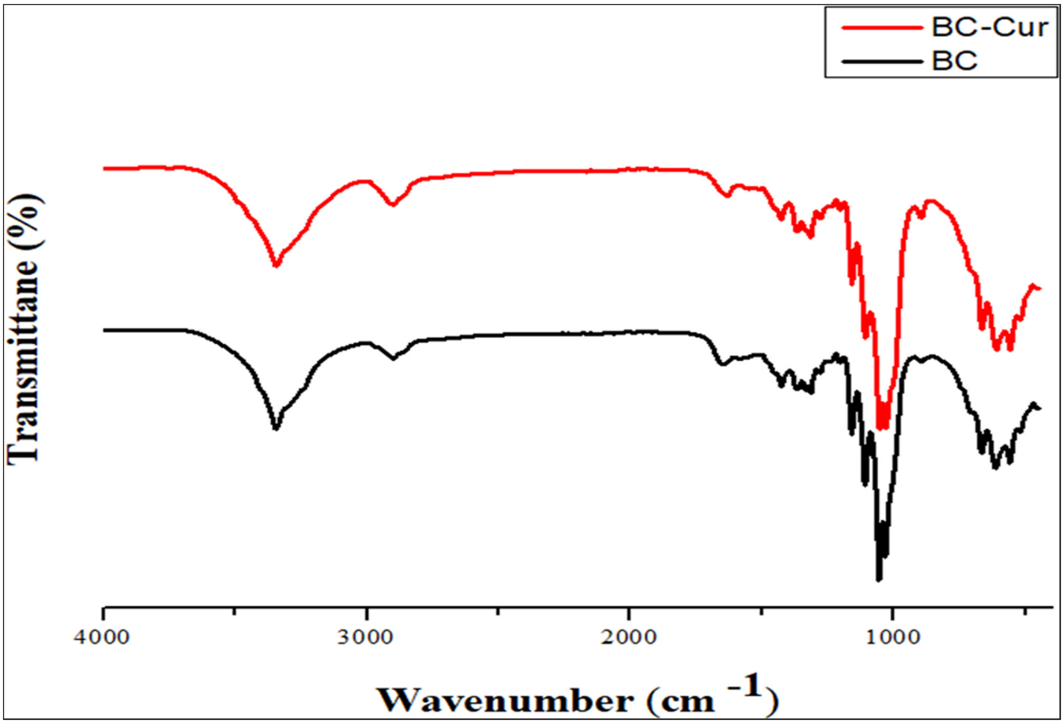

FIGURE 2 | Fourier transform-infrared spectral analysis of BC and BC-Cur nanocomposite.

The peaks for symmetric deformation and bending vibration appeared at 1435 cm^{-1} and 1415 cm^{-1}, respectively. A peak appeared at 1671 $cm^{-}1$, which was attributed to the glucose carbonyl (—CO) group, while the peak for C-O-C stretching vibration appeared at 1055 cm^{-1}. These characteristic peaks at respective positions confirmed the chemical structure of cellulose as well as purity of BC produced by *G. xylinus*, which is also in accordance with available literature (Ul-Islam et al., 2012; Ullah et al., 2016b). In contrast, the BC-Cur nanocomposite exhibited all characteristic peaks of BC; however, with a slight peak shift, which indicates an altered hydrogen-bonding pattern. For example, the peak for—CO group was slightly shifted from 1671 to 1663 cm^{-1}, which could be attributed to the interaction of BC with curcumin. In addition to the slight peak shift observation, the spectrum of BC-Cur nanocomposite exhibited additional peaks around 1512–1518 cm^{-1} due to the aromatic skeletal vibrations of the benzene ring, which are in agreement with previous studies (Chidambaram and Krishnasamy, 2014; Subtaweesin et al., 2018). These observations not only confirmed the importation of curcumin into the BC matrix but also its chemical interaction with the cellulose fibrils.

Bacterial cellulose is a semi-crystalline material and possesses cellulose I and cellulose II polymorphic structures, when produced by microbial and cell-free systems, respectively (Ullah et al., 2016b). It contains three characteristic crystalline peaks when examined through XRD. Impregnation of any material into its matrix can potentially alter the crystal structure of BC, thus can lead to an increased or decreased crystallinity. XRD analyses of pristine BC and BC-Cur nanocomposite were carried out to investigate the possible effect of curcumin impregnation into the BC matrix. Comparative XRD spectra of the extended linear scanning (10–40°) of pristine BC and BC-Cur nanocomposite are shown in **Figure 3**. As expected, the XRD spectrum of pristine BC showed three characteristic peaks; including two distinct peaks at $2\theta = 14.3°$ and 22.6° along a weak shoulder peak at 16.5°, corresponding to (1-1 0), (200), and (110) crystalline planes of cellulose I-β structure. These observations are in accordance with a well-characterized XRD spectrum of BC, as reported in available literature (French, 2014; Ul-Islam et al., 2014). Contrary, the XRD spectrum of BC-Cur nanocomposite showed similar peaks to pristine BC; however, with slight variation in the position and intensities of peaks. Specifically, the BC-Cur nanocomposite showed characteristic peaks at $2\theta = 14.1°$, 22.3°, and 16.2°corresponding to (1-1 0), (200), and (110) crystalline planes. The intensities of peaks at $2\theta = 16.2°$ and 22.3° were slightly increased while that at 14.1° was slightly decreased as evident from **Figure 3**. These variations in peak intensity were quantitatively determined by measuring the degree of crystallinity of BC and BC-Cur nanocomposite from the relative integrated area of crystalline and amorphous peaks using Eq. 1. The relative crystallinities of BC and BC-Cur nanocomposite were 56.61 and 63.88%, respectively. The increased crystallinity of BC-Cur nanocomposite could be attributed to the crystalline nature of curcumin nanoparticles. As a matter of fact, the calculated crystallinity of any sample deviates to some extent from the actual value due to the presence of small crystalline peaks which raise the background and in turn contribute to increasing the amorphous and total area under consideration

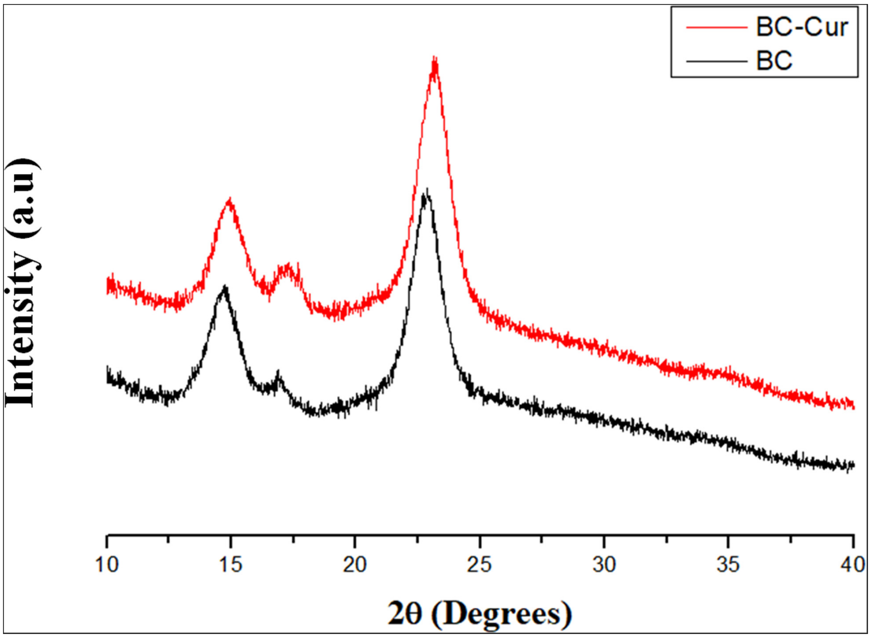

FIGURE 3 | X-ray diffraction patterns of BC and BC-Cur nanocomposite.

for calculating the crystallinity (French, 2014). Therefore, it is assumed that the calculated crystallinities of BC and BC-Cur nanocomposite might be slightly lower than the actual values.

Biocompatibility of BC and BC-Cur Nanocomposite With NIH 3T3 Cells

Curcuminoids are generally recognized as safe (GRAS) by the United States Food and Drug Administration (US-FDA). However, it may cause potential toxicity upon interaction with the plasma protein if excessively released into the blood stream. Therefore, in the current study, FDA-recommended safe concentration i.e., 1 wt.% of curcumin (Gupta et al., 2013; Dhakal et al., 2016) was used for the preparation of BC-Cur nanocomposite. *In vitro* biocompatibility of BC and BC-Cur nanocomposites were investigated using NIH 3T3 cells to evaluate their potential applications in wound healing. The mouse fibroblast cells were cultured on pristine BC and BC-Cur nanocomposites. In phase contrast, images were photographed on day 1 and 5. The results showed that there were few cells attached to the BC membrane surface (**Figure 4**). On the other hand, it can clearly be seen in images that more numbers of cells attached to the BC-Cur nanocomposite surface. In addition to increasing cell attachment, the BC-Cur nanocomposite showed distinguished behavior of the growth pattern as the cells appeared in the form of a colony or spheroids. For which further studies may need to elucidate the distinguished nature of BC-Cur nanocomposite. Furthermore, the cell attachment, spheroids formation, and spreading were confirmed by 4′,6-diamidino-2-phenylindole (DAPI) staining, as shown in **Figure 5**.

The SEM images showed a well porous morphology of BC and BC-Cur nanocomposite for potential cell adhesion and proliferation. Previously, it was observed that BC composites exhibited considerable cell adhesion and proliferation not only within the BC pores but also in its composites with other materials (Khan et al., 2016). The results showed that the addition of curcumin into BC improved the attachment and proliferation of NIH 3T3 cells, which is in accordance with a previous study, which reported that lower doses of curcumin enhance the cell growth and proliferation of fibroblast-derived from scar tissues (Kang et al., 2009). Another study reported that curcumin induces apoptosis of tumor cell lines; however, no apoptotic effect was observed on normal rat hepatocytes (Syng-ai et al., 2004). Thus, it can be concluded that the developed BC-Cur nanocomposite possesses a high level of biocompatibility, which makes it an ideal candidate for biomedical application, including skin tissue engineering.

Antibacterial Activity

The antibacterial activity of curcumin was determined against the classic burn wound pathogens such as *E. coli, P. aeruginosa*, *S. typhimurium*, and *S. aureus*, by measuring the zone of inhibition and percent inhibition, and the results are summarized in **Supplementary Table S1**, and representative photographs are shown in **Supplementary Figure S2**. Curcumin is known for its antibacterial activity and produced inhibition zones of 15 ± 0 mm, 16.3 ± 0.4 mm, 16 ± 0 mm, and 15.5 ± 0.4 mm against *E. coli, P. aeruginosa*, *S. typhimurium*, and *S. aureus*, respectively (**Supplementary Figure S2**). Literature review shows that curcumin lyse the bacterial cell by causing damage to the cell membrane or through a specialized mechanism as a possible mode of action in *E. coli* (Wang et al., 2017). In another study, Wang et al. reported that curcumin shows its

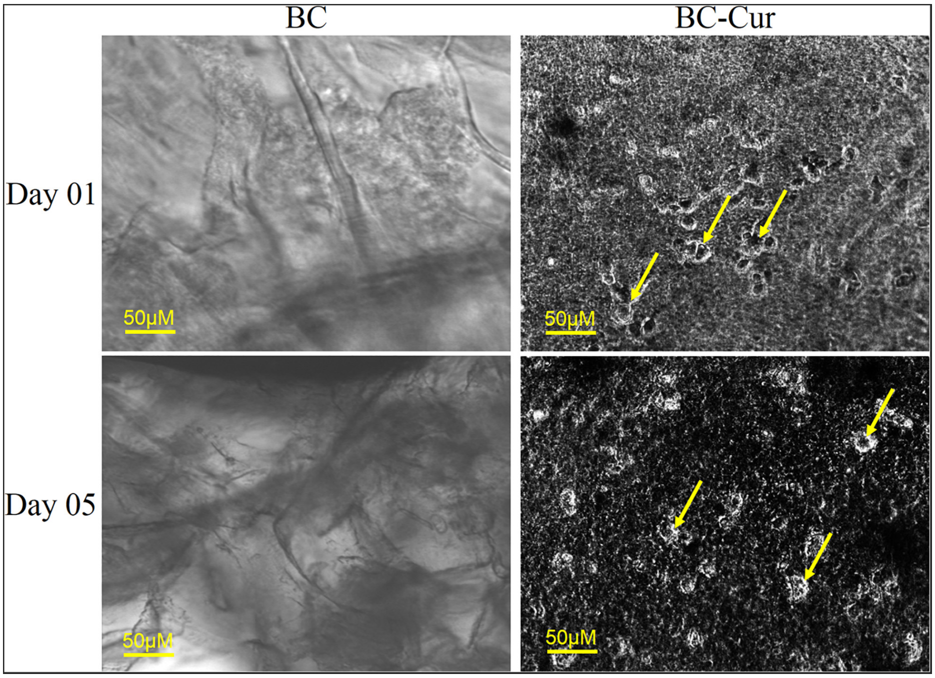

FIGURE 4 | Cell adhesion and proliferation on BC and BC-Cur nanocomposite, 3T3 mouse fibroblast cells were cultured on BC and their composite with Cur showing cell growth on day 1 and 5. Arrows representing cells.

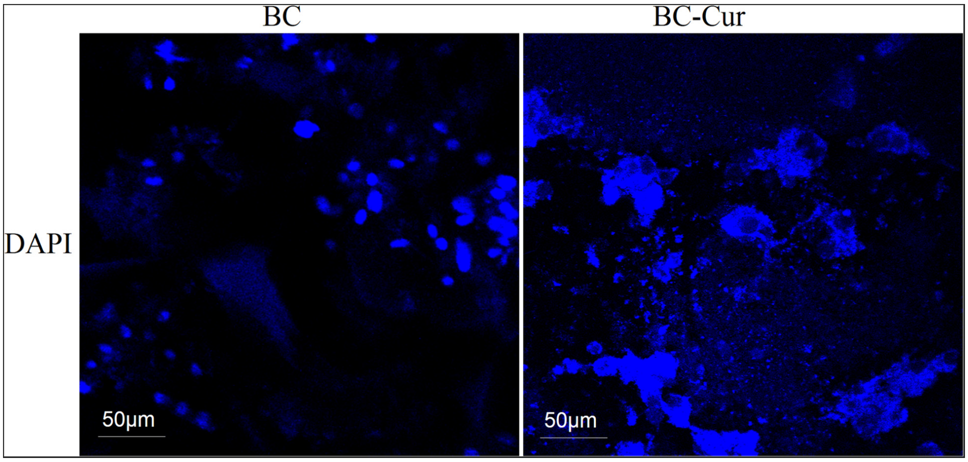

FIGURE 5 | 4′,6-diamidino-2-phenylindole (DAPI) staining of cells growth and attachment on BC and BC-Cur nanocomposites.

antibacterial activity against *S. aureus* by anchoring to the cell wall, break it, diffuse into the cell, and disrupt the structure of cellular organelles, and ultimately lead to apoptosis (Wang et al., 2017). Similarly, Yun and Lee (2016) in their study reported that curcumin induces the generation of reactive oxygen species (ROS), which accumulate inside the cell and damage the macromolecules, including proteins, nucleic acid (DNA/RNA), and lipid membranes, thus leading to apoptosis. These studies suggests that curcumin may induce the cell death through any of the above-described mechanisms. Overall, the findings suggest that the combination of BC and curcumin could be used as a smart antibacterial wound dressing system to treat the partial-thickness skin burn.

In vivo Evaluation of Wound Healing in Burn Animal Model

In the present study, BC-Cur nanocomposite was developed as a wound dressing system and investigated its potential wound healing capability in the burn animal model. The results in **Figure 6** show that the wound bed area started to contract on day 5 in each group and continued thereafter. Compared to

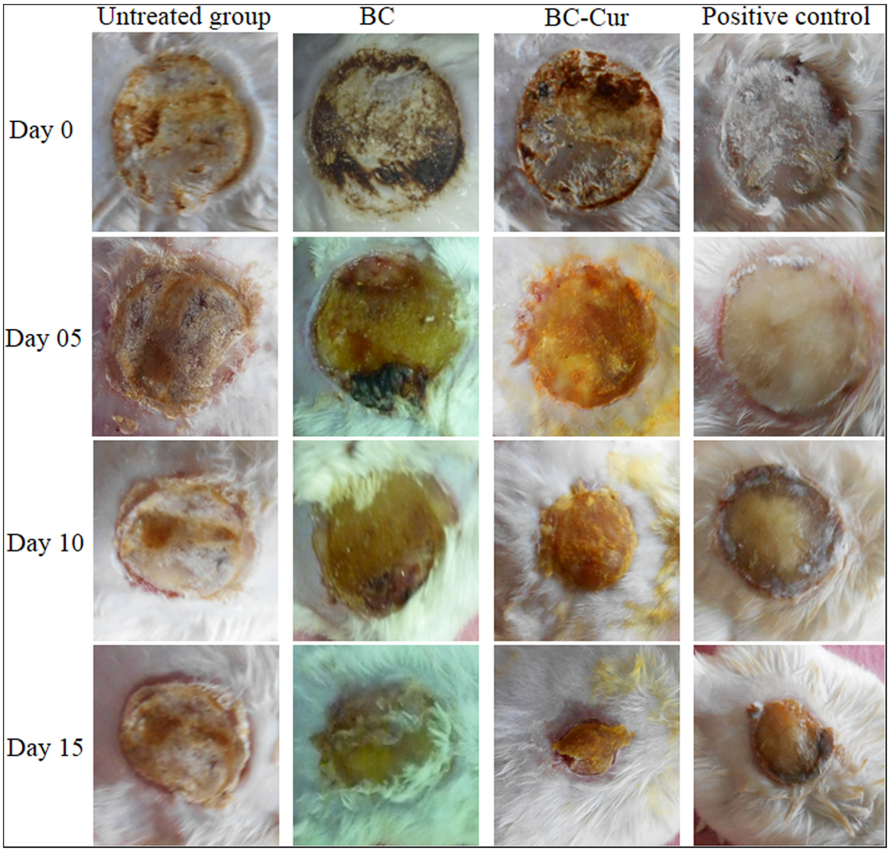

FIGURE 6 | The photographs of the wound healing process in untreated, pristine BC, BC-Cur nanocomposite and positive control groups at day 0, 5, 10, and 15. Each photograph is a representative of three mice in each group.

BC, positive control, and untreated groups, the wound closing was much higher in the BC-Cur nanocomposite group. In comparison to the positive control group (silver sulfadiazine treated), the BC-Cur nanocomposite treated group showed more wound healing. The results of wound healing for all groups under investigation are summarized in **Figure 6** and **Table 1**.

TABLE 1 | *In vivo* evaluation of wound healing in burn animal model.

	Average wound area (mm^2)			
	Untreated group	**BC**	**BC-Cur**	**Positive control**
Day 0	289 ± 0	289 ± 0	289 ± 0	289 ± 0
Day 5	348.33 ± 20.2	318 ± 9.8	289 ± 14.2*	284.66 ± 19.8
Day 10	219 ± 29.1	200.33 ± 8	210 ± 14	241 ± 11.1
Day 15	202 ± 3.2	169 ± 13	103.33 ± 12.2***	118.66 ± 13.1
Healing (%) at day 15	30.10%	41.60%	64.25%	59%

*The data represent the mean ± SD of three mice with percent healing. The statistical significance of wound reduction was evaluated at day 0, 5, 10, and 15 of post-wounding. $p \leq 0.05$ was considered statistically significant (asterisk (*) represents significant statistical differences at $p \leq 0.001$ ***, $p \leq 0.01$ **, $p \leq 0.05$ *, n = 3).*

Precisely, the wound area contraction in BC-Cur nanocomposite, pristine BC, positive control and negative control groups were 103.33 ± 12.24, 169 ± 13, 118.66 ± 13.14, and 202 ± 3.28, respectively, on day 15 (**Table 1**). Meanwhile, there was a significant difference in the percent wound healing of BC-Cur nanocomposite and other groups on day 15 of the experiment. The percent healing of the BC-Cur nanocomposite group was 64.25% in comparison to pristine BC, positive control, and the untreated group, which were found to be 41.60, 30, and 59%, respectively. These results indicate that the impregnation of curcumin into the BC matrix effectively enhanced its wound-healing capabilities. These observations are in agreement with previous studies reporting the therapeutic applications of BC and curcumin in wound healing. The nano-scale network structure of BC acts as a physical barrier to prevents the microorganisms from penetrating into the wound (Li et al., 2012a). El-Refaie et al. (2015) reported that curcumin-loaded gel-core hyaluosomes greatly enhanced the wound healing rate in a burn animal model. Similar results were shown by the curcumin-methoxy poly(ethylene glycol) (MPEG)-chitosan film in a rat model where the *N*,O-carboxymethyl chitosan-hydrogel effectively decreased the wound bed (Li et al., 2012b,a). Krausz et al., in their studies, demonstrated that curcumin nanocomposites inhibited the growth of burn-associated pathogens and enhanced wound healing (Krausz et al., 2015). It is reported that silver sulfadiazine, as a standard drug for burn wound treatment, cause delayed wound healing (Atiyeh et al., 2007) and significant cell impairment to human dermal fibroblast (Lee and Moon, 2003). In the current study, silver sulfadiazine showed less wound healing ability as compared to BC-Cur nanocomposite indicating a high wound healing potential of the developed nanocomposite, thus can find potential applications in skin burns.

In conclusion, the results of the current study demonstrate that the *ex situ* developed BC-Cur nanocomposite exhibits significant wound healing potential for skin burns. Hence, nano-structured BC might be a promising carrier for curcumin to accelerate the wound healing process with the possibility of inhibiting the penetration of microbes, better patient compliance, minimizing the scar formation, and provide excellent recovery medium for complete skin regeneration.

Histological Analysis

The tissue regeneration capabilities of BC and BC-Cur nanocomposite were assessed by histological analysis. For this purpose, the full thickness sections of both treated and untreated wounds were extracted on day 15 of the experiment and stained with H&E for microscopic examination of re-epithelialization, fibrogenesis, tissue regeneration, and formation of granulation tissues and the results are shown in **Figure 7**. The H&E stained microphotograph showed the migration of epithelium over the complete dermis, re-epithelialization, and granulation of tissues in the BC-Cur nanocomposite treated wound. Further, few inflammatory cells, with the absence of necrotic tissues and ulceration, were observed in the BC-Cur nanocomposite group (**Figure 7**), indicating its excellent wound healing and tissue regeneration capabilities. These results are in agreement with a previous study which demonstrated that curcumin administration increased the cell proliferation and collagen synthesis at the wound site and thus contributed to rapid wound healing in full-thickness excision wound model (Panchatcharam et al., 2006). On the other hand, the non-modified BC treated wound displayed mild inflammation, less ulceration, and absence of necrotic tissues in the H&E stained slide photograph (**Figure 7**). Moreover, the partial re-epithelialization, tissue regeneration, and presence of small granulation tissues indicate that the wound healing process was incomplete and still active. Histological analysis of both positive and negative controls was also performed to compare the wound healing, and tissue regeneration efficiencies of both BC and BC-Cur nanocomposite treated groups. The histological analysis of positive control presented a good wound healing capability; nevertheless, lower than BC-Cur nanocomposite treated group (**Figure 7**), which are also in agreement with *in vivo* evaluation of wound healing (**Figure 6**). While in the negative control group where animals were left untreated, a higher number of inflammatory cells, a dead slough of necrotic tissues, and ulceration were observed with no signs of re-epithelialization and tissue regeneration (**Figure 7**) which indicate that wound healing is still in an inflammatory phase. These results are summarized in **Table 2**. The results indicate that anti-inflammatory activity of curcumin and inherent wound healing properties of BC contributed to complete re-epithelialization, with well-formed differentiated epithelium and granulation tissue in the treated wounds. Therefore, these results of the efficient healing process in mouse models indicate the suitability of BC-Cur nanocomposite as a wound dressing system to treat partial-thickness skin burns.

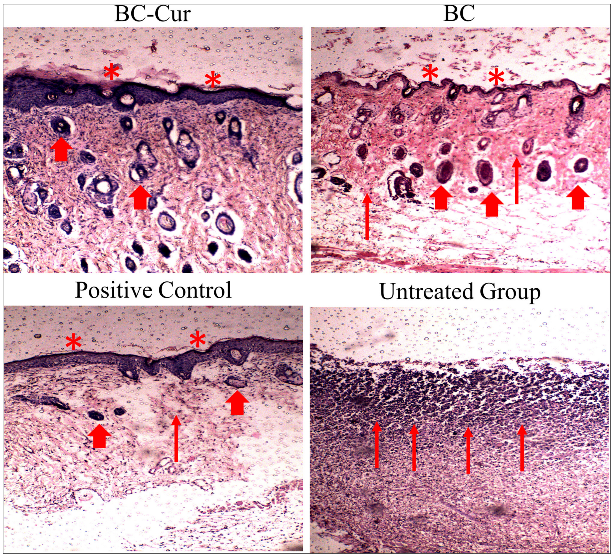

FIGURE 7 | H&E stained sections of the wounds of BC-Cur, BC, positive control and untreated group (negative control) at day 15 post wounding. Thin arrow represents granulation, thick arrow shows hairs follicles and asterisk represents epithelization of epidermis layer of skin.

TABLE 2 | Histological evaluation of different wound healing events in untreated, pristine BC, BC-Cur nanocomposite, and positive control groups.

Group	Untreated	BC	BC-Cur	Positive control
Inflammation	+++	++	–	–
Necrotic tissues	++	–	–	–
Ulceration	++	+	–	–
Re-epithelialization	–	+	+++	++
Granulation tissues	–	+	+++	++
Healing	–	+	+++	++

+++ (excellent); ++ (good); + (fair/mild); – (no).

CONCLUSION

Infectious burns are the most traumatic and challenging issue due to various pathological complications and microbial infections, which result in halted healing, scar formation, and uncontrolled necrosis of injured tissues. The *ex situ* modification allowed effective impregnation of curcumin into the BC matrix. FTIR spectroscopy confirmed chemical interaction between BC and curcumin. The addition of crystalline curcumin accounted for improved crystallinity of BC-Cur nanocomposite. The biocompatibility studies of the BC and BC-Cur nanocomposites confirmed their non-toxic nature for wound dressing application. The fabricated BC-Cur nanocomposite demonstrated accelerated wound healing, tissue regeneration, and wound contraction in a mouse burn model, thus showing the potential to be evaluated as a wound dressing material in treating partial thickness skin burns. The improved wound healing potential could be attributed to the additive effect of BC (inherently biocompatible) and curcumin (therapeutically active). These results suggest that the fabricated BC-Cur nanocomposite could be used as a potential topical antibacterial patch for wound healing and tissue regeneration in treating skin burns after further pre-clinical and clinical assessments.

DATA AVAILABILITY STATEMENT

The raw data supporting the conclusions of this article will be made available by the authors, without undue reservation.

ETHICS STATEMENT

The animal study was reviewed and approved by Research Ethics Committee COMSATS University Islamabad, Abbottabad Campus, Pakistan.

AUTHOR CONTRIBUTIONS

FW and FH conceived the project, supervised the research, and wrote the manuscript. WS and AK designed and performed the experiments, analyzed the results, wrote the manuscript, and prepared the figures. MWU and GY performed the characterization and wrote the manuscript. MI and SMS assisted in biocompatibility studies. RK assisted in characterization analysis and manuscript writing. All authors read and approved the manuscript.

FUNDING

This study was supported by the Higher Education Commission of Pakistan under the Start-Up Research Grant Program (SRGP) (Grant No. 21-211/SRGP/R&D/HEC/2014), National Natural Science Foundation of China (21774039, 51603079, and 31270150), and China Postdoctoral Science Foundation (2016M602291).

SUPPLEMENTARY MATERIAL

The Supplementary Material for this article can be found online at: https://www.frontiersin.org/articles/10.3389/fbioe.2020.553037/full#supplementary-material

REFERENCES

Aljohani, W., Ullah, M. W., Zhang, X., and Yang, G. (2018). Bioprinting and its applications in tissue engineering and regenerative medicine. *Int. J. Biol. Macromol.* 107, 261–275. doi: 10.1016/j.ijbiomac.2017.08.171

Atiyeh, B. S., Costagliola, M., Hayek, S. N., and Dibo, S. A. (2007). Effect of silver on burn wound infection control and healing: review of the literature. *Burns* 33, 139–148. doi: 10.1016/j.burns.2006.06.010

Azuma, K., Izumi, R., Osaki, T., Ifuku, S., Morimoto, M., Saimoto, H., et al. (2015). Chitin, chitosan, and its derivatives for wound healing: old and new materials. *J. Funct. Biomater.* 6, 104–142. doi: 10.3390/jfb6010104

Chidambaram, M., and Krishnasamy, K. (2014). Drug-drug/drug-excipient compatibility studies on curcumin using non-thermal methods. *Adv. Pharm. Bull.* 4, 309–312. doi: 10.5681/apb.2014.045

Coban, Y. K. (2012). Infection control in severely burned patients. *World J. Crit. Care Med.* 1, 94–101. doi: 10.5492/wjccm.v1.i4.94

Czaja, W., Krystynowicz, A., Bielecki, S., and Brown, R. M. (2006). Microbial cellulose - the natural power to heal wounds. *Biomaterials* 27, 145–151. doi: 10.1016/j.biomaterials.2005.07.035

Dhakal, S., Chao, K., Schmidt, W., Qin, J., Kim, M., and Chan, D. (2016). Evaluation of turmeric powder adulterated with metanil yellow using FT-Raman and FT-IR spectroscopy. *Foods* 5:36. doi: 10.3390/foods5020036

Di, Z., Shi, Z., Ullah, M. W., Li, S., and Yang, G. (2017). A transparent wound dressing based on bacterial cellulose whisker and poly(2-hydroxyethyl methacrylate). *Int. J. Biol. Macromol.* 105, 638–644. doi: 10.1016/j.ijbiomac.2017.07.075

Douglass, E. F., Avci, H., Boy, R., Rojas, O. J., and Kotek, R. (2018). A review of cellulose and cellulose blends for preparation of bio-derived and conventional membranes, nanostructured thin films, and composites. *Polym. Rev.* 58, 102–163. doi: 10.1080/15583724.2016.1269124

Duan, B., and Wang, M. (2010). Customized Ca-P/PHBV nanocomposite scaffolds for bone tissue engineering: design, fabrication, surface modification and sustained release of growth factor. *J. R. Soc. Interface* 7(Suppl. 5), S615–S629. doi: 10.1098/rsif.2010.0127.focus

El-Refaie, W. M., Elnaggar, Y. S. R., El-Massik, M. A., and Abdallah, O. Y. (2015). Novel curcumin-loaded gel-core hyaluosomes with promising burn-wound healing potential: development, in-vitro appraisal and in-vivo studies. *Int. J. Pharm.* 486, 88–98. doi: 10.1016/j.ijpharm.2015.03.052

Farooq, U., Ullah, M. W., Yang, Q., Aziz, A., Xu, J., Zhou, L., et al. (2020). High-density phage particles immobilization in surface-modified bacterial cellulose for ultra-sensitive and selective electrochemical detection of *Staphylococcus aureus*. *Biosens. Bioelectron.* 157:112163. doi: 10.1016/j.bios.2020.112163

Flora, G., Gupta, D., and Tiwari, A. (2013). Nanocurcumin: a promising therapeutic advancement over native curcumin. *Crit. Rev. Ther. Drug Carrier Syst.* 30, 331–368. doi: 10.1615/CritRevTherDrugCarrierSyst.2013007236

French, A. D. (2014). Idealized powder diffraction patterns for cellulose polymorphs. *Cellulose* 21, 885–896. doi: 10.1007/s10570-013-0030-4

Gupta, S. C., Patchva, S., and Aggarwal, B. B. (2013). Therapeutic roles of curcumin: lessons learned from clinical trials. *AAPS J.* 15, 195–218. doi: 10.1208/s12248-012-9432-8

Ho, J., Walsh, C., Yue, D., Dardik, A., and Cheema, U. (2017). Current advancements and strategies in tissue engineering for wound healing: a comprehensive review. *Adv. Wound Care* 6, 191–209. doi: 10.1089/wound.2016.0723

Hu, W., Chen, S., Yang, J., Li, Z., and Wang, H. (2014). Functionalized bacterial cellulose derivatives and nanocomposites. *Carbohydr. Polym.* 101, 1043–1060. doi: 10.1016/j.carbpol.2013.09.102

Huang, B., Liu, M., and Zhou, C. (2017). Cellulose–halloysite nanotube composite hydrogels for curcumin delivery. *Cellulose* 24, 2861–2875. doi: 10.1007/s10570-017-1316-8

Hussain, Z., Sajjad, W., Khan, T., and Wahid, F. (2019). Production of bacterial cellulose from industrial wastes: a review. *Cellulose* 26, 2895–2911. doi: 10.1007/s10570-019-02307-1

Jasim, A., Ullah, M. W., Shi, Z., Lin, X., and Yang, G. (2017). Fabrication of bacterial cellulose/polyaniline/single-walled carbon nanotubes membrane for potential application as biosensor. *Carbohydr. Polym.* 163, 62–69. doi: 10.1016/j.carbpol.2017.01.056

Kang, J., Huang, H., and Zhu, F. Q. (2009). Effect of curcumin on growth and function of fibroblast in human hyperplastic scar. *Zhongguo Zhong Xi Yi Jie He Za Zhi* 29, 1100–1103.

Khalid, A., Khan, R., Ul-Islam, M., Khan, T., and Wahid, F. (2017a). Bacterial cellulose-zinc oxide nanocomposites as a novel dressing system for burn wounds. *Carbohydr. Polym.* 164, 214–221. doi: 10.1016/j.carbpol.2017.01.061

Khalid, A., Ullah, H., Ul-Islam, M., Khan, R., Khan, S., Ahmad, F., et al. (2017b). Bacterial cellulose–TiO_2 nanocomposites promote healing and tissue regeneration in burn mice model. *RSC Adv.* 7, 47662–47668. doi: 10.1039/C7RA06699F

Khamrai, M., Banerjee, S. L., and Kundu, P. P. (2017). Modified bacterial cellulose based self-healable polyeloctrolyte film for wound dressing application. *Carbohydr. Polym.* 174, 580–590. doi: 10.1016/j.carbpol.2017.06.094

Khan, S., Ul-Islam, M., Ikram, M., Islam, S. U., Ullah, M. W., Israr, M., et al. (2018). Preparation and structural characterization of surface modified microporous bacterial cellulose scaffolds: a potential material for skin regeneration applications in vitro and in vivo. *Int. J. Biol. Macromol.* 117, 1200–1210. doi: 10.1016/j.ijbiomac.2018.06.044

Khan, S., Ul-Islam, M., Ikram, M., Ullah, M. W., Israr, M., Subhan, F., et al. (2016). Three-dimensionally microporous and highly biocompatible bacterial cellulose–gelatin composite scaffolds for tissue engineering applications. *RSC Adv.* 6, 110840–110849. doi: 10.1039/C6RA18847H

Khan, S., Ul-Islam, M., Khattak, W. A., Ullah, M. W., and Park, J. K. (2015a). Bacterial cellulose-titanium dioxide nanocomposites: nanostructural characteristics, antibacterial mechanism, and biocompatibility. *Cellulose* 22, 565–579. doi: 10.1007/s10570-014-0528-4

Khan, S., Ul-Islam, M., Ullah, M. W., Ikram, M., Subhan, F., Kim, Y., et al. (2015b). Engineered regenerated bacterial cellulose scaffolds for application in in vitro tissue regeneration. *RSC Adv.* 5, 84565–84573. doi: 10.1039/C5RA16985B

Kim, Y., Ullah, M. W., Ul-Islam, M., Khan, S., Jang, J. H., and Park, J. K. (2019). Self-assembly of bio-cellulose nanofibrils through intermediate phase in a cell-free enzyme system. *Biochem. Eng. J.* 142, 135–144. doi: 10.1016/j.bej.2018.11.017

Kirdponpattara, S., Khamkeaw, A., Sanchavanakit, N., Pavasant, P., and Phisalaphong, M. (2015). Structural modification and characterization of bacterial cellulose-alginate composite scaffolds for tissue engineering. *Carbohydr. Polym.* 132, 146–155. doi: 10.1016/j.carbpol.2015.06.059

Klemm, D., Schumann, D., Udhardt, U., and Marsch, S. (2001). Bacterial synthesized cellulose - Artificial blood vessels for microsurgery. *Prog. Polym. Sci.* 26, 1561–1603. doi: 10.1016/s0079-6700(01)00021-1

Krausz, A. E., Adler, B. L., Cabral, V., Navati, M., Doerner, J., Charafeddine, R. A., et al. (2015). Curcumin-encapsulated nanoparticles as innovative antimicrobial and wound healing agent. *Nanomedicine* 11, 195–206. doi: 10.1016/j.nano.2014.09.004

Lamboni, L., Li, Y., Liu, J., and Yang, G. (2016). Silk sericin-functionalized bacterial cellulose as a potential wound-healing biomaterial. *Biomacromolecules* 17, 3076–3084. doi: 10.1021/acs.biomac.6b00995

Lee, A.-R. C., and Moon, H. K. (2003). Effect of topically applied silver sulfadiazine on fibroblast cell proliferation and biomechanical properties of the wound. *Arch. Pharm. Res.* 26, 855–860. doi: 10.1007/BF02980032

Li, R., Cai, J., Zhang, L., Naresh, S., and Rajulu, A. V. (2014). Properties of cellulose/turmeric powder green composite films. *Cellulose Chem. Technol.* 48, 321–324.

Li, S., Jasim, A., Zhao, W., Fu, L., Ullah, M. W., Shi, Z., et al. (2018). Fabrication of pH-electroactive bacterial cellulose/polyaniline hydrogel for the development of a controlled drug release system. *ES Mater. Manuf.* 1, 41–49. doi: 10.30919/esmm5f120

Li, X., Chen, S., Zhang, B., Li, M., Diao, K., Zhang, Z., et al. (2012a). In situ injectable nano-composite hydrogel composed of curcumin, N,O-carboxymethyl chitosan and oxidized alginate for wound healing application. *Int. J. Pharm.* 437, 110–119. doi: 10.1016/j.ijpharm.2012.08.001

Li, X., Nan, K., Li, L., Zhang, Z., and Chen, H. (2012b). In vivo evaluation of curcumin nanoformulation loaded methoxy poly(ethylene glycol)-graft-chitosan composite film for wound healing application. *Carbohydr. Polym.* 88, 84–90. doi: 10.1016/j.carbpol.2011.11.068

Luo, N., Varaprasad, K., Reddy, G. V. S., Rajulu, A. V., and Zhang, J. (2012). Preparation and characterization of cellulose/curcumin composite films. *RSC Adv.* 2, 8483–8488. doi: 10.1039/c2ra21465b

Maneerung, T., Tokura, S., and Rujiravanit, R. (2008). Impregnation of silver nanoparticles into bacterial cellulose for antimicrobial wound dressing. *Carbohydr. Polym.* 72, 43–51. doi: 10.1016/j.carbpol.2007.07.025

McCarthy, R. R., Ullah, M. W., Booth, P., Pei, E., and Yang, G. (2019a). The use of bacterial polysaccharides in bioprinting. *Biotechnol. Adv.* 37:107448. doi: 10.1016/j.biotechadv.2019.107448

McCarthy, R. R., Ullah, M. W., Pei, E., and Yang, G. (2019b). Antimicrobial inks: the anti-infective applications of bioprinted bacterial polysaccharides. *Trends Biotechnol.* 37, 1153–1155. doi: 10.1016/j.tibtech.2019.05.004

Mohanty, C., and Sahoo, S. K. (2017). Curcumin and its topical formulations for wound healing applications. *Drug Discov. Today* 22, 1582–1592. doi: 10.1016/j.drudis.2017.07.001

Numata, Y., Mazzarino, L., and Borsali, R. (2015). A slow-release system of bacterial cellulose gel and nanoparticles for hydrophobic active ingredients. *Int. J. Pharm.* 486, 217–225. doi: 10.1016/j.ijpharm.2015.03.068

Oliveira Barud, H. G., Barud, H. D. S., Cavicchioli, M., Do Amaral, T. S., De Oliveira Junior, O. B., Santos, D. M., et al. (2015). Preparation and characterization of a bacterial cellulose/silk fibroin sponge scaffold for tissue regeneration. *Carbohydr. Polym.* 128, 41–51. doi: 10.1016/j.carbpol.2015.04.007

Panchatcharam, M., Miriyala, S., Gayathri, V. S., and Suguna, L. (2006). Curcumin improves wound healing by modulating collagen and decreasing reactive oxygen species. *Mol. Cell. Biochem.* 290, 87–96. doi: 10.1007/s11010-006-9170-2

Rajwade, J. M., Paknikar, K. M., and Kumbhar, J. V. (2015). Applications of bacterial cellulose and its composites in biomedicine. *Appl. Microbiol. Biotechnol.* 99, 2491–2511. doi: 10.1007/s00253-015-6426-3

Sajjad, W., Khan, T., Ul-islam, M., Khan, R., Hussain, Z., and Khalid, A. (2019). Development of modified montmorillonite-bacterial cellulose nanocomposites as a novel substitute for burn skin and tissue regeneration. *Carbohydr. Polym.* 206, 548–556. doi: 10.1016/j.carbpol.2018.11.023

Shah, N., Ha, J. H., and Park, J. K. (2010). Effect of reactor surface on production of bacterial cellulose and water soluble oligosaccharides by *Gluconacetobacter hansenii* PJK. *Biotechnol. Bioprocess Eng.* 15, 110–118. doi: 10.1007/s12257-009-3064-6

Shah, N., Ul-Islam, M., Khattak, W. A., and Park, J. K. (2013). Overview of bacterial cellulose composites: a multipurpose advanced material. *Carbohydr. Polym.* 98, 1585–1598. doi: 10.1016/j.carbpol.2013.08.018

Shehzad, A., Rehman, G., and Lee, Y. S. (2013). Curcumin in inflammatory diseases. *Biofactors* 39, 69–77. doi: 10.1002/biof.1066

Subtaweesin, C., Woraharn, W., Taokaew, S., Chiaoprakobkij, N., Sereemaspun, A., and Phisalaphong, M. (2018). Characteristics of curcumin-loaded bacterial cellulose films and anticancer properties against malignant melanoma skin cancer cells. *Appl. Sci.* 8:1188. doi: 10.3390/app8071188

Syng-ai, C., Kumari, A. L., and Khar, A. (2004). Effect of curcumin on normal and tumor cells : role of glutathione and bcl-2. *Mol. Cancer Ther.* 3, 1101–1108.

Takeda, N., Tamura, K., Mineguchi, R., Ishikawa, Y., Haraguchi, Y., Shimizu, T., et al. (2016). In situ cross-linked electrospun fiber scaffold of collagen for fabricating cell-dense muscle tissue. *J. Artif. Organs* 19, 141–148. doi: 10.1007/s10047-015-0871-8

Torgbo, S., and Sukyai, P. (2018). Bacterial cellulose-based scaffold materials for bone tissue engineering. *Appl. Mater. Today* 11, 34–49. doi: 10.1016/j.apmt.2018.01.004

Ul-Islam, M., Ha, J. H., Khan, T., and Park, J. K. (2013a). Effects of glucuronic acid oligomers on the production, structure and properties of bacterial cellulose. *Carbohydr. Polym.* 92, 360–366. doi: 10.1016/j.carbpol.2012.09.060

Ul-Islam, M., Khan, T., Khattak, W. A., and Park, J. K. (2013b). Bacterial cellulose-MMTs nanoreinforced composite films: novel wound dressing material with antibacterial properties. *Cellulose* 20, 589–596. doi: 10.1007/s10570-012-9849-3

Ul-Islam, M., Khan, T., and Park, J. K. (2012). Nanoreinforced bacterial cellulose-montmorillonite composites for biomedical applications. *Carbohydr. Polym.* 89, 1189–1197. doi: 10.1016/j.carbpol.2012.03.093

Ul-Islam, M., Khattak, W. A., Ullah, M. W., Khan, S., and Park, J. K. (2014). Synthesis of regenerated bacterial cellulose-zinc oxide nanocomposite films for biomedical applications. *Cellulose* 21, 433–447. doi: 10.1007/s10570-013-0109-y

Ul-Islam, M., Shah, N., Ha, J. H., and Park, J. K. (2011). Effect of chitosan penetration on physico-chemical and mechanical properties of bacterial cellulose. *Korean J. Chem. Eng.* 28, 1736–1743. doi: 10.1007/s11814-011-0042-4

Ul-Islam, M., Subhan, F., Islam, S. U., Khan, S., Shah, N., Manan, S., et al. (2019). Development of three-dimensional bacterial cellulose/chitosan scaffolds: analysis of cell-scaffold interaction for potential application in the diagnosis of ovarian cancer. *Int. J. Biol. Macromol.* 137, 1050–1059. doi: 10.1016/j.ijbiomac.2019.07.050

Ul-islam, M., Ullah, M. W., Khan, S., and Park, J. K. (2020). Production of bacterial cellulose from alternative cheap and waste resources: a step for cost reduction with positive environmental aspects. *Korean J. Chem. Eng.* 37, 925–937. doi: 10.1007/s11814-020-0524-3

Ullah, M. W., Ul Islam, M., Khan, S., Shah, N., and Park, J. K. (2017). Recent advancements in bioreactions of cellular and cell-free systems: a study of bacterial cellulose as a model. *Korean J. Chem. Eng.* 34, 1591–1599. doi: 10.1007/s11814-017-0121-2

Ullah, M. W., Ul-Islam, M., Khan, S., Kim, Y., Jang, J. H., and Park, J. K. (2016a). In situ synthesis of a bio-cellulose/titanium dioxide nanocomposite by using a cell-free system. *RSC Adv.* 6, 22424–22435. doi: 10.1039/C5RA26704H

Ullah, M. W., Ul-Islam, M., Khan, S., Kim, Y., and Park, J. K. (2016b). Structural and physico-mechanical characterization of bio-cellulose produced by a cell-free system. *Carbohydr. Polym.* 136, 908–916. doi: 10.1016/j.carbpol.2015.10.010

Ullah, M. W., Ul-Islam, M., Khan, S., Kim, Y., and Park, J. K. (2015). Innovative production of bio-cellulose using a cell-free system derived from a single cell line. *Carbohydr. Polym.* 132, 286–294. doi: 10.1016/j.carbpol.2015.06.037

Wang, H., Hao, L., Wang, P., Chen, M., Jiang, S., and Jiang, S. (2017). Release kinetics and antibacterial activity of curcumin loaded zein fibers. *Food Hydrocoll.* 63, 437–446. doi: 10.1016/j.foodhyd.2016.09.028

Yun, D. G., and Lee, D. G. (2016). Antibacterial activity of curcumin via apoptosis-like response in *Escherichia coli*. *Appl. Microbiol. Biotechnol.* 100, 5505–5514. doi: 10.1007/s00253-016-7415-x

Conflict of Interest: The authors declare that the research was conducted in the absence of any commercial or financial relationships that could be construed as a potential conflict of interest.

frontiers
in Bioengineering and Biotechnology

REVIEW
published: 23 November 2020
doi: 10.3389/fbioe.2020.593768

Latest Advances on Bacterial Cellulose-Based Antibacterial Materials as Wound Dressings

Lu Zheng[1]*, Shanshan Li*[1]*, Jiwen Luo*[2]** and Xiaoying Wang*[1]**

[1] State Key Laboratory of Pulp and Paper Engineering, South China University of Technology, Guangzhou, China, [2] Key Laboratory of Theoretical Chemistry of Environment, Ministry of Education, School of Chemistry and Environment, South China Normal University, Guangzhou, China

At present, there are various wound dressings that can protect the wound from further injury or isolate the external environment in wound treatment. Whereas, infection and slow self-healing still exist in wound healing process. Therefore, it is urgent to develop an ideal wound dressing with good biocompatibility and strong antibacterial activity to promote wound healing. Bacterial cellulose is a kind of promising biopolymer because it can control wound exudate and provide a moist environment for wound healing. However, the lack of antibacterial activity limits its application. In this paper, the advantages of bacterial cellulose as wound dressings were introduced, and the preparation and research progress of bacterial cellulose-based antibacterial composites in recent years were reviewed, including adding antibiotics, combining with inorganic antibacterial agents or organic antibacterial agents. Finally, the existing problems and future development direction of bacterial cellulose-based antibacterial wound dressings were discussed.

Keywords: bacterial cellulose, wound dressings, infection, antibacterial activity, sustained release

Edited by:
Muhammad Wajid Ullah,
Huazhong University of Science and Technology, China

Reviewed by:
Xin Zhao,
Hong Kong Polytechnic University, Hong Kong
Baolin Guo,
Xi'an Jiaotong University, China

Correspondence:
Xiaoying Wang
xyw@scut.edu.cn
Jiwen Luo
holdit@126.com

Specialty section:
This article was submitted to Biomaterials, a section of the journal Frontiers in Bioengineering and Biotechnology

Received: *11 August 2020*
Accepted: *27 October 2020*
Published: *23 November 2020*

Citation:
Zheng L, Li S, Luo J and Wang X (2020) Latest Advances on Bacterial Cellulose-Based Antibacterial Materials as Wound Dressings. Front. Bioeng. Biotechnol. 8:593768. doi: 10.3389/fbioe.2020.593768

INTRODUCTION

Human skin covers the whole body surface, which is the barrier between human body and external environment, and plays an important role in preventing pathogens from entering human body (Byrd et al., 2018). In addition, the skin can regulate a variety of body functions, has effects on protection, excretion, temperature regulation and external stimulus perception, and also supports blood vessels and nerves (Yildirimer et al., 2012). Wound repair is a dynamic process, which mainly consists of several stages (**Figure 1A**). The first reaction after injury is hemostasis, which occurs at the site of blood loss in the wound (Sinno and Prakash, 2013). The second stage is inflammation lasting from 24 h to 4–6 days, which begins with releasing proteolytic enzymes and proinflammatory cytokines from invasive immune cells into the wound area, and these inflammatory cells produce reactive oxygen species (ROS) to protect the organism from bacterial infection (Thomason et al., 2018). At this stage, all foreign bodies and tissue debris are removed from the wound bed by neutrophils and macrophages, thus preventing infection (Minutti et al., 2017). Furthermore, the release of cytokines and enzymes stimulate the growth of fibroblasts and myofibroblasts, and wound exudate ensures the necessary moisture for healing (Das and Baker, 2016; Suarato et al., 2018). The third stage is the proliferation stage, in which new granulation tissue forms and grows in the wound area to form the new extracellular matrix. The final stage of healing is remodeling. At this stage, the matrix composition changes and collagen III is replaced by collagen I, which leads to the increased tensile strength of new tissues (Bielefeld et al., 2013;

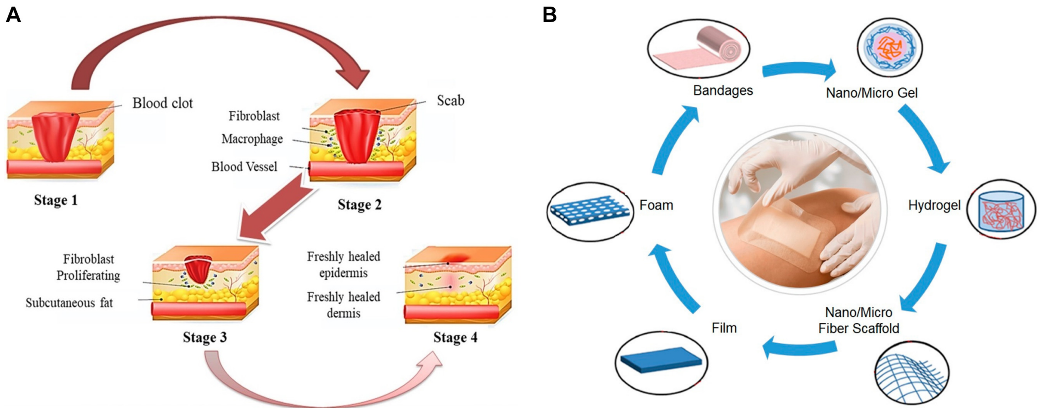

FIGURE 1 | (A) Wound self-healing process (Moeini et al., 2020). **(B)** Different forms of wound dressings (Teixeira et al., 2020).

Sinno and Prakash, 2013; Das and Baker, 2016). Skin wound repair is a complex physiological process, which is often affected by uncertain factors. Self-healing of wound is slow and susceptible to external infections, hence appropriate wound dressing is needed to promote and guide the healing process.

Optimal dressings are defined as being able to maintain high humidity at the wound site, remove excess exudates, have non-toxicity and non-allergy reaction, allow oxygen exchange, prevent microbial invasion, be comfortable, and cost-effective (Jannesari et al., 2011; Dart et al., 2019; Rezvani Ghomi et al., 2019; Felgueiras et al., 2020). Both natural and synthetic polymers can be used to prepare wound dressings, while natural polymers are widely used in wound dressings due to their biocompatibility, biodegradability, high bionic level and physicochemical properties. In particular, biopolymer based wound dressings, whose degradation rate should be synchronized with the wound healing process, should ensure the effective release of active substances at the same time (Suarato et al., 2018). Natural polymer materials that have been studied as wound dressing for the moment include agar, sodium alginate, hyaluronic acid, chitin, chitosan, carrageenan, cellulose, pectin, starch, collagen and so on. Moreover, different forms of wound dressings can be prepared, including bandages, hydrogel, film, sponge, foam, nanofiber mats, etc (Ambekar and Kandasubramanian, 2019; Teixeira et al., 2020; **Figure 1B**). On account of that wound dressings are the barrier to protect wounds, it is particularly significant to develop suitable wound dressings. The ideal wound dressings should promote healing and bring the least inconvenience to patients. At the same time, they can remove excessive exudate, improve autolysis debridement, and keep enough water for healing. In addition, wound dressings should also have certain applicability, flexibility, stability, barrier property, biodegradability, certain viscosity and be easy to remove, so as to speed up the healing speed and reduce the chance of infection (Boateng and Catanzano, 2015; Suarato et al., 2018).

Wound repair is a physiological process affected by many factors, and its complexity often leads to some uncertainties, such as slow wound healing, secondary infection, and inflammation (Au-Crane et al., 2020). Therefore, it is very important to choose appropriate wound dressing to promote and guide the healing process. Bacterial cellulose (BC), as a new type of wound dressing material, has attracted more and more attention. Various species of bacteria can produce cellulose in a biosynthesis pathway that involves the secretion of polysaccharides produced from carbon sources (Fernandes et al., 2020). This nanostructured cellulose has good physicochemical and mechanical properties, outstanding biocompatibility and biodegradability (Sulaeva et al., 2015). Compared with plant-derived cellulose, BC has high purity, simple purification process and three-dimensional (3D) network structure similar to extracellular matrix, so it is widely studied in tissue engineering and reconstruction of damaged tissues, wound healing and vascular regeneration (Li Z. et al., 2016; Frone et al., 2020; Pang et al., 2020). In addition, BC has the potential to be applied to various fields such as drug delivery, bioprinting, implants, artificial organs, and others (Ul-Islam et al., 2015; Ullah et al., 2016; Yang et al., 2018). BC has many excellent properties for wound healing, but the lack of antibacterial activity limits its application in wound dressings (Wei et al., 2011). The antibacterial activity of wound dressings plays an important role in anti-infection and promoting wound healing during wound treatment.

In order to endow BC with antibacterial properties, many studies have prepared BC-based composite materials with antibacterial function as wound dressing. The high porosity and surface area of BC allow the introduction and release of antimicrobial agents, drugs and other biological functional materials (Buruaga-Ramiro et al., 2020). This paper reviews the preparation methods and slow release behavior of BC-based antibacterial materials for wound dressings, as shown in **Figure 2**.

BACTERIAL CELLULOSE

Brief Description

Bacterial cellulose is a natural polymer produced by bacterial strains with 3D network structure composed of cellulose chains, and the network can be filled with a large amount of liquid to

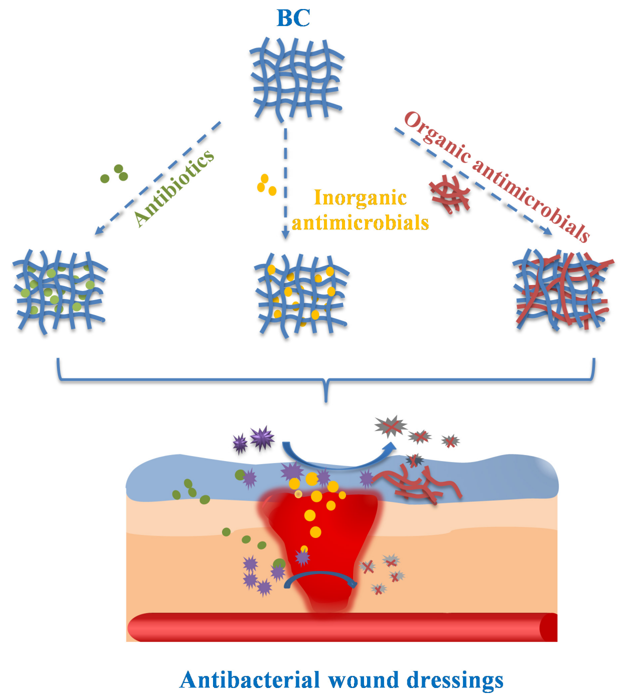

FIGURE 2 | The preparation and slow release behavior of BC-based antibacterial wound dressings.

support tissue regeneration (Sulaeva et al., 2015; **Figure 3A**). The production of BC dates back to 1886 (Brown, 1886). Various species of bacteria can produce cellulose in a biosynthesis pathway that involves the secretion of polysaccharides produced from carbon sources (Fernandes et al., 2020). Microorganisms that synthesize BC include *Acetobacter*, *Agrobacterium*, *Rhizobium*, *Sarcina*, etc., and carbon sources could be glucose, fructose, maltitol, sucralose, lactose, etc. Agricultural corn stalk, nutshell, other agricultural or industrial waste also could be carbon sources (Cheng et al., 2017; Dórame-Miranda et al., 2019; Ul-Islam et al., 2020). Besides, BC can also be synthesized in a cell-free system which does not have a complete cell structure but retains a biosynthetic cell extract. Ullah et al. (2015) hypothesized a synthetic pathway for bio-cellulose synthesis in the cell-free system, which can overcome some limitations of cellulose-producing cells and offers a wider scope for synthesizing cellulose composites with bactericidal elements. The production and yield of BC are influenced by carbon source concentration, species and other medium components. The majority of low-cost culture media have the potential to produce BC on an industrial scale (Velásquez-Riaño and Bojacá, 2017). Optimization strategies (conventional or statistical) have become relevant for the cost-effective production of BC (Fernandes et al., 2020).

Bacterial cellulose is known for its many desirable properties, such as sustainability, biocompatibility, biodegradability, extensive chemical modification capability, and high surface area. Although BC and plant-derived cellulose all have the same chemical structure of linear β-1,4-glucan chains, there are still many differences in physical properties between them (de Amorim et al., 2020). Plant-derived cellulose chains are closely related to hemicellulose, lignin, etc., while BC contains no other polymers so that it has high purity and simple purification (Klemm et al., 2011). The continuous spinning of cellulose ribbons by bacteria leads to the formation of 3D network structure of nanofibers stabilized by hydrogen bonds (Luo et al., 2014). The special fiber network structure endows BC with unique mechanical properties like high crystallinity and high Young's modulus, the highest of all two-dimensional organic materials (Dayal and Catchmark, 2016). As a result of the high aspect ratio of the fiber, BC with a high specific surface area can provide a liquid loading capacity of up to 99 wt.%. In the presence of water, about 90% of water molecules are tightly bound to a large number of hydroxyl groups in cellulose molecules (Bashari et al., 2018). Compared with plant-derived cellulose, BC has larger specific surface area. The water absorption of BC is 30% higher than that of cotton yarn, and the drying time is prolonged by 33% (Meftahi et al., 2010).

Bacterial Cellulose as Wound Dressings

The common biomass materials for wound dressings include chitosan, gelatin, hyaluronic acid, etc (Wu J. et al., 2018; İnal and Mülazımoğlu, 2019; Graça et al., 2020). These materials have good biocompatibility, degradability, mechanical properties, etc., but BC has unique advantage in the application of wound dressings for it has more excellent properties at the same time. The use of BC as a wound healing material is determined by its unique characteristics, including high tensile strength, good flexibility, strong water holding capacity, significant permeability to gas and liquid, great compatibility with living tissues and so on. In terms of biocompatibility, BC itself has no cytotoxicity and no toxic substances are introduced in the production process, and there are no adverse reactions produced when BC contacts with human body in short-term or long-term because of its histocompatibility and blood compatibility. These unique properties of BC are closely related to its source, structure and functional characteristics, which have a certain impact on wound healing (**Table 1**). In addition, pure BC can be modified specifically to meet all the necessary functional requirements as a wound dressing (Sulaeva et al., 2015; **Figure 3B**).

The normal progress of wound healing mechanism may be destroyed by many factors, resulting in the prolongation of healing time. In this case, the demand for dressings has risen to a new level that requires them to actively participate in the complex wound repair process. BC, as one of the promising wound dressing materials, can control wound exudate and provide moist environment for wound healing (Nuutila and Eriksson, 2020), but it lacks antibacterial activity that limits its application. Complications can easily occur in chronic wounds where severe physiological changes or tumorigenesis may happen, which can lead to excessive production of exudates containing high levels of tissue-destructive proteases and contamination of wounds by foreign bodies (e.g., bacteria) because of inflammatory reactions (Lindsay et al., 2017; Ruf et al., 2017). For example, more than 50% of diabetic chronic ulcers are infected, and the infection is one of the most common and serious sequelae during wound

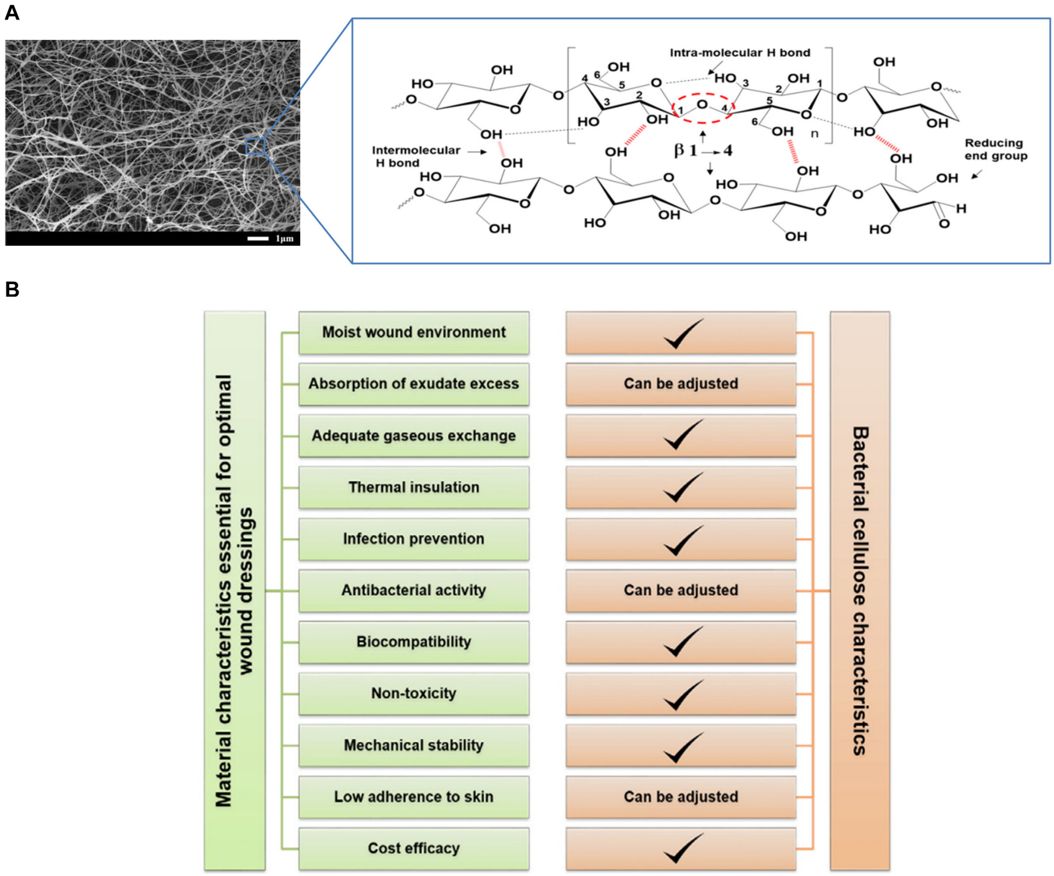

FIGURE 3 | (A) General introduction of BC tissue structure (Shao et al., 2016a; Tayeb et al., 2018). **(B)** An overview of BC characteristics with respect to the general requirements for wound dressing materials (Sulaeva et al., 2015).

healing and also the major factor in delayed healing (Alavi et al., 2014). Furthermore, due to the adverse effect of the patients' immune system and the extensive destruction of physical skin barrier, which cannot prevent the invasion of bacteria, the problem of microorganism colonization in the wounds of burn patients is particularly serious (Oryan et al., 2017). Therefore, the development of wound dressings with antibacterial activity is particularly important for reducing bacterial infection and promoting wound healing.

BACTERIAL CELLULOSE-BASED ANTIBACTERIAL WOUND DRESSINGS

In order to prepare BC-based composites with good antibacterial properties as wound dressings, three methods can be used: adding antibiotics, combining with inorganic antibacterial agents, and combining with organic antibacterial agents. Adding antibiotics is the most commonly used method, which has been widely used in clinical application. Inorganic antibacterial agents have excellent antibacterial properties and have a great application prospect in the field of biomedicine. Natural organic antibacterial substances have attracted wide attention due to their good biocompatibility and biodegradability.

Addition of Antibiotics

The antibacterial activity of BC-based wound dressings is often achieved by adding antibiotics. The most commonly used antibiotics are ciprofloxacin, ceftriaxone, tetracycline hydrochloride (TCH), amoxicillin and so on (**Figure 4A**). Chemical modification and the incorporation of antibiotics can further increase the potential of BC as a biomedical material. BC is composed of β-1,4-glucose, where there are three active hydroxyl groups in C2, C3, and C6 of glucopyranosyl ring. BC can be easily modified at these sites by oxidation, esterification or etherification to introduce new functional groups. Immersion method is the common method of combining BC with antibiotics, which is simple and easy to operate but may cause uneven distribution of antibiotics. For example, vancomycin and ciprofloxacin can be incorporated into bacterial nanocellulose (BNC) or modified BNC to provide bioactivity for wound dressing and tissue engineering scaffold (Vismara et al., 2019). The BC composite materials containing amikacin and ceftriaxone were prepared by immersing the dried BC films in different concentrations of antibiotics solution. And the

TABLE 1 | The relation among BC structures, BC properties, and wound healing.

BC structures	BC properties	Effects on wound healing	References
Composition of glucose monomer	Biocompatibility and biodegradability	have good compatibility with living tissue and avoid allergic reactions and foreign body rejection	Mohamad et al., 2017; Rühs et al., 2018; Torgbo and Sukyai, 2020
3D network structure	Mechanical stability and certain permeability to liquids and gases	1. Allow the absorption and evaporation of exudate and the oxygen exchange, and protect the wound from infection	Meftahi et al., 2010; Klemm et al., 2011; Luo et al., 2014; Dayal and Catchmark, 2016; Bashari et al., 2018; Portela et al., 2019; Nuutila and Eriksson, 2020
Fiber with high aspect ratio and high specific surface area	High tensile strength, good flexibility and high liquid loading capacity	2. Have stable mechanical properties, and easy to remove from the wound to avoid secondary injuries	
Abundant hydroxyl group	Strong hydrophilicity and water retention	3. Provide a warm and moist micro-environment for the wound, which is conducive to wound healing	

composites have obvious antibacterial activity against *Escherichia coli*, *Pseudomonas aeruginosa*, *Streptococcus pneumoniae*, and *Staphylococcus aureus*, so they are expected to be used as wound dressings (Volova et al., 2018). Moreover, it was observed that the bilayer BC film synthesized in different carbon sources (sugarcane molasses, syrup, and fructose) had the ability to retain and slowly release ceftriaxone, an antimicrobial drug (Lazarini et al., 2016).

The 3D network structure of BC is the basis for antibiotic to be contained and released continuously (Buruaga-Ramiro et al., 2020). The BC-TCH composite membrane loading TCH has good antibacterial activity, biocompatibility and controlled release of TCH (Shao et al., 2016a; **Figure 4B**). Amoxicillin is easy to degrade and then lose its antibacterial activity, so it is very important to limit the release of amoxicillin. Grafting antibiotics onto modified BC is also a commonly used method. Ye et al. (2018) designed a new biocompatible sponge with excellent antibacterial properties by grafting amoxicillin onto regenerated bacterial cellulose (RBC), and the grafted RBC enhanced the antibacterial activity against fungi, Gram-negative and Gram-positive bacteria, which had great potential in clinical application of wound dressings.

Combination With Inorganic Antimicrobials

Due to the overuse of antibiotics, many bacteria have developed resistance to antibiotics, which greatly reduces the antibacterial effect (Kuehn, 2018; Durand et al., 2019; Subramaniam and Girish, 2020). For the sake of finding new antibacterial agents that are not easy to produce drug resistance and have excellent antibacterial effect to replace antibiotics, people have focused on inorganic antibacterial agents, including various metal/metal oxide nanoparticles, carbon nanomaterials and nanosilicate materials. The combination of inorganic antibacterial agents and BC has always been a research hotspot, particularly nano antibacterial materials composed of metal/metal oxides and BC (**Table 2**). Dipping, reduction, deposition are commonly used composite methods, the choice of composite methods depends on different situations.

Metal/Metal Oxide Nanoparticles

Silver nanoparticles (Ag NPs) have attracted much attention due to their broad-spectrum antibacterial properties. A great deal of research has shown that these nanoparticles can kill bacteria, but the antibacterial mechanism of Ag NPs is still unclear. Some researchers believe that when silver ion (Ag^+) released from Ag NPs reaches a certain concentration range it will inhibit the growth of bacteria, destroy cell membrane and prevent DNA replication and transcription. In addition, silver or silver ions can promote the production of intracellular ROS, thus destroying the structure and function of bacterial cells (Le Ouay and Stellacci, 2015; Sukhorukova et al., 2017). BC can be combined with Ag NPs in different ways to obtain antibacterial BC-based materials. The aldehyde or carboxyl groups on BC are usually obtained through oxidation with oxidants, such as sodium periodate and 2,2,6,6-tetramethylpiperidinyloxy (TEMPO). Sodium periodate can selectively oxidize hydroxyl groups on C6 position of BC to form aldehyde group. Through using more sodium periodate and longer oxidation time, oxidized nanocellulose with higher aldehyde group content can be obtained (Sirvio et al., 2011). TEMPO can link on the surface of nanocellulose under aqueous condition and convert the hydroxyl group at C6 position into aldehyde or carboxyl functional groups (Cao et al., 2012). Wu C. -N. et al. (2018) prepared TEMPO-oxidized BC film (TOBCP), which then reacted in $AgNO_3$ solution. Ag NPs with a diameter of 16.5 nm were synthesized on the surface of TOBCP nanofibers by thermal reduction method without reducing agent (Wu C. -N. et al., 2018; **Figure 5A**). The prepared TOBCP/Ag NPs composites have good biocompatibility and high antibacterial activity against *E. coli* and *S. aureus* to be a promising wound dressing. It is also a common way to load Ag NPs on BC by dipping method (Mohite and Patil, 2016; Yang et al., 2017; Moniri et al., 2018b; Chatchawanwirote et al., 2019). For example, in the presence of sodium tripolyphosphate, using $AgNO_3$ solution as the precursor and BC film as the template, transparent Ag NPs/BC films were prepared though *in situ* dipping method, whose antibacterial rates to *E. coli* and *S. aureus* were 100% and 99.99%, respectively (Tabaii and Emtiazi, 2018). Because the films were transparent, the wound could be observed continuously without removing the dressing. Furthermore, ultraviolet irradiation can also be utilized for Ag NPs deposition on the BC gel network and Ag NPs combine with the cellulose fiber surface (Pal et al., 2017; **Figure 5B**). The composite has good antibacterial properties, and Ag/BC film has no obvious silver release after long time immersion.

Due to the potential cytotoxicity of Ag NPs (Mijnendonckx et al., 2013; Hu et al., 2015; Tian et al., 2020),

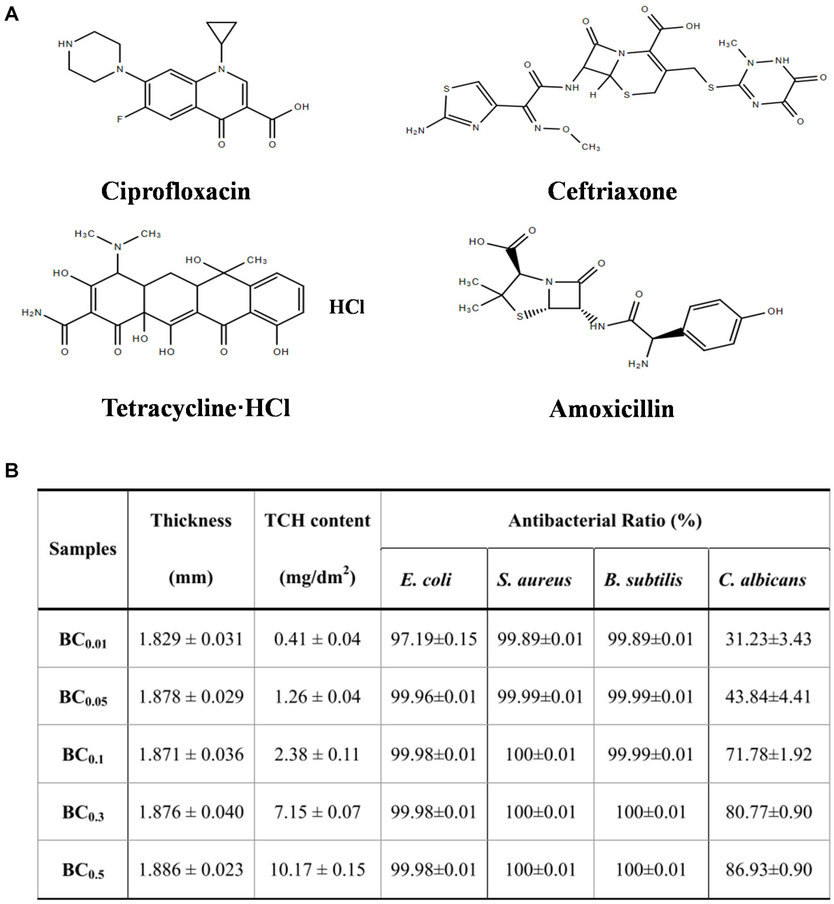

Samples	Thickness (mm)	TCH content (mg/dm^2)	Antibacterial Ratio (%)			
			E. coli	*S. aureus*	*B. subtilis*	*C. albicans*
BC$_{0.01}$	1.829 ± 0.031	0.41 ± 0.04	97.19±0.15	99.89±0.01	99.89±0.01	31.23±3.43
BC$_{0.05}$	1.878 ± 0.029	1.26 ± 0.04	99.96±0.01	99.99±0.01	99.99±0.01	43.84±4.41
BC$_{0.1}$	1.871 ± 0.036	2.38 ± 0.11	99.98±0.01	100±0.01	99.99±0.01	71.78±1.92
BC$_{0.3}$	1.876 ± 0.040	7.15 ± 0.07	99.98±0.01	100±0.01	100±0.01	80.77±0.90
BC$_{0.5}$	1.886 ± 0.023	10.17 ± 0.15	99.98±0.01	100±0.01	100±0.01	86.93±0.90

FIGURE 4 | (A) Structural formula of four common antibiotics. **(B)** Antibacterial properties of BC-TCH composite films with different TCH content (Shao et al., 2016a).

TABLE 2 | BC-based metal/metal oxide nano-antibacterial composites.

Metal/metal oxide	Preparation methods	Bacterial species	Mechanism	References
Ag	*In situ* reduction, dipping or photodeposition	*S. aureus* and *E. coli*	Ag^+ release inhibits cell growth, disrupts cell membrane and prevents DNA replication and transcription, or the generation of ROS destroys cell structure and function	Le Ouay and Stellacci, 2015; Mohite and Patil, 2016; Pal et al., 2017; Sukhorukova et al., 2017; Yang et al., 2017; Moniri et al., 2018b; Tabaii and Emtiazi, 2018; Wu C. -N. et al., 2018; Chatchawanwirote et al., 2019
Au	Dipping	*E. coli*, *MDR E. coli*, *P. aeruginosa* and *MDR P. aeruginosa*	Light excitation produces local heat to destroy cell structure, and Au NPs combine with ribosome subunits to prevent protein synthesis	Cui et al., 2012; Li et al., 2017; Nisar et al., 2019
Cu	Dipping or *in situ* reduction	*S. aureus*, *B. subtilis*, *C. albicans*, *E. coli* and *P. aeruginosa*	Cu^+ release destroys cell membranes and damages DNA and cell enzyme	Bogdanovic et al., 2014; Shao et al., 2016c; He et al., 2018
TiO_2	Dipping	*S. aureus* and *E. coli*	Photocatalytic generation of ROS to sterilize	Khalid et al., 2017b; Pathakoti et al., 2019
ZnO	*In situ* deposition or electrochemical deposition	*S. aureus* and *E. coli*	Zn^+ release and photocatalytic generation of ROS to sterilize	Janpetch et al., 2016; Khalid et al., 2017a; Joe et al., 2018; Luo et al., 2020
Fe_3O_4	*In situ* deposition	*S. aureus*, *S. epidermidis* and *P. aeruginosa*	Magnetic thermotherapy produces local heat for sterilization	Raval et al., 2017; Moniri et al., 2018a

people began to pay attention to other noble metal nanoparticles, such as gold nanoparticles (Au NPs), copper nanoparticles (Cu NPs) and so on. Au NPs have many unique properties, like low toxicity, photothermal effect, large specific surface area, multifunctional surface modification and multivalent effect, etc (Xianyu et al., 2014; Connor and Broome, 2018). For the excellent

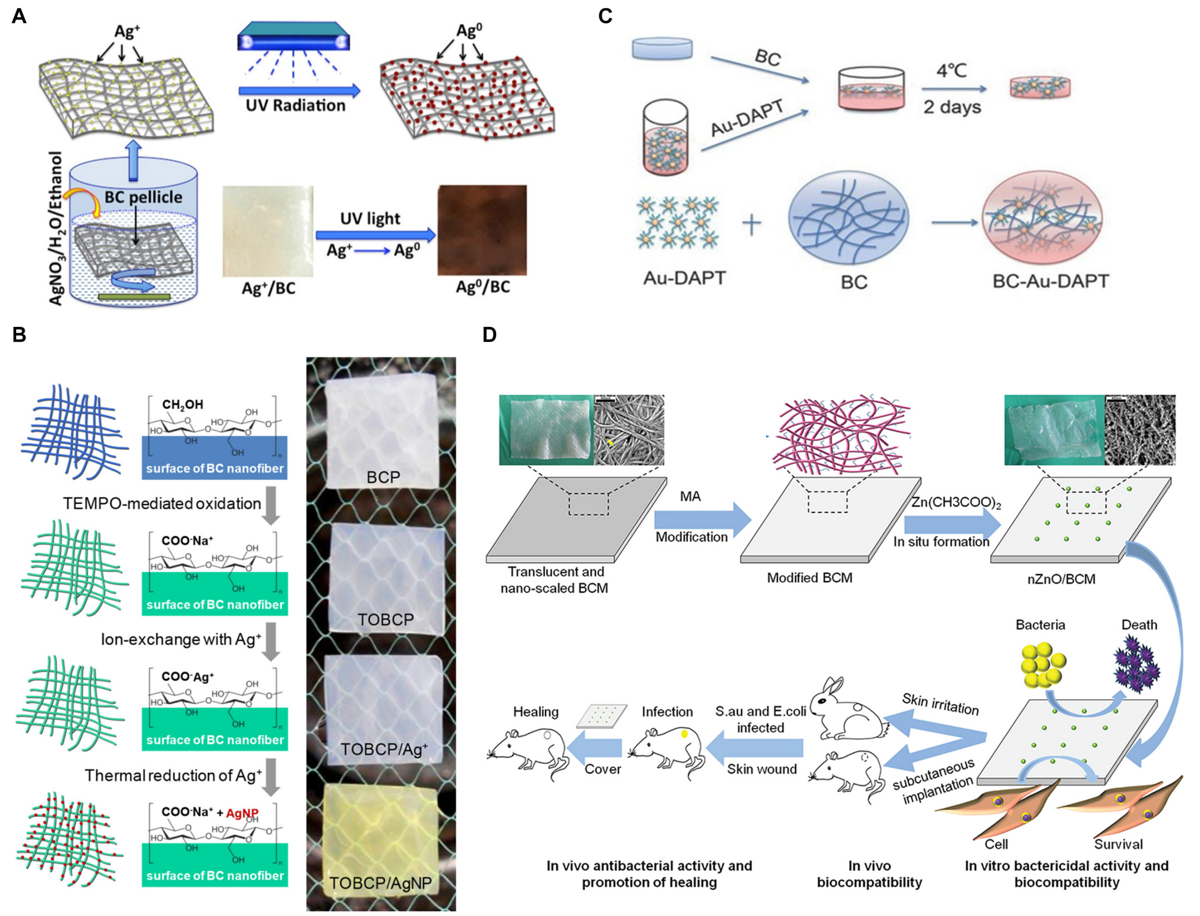

FIGURE 5 | (A) Ag/BC films prepared by photochemical deposition (Pal et al., 2017). **(B)** TOBCP/Ag NPs films prepared by thermal reduction method (Wu C. -N. et al., 2018). **(C)** BC-Au- DAPT nanocomposites prepared by solution dipping method (Li et al., 2017). **(D)** nZnO/BCM composites prepared by *in situ* deposition method (Luo et al., 2020).

photothermal effect of Au NPs, local heat is generated under laser irradiation, thus destroying the cell structure. In addition, Au NPs have been proved to bind to ribosomal subunits, which prevent the successful binding of ribosomes and tRNA, resulting in the failed synthesis of protein in bacterial cells (Cui et al., 2012; Nisar et al., 2019). The BC-Au-DAPT nanocomposites prepared by 4,6-diamino-2-pyrimidinethiol (DAPT) and BC have good physicochemical properties and better germicidal efficacy of Gram-negative bacteria than most antibiotics (**Figure 5C**). It can be used as dressing for the treatment of bacterial infection wounds (Li et al., 2017). In addition, Cu NPs can destroy bacterial cell membrane and damage DNA and cell enzyme via Cu ion (Cu^+) release (Bogdanovic et al., 2014). A series of RBC membranes loaded with Cu NPs were prepared by Shao et al. (2016c), and the antibacterial activities of RBC-Cu membranes against *S. aureus*, *Bacillus subtilis*, *Candida albicans*, *E. coli*, and *P. aeruginosa* were affected by the content of Cu NPs. *In situ* chemical reduction method was used to prepare BC-Cu NPs films, which showed high long-term antibacterial activity against *S. aureus* and *E. coli* and maintained the continuous release of Cu^+ after immersion in deionized water for 90 days (He et al., 2018). These results indicate that the antibacterial activity of wound dressing materials can be obtained by loading noble metal nanoparticles such as Ag NPs, Au NPs, and Cu NPs into BC membrane. The 3D network structure and high porosity of BC are conducive to the slow release of metal nanoparticles in composite materials, thus prolongs the antibacterial activity time.

Except noble metal nanoparticles, many metal oxide nanoparticles also have fantastic antibacterial properties, which have attracted the attention of researchers. Titanium dioxide (TiO_2), zinc oxide (ZnO), ferroferric oxide (Fe_3O_4) and other metal oxide nanoparticles were compounded with BC to prepare dressings with antibacterial activity and promoting wound healing. TiO_2 NPs have photocatalytic activity, which can produce ROS under sunlight to kill bacteria (Pathakoti et al., 2019). BC-TiO_2 nanocomposites have certain antibacterial activity against *E. coli* and *S. aureus*, good healing potential, faster speed of regenerative epithelialization and ability to accelerate wound contraction (Khalid et al., 2017b). ZnO NPs can kill bacteria through Zn ion (Zn^{2+}) release or ROS produced by photocatalysis (Joe et al., 2018). Based on maleic anhydride (MA) modified BC (BCM), the nZnO/BCM biocomposites were prepared using a simple and environmentally friendly method (**Figure 5D**), which not only showed excellent antibacterial activity against *S. aureus* and *E. coli*, but also prevented bacterial infection and promoted wound healing by accelerating reepithelization and wound contraction (Luo et al., 2020). Janpetch et al. (2016) synthesized ZnO NPs successfully by liquid-phase plasma discharge method without reducing agent, and deposited ZnO NPs into BC film with BC as template. The BC-ZnO composite showed strong antibacterial activity against *S. aureus* and *E. coli* to be used as antibacterial material in wound dressing. On the other hand, ZnO NPs can be directly impregnated into BC to obtain the composite with certain antibacterial activity and healing activity (Khalid et al., 2017a). In addition, Fe_3O_4 NPs, as a kind of magnetic nanoparticles, can generate local heat through magnetic thermotherapy to achieve sterilization (Raval et al., 2017). Moniri et al. (2018a) reported the formation and immobilization of spherical magnetic Fe_3O_4 NPs (15–30 nm), and BNC/Fe_3O_4 nanocomposites with non-toxic have nice antibacterial activity against *S. aureus*, *Staphylococcus epidermidis,* and *P. aeruginosa*. The composites also can increase the expression of other effective genes by reducing the expression of microRNA, thus leading to wound healing.

Carbon Nanomaterials

Graphene oxide (GO) is a potential wound dressing material with good biocompatibility and mechanical properties. Moreover, GO has high antibacterial activity against Gram-negative bacteria and Gram-positive bacteria. GO sheets can destroy the phospholipid bilayer along the edge of the sheet, that is, physical damage to bacterial cell membrane (Chen et al., 2014). It can also generate ROS under laser excitation or local heat under near-infrared light, so as to achieve antibacterial (Qiu et al., 2018). A new type of chitosan/BC nanofiber composite reinforced by GO nanosheets was developed. The addition of GO nanosheets reduced the average size of the fibers and affected their mechanical properties (Azarniya et al., 2016). Mohammadnejad et al. (2018) optimized the synthesis of GO-Ag nanohybrids by response surface methodology and impregnated them into BC. It was found that the GO-Ag nanohybrids exhibited synergetic enhanced antibacterial activity against *E. coli* and *S. aureus* at a relatively low dose. In another way, the BNC/polyacrylic acid/GO composite hydrogels were successfully synthesized by electron beam irradiation, and with the increase of GO concentration in hydrogels, their hardness and biocompatibility decreased, thus ensuring the durability and ease of wound dressings removal (Chen et al., 2019). BC was modified by amidation reaction between carboxylated BC and dopamine (DOPA). The BC-DOPA/rGO/Ag NPs composite membrane was prepared through the free hydroxyl group of BC-DOPA, and the composite membrane had antibacterial effect on Gram-positive and Gram-negative bacteria and accelerated the wound healing process because of rGO and Ag NPs (Khamrai et al., 2019; **Figure 6**).

Furthermore, a series of new BC/C-60 composites were prepared via *in situ* dehydration-rehydration method, which had high ROS production capacity under light conditions and strong antibacterial activity against *E. coli* and *S. aureus*, and could be used as multifunctional wound dressings (Chu et al., 2018). BC has the ability to carry and transfer drugs to assist wound healing. It has been studied that carbon quantum dots-TiO_2 (CQD-TiO_2) nanoparticles were added into BC as antibacterial agents, and the BC/CQD-TiO_2 nanostructure had good antibacterial properties and tensile strength, which provided an alternative method for making antibacterial wound dressings (Malmir et al., 2020).

Nanosilicates-Based Materials

Nanosilicates, such as montmorillonite (MMT), are composed of two silica tetrahedral sheets and a central octahedral alumina sheet, plate-shaped particles, and have antibacterial activity to clean and protect the skin, so that they have been widely used in the medical field. The BC/MMT membrane has excellent antibacterial activity against *E. coli* and *S. aureus* and potential therapeutic value in wound healing and tissue

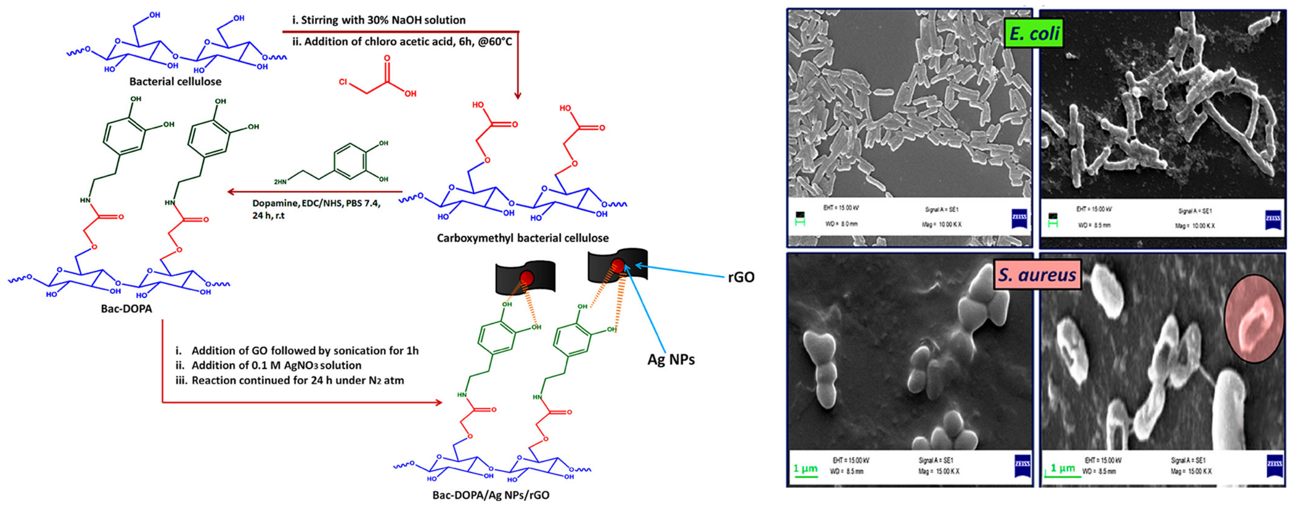

FIGURE 6 | Preparation process and antibacterial effect against *E. coli* and *S. aureus* of BC-DOPA/rGO/Ag NPs composite (Khamrai et al., 2019).

regeneration (Ul-Islam et al., 2013). Wasim et al. combined the wound healing characteristics of BC with the antibacterial activity of modified MMT (Cu-MMT, Na-MMT, and Ca-MMT) to obtain modified MMTs-BC nanocomposites that show enhanced wound healing activity and promoted functions of tissue regeneration, reepithelization, healthy granulation, and angiogenesis (Sajjad et al., 2019).

Combination With Organic Antimicrobials

Considering that there are some noble metal/metal oxide nanoparticles and carbon materials whose residues after use will pollute the environment to a certain extent (Tian et al., 2019), or cause long-term potential toxicity problems in the body and so on (Baker et al., 2014; Vimbela et al., 2017), people are looking for safer antibacterial materials with the least negative impact to the environment and human body. Organic antibacterial agents, including natural polymers (such as chitosan, curcumin, amino acids) and synthetic polymers (such as polyhexamethylene biguanidine), can be combined with BC to prepare antibacterial wound dressings. Among them, natural polymers have attracted more and more attention due to their excellent biocompatibility and degradability. The methods of combining BC with organic antimicrobials include immersion, physical blending, *in situ* synthesis, chemical fixation, electrostatic self-assembly and so on.

Natural Polymers

Chitosan (CS) is considered as a natural antibacterial compound, which can resist a variety of microorganisms, including bacteria, yeast, and mold (Li and Zhuang, 2020; Li et al., 2020). Low molecular weight CS can pass through the bacterial cell membrane and combine with negatively charged nucleic acid, while high molecular weight CS can adhere to the cell membrane and form a membrane on the surface of bacteria, thus hindering the transportation of nutrients (Li J. et al., 2016; Liu et al., 2020). A highly efficient dynamic culture method which retain nanofiber structure can be used to prepare CS/BC nanofiber hydrogel with high mechanical properties and great antibacterial activity against *E. coli* and *S. aureus* (Zhang et al., 2016). In addition, biopolymer blends based on BC membrane modified by low molecular weight chitosan (Chi) were developed for the controlled release of ciprofloxacin (CIP), and Chi had synergistic effect on CIP antibacterial activity (Cacicedo et al., 2020; **Figure 7A**). A novel hemostatic nanocomposite (OBC/COL/CS) was prepared by coupling oxidized bacterial cellulose (OBC), CS and collagen (COL) (Yuan et al., 2020; **Figure 7B**). In the electrostatic self-assembly process of OBC and CS, COL was skillfully attached as a functional component by the electrostatic adsorption between cationic CS and anionic OBC. The introduction of COL was expected to enhance hemostasis and promote wound healing, while CS provided antibacterial effect, so the composite material had rapid and efficient hemostatic effect and good antibacterial property.

Curcumin is a natural polyphenol compound, also a hydrophobic drug, with antibacterial activity and wound healing ability, so it is considered as a wound healing agent. Moreover, it is a natural reducing agent, which can be used for green synthesis of nanoparticles. The microencapsulation of curcumin in cyclodextrin (CD) has overcome the hydrophobicity of curcumin (Gupta et al., 2019). It has been studied that the compounds (cAgNP) containing Ag NPs were prepared with curcumin and hydroxypropyl-β-CD and then were loaded

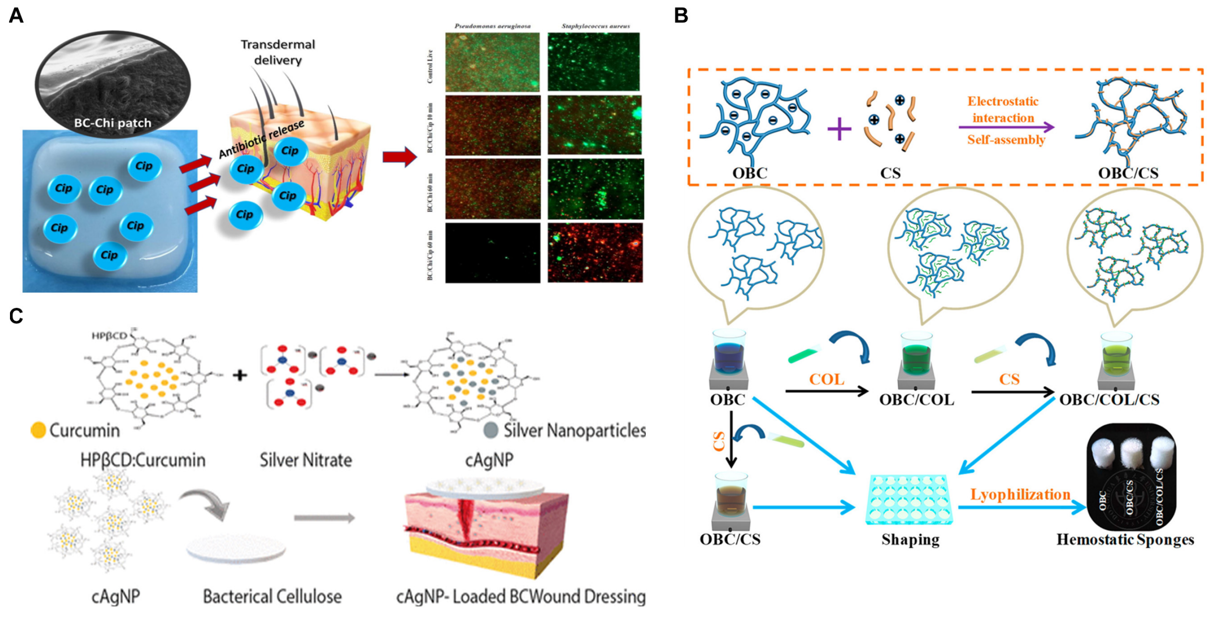

FIGURE 7 | (A) BC-Chi-CIP membrane for CIP controlled release with synergistic antibacterial effect of Chi and CIP (Cacicedo et al., 2020). **(B)** The preparation scheme of OBC/COL/CS hemostatic sponge with CS as antibacterial agent (Yuan et al., 2020). **(C)** Schematic representation of the preparation of cAgNP loaded BC-based wound dressing with synergistic antibacterial effect of curcumin and Ag NPs (Gupta et al., 2020).

into BC hydrogels with moist wound healing properties. The new dressing had not only high biocompatibility but also antibacterial activity to three common pathogenic bacteria in wound infections, *S. aureus*, *P. aeruginosa*, and *Candida* (Gupta et al., 2020; **Figure 7C**). Hydroxypropyl-β-CD enhanced the water solubility of curcumin and allowed it to be loaded in BC hydrogels, and BC hydrogels could be used for wound treatment, which also had good blood compatibility, cytocompatibility, anti-staphylococci, and antioxidant capacity (Gupta et al., 2019). Besides, a self-healing polyelectrolyte membrane was produced by crosslinking cationic charged CS with anionic modified BC, and the membrane could deliver curcumin (Khamrai et al., 2017). In another way, curcumin was encapsulated in pluronic and prepared into granules by extrusion method, and then the granules were coated with CS, which finally were successfully fixed on the surface of mBNC by EDC/NHC chemical method. The particles attached to the surface of mBNC could control the release of curcumin in a sustained and good way, which made the potential wound dressing have prolonged bioactivity (Rojewska et al., 2017).

In addition, lignin and its derived compounds also have antibacterial properties. In order to develop a highly effective antibacterial dressing for treating chronic wounds, a composite hydrogel (BC-DHP) of BC and lignin dehydrogenate polymer (DHP) was designed, and the BC-DHP hydrogel could release DHP oligomer with antibacterial activity (Zmejkoski et al., 2018).

Bioactive Substances

Lysine, tyrosine, arginine and other bioactive substances can promote cell proliferation and collagen deposition related to skin growth, thus accelerating wound healing, and some amino acids can also obtain antibacterial activity after modification. For the sake of exploring the practical application value of BC and developing new wound dressings, a series of BC/PILs composite membranes with antibacterial activity were synthesized by *in situ* synthesis method (He et al., 2020). Polymer ionic liquids (PILs) were formed by choline and different amino acids. Several BC/PILs membranes showed good biocompatibility and high antibacterial activity against Gram-positive and Gram-negative bacteria and fungi. ε-poly-L-lysine (ε-PLL) is a kind of non-toxic biopolymer with broad-spectrum antibacterial activity, and the ε-PLL functionalized BC can be used in wound dressing (Fursatz et al., 2018). Tyrosine (Tyr) is a natural amino acid, which can form non-covalent cation-pi interaction with positively charged ethylenediamine (EDA). A novel compound [EDA][DLA-Tyr] was synthesized by simple coupling reaction based on the dilinoleic acid (DLA) and Tyr. BC impregnated with [EDA][DLA-Tyr] showed strong and long-term antibacterial activity against *S. aureus* and *S. epidermidis*, as a promising new wound dressing (Zywicka et al., 2018).

Synthetic Compounds

Polyhexamethylene biguanide (PHMB) is a fungicide (**Figure 8A**), which has antibacterial effect on Gram-positive bacteria and Gram-negative bacteria. It has been studied that PHMB was mixed with BNC to improve the antibacterial effect of BC-based wound dressing (De Mattos et al., 2019). Napavichayanun et al. (2016) tried to develop a new type of BNC dressing, which was composed of PHMB as an antibacterial agent and sericin as a component for promoting wound healing. The antibacterial PHMB component played a role in reducing infection and inflammatory reaction, so the composite could be used as a safe and effective wound dressing material. The physical and biological properties of BC dressing were improved by adding silk fibroin (SS), PHMB and glycerin, because the dehydration rate of BC dressing decreased with the addition of glycerol to prevent adhesion to the wound, and SS promoted the formation of collagen and tissue in wound

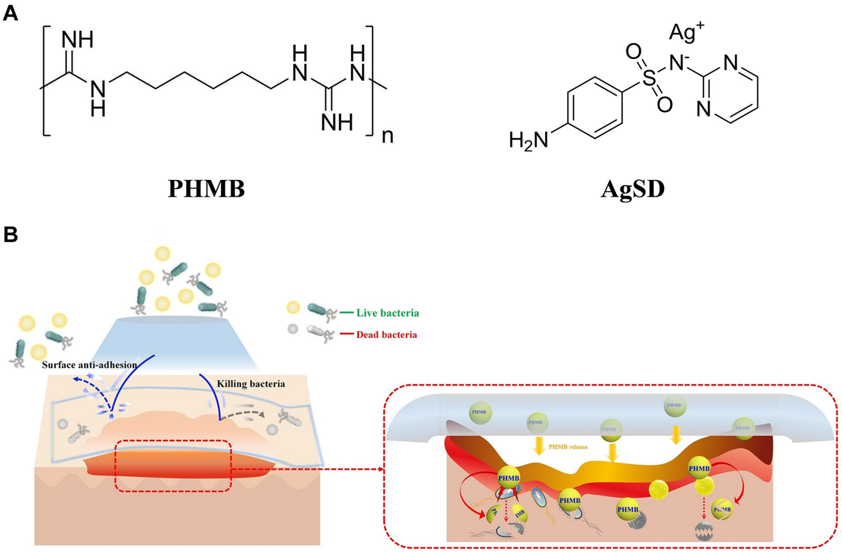

FIGURE 8 | (A) Molecular formula of fungicides PHMB and AgSD. **(B)** Multifunctional antibacterial effect of PHMB-PBC composites (Wang et al., 2019).

surface (Napavichayanun et al., 2018). Another new composite material (PHMB-PBC) composed of BC, polyethylene glycol and PHMB also has good physical and chemical properties, especially transparency, water holding capacity, flexibility and anti-adhesion force (Wang et al., 2019). Moreover, the composite has good biocompatibility and strong antibacterial activity, which can effectively promote the healing and regeneration of rat skin wounds (**Figure 8B**). In addition, silver sulfadiazine (AgSD) is also an antibacterial agent widely used in local burn management (**Figure 8A**), which has a wide range of antibacterial and antifungal effects, and its mechanism of action is related to the ionization and release of Ag^+ (Dellera et al., 2014). When the ions are released too much, cytotoxicity may appear. Combination with BC can reduce the possible cytotoxicity (Liu et al., 2019), enhance the antibacterial activity and promote wound healing. For example, AgSD can be impregnated into BC matrix, and the obtained composite has pH sensitive controlled-release behavior and good antibacterial activity against *S. aureus* and *C. albicans* (Shao et al., 2016b).

PROBLEMS AND CHALLENGES

Through the summary of the preparation and research progress of BC-based antibacterial wound dressing, we can find that there are still many problems in the composite materials, including the preparation methods and antibacterial activity. The commonly used method of adding antibiotics has been widely used in clinical practice. BC with 3D network structure can help retain and slowly release antibiotics, but the problem of resistance to antibiotics is still under study until now. People are willing to find a new therapy to fight against drug-resistant bacteria, for example, there are antibodies, probiotics and vaccines in the early stage (Czaplewski et al., 2016). Later, it is found that antibacterial nanomaterials are expected to replace antibiotics, however, nanoparticles have the disadvantages of easy aggregation, uncontrollable ion release trend and potential cytotoxicity, which limit their application (Sulaeva et al., 2015). Therefore, it is worth studying to prevent the aggregation of nanoparticles, facilitate immobilization and controlled release of nanoparticles, and improve sterilization efficiency while reducing the use of nanoparticles. Due to a large number of active functional groups, BC and its modified products can be used as the green reducing agent, stabilizer, template or immobilization material for nanoparticles, which is beneficial to reduce the agglomeration of nanoparticles and control the release rate. People have been pursuing the development of antibacterial materials without drug resistance, cytotoxicity and pollution, but long-term controllable antibacterial activity. Although natural organic antimicrobials have wide sources and good biodegradability, they have some problems such as inadequate antibacterial properties or unstable antibacterial activities. On the contrary, synthetic organic antimicrobials have some limitations in biodegradability. Therefore, there is no defect-free BC-based wound dressings material, and developing multifunctional BC-based composites is a major direction of future research. The materials compounded with BC should not only give antibacterial activity, but also improve other physical and chemical properties of composites to help wound healing.

Low yield, high capital investment requirements, and associated high operating costs present major economic constraints to the commercialization of BC production. How to reduce the energy consumption and cost of material preparation is still a big challenge. The BC potential in advanced material applications are hindered by a limited knowledge of optimal BC production conditions, efficient process scale-up, separation methods, and purification methods (Reiniati et al., 2017), so BC-based wound dressings have not been widely used in clinic. By utilizing low-cost substrates and wastes from agro-industry, breweries, food producers, and municipalities, it is possible to devise an economically feasible biotechnological process for BC production, but its high selling cost still restrict BC to high-value markets (Ul-Islam et al., 2020). In conclusion, BC-based wound dressings should be developed in the direction of low cost, simple process, green environmental protection, safety, no potential toxicity, excellent physical and chemical properties, and sustainably controlled sterilization.

CONCLUSION

Wound repair is a physiological process affected by many factors, and its complexity often leads to some uncertainties, such as slow wound healing, secondary infection and inflammation. BC-based materials are a kind of promising wound dressing materials with many excellent properties that are beneficial to wound healing, such as providing a moist wound environment, good biocompatibility, and stable mechanical properties. However, they lack antibacterial properties. The antibacterial activity of wound dressings plays an important role in anti-infection and promoting wound healing during wound treatment. In order to obtain antibacterial activity and accelerate wound healing, different kinds of antibacterial substances were compounded with BC, including metal or metal oxide nanoparticles, carbon nanomaterials, nanosilicates, antibiotics, natural polymers, bioactive substances, and synthetic polymers. Wound dressings consisted of BC and antibiotics are most frequently used with potential clinical application value, while BC combined with metal or metal oxide nanoparticles have great antibacterial effect. Moreover, wound dressings possess excellent biocompatibility and degradability without potential toxicity and pollution when they are made of BC and natural polymers. BC-based antibacterial materials obtained with these methods have significant antibacterial activity and the potential to reduce infection and promote wound healing. Nevertheless, there are also some problems, such as drug resistance caused by abuse of antibiotics, environmental pollution, potential toxicity of metal/metal oxides, and unstable antibacterial activity of natural antibacterial polymers. Overcoming these problems is also an important direction for future development. Furthermore, organic/inorganic hybrid materials, natural/synthetic hybrid materials and emerging nanomaterials are all research hotspots, as they can be used to construct new antibacterial wound dressings by combination with BC.

AUTHOR CONTRIBUTIONS

LZ and XW conceived the scope of this work. LZ drafted the manuscript. SL, JL, and XW involved in revising and editing the manuscript. All authors approved the submitted version and agreed both to be personally accountable for the author's own contributions and to ensure that questions related to the accuracy or integrity of any part of the work.

FUNDING

This work was financially supported by the National Natural Science Foundation of China (No. 22078119) and the Fundamental Research Funds for the Central Universities (No. 2020ZYGXZR066).

REFERENCES

Alavi, A., Sibbald, R. G., Mayer, D., Goodman, L., Botros, M., Armstrong, D. G., et al. (2014). Diabetic foot ulcers: Part II. Management. *J. Am. Acad. Dermatol.* 70:21.

Ambekar, R. S., and Kandasubramanian, B. (2019). Advancements in nanofibers for wound dressing: a review. *Eur. Polym. J.* 117, 304–336. doi: 10.1016/j.eurpolymj.2019.05.020

Au-Crane, M. J., Au-Henry, W. L. Jr., Au-Tran, H. L., Au-Albina, J. E., and Au-Jamieson, A. M. (2020). Assessment of acute wound healing using the dorsal subcutaneous polyvinyl alcohol sponge implantation and excisional tail skin wound models. *J. Vis. Exp.* 157:e60653.

Azarniya, A., Eslahi, N., Mahmoudi, N., and Simchi, A. (2016). Effect of graphene oxide nanosheets on the physico-mechanical properties of chitosan/bacterial cellulose nanofibrous composites. *Compos. Part A Appl. Sci. Manuf.* 85, 113–122. doi: 10.1016/j.compositesa.2016.03.011

Baker, T. J., Tyler, C. R., and Galloway, T. S. (2014). Impacts of metal and metal oxide nanoparticles on marine organisms. *Environ. Pollut.* 186, 257–271. doi: 10.1016/j.envpol.2013.11.014

Bashari, A., Rouhani Shirvan, A., and Shakeri, M. (2018). Cellulose-based hydrogels for personal care products. *Polym. Adv. Technol.* 29, 2853–2867. doi: 10.1002/pat.4290

Bielefeld, K. A., Amini-Nik, S., and Alman, B. A. (2013). Cutaneous wound healing: recruiting developmental pathways for regeneration. *Cell. Mol. Life Sci.* 70, 2059–2081. doi: 10.1007/s00018-012-1152-9

Boateng, J., and Catanzano, O. (2015). Advanced therapeutic dressings for effective wound healing-a review. *J. Pharm. Sci.* 104, 3653–3680. doi: 10.1002/jps.24610

Bogdanovic, U., Lazic, V., Vodnik, V., Budimir, M., Markovic, Z., and Dimitrijevic, S. (2014). Copper nanoparticles with high antimicrobial activity. *Mater. Lett.* 128, 75–78. doi: 10.1016/j.matlet.2014.04.106

Brown, A. J. (1886). XLIII.—On an acetic ferment which forms cellulose. *J. Chem. Soc. Transact.* 49, 432–439. doi: 10.1039/ct8864900432

Buruaga-Ramiro, C., Valenzuela, S. V., Valls, C., Roncero, M. B., Pastor, F. I. J., Díaz, P., et al. (2020). Development of an antimicrobial bioactive paper made from bacterial cellulose. *Int. J. Biol. Macromol.* 158, 587–594. doi: 10.1016/j.ijbiomac.2020.04.234

Byrd, A. L., Belkaid, Y., and Segre, J. A. (2018). The human skin microbiome. *Nat. Rev. Microbiol.* 16, 143–155.

Cacicedo, M. L., Pacheco, G., Islan, G. A., Alvarez, V. A., Barud, H. S., and Castro, G. R. (2020). Chitosan-bacterial cellulose patch of ciprofloxacin for wound dressing: preparation and characterization studies. *Int. J. Biol. Macromol.* 147, 1136–1145. doi: 10.1016/j.ijbiomac.2019.10.082

Cao, X., Ding, B., Yu, J., and Al-Deyab, S. S. (2012). Cellulose nanowhiskers extracted from TEMPO-oxidized jute fibers. *Carbohydr. Polym.* 90, 1075–1080. doi: 10.1016/j.carbpol.2012.06.046

Chatchawanwirote, L., Chuysinuan, P., Thanyacharoen, T., Ekabutr, P., and Supaphol, P. (2019). Green synthesis of photomediated silver nanoprisms via a light-induced transformation reaction and silver nanoprism-impregnated bacteria cellulose films for use as antibacterial wound dressings. *J. Drug Deliv. Sci. Technol.* 54:101305. doi: 10.1016/j.jddst.2019.101305

Chen, J., Peng, H., Wang, X., Shao, F., Yuan, Z., and Han, H. (2014). Graphene oxide exhibits broad-spectrum antimicrobial activity against bacterial phytopathogens and fungal conidia by intertwining and membrane perturbation. *Nanoscale* 6, 1879–1889. doi: 10.1039/c3nr04941h

Chen, X. Y., Low, H. R., Loi, X. Y., Merel, L., and Iqbal, M. A. M. C. (2019). Fabrication and evaluation of bacterial nanocellulose/poly(acrylic acid)/graphene oxide composite hydrogel: characterizations and biocompatibility studies for wound dressing. *J. Biomed. Mater. Res. Part B Appl. Biomater.* 107, 2140–2151. doi: 10.1002/jbm.b.34309

Cheng, Z., Yang, R., Liu, X., Liu, X., and Chen, H. (2017). Green synthesis of bacterial cellulose via acetic acid pre-hydrolysis liquor of agricultural corn stalk used as carbon source. *Bioresour. Technol.* 234, 8–14. doi: 10.1016/j.biortech.2017.02.131

Chu, M., Gao, H., Liu, S., Wang, L., Jia, Y., Gao, M., et al. (2018). Functionalization of composite bacterial cellulose with C-60 nanoparticles for wound dressing and cancer therapy. *RSC Adv.* 8, 18197–18203. doi: 10.1039/c8ra03965h

Connor, D.M., and Broome, A.-M. (2018). "Chapter Seven - Gold nanoparticles for the delivery of cancer therapeutics," in *Advances in Cancer Research*, ed. A.-M. Broome (Cambridge, MA: Academic Press), 163-184.

Cui, Y., Zhao, Y., Tian, Y., Zhang, W., Lü, X., and Jiang, X. (2012). The molecular mechanism of action of bactericidal gold nanoparticles on *Escherichia coli*. *Biomaterials* 33, 2327–2333. doi: 10.1016/j.biomaterials.2011.11.057

Czaplewski, L., Bax, R., Clokie, M., Dawson, M., Fairhead, H., Fischetti, V. A., et al. (2016). Alternatives to antibiotics-a pipeline portfolio review. *Lancet Infect. Dis.* 16, 239–251. doi: 10.1016/s1473-3099(15)00466-1

Dart, A., Bhave, M., and Kingshott, P. (2019). Antimicrobial peptide-based electrospun fibers for wound healing applications. *Macromol. Biosci.* 19:e1800488.

Das, S., and Baker, A. B. (2016). Biomaterials and nanotherapeutics for enhancing skin wound healing. *Front. Bioeng. Biotechnol.* 4:82. doi: 10.3389/fbioe.2016.00082

Dayal, M. S., and Catchmark, J. M. (2016). Mechanical and structural property analysis of bacterial cellulose composites. *Carbohydr. Polym.* 144, 447–453. doi: 10.1016/j.carbpol.2016.02.055

de Amorim, J. D. P., De Souza, K. C., Duarte, C. R., Da Silva Duarte, I., De Assis Sales Ribeiro, F., Silva, G. S., et al. (2020). Plant and bacterial nanocellulose: production, properties and applications in medicine, food, cosmetics, electronics and engineering. A review. *Environ. Chem. Lett.* 18, 851–869. doi: 10.1007/s10311-020-00989-9

De Mattos, I. B., Holzer, J. C. J., Tuca, A.-C., Groeber-Becker, F., Funk, M., Popp, D., et al. (2019). Uptake of PHMB in a bacterial nanocellulose-based wound dressing: a feasible clinical procedure. *Burns* 45, 898–904. doi: 10.1016/j.burns.2018.10.023

Dellera, E., Bonferoni, M. C., Sandri, G., Rossi, S., Ferrari, F., Del Fante, C., et al. (2014). Development of chitosan oleate ionic micelles loaded with silver sulfadiazine to be associated with platelet lysate for application in wound healing. *Eur. J. Pharm. Biopharm.* 88, 643–650. doi: 10.1016/j.ejpb.2014.07.015

Dórame-Miranda, R. F., Gámez-Meza, N., Medina-Juárez, L. Á., Ezquerra-Brauer, J. M., Ovando-Martínez, M., and Lizardi-Mendoza, J. (2019). Bacterial cellulose production by *Gluconacetobacter entanii* using pecan nutshell as carbon source and its chemical functionalization. *Carbohydr. Polym.* 207, 91–99. doi: 10.1016/j.carbpol.2018.11.067

Durand, G. A., Raoult, D., and Dubourg, G. (2019). Antibiotic discovery: history, methods and perspectives. *Int. J. Antimicrob. Agents* 53, 371–382. doi: 10.1016/j.ijantimicag.2018.11.010

Felgueiras, H. P., Teixeira, M. A., Tavares, T. D., Homem, N. C., Zille, A., and Amorim, M. T. P. (2020). Antimicrobial action and clotting time of thin, hydrated poly(vinyl alcohol)/cellulose acetate films functionalized with LL37 for prospective wound-healing applications. *J. Appl. Polym. Sci.* 137:48626. doi: 10.1002/app.48626

Fernandes, I. D. A. A., Pedro, A. C., Ribeiro, V. R., Bortolini, D. G., Ozaki, M. S. C., Maciel, G. M., et al. (2020). Bacterial cellulose: from production optimization to new applications. *Int. J. Biol. Macromol.* 164, 2598–2611. doi: 10.1016/j.ijbiomac.2020.07.255

Frone, A. N., Panaitescu, D. M., Nicolae, C. A., Gabor, A. R., Trusca, R., Casarica, A., et al. (2020). Bacterial cellulose sponges obtained with green cross-linkers for tissue engineering. *Mater. Sci. Eng. C* 110:110740. doi: 10.1016/j.msec.2020.110740

Fursatz, M., Skog, M., Sivler, P., Palm, E., Aronsson, C., Skallberg, A., et al. (2018). Functionalization of bacterial cellulose wound dressings with the antimicrobial peptide epsilon-poly-L-Lysine. *Biomed. Mater.* 13:025014. doi: 10.1088/1748-605x/aa9486

Graça, M. F. P., Miguel, S. P., Cabral, C. S. D., and Correia, I. J. (2020). Hyaluronic acid—Based wound dressings: a review. *Carbohydr. Polym.* 241:116364. doi: 10.1016/j.carbpol.2020.116364

Gupta, A., Briffa, S. M., Swingler, S., Gibson, H., Kannappan, V., Adamus, G., et al. (2020). Synthesis of Silver Nanoparticles Using Curcumin-Cyclodextrins Loaded Into Bacterial Cellulose-Based Hydrogels For Wound Dressing Applications. *Biomacromolecules* 21, 1802–1811. doi: 10.1021/acs.biomac.9b01724

Gupta, A., Keddie, D. J., Kannappan, V., Gibson, H., Khalil, I. R., Kowalczuk, M., et al. (2019). Production and characterisation of bacterial cellulose hydrogels loaded with curcumin encapsulated in cyclodextrins as wound dressings. *Eur. Polym. J.* 118, 437–450. doi: 10.1016/j.eurpolymj.2019.06.018

He, W., Huang, X., Zheng, Y., Sun, Y., Xie, Y., Wang, Y., et al. (2018). In situ synthesis of bacterial cellulose/copper nanoparticles composite membranes with long-term antibacterial property. *J. Biomater. Sci. Polym. Ed.* 29, 2137–2153. doi: 10.1080/09205063.2018.1528518

He, X., Yang, Y., Song, H., Wang, S., Zhao, H., and Wei, D. (2020). Polyanionic composite membranes based on bacterial cellulose and amino acid for antimicrobial application. *ACS Appl. Mater. Interfaces* 12, 14784–14796. doi: 10.1021/acsami.9b20733

Hu, G., Cai, Y., Tu, Z., Luo, J., Qiao, X., Chen, Q., et al. (2015). Reducing the cytotoxicity while improving the anti-cancer activity of silver nanoparticles through α-tocopherol succinate modification. *RSC Adv.* 5, 82050–82055. doi: 10.1039/c5ra12911g

İnal, M., and Mülazımoğlu, G. (2019). Production and characterization of bactericidal wound dressing material based on gelatin nanofiber. *Int. J. Biol. Macromol.* 137, 392–404. doi: 10.1016/j.ijbiomac.2019.06.119

Jannesari, M., Varshosaz, J., Morshed, M., and Zamani, M. (2011). Composite poly(vinyl alcohol)/poly(vinyl acetate) electrospun nanofibrous mats as a novel wound dressing matrix for controlled release of drugs. *Int. J. Nanomed*. 6, 993–1003. doi: 10.2147/ijn.s17595

Janpetch, N., Saito, N., and Rujiravanit, R. (2016). Fabrication of bacterial cellulose-ZnO composite via solution plasma process for antibacterial applications. *Carbohydr. Polym.* 148, 335–344. doi: 10.1016/j.carbpol.2016.04.066

Joe, A., Park, S.-H., Kim, D.-J., Lee, Y.-J., Jhee, K.-H., Sohn, Y., et al. (2018). Antimicrobial activity of ZnO nanoplates and its Ag nanocomposites: insight into an ROS-mediated antibacterial mechanism under UV light. *J. Solid State Chem.* 267, 124–133. doi: 10.1016/j.jssc.2018.08.003

Khalid, A., Khan, R., Ul-Islam, M., Khan, T., and Wahid, F. (2017a). Bacterial cellulose-zinc oxide nanocomposites as a novel dressing system for burn wounds. *Carbohydr. Polym.* 164, 214–221. doi: 10.1016/j.carbpol.2017.01.061

Khalid, A., Ullah, H., Ul-Islam, M., Khan, R., Khan, S., Ahmad, F., et al. (2017b). Bacterial cellulose-TiO2 nanocomposites promote healing and tissue regeneration in burn mice model. *RSC Adv.* 7, 47662–47668. doi: 10.1039/c7ra06699f

Khamrai, M., Banerjee, S. L., and Kundu, P. P. (2017). Modified bacterial cellulose based self-healable polyeloctrolyte film for wound dressing application. *Carbohydr. Polym.* 174, 580–590. doi: 10.1016/j.carbpol.2017.06.094

Khamrai, M., Banerjee, S. L., Pau, S., Ghosh, A. K., Sarkar, P., and Kundu, P. P. (2019). A mussel mimetic, bioadhesive, antimicrobial patch based on dopamine-modified bacterial cellulose/rGO/Ag NPs: a green approach toward wound-healing applications. *ACS Sustain. Chem. Eng.* 7, 12083–12097.

Klemm, D., Kramer, F., Moritz, S., Lindstrom, T., Ankerfors, M., Gray, D., et al. (2011). Nanocelluloses: a new family of nature-based materials. *Angew. Chem. Int. Ed.* 50, 5438–5466. doi: 10.1002/anie.201001273

Kuehn, B. (2018). Antibiotic resistance challenge. *JAMA* 320:1851. doi: 10.1001/jama.2018.16587

Lazarini, S. C., De Aquino, R., Amaral, A. C., Corbi, F. C. A., Corbi, P. P., Barud, H. S., et al. (2016). Characterization of bilayer bacterial cellulose membranes with different fiber densities: a promising system for controlled release of the antibiotic ceftriaxone. *Cellulose* 23, 737–748. doi: 10.1007/s10570-015-0843-4

Le Ouay, B., and Stellacci, F. (2015). Antibacterial activity of silver nanoparticles: a surface science insight. *Nano Today* 10, 339–354. doi: 10.1016/j.nantod.2015.04.002

Li, J., Wu, Y., and Zhao, L. (2016). Antibacterial activity and mechanism of chitosan with ultra high molecular weight. *Carbohydr. Polym.* 148, 200–205. doi: 10.1016/j.carbpol.2016.04.025

Li, J., and Zhuang, S. (2020). Antibacterial activity of chitosan and its derivatives and their interaction mechanism with bacteria: current state and perspectives. *Eur. Polym. J.* 138:109984. doi: 10.1016/j.eurpolymj.2020.109984

Li, Y., Chi, Y.-Q., Yu, C.-H., Xie, Y., Xia, M.-Y., Zhang, C.-L., et al. (2020). Drug-free and non-crosslinked chitosan scaffolds with efficient antibacterial activity against both Gram-negative and Gram-positive bacteria. *Carbohydr. Polym.* 241:116386. doi: 10.1016/j.carbpol.2020.116386

Li, Y., Tian, Y., Zheng, W., Feng, Y., Huang, R., Shao, J., et al. (2017). Composites of bacterial cellulose and small molecule-decorated gold nanoparticles for treating gram-negative bacteria-infected wounds. *Small* 13:1700130. doi: 10.1002/smll.201700130

Li, Z., Lv, X., Chen, S., Wang, B., Feng, C., Xu, Y., et al. (2016). Improved cell infiltration and vascularization of three-dimensional bacterial cellulose nanofibrous scaffolds by template biosynthesis. *RSC Adv.* 6, 42229–42239. doi: 10.1039/c6ra07685h

Lindsay, S., Oates, A., and Bourdillon, K. (2017). The detrimental impact of extracellular bacterial proteases on wound healing. *Int. Wound J.* 14, 1237–1247. doi: 10.1111/iwj.12790

Liu, X., Gan, H., Hu, C., Sun, W., Zhu, X., Meng, Z., et al. (2019). Silver sulfadiazine nanosuspension-loaded thermosensitive hydrogel as a topical antibacterial agent. *Int. J. Nanomed.* 14, 289–300. doi: 10.2147/ijn.s187918

Liu, Y., Yuan, Y., Duan, S., Li, C., Hu, B., Liu, A., et al. (2020). Preparation and characterization of chitosan films with three kinds of molecular weight for food packaging. *Int. J. Biol. Macromol.* 155, 249–259. doi: 10.1016/j.ijbiomac.2020.03.217

Luo, H., Zhang, J., Xiong, G., and Wan, Y. (2014). Evolution of morphology of bacterial cellulose scaffolds during early culture. *Carbohydr. Polym.* 111, 722–728. doi: 10.1016/j.carbpol.2014.04.097

Luo, Z., Liu, J., Lin, H., Ren, X., Tian, H., Liang, Y., et al. (2020). *In situ* Fabrication of Nano ZnO/BCM biocomposite based on MA modified bacterial cellulose membrane for antibacterial and wound healing. *Int. J. Nanomed.* 15, 1–15. doi: 10.2147/ijn.s231556

Malmir, S., Karbalaei, A., Pourmadadi, M., Hamedi, J., Yazdian, F., and Navaee, M. (2020). Antibacterial properties of a bacterial cellulose CQD-TiO2 nanocomposite. *Carbohydr. Polym.* 234:115835. doi: 10.1016/j.carbpol.2020.115835

Meftahi, A., Khajavi, R., Rashidi, A., Sattari, M., Yazdanshenas, M. E., and Torabi, M. (2010). The effects of cotton gauze coating with microbial cellulose. *Cellulose* 17, 199–204. doi: 10.1007/s10570-009-9377-y

Mijnendonckx, K., Leys, N., Mahillon, J., Silver, S., and Van Houdt, R. (2013). Antimicrobial silver: uses, toxicity and potential for resistance. *Biometals* 26, 609–621. doi: 10.1007/s10534-013-9645-z

Minutti, C. M., Knipper, J. A., Allen, J. E., and Zaiss, D. M. W. (2017). Tissue-specific contribution of macrophages to wound healing. *Semin. Cell Dev. Biol.* 61, 3–11. doi: 10.1016/j.semcdb.2016.08.006

Moeini, A., Pedram, P., Makvandi, P., Malinconico, M., and D'ayala, G. G. (2020). Wound healing and antimicrobial effect of active secondary metabolites in chitosan-based wound dressings: a review. *Carbohydr. Polym.* 233:115839. doi: 10.1016/j.carbpol.2020.115839

Mohamad, N., Buang, F., Mat Lazim, A., Ahmad, N., Martin, C., and Mohd Amin, M. C. I. (2017). Characterization and biocompatibility evaluation of bacterial cellulose-based wound dressing hydrogel: effect of electron beam irradiation doses and concentration of acrylic acid. *J. Biomed. Mater. Res. Part B Appl. Biomater.* 105, 2553–2564. doi: 10.1002/jbm.b.33776

Mohammadnejad, J., Yazdian, F., Omidi, M., Rostami, A. D., Rasekh, B., and Fathinia, A. (2018). Graphene oxide/silver nanohybrid: optimization, antibacterial activity and its impregnation on bacterial cellulose as a potential wound dressing based on GO-Ag nanocomposite-coated BC. *Eng. Life Sci.* 18, 298–307. doi: 10.1002/elsc.201700138

Mohite, B. V., and Patil, S. V. (2016). *In situ* development of nanosilver-impregnated bacterial cellulose for sustainable released antimicrobial wound dressing. *J. Appl. Biomater. Funct. Mater.* 14, 53–58.

Moniri, M., Moghaddam, A. B., Azizi, S., Rahim, R. A., Saad, W. Z., Navaderi, M., et al. (2018a). Molecular study of wound healing after using biosynthesized BNC/Fe3O4 nanocomposites assisted with a bioinformatics approach. *Int. J. Nanomed.* 13, 2955–2971. doi: 10.2147/ijn.s159637

Moniri, M., Moghaddam, A. B., Azizi, S., Rahim, R. A., Zuhainis, S. W., Navaderi, M., et al. (2018b). *In vitro* molecular study of wound healing using biosynthesized bacteria nanocellulose/silver nanocomposite assisted by bioinformatics databases. *Int. J. Nanomed.* 13, 5097–5112. doi: 10.2147/ijn.s164573

Napavichayanun, S., Yamdech, R., and Aramwit, P. (2016). The safety and efficacy of bacterial nanocellulose wound dressing incorporating sericin and polyhexamethylene biguanide: *in vitro*, *in vivo* and clinical studies. *Arch. Dermatol. Res.* 308, 123–132. doi: 10.1007/s00403-016-1621-3

Napavichayanun, S., Yamdech, R., and Aramwit, P. (2018). Development of bacterial cellulose incorporating silk sericin, polyhexamethylene biguanide, and glycerin with enhanced physical properties and antibacterial activities for wound dressing application. *Int. J. Polym. Mater. Polym. Biomater.* 67, 61–67. doi: 10.1080/00914037.2017.1297943

Nisar, P., Ali, N., Rahman, L., Ali, M., and Shinwari, Z. K. (2019). Antimicrobial activities of biologically synthesized metal nanoparticles: an insight into the mechanism of action. *J. Biol. Inorg. Chem.* 24, 929–941. doi: 10.1007/s00775-019-01717-7

Nuutila, K., and Eriksson, E. (2020). Moist wound healing with commonly available dressings. *Adv. Wound Care.* doi: 10.1089/wound.2020.1232 [Epub ahead of print].

Oryan, A., Alemzadeh, E., and Moshiri, A. (2017). Burn wound healing: present concepts, treatment strategies and future directions. *J. Wound Care* 26, 5–19. doi: 10.12968/jowc.2017.26.1.5

Pal, S., Nisi, R., Stoppa, M., and Licciulli, A. (2017). Silver-functionalized bacterial cellulose as antibacterial membrane for wound-healing applications. *ACS Omega* 2, 3632–3639. doi: 10.1021/acsomega.7b00442

Pang, M., Huang, Y., Meng, F., Zhuang, Y., Liu, H., Du, M., et al. (2020). Application of bacterial cellulose in skin and bone tissue engineering. *Eur. Polym. J.* 122:109365. doi: 10.1016/j.eurpolymj.2019.109365

Pathakoti, K., Manubolu, M., and Hwang, H.-M. (2019). Effect of size and crystalline phase of TiO2 nanoparticles on photocatalytic inactivation of *Escherichia coli*. *J. Nanosci. Nanotechnol.* 19, 8172–8179. doi: 10.1166/jnn.2019.16757

Portela, R., Leal, C. R., Almeida, P. L., and Sobral, R. G. (2019). Bacterial cellulose: a versatile biopolymer for wound dressing applications. *Microb. Biotechnol.* 12, 586–610. doi: 10.1111/1751-7915.13392

Qiu, J., Liu, L., Zhu, H., and Liu, X. (2018). Combination types between graphene oxide and substrate affect the antibacterial activity. *Bioact. Mater.* 3, 341–346. doi: 10.1016/j.bioactmat.2018.05.001

Raval, Y. S., Fellows, B. D., Murbach, J., Cordeau, Y., Mefford, O. T., and Tzeng, T.-R. J. (2017). Multianchored glycoconjugate-functionalized magnetic nanoparticles: a tool for selective killing of targeted bacteria via alternating magnetic fields. *Adv. Funct. Mater.* 27:1701473. doi: 10.1002/adfm.201701473

Reiniati, I., Hrymak, A. N., and Margaritis, A. (2017). Recent developments in the production and applications of bacterial cellulose fibers and nanocrystals. *Crit. Rev. Biotechnol.* 37, 510–524. doi: 10.1080/07388551.2016.1189871

Rezvani Ghomi, E., Khalili, S., Nouri Khorasani, S., Esmaeely Neisiany, R., and Ramakrishna, S. (2019). Wound dressings: current advances and future directions. *J. Appl. Polym. Sci.* 136:47738. doi: 10.1002/app.47738

Rojewska, A., Karewicz, A., Boczkaja, K., Wolski, K., Kepczynski, M., Zapotoczny, S., et al. (2017). Modified bionanocellulose for bioactive wound-healing dressing. *Eur. Polym. J.* 96, 200–209. doi: 10.1016/j.eurpolymj.2017.09.010

Ruf, M.-T., Andreoli, A., Vujic, G., Itin, P., Pluschke, G., and Schmid, P. (2017). Exudate collection using wound sponges—An easy, non-invasive and reliable method to explore protease activities in ulcers. *Wound Repair Regen.* 25, 320–326. doi: 10.1111/wrr.12517

Rühs, P. A., Storz, F., López Gómez, Y. A., Haug, M., and Fischer, P. (2018). 3D bacterial cellulose biofilms formed by foam templating. *NPJ Biofilms Microbiomes* 4:21.

Sajjad, W., Khan, T., Ul-Islam, M., Khan, R., Hussain, Z., Khalid, A., et al. (2019). Development of modified montmorillonite-bacterial cellulose nanocomposites as a novel substitute for burn skin and tissue regeneration. *Carbohydr. Polym.* 206, 548–556. doi: 10.1016/j.carbpol.2018.11.023

Shao, W., Liu, H., Wang, S., Wu, J., Huang, M., Min, H., et al. (2016a). Controlled release and antibacterial activity of tetracycline hydrochloride-loaded bacterial cellulose composite membranes. *Carbohydr. Polym.* 145, 114–120. doi: 10.1016/j.carbpol.2016.02.065

Shao, W., Liu, H., Wu, J., Wang, S., Liu, X., Huang, M., et al. (2016b). Preparation, antibacterial activity and pH-responsive release behavior of silver sulfadiazine loaded bacterial cellulose for wound dressing applications. *J. Taiwan Inst. Chem. Eng.* 63, 404–410. doi: 10.1016/j.jtice.2016.02.019

Shao, W., Wang, S., Wu, J., Huang, M., Liu, H., and Min, H. (2016c). Synthesis and antimicrobial activity of copper nanoparticle loaded regenerated bacterial cellulose membranes. *RSC Adv.* 6, 65879–65884. doi: 10.1039/c6ra07984a

Sinno, H., and Prakash, S. (2013). Complements and the wound healing cascade: an updated review. *Plast. Surg. Int.* 2013:146764.

Sirvio, J., Hyvakko, U., Liimatainen, H., Niinimaki, J., and Hormi, O. (2011). Periodate oxidation of cellulose at elevated temperatures using metal salts as cellulose activators. *Carbohydr. Polym.* 83, 1293–1297. doi: 10.1016/j.carbpol.2010.09.036

Suarato, G., Bertorelli, R., and Athanassiou, A. (2018). Borrowing from nature: biopolymers and biocomposites as smart wound care materials. *Front. Bioeng. Biotechnol.* 6:137. doi: 10.3389/fbioe.2018.00137

Subramaniam, G., and Girish, M. (2020). Antibiotic resistance — a cause for reemergence of infections. *Indian J. Pediatr.* 87, 937–944. doi: 10.1007/s12098-019-03180-3

Sukhorukova, I. V., Sheveyko, A. N., Shvindina, N. V., Denisenko, E. A., Ignatov, S. G., and Shtansky, D. V. (2017). Approaches for controlled Ag+ ion release: influence of surface topography, roughness, and bactericide content. *ACS Appl. Mater. Interfaces* 9, 4259–4271. doi: 10.1021/acsami.6b15096

Sulaeva, I., Henniges, U., Rosenau, T., and Potthast, A. (2015). Bacterial cellulose as a material for wound treatment: properties and modifications. A review. *Biotechnol. Adv.* 33, 1547–1571. doi: 10.1016/j.biotechadv.2015.07.009

Tabaii, M. J., and Emtiazi, G. (2018). Transparent nontoxic antibacterial wound dressing based on silver nano particle/bacterial cellulose nano composite synthesized in the presence of tripolyphosphate. *J. Drug Deliv. Sci. Technol.* 44, 244–253. doi: 10.1016/j.jddst.2017.12.019

Tayeb, A. H., Amini, E., Ghasemi, S., and Tajvidi, M. (2018). Cellulose nanomaterials-binding properties and applications: a review. *Molecules* 23:2684. doi: 10.3390/molecules23102684

Teixeira, M. A., Paiva, M. C., Amorim, M. T. P., and Felgueiras, H. P. (2020). Electrospun nanocomposites containing cellulose and its derivatives modified with specialized biomolecules for an enhanced wound healing. *Nanomaterials* 10:557. doi: 10.3390/nano10030557

Thomason, H. A., Lovett, J. M., Spina, C. J., Stephenson, C., Mcbain, A. J., and Hardman, M. J. (2018). Silver oxysalts promote cutaneous wound healing independent of infection. *Wound Repair Regen.* 26, 144–152. doi: 10.1111/wrr.12627

Tian, H., Kahl, M., and Kariman, K. (2019). Are nanoparticles a threat to mycorrhizal and rhizobial symbioses? A critical review. *Front. Microbiol.* 10:1660. doi: 10.3389/fmicb.2019.01660

Tian, S., Saravanan, K., Mothana, R. A., Ramachandran, G., Rajivgandhi, G., and Manoharan, N. (2020). Anti-cancer activity of biosynthesized silver nanoparticles using Avicennia marina against A549 lung cancer cells through ROS/mitochondrial damages. *Saudi J. Biol. Sci.* 27, 3018–3024. doi: 10.1016/j.sjbs.2020.08.029

Torgbo, S., and Sukyai, P. (2020). Biodegradation and thermal stability of bacterial cellulose as biomaterial: the relevance in biomedical applications. *Polym. Degrad. Stab.* 179:109232. doi: 10.1016/j.polymdegradstab.2020.109232

Ul-Islam, M., Khan, S., Ullah, M. W., and Park, J. K. (2015). Bacterial cellulose composites: synthetic strategies and multiple applications in bio-medical and electro-conductive fields. *Biotechnol. J.* 10, 1847–1861. doi: 10.1002/biot.201500106

Ul-Islam, M., Khan, T., Khattak, W. A., and Park, J. K. (2013). Bacterial cellulose-MMTs nanoreinforced composite films: novel wound dressing material with antibacterial properties. *Cellulose* 20, 589–596. doi: 10.1007/s10570-012-9849-3

Ul-Islam, M., Ullah, M. W., Khan, S., and Park, J. K. (2020). Production of bacterial cellulose from alternative cheap and waste resources: a step for cost reduction with positive environmental aspects. *Korean J. Chem. Eng.* 37, 925–937. doi: 10.1007/s11814-020-0524-3

Ullah, H., Santos, H. A., and Khan, T. (2016). Applications of bacterial cellulose in food, cosmetics and drug delivery. *Cellulose* 23, 2291–2314. doi: 10.1007/s10570-016-0986-y

Ullah, M. W., Ul-Islam, M., Khan, S., Kim, Y., and Park, J. K. (2015). Innovative production of bio-cellulose using a cell-free system derived from a single cell line. *Carbohydr. Polym.* 132, 286–294. doi: 10.1016/j.carbpol.2015.06.037

Velásquez-Riaño, M., and Bojacá, V. (2017). Production of bacterial cellulose from alternative low-cost substrates. *Cellulose* 24, 2677–2698. doi: 10.1007/s10570-017-1309-7

Vimbela, G. V., Ngo, S. M., Fraze, C., Yang, L., and Stout, D. A. (2017). Antibacterial properties and toxicity from metallic nanomaterials. *Int. J. Nanomed.* 12, 3941–3965. doi: 10.2147/ijn.s134526

Vismara, E., Bernardi, A., Bongio, C., Fare, S., Pappalardo, S., Serafini, A., et al. (2019). Bacterial nanocellulose and its surface modification by glycidyl methacrylate and ethylene glycol dimethacrylate. incorporation of vancomycin and ciprofloxacin. *Nanomaterials* 9:1668. doi: 10.3390/nano9121668

Volova, T. G., Shumilova, A. A., Shidlovskiy, I. P., Nikolaeva, E. D., Sukovatiy, A. G., Vasiliev, A. D., et al. (2018). Antibacterial properties of films of cellulose composites with silver nanoparticles and antibiotics. *Polym. Test.* 65, 54–68. doi: 10.1016/j.polymertesting.2017.10.023

Wang, Y., Wang, C., Xie, Y., Yang, Y., Zheng, Y., Meng, H., et al. (2019). Highly transparent, highly flexible composite membrane with multiple antimicrobial effects used for promoting wound healing. *Carbohydr. Polym.* 222:114985. doi: 10.1016/j.carbpol.2019.114985

Wei, B., Yang, G., and Hong, F. (2011). Preparation and evaluation of a kind of bacterial cellulose dry films with antibacterial properties. *Carbohydr. Polym.* 84, 533–538. doi: 10.1016/j.carbpol.2010.12.017

Wu, C. -N., Fuh, S.-C., Lin, S.-P., Lin, Y.-Y., Chen, H.-Y., Liu, J.-M., et al. (2018). TEMPO-Oxidized bacterial cellulose pellicle with silver nanoparticles for wound dressing. *Biomacromolecules* 19, 544–554. doi: 10.1021/acs.biomac.7b01660

Wu, J., Su, C., Jiang, L., Ye, S., Liu, X., and Shao, W. (2018). Green and facile preparation of chitosan sponges as potential wound dressings. *ACS Sustain. Chem. Eng.* 6, 9145–9152. doi: 10.1021/acssuschemeng.8b01468

Xianyu, Y., Wang, Z., and Jiang, X. (2014). A plasmonic nanosensor for immunoassay via enzyme-triggered click chemistry. *ACS Nano* 8, 12741–12747. doi: 10.1021/nn505857g

Yang, G., Wang, X., and Xie, J. (2017). Bacterial cellulose-silver antibacterial composites: effects of drying processes of bacterial cellulose. *J. Donghua Univ.* 34, 254–258.

Yang, J., Wang, L., Zhang, W., Sun, Z., Li, Y., Yang, M., et al. (2018). Reverse reconstruction and bioprinting of bacterial cellulose-based functional total intervertebral disc for therapeutic implantation. *Small* 14:1702582. doi: 10.1002/smll.201702582

Ye, S., Jiang, L., Wu, J., Su, C., Huang, C., Liu, X., et al. (2018). Flexible amoxicillin-grafted bacterial cellulose sponges for wound dressing: *in vitro* and *in vivo* evaluation. *ACS Appl. Mater. Interfaces* 10, 5862–5870. doi: 10.1021/acsami.7b16680

Yildirimer, L., Thanh, N. T. K., and Seifalian, A. M. (2012). Skin regeneration scaffolds: a multimodal bottom-up approach. *Trends Biotechnol.* 30, 638–648. doi: 10.1016/j.tibtech.2012.08.004

Yuan, H., Chen, L., and Hong, F. F. (2020). A Biodegradable antibacterial nanocomposite based on oxidized bacterial nanocellulose for rapid hemostasis and wound healing. *ACS Appl. Mater. Interfaces* 12, 3382–3392. doi: 10.1021/acsami.9b17732

Zhang, P., Chen, L., Zhang, Q., and Hong, F. F. (2016). Using *in situ* dynamic cultures to rapidly biofabricate fabric-reinforced composites of chitosan/bacterial nanocellulose for antibacterial wound dressings. *Front. Microbiol.* 7:260. doi: 10.3389/fmicb.2016.00260

Zmejkoski, D., Spasojevic, D., Orlovska, I., Kozyrovska, N., Sokovic, M., Glamoclija, J., et al. (2018). Bacterial cellulose-lignin composite hydrogel as a promising agent in chronic wound healing. *Int. J. Biol. Macromol.* 118, 494–503. doi: 10.1016/j.ijbiomac.2018.06.067

Zywicka, A., Fijalkowski, K., Junka, A. F., Grzesiak, J., and El Fray, M. (2018). Modification of bacterial cellulose with quaternary ammonium compounds based on fatty acids and amino acids and the effect on antimicrobial activity. *Biomacromolecules* 19, 1528–1538. doi: 10.1021/acs.biomac.8b00183

Conflict of Interest: The authors declare that the research was conducted in the absence of any commercial or financial relationships that could be construed as a potential conflict of interest.

frontiers
in Bioengineering and Biotechnology

ORIGINAL RESEARCH
published: 02 December 2020
doi: 10.3389/fbioe.2020.603407

Production of Bacterial Cellulose Aerogels With Improved Physico-Mechanical Properties and Antibacterial Effect

Viktor V. Revin, Natalia B. Nazarova, Ekaterina E. Tsareva, Elena V. Liyaskina, Vadim D. Revin and Nikolay A. Pestov*

Department of Biotechnology, Bioengineering and Biochemistry, National Research Ogarev Mordovia State University, Saransk, Russia

Aerogels have gained significant interest in recent decades because of their unique properties such as high porosity, low density, high surface area, and excellent heat and noise insulation. However, their high cost and low mechanical strength limit their practical application. We developed appropriate conditions to produce aerogels with controlled density, high mechanical strength, and thermal characteristics from bacterial cellulose (BC) synthesized by the strain *Komagataeibacter sucrofermentans* H-110. Aerogels produced using TEMPO oxidized BC (OBC) exhibited high mechanical strength and lower shrinkage than those from native bacterial cellulose (NBC). Compared to the NBC, the use of TEMPO-oxidized BC with oxidation degrees (OD) of 1.44 and 3.04% led to the reduction of shrinkage of the aerogels from 41.02 to 17.08%. The strength of the aerogel produced from the TEMPO-oxidized BC with an oxidation degree of 1.44% was twice that of the aerogel produced from NBC. The addition of Mg^{2+}at concentrations of 20 and 40 mM during the preparation of the aerogels increased the strength of the aerogels by 4.9 times. The combined use of TEMPO-oxidized BC and Mg^{2+} allowed pore size reduction from 1,375 to 197.4 μm on the outer part of the aerogels, thereby decreasing the thermal conductivity coefficient from 0.036 to 0.0176 W/(m•K). Furthermore, novel biocomposites prepared from the aerogels based on NBC and OBC and sodium fusidate, which have high antibiotic activity against *Staphylococcus aureus*, were obtained. Owing to their antibacterial properties, these aerogels can be used as functional biomaterials in a wide range of applications such as in tissue engineering and fabrication of wound dressing materials.

Keywords: biocomposites, antibacterial activity, bacterial cellulose, TEMPO oxidation, aerogels

Edited by:
Muhammad Wajid Ullah,
Huazhong University of Science and Technology, China

Reviewed by:
Ahmed El-Fiqi,
Dankook University, South Korea
Adil Denizli,
Hacettepe University, Turkey

****Correspondence:***
Nikolay A. Pestov
pestov79@gmail.com

Specialty section:
This article was submitted to Biomaterials, a section of the journal Frontiers in Bioengineering and Biotechnology

Received: *06 September 2020*
Accepted: *13 November 2020*
Published: *02 December 2020*

Citation:
Revin VV, Nazarova NB, Tsareva EE, Liyaskina EV, Revin VD and Pestov NA (2020) Production of Bacterial Cellulose Aerogels With Improved Physico-Mechanical Properties and Antibacterial Effect. Front. Bioeng. Biotechnol. 8:603407. doi: 10.3389/fbioe.2020.603407

INTRODUCTION

Aerogels are one of the most interesting materials of the twenty-first century (Barrios et al., 2019). They have gained considerable interest because of their unique properties such as high porosity, low density, high surface area, and excellent heat and noise insulations. However, high production costs and low mechanical strength limit their practical application (Nita et al., 2020).

Aerogels are highly porous nanostructured materials that were first created by Kistler in 1931 (Kistler, 1931; Nita et al., 2020). They can be produced by two methods–supercritical drying or freeze-drying. In both, the microporous structure of the material is preserved during drying. Therefore, this material has a high porosity, an extremely low density, and a high specific surface area. The first aerogel produced by Kistler was a silica aerogel obtained through supercritical drying. The precursors used to produce silica aerogels are toxic, and the resulting aerogel is not biodegradable and has unsatisfactory strength (Katti et al., 2006). The high production cost for such an aerogel combined with the above disadvantages, is the main reason that this material is not widely used.

Aerogels can be inorganic, organic, or hybrid (Novak et al., 1994; Nita et al., 2020) depending on the material used for their production. Organic aerogels are obtained from biopolymers that are based on renewable raw materials. The most common biopolymer on Earth is cellulose. In applications that require biodegradability and biocompatibility, cellulose aerogels can be an excellent alternative to silica aerogels. These applications include medicinal purposes—where the aerogel can be used for directed drug delivery—and tissue engineering and regenerative medicine (Bhandari et al., 2017; Nita et al., 2020; Zheng et al., 2020). The high sorption capacity of cellulose aerogels for heavy metals and toxic organic compounds allows them to be used for removing undesirable pollutants from the environment (Nguyen et al., 2014; Maleki, 2016; Wang et al., 2019). Owing to the formation of an open-cell structure the aerogel can act as an effective heat-insulator (Nguyen et al., 2014).

Cellulose of various origins, such as the common vegetable cellulose from wood (Gupta et al., 2018), plant cellulose, and bacterial cellulose (BC) (Pircher et al., 2016; Revin et al., 2019), can be used to produce aerogels (Long et al., 2018). BC is an extracellular product of the metabolism of certain bacteria, and the main function of this polymer is to deliver bacterial cells to the upper layers of the nutrient medium, wherein their oxygen demand is met. The most promising producers of BC are bacteria of the genus *Komagataeibacter* (formerly the genus *Gluconacetobacter*) (Yamada et al., 2011). Moreover, BC has the same chemical composition as plant cellulose; however, its structure differs from the plant polymer. These differences arise because BC is synthesized in a chemically pure form, the thickness of its fibrils is much less (20–80 nm) than that of the plant polymer, and has a higher degree of crystallinity (Revin et al., 2018). BC has several biorelevant properties including biological compatibility, high mechanical strength, and high sorption capacity. This makes it a unique carrier matrix for enzymes, cells, and various medications, particularly with hemostatic, antibacterial, and regenerative effects.

Recently, BC has attracted significant attention because it can be used to produce a wide range of functional and structural materials (Choi and Shin, 2020). It has excellent potential for applications in medicine such as a biomaterial for tissue engineering (Carvalho et al., 2019; Hickey and Pelling, 2019; Luo et al., 2019), wound dressing (Sulaeva et al., 2015; Carvalho et al., 2019; Portela et al., 2019; Teixeira et al., 2020), and controlled drug delivery (Carvalho et al., 2019). Furthermore, BC can be used in dietetics as a carrier of additives for balanced nutrition, in industrial electronics to produce optically transparent compounds with an ultra-low thermal expansion coefficient, and in manufacturing of acoustic diaphragms. It is a promising source for obtaining nanocrystalline cellulose, and biocomposite materials (Sharma et al., 2019; Choi and Shin, 2020). Currently, it is prevalent in the production of several biocomposites that have antibacterial and hemostatic properties. Biocomposites with high antibacterial activity are produced based on BC and silver nanoparticles (Wu et al., 2018), copper (Ma et al., 2016), zinc (Jebel and Almasi, 2016), and a few antibiotics such as tetracycline, gentamicin, and amoxicillin (Kaplan et al., 2014; Shao et al., 2016). Biocompatible Au nanoclusters (AuNCs) were synthesized and added to a cellulose nanofibril dispersion to prepare a novel antibacterial film (Wang et al., 2020). A previous study reported the synthesis of biocomposites that are based on BC and chitosan (Zang et al., 2016). A review by Zheng et al. covers the challenges in obtaining medical biomaterials in the form of aerogels for wound coverings, bone regeneration, and directed drug delivery (Zheng et al., 2020).

Most of the practical applications of aerogels require certain strength characteristics. Hence, it is particularly important to identify and understand the factors that affect the strength of the aerogels. The strength characteristics of a BC aerogel depend on both its density and microporous structure (Revin et al., 2019). Chemical modification methods are widely used to adjust the properties of cellulose and its derivative materials (Dufresne, 2013). Cellulose oxidation is a common method for modifying the properties of this biopolymer. There are two main methods to oxidize BC: TEMPO (2,2,6,6-tetramethylpiperidin-1-yl)oxyl) oxidation, in which the primary hydroxymethyl group is selectively oxidized to a carboxyl group, and periodate oxidation, in which the C2–C3 bond is broken to form two aldehyde groups.

The purpose of this work is to obtain BC aerogels with specified properties, such as controllable density, strength, and corresponding typical characteristics. Considering the properties of aerogels, another important task is to obtain biocomposites in aerogel forms for biomedical applications, which is one of the novel contributions of this work.

MATERIALS AND METHODS

Preparation of BC

BC was produced in a static culture medium by *Komagataeibacter sucrofermentans* H-110, which was isolated from Kombucha tea and identified by sequencing the amplified product of 16S rRNA (Revin et al., 2020). A strain was deposited in the Russian National Collection of Industrial Microorganisms (VKPM) (Accession No. VKPM: B-11267). For the production of BC, a Hestrin and Schramm (HS) medium that contained glucose (20 g/L), peptone (5 g/L), yeast extract (5 g/L), citric acid (1.15 g/L), and disodium hydrogen phosphate (2.7 g/L) at a pH of 6.0 was used. The culture medium was autoclaved for 20 min at 120°C. Further, the medium was inoculated with 10% (v/v) inoculum. To prepare the inoculum, *K. sucrofermentans*H-110 was transferred aseptically from an agar plate to a 250-ml Erlenmeyer flask containing 100 ml of culture medium and incubated in a shaker incubator (Model ES-20/60, BIOSAN, Latvia) at 28°C for 24 h at 250 rpm. The BC was produced in static conditions at 28°C for 5 days. After the incubation, the BC was collected, washed thoroughly with de-ionized water to remove medium components, and treated with 1% (w/v) sodium hydroxide solution at 80°C for 1 h to eliminate the bacterial cells. Further, the BC was rinsed extensively with 6% (v/v) acetic acid and then de-ionized water until the pH became neutral. If necessary, the purified BC was dried to a constant weight at 60°C.

TEMPO Oxidation of Bacterial Cellulose

In this study, 10 ml of distilled water containing 48 mg NaBr and 0.2 mg TEMPO was added to 8 g of the BC gel film. The pH of the solution was adjusted to 10.0 by adding 0.5 M NaOH. Further, 3 ml of 5% NaClO was added to the solution. The reaction was performed at 22°C for 15, 30, 45 and 60 min. The reaction was stopped by adding 5 ml ethanol to decompose the residual NaOCl. After oxidation, to remove the reagents, the gel film of oxidized BC was thoroughly washed with distilled water until a pH value of 5.5 was reached. This pH value should remain stable for 3 h.

The oxidation degree (OD) of BC was determined by conductometric titrations using a S70-K SevenMulti conductivity meter. Eight gram of BC gel film was suspended into 50 mL of 0.01 M hydrochloric acid solution. After 60 min of stirring, the suspensions were titrated with 0.01 M NaOH. The relative amount of carboxyl groups on the BC, which is indicated by OD, was calculated using the following equation (Perez et al., 2003):

$$OD = 162\,(V2 - V1)\,c\,[w - 36\,(V2 - V1)\,c]^{-1}$$

where V2 is the amount of NaOH (in L) required for the titration of excess of HCl and weak acid corresponding to the carboxyl content and V1 is the amount of NaOH (in L) required for the titration of excess of HCl, c is the NaOH concentration (mol/L), and w is the weight of oven-dried sample (g).

Aerogel Production

The BC aerogels were obtained using the freeze-drying method. The hydrogel was produced by grinding the cellulose obtained from the cultivated bacteria under static conditions using a laboratory homogenizer for 5 min. The BC hydrogel was frozen in a single step in a foil with the required shape. The resulting BC hydrogel was placed in a −50°C freezer for 24 h. Freeze-drying was conducted using a FreeZone Plus freeze-dryer lyophilizer (Labconco, USA) for 72 h.

To obtain aerogels from the TEMPO-oxidized BC containing divalent metals, an appropriate amount of salts of the corresponding metals was added to the obtained BC hydrogel until the required concentration was obtained. The following salts were used as the sources of the divalent metals: $MgSO_4$, $MnSO_4$, $CoSO_4$, $ZnSO_4$, $CuSO_4$, $NiSO_4$, $CaCl_2$, and $ZnSO_4$.

Production of Biocomposites Based on BC Aerogels and Sodium Fusidate (SF)

Biocomposites based on the BC aerogels and SF were obtained using the freeze-drying of hydrogels from native bacterial cellulose (NBC) and oxidized bacterial cellulose (OBC) with an OD of 1.44%. To impart the antimicrobial properties, the antibiotic SF, at concentrations of 500 µg/g, was added to the hydrogel. To obtain the aerogels, the hydrogels were frozen in a low-temperature cooler MDF-U53V (SANYO, Japan) at −50 °C for 24 h, and further dried on a FreeZone Plus freeze-dryer lyophilizer (Labconco, USA). The obtained aerogels were cut into round pieces with a diameter of 10 mm, weighing 0.002 g and containing 100 µg of SF. The final composites were identified as NBC/SF_{100}, and OBC/SF_{100}.

Determination of Aerogel Properties

The density of the aerogels was determined by volume and weight measurement. The aerogel volume was determined based on its linear dimensions.

The strength of aerogels from NBC and OBC was determined using digital force gauge ISF-DF5, "Insize." For this study, cylindrical aerogels with a diameter of 14 mm and a height of 10 mm were used.

Scanning electron microscopy (SEM) of the BC aerogels was performed using a Quanta 200 I 3D FEI scanning electron microscope (USA). Average pore sizes were determined using the image analysis software FEI xT microscope server. At least 100 pores on each SEM image were measured. To determine the pore area, the total area occupied by the pores having the same size was calculated. The area of a single pore was determined based on the linear dimensions of each pore.

The shrinkage of the aerogels was determined using the following equation:

$$Shrinkage = \frac{(\mathbf{V}_{initial} - V_{final})}{V_{initial}} \times 100$$

where $V_{initial}$ and V_{final} are the volumes of the BC hydrogel that was used to produce the aerogel and the aerogel obtained after freeze-drying, respectively.

The porosity of the aerogels was determined using the following equation:

$$Porosity(\%) = \left(1 - \frac{\rho_{apparent}}{\rho_{actual}}\right) \times 100$$

where $\rho_{apparent}$ is the apparent density that was determined based on the linear size of the aerogel, and ρ_{actual} is the density of BC, which is 1.38 g/cm^3 (Wang et al., 2017).

The thermal conductivity coefficient of the sample (λ) was determined using the following equation:

$$\lambda = \frac{dq}{\Delta T}$$

where d is the thickness of the sample (in m), q is the heat flow density, and ΔT is the temperature difference between the sample facets.

The measurement of the heat flow density and the temperatures of the opposite face sides was performed using a digital device for measuring heat flow density (HFM-2). We considered the heat flow, which flowed through a test sample with dimensions of 60 × 40 × 10 mm, to be established if the values of the sample thermal conductivity, calculated from the results of five consecutive measurements, differed from each other by <1%.

Thermogravimetric analysis was performed using a TG 209 F1 Libra thermobalance (Netzsch, Germany).

Fourier-Transform Infrared (FTIR) Spectra of BC

The BC was freeze-dried and crushed into a powder form, mixed with potassium bromide, and pressed into a small tablet that was subjected to FTIR spectroscopy using an FTIR spectrometer IRPrestige-21 (Shimadzu, Japan) in the absorption mode. For each sample, 32 scans at a resolution of 4 cm^{-1} at wavenumbers ranging from 4,000 to 400 cm^{-1} were collected.

AFM Micrographs of BC

The surface morphologies of BC were studied by contact atomic force microscopy (AFM) using an SPM 9600 (Shimadzu, Japan) microscope. The BC samples were air-dried on a glass slide in the form of a thin film. A silicon nitride cantilever with a nominal radius of 2 nm of the pyramidal tip was used. The scan rates ranged between 0.6 and 1.0 Hz/s. An image resolution of 256 × 256 points was set.

Antibacterial Activity

The antibacterial activities of the prepared aerogels were studied by the disc diffusion method against *Staphylococcus aureus* 209 P from VKPM (VKPM B-6646, ATCC 6538P). The antibacterial capacity is determined by measuring the diameter of the clear zone of inhibition around the samples after 18 h of incubation at 37°C.

In vitro Release Assays

The release behavior of SF was studied in 100 mL of phosphate buffer solution at pH 7.4. The quantitative analysis of SF was performed using a microbiological method (Hikalx et al., 1982). An agar plate diffusion technique was employed using *S. aureus*209 P as the test organism. After the agar had solidified, wells (10-mm i.d.) were punched out, and 0.1 mL of a standard or test dilution was applied. Standard dilutions contained 100, 200, 300, 400, 500, 600, 700, 800, 900, and 1,000 μg/mL of SF. The zone of inhibition diameter was measured after 18 h of incubation at 37°C.

Cytotoxicity Tests

The study was made on mouse fibroblast cell culture L929 (obtained from tissue culture collections of D.I. Ivanovsky Institute of Virology, Russia). The cells were cultured in Dulbecco's modified Eagle's medium (DMEM) (Paneko, Russia) with 10% fetal bovine serum (FBS) (HyClone, USA) and antibiotics (penicillin, streptomycin) under the standard conditions: 5% CO_2 atmosphere, $t = 37°C$, 5% humidity in an incubator MCO-170M (Sanyo, Japan). For the study, cells in the exponential growth phase were dispersed in a 96-well plate (5 × 10^3 cells/well). After 24 h, the medium in the 96-well plate was replaced by fresh medium containing the aerogels extracts followed by incubation for 24 h. The aerogels NBC/SF_{100} and OBC/SF_{100} were extracted by immersion of the aerogels in DMEM at 37°C for 24 h. Wells containing only the cells were used as control. After the incubation time the morphological structures was observed by an inverted optical microscope (Micromed, Russia). The cytotoxicity was measured using the MTT assay method. The medium was replaced with the fresh one with 5 mg/mL dimethyl thiazolyl diphenyl (MTT) solution. After 4 h incubation time the medium was removed, 150 μL DMSO was added. Optical density was measured on a microplate reader EFOS 9305 (Russia) at a wavelength of 492 nm with a reference wavelength of 620 nm. Cell viability was determined as the ratio of the optical density of the sample to the control expressed as a percentage.

Statistical Analysis

All the presented data are averages of at least three rounds of experiments, which were performed with three to six replicates of the mean. The standard deviations of the means were calculated using Microsoft Excel 2013 (Microsoft Corporation, Redmond, USA). The obtained data were statistically analyzed by a student *t*-test: two-sample assuming equal variances. The differences were considered significant at the level of $p < 0.05$.

RESULTS

Morphology of BC

The macrostructure morphology of BC varied depending on the different culture methods (Wang et al., 2019). In an agitated culture, the cellulose was synthesized in deep medium in the form of fibrous suspensions, pellets, and irregular masses (Revin et al., 2018). In a stationary culture, a gelatinous cellulose film was formed at the air/liquid interface of the medium. When cultivating bacterium *K. sucrofermentans* H-110 at static conditions in the HS growing medium for 5 days, a BC gel film was formed on the surface of the medium (**Figure 1A**). After treatment, the gel film became colorless and transparent (**Figure 1B**). **Figure 1C** shows a general scheme for producing NBC or OBC aerogels containing Mg^{2+} or SF.

AFM was used to study the microscopic details of the biopolymer. The micromorphology of the BC, that exhibited a nanoporous three-dimensional (3D) network structure with a random arrangement of the ribbon-shaped fibrils, is shown in **Figure 2**. The average thickness of the BC fibrils formed on the standard HS medium was 50–90 nm.

Oxidation of BC

BC aerogels can be obtained from BC synthesized under static and dynamic cultivation conditions (Revin et al., 2019). An important parameter that determines the consumer qualities of the aerogels is the strength of the material. These characteristics strongly depend on the density of the aerogels obtained from the BC (Revin et al., 2019). Therefore, it is required that the strength of the BC aerogels be increased without increasing their densities. To modify the properties of the BC, chemical modification methods can be used. In this work, TEMPO oxidation was used for the BC gel film modification. The oxidation of cellulose using a TEMPO reagent leads to

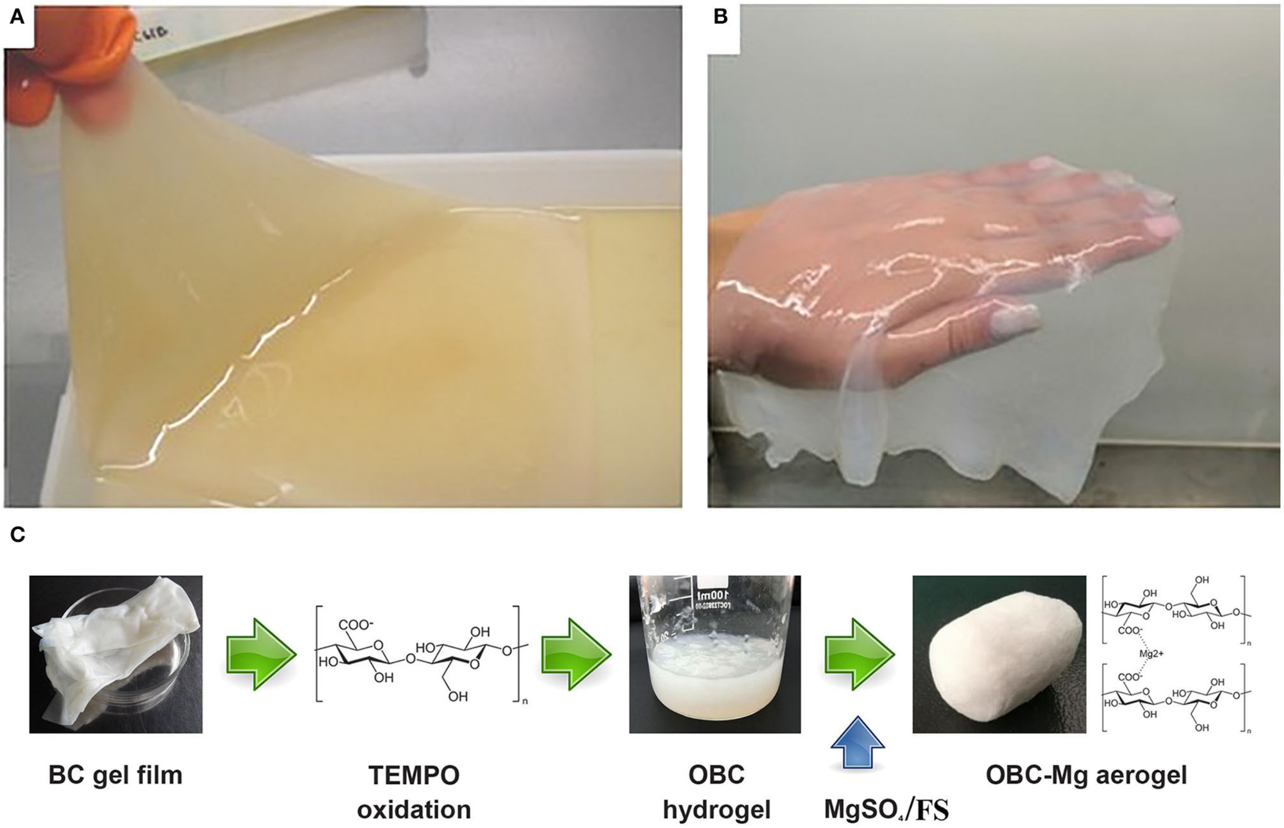

FIGURE 1 | A BC gel film on the surface of the HS medium **(A)**, after its purification **(B)**, and scheme for producing NBC or OBC aerogels **(C)**.

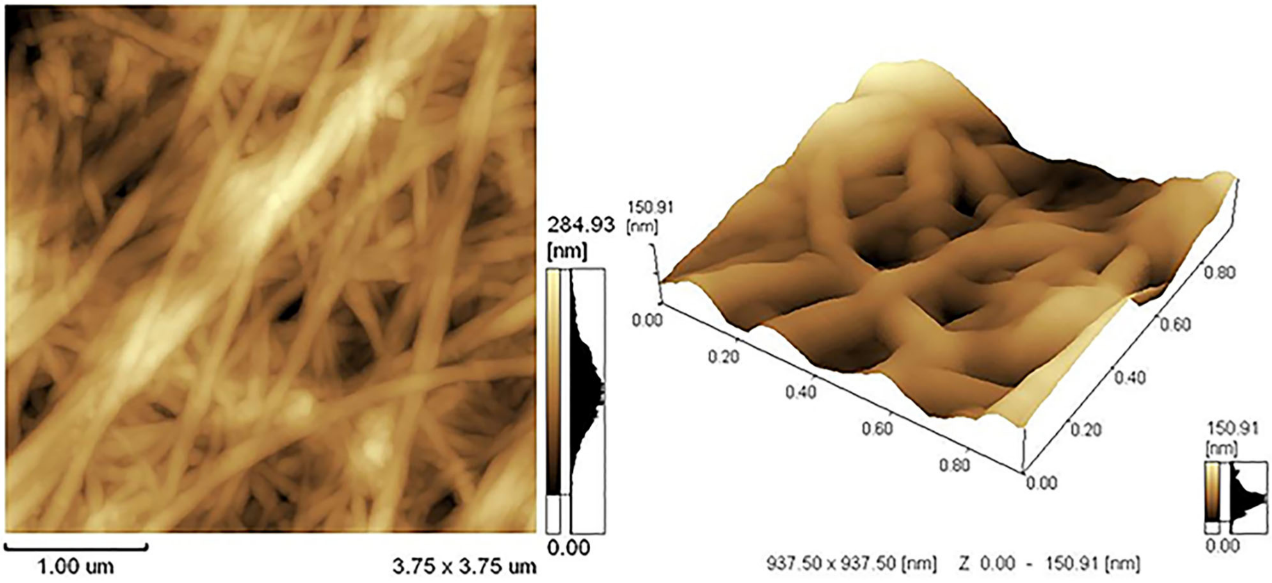

FIGURE 2 | AFM image of the BC.

a specific oxidation of the primary $-CH_2OH$ group of the glucopyranose unit to –COOH. The qualitative analysis of the TEMPO oxidation of the BC was determined by infrared (IR) spectroscopy (**Figure 3**).

The IR spectrum of the native BC gel film showed absorption peaks that are typical of this polymer. The absorption peak in the 3,000–3,600 cm^{-1} region can be distinguished, and corresponds to the stretching vibrations of the cellulose hydroxyl groups involved in the formation of hydrogen bonds. A wide and less-intense band at 2,800–3,000 cm^{-1} corresponds to the stretching vibrations of the C–H bonds of the cellulose methylene groups (Kondo and Sawatari, 1996). The peak in the 1,650 cm^{-1} area is due to the deformation vibrations of the –OH groups from adsorbed water. The peak at 1,431 cm^{-1} is caused by the symmetric $-CH_2$ bending (Cael et al., 1975). The intense band at 1,000–1,047 cm^{-1} corresponds to the valence vibrations of the C–O bonds. The peak in the 1,162–1,125 cm^{-1} region is caused by the asymmetric bending of C–O–C (Oh et al., 2005). The oxidation of BC leads to the appearance of the –COOH groups in this polymer. The absorption of the –COOH group depends on its protonation state. When the carboxyl group is protonated, a peak appears at 1,730 cm^{-1} (Naumann et al., 1982; Jiang et al., 2004).

The TEMPO oxidation of the BC led to the appearance of a peak that exhibits the IR spectrum characteristics of the –COOH group. Particularly, a pronounced peak at 1,730 cm^{-1}, which indicates the successful oxidation of the BC, was observed after the transition of the –COOH groups in the protonated state.

Influence of the OD of BC on the Properties of Produced Aerogels

By changing the oxidation conditions of the BC, it is possible to obtain samples of the oxidized BC gel film with different ODs. During the oxidation of the BC, samples of the OBC were obtained with ODs of 1.03, 1.44, 3.04, and 4.15%. The ODs were determined by conductometric titrations.

Obtaining aerogels through freeze-drying was accompanied by a decrease in the volume of the aerogels, which is called aerogel shrinkage (Long et al., 2018). In the freeze-drying method for producing aerogels from the NBC, the shrinkage of the resulting material reached 41% (**Table 1**).

The oxidation of the BC allowed shrinkage of the BC aerogel to be reduced from 41 to 17.8%. It is worth noting that the OD of the BC affected the amount of the aerogel shrinkage. At the ODs of 1.44 and 3.04%, the shrinkage of the aerogel was minimal (17.8%). At the minimum OD of 1.03%, the aerogel shrinkage value was 31.62%, which was lower than that of the control sample of the NBC aerogel. An increase in the OD of the BC to 4.15% led to an increase in the aerogel shrinkage from 17.8 to 21.27%. Thus, the obtained results indicate an optimal influence of BC OD is possible on the aerogel shrinkage during its production through the freeze-drying process.

The study of the strength of the OBC aerogels showed that the TEMPO oxidation of the BC led to a change in the strength of the aerogels (**Figure 4**).

Compared to the control aerogel obtained from NBC, the aerogel obtained from the OBC, which had an OD of 1.44%, exhibited the most pronounced effect. Compressing an aerogel

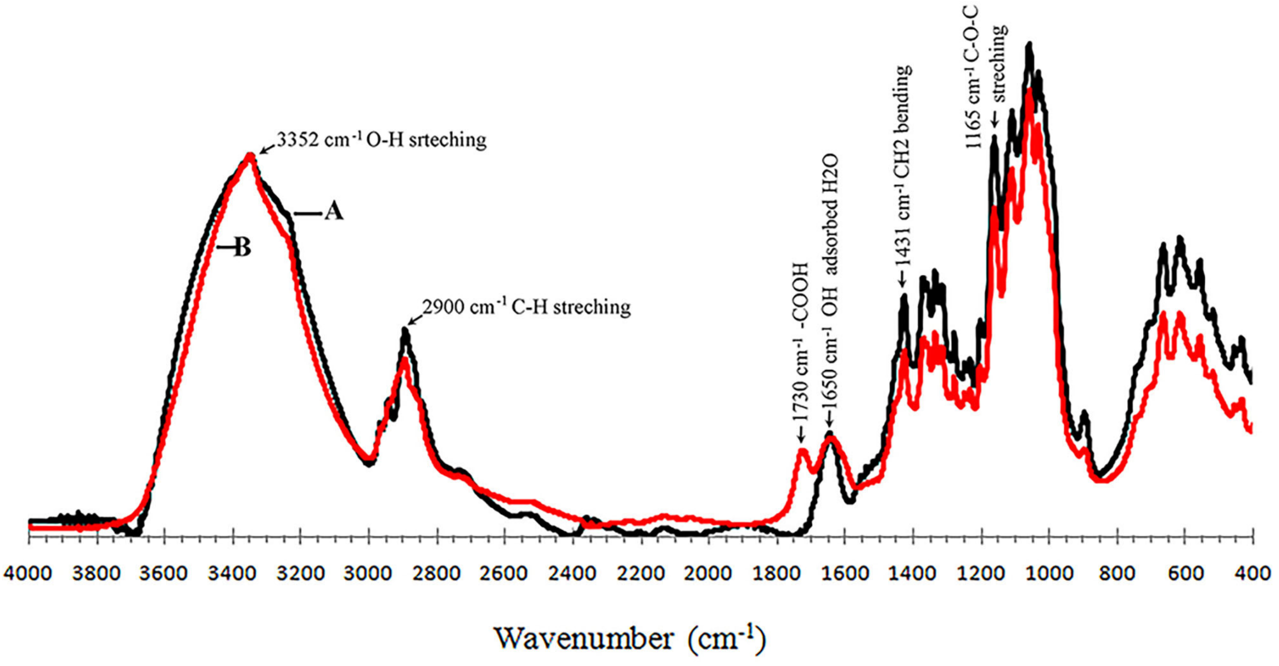

FIGURE 3 | IR spectra of purified NBC **(A)** and TEMPO-oxidized BC **(B)**.

TABLE 1 | Effect of BC gel film oxidation on the aerogel properties.

Parameters	Aerogel produced from NBC	Aerogel produced from TEMPO-oxidized BC with an oxidation degree, %			
		1.03	1.44	3.04	4.15
Volume, cm^3	2.654 ± 0.013	3.077 ± 0.015	3.697 ± 0.018	3.699 ± 0.018	3.543 ± 0.017
Porosity, %	99.16 ± 0.10	99.25 ± 0.09	99.42 ± 0.09	99.39 ± 0.09	99.32 ± 0.09
Shrinkage, %	41.02	31.62	17.84	17.80	21.27

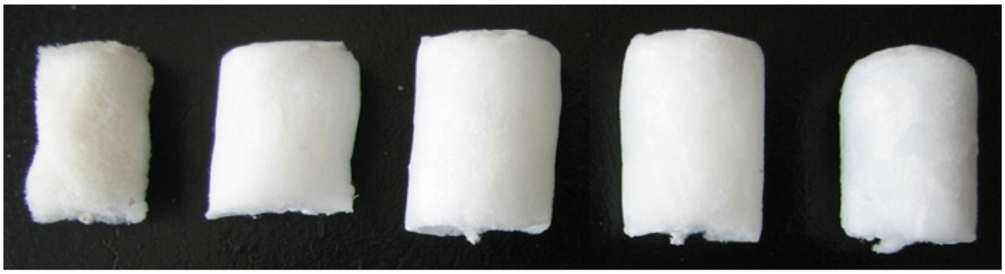

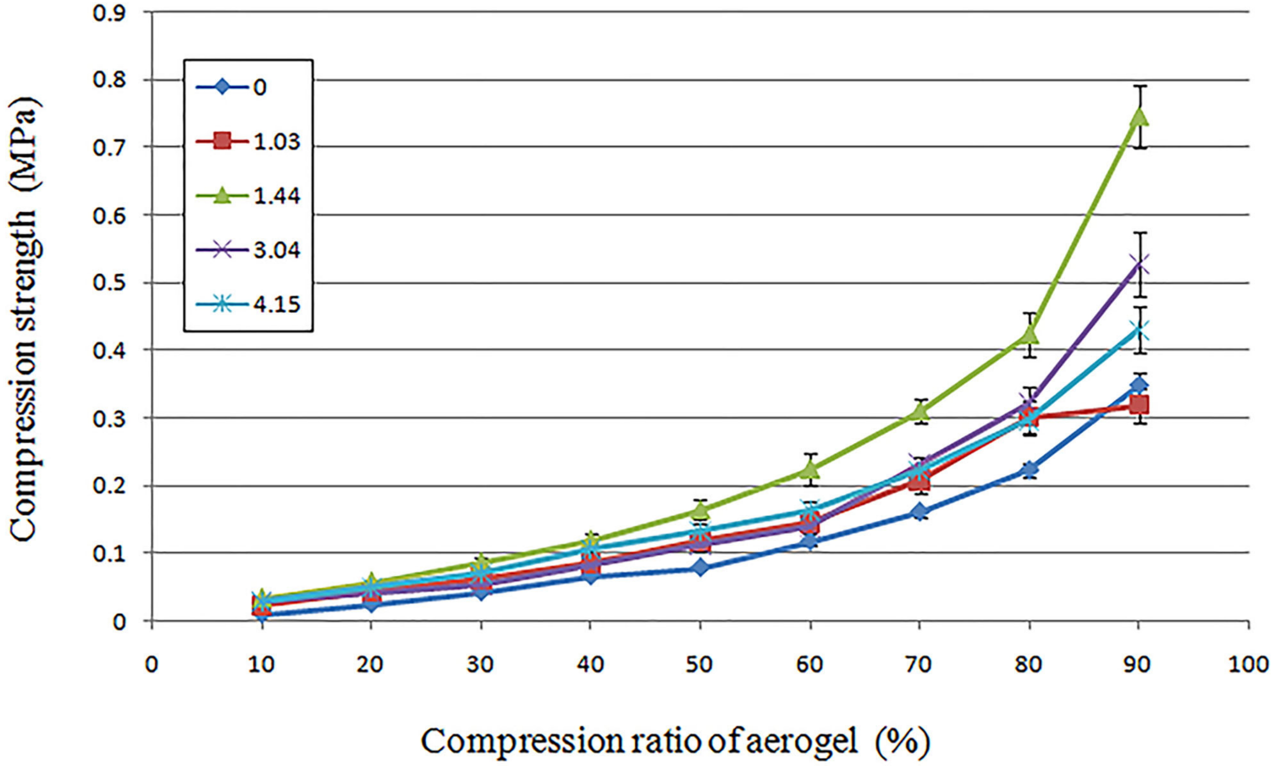

FIGURE 4 | Effect of the ODs of BC on the strength properties of the produced aerogels.

sample from the BC with an OD of 1.44% required twice strength compared to an aerogel sample obtained from the NBC. An increase in the OD to 3.04 and 4.15% led to a decrease in the strength of the OBC aerogels, which was nevertheless higher than the NBC control aerogels.

Effect of Divalent Metals on the Strength of Aerogels Made of Oxidized BC

The introduction of the–COOH groups in the BC by TEMPO oxidation enables further increase in the strength properties of the OBC aerogels by forming cross-links between two –COOH groups with help of divalent cations. For this purpose, $Mg^{2+}$of specific concentration was added to the OBC hydrogel with an OD of 1.44%, and the strength of the obtained samples was compared (**Figure 5**).

The addition of Mg^{2+} resulted in an increase in the compressive force applied to the aerogel sample to achieve a certain degree of the sample compression. The largest increment in the compressive force on an OBC aerogel sample with an OD of 1.44% was achieved when Mg^{2+} was added at concentrations of 20 and 40 mM. To achieve 50% sample compression of the samples with an OD of 1.44% containing 20 or 40 mm Mg^{2+}, compressive forces four- and five-fold higher than those applied on the NBC aerogel were required.

Owing to the fact that the introduction of Mg^{2+} into the BC aerogel improved the strength properties of the material, the influence of other divalent ions, such as Mn^{2+}, Co^{2+}, Cu^{2+}, Ni^{2+}, Ca^{2+}, and Zn^{2+}, on the strength of the OBC aerogels with an OD of 1.44% was also evaluated. These ions were added to the BC hydrogels in the amount necessary to achieve a final concentration of 20 mM (**Figure 6A**). The changes in strength properties were determined for the obtained aerogels (**Figure 6B**).

Before achieving 50% sample compression, the OBC aerogel with Mg^{2+} ions was observed to be the most durable aerogel. At a sample compression of 60–80%, the strength of the aerogels containing Mg^{2+}ions was comparable to that of the aerogels containing Zn^{2+}or Mn^{2+} ions. Further, Co^{2+}, Ni^{2+}, and Ca^{2+} had the least influence on the strength of the aerogels. However, all the metals increased the strength of the aerogels prepared from the TEMPO-oxidized BC. The simplicity of this approach is primarily attributed to the use of divalent ions as a cross-linking agent, which does not require further modification of BC, because chemical modification always destroys the weak interactions that play a major role in aerogel stabilization.

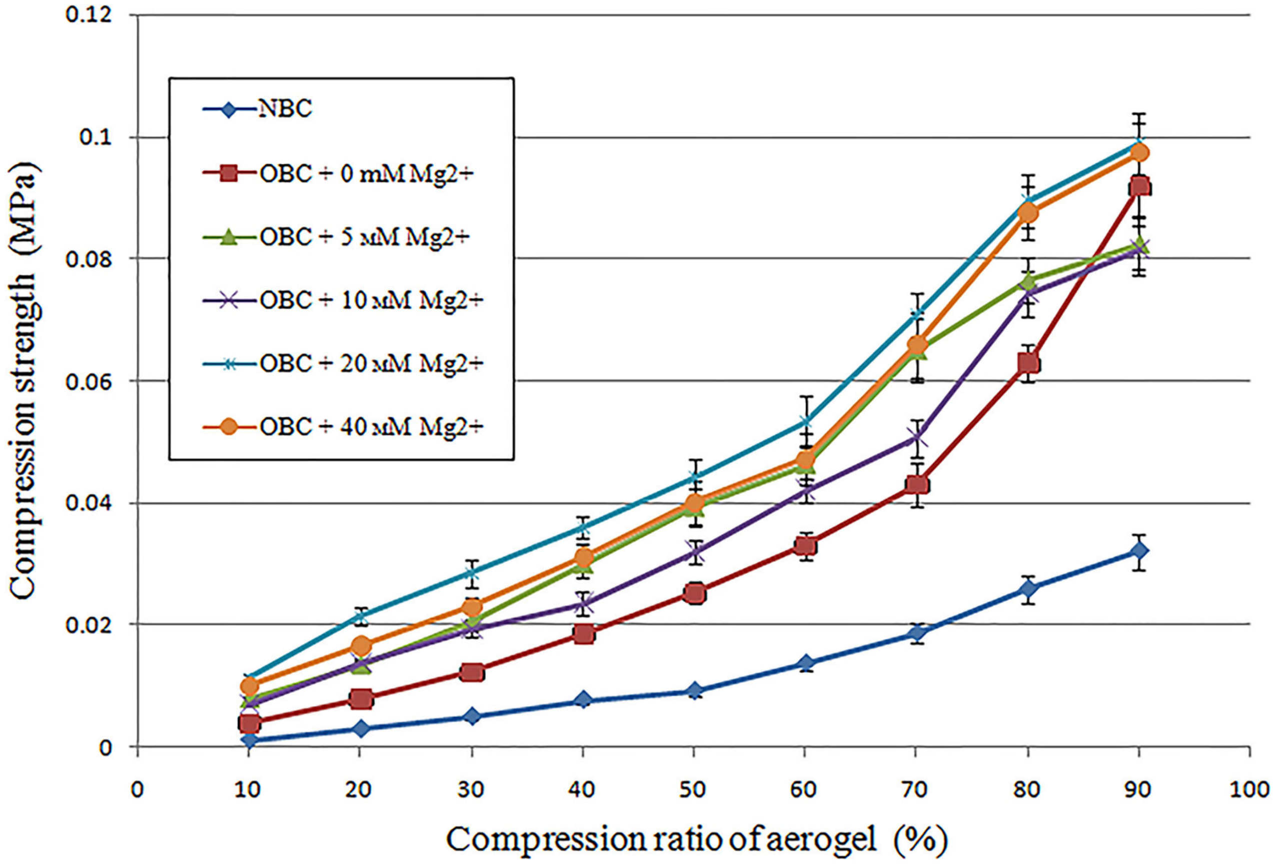

FIGURE 5 | Changes in the strength properties of the aerogels obtained from the TEMPO-oxidized BC (OBC), with an OD of 1.44% depending on the concentration of Mg^{2+}, compared with the aerogel obtained from the NBC.

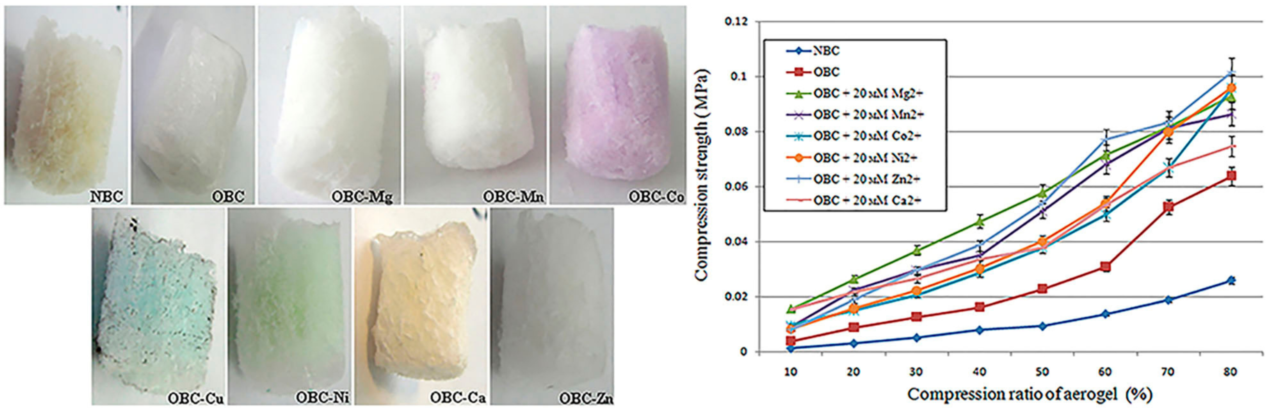

FIGURE 6 | Samples of BC aerogels and changes in their strength. **(A)** BC aerogels produced from NBC and TEMPO-oxidized BC with an OD of 1.44% with presence of 20 mM of corresponding divalent metals: Mg^{2+}, Mn^{2+}, Co^{2+}, Cu^{2+}, Ni^{2+}, Ca^{2+}, and Zn^{2+}. **(B)** Changes in the strength of the aerogels prepared from the TEMPO-oxidized BC with an OD of 1.44% depending on the presence of 20 mM of divalent metals.

Thus, oxidation of the BC solved several problems at once in the process of obtaining an aerogel from the BC. The oxidation of the BC resulted in reduced shrinkage of the OBC aerogel, and increased the strength of the OBC aerogels, which can be further enhanced by the introduction of divalent metal ions.

Microporous Structure of Aerogels Obtained From NBC or OBC

Utilizing the TEMPO-oxidized BC to produce aerogels resulted in both a decrease in the aerogel shrinkage and an increase in the porosity and strength of the material. Obviously, these changes are correlated to the microporous structure changes of the BC aerogels. The porous structures of the aerogels obtained from the NBC and the TEMPO-oxidized BC with an OD of 1.44% were studied, in the absence or presence of 20 mM Mg^{2+}. The microporous structure in the central and outer parts of the aerogels was studied using cylindrical aerogels with a diameter of 14 mm and a height of 10 mm.

In the central part of the aerogels obtained from the NBC or OBC, no significant change in the microporous structure was observed; however, the aerogel obtained from TEMPO-oxidized BC has a tendency to increase the number of smaller pores. The oxidation of the BC reduced the maximum pore size in the central part of the aerogel from 206 to 188 μm (**Figure 7**). This reduction is not significant; however, the total area of the pores, the size of which does not exceed 100 μm in the aerogel from TEMPO-oxidized BC, increased from 40.6 to 44.6%. The addition of 20 mM Mg^{2+} to the aerogels obtained from the TEMPO-oxidized BC further reduced the maximum pore size to 175.6 μm. Simultaneously, the area of the pores, with pore sizes <100 μm, in this aerogel increased to 68.4%. Thus, the central part of the aerogels obtained from the TEMPO-oxidized BC, particularly with the Mg^{2+} ions, was characterized by a more developed porous structure that has a decreased maximum pore size and an increased number of smaller pores.

In contrast to the central part of aerogels, the porous structures of the outer part of the aerogels prepared from the NBC or TEMPO-oxidized BC varied significantly (**Figure 8**). The NBC aerogels had a significant number of pores larger than 1 mm, and these large pores account for most of the occupied area and volume. For example, the proportion of the pores with sizes < 100 μm in the NBC aerogel accounts for up to 70.7% of their total number. However, these pores occupy only 3.9% of the total pore area. Utilizing the TEMPO-oxidized BC reduced the maximum average pore size from 1,375 to 611 μm. The amount of pores with pore sizes <100 μm in the aerogel obtained from the TEMPO-oxidized BC with an OD of 1.44 was 90.5% of the total number of pores, and the total area occupied by these pores increased to 21.2% of the total pore area. Despite the decrease in the average pore size of the TEMPO-oxidized BC aerogel, the maximum pore size in the outer part of the aerogel was three times larger than in the central part. The addition of 20 mM Mg^{2+} to the TEMPO-oxidized BC aerogel resulted in a noticeable reduction in the average pore size compared to the pore sizes of the NBC aerogels. The microporous structure of the outer part of the aerogel was like that of its central part. The average maximum pore size was 197.4 μm. In the TEMPO-oxidized BC aerogel with an OD of 1.44% containing Mg^{2+}, the proportion of pores with pore sizes < 100 μm was 99.1%, and the total area occupied by these pores increased to 81.6%.

These results suggest that the introduction of negatively charged groups, such as –COOH, into the BC enabled the stabilization of the BC hydrogel because of their mutual repulsion during freeze-drying. The addition of Mg^{2+} during the preparation of the aerogel from the TEMPO-oxidized BC stabilized the fibrils of the BC in the freezing process more effectively through the ionic bonds between the –COOH groups and the Mg^{2+} ions.

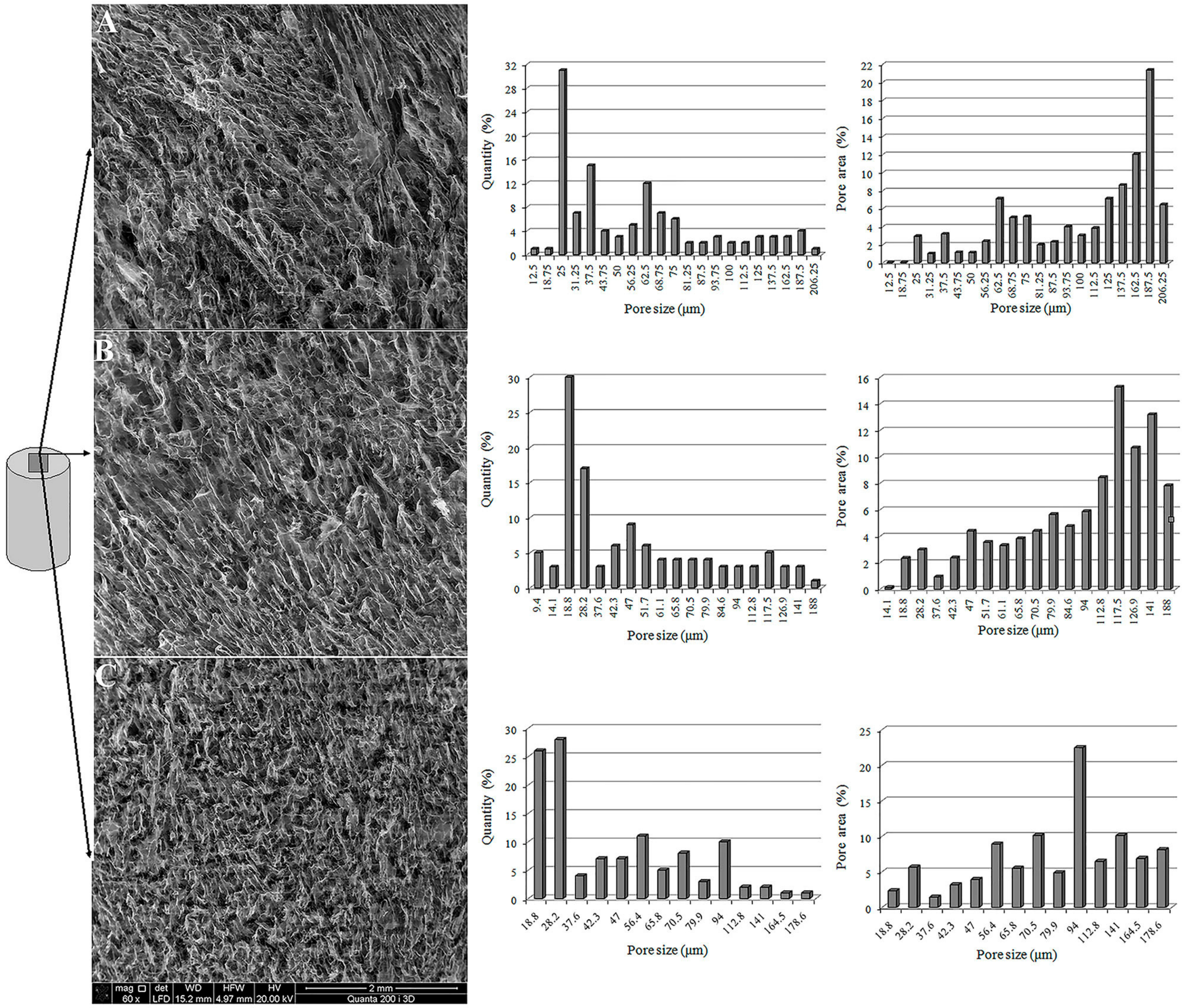

FIGURE 7 | SEM image of the central part of the aerogels prepared from the NBC **(A)**, TEMPO-oxidized BC with an OD of 1.44% **(B)**, and TEMPO-oxidized BC with an OD of 1.44% containing 20 mM Mg^{2+} **(C)**.

Determination of Thermal Properties of Aerogels Obtained From Native or Oxidized Bacterial Cellulose

The temperature stability of BC aerogels is an important characteristic, especially in high-temperature applications of this material. Therefore, we conducted a thermogravimetric study of BC aerogels produced from the NBC and TEMPO-oxidized BC with an OD of 1.44% with or without of 20 mM of Mg^{2+} (**Figure 9**). Generally, NBC aerogel shows initial decomposition in one step ranging from 275 to 330″C The weight loss of the NBC aerogel started at 57°C, and upon reaching a temperature of 250°C, the NBC aerogel lost 7.5% of its mass. This weight loss is caused by the evaporation of bacterial-cellulose-related water (Huang et al., 2014). Thermogravimetric analysis showed that the thermal decomposition of the NBC aerogel began at 275°C, and by the time the temperature reached 330°C, there was a loss of 70% of the NBC aerogel mass in the oxidizing atmosphere. This result is consistent with thermogravimetric characteristic of the thermal stability of BC film (Revin et al., 2019). The main mass loss in the OBC aerogel or OBC-Mg aerogel also began at 275°C and continued till 330 and 300°C, respectively. The mass loss under these conditions was 43% and 39% for the OBC aerogel and OBC-Mg aerogel, respectively. When the temperature reached 500°C, the mass loss for the OBC and OBC-Mg aerogels was 63 and 60%, respectively, while for the NBC aerogel, the mass loss at this temperature was 99%. The results show that the TEMPO oxidation of BC does not lead to changes in the thermal stability of the material however, the nature of the thermal degradation of the material depended on the oxidation of BC and the presence of Mg^{2+}.

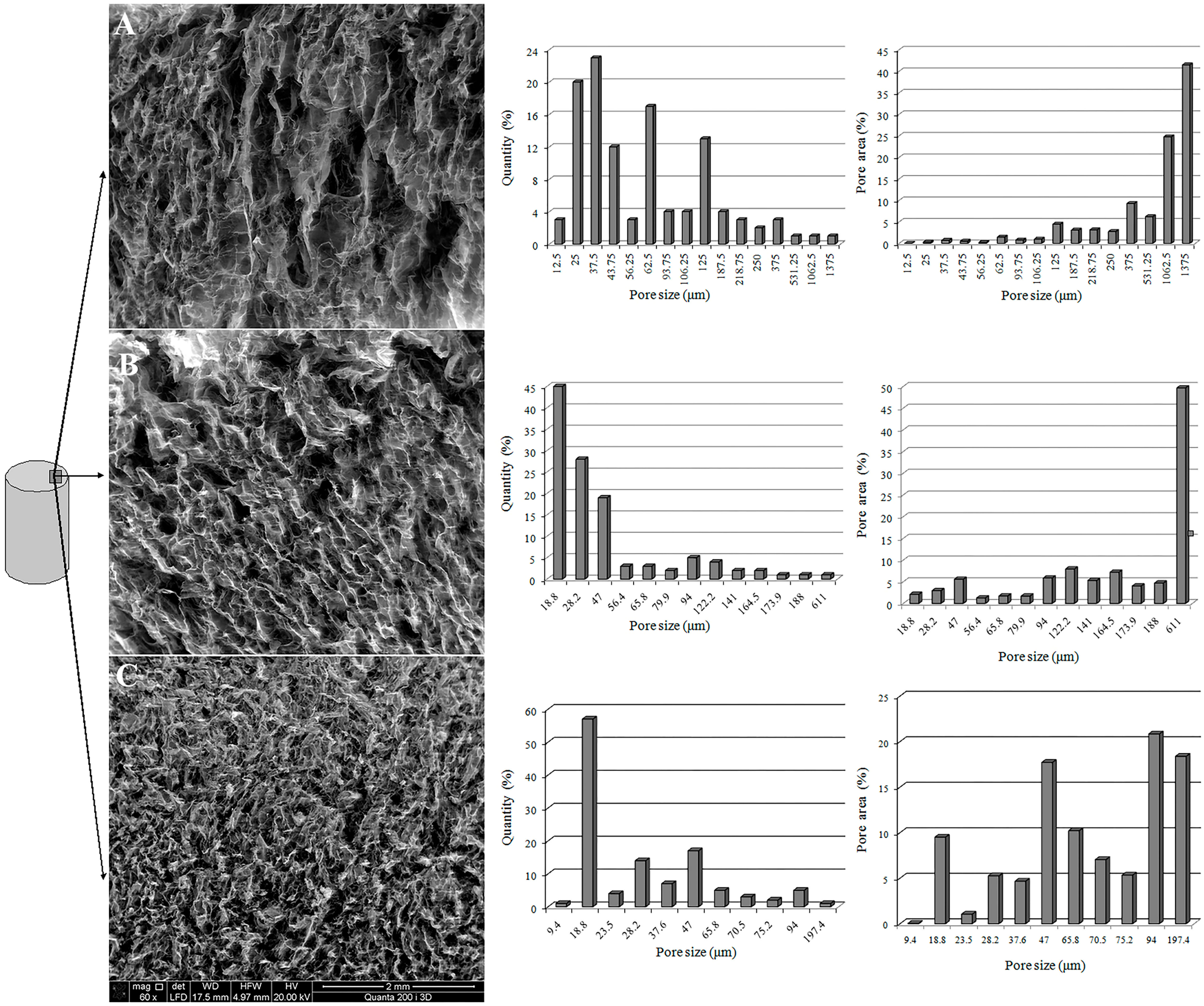

FIGURE 8 | SEM image of the outer part of the aerogels prepared from the NBC **(A)**, TEMPO-oxidized BC with an OD of 1.44% **(B)**, and TEMPO-oxidized BC with an OD of 1.44% containing 20 mM Mg^{2+} **(C)**.

Owing to the changes in the microporous structure of the aerogels from the TEMPO-oxidized BC, and owing to the fact that the aerogel obtained from the BC is a highly porous material that can be used as a heat-insulating material, it was interesting to determine how the oxidation of the BC will affect the thermal conductivity of this material. To understand this, we compared the coefficients of thermal conductivity of the aerogels obtained from the NBC, TEMPO-oxidized BC, and TEMPO-oxidized BC containing Mg^{2+} (**Table 2**). While measuring the coefficient of thermal conductivity, the temperature on the warm side of the sample was 50°C and that on the cold side of the sample was 40°C. Under these conditions, the coefficient of thermal conductivity of air was 0.0283 W/(m•K). The aerogel obtained from the NBC had the highest coefficient of thermal conductivity, most likely because of the presence of the heterogeneous porous structure of the aerogel, which facilitated the transfer of heat. Utilizing the TEMPO-oxidized BC to produce aerogels made it possible to obtain a material with a more uniform porous structure over the entire volume of the sample as compared to the native cellulose aerogel. This led to a decrease in the thermal conductivity coefficient from 0.036 to 0.0225 W/(m•K). The preparation of the aerogel from the TEMPO-oxidized BC with an OD 1.44% and Mg^{2+} led not only to an increase in the strength of the aerogels and a more uniform porous structure, but also to a further decrease in the coefficient of thermal conductivity to 0.0176 W/(m•K).

Preparation of Aerogels With Antibacterial Properties Based on Native and Oxidized BC

The aerogels obtained in this work can be used as functional biomaterials for a wide range of applications, particularly in biomedicine. This work shows that the strength of an aerogel

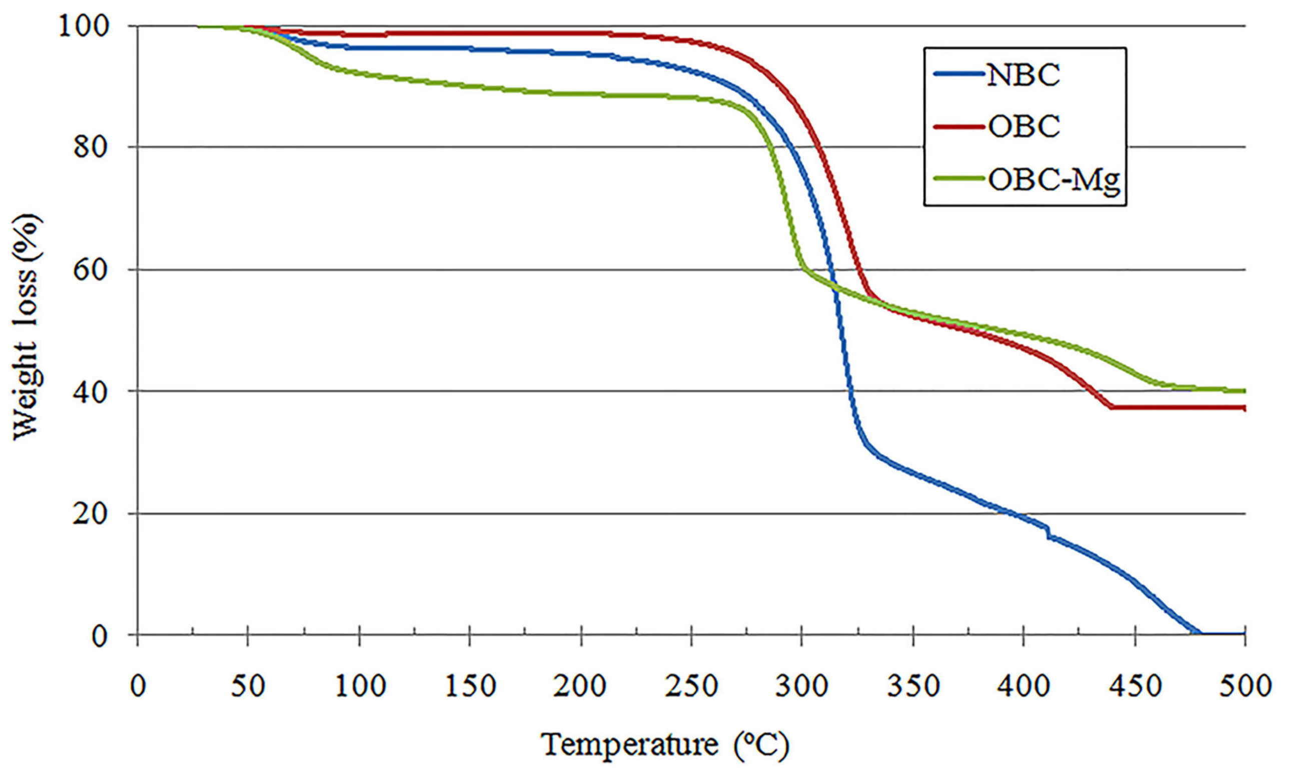

FIGURE 9 | Thermogravimetric analysis of BC aerogels produced from the NBC, TEMPO-oxidized BC with an OD of 1.44% with or without of 20 mM of Mg^{2+}.

TABLE 2 | Coefficients of thermal conductivity of the aerogels obtained from the NBC and the TEMPO-oxidized BC.

Aerogels prepared from:	Coefficient of thermal conductivity, W/(m·K)
NBC	0.036
TEMPO-oxidized BC with oxidation degree 1.44%	0.0225
TEMPO-oxidized BC with oxidation degree 1.44%, 20 MM Mg^{2+}	0.0176

with an OD of 1.44% doubled compared to that of the aerogels obtained from the NBC. Therefore, we used the TEMPO-oxidized BC with an OD of 1.44% and NBC as a control to obtain antibacterial biocomposites.

The BC has many characteristics of an ideal wound dressing. However, in the native state, it does not show any antimicrobial effects. To produce aerogels with antibacterial properties, we used the antibiotic SF, which is gaining interest in the treatment of skin infections (Siala et al., 2018). Fusidic acid (FA) is used to treat a variety of infections caused by Gram-positive bacteria and is particularly effective against infections caused by staphylococci, including strains resistant to penicillin and other antimicrobials as an alternative for the treatment of infections caused by methicillin resistant *Staphylococcus aureus* (MRSA). In addition, it is a hypoallergenic drug with low toxicity, low drug resistance, and no cross-resistance with other clinically used antibiotics (Curbete and Salgado, 2016).

In the present study, novel biocomposites in the form of aerogels based on the NBC and SF (NBC/SF) and the TEMPO-oxidized BC and SF (OBC/SF) with antibacterial activities were obtained for the first time by the incorporation of SF with the NBC and the OBC hydrogel. **Figure 10** shows the FTIR spectra of the NBC, SF and NBC/SF composite. The typical FTIR spectrum of the NBC for this polymer is shown, where the absorption in the region of 3,200–3,500 cm^{-1} is due to the valence vibration of the hydrogen-bonded OH groups (Shao et al., 2016). In the C–O stretching vibration region, the peaks at 1,164, and 1,061 cm^{-1} correspond to the C–O–C asymmetric stretching and the C–C, C–OH, C–H ring and side group vibrations, respectively. The infrared spectrum of pure SF exhibited three characteristic bands at 3,420, 1,725, 1,260 cm^{-1}. The absorption at the 3,420 and 1,725 cm^{-1} were caused by the valence vibration of the hydrogen-bonded OH groups and carboxyl groups of the SF. In the case of the NBC/SF composite, the FTIR spectrum showed typical bands for the NBC and SF at 1,725 and 1,260 cm^{-1}. The presence of these peaks at the FTIR spectrum of the NBC/SF indicates the presence of the SF in the obtained composite.

The antibacterial activities of the prepared aerogels were studied by the disc diffusion method. The antibacterial capacity was determined by measuring the diameter of the clear zone of the inhibition around the samples after 18 h incubation, as shown in **Figure 11**.

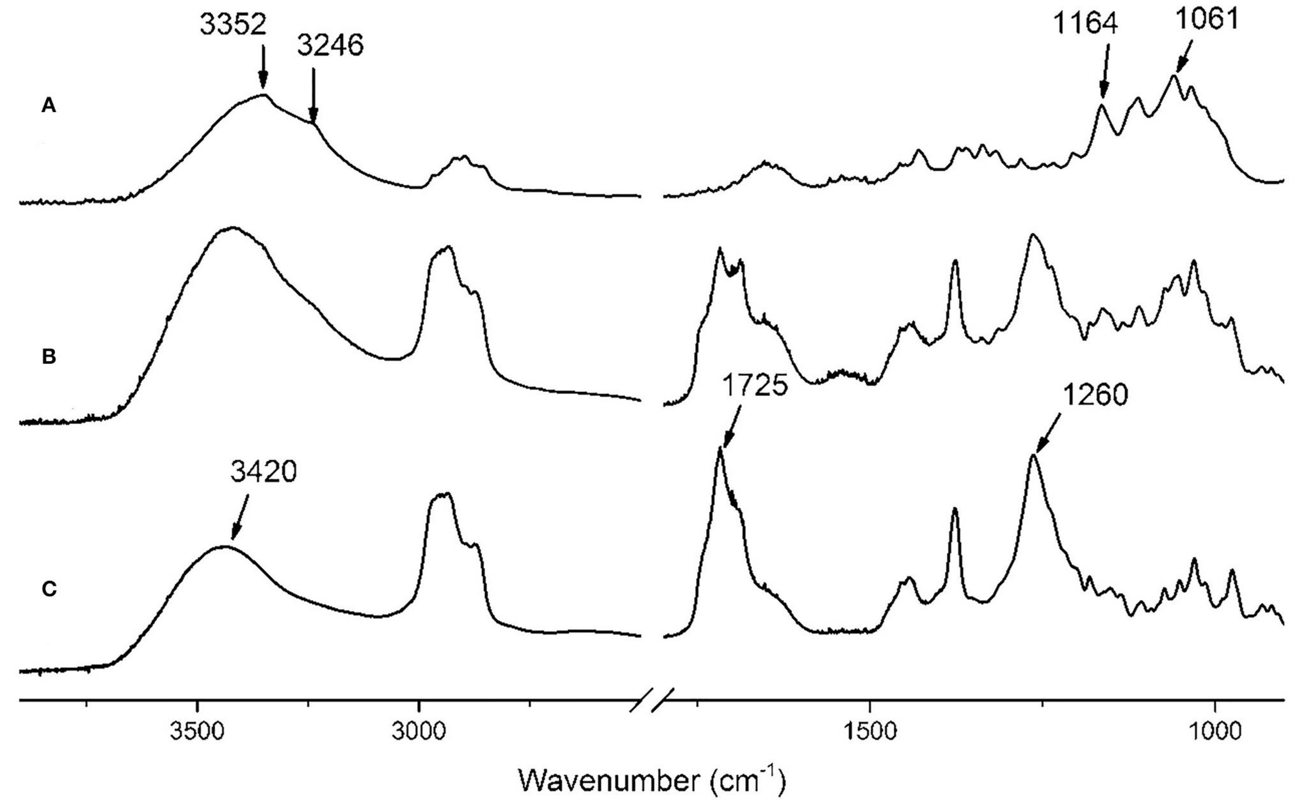

FIGURE 10 | FTIR spectra of the aerogels: NBC **(A)**, NBC/SF **(B)**, and SF **(C)**.

As expected, no inhibition zones were observed for the NBC as control, or the OBC, demonstrating that the NBC and OBC do not have any antibacterial abilities. The biocomposites NBC/SF$_{100}$ and OBC/SF$_{100}$ exhibited high antibacterial activities, and the diameters of their zones of inhibition for *S. aureus* were 28 ± 1 and 27 ± 1 mm, respectively. This study clearly illustrates that the prepared aerogels show excellent antibacterial activities. There was no significant difference to be found between the NBC/SF and OBC/SF aerogels. However, as shown in our study, the aerogels obtained from the OBC have greater strength and the functional biomaterials obtained from it will have a wide range of applications, particularly for biomedicine.

For an antimicrobial material, the release ratio of the antimicrobial agent is important for its practical applications. An antimicrobial agent exhibiting optimally stable and prolonged release is favored. In this study, SF was adsorbed on the nanofibres of NBC and OBC. To study the release behavior of aerogels loaded with SF, the samples were placed in a phosphate buffer solution at pH 7.4 for observation. As shown in **Figure 12**, the release amount changed with the increase in the sustained release time. It was found that the amount of drug released from NBC/SF and OBC/SF reached 75% and 65% in 24 h, respectively. SF loaded into NBC and OBC can obviously slow the release activity, which suggests that NBC and OBC could be used for the controlled release of drugs that reduce infection and inflammation. The drug release results showed that cellulose aerogels have controlled SF release performance.

Cytotoxicity studies were performed to investigate the effect of SF in the NBC and OBC matrix on proliferation of mouse fibroblast cell culture L929. The cell viability of L929 cells was evaluated by MTT assay. The cell cytotoxicity imparted by NBC/SF$_{100}$ and OBC/SF$_{100}$ aerogels extracts was studied. The MTT results are shown in **Figure 13A**. All the materials showed negligible toxicity. No reduced cell viability following their incubation with NBC/SF and OBC/SF extracts was shown. The results showed that SF does not inhibit the proliferation of L929 cells. To determine whether the morphology of L929 cells was affected by NBC/SF and OBC/SF biocomposites, the cells were observed by an inverted optical microscope (**Figure 13B**). The morphologies of L929 cells treated with NBC/SF and OBC/SF extracts were similar to the blank one. Thus, the prepared biocomposites displayed no effect on L929 cells morphology. These results showed that NBC/SF and OBC/SF biocomposites are promising candidates for wound dressing and tissue engineering applications.

DISCUSSION

The utilization of the freeze-drying method for preparing aerogels from BC indicates the presence of a step for pre-freezing

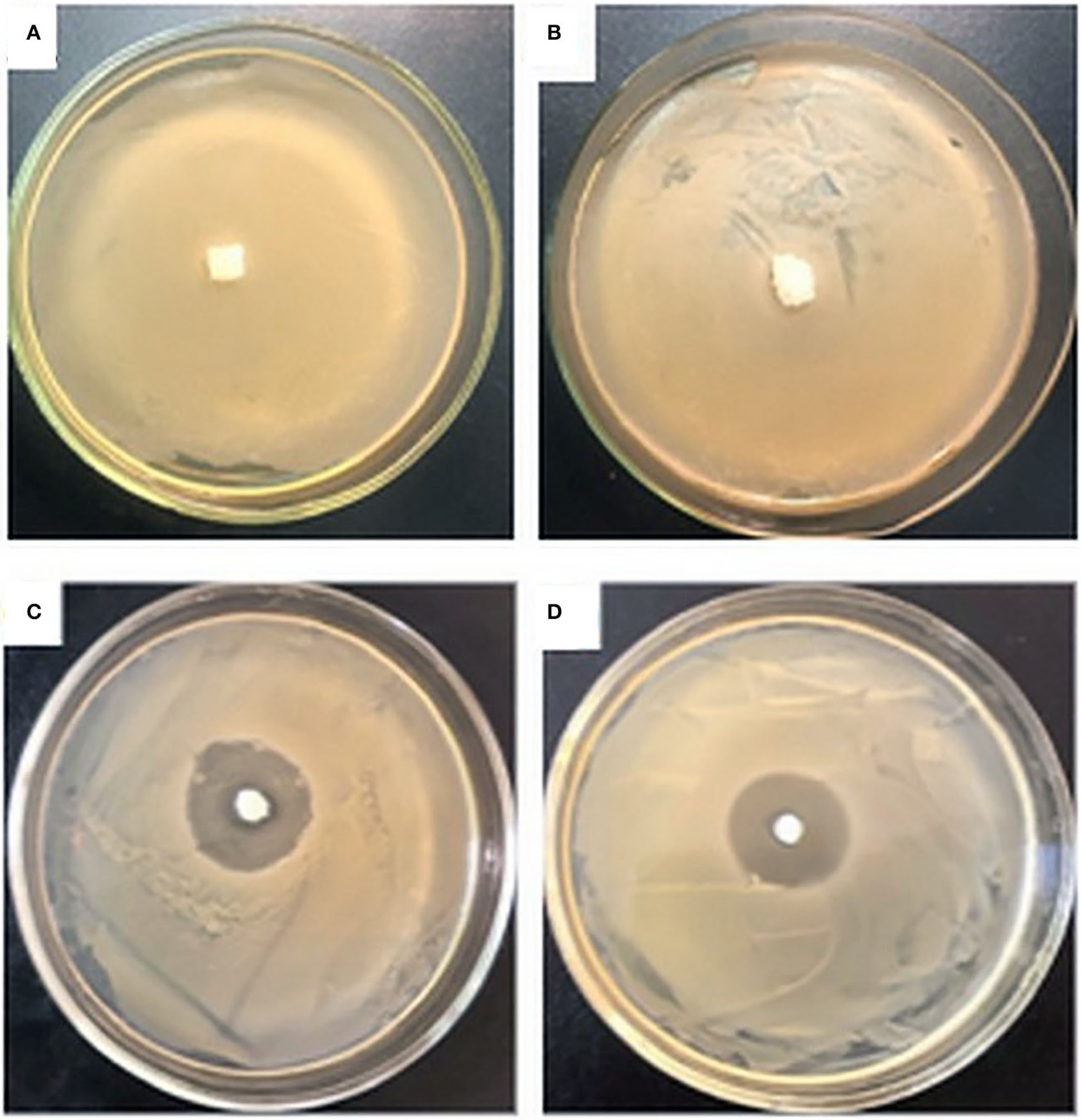

FIGURE 11 | Antimicrobial activities of aerogels against *S. aureus*: NBC **(A)**, OBC **(B)**, biocomposite NBC/SF$_{100}$ **(C)**, biocomposite OBC/SF$_{100}$ **(D)**.

the hydrogel of BC. This step will ultimately determine the microporous structure of the aerogel, which, in turn, will determine the aerogel properties such as thermal conductivity, strength, and porosity (Revin et al., 2019). Obviously, the freezing process will not only be determined by the freezing mode but also will depend on parameters such as volume of the frozen sample. It is known that the production of aerogels from BC by freeze-drying is accompanied with their shrinkage, which is expressed as a decrease in their volume, a change in porosity (as observed in our studies), and the existence of heterogeneity of the microporous structure in different sections of the aerogel. According to our data, the shrinkage volume can be significant and reach 40% or more (**Table 1**). Moreover, the central part of the aerogel obtained from BC was denser than the aerogel sections located on the outer part of the sample. The presence of such heterogeneity in the structure will undoubtedly become more pronounced with an increase in the volume of the aerogels, and will make it difficult to design functional materials based on them.

It is possible that the shrinkage of the aerogel may be caused by the freezing-out of the material during its freezing. Accordingly, prevention of such an undesirable phenomenon by changing the properties of BC is possible. It is known that the chemical modification of cellulose is widely conducted to change the properties of this polymer as well as to overcome some difficulties, for example barrier properties, in preparing

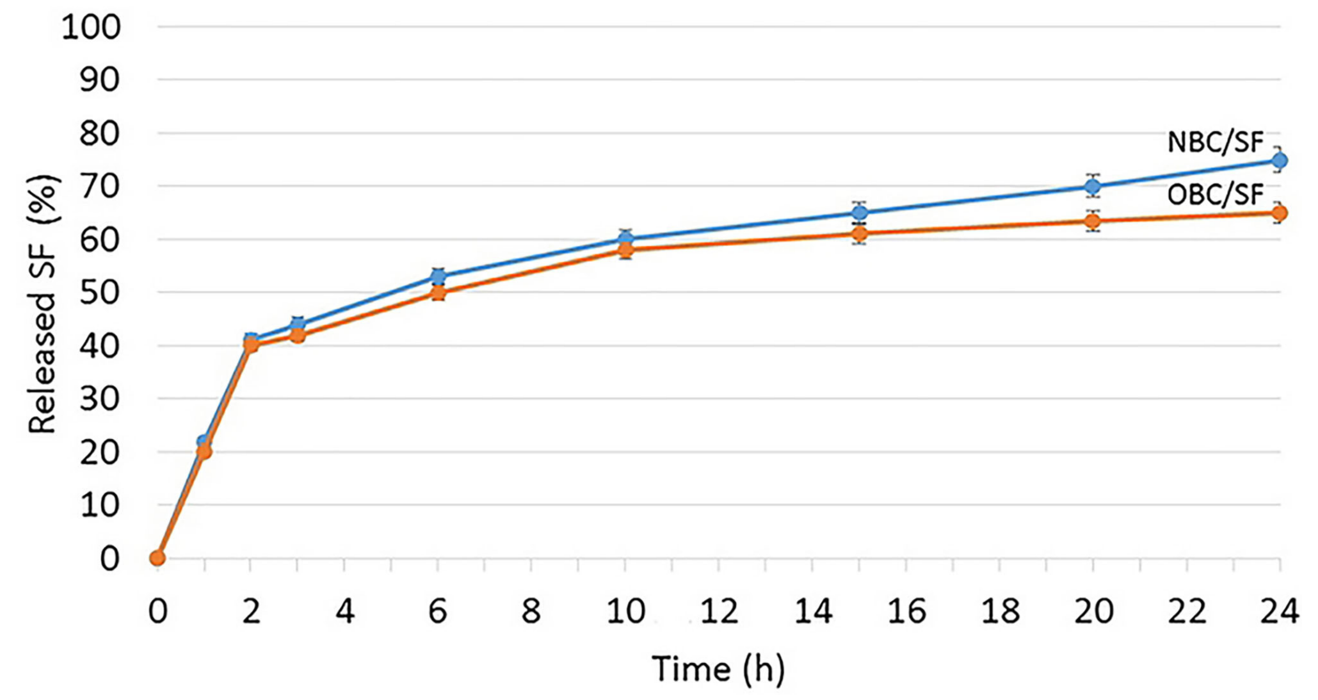

FIGURE 12 | Cumulative release profiles of SF from NBC/SF and OBC/SF biocomposites.

functional materials (Aulin et al., 2010; Habibi et al., 2010; Rodionova et al., 2010; Kang et al., 2015).

Because it is assumed that the formation and stabilization of the structures of the BC hydrogel and the aerogel obtained from it are dependent on the formation of hydrogen bonds, the introduction of additional functional groups into this system could lead to changes that would reduce shrinkage and increase the homogeneity of the microporous structure of aerogels. The role of such additional functional groups is well-aligned with the carboxyl group which can easily be introduced into BC during its TEMPO oxidation. Our results showed that the introduction of carboxyl groups into BC resulted in a decrease in the shrinkage of aerogels from 41.02 to 17.8% and an increase in the strength of this material (**Table 1**, **Figure 4**). Moreover, the nature of these changes was directly dependent on the number of carboxyl groups introduced. It is assumed that a decrease in the shrinkage observed with the introduction of carboxyl groups into BC could be due to mutual repulsion of negatively charged carboxyl groups, which, in turn, could lead to the stabilization of the hydrogel of BC during its freezing at a given OD. An excessive increase in the OD, resulting from the introduction of a large number of carboxyl groups, could lead to the destruction of the system of stabilizing hydrogen bonds, which negatively affects both the shrinkage and strength of the aerogel. The results obtained on the effect of chemical modification on the such parameter as shrinkage are in good agreement with the data on the effect of chemical modification on the properties of functional materials from BC obtained in the studies of other authors (Aulin et al., 2010; Habibi et al., 2010; Rodionova et al., 2010; Kang et al., 2015).

Thus, the oxidation of BC solved several problems associated with the process of obtaining aerogel from BC. First, the oxidation of BC resulted in reduced shrinkage of the aerogels from OBC. Secondly, the oxidation of BC led to an increase in the strength of the aerogels from OBC. This high strength of BC aerogels is extremely advantageous for applications such as a thermal insulator or in the fabrication of a composite material for medical purposes. According to our data, the aerogels from BC with a lower density had a lower coefficient of thermal conductivity (Revin et al., 2019). Moreover, although the strength of the BC aerogels significantly decreased with a decrease in their density, for this field of application, it is necessary to maintain a high strength of the material at a low density. This problem can be solved by the introduction of additional cross-links. In this work, divalent metal ions were used to create cross-links between two carboxyl groups located close to each other. Thus, the inclusion of 20 mM Mg^{2+} in the aerogel resulted in a four- to five-fold increase in the strength of aerogels prepared from TEMPO-oxidized BC compared to that of aerogels prepared from NBC (**Figure 5**). The use of divalent ions as a cross-linking agent was primarily due to the simplicity of this approach, which does not require further modification of BC, because chemical modification always destroys the weak interactions that play a major role in aerogel stabilization. However, the development of the material is also based on its applications. The use of these aerogels as a functional element of a structural material, such as a heat-insulating material (because it has a

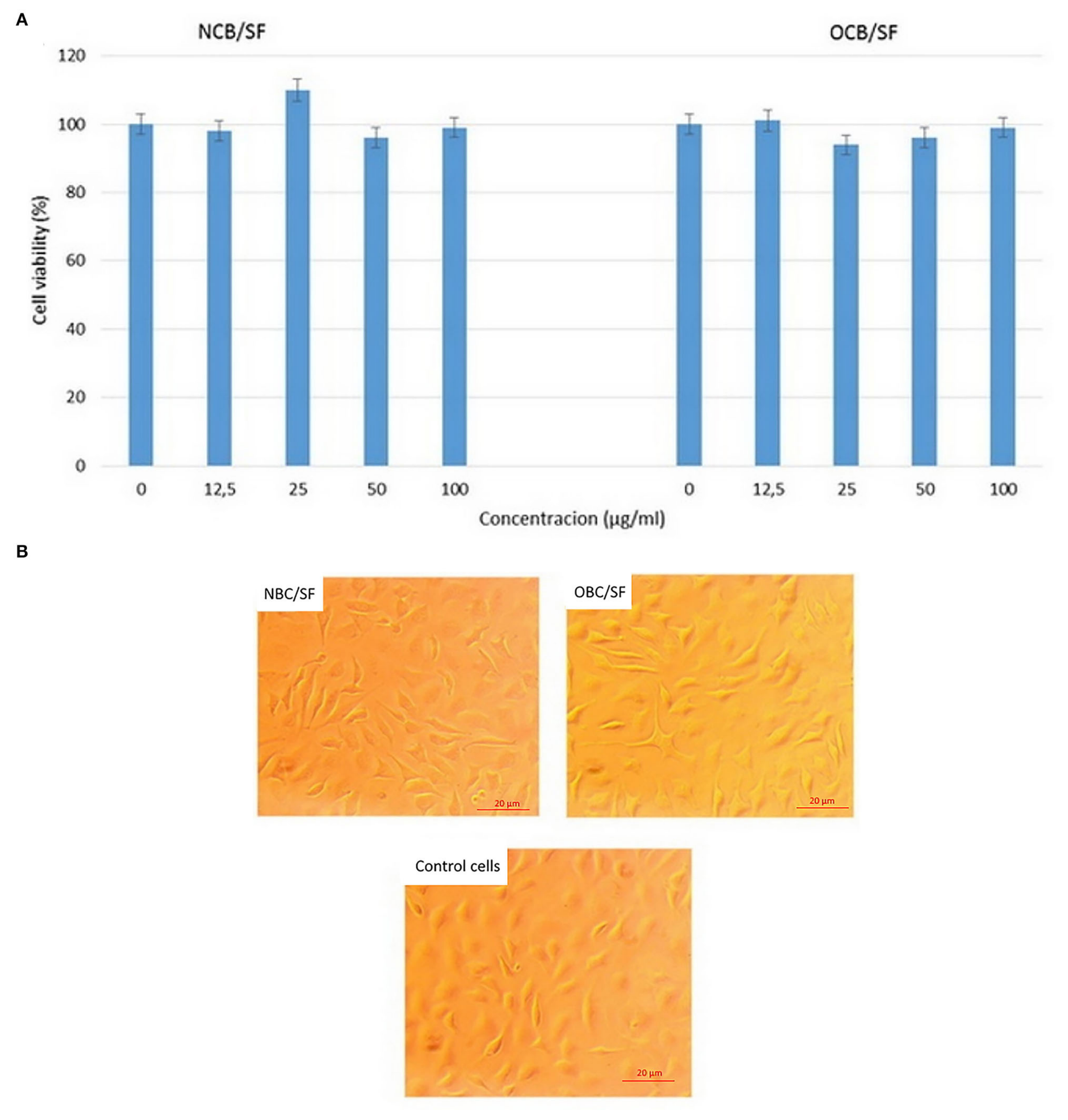

FIGURE 13 | Cell viabilities **(A)** and cell morphologies **(B)** of the mouse fibroblast cell culture L929 treated with NBC/SF and OBC/SF extracts.

low coefficient of thermal conductivity, as shown in this study), would be possible. Moreover, the aerogels can be used as a sound-insulating material, because it has sufficiently high sound absorption coefficients in the region of 1,600–5,000 Hz (Revin et al., 2019). However, in either of these applications, the use of divalent metals related to heavy metals will be impossible for environmental reasons. In contrast, when preparing medical materials, the use of divalent metals including heavy metals may be advisable because some of them have pronounced antimicrobial properties (Robinson et al., 2010; Argueta-Figueroa et al., 2014).

The inclusion of Mg^{2+} in the composition of the aerogel from TEMPO-oxidized BC resulted in a more uniform microporous structure of the aerogel with maximal pore sizes in the central and outer parts of the aerogel 178 and 197 μm, respectively, unlike the structure of aerogel prepared from NBC (for which the maximum pore size varied from 206 μm in the central part of the aerogel to 1,375 μm in the outer part of the sample). Apparently, changing of the aerogel microporous structure caused a decrease in the thermal conductivity coefficient of the aerogel from TEMPO-oxidized BC containing Mg^{2+} from 0.036 to 0.0176 W/(m•K) (**Table 2**) compared to that of the aerogel from NBC.

Thermogravimetric analysis has showed that the oxidation of BC or the inclusion of Mg^{2+} in the aerogel from OBC did not lead to a change in the temperature at the beginning of thermal degradation of the material, but the pattern of change of thermal degradation of the aerogels depended on the oxidation of BC and the presence of Mg^{2+}. This may be due to the fact that the number of carboxyl groups included in BC was not large enough, since the calculation of the percentage of carboxyl groups reflects only the number of primary CH_2OH groups subjected to oxidation. It is necessary to note that the thermal stability of the obtained aerogel will only be important in certain potential applications of this material. There is a large opportunity for creating materials for medicine, including those based on BC, where in thermally stable materials are not required.

The resulting aerogels can be used as functional biomaterials in a wide range of applications, particularly in biomedicine. Recently, aerogels were incorporated in the field of biomaterials (Nita et al., 2020) because of their properties such as high porosity, high internal surfaces, and controlled pore diameter and their 3D interconnected structure. Bio-based aerogels also exhibit high cytocompatibility, biocompatibility, and biodegradability and can be used successfully in biomedical applications such as tissue engineering and drug delivery and as antibacterial materials (El-Naggar et al., 2020; Nita et al., 2020). In this study, the TEMPO-oxidized BC with an OD of 1.44% and NBC were used to produce antibacterial biocomposites.

The BC has the characteristics of an ideal wound dressing. BC-based dressings have nanofibrous structures with a high capability of absorbing and retaining water and wound exudate and can control the environment for wound healing (Li et al., 2018). Therefore, BC must be considered as a physical barrier between the wound and the surrounding environment, thereby preventing microbial infections. There have been several successful attempts to impart antimicrobial properties to BC. BC-silver nanocomposites exhibited excellent antibacterial activity (Wu et al., 2018; Wang et al., 2020). The synthesis of BC/chitosan composites with high mechanical reliability and antibacterial activity has also been reported (Zang et al., 2016). Aerogels with antimicrobial properties based on chitosan (Zheng et al., 2020) and cellulose with amoxicillin (Ye et al., 2018) have also been reported.

Among the technologies for constructing antibacterial materials, adding antibiotics in the BC is a facile method to obtain an antibacterial film that can be used as a wound dressing material (Kaplan et al., 2014). Previously, we obtained biocomposites with high antibacterial activity based on BC and FA in the form of films (Liyaskina et al., 2017). FA, an antibiotic produced from the *Fusidium coccineum* fungus, belongs to the class of steroids, but it has no corticosteroid effects (Liu et al., 2020). FA is characterized as an α, β-unsaturated carboxylic acid; its molecular formula is $C_{31}H_{48}O_6$, containing one acetoxyl and two hydroxyl groups. The most active derivative is its sodium salt (sodium fusidate), which was first used clinically for the treatment of staphylococcal infections. FA has been widely used in the systemic and topical treatments of staphylococcal infections, including those caused by strains resistant to penicillin and other antimicrobials, thereby making it an alternative for the treatment of diseases caused by the MRSA strains (Fernandes, 2016). In recent years, the inhibitory effect of FA on the biofilm formation of *S. aureus* (Siala et al., 2018) was reported. FA can effectively reduce the virulence of *S. aureus* by inhibiting the expression of α-toxin (Liu et al., 2020). Oral FS is currently being re-developed in the US for skin and orthopedic infections, in which biofilms play a major role (Siala et al., 2018).

Drugs can be incorporated into aerogels by two methods (Nita et al., 2020). In the first method, which is considered the simpler method, the drug is added *in situ* during the gelling process. The second method consists of the *ex situ* addition of the drug by absorption or precipitation in a dry aerogel. By this method, the drug in a liquid or gaseous phase is incorporated into the aerogel matrix. However, this latter method has some restrictions; specifically, the slow diffusion capacity of the drug through the pores of the matrix.

In this work, novel biocomposites with antibacterial properties based on native and oxidized BC and SF in the form of aerogels, by including SF in the hydrogels of native and oxidized BC, were obtained for the first time. These biocomposites exhibit high antibiotic activity against *S. aureus* and can be used in medicine as a wound dressing. Aerogels prepared from OBC have high strength and, therefore, are advantageous for use as functional biomaterials for a wide range of applications, including in biomedicine.

CONCLUSION

In this study, we developed appropriate conditions for obtaining aerogels with controlled density, strength, and thermal characteristics from BC such that they can be used as functional biomaterials for a wide range of applications, particularly in biomedicine. It was found that the aerogels prepared from OBC are more durable and have a lower aerogel shrinkage compared to the aerogels obtained from NBC. Furthermore, the TEMPO oxidation of the BC along with the addition of Mg^{2+} can produce aerogels with significantly increased strength and a more uniform microporous structure. Furthermore, in this study for the first time, novel biocomposites were formed from aerogels based on either the NBC or the OBC and SF, which had a high antibacterial activity against *S. aureus*. These results can be helpful in the further development of antibacterial wound dressing materials as well as other new antibacterial products for biomedical applications.

DATA AVAILABILITY STATEMENT

The raw data supporting the conclusions of this article will be made available by the authors, without undue reservation.

AUTHOR CONTRIBUTIONS

VR, NP, and EL contributed toward conception and design of the study. ET, NN, and NP performed the experimental work. NP and EL wrote the first draft of the manuscript and contributed toward data analysis and manuscript revision. All the authors have read and approved the submitted version.

FUNDING

This work was financed by Russian Foundation for Basic Research (project No. 19-515-80002\19). The results of section Determination of Thermal Properties of Aerogels Obtained from Native or Oxidized Bacterial Cellulose were obtained within the state assignment of Ministry of Science and Higher Education of the Russian Federation (Grant No. FZRS-2020-0003).

REFERENCES

Argueta-Figueroa, L., Morales-Luckie, R. A., Scougall-Vilchis, R. J., and Olea-Mejía, O. F. (2014). Synthesis, characterization and antibacterial activity of copper, nickel and bimetallic Cu–Ni nanoparticles for potential use in dental materials. *Prog. Nat. Sci. Mater. Int.* 24, 321–328. doi: 10.1016/j.pnsc.2014.07.002

Aulin, C., Gallstedt, M., and Lindstrom, T. (2010). Oxygen and oil barrier properties of microfibrillated cellulose films and coatings. *Cellulose* 17, 559–574. doi: 10.1007/s10570-009-9393-y

Barrios, E., Fox, D., Li Sip, Y. Y., Catarata, R., Calderon, J. E., Azim, N., et al. (2019). Nanomaterials in advanced, high-performance aerogel composites: a review. *Polymers* 11:726. doi: 10.3390/polym11040726

Bhandari, J., Mishra, H., Mishra, P. K., Wimmer, R., Ahmad, F. J., and Talegaonkar, S. (2017). Cellulose nanofiber aerogel as a promising biomaterial for customized oral drug delivery. *Int. J. Nanomed.* 12, 2021–2031. doi: 10.2147/IJN.S124318

Cael, J. J., Gardner, K. H., Koenig, J. L., and Blackwell, J. (1975). Infrared and Raman spectroscopy of carbohydrates. Paper V. Normal coordinate analysis of cellulose I. *J. Chem. Phys.* 62, 1145–1153. doi: 10.1063/1.430558

Carvalho, T., Guedes, G., Sousa, F. L., Freire, C. S., and Santos, H. A. (2019). Latest advances on bacterial cellulose-based materials for wound healing, delivery systems, and tissue engineering. *Biotechnol. J.* 14:1900059. doi: 10.1002/biot.201900059

Choi, S. M., and Shin, E. J. (2020). The nanofication and functionalization of bacterial cellulose and its applications. *Nanomaterials* 10:406. doi: 10.3390/nano10030406

Curbete, M. M., and Salgado, H. R. N. (2016). A critical review of the properties of fusidic acid and analytical methods for its determination. *Crit. Rev. Anal. Chem.* 46, 352–360. doi: 10.1080/10408347.2015.1084225

Dufresne, A. (2013). Nanocellulose: a new ageless bionanomaterial. *Mater. Today.* 16, 16220–16227. doi: 10.1016/j.mattod.2013.06.004

El-Naggar, M. E., Othman, S. I.;, Allam, A. A., and Morsy, O. M. (2020). Synthesis, drying process and medical application of polysaccharide-based aerogels. *Int. J. Biol. Macromol.* 145, 1115–1128. doi: 10.1016/j.ijbiomac.2019.10.037

Fernandes, P. (2016). Fusidic acid: a bacterial elongation factor inhibitor for the oral treatment of acute and chronic staphylococcal infections. *Cold Spring Harb. Perspect. Med.* 6:a025437. doi: 10.1101/cshperspect.a025437

Gupta, P., Singh, B., Agrawal, A. K., and Maji, P. K. (2018). Low density and high strength nanofibrillated cellulose aerogel for thermal insulation application. *Mater. Design.* 158, 224–236. doi: 10.1016/j.matdes.2018.08.031

Habibi, Y., Lucia, L. A., and Rojas, O. J. (2010). Cellulose nanocrystals: Chemistry, self-assembly, and applications. *Chem. Rev.* 110, 3479–3500. doi: 10.1021/cr900339w

Hickey, R. J., and Pelling, A. E. (2019). Cellulose biomaterials for tissue engineering. *Front. Bioeng. Biotechnol.* 7:45. doi: 10.3389/fbioe.2019.00045

Hikalx, A. H., Shibl, A., and El-Hoofy, S. (1982). Determination of sodium fusidate and fusidic acid in dosage forms by high-performance liquid chromatography and a microbiological method. *J. Pharm. Sci.* 71, 1297–1298. doi: 10.1002/jps.2600711130

Huang, Z., Li, H., Miao, H., Guo, Y., and Teng, L. (2014). Modified supercritical CO_2 extraction of amine template from hexagonal mesoporous silica (HMS) materials: effects of template identity and matrix Al/Si molar ratio. *Chem. Eng. Res. Des.* 92, 1371–1380. doi: 10.1016/j.cherd.2013.10.023

Jebel, F. S., and Almasi, H. (2016). Morphological, physical, antimicrobial and release properties of ZnO nanoparticles-loaded bacterial cellulose films. *Carbohydr. Polym.* 149, 8–19. doi: 10.1016/j.carbpol.2016.04.089

Jiang, W., Saxena, A., Song, B., Ward, B. B., Beveridge, T. J., and Myneni, S. C. (2004). Elucidation of functional groups on gram-positive and gram-negative bacterial surfaces using infrared spectroscopy. *Langmuir* 20, 11433–11442. doi: 10.1021/la049043+

Kang, H., Liu, R., and Huang, Y. (2015). Graft modification of cellulose: Methods, properties and applications. *Polymer* 70, A1–A16. doi: 10.1016/j.polymer.2015.05.041

Kaplan, E., Ince, T., Yorulmaz, E., Yener, F., Harputlu, E., and Lacin, N. T. (2014). Controlled delivery of ampicillin and gentamycin from cellulose hydrogels and their antibacterial efficiency. *J. Biomater. Tissue Eng.* 7, 543–549. doi: 10.1166/jbt.2014.1198

Katti, A., Shimpi, N., Roy, S., Lu, H., Fabrizio, E. F., Dass, A., et al. (2006). Chemical, physical, and mechanical characterization of isocyanate cross-Linked amine-modified silica aerogels. *Chem. Mater.* 18, 285–296. doi: 10.1021/cm0513841

Kistler, S. S. (1931). Coherent expanded aerogels and jellies. *Nature* 127, 741–741. doi: 10.1038/127741a0

Kondo, T., and Sawatari, C. A. (1996). Fourier transform infra-red spectroscopic analysis of the character of hydrogen bonds in amorphous cellulose. *Polymer* 37, 393–399. doi: 10.1016/0032-3861(96)82908-9

Li, J. J., Cha, R., Mou, K., Zhao, X. H., Long, K. Y., Luo, H., et al. (2018). Nanocellulose-based antibacterial materials. *Adv. Healthc. Mater.* 20:1800334. doi: 10.1002/adhm.201800334

Liu, L., Shen, X., Yu, J., Cao, X., Zhan, Q., Guo, Y., et al. (2020). Subinhibitory Concentrations of Fusidic Acid May Reduce the Virulence of S. *aureus by down-regulating sara and saers to reduce biofilm formation and α-toxin expression. Front. Microbiol.* 11:25. doi: 10.3389/fmicb.2020.00025

Liyaskina, E., Revin, V., Paramonova, E., Nazarkina, M., Pestov, N., Revina, N., et al. (2017). Nanomaterials from bacterial cellulose for antimicrobial wound dressing. *J. Phys.* 784:012034. doi: 10.1088/1742-6596/784/1/012034

Long, L.-Y., Weng, Y.-X., and Wang, Y.-Z. (2018). Cellulose aerogels: synthesis, applications, and prospects. *Polymers* 10:623. doi: 10.3390/polym10060623

Luo, H., Cha, R., Li, J., Hao, W., Zhang, Y., and Zhou, F. (2019). Advances in tissue engineering of nanocellulose-based scaffolds: a review. *Carbohyd. Polym.* 224:115144. doi: 10.1016/j.carbpol.2019.115144

Ma, B, Huang, Y, Zhu, C, Chen, C, Chen, X, Fan, M. et al. (2016). Novel CuSiO2 / bacterial cellulose nanofibers: Preparation and excellent performance in antibacterial activity. *Mater. Sci. Eng. C Mater. Biol. Appl.* 62, 656–661. doi: 10.1016/j.msec.2016.02.011

Maleki, H. (2016). Recent advances in aerogels for environmental remediation applications: a review. *Chem. Eng. J.* 300, 98–118. doi: 10.1016/j.cej.2016.04.098

Naumann, D., Barnickel, G., Bradaczek, H., Labischinski, H., and Giesbrecht, P. (1982). Infrared spectroscopy, a tool for probing bacterial peptidoglycan potentialities of infrared spectroscopy for cell wall analytical studies and rejection of models based on crystalline chitin. *Eur. J. Biochem.* 125, 505–515. doi: 10.1111/j.1432-1033.1982.tb06711.x

Nguyen, S. T., Feng, J., Ng, S. K., Wong, J. P. W., Tan, V. B. C., and Duong, H. M. (2014). Advanced thermal insulation and absorption properties of recycled cellulose aerogels. *Colloids Surf. A* 445, 128–134. doi: 10.1016/j.colsurfa.2014.01.015

Nita, L. E., Ghilan, A., Rusu, A. G., Neamtu, I., and Chiriac, A. P. (2020). New trends in bio-based aerogels. *Pharmaceutics* 12:449. doi: 10.3390/pharmaceutics12050449

Novak, B. M., Auerbach, D., and Verrier, C. (1994). Low-density, mutually interpenetrating organic-inorganic composite materials via supercritical drying techniques. *Chem. Mater.* 6, 282–286. doi: 10.1021/cm00039a006

Oh, S. Y., Yoo, D. I., Shin, Y., and Seo, G. (2005). FTIR analysis of cellulose treated with sodium hydroxide and carbon dioxide. *Carbohydr. Res.* 340, 417–428. doi: 10.1016/j.carres.2004.11.027

Perez, D. S., Montanari, S., and Vignon, V. R. (2003). TEMPO-mediated oxidation of cellulose III. *Biomacromolecules* 4, 1417–1425. doi: 10.1021/bm034144s

Pircher, N., Carbajal, L., Schimper, C., Bacher, M., Rennhofer, H., Nedelec, J. M., et al. (2016). Impact of selected solvent systems on the pore and solid structure of cellulose aerogels. *Cellulose* 23, 1949–1966. doi: 10.1007/s10570-016-0896-z

Portela, R., Leal, C. R., Almeida, P. L., and Sobral, R. G. (2019). Bacterial cellulose: a versatile biopolymer for wound dressing applications. *Microb. Biotechnol.* 12, 586–610. doi: 10.1111/1751-7915.13392

Revin, V., Liyaskina, E., Nazarkina, M., Bogatyreva, A., and Shchankin, M. (2018). Cost-effective production of bacterial cellulose using acidic food industry by-products. *Braz. J. Microbiol.* 49, 151–159. doi: 10.1016/j.bjm.2017.12.012

Revin, V. V., Liyas'kina, E. V., Sapunova, N. B., and Bogatyreva, A. O. (2020). Isolation and characterization of the strains producing bacterial cellulose. *Microbiology* 14, 86–95. doi: 10.1134/S0026261720010130

Revin, V. V., Pestov, N. A., Shchankin, M. V., Mishkin, V. P., Platonov, V. I., Petrov, P. S., et al. (2019). A study of the physical and mechanical properties of aerogels obtained from bacterial cellulose. *Biomacromolecules* 20, 1401–1411. doi: 10.1021/acs.biomac.8b01816

Robinson, D. A., Griffith, R. W., Shechtman, D., Evans, R. B., and Conzemius, M. G. (2010). *In vitro* antibacterial properties of magnesium metal against *Escherichia coli*, *Pseudomonas aeruginosa,* and *Staphylococcus aureus*. *Acta Biomater.* 6, 1869–1877. doi: 10.1016/j.actbio.2009.10.007

Rodionova, G., Lenes, M., Eriksen, O., and Gregersen, O. (2010). Surface chemical modification of microfibrillated cellulose: improvement of barrier properties for packaging applications. *Cellulose* 18, 127–134. doi: 10.1007/s10570-010-9474-y

Shao, W., Liu, H., Wang, S., Wu, J., Huang, M., Min, H. et al. (2016). Controlled release and antibacterial activity of tetracycline hydrochloride-loaded bacterial cellulose composite membranes. *Carbohydr. Polym.* 145, 114–120. doi: 10.1016/j.carbpol.2016.02.065

Sharma, A., Thakur, M., Bhattacharya, M., Mandal, T., and Goswami, S. (2019). Commercial application of cellulose nano-composites - a review. *Biotechnol. Rep.* 21:e00316. doi: 10.1016/j.btre.2019.e00316

Siala, W., Rodriguez-Villalobos, H., Fernandes, P., Tulkens, P. M., and Van Bambeke, F. (2018). Activities of combinations of antistaphylococcal antibiotics with fusidic acid against staphylococcal biofilms in *in vitro* static and dynamic models. *Antimicrob. Agents Chemother.* 62, e00598–18. doi: 10.1128/AAC.00598-18

Sulaeva, I., Henniges, U., Rosenau, T., and Potthast, A. (2015). Bacterial cellulose as a material for wound treatment: properties and modifications. A review. *Biotechnol. Adv.* 33, 1547–1571. doi: 10.1016/j.biotechadv.2015.07.009

Teixeira, M. A., Paiva, M. C., Amorim, T. P., and Felgueiras, H. P. (2020). Electrospun nanocomposites containing cellulose and its derivatives modified with specialized biomolecules for an enhanced wound healing. *Nanomaterials* 10:557. doi: 10.3390/nano10030557

Wang, J., Tavakoli, J., and Tang, Y. (2019). Bacterial cellulose production, properties and applications with different culture methods – a review. *Carbohydr. Polym.* 219, 63–76. doi: 10.1016/j.carbpol.2019.05.008

Wang, P., Yin, B., Dong, H., Zhang, Y., Zhang, Y., Chen, et al. (2020). Coupling biocompatible au nanoclusters and cellulose nanofibrils to prepare the antibacterial nanocomposite films. *Front. Bioeng. Biotechnol.* 8:986. doi: 10.3389/fbioe.2020.00986

Wang, S., Jiang, F., Xu, X., Kuang, Y., Fu, K., Hitz, E., et al. (2017). Super-strong, super-stiff macrobers with aligned, long bacterial cellulose nanofibers. *Adv. Mater.* 29:1702498. doi: 10.1002/adma.201702498

Wu, C.-N., Fuh, S.-C., Lin, S.-P., Lin, Y.-Y., Chen, H.-Y., Liu, J.-M., et al. (2018). TEMPO-oxidized bacterial cellulose pellicle with silver nanoparticles for wound dressing. *Biomacromolecules* 19, 544–554. doi: 10.1021/acs.biomac.7b01660

Yamada, Y., Yukphan, P., Vu, H. T. L., Muramatsu, Y., Ochaikul, D., and Nakagawa, Y. (2011). Subdivision of the genus *Gluconacetobacter* Yamada, Hoshino and Ishikawa 1998: the proposal of *Komagatabacter* gen. nov., for strains accommodated to the Gluconacetobacter xylinus group in the α-Proteobacteria. *Ann. Microbiol.* 62, 849–859. doi: 10.1007/s13213-011-0288-4

Ye, S., He, S., Su, C., Jiang, L., Wen, Y., Zhu, Z., et al. (2018). Morphological, release and antibacterial performances of amoxicillin-loaded cellulose aerogels. *Molecules* 23:2082. doi: 10.3390/molecules23082082

Zang, P., Chen L., Zhang, Q., and Hong, F. F. (2016). Using in sity dynamic cultures to rapidly biofabricate fabric-reinforsed composites of chitosan/bacterial nanocellulose for antibacterial wound dressings. *Front. Microbiol.* 7:260. doi: 10.3389/fmicb.2016.00260

Zheng, L., Zhang, S., Ying, Z., Liu, J., Zhou, Y., and Chen, F. (2020). Engineering of aerogel-based biomaterials for biomedical applications. *Int. J. Nanomed.* 15, 2363–2378. doi: 10.2147/IJN.S238005

Conflict of Interest: The authors declare that the research was conducted in the absence of any commercial or financial relationships that could be construed as a potential conflict of interest.

frontiers in Bioengineering and Biotechnology

ORIGINAL RESEARCH
published: 03 December 2020
doi: 10.3389/fbioe.2020.579404

Development and Evaluation of Drug Loaded Regenerated Bacterial Cellulose-Based Matrices as a Potential Dosage Form

Munair Badshah[1], Hanif Ullah[1], Feng He[2]*, Fazli Wahid[3], Umar Farooq[1], Mattias Andersson[4] and Taous Khan[1]*

[1] Department of Pharmacy, COMSATS University Islamabad, Abbottabad, Pakistan, [2] Hubei Key Laboratory of Economic Forest Germplasm Improvement and Resources Comprehensive Utilization, Huanggang Normal University, Huanggang, China, [3] Department of Biomedical Sciences, Pak-Austria Fachhochschule: Institute of Applied Sciences and Technology, Haripur, Pakistan, [4] Department of Chemistry and Chemical Engineering, Chalmers University of Technology, Gothenburg, Sweden

Bacterial cellulose (BC) is a highly pure form of cellulose and possesses superior physico-mechanical properties with wide range of applications. These properties of BC can further be improved by various modifications, including its regeneration from the BC solution. In the current research work, regenerated BC (R-BC) matrices were prepared using N-methyl-morpholine-oxide (NMMO; 50% w/w solution in water) and loaded with model drugs, i.e., famotidine or tizanidine. The characterization of drug loaded regenerated BC (R-BC-drug) matrices was carried out using Fourier transform infrared spectroscopy (FTIR), x-ray diffraction (XRD) analysis, scanning electron microscopy (SEM) and thermogravimetric analysis (TGA), which revealed the stability of matrices and successful drug loading. Results of dissolution studies showed immediate (i.e., > 90%) drug release in 30 min. The drugs release data was found to best fit into first order kinetics model having R^2 values >0.99 for all the formulations. These results indicated that regenerated BC-based matrices had the ability to be used for delivery of orally administered drugs.

Keywords: bacterial cellulose, drug delivery, famotidine, tizanidine, regeneration

Edited by:
*Ronan McCarthy,
Brunel University London,
United Kingdom*

Reviewed by:
*Diego Mantovani,
Laval University, Canada
Adil Denizli,
Hacettepe University, Turkey*

***Correspondence:**
*Taous Khan
taouskhan@cuiatd.edu.pk
Feng He
hfeng@hust.edu.cn*

Specialty section:
*This article was submitted to
Biomaterials,
a section of the journal
Frontiers in Bioengineering and
Biotechnology*

Received: *02 July 2020*
Accepted: *12 November 2020*
Published: *03 December 2020*

Citation:
*Badshah M, Ullah H, He F, Wahid F,
Farooq U, Andersson M and Khan T
(2020) Development and Evaluation of
Drug Loaded Regenerated Bacterial
Cellulose-Based Matrices as a
Potential Dosage Form.
Front. Bioeng. Biotechnol. 8:579404.
doi: 10.3389/fbioe.2020.579404*

INTRODUCTION

Cellulose is the most abundant, inexpensive, biodegradable, and renewable biomaterial obtained from cotton, wood, and other plant sources, which often contains pectin, lignin, and hemicellulose as biogenic contaminations (Khan et al., 2015; Hickey and Pelling, 2019). In contrast, bacterial cellulose (BC) is highly pure, non-cytotoxic and non-pyrogenic biomaterial, obtained by culturing the colonies of selected bacterial species, particularly *Gluconacetobacter xylinus* (*G. xylinus*) (Ávila et al., 2015; Ullah et al., 2016a). The features like molding ability into the desired shape, ultrafine, and well-organized fibrous network, and ability of absorption and retention of water make BC superior to plant based cellulose (Sajjad et al., 2020; Souza et al., 2020). BC finds applications in the preparation of medical devices, tissue engineering and reconstructive surgery, and as supportive scaffold for reconstruction of auricular cartilage (Ávila et al., 2015; Möller et al., 2017). In addition, BC has been studied for potential applications, such as tissue proliferation, cell growth, treatment of wounds, mesenchymal cells differentiation, enzymes and bioactive compounds delivery (Klinthoopthamrong et al., 2020), and as-synthesized as well as surface modified matrices (Badshah et al., 2017,18) and capsules shells for oral drug delivery (Ullah et al., 2017).

To meet the current research demand and to explore further potential applications of BC in various fields, several physical and chemical procedures have been reported in the literature for preparation of BC based nano-composites (Ullah et al., 2016a,b) and bio-functionalized polymers (Badshah et al., 2018). Out of these methods, the most popular are the surface modification, and novel dissolution and regeneration process (Khalid et al., 2017; Ullah et al., 2019). Limited data is available regarding biomedical and pharmaceutical applications of regenerated bacterial cellulose (R-BC). The applications of R-BC include microfluidic column for protein separation, electricity conducting multi-walled carbon nano-tubes (Phisalaphong et al., 2008; Chen et al., 2016), novel nano-porous membrane for filtration and diode for light emission (Chen et al., 2009, 2016). In addition, R-BC has been studied as wound dressing material for the delivery of nanoparticles, as scaffold for tissue regeneration (Ul-Islam et al., 2014), delivery of antibacterial agents and for biomedical tissue engineering (Shafiei et al., 2014; Reddy and Yang, 2015). In addition to above-mentioned applications, BC forms a single excipient based intact oral dosage form due its higher tensile strength in comparison to the existing conventional solid dosage forms. Moreover, the as-synthesized BC membrane has limited thickness and more time is required to obtain desired thickness. In case of regenerated BC, the matrices with desired thickness can be easily produced by increasing the quantity or concentration of BC solution (Badshah et al., 2017, p. 18; Ullah et al., 2017). Similarly, R-BC is more amorphous and easily biodegrade in comparison to as-synthesized BC and thus have high potential for drug delivery to the body parts, wherein degradation of BC is desired (Ullah et al., 2019).

The process of BC regeneration is associated with certain shortcomings, such as its limited solubility in solvents (commonly used for plant cellulose) and inability to tailor the polymeric properties after regeneration (Reddy and Yang, 2015). The literature studies showed that N-methyl-morpholine-oxide (NMMO) is an environment friendly and recyclable solvent (Shafiei et al., 2014; Reddy and Yang, 2015), and possesses better cellulose dissolution properties as compared to other chemicals (El-Wakil and Hassan, 2008; Xu et al., 2015). The use of NMMO revolutionized the regeneration process of cellulose, and expanded its applications from textiles and cotton fiber spinning industry (Xu et al., 2015) to biomedical field (Isogai and Atalla, 1998; Zhu et al., 2006). Literature revealed the availability of several studies on the dissolution and regeneration of plant based cellulose, but little data is available related to BC regeneration. In addition, no studies have been reported regarding R-BC applications as matrices for oral delivery of drugs. Therefore, the current research was designed to dissolve and regenerate BC for drug delivery using NMMO as solvent.

In the current research work, R-BC-drug (famotidine and tizanidine) matrices were prepared for the first time using NMMO as solvent. The matrices were characterized using FTIR, XRD, SEM and TGA. The matrices were evaluated (*in-vitro)* using simulated gastric conditions with objective to explore the possible applications of R-BC in oral drug delivery.

MATERIALS AND METHODS

Materials

Anhydrous D-glucose (Dae-Jung, Gyeonggi-do, Korea), agar and peptone (Oxide, Hants, UK), sodiumhydroxide (Sigma Aldrich, St. Louis, USA), citric acid monohydrate (RDH, Seelze, Germany), sodium dihydrogen phosphate and yeast extract (Merk, Darmstadt, Germany), NMMO 50% (w/w) aqueous solution (a kind gift from Amines and Plasticizer, Mumbai, India), tizanidine HCl (JPN Pharma, Mumbai, India), famotidine (Suleshvari Pharma, Gujarat, India), and hydrochloric acid (Fishers Chemicals Ltd, Loughborough, UK) were used. The solvents and chemicals received were used without further processing.

Methods

Biosynthesis of BC

Hestrin Schramm (HS) liquid medium, containing glucose anhydrous 2% citric acid monohydrate 0.11%, yeast extract 0.5%, peptone 0.5%, NaH_2PO_4 0.27% and distilled-water, was prepared (pH 6.0) and sterilized (121°C for 20 min). For the preparation of the pre-culture, the colonies of *G. xylinus* were added into HS medium (50 mL) in conical flask (100 mL) and incubated for 24 h at 30°C and 150 rpm in shaking orbital incubator (J.P. Selecta S.A, Spain). Then, 20 mL of the pre-cultured medium was added into basal HS medium in a rectangular container (6 cm × 24 cm × 18 cm) and kept in static incubator (Memmert, 100–800, Germany) at 28°C for 7 to 15 days. The prepared BC sheets was thoroughly washed using distilled water followed by addition of 0.3 M sodium hydroxide and sterilized at 121°C for 20 min, to remove culture medium remnants and bacterial colonies. Then, distilled water was used for complete washing of BC till the pH became neutral and stored in distilled water at 4°C for further use (Badshah et al., 2017; Ullah et al., 2017).

TABLE 1 | Summary of R-BC-drug matrices thickness, friability and drug loading data.

Formulation	R-BC : Drug (g)	Thickness (mm) ($n = 3$)	Friability ($n = 20$)	Drug Loading (%) ($n = 3$)
F1	1 : 0.25	3.50	0	22.97 ± 0.81
F2	1 : 0.50	3.25	0	24.62 ± 3.98
F3	1 : 0.75	3.20	0	27.70 ± 3.24
G1	1 : 0.085	2.50	0	17.65 ± 1.80
G2	1 : 0.17	2.45	0	24.79 ± 3.27
G3	1 : 0.25	2.65	0	28.32 ± 1.00

Preparation of Regenerated Bacterial Cellulose Drug Matrices

BC was dried at 60°C for 10 h in a heating oven (SANFA, DHG-9202, Jiangsu Jinyi, China), followed by grinding to convert it into powder form. Then, powdered BC (2 g) was gradually added to NMMO solution (50 g) in glass petri plates (90 mm × 10 mm) and heated at 70°C for 24 h to dissolve it. The BC solution was added with different concentrations of famotidine and tizanidine (**Table 1**) and thoroughly stirred until dispersed uniformly. The BC-drug mixtures were allowed to stand at room temperature (25°C) until solidification (6 h). In order to remove NMMO, the R-BC-drug sheets were incubated in 50 mL distilled water for 96 h with regular replacement of fresh washing medium each 24 h (4 times) and finally freeze-dried (FreeZone 6, catalog No. 7752030, LABCONCO, USA) at −33°C and 0.025 mbar (Ul-Islam et al., 2014; Khan et al., 2015). Round shaped matrices were prepared from the R-BC-drug sheets using a specially designed fabricator with 12 mm diameter. **Figure 1** illustrates the important steps used in the preparation of R-BC-drug matrices.

Characterization

Fourier-Transform Infrared Spectroscopy

The samples were dried at 50°C for 24 h prior to measurement. FTIR spectra for R-BC, drugs and R-BC-drug matrices was recorded using FTIR spectrophotometer (Perkin-Elmer Frontier FTIR Spectrometer, USA) in the spectral range of 4,000–400 cm^{-1} at resolution rate of 4 cm^{-1}, with an ATR Pike Gladi ATR diamond crystal.

X-Ray Diffraction Analysis

XRD measurements were employed by means of x-ray diffractometer (D8 ADVANCE, BRUKER, Co. USA) with radiation Cu Kα at 2.29 Å and operated at room temperature for the determination of crystallinity of R-BC, drugs and R-BC-drug matrices. The sample scanning speed was 6°/min and the angle for scanning (2θ) used was in the range of 10–60°.

Field Emission Scanning Electron Microscopy

The surface morphology analysis of R-BC and R-BC-drug matrices was carried out with field emission scanning electron microscopy (LEO Ultra 55, LEO Electron Microscopy Ltd, Cambridge, UK). The samples for cross section analysis were prepared under the liquid nitrogen conditions. All the samples were fixed on the SEM holder using adhesive tape prior to proceeding for analysis. The samples were exposed for 1 min for sputter coating with gold in an atmosphere provided with Argon (S150B Sputter Coater, Edwards, England) to determine the surface topography and morphology.

Thermogravimetric Analysis

Thermal stability analysis of the R-BC-drug matrices was carried out with the help of thermogravimetric analyzer (TGA/DSC 3^{+}, Mettler Toledo, UK). Thermogram of samples was attained in the temperature range of 35 to 800°C with an increment of 10°C/min under the nitrogen atmospheric conditions.

Thickness and Drug Loading Efficiency (%)

The R-BC-drug matrices thickness was measured using a Vernier caliper (SparkFun, USA). Percent drug loading of the matrices were calculated by averaging the amount of drug released of all

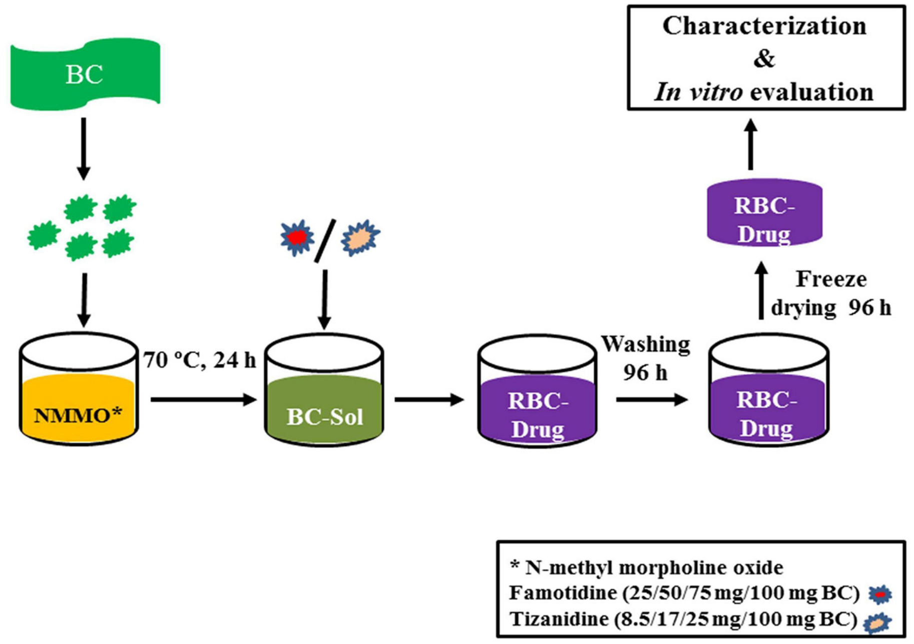

FIGURE 1 | Schematic diagram showing the general process of BC regeneration, drug loading, and matrices preparation.

the formulations during dissolution. The following equation was used to calculate matrices percent drug loading.

$$\textit{Drug laoding efficiency}\ (\%) = \frac{\textit{Loaded drug (based on the released amount)}}{\textit{Amount of drug feed initially}} \times 100$$

Friability Test

Friability test of the matrices was performed using a Friability Tester (FT-L, Galvano Scientific, Pakistan) having speed of 25 rpm and time limit of 4 min (Badshah et al., 2017). The change in weight of the matrices was calculated using the following equation:

$$x = \frac{(W1 - W2)}{W1} \times 100$$

Where W1 represents pre-test weight of matrices, W2 denotes the weight of matrices after test and x show the percent weight loss.

In-vitro Drug Release

The release of drugs from the R-BC-drug matrices was performed in simulated gastric conditions, i.e., 0.1 N HCl solution (900 mL) maintained at 37 ± 0.5°C using USP type-I dissolution apparatus (Dissolutest, Prolabo, France). The paddle rotation speed was in tune of 50 rpm. Samples (5 mL) from the medium were withdrawn at designated time intervals and replaced with an equal amount of fresh medium. The amount of drug released was tested using UV-spectrophotometer (Cary 60 UV-Vis, Agilent Technologies, USA) at 265 nm and 320 nm for famotidine and tizanidine, respectively. All the drug release experiments were performed in triplicate. The data obtained was averaged and presented as cumulative percent release vs. time (Badshah et al., 2017, 2018).

Drug Release Kinetics

The mechanism for drug release from R-BC-drug matrices was studied by applying selected kinetics models including

$$\text{Zero order}(Q_t = Q_0 + K_0 t),$$

Where "Qt" is the cumulative amount of drug release at time "t"

"Q_0" is the initial amount of drug at time "0," "K_0" is zero order rate constant and "t" is the time.

$$\text{First order}(\text{Log } Q_t = \text{Log } Q_0 + K_t/2.303),$$

Where "Q_t" is the cumulative amount of drug release at time "t"

"Q_0" is the initial amount of drug at time "0," "K_t" is first order rate constant and "t" is the time.

$$\text{Higuchi}(Q_t = K_H\, t^{1/2})$$

Where "Q_t" is the cumulative amount of drug release at time "t" and "K_H" is Higuchi rate constant and "t" is the time,
and

$$\text{Korsmeyer} - \text{Peppas}(Q_t/Q = K_{kp} t^n)$$

Whereas "Q_t" is drug cumulative amount released at time "t," "Q" is the total amount of drug in the dosage form, "K_{kp}" is Korsmeyer-Peppas rate constant, "t" is the time and "n" is diffusion or release exponent (Gouda et al., 2017; Ullah et al., 2017).

Statistical Analysis

The results obtained from three independent replicate experiments were presented as mean ± SD. The results were analyzed using GraphPad Prism 5.0 software (GraphPad Software Inc. USA). The statistical analysis was performed using one way ANOVA with *post-hoc* Tukey's test, keeping the level of significance with probabilities of $^{*}p < 0.05$, $^{**}p < 0.01$, and $^{***}p < 0.001$.

RESULTS AND DISCUSSION

Preparation of R-BC-Drug Matrices

In the current study, BC was successfully dissolved in NMMO, incorporated with model drugs in various concentrations and finally regenerated. Several solvents can dissolve BC, however, NMMO was selected in the current study because it is recyclable and environment friendly solvent (Gao et al., 2011; Shafiei et al., 2014). The BC dissolution and regeneration require high temperature and longer duration, which have strong impact on the BC intra- and intermolecular hydrogen bonds breaking, crystallinity, surface morphology, thermal stability and mechanical properties (Gao et al., 2011; Xu et al., 2015). Moreover, the R-BC-drug matrices were subjected to various characterization techniques to study the effects of temperature and chemical changes (if any) during this process (Gao et al., 2011 Ul-Islam et al., 2014).

Physical Evaluation of R-BC-Drug Matrices

The prepared matrices were subjected to various physical tests. The matrices thickness was observed to be directly proportional to the initial concentration of drug for loading (**Table 1**). The data of friability test showed no weight loss during the test (Chen et al., 2009; Badshah et al., 2017). Similarly, the amount of drug loaded into R-BC was directly proportional to the initial concentration of the drug added to BC solution before the regeneration (**Table 1**). In case of tizanidine, the drug loading efficiency was directly proportional to the amount of drug used in the loading process. However, in case of famotidine, the drug loading efficiency was almost constant irrespective of the amount of drug used in the loading process. The possible reason for this constant loading might be that a fixed quantity of BC is available for absorption of drug (Sharma et al., 2016) and the drug concentrations beyond the maximum saturation capacity of the BC cannot be absorbed.

Characterization of R-BC-Drug Matrices

Fourier-Transform Infrared Analysis

FTIR technique was used to study the compatibility and structural changes of the formulations ingredients, i.e., R-BC and drug loaded R-BC. FTIR spectra for BC, R-BC, famotidine, R-BC-famotidine, tizanidine and R-BC-tizanidine have been shown in **Figure 2**. The spectrum of as-synthesized BC showed

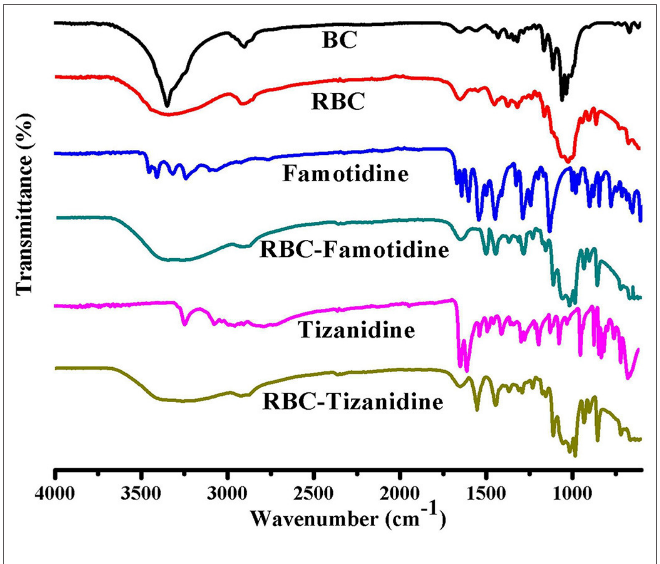

FIGURE 2 | FTIR spectrum of the prepared BC, R-BC, famotidine, R-BC-famotidine, tizanidine, and R-BC-tizanidine matrices for comparison.

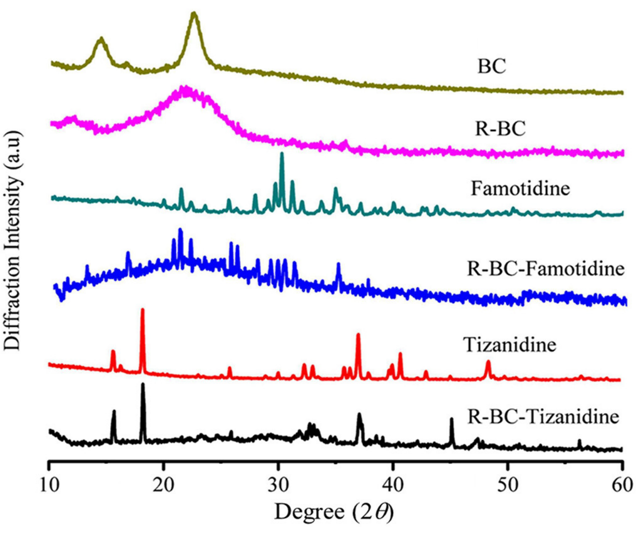

FIGURE 3 | XRD pattern of R-BC, famotidine, R-BC-famotidine, tizanidine, and R-BC-tizanidine.

characteristic band at 3,500–3,200 cm^{-1} and at 1,160 and 1,068 cm^{-1}, which are assigned to OH stretching, OH wagging and C-O-C pyranose ring (Chen et al., 2009; Badshah et al., 2017). The spectrum of R-BC has broad peaks at 3,500–3,200 cm^{-1}, representing OH stretching due to breakage of inter and intra molecular hydrogen bonding. In addition, the appearance of peaks in as-synthesized and regenerated BC at 1,160 and 1,068 cm^{-1} represent the C-H scissor vibration (Gao et al., 2011; Shafiei et al., 2014). The IR spectra of R-BC-famotidine revealed a broad band between 3,500 and 3,200 cm^{-1}, which may arise due to the merger of –OH and NH_2 groups of R-BC and famotidine, respectively. Similarly, the region of 2,850–2,950 cm^{-1} represents the C–H bending of R-BC vibration (Sagdinc and Bayari, 2005; Arima and Iwata, 2007). The band at 1,553 cm^{-1} represent NH_2 group, while at 1,290 and 1,135 cm^{-1} revealed CH_2=S and SO_2 groups of famotidine, respectively (Sagdinc and Bayari, 2005; Cheng and Lin, 2008). The peaks at 1,078 and 990 cm^{-1} represent bending vibration due to NH_2 group of famotidine and CH_2 group of R-BC (Sagdinc and Bayari, 2005; Souza et al., 2020). The band at 895 cm^{-1} represent glycosidic linkage of R-BC and 850 cm^{-1} has been assigned to the CH_2 skeleton of famotidine and R-BC (Sagdinc and Bayari, 2005; Gao et al., 2011).

The IR spectrum of R-BC-tizanidine IR displayed bands at 3,200–3,500 cm^{-1} that represent OH and NH_2 groups of R-BC and tizanidine, respectively. Similarly, bands at 1,665 cm^{-1} indicates the C=C aromatic stretching of tizanidine (Aamir and Ahmad, 2010; Badshah et al., 2018). The peaks at 1,450–1,200 cm^{-1} indicates R-BC C–H stretching vibration. The C–N stretching was confirmed by peak at 1,290 and 1,187 cm^{-1}, while bands at 1,113 and 1,068 cm^{-1} confirm the C–Cl group of tizanidine (Aamir and Ahmad, 2010; Badshah et al., 2017, 2018). The presence of characteristic absorption bands of respective drug functional groups with slight shift shows drug incorporation into the R-BC. There has been no new peak appearance in the FTIR spectrum of the respective R-BC-drug composites, which show absence of any chemical boding formation between the components.

X-Ray Diffraction Analysis

Change in the crystallinity of the R-BC and drug loaded matrices was evaluated using XRD technique. XRD patterns of BC, R-BC, famotidine, R-BC-famotidine, tizanidine HCl and R-BC-tizanidine HCl have been displayed in **Figure 3**. BC has appearance of characteristic peaks at 14.5, 16.5, and 22.5°. R-BC showed comparative peak broadening at 19.8 and 22.7°, which confirmed the conversion of BC to amorphous form as a result of inter and intra molecular hydrogen bonding disruption during the dissolution process (Lee et al., 2014; Badshah et al., 2017). The pattern for famotidine displayed crystalline nature and the R-BC-famotidine showed few and shorter peaks, which indicated lower crystalline nature and amount of drug loaded. The peaks at 15, 22, 25.6, 30, and 35.5° also showed the presence of famotidine in crystalline form (Razavi et al., 2014). In case of R-BC-tizanidine, distinct peaks at 16, 18.7, and at 32.55, 37.55, and 41.5° with reduced intensity confirmed the presence of tizanidine in crystalline form (Aamir and Ahmad, 2010; Badshah et al., 2017). The presence of the respective drug specified peaks confirmed the effective loadings of drugs into the R-BC-drug matrices in crystalline form. The nanoporous BC can convert the drug into amorphous form when loaded into the pores (Ullah et al., 2019), however, the drug is also present in crystalline form on the surface of matrices due to excessive loading, which is further confirmed by the SEM analysis as shown in **Figure 4**.

Scanning Electron Microscopy

Surface morphology of R-BC and the matrices with loaded drugs was studied using SEM. The SEM micrographs of surface and cross section of R-BC and R-BC-drugs matrices

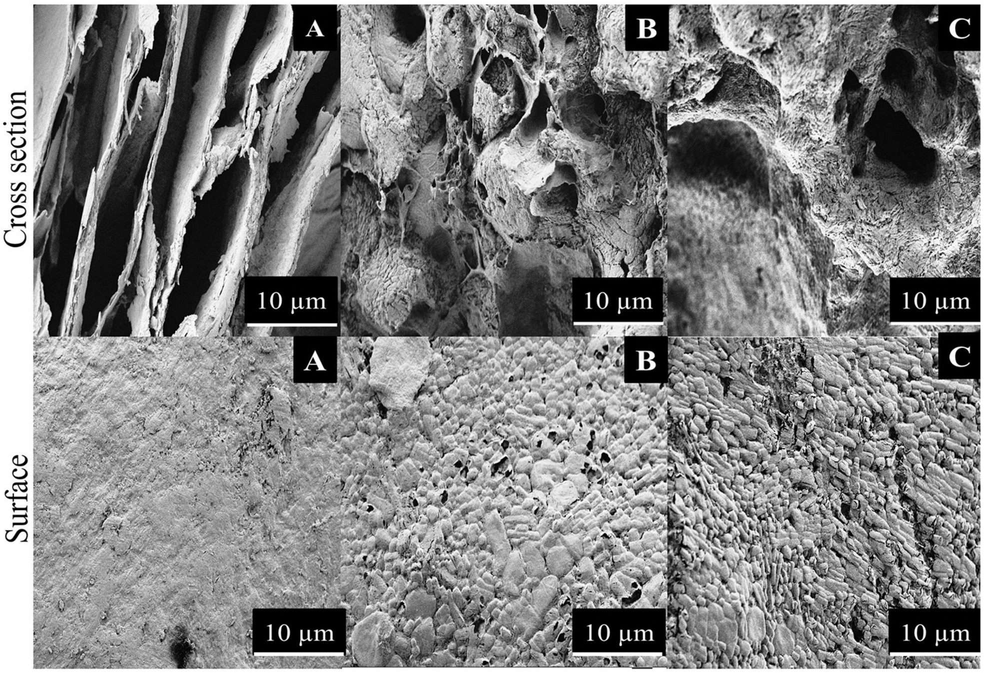

FIGURE 4 | SEM images of **(A)** R-BC, **(B)** R-BC-famotidine, and **(C)** R-BC-tizanidine matrices.

were obtained at varying magnifications. **Figure 4** shows the typical microphotographs for R-BC, R-BC-famotidine and R-BC-tizanidine. The cross-section for R-BC (**Figure 4A**) showed porous layers of different dimensions. These pores may be attributed to the water crystallization during R-BC regeneration process (El-Wakil and Hassan, 2008; Xu et al., 2015). The cross sectional micrograph for the R-BC did not show formation of fibrous structure, which is the confirmation of the native BC fiber network destruction/annihilation during the regeneration process. Similarly, the surface morphology of the R-BC also showed smooth appearance and absence of fibrous network, which confirmed the dissolution of BC followed by regeneration (Wan et al., 2006; Ul-Islam et al., 2014). The cross sectional images of the R-BC famotidine (**Figure 4B**) and R-BC-tizanidine (**Figure 4C**) showed comparatively less porous structure than pure R-BC. The possible reason may be that the loaded drugs have filled most of the spaces produced. In addition to this, the probable reason of pores formation may be the wash out of some of the loaded drug during the solvent exchange of NMMO with deionized water and the forced migration of the loaded drug content to the surfaces during the freeze drying of the matrices. The micrographs revealed the presence of drug crystals on the surface of the R-BC film, which confirms successful drug loading.

Thermogravimetric Analysis

In order to study the thermal stability of R-BC and drugs loaded matrices, thermal analysis was carried out. Thermogram of BC, R-BC, and R-BC-drugs matrices were obtained in order to study the thermal behavior of these samples (**Figure 5**). In the initial phase of degradation, BC showed 5% weight loss at temperature up to 280°C possibly due to evaporation of adsorbed water. In the second phase, there is a sharp decline in weight (70%) at a temperature between 280 and 380°C due to breakdown of glycosidic linkages. The rest of the content (25%) remained as ash till 800°C. These results are in agreement with the previous studies (Chen et al., 2016). Similarly, the R-BC displayed 5% weight loss up to 220°C followed by a sudden decline (70%) due to depolymerization and breaking down of glycosidic backbone in the temperature range of 220–380°C. The remaining portion (25%) existed as ash till 800°C. These results were also consistent with the reported thermal studies for regenerated BC (El-Wakil and Hassan, 2008; Gao et al., 2011). On the other hand, R-BC-famotidine and R-BC-tizanidine displayed 6 and 8% loss in weight up to 100°C, respectively. This weight loss may be due to evaporation of surface adsorbed water molecules in R-BC-drug matrices (Badshah et al., 2017). With the rise in temperature from 100 to 200°C, the weight loss count for both drugs of matrices was 80% and the possible reason may be the elimination of hydroxyl groups and combustion of the organic part of R-BC. In addition, the melting temperature of the loaded drug might have caused the abrupt weight loss (El-Wakil and Hassan, 2008; Gao et al., 2011). The data showed that R-BC-famotidine and R-BC tizanidine was maximally degraded (marked as ash) till 800°C (Badshah et al., 2017).

In-vitro Drug Release Studies

The release of drugs from the R-BC-drug matrices was studied in simulated gastric fluid, i.e., 0.1 N HCl solution using USP type-I dissolution apparatus under predefined conditions. **Figure 6** and **Figure 7** show the *in-vitro* drug release profile from

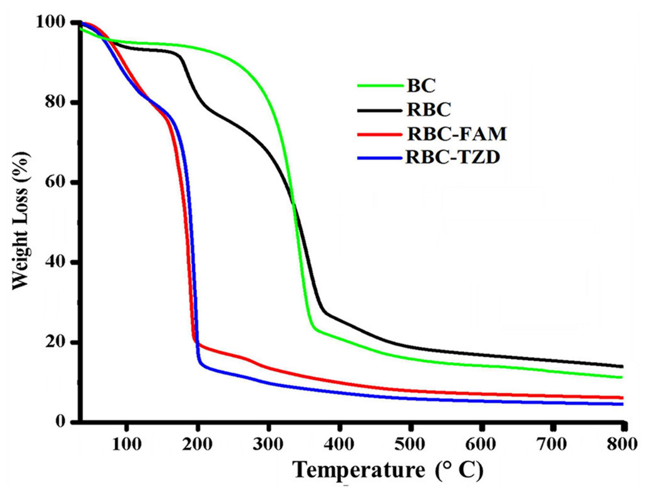

FIGURE 5 | Curves of the thermogravimetric analysis for the prepared matrices of R-BC, R-BC-famotidine, and R-BC-tizanidine.

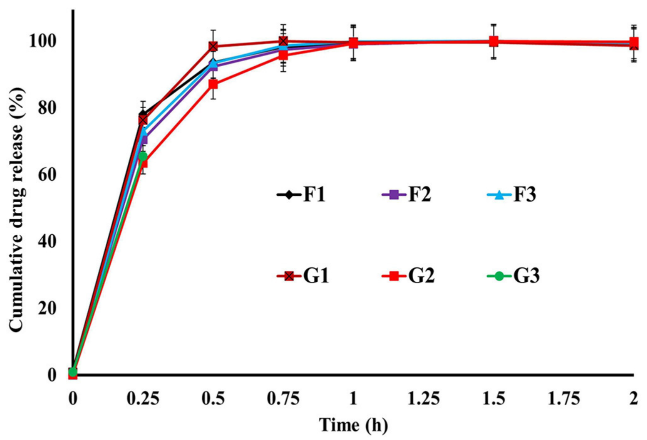

FIGURE 6 | *In-vitro* drug release profile of R-BC-famotidine (F1–F3) and R-BC-tizanidine (G1–G3) matrices using USP type-I dissolution apparatus.

R-BC-famotidine matrices (F1–F3) and tizanidine loaded R-BC matrices (G1–G3). The matrices F1, F2, and F3 released 78.03 ± 3.77, 70.52 ± 6.52, and 73.04 ± 2.85% of the drug content, respectively, in the initial 15 min ($p < 0.001$) (**Figure 7**). The formulation F1 released higher concentration of drug than F2 and F3, whereas, no significant difference was observed between F2 and F3. Similarly, 93.57 ± 2.36, 92.28 ± 5.30, and 93.40 ± 3.00% of the drug was released has been shown by F1, F2, and F3 matrices after 30 min, which is not significant. However, at later time point i.e., 45 min, it was observed that regardless of the concentrations of loaded drug (**Table 1**), the matrices released most of the drug content (>95%), which was observed as 98.25 ± 0.78, 97.34 ± 2.99, and 98.58 ± 1.36% for F1, F2, and F3, respectively. In contrast to famotidine loaded matrices, the drug release from the R-BC-tizanidine matrices, i.e., G1, G2, and G3 was 76.260 ± 5.20, 63.40 ± 7.74, and 65.43 ± 7.73% at 15 min, respectively. These results reveals significant difference in drug release ($p < 0.05$) between formulations G1 with G2 and G3, whereas G2 and G3 have no significant difference. Moreover, 98.30 ± 0.4, 86.98 ± 5.59, and 91.33 ± 4.93% of the drug was released ($p < 0.05$), respectively, after 30 min from these matrices. This shows that G1 has released higher concentrations of the loaded drug as compared to G2 and G3. This behavior of comparatively slow drug release from G2 and G3 might be due to the higher concentrations of the drug (remained intact with R-BC) into matrices (**Table 1**). The R-BC-tizanidine matrices released most of the drug (>95%) after 45 min of studies and was found to be 99.91 ± 0.15, 95.65 ± 2.21, and 99.36 ± 0.72% for the formulations G1, G2, and G3 ($p < 0.01$), respectively. It was observed that $t_{90\%}$ (time in which 90% of the drug was released) is <1 h for both of the drug loaded matrices. The comparison of drug release from F1–F3 and G1–G3 show that famotidine loaded matrices have released higher concentrations of drug as compared to tizanidine in the initial 15 min. This might become possible due to larger exposed surface of R-BC for binding of the lower concentration of tizanidine as compared to famotidine loaded formulations (Kolakovic et al., 2013). However, after 30 min there have been no significant changes observed in drug release between F1–F3 and G1–G3. The possible reasons for the faster release of drugs from all formulations may be the aqueous solubility of the drugs (Badshah et al., 2017) and breakdown of the interconnected fibrous network hydrogen bonding of the BC as result of dissolution (Lee et al., 2014; Xu et al., 2015). R-BC has higher hydrophilic nature and absorbs aqueous solution faster. This feature might have facilitated the rapid penetration of dissolution medium into matrices, which resulted in faster dissolution and release of drugs (Gao et al., 2011; Badshah et al., 2017). In addition, the presence of loaded drug particles might have effected the film and pores formation (**Figure 4**) during the regeneration process, which have made the system strongly hydrophilic and thus facilitateed the rapid diffusion of dissolution medium into the matrices. These factors may resulted in the faster drug release from the matrices (Fink et al., 2001). Furthermore, the matrices washing for the removal of NMMO and freeze-drying may have facilitated the drug migration toward the surfaces, which has resulted in faster dissolution of the drugs and speedy release. This behavior might have facilitated the desired concentrations of the drugs to be released in the dissolution medium effectively (Isogai and Atalla, 1998; Ávila et al., 2015). It was also observed that early drug release behavior of R-BC have the potential for designing immediate release formulations (i.e., in stomach) based on single polymer. As mentioned above, the drug release is limited to few hours; however, the drug release could further be tailored by using other strategies with altered drugs aqueous solubility and their interactions with the BC nanofibers (Kolakovic et al., 2012). For statistical calculations of the effect of BC regeneration on the drug release from the mentioned formulations (F1–F3 and G1–G3), drug release results from as-synthesized BC matrices (F0 and G0) were used as reference (**Figure 7**).

It is evident from our current and previous studies that in comparison to the existing conventional dosage forms, BC forms a single excipient based intact oral dosage form due its higher

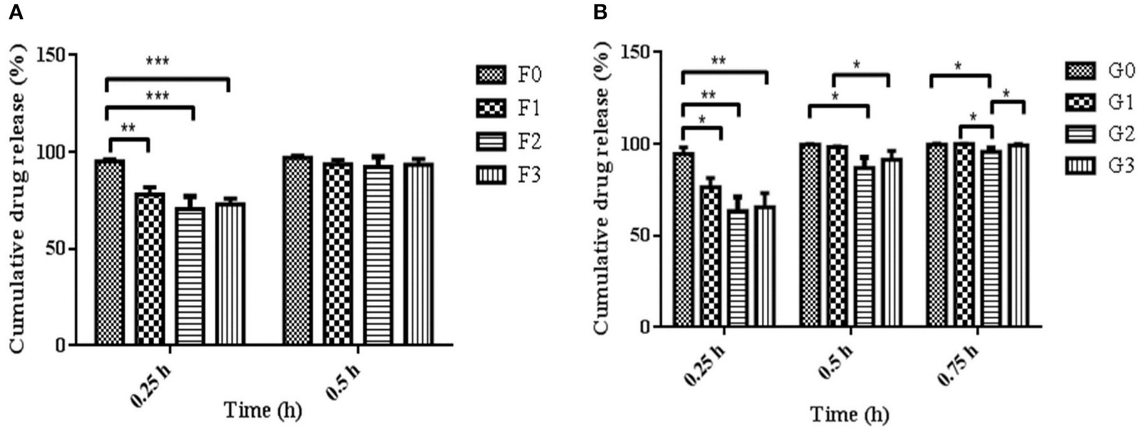

FIGURE 7 | Comparison of R-BC matrices drug release data at various intervals of time i.e., **(A)** represent R-BC-famotidine matrices (F1–F3), at 0.25 and 0.5 h, whereas **(B)** denote R-BC-tizanidine matrices (G1–G3) at 0.25, 0.5, and 0.75 h, using one way ANOVA with *post-hoc* Tukey's test, keeping the level of significance with probabilities of $^{*}p < 0.05$, $^{**}p < 0.01$, and $^{***}p < 0.001$. Data is presented as mean ± SD ($n = 3$).

TABLE 2 | Drug release kinetics of famotidine and tizanidine from the R-BC-drug matrices.

Formulation	Zero order		First order		Higuchi		Korsmeyer	
	R^2	$K_0 h^{-1}$	R^2	$K_1 h^{-1}$	R^2	$K_H h^{-0.5}$	*n*	R^2
F1	0.4896	72.276	0.9993	5.936	0.5722	91.901	0.101	0.9879
F2	0.3376	71.847	0.9997	4.935	0.6440	91.047	0.136	0.9771
F3	0.3753	72.206	0.9998	5.298	0.6208	91.750	0.122	0.9790
G1	0.5115	72.526	0.9980	6.025	0.5404	92.520	0.098	0.9757
G2	0.1349	71.326	0.9998	4.064	0.7337	89.766	0.182	0.9717
G3	0.2580	71.947	0.9978	4.510	0.6758	90.967	0.158	0.9626

tensile strength. Moreover, the as-synthesized BC membrane has limited thickness and more time is required to obtain desired thickness (Badshah et al., 2017; Ullah et al., 2017). In case of R-BC, the matrices with desired thickness can be easily produced by increasing the concentration of BC solution. Similarly, R-BC is more amorphous and easily biodegraded compared to as-synthesized BC and thus have high potential for drug delivery to the body parts, wherein degradation of BC is desired (Ullah et al., 2019).

Drug Release Kinetics From the R-BC-Drug Matrices

The drug release kinetics studies revealed that the release of drugs from the R-BC-drug matrices was dependent on the drug concentration. The hydrophilic property of R-BC might facilitate the diffusion of the medium into the matrices. It was observed that drug release during dissolutions was best fitted into the first order kinetics model with R^2 value more than 0.99. The release exponent *"n"* value of Korsmeyer-Pappas model was different for *in-vitro* dissolution. In case of the dissolution studies, the value of *"n"* was <0.5, which showed that release mechanism was following Fickian diffusion (Badshah et al., 2017, 2018) as presented in **Table 2**.

CONCLUSION

The current research work was carried out for the first time to evaluate the potential applications of regenerated BC for drug delivery. The R-BC-drug matrices were prepared using NMMO as solvent. Characterization data showed that R-BC-drug matrices were chemically and thermally stable. The drug loading and *in-vitro* drug release studies revealed that R-BC-drug matrices released more than 90% of the loaded amount of drugs in the initial 30 min during dissolution studies, which followed the criteria for immediate release drug delivery system. It can be concluded that R-BC, a novel and physically modified form of BC, has the ability for designing matrices for the delivery of drugs via oral route. However, further research work is required for the exploration of its potential applications in drug delivery via other routes of administration using other drugs.

DATA AVAILABILITY STATEMENT

The raw data supporting the conclusions of this article will be made available by the authors, without undue reservation.

AUTHOR CONTRIBUTIONS

TK, FW, and FH conceived the project, supervised the research, and writing of the manuscript. MB carried out the research work and wrote the manuscript basic draft in collaboration with HU and UF. MA has contributed in the characterization of samples and reviewed the manuscript critically. All authors contributed to the article and approved the submitted version.

FUNDING

This research was partially supported by The Higher Education Commission of Pakistan under the IRSIP award (Ref. No. 1-8/HEC/HRD/2015/4061).

ACKNOWLEDGMENTS

We thank Prof. Dr. Annette Larsson, Chalmers University of Technology, Sweden for assistance with characterization techniques and providing space in laboratory to carry out research work. We are also thankful to Mr. H. K. Ruia of Amines & Plasticizers Limited, India for providing NMMO as donation for this research work.

SUPPLEMENTARY MATERIAL

The Supplementary Material for this article can be found online at: https://www.frontiersin.org/articles/10.3389/fbioe.2020.579404/full#supplementary-material

REFERENCES

Aamir, M. N., and Ahmad, M. (2010). Production and stability evaluation of modified-release microparticles for the delivery of drug combinations. *AAPS Pharm. Sci. Tech*. 11, 351–355. doi: 10.1208/s12249-010-9392-1

Arima, Y., and Iwata, H. (2007). Effect of wettability and surface functional groups on protein adsorption and cell adhesion using well-defined mixed self-assembled monolayers. *Biomaterials* 28, 3074–3082. doi: 10.1016/j.biomaterials.2007.03.013

Ávila, H. M., Feldmann, E. M., Pleumeekers, M. M., Nimeskern, L., Kuo, W., de Jong, W. C., et al. (2015). Novel bilayer bacterial nanocellulose scaffold supports neocartilage formation *in vitro* and *in vivo*. *Biomaterials* 44, 122–133. doi: 10.1016/j.biomaterials.2014.12.025

Badshah, M., Ullah, H., Khan, A. R., Khan, S., Park, J. K., and Khan, T. (2018). Surface modification and evaluation of bacterial cellulose for drug delivery. *Int. J. Boil. Macromol*. 113, 526–533. doi: 10.1016/j.ijbiomac.2018.02.135

Badshah, M., Ullah, H., Khan, S. A., Park, J. K., and Khan, T. (2017). Preparation, characterization and *in-vitro* evaluation of bacterial cellulose matrices for oral drug delivery. *Cellulose* 24, 5041–5052. doi: 10.1007/s10570-017-1474-8

Chen, C., Zhu, C., Huang, Y., Nie, Y., Yang, J., Shen, R., et al. (2016). Regenerated bacterial cellulose microfluidic column for glycoproteins separation. *Carbohydr. Polym*. 137, 271–276. doi: 10.1016/j.carbpol.2015.10.081

Chen, P., Kim, H. S., Kwon, S. M., Yun, Y. S., and Jin, H. J. (2009). Regenerated bacterial cellulose/multi-walled carbon nanotubes composite fibers prepared by wet-spinning. *Curr. Appl. Phys.* 9, e96–e99. doi: 10.1016/j.cap.2008.12.038

Cheng, W. T., and Lin, S. Y. (2008). Famotidine polymorphic transformation in the grinding process significantly depends on environmental humidity or water content. *Int. J. Pharm*. 357, 164–168. doi: 10.1016/j.ijpharm.2008.01.048

El-Wakil, N. A., and Hassan, M. L. (2008). Structural changes of regenerated cellulose dissolved in FeTNa, NaOH/thiourea, and NMMO systems. *J Appl Polym Sci*. 109, 2862–2871. doi: 10.1002/app.28351

Fink, H. P., Weigel, P., Purz, H. J., and Ganster, J. (2001). Structure formation of regenerated cellulose materials from NMMO-solutions. *Prog. Polym. Sci*. 26, 1473–1524. doi: 10.1016/S0079-6700(01)00025-9

Gao, Q., Shen, X., and Lu, X. (2011). Regenerated bacterial cellulose fibers prepared by the NMMO· H2O process. *Carbohydr. Polym*. 83, 1253–1256. doi: 10.1016/j.carbpol.2010.09.029

Gouda, R., Baishya, H., and Qing, Z. (2017). Application of mathematical models in drug release kinetics of carbidopa and levodopa ER tablets. *J. Dev. Drugs* 6, 1–8. doi: 10.4172/2329-6631.1000171

Hickey, R. J., and Pelling, A. E. (2019). Cellulose biomaterials for tissue engineering. *Front. Bioeng. Biotechnol*. 7:45. doi: 10.3389/fbioe.2019.00045

Isogai, A., and Atalla, R. H. (1998). Dissolution of cellulose in aqueous NaOH solutions. *Cellulose* 5, 309–319. doi: 10.1023/A:1009272632367

Khalid, A., Ullah, H., Ul-Islam, M., Khan, R., Khan, S., Ahmad, F., et al. (2017). Bacterial cellulose–TiO 2 nanocomposites promote healing and tissue regeneration in burn mice model. *RSC Adv*. 7, 47662–47668. doi: 10.1039/C7RA06699F

Khan, S., Ul-Islam, M., Ullah, M. W., Ikram, M., Subhan, F., Kim, Y., et al. (2015). Engineered regenerated bacterial cellulose scaffolds for application in *in vitro* tissue regeneration. *RSC Adv*. 5, 84565–84573. doi: 10.1039/C5RA16985B

Klinthoopthamrong, N., Chaikiawkeaw, D., Phoolcharoen, W., Rattanapisit, K., Kaewpungsup, P., Pavasant, P., et al. (2020). Bacterial cellulose membrane conjugated with plant-derived osteopontin: preparation and its potential for bone tissue regeneration. *Int. J. Biol. Macromol*. 149, 51–59. doi: 10.1016/j.ijbiomac.2020.01.158

Kolakovic, R., Peltonen, L., Laukkanen, A., Hellman, M., Laaksonen, P., Linder, M. B., et al. (2013). Evaluation of drug interactions with nanofibrillar cellulose. *Eur. J. Pharm. Biopharm*. 85, 1238–1244. doi: 10.1016/j.ejpb.2013.05.015

Kolakovic, R., Peltonen, L., Laukkanen, A., Hirvonen, J., and Laaksonen, T. (2012). Nanofibrillar cellulose films for controlled drug delivery. *Eur. J. Pharm. Biopharm*. 82, 308–315. doi: 10.1016/j.ejpb.2012.06.011

Lee, S., Pan, H., Hse, C. Y., Gunasekaran, A. R., and Shupe, T. F. (2014). Characteristics of regenerated nanocellulosic fibers from cellulose dissolution in aqueous solutions for wood fiber/polypropylene composites. *J. Therm. Comp. Mater*. 27, 558–570. doi: 10.1177/0892705713484739

Möller, T., Amoroso, M., Hägg, D., Brantsing, C., Rotter, N., Apelgren, P., et al. (2017). *In vivo* chondrogenesis in 3D bioprinted human cell-laden hydrogel constructs. *Plastic Reconstruct. Surg. Glob. Open* 5:1227. doi: 10.1097/GOX.0000000000001227

Phisalaphong, M., Suwanmajo, T., and Sangtherapitikul, P. (2008). Novel nanoporous membranes from regenerated bacterial cellulose. *J. Appl. Polym. Sci*. 107, 292–299. doi: 10.1002/app.27118

Razavi, M., Nyamathulla, S., Karimian, H., and Noordin, M. I. (2014). Novel swellable polymer of orchidaceae family for gastroretentive drug delivery of famotidine. *Drug Design Dev. Therap*. 8:1315. doi: 10.2147/DDDT.S68517

Reddy, N., and Yang, Y. (2015). "The N-methylmorpholine-N-oxide (NMMO) process of producing regenerated fibers," in *Innovative Biofibers From Renewable Resources* (Berlin; Heidelberg: Springer), 65–71. doi: 10.1007/978-3-662-45136-6_18

Sagdinc, S., and Bayari, S. (2005). Experimental and theoretical infrared spectra of famotidine and its interaction with ofloxacin. *J. Mol. Struct*. 744, 369–376. doi: 10.1016/j.molstruc.2004.12.013

Sajjad, W., He, F., Ullah, M. W., Ikram, M., Shah, S. M., Khan, R., et al. (2020). Fabrication of bacterial cellulose-curcumin nanocomposite as a novel dressing for partial thickness skin burn. *Front. Bioeng. Biotechnol*. 8:1089. doi: 10.3389/fbioe.2020.553037

Shafiei, M., Karimi, K., Zilouei, H., and Taherzadeh, M. J. (2014). Enhanced ethanol and biogas production from pinewood by NMMO pretreatment and detailed biomass analysis. *Biomed Res. Int*. 2014:469378. doi: 10.1155/2014/469378

Sharma, N., Madan, P., and Lin, S. (2016). Effect of process and formulation variables on the preparation of parenteral paclitaxel-loaded biodegradable polymeric nanoparticles: a co-surfactant study. *Asian J. Pharm. Sci*. 11, 404–416. doi: 10.1016/j.ajps.2015.09.004

Souza, E. F., Furtado, M. R., Carvalho, C. W., Freitas-Silva, O., and Gottschalk, L. M. (2020). Production and characterization of *Gluconacetobacter xylinus* bacterial cellulose using cashew apple juice and soybean molasses. *Int. J. Biol. Macromol*. 146, 285–289. doi: 10.1016/j.ijbiomac.2019.12.180

Ul-Islam, M., Khattak, W. A., Ullah, M. W., Khan, S., and Park, J. K. (2014). Synthesis of regenerated bacterial cellulose-zinc oxide nanocomposite films for biomedical applications. *Cellulose* 21, 433–447. doi: 10.1007/s10570-013-0109-y

Ullah, H., Badshah, M., Correia, A., Wahid, F., Santos, H. A., and Khan, T. (2019). Functionalized bacterial cellulose microparticles for drug delivery in biomedical applications. *Curr. Pharm. Des*. 25, 3692–3701. doi: 10.2174/1381612825666191011103851

Ullah, H., Badshah, M., Mäkil,ä, E., Salonen, J., Shahbazi, M. A., Santos, H. A., et al. (2017). Fabrication, characterization and evaluation of bacterial cellulose-based capsule shells for oral drug delivery. *Cellulose* 24, 1445–1454. doi: 10.1007/s10570-017-1202-4

Ullah, H., Santos, H. A., and Khan, T. (2016b). Applications of bacterial cellulose in food, cosmetics and drug delivery. *Cellulose* 23, 2291–2314. doi: 10.1007/s10570-016-0986-y

Ullah, H., Wahid, F., Santos, H. A., and Khan, T. (2016a). Advances in biomedical and pharmaceutical applications of functional bacterial cellulose-based nanocomposites. *Carbohydr. Polym*. 150, 330–352. doi: 10.1016/j.carbpol.2016.05.029

Wan, Y. Z., Hong, L., Jia, S. R., Huang, Y., Zhu, Y., Wang, Y. L., et al. (2006). Synthesis and characterization of hydroxyapatite–bacterial cellulose nanocomposites. *Comp. Sci. Technol*. 66, 1825–1832. doi: 10.1016/j.compscitech.2005.11.027

Xu, F., Yang, Y., Zhang, G., Zhang, F., and Zhang, Y. (2015). A self-stiffness finishing for cotton fabric with N-methylmorpholine-N-oxide. *Cellulose* 22, 2837–2844. doi: 10.1007/s10570-015-0686-z

Zhu, S., Wu, Y., Chen, Q., Yu, Z., Wang, C., Jin, S., et al. (2006). Dissolution of cellulose with ionic liquids and its application: a mini-review. *Green Chem*. 8, 325–327. doi: 10.1039/b601395c

Conflict of Interest: The authors declare that the research was conducted in the absence of any commercial or financial relationships that could be construed as a potential conflict of interest.

frontiers
in Bioengineering and Biotechnology

ORIGINAL RESEARCH
published: 18 December 2020
doi: 10.3389/fbioe.2020.602318

A Dual-Crosslinked and Anisotropic Regenerated Cellulose/Boron Nitride Nanosheets Film With High Thermal Conductivity, Mechanical Strength, and Toughness

Xuran Xu [1]†, Yichuan Su [1,2]†, Yongzheng Zhang [1,2], Shuaining Wu [1], Kai Wu [1,2,3] and Qiang Fu [2]**

[1] State Key Laboratory of Polymer Materials Engineering, College of Polymer Science and Engineering, Sichuan University, Chengdu, China, [2] Key Laboratory for Soft Chemistry and Functional Materials of the Ministry of Education, School of Chemical Engineering, Nanjing University of Science and Technology, Nanjing, China, [3] Key Laboratory of Advanced Technologies of Materials, Ministry of Education China, Southwest Jiaotong University, Chengdu, China

OPEN ACCESS

Edited by:
Guang Yang,
Huazhong University of Science and Technology, China

Reviewed by:
PaYaM ZarrinTaj,
Oklahoma State University, United States
Anna Tarakanova,
University of Connecticut, United States

***Correspondence:**
Kai Wu
kaiwu@scu.edu.cn
Qiang Fu
qiangfu@scu.edu.cn

† These authors have contributed equally to this work

Specialty section:
This article was submitted to Biomaterials, a section of the journal Frontiers in Bioengineering and Biotechnology

Received: *03 September 2020*
Accepted: *09 November 2020*
Published: *18 December 2020*

Citation:
Xu X, Su Y, Zhang Y, Wu S, Wu K and Fu Q (2020) A Dual-Crosslinked and Anisotropic Regenerated Cellulose/Boron Nitride Nanosheets Film With High Thermal Conductivity, Mechanical Strength, and Toughness. Front. Bioeng. Biotechnol. 8:602318. doi: 10.3389/fbioe.2020.602318

The highly thermo-conductive but electrically insulating film, with desirable mechanical performances, is extremely demanded for thermal management of portable and wearable electronics. The integration of boron nitride nanosheets (BNNSs) with regenerated cellulose (RC) is a sustainable strategy to satisfy these requirements, while its practical application is still restricted by the brittle fracture and loss of toughness of the composite films especially at the high BNNS addition. Herein, a dual-crosslinked strategy accompanied with uniaxial pre-stretching treatment was introduced to engineer the artificial RC/BNNS film, in which partial chemical bonding interactions enable the effective interfiber slippage and prevent any mechanical fracture, while non-covalent hydrogen bonding interactions serve as the sacrifice bonds to dissipate the stress energy, resulting in a simultaneous high mechanical strength (103.4 MPa) and toughness (10.2 MJ/m^3) at the BNNS content of 45 wt%. More importantly, attributed to the highly anisotropic configuration of BNNS, the RC/BNNS composite film also behaves as an extraordinary in-plane thermal conductivity of 15.2 W/m·K. Along with additional favorable water resistance and bending tolerance, this tactfully engineered film ensures promised applications for heat dissipation in powerful electronic devices.

Keywords: regenerated cellulose, thermal conductivity, boron nitride nanosheets, dual-crosslink, urea

INTRODUCTION

With the rapid development of the highly integrated electronic devices toward high power and increasing miniaturization, research on the flexible thermo-conductive material becomes urgent to satisfy the thermal management requirements in portable and wearable applications (Li et al., 2015; Chen et al., 2018a; Wu et al., 2020). Regenerated cellulose (RC), a green and biodegradable biomass macromolecule that is constructed simply by physical dissolution and then regeneration into the fibrous configuration without abundant consumption of chemical reagents (Ray et al., 2020; Tu et al., 2020; Wågberg and Erlandsson, 2020), is a sustainable choice for conformation of thermo-conductive paper-like material, broadening its extensive usage in our real life (Wang et al., 2016; Zhu et al., 2016). Typically, boron nitride nanosheets (BNNS), one type of two-dimensional thermo-conductive but electrically insulating nanofiller (Weng et al., 2016), with the prominent basal thermal conductivity (TC) up to 400 W/m·K (Guerra et al., 2019), is attractive for integration with RC for the fabrication of a thermo-conductive film (Yao et al., 2016; Ye et al., 2019). The essential issue is to balance the contradiction between tremendous enhancement of TC, and simultaneous achievement of high mechanical strength and toughness, which remains a great challenge (Yao et al., 2018; Yin et al., 2019).

In the past, some researches have tried to hybrid BNNS with RC for fabrication of flexible RC/BNNS nanocomposite films (Pickering et al., 2016; Wu K. et al., 2019; Li et al., 2020). For example, a green pathway that is using NaOH/urea aqueous solution as the dissolving agent was reported (Cai and Zhang, 2005), in which BNNSs were intensely mixed with RC by direct mechanical stirring, resulting in an in-plane TC of 2.97 W/m K, mechanical strength of 70 MPa, and elongation of 14% at a BNNS addition of 30 wt% (Lao et al., 2018). These limited in-plane TC, mechanical strength, and toughness are mainly attributed to the following reasons: (i) Low BNNS addition, derived from the challenging dispersion of BNNSs in aqueous solution of cellulose, leads to insufficient BNNS–BNNS interconnections and thus discontinuous phonon pathways within the RC matrix (Cai et al., 2017; Ma et al., 2020). (ii) Isotropic alignment of BNNS without adequate in-plane orientation could not take advantage of the highly thermo-conductive trait of BNNSs to the fullest (Wang et al., 2019; Liu et al., 2020). (iii) Weak bonding interactions merely by intermolecular hydrogen bonds of cellulose and their random molecular configuration is easy to give rise to mechanical fracture during uniaxial stretching, without enough interfiber slippage to dissipate the stress energy (Osorio-Madrazo et al., 2012; Tu et al., 2020).

The key to achieve simultaneous high mechanical properties and in-plane TC is to tactfully tailor the structural features of building blocks (BNNS and cellulose nanofiber) with favorable arrangements in the in-plane direction (Yuan et al., 2015; Cho et al., 2016; Han et al., 2019), resulting in the formation of highly anisotropic configurations (Zhang et al., 2018; Tarhini and Tehranibagha, 2019). Moreover, in comparison with self-assembled fibrous nanocellulose, the RC film built from regeneration and then assembly of cellulose chains is provided with much more tunable chemistry and functionality (Li et al., 2018; Wu Y. et al., 2019; Yang et al., 2019). For example, a synergistic strategy based on chemical (interfiber covalent crosslinking) and physical (non-covalent interactions via the hydrogen bonds) crosslinks is effective to tailor the structural characteristics for the purpose of high mechanical properties (Rodell et al., 2016; Song et al., 2017; Liu et al., 2018).

In this study, a dual-crosslinking assisted with pre-orientation strategy is adopted to engineer the thermo-conductive RC/BNNS composite film, in which epoxy chloropropane (ECH) was used for the covalent crosslinking, while the RC nanofibers are also non-covalently bonded by hydrogen bonding interaction between adjacent RC nanofibers. Compared with the conventional vacuum–filtration strategy (Yang et al., 2017; Cao et al., 2018; Chen et al., 2018b) in which nanocellulose is mainly assembled merely via intermolecular hydrogen interactions, this synergistic effect not only enables the effective interfiber slippage and prevent any mechanical fracture through partial chemical bonding interactions but also non-covalent hydrogen bonding interactions serve as the sacrifice bonds to dissipate the stress energy, ensuring a simultaneous high mechanical strength and toughness at the high loading of BNNSs (45 wt%). More importantly, ascribed to the high-loading but homogeneous BNNS, and the anisotropic BNNS alignment due to the uniaxial stretching treatment, the RC/BNNS composite film also behaves at an extraordinary in-plane thermal conductivity up to 15.2 W/m·K. Along with an additional favorable water resistance and bending tolerance (>10,000 times), this tactfully engineered film broadens its applications in next-generation portable and wearable electronic devices for efficient heat dissipation.

MATERIALS AND METHODS

Materials

Lithium hydroxide (LiOH, 98%), lithium chloride (LiCl, 99.0%), phytic acid (70%), epoxy chloropropane (ECH, 99.5%), and urea (99.0%) were obtained from Aladdin Reagent Co., Ltd. Cotton linter pulp was obtained from Jilin Chemical Fiber Group Co., Ltd. These chemicals were used as received without further purification. Boron nitride (99.9%, 1 2 μm) was obtained from Sigma-Aldrich Co., Ltd and was exfoliated according to our previous study.

Fabrication of the Dual-Crosslinked RC/BNNS Films

Dual-crosslinked RC/BNNS composite films were fabricated as shown in **Figure S1**. First, cotton linter pulp was immersed in a precooled 4.6 wt% urea/15 wt% LiOH aqueous solvent (−12°C) and stirred at 950 rpm until the temperature approached to 5°C, then the solution in liquid nitrogen was quickly frozen and diluted to 6 wt%. The stirring and freezing procedures were repeated until the solution was clear and sticky. Simultaneously, the BNNSs were immersed in the above LiOH/urea solvent under stirring at 500 rpm, following a ball milling process for 2 h, and then frozen in liquid nitrogen. Afterward, 21.2 g of the cellulose solution was mixed with the BNNS solution at different mass ratios of BNNS/cellulose from 0 to 60 wt%, and 0.23 g ECH was added into the mixture under stirring at 950 rpm. After defoaming, the solution was poured into molds and kept at 5°C for 30 h. Subsequently, the as-prepared RC/BNNS gels were pre-stretched to specific strains ranging from 100 to 400% and then immersed in the 5-wt% phytic acid aqueous solution for 30 min to achieve the physical crosslinking. Last, the gels were immersed in deionized water for 48 h, and the anisotropic and dual-crosslinked RC/BNNS films were obtained by air drying the gels at room temperature. To verify the effect of RC fibers on the structure and mechanical properties of the materials, a merely physical cross-linked RC film and dual-crosslinked RC films with 100 and 300% pre-stretching were also prepared without RNNS addition for comparison.

Characterization

The structures and morphologies of the fabricated samples were observed by atomic force microscopy (AFM, Bruker Veeco Multimode 8), scanning electron microscopy (SEM, Hitachi S-4800), and transmission electron microscopy (TEM, TECNAI G2-20 LaB6). The Fourier transform infrared (FT-IR) spectra were collected on a Thermo Scientific Nicolet iS5 spectrometer with scanning wavelengths from 500 to 4,000 cm^{-1}. The 2D wide-angle X-ray diffraction (WAXD) measurements were performed on a WAXD diffractometer (Rigaku D/MAX-1200). The X-ray diffraction (XRD) patterns were obtained by using a Bruker AXS D8 advanced diffractometer. The dispersion degree of the suspension was analyzed by a polarizing microscope (BM2100 POL). The TC of the sample was calculated according the equation $TC = \alpha \times \rho \times C$, where α, ρ, and C, correspond to the thermal diffusivity, density, and specific heat capacity of the sample, respectively. The in-plane and out-of-plane thermal diffusivity of the samples were measured by a flash thermal conductivity analyzer (Netzsch LFA 467) at a voltage of 250 V and pulse width of 300 μs. The rheological properties of the samples were tested by rotational rheometer (TA AR2000ex). Thermogravimetric analysis was carried out on a synchronized thermogravimetric analyzer (TGA/DSC, Mettler Toledo TGA/DSC1/1100LF), and the samples were heated from 25 to 700°C at a heating rate of 20°C/min. Surface wettability of the samples were tested by a contact angle tester (Solon SL200B).

Finite Element Simulation

Finite element analysis was carried out to visualize the temperature and heat flux distribution within RCF/BNNS during heat dissipation. The simulation was based on classical Fourier Law [$q = -\kappa \times \text{grad}(T)$], where q, κ, and grad (T) corresponds to heat flux, thermal conductivity, and temperature gradient, respectively.

RESULTS AND DISCUSSIONS

The anisotropic and dual-crosslinked RC/BNNS films were well-designed through a pre-orientation assisted with dual cross-linking strategy (**Figure 1a**). First of all, so as to improve the compatibility of RC and BNNS, BNNSs with a lateral size of 200–300 nm and thickness of 1–2 nm (**Figures 1b,c**) were fabricated with a typical ball-milling treatment with alkali/urea solvent. Dissolved cellulose solution was obtained via a typical alkali/urea solvent, in which abundant cellulose nanofibers with a diameter of ∼30 nm exist in the solution (**Figure 1d**). After mixing them together, the cellulose/BNNS suspension could present a very uniform dispersion according to the optical microscope result (**Figure 1e**, no obvious BNNS aggregations), and it was verified that the BNNS sheets could remain stable and dispersive in the suspension after long standing according to the TGA test of the supernatant (**Figure 1f** and **Figure S2**). Epichlorohydrin (ECH) was employed to give rise to firm chemical crosslinked bonds by introducing the epoxy groups, which would crosslink the adjacent RC nanofibers, leading to the construction of the chemical gels with a sudden increase in viscosity (**Figure S3**). The rheological test results (**Figure 1g**) show that, as the oscillation strain increased, both the cellulose solution and the cellulose/BNNS suspension possessed higher values of loss modulus than that of the storage modulus, behaving in a liquid-like state (Zhang et al., 2020), while the RC/BNNS/ECH composite exhibited the opposite result, showing a gel-like state, which further proved the formation of the hydroxyl gel. However, the cross-linking amount of such homogeneous and isotropic gel was low, and its mechanical strength is needed to be further improved for practical application. Therefore, a stretch force was applied to both sides of the gel to guide the anisotropic arrangement of the RC chains and BNNS, following a phytic acid bath to destroy the alkali/urea solvent shells and fix the pre-stretched structure of the composites. Upon pre-stretching, the RC chain exhibited an anisotropic arrangement along the direction of the stretching force. Simultaneously, the stretch force of pre-stretching and restriction of RC endow the BNNS with an orientated topology in the film. In the wake of phytic acid bath, the alkali/urea solvent system, which was broken and physical crosslinked within the hydrogen bond, was therefore formed. Finally, the dual cross-linked RC/BNNS hydrogels were fixed to prevent the shrinkage and air dried to form the anisotropic structure of the RC and BNNS, which is expected to achieve a much higher tensile strength and in-plane thermal conductivity of the films.

The FT-IR spectra of the physical crosslinked RC, dual-crosslinked RC, physical crosslinked RC/BNNS, and dual-crosslinked RC/BNNS films confirmed the reaction and hydrogen bond interactions between the cellulose chains of the samples (**Figure S4**). The physical crosslinked RC film exhibited a series of characteristic peaks at 3,450, 2,880, and 1,644 cm^{-1} that correspond to –OH stretching, $-CH_2$ stretching, and H–O–H stretching, respectively. The absorption bands of the RC were 1,350, 1,160, and 1,060 cm^{-1}, which were attributed to C–H scissor vibration, –OH wagging vibration, and C–O and C–C stretching vibration, respectively (Gao et al., 2011; Zhao et al., 2016). However, after crosslinking by the ECH, the intensities of these absorption peaks decreased. This result indicated that the hydroxyl groups on the cellulose chains partially reacted with ECH to form covalent crosslinking. After blending with BNNS nanosheets, two typical peaks of BN at 819 cm^{-1} (deformation of B–N bonds) and 1,370 cm^{-1} (stretching vibrations of B–N bonds) appeared in the spectra of both physical crosslinked and dual-crosslinked RC/BNNS films (Yu et al., 2016). The thermal degradation behavior of RC and RC/BNNS films with and without chemical crosslinking were compared by TGA and DSC curves (**Figure S5**). The physical crosslinked RC film exhibited a major weight loss between 300 and 400°C, while the initial decomposition temperature of the dual-crosslinked RC film was relatively lower, and the residual weight ratio was a little higher than the physical crosslinked RC film due to the

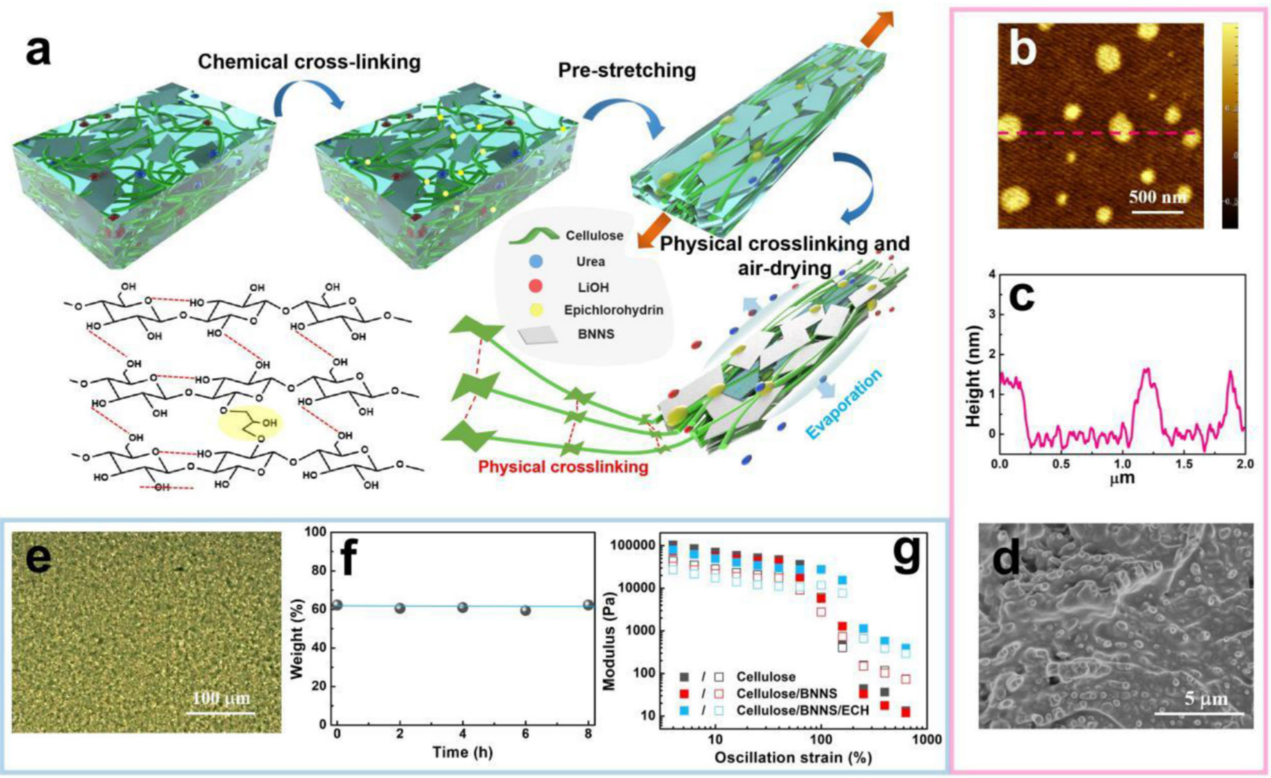

FIGURE 1 | (a) Schematic illustration of the fabrication process of the dual-crosslinked regenerated cellulose (RC)/boron nitride nanosheet (BNNS) film. **(b)** Atomic force microscopy (AFM) micrograph and **(c)** the corresponding height information of BNNS. **(d)** *In situ* scanning electron microscopy (SEM) image of cellulose nanofibers within the precipitated RC paper. **(e)** Microscopic image of the cellulose/BNNS suspension. **(f)** Weight fraction of BNNS in the supernatant of cellulose/BNNS suspension by thermogravimetric analyzer (TGA) test. **(g)** Rheological test results of the cellulose, cellulose/BNNS, and cellulose/BNNS/epoxy chloropropane (ECH) suspension.

existence of the ECH. After adding the BNNS, the residual weight ratios of both of the films were increased remarkably, which were consistent with the mass ratios of BNNSs. To clarify the impact of the dual-crosslinked structure and stretching effect on the material properties, the stress–strain curves of the pristine RC, dual-crosslinked RC, and dual-crosslinked RC in 300% stretch film were compared as shown in **Figure 2a**. For the RC film with only physical crosslinking by hydrogen bonding interactions, the tensile strength and elongation at break were 84.2 MPa and 23.1%, respectively. Nevertheless, the introduction of the chemical cross-linking effect of ECH was used as a kind of supporting bond to prevent the interfiber slippage in the stretching process. The elongation at break of the film increased to 45.7%, while the tensile strength was almost unchanged, which was attributed to the slip of the RC chain before break and chemical crosslink between the RC nanofiber. Furthermore, when the RC film was pre-stretched to a strain of 300%, the cellulose molecular chains or embedded cellulose nanofibers would be induced to orientation, and the slip distance between molecular chains or nanofibers would be reduced, which not only greatly improved the tensile strength of the film but also maintained a high material toughness under the interaction of dual-crosslinking. **Figures 2b–d** show the WAXS patterns and their corresponding orientation factors of the dual-crosslinked RC films after 100 and 300% stretching in a synchrotron radiation facility. For the film without stretching, the WAXS pattern shows a very uniform diffraction pattern at all azimuthal angles. Differently, the WAXS pattern of the dual-crosslinked RC film with 300% stretching shows clear equatorial arcs with two obvious peaks of integrated intensity, revealing the changes of the dual-crosslinked structure from isotropy to anisotropy (Pan et al., 2019; Wang et al., 2020). Therefore, as illustrated in **Figure 2e**, it is considered that the dual interactions could provide prominent mechanical enhancement, in which chemical crosslinking interactions offer the effective interfiber slip and prevent any fracture, while intermolecular hydrogen bonding interactions serve as the sacrifice bonds to dissipate the stress energy, resulting in a simultaneous high mechanical strength and toughness.

To further study the effect of BNNS content on the dual-crosslinked composite films, taking a stretching ratio of 300% as an example, the pre-stretched RC/BNNS samples with a BNNS weight ratio from 0 to 60 wt% were compared through stress–strain test in **Figure 2f**. Compared with pure RC film, when 10 wt% of BNNS was added, the tensile strength and elongation at break of the RC film was slightly improved to

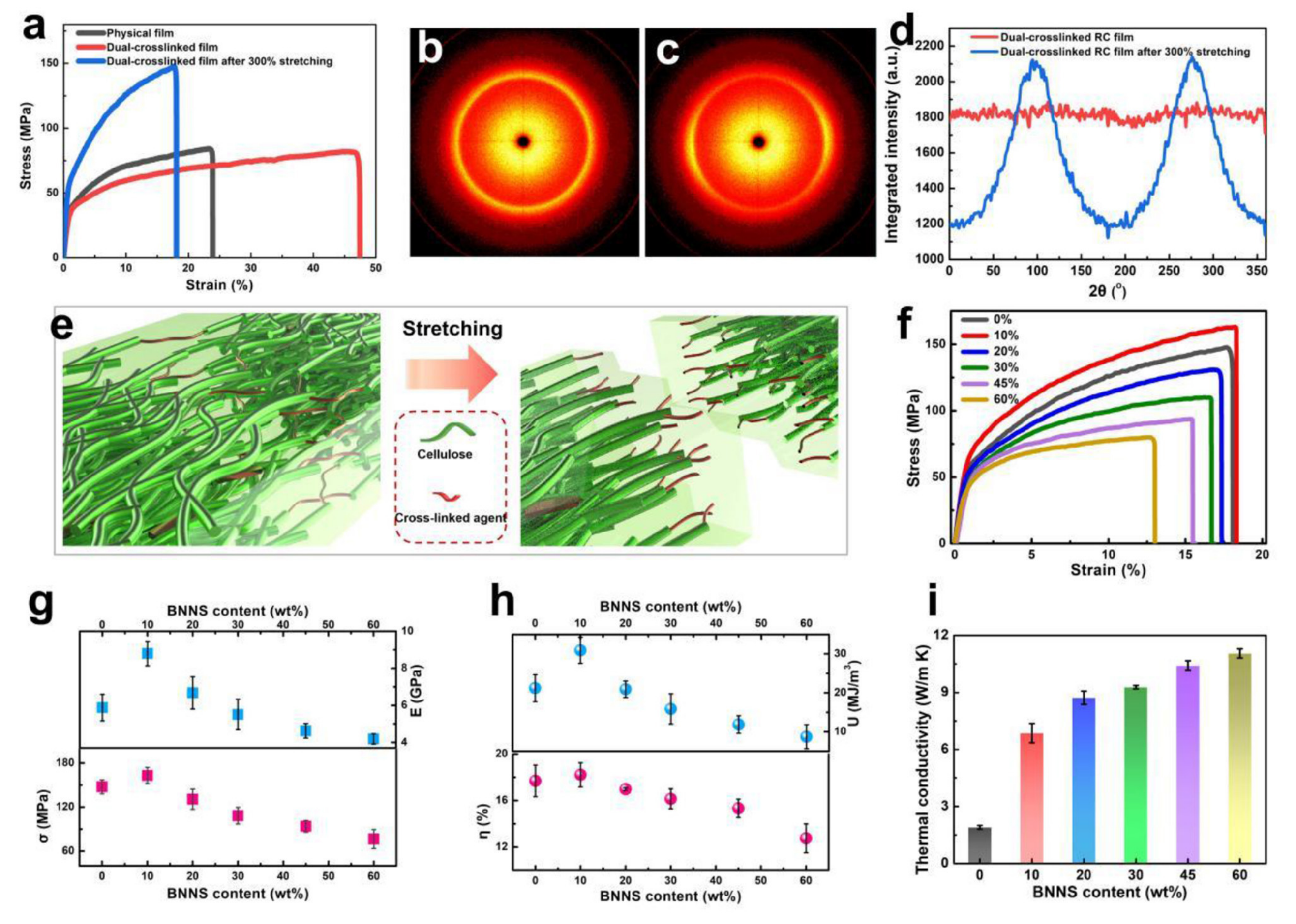

FIGURE 2 | **(a)** Stress–strain curves of the RC films with different crosslinking states; WAXS patterns of **(b)** the dual-crosslinked RC film without pre-stretching and **(c)** the dual-crosslinked RC film after 300% stretching, and **(d)** the corresponding azimuthal-integrated intensity distribution curves. **(e)** Mechanism diagram of the dual-crosslinking enhancement of the RC/BNNS film. **(f)** Stress–strain curves, **(g)** modulus and tensile strength, **(h)** toughness and elongation at break, and **(i)** thermal conductivities of the dual-crosslinked RC/BNNS film with 0–60 wt% of BNNS additions.

163.1 MPa and 18.2%, respectively. It is due to the good interfacial interaction between RC and BNNS, which deliver the force from RC to BNNS when stretched. However, with the increase in BNNS content, more defects between excess BNNS and the substrate occurred, leading to gradual decrease in the tensile strength, elongation at break, toughness, and modulus of the composite film (**Figures 2g,h**). Especially, when the BNNS content increased from 45 to 60 wt%, the toughness and elongation at break of the composite film decreased significantly, which were caused by the structural defects as shown in **Figure S6**. Besides, the thermal conductivities of the above samples are compared in **Figure 2i**. It is noted that the in-plane-orientated BNNS obviously enhanced the thermal conductivity, indicating that the thermally conductive path was formed (Wu Y. et al., 2019). With the increase in BNNS content, abundant thermal conductive phonon pathways were established, and the thermal conductivity of the composite film was increased accordingly. When the BNNS content increased from 45 to 60 wt%, the thermal conductivity was increasing not obviously from 10.4 to 11.0 W/m·K, corresponding to the beforehand establishment of the conductive path. Therefore, the dual crosslinking strategy accompanied by the optimal BNNS content of 45 wt% was chosen to prepare the highly thermo-conductive RC/BNNS film.

The structural alignment of the BNNS in the dual-crosslinked RC/BNNS film is mainly induced by the pre-stretching before the physical crosslinking process. During pre-stretching, the BNNSs were limited in an in-plane-oriented arrangement, which results from the RC chain getting orientated along the force direction and the film punchout along the vertical direction. Generally, the more pre-stretching ratio of the film, the higher the orientation it will have. It is known that BNNS exhibits high TC along the (002) lattice plane, whereas the TC value is considerably declined along the (100) lattice plane. Hence, the ratio between the intensity of the (002) peak (I_{002}) and the (100) peak (I_{100}) is represented to characterize the anisotropic degree of BNNSs by XRD test in **Figure S7**, and the calculated I_{002}/I_{100} values, which could reflect the in-plane-orientated degree of

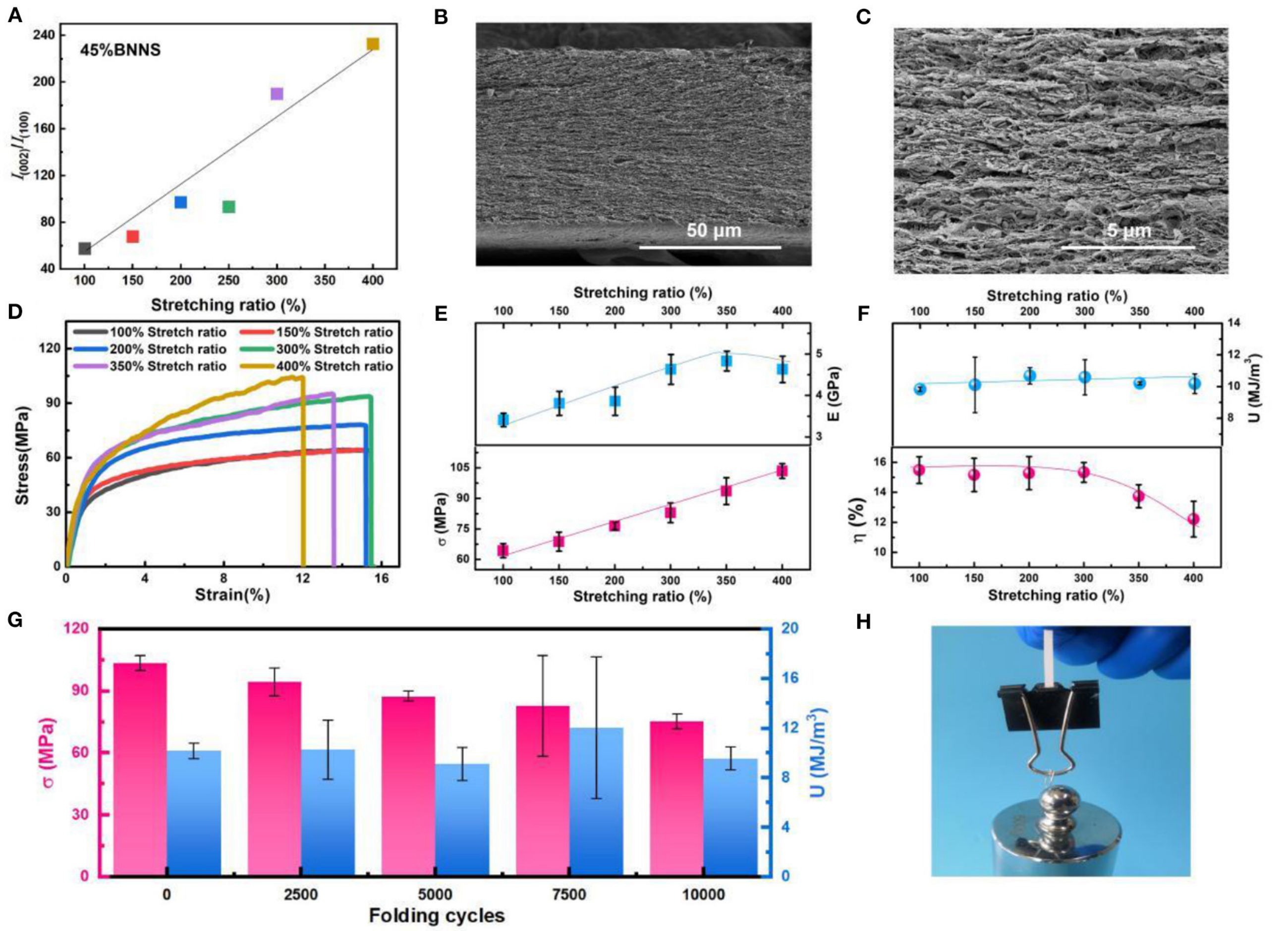

FIGURE 3 | (A) I_{002}/I_{100}values calculated from the X-ray diffraction (XRD) information of the dual-crosslinked RC/BNNS films after 100–400% stretching. **(B)** Cross-section SEM image and **(C)** the partial enlarged detail of the dual-crosslinked RC/BNNS film after 400% stretching. **(D)** Stress–strain curves, **(E)** tensile strength and modulus, **(F)** elongation at break and toughness of the dual-crosslinked RC/BNNS films after 100–400% stretching. **(G)** Tensile strength and toughness after repeated folding cycles. **(H)** Digital image of the folded RC/BNNS film after 400% stretching that can withstand a weight of 500 g.

BNNS, are illustrated in **Figure 3A**. With the increase in the pre-stretching ratio from 100 to 400%, the value of I_{002}/I_{100}revealed a growing trend from 48 to 226, indicating that the orientation of the BNNS tend to be more prominent in the composite film after stretching. The cross-section SEM image of the dual-crosslinked RC/BNNS film after 400% stretching (**Figure 3B**) and its partial enlarged detail (**Figure 3C**) displayed that the BNNS lie horizontally along the in-plane direction of the composite film, which was visibly different from the disordered orientation of the BNNS in the dual-crosslinked RC/BNNS film without pre-stretching (**Figure S8**). Moreover, with the formation of the RC/BNNS anisotropic structure, the mechanical properties of the film were also affected to some extent. **Figure 3D** shows the stress–strain curves of the dual-crosslinked RC/BNNS films after different degrees of pre-stretching. As can be seen, in the increase of the stretching ratio, dual-crosslinked RC/BNNS film with 400% stretching ratio behaves with much enhanced tensile strength (107 MPa), but with depressed elongation, it can be explained as the decrease in slidable RC chain. By the way, exorbitant pre-stretching will spoil the mechanical properties of the film when it is over a ratio of 300% (**Figures 3E,F**). The exorbitant pre-stretching may cause the crack in the chemical crosslinking between the RC chain, so that it will weaken the modulus and toughness. In addition, the mechanical properties of the optimal RC/BNNS film were tested under 10,000 times of folding (**Figure 3G**), and the results show that the tensile strength declined slowly, while the toughness could be well-preserved, which is a direct evidence for its excellent flexibility. Moreover, this folded film could also withstand a 500-g weight that is almost 20,000 times of its own weight (**Figure 3H**), further proving its strong and flexible performance.

For the BNNS-based thermo-conductive material, the thermal conductivity is greatly affected by the directional arrangement of the BNNS in the matrix. As a result, with the increase in the pre-stretching ratio from 100 to 400%, the thermal conductivity of the dual-crosslinked RC/BNNS film was increased accordingly (**Figure 4A**). Note that the value of the film with 400% of pre-stretching reached to a high level of 15.2 W/m·K, which was

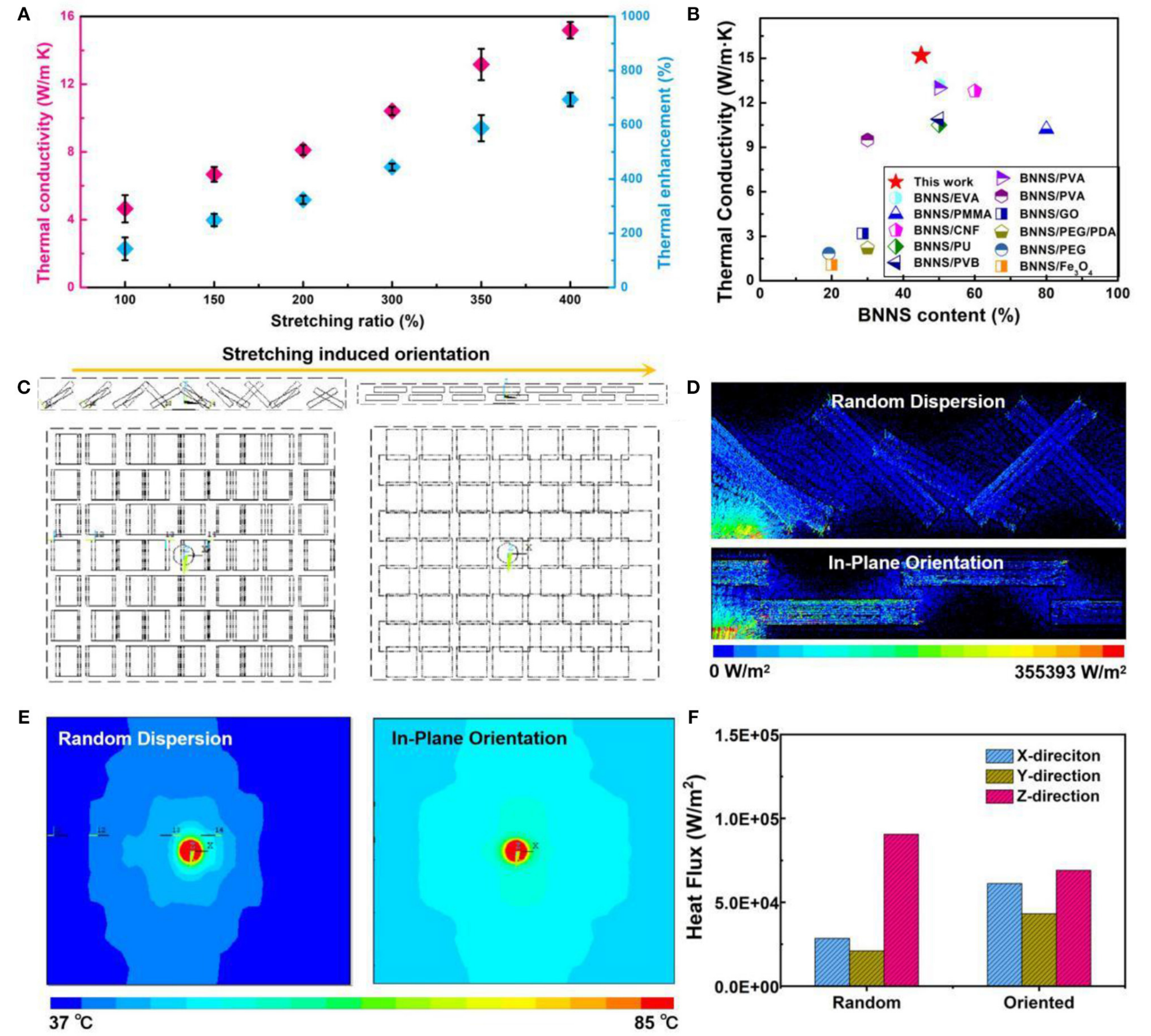

FIGURE 4 | (A) Thermal conductivity (TC) and the corresponding thermal enhancements of the dual-crosslinked films after 100–400% stretching. **(B)** Comparison of TC as a function of BNNS content with previous reports. **(C)** The simulated arrangements of the BNNSs with random dispersion and in-plane orientation. Map of the **(D)** cross-section thermal distribution, **(E)** in-plane thermal distribution, and **(F)** the corresponding heat flux results of the BNNS-based models with random dispersion and in-plane orientation.

almost 7.9 times higher than the pure RC film and 3.2 times higher than the film without pre-stretching. We also compare this composite film with most of the BNNS-based thermal conducting materials (**Figure 4B**); our dual-crosslinked RC/BNNS film after 400% stretching behaves with a much higher TC value at a low BNNS content (Lim et al., 2013; Ahn et al., 2014; Morishita and Okamoto, 2016; Yang et al., 2016a,b, 2018; Hong et al., 2017; Wu et al., 2017; Wang et al., 2020). Much of the researches (Wei et al., 2011; Yang et al., 2019) verified that the in-plane thermal conductivity of BNNSs is dozens of times higher than that in the out-plane direction. The thermal enhancement profits from the in-plane-arranged orientation of the BNNSs, which maximized the utilization of the in-plane thermal conductivity of BNNSs. An increasing number of orientated BNNSs, arranged along the in-plane of the film with the stretch ratio improved, led to the intensive thermal conductivity, which corresponds to the I_{002}/I_{100} values calculated from XRD (**Figure 3A**). Considering the relative mechanical properties of the composite film, the pre-stretching ratio of 400% was regarded as the optimized one in this study. Furthermore, to realize a visual analysis of the enhancement on the thermal conductivity, the finite element (FE) analysis was provided to simulate the heat fluxes and temperature

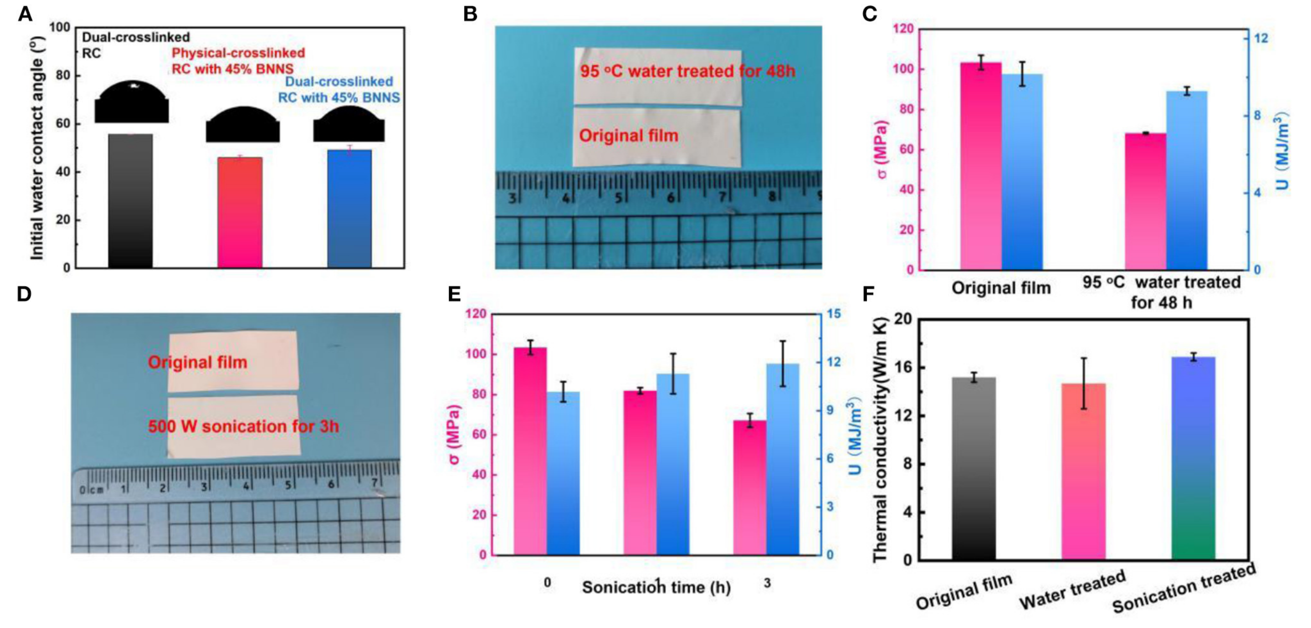

FIGURE 5 | (A) Initial water contact angle results and photographs of water droplets on the surface of the samples. **(B)** Digital images and **(C)** mechanical properties of the original film and the film treated in 95°C water for 48 h. **(D)** Digital images and **(E)** mechanical properties of the original film and the film treated by 500 W sonication for 3 h. **(F)** Thermal conductivity of the RC/BNNS samples.

distribution of the dual-crosslinked RC/BNNS films. The detailed simulation and parameters are listed in **Figures S9**, **S10** and **Table S1**. **Figure 4C** illustrates two simulated arrangements of the BNNS with random dispersion and in-plane orientation in the RC matrix, and the hotspots were set in the middle of the upper surface. After heating, the radial heat flux transfer rate of the randomly dispersed model was obviously lower than that of the oriented model along the in-plane direction (x-direction and y-direction) as time went by **Figure 4D**. The heat diffusion of the oriented film was more obvious than that of the film with inefficient BNNS orientation, and the heat distribution was more uniform (**Figure 4E**). For intuitive represention of the heat flux along the different orientations, we count the heat flux distribution in the x-, y-, and z-directions (**Figure 4F**). The in-plane heat flux of the oriented model was superior to the random model, but with an inferior heat flux along the z-direction. Combined with **Figure 4C**, it is indicated that the in-plane heat flux seizes the principal position in the oriented model, which attributes to the in-plane-arranged orientation of the BNNSs.

To investigate the water resistance of the thermo-conductive film, the surface hydrophilicity of the dual-crosslinked RC film, the physical crosslinked RC/BNNS film with 45% BNNS, and the dual-crosslinked RC/BNNS film with 45% BNNS were characterized first by water contact angle measurements (**Figure 5A**). The RC film exhibited a contact angle of 55.7°, while the two other samples exhibited slightly reduced contact angles, suggesting that the dual-crosslinked composite film maintained good hydrophilicity of cellulose. For the final optimized RC/BNNS film, the shape and mechanical properties were tested at 95°C water treated for 48 h (**Figures 5B,C**) and 500 W sonication for 3 h (**Figures 5D,E**), respectively. After being treated by the above two situations, the shape of the film was almost unchanged, and more importantly, the tensile strength and toughness were maintained at high levels. In addition, the thermal conductivity of the original, water treated, and sonication-treated films were also compared in **Figure 5F**, and the results further verify the qualified water resistance of the films.

CONCLUSIONS

In summary, we report the fabrication of a strong, tough, and flexible RC/BNNS composite film by combining chemically and physically dual-crosslinking strategy. By stretching-induced orientation, the composite film possessed an anisotropic structure with highly ordered cellulose and BNNSs in the plane direction. As a result, the dual-crosslinked RC/BNNS composite film exhibited high tensile strength (103.4 MPa), high toughness (10.18 MJ/m^3), and excellent thermal conductivity (15.2 W/m·K) with 400% pre-stretching. These properties were consistent with the results through finite element modeling calculation. Furthermore, the optimized RC/BNNS composite film presented excellent folding endurance of more than 10,000 times, and qualified stability under sonication and hydrothermal treatment. Such comprehensive properties greatly exceed that of conventional isotropic thermal conductive materials, which will broaden the practical applications in the portable and wearable electronic devices.

DATA AVAILABILITY STATEMENT

The original contributions presented in the study are included in the article/**Supplementary Material**, further inquiries can be directed to the corresponding authors.

AUTHOR CONTRIBUTIONS

The manuscript was written through contributions of all authors. All authors have given approval to the final version of the manuscript. All authors contributed equally.

FUNDING

This work was financially supported by the Natural Science Foundation of Jiangsu Province (BK20200501), the Research Start-Up Fund of the Nanjing University of Science and Technology (AE89991/222), the 2020 open projects (No. KLATM202010) of the Key Laboratory of Advanced Technologies of Materials, Ministry of Education of China, Southwest Jiaotong University, the Fundamental Research Funds for the Central Universities (Grant No. 30920021121), the China Postdoctoral Science Foundation (2020M671497 and 2020T130300), and the National Natural Science Foundation of China (Grant Nos. 51573102 and 51421061).

SUPPLEMENTARY MATERIAL

The Supplementary Material for this article can be found online at: https://www.frontiersin.org/articles/10.3389/fbioe.2020.602318/full#supplementary-material

Supplementary Figure 1 | Schematic diagram of the fabrication process of the anisotropic dual-crosslinked RC/BNNS films.

Supplementary Figure 2 | TGA test of cellulose/BNNS supernatan.

Supplementary Figure 3 | Viscosity test results of the pure cellulose solution, the cellulose/BNNS suspension, and the cellulose/BNNS/ECH suspension.

Supplementary Figure 4 | FT-IR spectra of RC or RC/BNNS films.

Supplementary Figure 5 | TGA and DSC curves of RC or RC/BNNS films.

Supplementary Figure 6 | Cross-section SEM image and the partial enlarged detail of the dual-crosslinked RC/BNNS film with 60 wt% BNNS content after 300% pre-stretching.

Supplementary Figure 7 | XRD results of the dual-crosslinked RC/BNNS films with different BNNS contents.

Supplementary Figure 8 | Cross-section SEM image of the dual-crosslinked RC/BNNS film without pre-stretching.

Supplementary Figure 9 | Heat flux in RC/BNNS films.

Supplementary Figure 10 | FE analysis detail.

Supplementary Table 1 | FE analysis detail.

REFERENCES

Ahn, H. J., Eoh, Y. J., Park, S. D., and Kim, E. S. (2014). Thermal conductivity of polymer composites with oriented boron nitride. *Thermochim. Acta* 590, 138–144. doi: 10.1016/j.tca.2014.06.029

Cai, J., and Zhang, L. (2005). Rapid dissolution of cellulose in LiOH/Urea and NaOH/Urea aqueous solutions. *Macromol. Biosci.* 5, 539–548. doi: 10.1002/mabi.200400222

Cai, Q., Scullion, D., Falin, A., Watanabe, K., Taniguchi, T., Chen, Y., et al. (2017). Raman signature and phonon dispersion of atomically thin boron nitride. *Nanoscale* 9, 3059–3067. doi: 10.1039/C6NR09312D

Cao, W., Chen, F., Zhu, Y., Zhang, Y., Jiang, Y., Ma, M., et al. (2018). Binary strengthening and toughening of MXene/cellulose nanofiber composite paper with nacre-inspired structure and superior electromagnetic interference shielding properties. *ACS Nano* 12, 4583–4593. doi: 10.1021/acsnano.8b00997

Chen, C., Wang, J., Liu, D., Yang, C., Liu, Y., Ruoff, R. S., et al. (2018a). Functionalized boron nitride membranes with ultrafast solvent transport performance for molecular separation. *Nat. Commun.* 9:1902. doi: 10.1038/s41467-018-04294-6

Chen, J., Huang, X., Sun, B., and Jiang, P. (2018b). Highly thermally conductive yet electrically insulating polymer/boron nitride nanosheets nanocomposite films for improved thermal management capability. *ACS Nano* 13, 337–345. doi: 10.1021/acsnano.8b06290

Cho, H., Nakayama, T., Suematsu, H., Suzuki, T., Jiang, W., Niihara, K., et al. (2016). Insulating polymer nanocomposites with high-thermal-conduction routes via linear densely packed boron nitride nanosheets. *Compos. Sci. Technol.* 129, 205–213. doi: 10.1016/j.compscitech.2016.04.033

Gao, Q., Shen, X., and Lu, X. (2011). Regenerated bacterial cellulose fibers prepared by the NMMO·H2O process. *Carbohydr. Polym.* 83, 1253–1256. doi: 10.1016/j.carbpol.2010.09.029

Guerra, V., Wan, C., and Mcnally, T. (2019). Thermal conductivity of 2D nano-structured boron nitride (BN) and its composites with polymers. *Prog. Mater. Sci.* 100, 170–186. doi: 10.1016/j.pmatsci.2018.10.002

Han, J., Du, G., Gao, W., and Bai, H. (2019). An anisotropically high thermal conductive boron nitride/epoxy composite based on nacre-mimetic 3D network. *Adv. Funct. Mater.* 29:1900412. doi: 10.1002/adfm.201900412

Hong, H.-J., Kwan, S. M., Lee, D. S., Kim, S. M., Kim, Y. H., Lim, J. S., et al. (2017). Highly flexible and stretchable thermally conductive composite film by polyurethane supported 3D networks of boron nitride. *Compos. Sci. Technol.* 152, 94–100. doi: 10.1016/j.compscitech.2017.09.020

Lao, J., Xie, H., Shi, Z., Li, G., Li, B., Hu, G., et al. (2018). Flexible regenerated cellulose/boron nitride nanosheet high-temperature dielectric nanocomposite films with high energy density and breakdown strength. *ACS Sustain. Chem. Eng.* 6, 7151–7158. doi: 10.1021/acssuschemeng.8b01219

Li, Q., Chen, L., Gadinski, M. R., Zhang, S., Zhang, G., Li, H., et al. (2015). Flexible high-temperature dielectric materials from polymer nanocomposites. *Nature* 523, 576–579. doi: 10.1038/nature14647

Li, Q., Xue, Z., Zhao, J., Ao, C., Jia, X., Xia, T., et al. (2020). Mass production of high thermal conductive boron nitride/nanofibrillated cellulose composite membranes. *Chem. Eng. J.* 383:123101. doi: 10.1016/j.cej.2019.123101

Li, T., Song, J., Zhao, X., Yang, Z., Pastel, G., Xu, S., et al. (2018). Anisotropic, lightweight, strong, and super thermally insulating nanowood with naturally aligned nanocellulose. *Sci. Adv.* 4:eaar3724. doi: 10.1126/sciadv.aar3724

Lim, H. S., Oh, J. W., Kim, S. Y., Yoo, M.-J., Park, S.-D., and Lee, W. S. (2013). Anisotropically alignable magnetic boron nitride platelets decorated with iron oxide nanoparticles. *Chem. Mater.* 25, 3315–3319. doi: 10.1021/cm401488a

Liu, B., Li, Y., Fei, T., Han, S., Xia, C., Shan, Z., et al. (2020). Highly thermally conductive polystyrene/polypropylene/boron nitride composites with 3D segregated structure prepared by solution-mixing and hot-pressing method. *Chem. Eng. J.* 385:123829. doi: 10.1016/j.cej.2019.123829

Liu, S., Oderinde, O., Hussain, I., Yao, F., and Fu, G. (2018). Dual ionic cross-linked double network hydrogel with self-healing, conductive, and force sensitive properties. *Polymer* 144, 111–120. doi: 10.1016/j.polymer.2018.01.046

Ma, T., Zhao, Y., Ruan, K., Liu, X., Zhang, J., Guo, Y., et al. (2020). Highly thermal conductivities, excellent mechanical robustness and flexibility, and outstanding thermal stabilities of aramid nanofiber composite papers with nacre-mimetic layered structures. *ACS Appl. Mater. Interfaces* 12, 1677–1686. doi: 10.1021/acsami.9b19844

Morishita, T., and Okamoto, H. (2016). Facile exfoliation and noncovalent superacid functionalization of boron nitride nanosheets and their use for highly thermally conductive and electrically insulating polymer nanocomposites. *ACS Appl. Mater. Interfaces* 8, 27064–27073. doi: 10.1021/acsami.6b08404

Osorio-Madrazo, A., Eder, M., Rueggeberg, M., Pandey, J. K., Harrington, M. J., Nishiyama, Y., et al. (2012). Reorientation of cellulose nanowhiskers in agarose hydrogels under tensile loading. *Biomacromolecules* 13, 850–856. doi: 10.1021/bm201764y

Pan, X., Shen, L., Schenning, A. P. H. J., and Bastiaansen, C. W. M. (2019). Transparent, high-thermal-conductivity ultradrawn polyethylene/graphene nanocomposite films. *Adv. Mater.* 31:1904348. doi: 10.1002/adma.201904348

Pickering, K. L., Efendy, M. G. A., and Le, T. M. (2016). A review of recent developments in natural fibre composites and their mechanical performance. *Compos. Part A Appl. Sci. Manuf.* 83, 98–112. doi: 10.1016/j.compositesa.2015.08.038

Ray, U., Zhu, S., Pang, Z., and Li, T. (2020). Mechanics design in cellulose-enabled high-performance functional materials. *Adv. Mater.* doi: 10.1002/adma.202002504. [Epub ahead of print].

Rodell, C. B., Dusaj, N. N., Highley, C. B., and Burdick, J. A. (2016). Injectable and cytocompatible tough double-network hydrogels through tandem supramolecular and covalent crosslinking. *Adv. Mater.* 28, 8419–8424. doi: 10.1002/adma.201602268

Song, N., Jiao, D., Cui, S., Hou, X., Ding, P., and Shi, L. (2017). Highly anisotropic thermal conductivity of layer-by-layer assembled nanofibrillated cellulose/graphene nanosheets hybrid films for thermal management. *ACS Appl. Mater. Interfaces* 9, 2924–2932. doi: 10.1021/acsami.6b11979

Tarhini, A. A., and Tehranibagha, A. R. (2019). Graphene-based polymer composite films with enhanced mechanical properties and ultra-high in-plane thermal conductivity. *Compos. Sci. Technol.* 184:107797. doi: 10.1016/j.compscitech.2019.107797

Tu, H., Zhu, M., Duan, B., and Zhang, L. (2020). Recent progress in high-strength and robust regenerated cellulose materials. *Adv. Mater.* doi: 10.1002/adma.202000682. [Epub ahead of print].

Wågberg, L., and Erlandsson, J. (2020). The use of layer-by-layer self-assembly and nanocellulose to prepare advanced functional materials. *Adv. Mater.* doi: 10.1002/adma.202001474. [Epub ahead of print].

Wang, H., Ding, D., Liu, Q., Chen, Y., and Zhang, Q. (2019). Highly anisotropic thermally conductive polyimide composites via the alignment of boron nitride platelets. *Compos. B. Eng.* 158, 311–318. doi: 10.1016/j.compositesb.2018.09.104

Wang, S., Lu, A., and Zhang, L. (2016). Recent advances in regenerated cellulose materials. *Prog. Polym. Sci.* 53, 169–206. doi: 10.1016/j.progpolymsci.2015.07.003

Wang, Z.-G., Liu, W., Liu, Y.-H., Ren, Y., Li, Y.-P., Zhou, L., et al. (2020). Highly thermal conductive, anisotropically heat-transferred, mechanically flexible composite film by assembly of boron nitride nanosheets for thermal management. *Compos. B. Eng.* 180:107569. doi: 10.1016/j.compositesb.2019.107569

Wei, Z., Ni, Z., Bi, K., Chen, M., and Chen, Y. (2011). In-plane lattice thermal conductivities of multilayer graphene films. *Carbon* 49, 2653–2658. doi: 10.1016/j.carbon.2011.02.051

Weng, Q., Wang, X., Wang, X., Bando, Y., and Golberg, D. (2016). Functionalized hexagonal boron nitride nanomaterials: emerging properties and applications. *Chem. Soc. Rev.* 45, 3989–4012. doi: 10.1039/C5CS00869G

Wu, K., Fang, J., Ma, J., Huang, R., Chai, S., Chen, F., et al. (2017). Achieving a collapsible, strong, and highly thermally conductive film based on oriented functionalized boron nitride nanosheets and cellulose nanofiber. *ACS Appl. Mater. Interfaces* 9, 30035–30045. doi: 10.1021/acsami.7b08214

Wu, K., Wang, J., Liu, D., Lei, C., Liu, D., Lei, W., et al. (2020). Highly thermoconductive, thermostable, and super-flexible film by engineering 1D rigid rod-like aramid nanofiber/2D boron nitride nanosheets. *Adv. Mater.* 32:1906939. doi: 10.1002/adma.201906939

Wu, K., Yu, L., Lei, C., Huang, J., Liu, D., Liu, Y., et al. (2019). Green production of regenerated cellulose/boron nitride nanosheet textiles for static and dynamic personal cooling. *ACS Appl. Mater. Interfaces* 11, 40685–40693. doi: 10.1021/acsami.9b15612

Wu, Y., Ye, K., Liu, Z., Wang, B., Yan, C., Wang, Z., et al. (2019). Cotton candy-templated fabrication of three-dimensional ceramic pathway within polymer composite for enhanced thermal conductivity. *ACS Appl. Mater. Interfaces* 11, 44700–44707. doi: 10.1021/acsami.9b15758

Yang, J., Qi, G.-Q., Tang, L.-S., Bao, R.-Y., Bai, L., Liu, Z.-Y., et al. (2016a). Novel photodriven composite phase change materials with bioinspired modification of BN for solar-thermal energy conversion and storage. *J. Mater. Chem. A* 4, 9625–9634. doi: 10.1039/C6TA03733J

Yang, J., Tang, L.-S., Bai, L., Bao, R.-Y., Liu, Z., Xie, B.-H., et al. (2018). Photodriven shape-stabilized phase change materials with optimized thermal conductivity by tailoring the microstructure of hierarchically ordered hybrid porous scaffolds. *ACS Sustain. Chem. Eng.* 6, 6761–6770. doi: 10.1021/acssuschemeng.8b00565

Yang, J., Tang, L.-S., Bao, R.-Y., Bai, L., Liu, Z.-Y., Yang, W., et al. (2016b). An ice-templated assembly strategy to construct graphene oxide/boron nitride hybrid porous scaffolds in phase change materials with enhanced thermal conductivity and shape stability for light–thermal–electric energy conversion. *J. Mater. Chem. A* 4, 18841–18851. doi: 10.1039/C6TA08454K

Yang, W., Zhao, Z., Wu, K., Huang, R., Liu, T., Jiang, H., et al. (2017). Ultrathin flexible reduced graphene oxide/cellulose nanofiber composite films with strongly anisotropic thermal conductivity and efficient electromagnetic interference shielding. *J. Mater. Chem. C* 5, 3748–3756. doi: 10.1039/C7TC00400A

Yang, X., Guo, Y., Han, Y., Li, Y., Ma, T., Chen, M., et al. (2019). Significant improvement of thermal conductivities for BNNS/PVA composite films via electrospinning followed by hot-pressing technology. *Compos. B Eng.* 175:107070. doi: 10.1016/j.compositesb.2019.107070

Yao, Y., Sun, J., Zeng, X., Sun, R., Xu, J., and Wong, C. (2018). Construction of 3D skeleton for polymer composites achieving a high thermal conductivity. *Small* 14:1704044. doi: 10.1002/smll.201704044

Yao, Y., Zeng, X., Wang, F., Sun, R., Xu, J., and Wong, C.-P. (2016). Significant Enhancement of thermal conductivity in bioinspired freestanding boron nitride papers filled with graphene oxide. *Chem. Mater.* 28, 1049–1057. doi: 10.1021/acs.chemmater.5b04187

Ye, D., Lei, X., Li, T., Cheng, Q., Chang, C., Hu, L., et al. (2019). Ultrahigh tough, super clear, and highly anisotropic nanofiber-structured regenerated cellulose films. *ACS Nano* 13, 4843–4853. doi: 10.1021/acsnano.9b02081

Yin, C., Ma, Y., Liu, Z., Fan, J., Shi, P., Xu, Q., et al. (2019). Multifunctional boron nitride nanosheet/polymer composite nanofiber membranes. *Polymer* 162, 100–107. doi: 10.1016/j.polymer.2018.12.038

Yu, B., Xing, W., Guo, W., Qiu, S., Wang, X., Lo, S., et al. (2016). Thermal exfoliation of hexagonal boron nitride for effective enhancements on thermal stability, flame retardancy and smoke suppression of epoxy resin nanocomposites via sol–gel process. *J. Mater. Chem. A,* 4, 7330–7340. doi: 10.1039/C6TA01565D

Yuan, C., Duan, B., Li, L., Xie, B., Huang, M., and Luo, X. (2015). Thermal Conductivity of polymer-based composites with magnetic aligned hexagonal boron nitride platelets. *ACS Appl. Mater. Interfaces* 7, 13000–13006. doi: 10.1021/acsami.5b03007

Zhang, J., Uzun, S., Seyedin, S., Lynch, P. A., Akuzum, B., Wang, Z., et al. (2020). Additive-free MXene liquid crystals and fibers. *ACS Central Sci.* 6, 254–265. doi: 10.1021/acscentsci.9b01217

Zhang, S., Li, J., Wu, H., Li, X., and Guo, W. (2018). Direct synthesizing in-plane heterostructures of graphene and hexagonal boron nitride in designed pattern. *Adv. Mater. Interfaces* 5:1800208. doi: 10.1002/admi.201800208

Zhao, D., Huang, J., Zhong, Y., Li, K., Zhang, L., and Cai, J. (2016). High-strength and high-toughness double-cross-linked cellulose hydrogels: a new strategy using sequential chemical and physical cross-linking. *Adv. Funct. Mater.* 26, 6279–6287. doi: 10.1002/adfm.201601645

Zhu, Y., Romain, C., and Williams, C. K. (2016). Sustainable polymers from renewable resources. *Nature* 540, 354–362. doi: 10.1038/nature21001

Conflict of Interest: The authors declare that the research was conducted in the absence of any commercial or financial relationships that could be construed as a potential conflict of interest.

frontiers
in Bioengineering and Biotechnology

REVIEW
published: 22 December 2020
doi: 10.3389/fbioe.2020.605374

Industrial-Scale Production and Applications of Bacterial Cellulose

*Chunyan Zhong**

Hainan Yeguo Foods Co. Ltd., Hainan, China

Bacterial cellulose (BC) is a natural biomaterial synthesized by bacteria. It possesses a unique structure of cellulose nanofiber-weaved three-dimensional reticulated network that endows it excellent mechanical properties, high water holding capability and outstanding suspension stability. It is also characterized with high purity, high degree of crystallinity, great biocompatibility and biodegradability. Due to these advantages, BC has gained great attentions in both academic and industrial areas. This critical review summarizes the up-to-date development of BC production and application from an industrial perspective. Firstly, a fundamental knowledge of BC's biosynthesis, structure and properties is described, and then recent developments in the industrial fermentation of BC are introduced. Subsequently, the latest commercial applications of BC in the areas of food, personal care, household chemicals, biomedicine, textile, composite resin are summarized. Finally, a brief discussion of future development of BC industry is presented at the end.

Keywords: bacterial cellulose, nanofiber, industrial fermentation, commercial applications, three-dimensional reticulated network

Edited by:
Guang Yang,
Huazhong University of Science and Technology, China

Reviewed by:
Wenfu Zheng,
National Center for Nanoscience and Technology (CAS), China
Jaehwan Kim,
Inha University, South Korea
Fida Hussain,
Pak-Austria Fachhochschule Institute of Applied Sciences and Technology, Pakistan

***Correspondence:**
Chunyan Zhong
yeguohome@163.com

Specialty section:
This article was submitted to Biomaterials,
a section of the journal Frontiers in Bioengineering and Biotechnology

***Received:** 12 September 2020*
***Accepted:** 20 November 2020*
***Published:** 22 December 2020*

Citation:
Zhong C (2020) Industrial-Scale Production and Applications of Bacterial Cellulose.
Front. Bioeng. Biotechnol. 8:605374.
doi: 10.3389/fbioe.2020.605374

INTRODUCTION

Cellulose is the most abundant natural polymers on the earth. It is chemically a linear homo-polysaccharide composed of repeating β-D-glucopyranose units linked by β-1,4 glycosidic bonds (**Figure 1**; Moon et al., 2011). Cellulose is sustainably synthesized by diverse life entities among the Plantae, Animalia, Fungi, and Bacteria Kingdoms (Iguchi et al., 2000; Abeer et al., 2014; Thomas et al., 2018). The key chemical profile of cellulose molecules is their plentiful hydroxyl groups existed along the polymer chain (one anhydroglucose has three hydroxyl groups; Ross et al., 1991). As a result, a large number of hydrogen bonds are formed between hydroxyl groups and oxygen atoms of anhydroglucose units (Pogorelova et al., 2020). The hydrogen bonding and van der Waals force promote a parallel stacking of cellulose molecules into crystalline nanofibers, which further assemble into cellulose microfibrils (Chen W. S. et al., 2018). The supermolecular structure having hierarchical order imparts cellulose microfibrils excellent mechanical strength, allowing them to act as a reinforcing component strengthening the natural architectures of organisms (Klemm et al., 2018). In human history, cellulose-based materials obtained from wood, cotton, and bamboo have been widely used for thousands of years as fundamental engineering materials for paper, construction, energy, textile, and furniture. However, the inefficient use of cellulose no longer meets the requirement of human society development. Additionally, the tremendous use of non-degradable petroleum-based plastics has caused a world-wide serious problem of white pollution (Arena et al., 2011). Thus, a public appeal from individuals and governments for the use of renewable and degradable materials instead of petroleum-based ones is continuously growing.

Therefore, the exploitation of more advanced and wide utilization of cellulose-based materials is urgently required.

In the recent decades, nanotechnology has gained a great progress regarding cellulose. Cellulose nanoparticles including cellulose nanocrystals and cellulose nanofibers are successfully extracted from the woods, cottons, and other plants by using chemical, mechanical, and/or enzymatic methods (Klemm et al., 2011). Since the petroleum-based polymers are non-renewable and degradable to cause energy constraint and white pollution, cellulose nanoparticles are an ideal material based on which to build up a new biopolymer composites industry (Mokhena and John, 2020). Cellulose nanoparticles have a larger mechanical strength but a lower mass density compared with steel (Abitbol et al., 2016). They also possess an extremely low coefficient of thermal expansion similar with that of quartz (Hori and Wada, 2005). Moreover, they are also biocompatible and biodegradable (Roman, 2015). These advantages make cellulose nanoparticles become an attractive nanomaterial in both academic and industrial areas. To date, several kinds of cellulose nanofibers like 2,2,6,6-tetrametylpiperidine-1-oxyl (TEMPO)-oxidized (Isogai et al., 2011), carboxymethylated (Im et al., 2019), and phosphorylated cellulose nanofibers (Noguchi et al., 2020) have been developed to the stages of commercial production and application.

Beyond cellulose nanoparticles obtained from plants, algae, fungi, and bacteria can also produce cellulose, namely microbial cellulose (Abeer et al., 2014). Among them, bacterial cellulose (BC) is a natural nanomaterial produced by some species of bacteria (Reiniati et al., 2017). In comparison, the plant cellulose nanoparticles are obtained via the top-down methods, meanwhile BC is bottom-up synthesized nanofibers. To date, BC has been successfully produced via industrial fermentation (Keshk, 2014). BC is chemically equivalent to plant cellulose, but it has high degree of crystallinity and high purity (free of lignin, hemicellulose, pectin, and other biogenic components) as well as a unique structure of cellulose nanofiber-weaved three-dimensional (3D) reticulated network (Jozala et al., 2016). The unique structure endows BC distinct properties involving high wet tensile strength, large surface area, high water holding capacity, excellent permeability, flexibility, elasticity, and durability (Romling and Galperin, 2015). These advantages make BC an ideal candidate for renewable sources of cellulose materials. Indeed, BC has been commercially produced and used in our life.

This critical review introduces the up-to-date development of BC from an industrial perspective. The biosynthesis, structure and properties of BC are firstly described, and then the development of industrial production of BC is presented. Finally, the commercial applications of BC in the areas of food, personal care, household chemicals, biomedicine, textile, and composite resin are summarized.

BIOSYNTHESIS AND ASSEMBLY OF BC

BC can be synthesized by a series of bacteria such as the genera *Gluconacetobacter, Aerobacter, Rhizobium, Sarcina, Azotobacter, Agrobacterium*, *Pseudomonas,* and *Alcaligenes* (Jonas and Farah, 1998). Among them, *Gluconacetobacter xylinus* (*G. xylinus*, previously named *Acetobacter xylinus*) is the earliest discovered and most widely studied microorganism to produce BC (Zhong et al., 2013). It is a Gram-negative, aerobic and rod-like bacterium discovered by Brown (1886). In the latest bacterial systematics, *G. xylinus* has been combined into the genus *Komagataeibacter,* which is named in honor of Dr. Kazuo Komagata for his contribution to the bacterial systematics of acetic acid bacteria (Yamada et al., 2012). Therefore, *G. xylinus* is also called as *Komagataeibacter xylinus* (*K. xylinus*) now. The efficiency of *G. xylinus* to produce BC is extremely high. A single bacterium *G. xylinus* enables to polymerize 200000 glucose molecules into β-1,4 glucan chains and meanwhile arrange the polymer chains into nanofibers in 1 s (Chen et al., 2011). Due to the high yield, *G. xylinus* has been employed as a model microorganism for the mechanism study of BC synthesis and as industrial strains for the commercial fermentation (Keshk, 2014). Interestingly, a cell-free enzyme system is also developed to produce BC, which might transform into a cell-free factory for BC production in the future. The cell-free enzyme system is developed from BC-producing strains, and contains the whole enzymes and cofactors required for BC synthesis. The quantitative analysis reveals that the system produces BC with a higher yield than the corresponding bacteria (Ullah et al., 2015). Further study demonstrates that the cell-free enzyme system produces BC via an anaerobic biosynthesis process, and the premature BC pellicles formed in the culture media move to the air-liquid interface and assemble into a sheet (Kim et al., 2019).

However, the biosynthesis of BC by *G. xylinus* is complicated. It can be divided into two stages: (I) the intracellular polymerization of glucose molecules into cellulose polymers, and (II) the self-assembly of cellulose polymer chains into crystalline nanofibers (**Figure 2**; Czaja et al., 2007). The biochemical synthesis of cellulose occurs in bacteria, which commonly contains four enzyme catalyzed reactions (**Figure 2**; Moniri et al., 2017; Portela et al., 2019): (a) a glucose molecule is first converted to glucose 6-phosphate (glucose 6-P) by glucokinase; (b) a glucose 6-P molecule is isomerized into glucose 1-phosphate (glucose 1-P) by phosphoglucomutase; (c) a glucose 1-P molecule reacts with uridine triphosphate (UTP) to generate uridine diphosphate glucose (UDP-glucose), which is catalyzed by pyrophosphorylase; (d) UDP-glucoses are finally polymerized into linear β-1,4 glucan chains, which is catalyzed by cellulose synthase. If other types of carbon sources such as disaccharides are used for BC production, they are first hydrolyzed into monosaccharides such as glucose and fructose (Mohammadkazemi et al., 2015; Singhsa et al., 2018). If fructose used as carbon source, it is converted into fructose1-phosphate (fructose1-P), fructose-6-phosphate (fructose 6-P), and glucose 6-P via a number of enzymatic reactions (**Figure 2**; Chao et al., 2001). After the intracellular polymerization, the cellulose polymer chains are ejected out of the cell membrane by bacteria, following by a self-assembly process driving by van der Waals force and the intra- and inter-molecular hydrogen bonding between hydroxyl groups and oxygen atoms in the anhydroglucose units (**Figure 3**; Nishiyama et al., 2008; Ruan

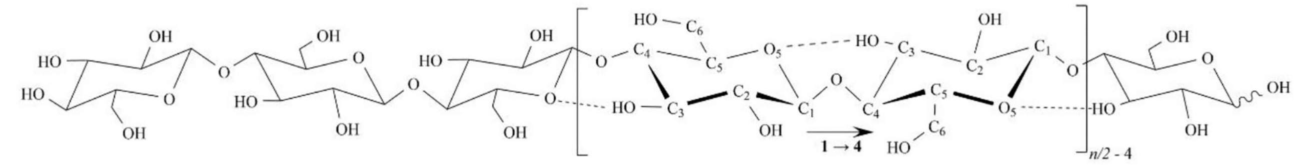

FIGURE 1 | Chemical structure of cellulose molecule (n = degree of polymerization).

et al., 2016). The bacterium *G. xylinus*, likes a missile submarine, holds 50–80 terminal complexes (TGs) aligned along the long axis of bacterial cell (**Figure 2**; Kimura et al., 2001; Krasteva et al., 2017). From the TGs, the cellulose polymer chains are sprayed out, and then self-assemble into semi-crystalline nanofibers (**Figure 2**). In detail, the process involves two steps: (a) the cellulose molecules extruded from the same extrusion pore first assemble into a single elementary nanofiber with a diameter size of ∼1.5 nm; (b) the elementary nanofibers are then gathered into a ribbon-like nanofiber with 3–4 nm thickness and 70–80 nm wideness in the cross-section (**Figure 2**; Portela et al., 2019). The ribbon-like microfibers further weave into 3D reticulated network to generate a gelatinous pellicle floating at the surface of culture media in a static fermentation, which innately provides an oxygen-rich, humid, and safe environment for the non-motile and aerobic bacteria to grow well and protects them from drying, radiation, and damage (Portela et al., 2019).

STRUCTURE AND PROPERTIES OF BC

Structurally, BC is ribbon-like cellulose nanofibers that further weave into 3D reticulated network (**Figure 4**; Ruka et al., 2014). It is characterized with high purity, high degree of polymerization and high crystallinity (Choi and Shin, 2020). BC is free of the symbiotic components in plants such as lignin, hemicellulose, and pectin. The raw pellicle harvested from microbial fermentation contains bacterial cells, residual nutrients and metabolic by-products, which can be easily detached from BC network to yield highly pure product. BC generally has a higher degree of polymerization than plant cellulose (Tabuchi et al., 1998). It varies depending on a series of factors including bacterial genera/strains, fermentation conditions, and nutrient sources (Tahara et al., 1997). BC also has a high crystallinity up to 90% (Sijabat et al., 2020). Like plant cellulose, there are also both crystalline and non-crystalline regions in the structure of BC (Moon et al., 2011). Since BC has high crystallinity, the crystalline regions are the major component of BC structure with short disordered sections as intervals, which probably attributes to both the high mechanical strength and flexibility of BC. The crystalline cellulose has different polymorphs including cellulose I, II, III, and IV (O'Sullivan, 1997). Among them, cellulose I exists in the natural products (Moon et al., 2011). Cellulose I also has two kinds of crystal structures, triclinic (Iα) and monoclinic structure (Iβ) (Azizi Samir et al., 2005). It is demonstrated that cellulose Iα can be irreversibly converted into cellulose Iβ in an alkaline solution by hydrothermal treatment, which suggests that cellulose Iβ represents a relative lower thermodynamic stability than cellulose Iα (Watanabe et al., 2007; Kose et al., 2011). Moreover, the hydrogen binding in cellulose Iα and Iβ is different, which should attribute to the differences in their thermodynamic stability (Moon et al., 2011). In natural products, the two allomorphs co-exist at different ratio proportions in biological species (VanderHart and Atalla, 1984). For instance, cellulose Iα is rich in BC with a mass fraction of ∼0.6, while cellulose Iβ is dominant in the higher plants with a mass fraction of ∼0.8 (Drahushuk et al., 1997). In bacteria, the proportions of cellulose Iα also vary depending on the genera and strains (Drahushuk et al., 1997). Moreover, the factors in fermentation such as temperatures, stirring and additives also influence the ratio proportions of cellulose Iα and Iβ in BC (Yamamoto and Horn, 1994; Kose et al., 2011). For instance, additives such as carboxymethylcellulose (CMC), xyloglucan, and acetyl glucomannan can disturb the crystallization and assembly of BC, resulting in the changes of both component and morphology (Tokoh et al., 1998; Chen et al., 2011). Moreover, glucose derivatives can also be integrated into BC during the fermentation (Gao et al., 2019). As a result, thinner nanofibers majorly composed of cellulose Iβ and coated with the additives are obtained (**Figure 2**; Yamamoto et al., 1996). Tokoh et al. have done a detail study over the structure and morphology changes of BC in the presence of acetyl glucomannan (Tokoh et al., 1998). A single bacterium *G. xylinus* produces a tightly-assembled nanofiber in the Hestrin-Schramm (HS) medium, but it sprays out loosely-gathered nanofibers in HS medium containing acetyl glucomannan (**Figures 5a,b**; Tokoh et al., 1998). The zooming-in images reveal that BC obtained from HS medium is an orderly-assembled and ribbon-like nanofiber with striations and twists in the structure, and BC harvested from acetyl glucomannan-containing medium is a bundle of loosely-gathered nanofibers with obvious gaps among them (**Figures 5c,d**; Tokoh et al., 1998). Ul-Islam et al. have done a comparative study over the properties of regenerated BC and plant cellulose (Ul-Islam et al., 2019). They demonstrate that the regenerated BC gel shows a better porosity, water absorption capability and water retention ability than that of plant cellulose. Moreover, the mechanical, thermal, and physiological properties of the regenerated BC gel are also better than these properties of the regenerated gel of plant cellulose.

BC is characterized with the unique structure of nanofiber-weaved 3D reticulated network (Yamanaka and Sugiyama, 2000). The reticulated network originally provides a safe and nutrient- and oxygen-rich living environment for bacteria

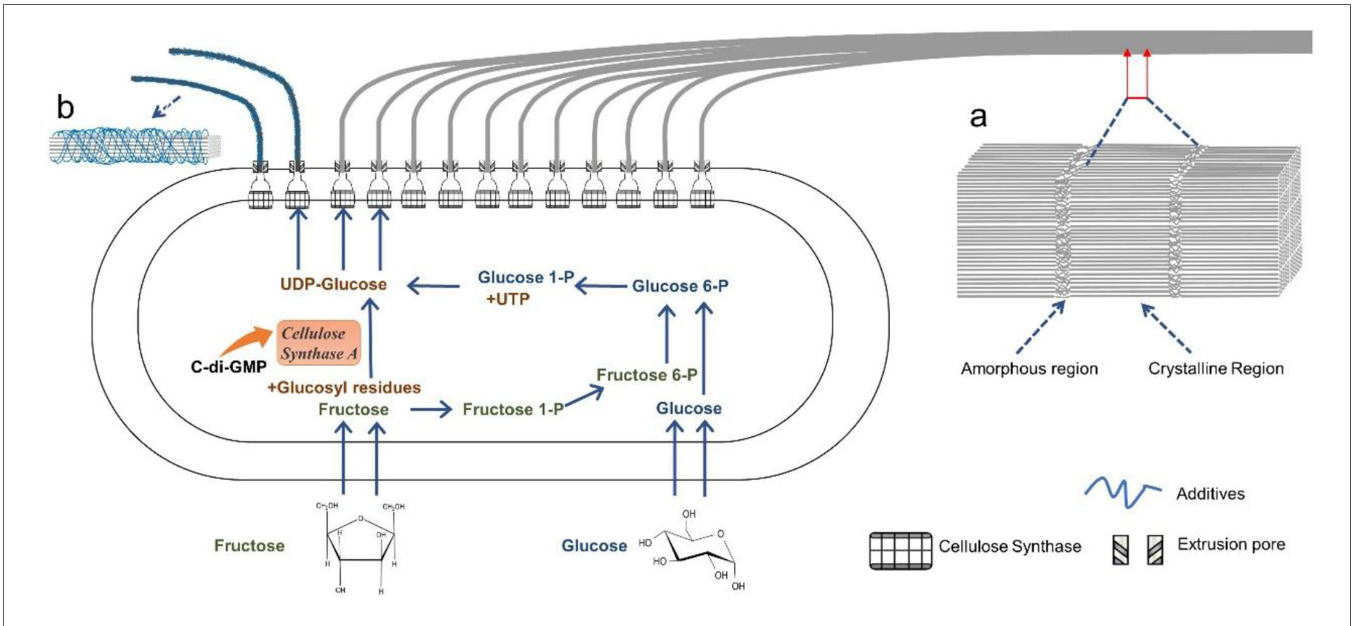

FIGURE 2 | Schematic illustration of the intracellular biosynthesis of cellulose molecules and the extracellular assembly of cellulose molecules into nanofibers by a bacterium. A ribbon-like nanofiber is produced in standard fermentation **(a)**, and loosely-gathered nanofibers are harvested in the presence of additives **(b)**.

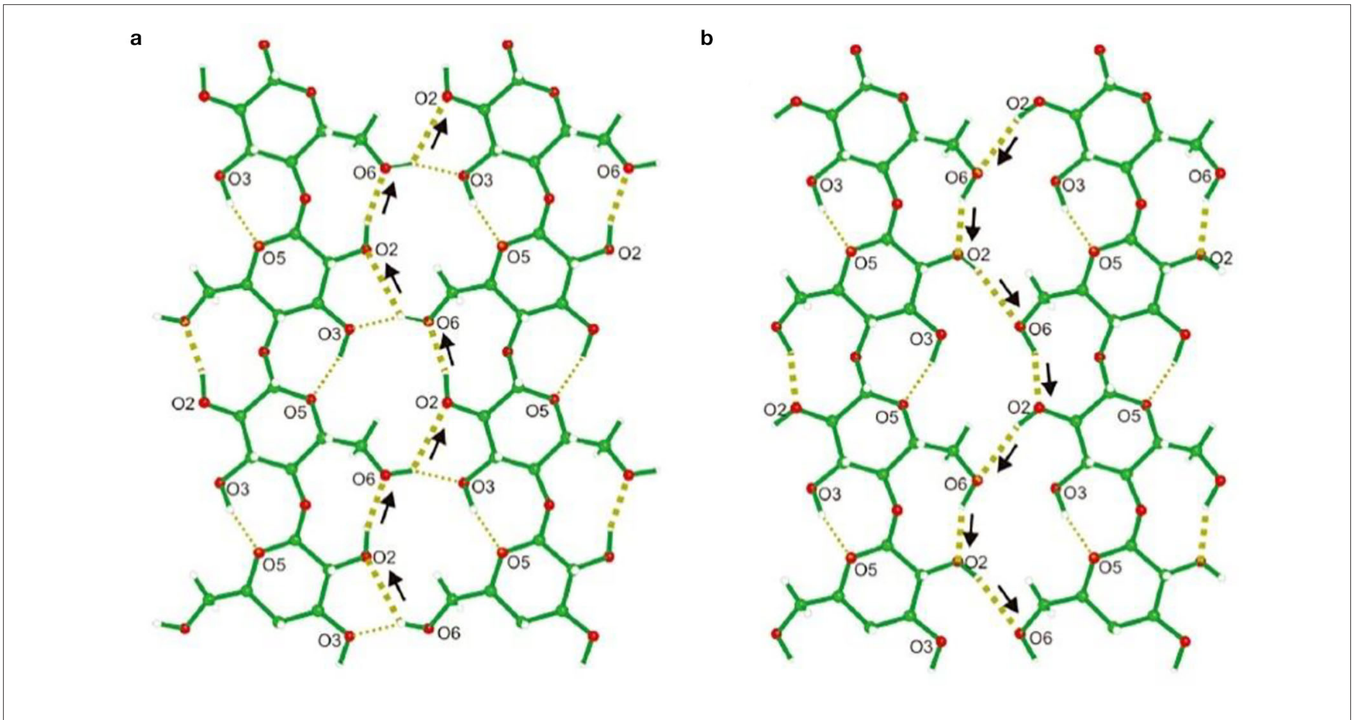

FIGURE 3 | Hydrogen bonding network A **(a)** and B **(b)**. Thick dotted lines show the hydrogen bonding cooperation, and thin dotted lines indicate intra- and inter-molecular hydrogen bonds. The arrows highlight the donor-acceptor-donor directions. Reproduced with permission from Nishiyama et al. (2008).

(Portela et al., 2019). In the term of performances, the unique structure endows BC outstanding mechanical properties, high water holding capability, high suspension stability, and excellent gas permeability (Liu et al., 2020). It is demonstrated that BC has a very high wet tensile strength, although it varies depending on the genera and strains of bacteria as well as the fermentation conditions (Krystynowicz et al., 2002; Yuan et al., 2018). Recently, the mechanical properties of wet BC pellicles and dry films are well-determined by Natalia et al. (Pogorelova et al., 2020). The wet BC pellicles have an average

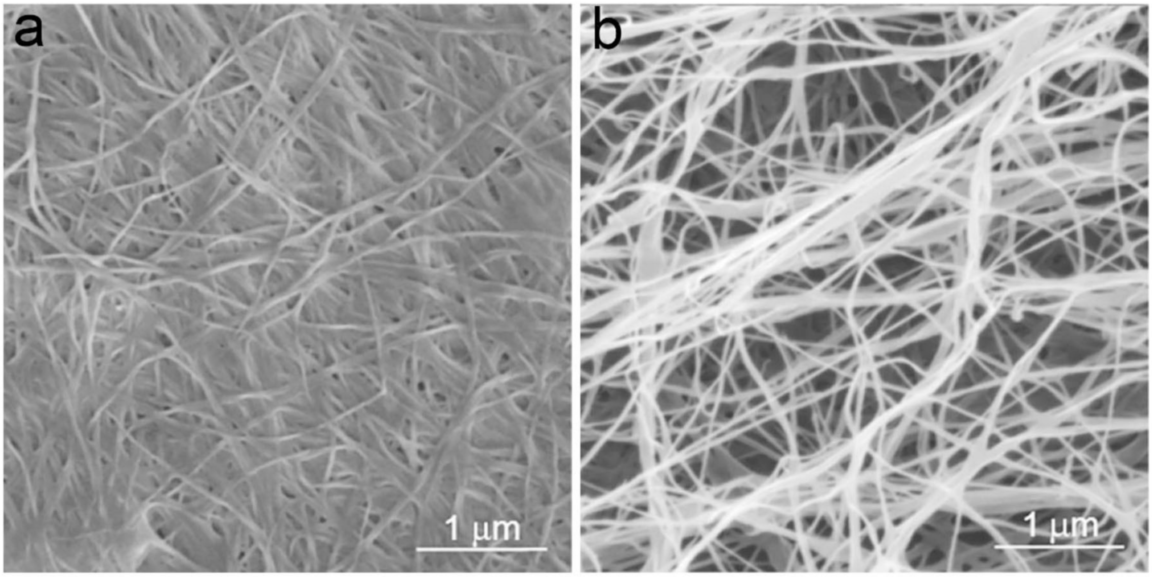

FIGURE 4 | SEM images of BC. **(a)** BC pellicle harvested from static fermentation and **(b)** nanofibers detached from BC pellicle obtained via sonication. Reproduced with permission from Ruka et al. (2014).

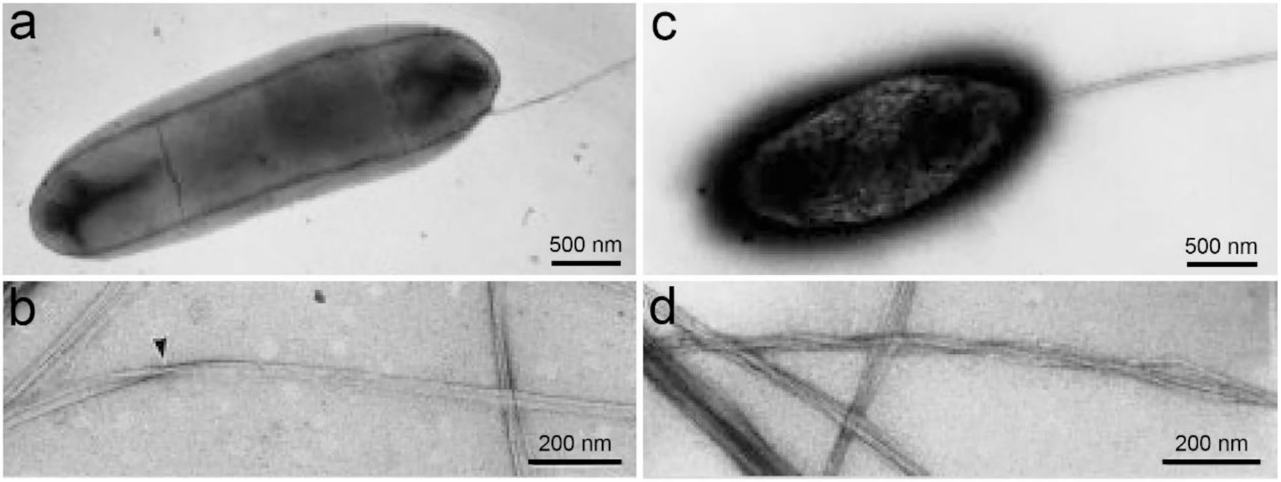

FIGURE 5 | BC structure influenced by acetyl glucomannan. **(a,b)** A negatively-stained bacterium *G. xylinus* producing BC in HS medium **(a)**, and the produced BC nanofibers having a ribbon-like structure with striations and twists **(b)**. **(c,d)** A negatively-stained bacterium *G. xylinus* producing BC in HS medium containing acetyl glucomannan **(c)**, and the produced BC is a bundle of loosely-gathered nanofibers. Reproduced with permission from Tokoh et al. (1998).

Young's modulus of 1.5 ± 0.3 MPa and an average elongation of 49.0 ± 3.6% (Pogorelova et al., 2020). The dry BC films show a higher Young's modulus of 428.0 ± 24.1 MPa but a decreased deformability (7.5 ± 0.4%; Pogorelova et al., 2020). After rehydration, the BC films represent a compromise Young's modulus of 250.4 ± 20.1 MPa and an elongation of 18.5 ± 0.8% (Pogorelova et al., 2020). The water holding capability of BC wet films ranges from 60 to 700 times of its dry weights (Portela et al., 2019). In general, BC pellicles obtained from static fermentation is composed of ∼1 wt % BC and ∼99 wt % water (Yamanaka et al., 1989). Such high-water holding capability should attribute to the plentiful hydroxyl groups of cellulose. It is suggested that only 10% of the water molecules in BC pellicles are free, and the others are trapped by cellulose hydroxyl groups via hydrogen bonding (Mariani et al., 2007). Moreover, it is indicated that water in BC pellicle seems to be trapped in small "lakes" rather than form continuous phase throughout the pellicle (Mariani et al., 2007). BC produced from agitated fermentation is generally a pot of millimeter-scale small pellets with irregular shapes (Gorgieva, 2020). Such small pellets enable to suspend diverse particulates without obviously enhancing the viscosity, and moreover they exhibit excellent suspension stability to tolerate acid, salts, and ethanol (San-Ei Gen, 2020). In the wet condition, BC is also demonstrated to permit water vapor and gas exchange but do not allow liquid to transport, which also benefits a series of applications especially in biomedical areas (Gorgieva and Trcek, 2019; Pang et al., 2020). BC is naturally non-toxic and biocompatible (Roman, 2015). The 3D reticulated network of BC is similar with the collagen fiber-weaved extracellular matrix, which is also beneficial to its biocompatibility (Torres et al., 2012). BC represents good hemocompatibility (Andrade et al., 2011). The *in vivo* studies demonstrated that BC has no foreign body reaction and no chronic inflammatory during long-term implantation (Torres et al., 2012). The above-mentioned properties along with the other advantages such as flexibility, elasticity, durability, and biodegradability make BC a unique and universal nanomaterial in diverse applications.

PRODUCTION AND PURIFICATION OF BC

BC is majorly produced by two kinds of methods, static and agitated fermentation (**Figure 6**). The choice between the methods for BC production depends on the application scenarios as the morphologies and properties of BC yielded by the two methods are very different (Islam et al., 2017; Pang et al., 2020). In a static fermentation, a gelatinous pellicle is formed at the air-liquid interface of the culture media (**Figures 6a,b**). In an agitated fermentation, small irregular pellets are fully suspended in the culture media (**Figures 6c,d**). The bacterial strains cultured in static fermentation represent a higher genetic stability to continuously produce BC in high yield, but the production efficiency is limited by fermentation method (Ross et al., 1991). The agitated fermentation is easily amplified to a large scale of industrial production (Chen G. et al., 2018), but it frequently induces an adverse conversion of bacteria into the non-cellulose producing mutants that reduce the yield (Sani and Dahman, 2010). Although BC gels produced by the two methods show very different macroscopic morphologies, they maintain the same microstructure of 3D reticulated network (CPKelco Inc, 2020). Furthermore, BC obtained in agitated culture has a lower degree of polymerization and a lower crystallinity in comparison with that produced in static culture (Watanabe et al., 1998). The CP/MAS ^{13}C NMR analysis reveals that the ratio proportion of cellulose Iα in BC obtained in agitated culture is lower than that in BC produced in static culture, and accordingly the amount of cellulose Iβ in BC obtained in agitated culture is increased (Watanabe et al., 1998). The mechanical properties of BC produced by the two methods are also different. BC yielded in static culture represents a higher Yong's modulus compared with that produced in agitated culture (Krystynowicz et al., 2002). However, BC from agitated culture has a higher water holding capability and suspension viscosity than that from static culture (Krystynowicz et al., 2002). In view of the differences in morphologies and properties, the applications of BC produced by the two methods are also dissimilar. For instance, the static fermentation is preferred for the production of raw materials requiring fixed geometries, well wet tensile strength and high-water holding capability, such as nano de coco, wound dressing, and face mask etc. On the other hand, BC produced by agitated fermentation represents the superiority in suspending stability, which is majorly used for particulate suspension in the beverages.

For both static and agitated methods, culture medium is the most important part for BC production, which not only provides the necessary nutrients for bacterial growth and BC production, but also significantly impacts structures and yields of BC as well as its mechanical and physical properties (Jozala et al., 2016). A typical fermentation medium is at least comprised of a carbon source, a nitrogen source, and certain nutrient elements such as phosphorus, potassium, sulfur, and magnesium (Andriani et al., 2020). The typical culture medium used for BC production is first described by Hestrin and Schramm (1954). It contains 2.0 wt % glucose, 0.5 wt % peptone, 0.5 wt % yeast extract, 0.27 wt % Na_2HPO_4, and 0.115 wt % citric acid (Hestrin and Schramm, 1954), in which glucose serves as a carbon source, peptone, and yeast extract act as nitrogen sources. The pH value of the medium is adjusted to 6.0 by using HCl or NaOH.

However, the production cost is too high to impede the industrial process of BC. There are two routes to reduce the production cost. One way is to enhance the BC production efficiency, and the other way is to seek cost-effective nutrient sources as the culture media account for ∼30% of the total production cost (Rivas et al., 2004). To date, there are several ways to promote the yield of BC: (I) isolating new bacterial strains that efficiently produce BC from the nature (Yang et al., 2013; Aydin and Aksoy, 2014); (II) employing traditional mutagenic methods (such as ultra-violet and chemical mutagenesis) and genetic engineering techniques to screen high-yield strains (Li et al., 2016); (III) optimizing the culture conditions (Krystynowicz et al., 2002; Cheng et al., 2009). The standard HS medium is expensive due to the high-cost of nutrients. However, the bacteria can be fed with different carbon sources (such as glucose, sucrose, fructose, mannitol, arabitol, and molasses) and nitrogen sources (such as yeast extract, peptone, and corn steep liquor; Keshk and Sameshima, 2005; Buldum et al., 2018). In recent years, the agricultural and/or industrial residues such as coconut water/milk, beet molasses, waste beer yeast, rotten fruit culture, liquid fermentation wastewater, and citrus juice have also been successfully exploited as nutrient sources for BC production (Kongruang, 2008; Wu and Liu, 2013; Velásquez-Riaño and Bojacá, 2017; Cao et al., 2018; Julia et al., 2019). The use of these substituted nutrients significantly reduces the production cost of BC and additionally alleviates environmental pollution induced by the improper discard of the industrial wastes.

After fermentation, the raw BC pellets are not pure, which contain bacterial cells, nutrient residues, and metabolic substances. Thus, a purification process is required to obtain high purity of BC. Cellulose in plant cells tightly co-exists with hemicellulose, lignin and pectin, which are not easily removed. However, BC can be easily purified via a routine method (Moniri et al., 2017). It involves three steps: (I) treat BC pellets with alkaline solutions at 100°C for 15–20 min to remove bacterial cells; (II) isolate BC pellets from the alkaline solution; (III) wash

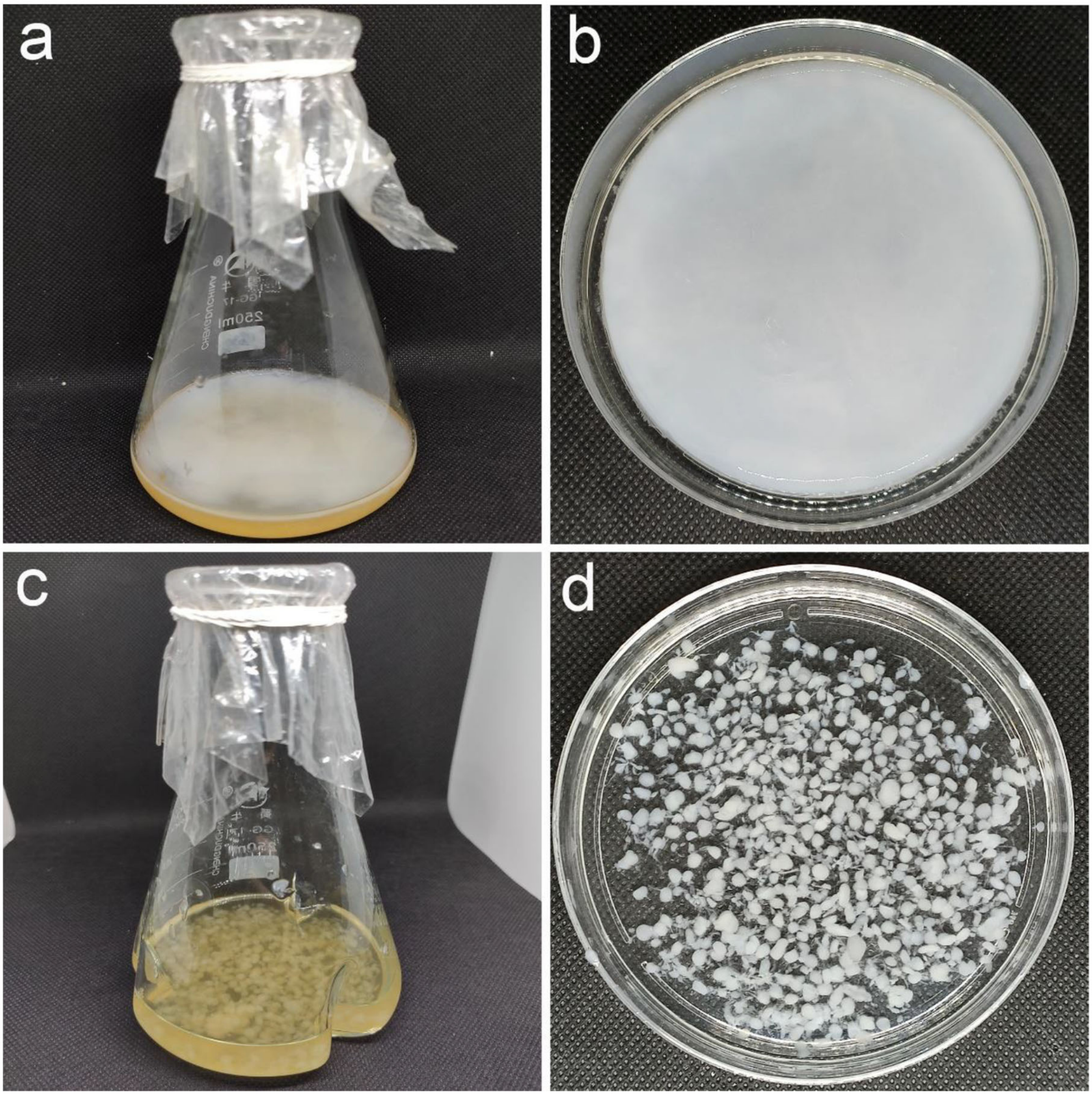

FIGURE 6 | BC produced via static and agitated fermentation. **(a,b)** BC pellicle formed at the air-liquid interface of the medium in a static fermentation **(a)** and the purified BC pellicle with uniform texture **(b)**. **(c,d)** BC pellets fully filled in the medium in an agitated fermentation **(c)** and the purified BC pellets with irregular shapes.

BC pellets by distilled water to recover neutral pH value. The endotoxin in BC can also be controlled under 20 endotoxin units/device, which is acceptable as specified by the US Food and Drug Administration (FDA; Petersen and Gatenholm, 2011).

INDUSTRIAL PRODUCTION OF BC

Currently, BC has been industrially produced and widely used in diverse areas. Donini et al. estimate that the fermentation production of BC can achieve a comparable production efficiency with the growth of plant cellulose when the yield of BC reaches up to 15 g/L in 50 h (Donini et al., 2010). Moreover, the production area required for BC fermentation is much smaller than that needed for the plant growth, and the purification of BC is simple and less of pollution compared with the procedure of cellulose extraction from woods. Additionally, the agricultural and industrial wastes are commonly utilized in the commercial fermentation, which not only reduces the cost but also diminishes the waste-induced pollution (Hussain et al., 2019). Therefore, BC can be a competitive alternative for plant-based cellulose nanofibers in certain application areas.

BC-based products have gained a huge market success, especially in food areas. According to a report from ResearchMoz, the BC market is around US$ 207.36 million in 2016, and is expected to be US$ 497.76 million in 2022 and to surpass US$ 700 million in 2026 (ResearchMoz and

QYResearch, 2017). Nata de coco is so far the main commercial product of BC, which is harvested from static fermentation by using coconut water as nutrient source. It is sold in the terms of slabs and diced pieces in the market depending on the customer's requirements. The price of nata de coco is varied in a range of US$ 200–1000 per ton, which is changed among different manufacturers and is dependent on the forms and quality of final products (Ul-Islam et al., 2020). A techno-economic analysis of industrial-scale fermentation of BC has been performed using Super-Pro Designer software by Dourado et al. (2016a). The software estimated that the capital investment of an industrial manufactory to produce 504 tons of BC per year is around US$ 13 million. The manufacturing cost of BC is estimated to be US$ 7.4 million per year, and the net profit to be US$ 3.3 million per year. Although BC production is highly capital-intensive, researchers, and manufacturers have been working on the development of new ways to reduce the production cost via isolation of high yield of strains, optimization of fermentation reactors, and utilization of low-cost nutrient substrates (Ul-Islam et al., 2020).

To date, both the static and agitated fermentations have been successfully used for the industrial production of BC (**Figure 7**). The *G. xylinus* strains are employed as the main bacteria for BC production (Keshk, 2014). To reduce the cost of culture media, the food industrial wastes such as coconut water/milk and beet molasses are used as the nutrient sources (Zhong, 1996; Kusano Sakko Inc, 2020). The static fermentation is first used for the industrial production of BC, which can be early traced back to 1970s in Philippine to produce nata de coco (Iguchi et al., 2000). The nata de coco holds a series of unique properties of jelly-like morphology, cool and crisp tastes, and near-zero cholesterol (Ullah et al., 2016). Therefore, it becomes into a very popular raw food material that is widely used as dessert, additives to drinks, sauce and stuffing, and garnish to dishes (Azeredo et al., 2019). Later, the nata de coco is prevalent in Japan and other south Asian countries, which accelerates the industrial production of BC. In China, the industrial production of BC is initiated by Zhong (1996). She isolated a *G. xylinus* strain from the fermented coconut water, and then started up Hainan Yeguo Foods Co. Ltd. for production and application development of BC (Hainan Yeguo Foods Co., Ltd, 2020). The *G. xylinus* strain 323 is stored in China General Microbiological Culture Collection Center (No.1186; Zhong, 2009). They majorly adopt the static fermentation to produce BC (**Figures 7a,b**). Up to now, this company has developed into one of the biggest manufacturers for BC products in the world.

A series of problems are encountered during the industrialized process of static fermentation of BC. The optimum fermentation temperature of *G. xylinus* is around 30°C (Son et al., 2001), and thus the BC production is majorly restricted in the regions of Southeast Asia such as Philippines, Indonesia, Vietnam, and Thailand. In Hainan province of China, heating is required to maintain a high temperature for BC production in winter, which inevitably increases the energy consumption. Moreover, high temperature frequently induces microbial contamination, causing a series of issues related to food safety, production capacity, and environment pollution. To solve the problem, Zhong and co-workers utilize a low-temperature domestication method to reduce the optimum fermentation temperature of bacteria for BC production, and they successfully screen out a low-temperature resistant strain that can produce BC at 10–20°C with high yield (Zhong, 2009). This technology enables BC production to be carried out in the cold regions.

The agricultural and industrial wastes are used as nutrient sources for BC production to reduce the cost. So far, the major nutrient source for commercial production of BC has still been coconut water (Hainan Yeguo Foods Co., Ltd, 2020). Although the coconut water is once an industrial waste, the huge market demand makes it scarce, thus causing its price to rise. Zhong et al. develop a two-step fermentation method to use other raw materials instead of coconut water (Zhong, 2008b). They find the culture media previously fermented by acetic acid bacteria or lactic acid bacteria can obviously enhance the yield of BC. Therefore, they utilize the agricultural or industrial wastes such as corncob, alcohol waste liquor, pineapple peel, citrus juice, and apple juice to conduct a former fermentation and then used for BC production. This method achieves a comparable yield with the fermentation by using coconut water, thus broadening the nutrient sources for BC production.

The cost of transportation and storage of BC is very high due to its high-water holding content (∼99 wt %; Yamanaka et al., 1989). In order to low the transport and storage cost, the water in BC is reduced to ∼10 wt % through a two-step compression method followed by an organic acid dipping treatment (Zhong, 2008a). The strategy prevents the destruction of the network structure in BC, and also maintains its excellent rehydration capability (rehydration rate up to 95%). The method not only reduces the transport and storage cost of BC, but also endows BC diverse flavor as raw food materials.

The agitated fermentation has also been successfully used for industrial BC production (**Figures 7c,d**). It has been commercially exploited as a thickener and/or suspending agent especially for suspension of particles due to its unique structure with 3D reticulated network (Swazey, 2014). The raw BC after purification from agitated fermentation is full of water, which is not suitable for transport and storage. CPKelco, a global company to produce nature-based hydrocolloids, produces BC named as fermentation-derived cellulose via agitated fermentation (CPKelco Inc, 2020). Initially, a wet cake form of BC is commercially produced by CPKelco, which contains 10–20% solids and the other balance water (Swazey et al., 2013). Furthermore, dry powder forms are also exploited by adding different compound additives (Swazey, 2014). Currently, a product with the trade name of CELLULON^{TM} Cellulose Liquid is assessable in its website, which is developed as hydrocolloid for suspension of actives, decorative particles, or perfumed nanoparticles with minimal influence to the viscosity (CPKelco Inc, 2020). A Japanese company, San-Ei Gen F. F. I., Inc. also provides BC via agitated fermentation with a trade name of Sun Artist$^{@}$, which is also exploited as suspending agent majorly in food areas (San-Ei Gen, 2020). Kusano Sakko Inc., another company in Japan, has also produced BC with a trade name of Fibnano (**Figures 7c,d**; Kusano Sakko Inc, 2020). They use

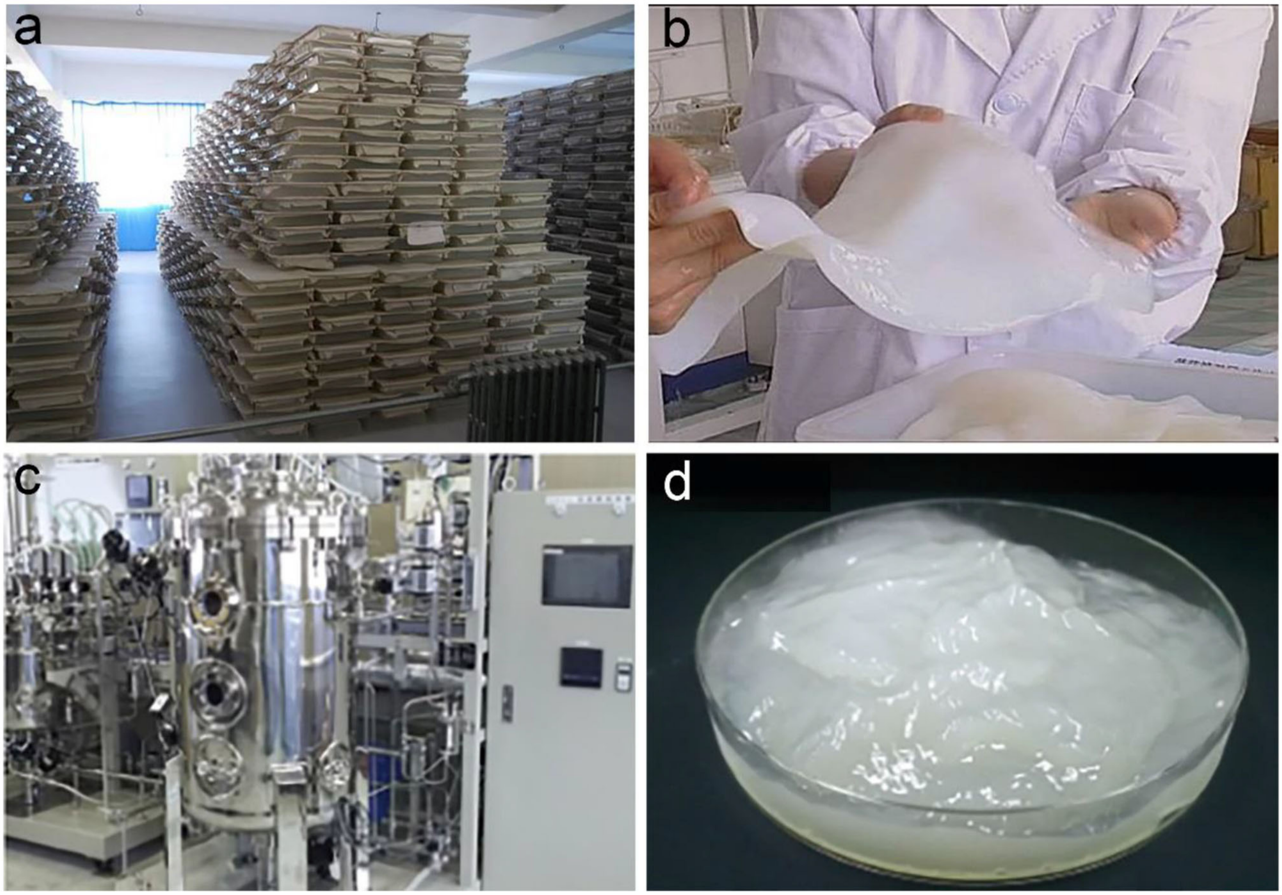

FIGURE 7 | Industrial production of BC via static and agitated fermentation. **(a,b)** Shallow tray fermentation used for industrial production of BC **(a)** and the purified BC pellicle **(b)**. Reproduced with permission from Hainan Yeguo Foods Co., Ltd (2020). **(c,d)** Agitated fermentation used for industrial production of BC **(c)** and the harvested BC slurry **(d)**. Reproduced with permission from Kusano Sakko Inc (2020).

molasses, a waste by-product in sugar industry instead of coconut water for BC fermentation, as they produce sugar by using sugar beet and sugar cane. Since 2012, they have put great effort in the production and application development of BC, and has given out various potential applications including medical care, food, personal care products, special paper, and resin filler (Kusano Sakko Inc, 2020).

APPLICATIONS OF BC

BC has been widely used in the commercial areas of food industry, personal care products, house hold chemicals, biomedicine, textile, composite materials etc. The detail of the applications in each area is described in the following sections.

APPLICATIONS IN FOOD INDUSTRY

BC has been considered as a "generally recognized as safe (GRAS)" food additives by FDA since 1992 (Shi et al., 2014). It has the potential uses in traditional dessert, low cholesterol diet, vegetarian meat, food/beverage additives, and food packaging etc. (Azeredo et al., 2019). In commercial applications, the forms and functions of BC are varied depending on the fermentation methods. BC produced from static fermentation with a jelly-like pellicle is majorly used as raw materials for food dessert and food ingredients (**Figures 8A,B**; Hainan Yeguo Foods Co., Ltd, 2020), and meanwhile BC obtained from agitated fermentation with hydrocolloid nature is exploited as thickeners and suspension agents in beverages (**Figure 8C**; San-Ei Gen, 2020). The human body lacks cellulase. Therefore, BC cannot be digested and absorbed in the gastrointestinal system, and is eliminated out of the body in the feces (Fontana et al., 2017).

The earliest application of BC in food can be dated to the 1960-1970s in Philippines (Iguchi et al., 2000). Nata de coco is praised for the high and pure fiber content, near-zero calories, and cholesterol counts (Ullah et al., 2016). Thus, it like the dietary fiber taken from daily foods to benefit the human health via reducing the risk of chronic diseases such as diabetes, obesity, and cardiovascular disease etc. (Anderson et al., 2009). Nata de coco is generally cut into cubes and pickled into different

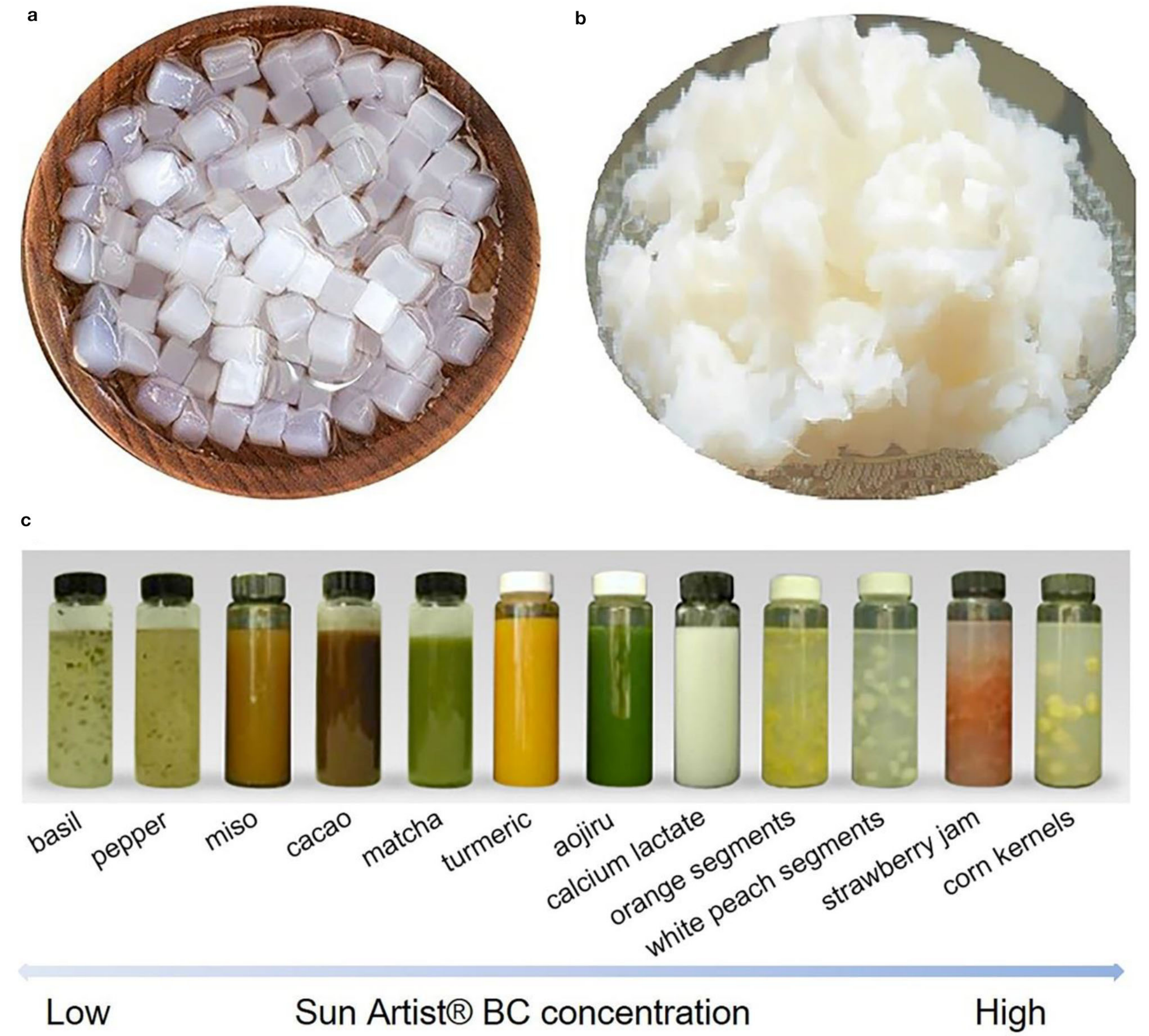

FIGURE 8 | BC particles used in food products as additives. **(a)** Cube-shaped BC obtained from static fermentation followed by cutting process, and **(b)** the compressed ones harvested via a two-step compression method. Reproduced with permission from Hainan Yeguo Foods Co., Ltd (2020). **(c)** Sun Artist® BC used for the suspension of diverse solid food ingredients with high stability. Reproduced with permission from San-Ei Gen (2020).

flavors (**Figures 8A,B**; Hainan Yeguo Foods Co., Ltd, 2020). Moreover, during the fermentation process, BC can be produced with different shapes and textures as well as diverse flavors by varying the fermentation conditions and/or the recipes of culture media, thus significantly enriching the variety of BC products (Gatenholm and Klemm, 2010). It is early enjoyed as a dessert due to the cool and smooth feeling, crunchy texture, as well as juicy taste. It is also exploited as an additive to endow the food new texture and flavor (Shi et al., 2014). Now, nata de coco can be found in a variety of foods such as drinks, yogurt, pies, sausages, and salads. It is early prevalent in Philippines, and then prevalent in Japan and other Asian countries in the 1990s (Dourado et al., 2016b).

On the other hand, BC is employed as a functional additive for the food industry. There are plenty of beverages and liquid foods that have particulate components such as milk beverages, coffee, porridge, and soybean milk, which need suspension. Generally, thickeners and surfactant agents like xanthan gum, pectin, CMC, soybean polysaccharide are added in the liquid products to suspend particulates (Dourado et al., 2016b). However, these formulations commonly represent a poor suspension stability, and are often troubled with transparency interferences and phase separation (John McArthur Swazey and Madison, 2010). Moreover, the high viscosity also causes unpleasant taste to customers. Therefore, new suspension agents with excellent dispersion stability and low viscosity are required. Under this condition, BC pellets produced by agitated fermentation are found to have the great characteristic to well fulfill the function to suspend particulates (**Figure 8C**; San-Ei Gen, 2020).

BC has a unique structure of nanofiber-weaved 3D reticulated network, which endows it excellent capability to suspend insoluble particulates with low viscosity (Swazey, 2014). It can well perform the suspension function at a low concentration, and it also works well even in the presence of high concentrations of surfactants and thickeners. Moreover, BC is suspended rather than solubilized in solution, and it is uncharged. This feature allows BC to be minimally affected by environment factors such as acidity and ionic strength (Swazey, 2014). Therefore, BC maintains the suspension capability in a wide range of pH values, and has great toleration with salts. Due to the high degree of crystallinity, BC also represents an excellent enzyme resistant (Torres et al., 2019). Finally, BC also exhibits undiminished suspension stability at a high temperature up to 80°C (San-Ei Gen, 2020). These advantages make BC a cost-effective and non-substitutable suspension agent for particulates.

To date, there are several companies such as CPKelco, San-Ei Gen, and Kusano Sakko have commercially applied BC from agitated fermentation as a suspension agent in the food areas. Originally, CPKelco commercially produces BC in the form of a wet cake typically with 10–20% solid and the other balance water (Swazey et al., 2013). In this formulation, sorbic acid is also added to prevent mold (Swazey et al., 2013). The wet cake is activated via high-speed shearing to recover the dispersed form in solution. Dry powder forms are also exploited by CPKelco with the trade name of AxCel®PX, AxCel®CG-PX, AxCel®PG, Cellulon™PX, and "K"-named series (John McArthur Swazey and Madison, 2010). These dry powder forms are generally composed of BC and one or more surfactants and/or thickeners such as xanthan gum, CMC, pectin, carrageenan etc. (Swazey, 2014). These co-agents allow BC to recover the dispersed state when meet water. However, the co-agents somehow adversely affect the suspension stability of BC, as they are commonly charged polymers. When the dry powder used in a solution with low acidic value or high ionic strength, these charged polymers may become insoluble to lose their functions, and thus inversely cause the suspension system to become unstable or non-transparent (John McArthur Swazey and Madison, 2010). The patent (John McArthur Swazey and Madison, 2010) applied by CPKelco gives out a solution method that involves a polymer degrader within the dry powder form. The polymer degraders can be enzymes, oxidizers and metal ions, which can selectively degrade the co-agents without interfering the function of BC (John McArthur Swazey and Madison, 2010). San-Ei Gen has its BC product in a liquid form with the trade name of "Sun Artist®" (San-Ei Gen, 2020). San-Ei Gen well displays the functions and applications of the Sun Artist® BC in diverse beverages and liquid foods such as basil, pepper, miso, cacao, matcha, turmeric, aojiru, calcium lactate, orange segments, white peach segments, strawberry jam, and corn kernels (**Figure 8C**; San-Ei Gen, 2020). They have also demonstrated that BC is able to prevent the sedimentation of particulates for a long period (over 1 month), and BC has an excellent resistance to acid, salt and heat (San-Ei Gen, 2020). Kusano Sakko Inc. shows that they are trying to use BC as a thickener and emulsion stabilizers in the food areas. Taken together, these commercialized applications suggest that BC has a huge market in the food industry areas (Shi et al., 2014).

FIGURE 9 | BC-based raw materials for face mask. Reproduced with permission from Hainan Yeguo Foods Co., Ltd (2020).

APPLICATION IN PERSONAL CARE PRODUCTS AND HOUSEHOLD CHEMICALS

The second large application area of BC is personal care products and household chemicals (Bianchet et al., 2020). The component materials used in personal care products should be non-toxic and biocompatible. Thus, natural product with high purity and high safety is favored by costumers. BC is a natural product generated via microbial fermentation, which has been demonstrated to be highly biocompatible (Roman, 2015). In the personal care products, BC pellicles harvested from static fermentation have been exploited as raw materials for face masks (**Figure 9**; Hainan Yeguo Foods Co., Ltd, 2020). In comparison with non-woven cellulose or silk face masks, BC-composed face masks have more excellent water holding capability and give a favorable feeling of coolness and smoothness owing to its nanoscale 3D reticulated network (Amnuaikit et al., 2011; Pacheco et al., 2018). Moreover, the highly porous microstructure allows BC to load various nutrients and even ingredients with therapeutic functions (Chantereau et al., 2020). The porous microstructure also imparts BC pellicle a function to control the release of these entrapped agents (Numata et al., 2015; Perugini et al., 2018). Based on this function, the BC-composed face masks can also be used in cosmeceuticals and treatment of mild skin diseases (Almeida et al., 2014; Morais et al., 2019).

Moreover, BC obtained from agitated fermentation also serves as a suspension agent, like the function in foods, to offer an excellent suspension stability for particulates such as decorative micro beads, encapsulated fragrance, and encapsulated enzymes etc. (Swazey and Morrison, 2015a,b). Both companies of CPKelco and Kusano Sakko have exploited their products in the applications of liquid laundry, detergent, and personal care fields (CPKelco Inc, 2020; Kusano Sakko Inc, 2020).

APPLICATION IN BIOMEDICAL AREAS

BC has great potential in diverse biomedical applications including wound dressing, artificial skin, dental implant, drug delivery, hemostatic materials, vascular grafts, scaffolds for tissue engineering, biosensor and diagnosis (Rajwade et al., 2015; Anton-Sales et al., 2019; Carvalho et al., 2019). The high purity and biocompatibility of BC are the prerequisite for all the biomedical applications. The endotoxin in BC is also well controlled under 20 endotoxin units/device, which meets the requirement of FDA for the *in vivo* usage (Petersen and Gatenholm, 2011). Moreover, BC possesses unique 3D reticulated network, which endows a series of advantages like large surface areas, excellent water holding capability, well liquid/gas permeability, remarkable mechanical properties and transparent nature (Thomas, 2008; Sulaeva et al., 2015). These distinctive characteristics make BC a very special material to demonstrate its superiority in biomedical applications. BC-based wound dressing devices have been successfully commercialized in the market, and there are also several products related to drug delivery, contact lens, vascular grafts, tympanic membrane replacement on the way of commercial transformation (Coelho et al., 2019).

Skin is the largest organ of the human body. It protects us from microorganisms, maintains body homeostasis, regulates body temperature, and feels sensations (Zhang et al., 2019). The diseased skin will lose these functions and cause severe consequences. There are diverse conditions to induce traumatic skin loss by either internal factors such as vascular disease, heart disease and diabetes, or external reasons such as accidents, suffering burn or scald and surgical operations (Vogelnest, 2017). To regenerate skin, a common treatment procedure involves a routine surgical treatment followed by complete coverage of the skin lesion by using wound dressing. An ideal wound dressing should maintain moisture of the wound lesion, eliminate exudates, allow perspiration and oxygen exchange, reduce electrolyte and protein loss, avoid infections, reduce pain, and finally accelerate wound healing (Portela et al., 2019). However, the conventional wound dressings such as gauze and synthetic materials can not satisfy these requirements.

BC is initially exploited as wound dressing due to its well moisture control, high wet tensile strength, permeability, flexibility, semitransparent nature, and great biocompatibility (Curvello et al., 2019). After the practical use, it is found that BC has a series of additional advantages including eliminating exudates meanwhile allowing perspiration and gas exchange, reducing pain and loss of electrolyte and protein, preventing infections, and accelerating wound closure (Abeer et al., 2014). These distinguished advantages give birth to BC in the market of wound dressing devices. As a result, a series of BC-based wound dressings are commercialized under the trademarks of Nanoderm™, Bionext®, Membracell®, Suprasorb® X, Biofill®, Gengiflex®, Xcell® etc. (Abeer et al., 2014). BC-based wound dressings show higher efficiency in comparison with these traditionally-used gauze or synthetic materials, and are widely used for the treatment of arterial and venous ulcers, diabetic ulcers, pressure ulcers, burns, post-operative surgical wounds, skin grafts, skin graft sites, abrasions, lacerations etc. (Portela et al., 2019). BC-based wound dressings on the market are formulated in a moisture membrane or a dry film (**Figure 10**). For instance, the Suprasorb® X wound dressing is a wet pellicle composed of 1.5–4.3% of BC and the other balance water (**Figure 10a**; Lohmann and Rauscher International GmbH & Co., 2020; Suprasorb® X + PHMB Lohmann Rauscher International, 2020), which is commercialized by a German company, Lohmann & Rauscher International. The Suprasorb® X wound dressing enables to balance the moisture in the chronic wound lesion. It absorbs fluid exudate of 20–200% its weight from exuding wound lesions, and is able to transfer moisture to dry or necrotic wound lesions by more than 75% of its weight (**Figure 10b**; Lohmann and Rauscher International GmbH & Co., 2020; Suprasorb® X Lohmann Rauscher International, 2020). Suprasorb® X wound dressing is used for the treatment of non-infected superficial or deep wounds with low to moderate levels of exudate. The indications involve arterial and venous ulcers, diabetic ulcers, pressure ulcers, superficial 2nd degree burns, post-operative surgical wounds, skin grafts and skin graft sites, abrasions, lacerations (Lohmann and Rauscher International GmbH & Co., 2020; Suprasorb® X Lohmann Rauscher International, 2020). The benefits include reducing pain, exudate management, accelerated wound healing, high wearing comfort, better cosmetic outcome, and it is also cost-effective in use due to a long dressing change interval (Lohmann and Rauscher International GmbH & Co., 2020; Suprasorb® X Lohmann Rauscher International, 2020). Furthermore, they developed an advanced wound dressing containing polyhexamethylene biguanide (PHMB), a widely-used and safe antimicrobial agent for the care of microorganism-infected wound (Lohmann and Rauscher International GmbH & Co., 2020; Suprasorb® X + PHMB Lohmann Rauscher International, 2020). Therefore, the Suprasorb® X + PHMB wound dressing is imparted with additional function of reducing infections. The Nanoderm™ wound dressing is a dry BC film developed by Axcelon Dermacare Inc. (**Figure 10c**; Axcelon Dermacare Inc, 2020). The Nanoderm™ wound dressing is accurately a semitransparent BC film with an average thickness of 0.05 mm (**Figure 10c**; Axcelon Dermacare Inc, 2020). The dry film can be stored easily without worrying about contamination and growth of mold and bacteria. It has the similar functions and benefits with the wet wound dressing, and has been widely used for treatment of skin diseases. For instance, Nanoderm™ wound dressing is used for the treatment of skin donor site, which well protects the skin-lost lesions and helps the skin regeneration in 12 days (**Figure 10e**; Axcelon Dermacare Inc, 2020). They also promoted another advanced wound dressing, Nanoderm™ Ag for the treatment of infected wounds (Axcelon Dermacare Inc, 2020). The chemically-reduced Ag nanoparticles bonded on

BC, which slowly release Ag ions to perform the antimicrobial action. Nanoderm^{TM} Ag also prolongs the interval time for dressing changes due to its antibacterial properties. Moreover, Nanoderm^{TM} series products are economical compared with the traditional wound dressing (**Figure 10d**; Axcelon Dermacare Inc, 2020).

Except commercialized wound dressing, BC also exhibits great potential in other biomedical application areas (Picheth et al., 2017; Pacheco et al., 2018). Kusano Sakko Inc. announces that they use BC as a drug carrier to deliver anticancer agent, and find that BC can improve the controlled release of drugs (Kusano Sakko Inc, 2020). In the further, they aim to use BC as a fundamental material in pharmaceuticals to improve the functions of drug delivery. Axcelon Dermacare Inc. also claims that they are developing an oral vaccine by using BC as drug carrier to maintain the activity of vaccine during transportation in stomach (Axcelon Dermacare Inc, 2020). Axcelon Dermacare Inc. also announces that they are developing several other BC-based medical devices including contact lens, vascular grafts, and artificial tympanic membranes (Axcelon Dermacare Inc, 2020). BC has also been studied a lot for the fabrication of vascular grafts (Pacheco et al., 2018). Its excellent wet mechanical strength and high biocompatibility make it an ideal candidate for vascular grafts. Jenpolymer Materials Ltd. & Co. developed vascular grafts with the trade-brand Basyc for coronary artery bypass surgery (Schumann et al., 2009; Picheth et al., 2017). Other companies like Innovatec and Axcelon Dermacare Inc. also announce their device pipeline for BC-based vascular grafts (Czaja et al., 2007; Portela et al., 2019; Axcelon Dermacare Inc, 2020).

APPLICATION IN TEXTILE

BC has also been commercially exploited as a raw material source for plant-free rayon and fabric (Huang et al., 2014). The heavy use of petroleum-based chemical fibers such as nylon, acrylon, terylene, and polypropylene has caused severe environment pollution problems due to their non-degradable nature (Wei and Zimmermann, 2017). Plant-based regenerated fibers such as rayon, cuprammonuium are generally derived from wood and cotton pulps. Although they are degradable, the pulping process generally consumes large amount of energy and causes environmental pollution as tremendous chemicals are used. Nanollose Ltd., an Australian technology company, is a pioneer that devotes to converting BC into eco-friendly fibers for textiles and other industrial applications (Nanollose Ltd, 2020). In comparison with plant cellulose, BC is easy to be purified, thus reducing the environment impacts. They have successfully converted BC into viscose-rayon fibers, providing an alternative for plant-based fibers (Nanollose Ltd, 2020). In 2018, Nanollose has collaborated with PT Supra Natami Utama, an Indonesian company, to develop a commercial scale factory to produce textile grade BC via fermentation by using coconut water (Nanollose Ltd, 2020). Nanollose transforms BC into viscose-rayon fiber, Nullarbor^{TM} fiber by using their own developed technique, which is further spun into yarn, fabric, and a garment (**Figure 11**; Nanollose Ltd, 2020). The future market of Nullarbor^{TM} fibers can be expanded in all the application areas of traditional rayon including shirts, sports, dresses, athleisure, and home furnishings (Nanollose Ltd, 2020). They denote that their plant-free viscose rayon fibers have a series of advantages in several aspects compared with plant-based fibers. In cellulose source, they use industrial wastes instead of wood pulp harvested via harsh chemical process. The fermentation process is also more efficient than plant growth in both time and land requirements. Finally, the process to produce rayon from BC fermentation is of low-energy and low-water exhausting. Taken together, it should be a promising direction for BC application that provides a sustainable alternative for plant-based rayon fibers.

APPLICATION IN COMPOSITE MATERIALS

During the fermentation process, polymers can be added into the culture media to produce BC with different physiochemical properties (Chen et al., 2011). For plant cellulose, obtaining cellulose nanofibers with different chemical and physical properties is majorly via chemical modification, which is generally a cumbersome and complicated process (Thomas et al., 2018). It is indicated that the additives such as CMC and xyloglucan not only disturb the crystal structures and aggregation of BC, but also influence on their surface chemistry and solubility (Hirai et al., 1998; Tokoh et al., 1998). This provides a route to produce BC with diverse properties. Kusano Sakko Inc. has successfully developed diverse BC with the trade name of Fibnano (Tajima et al., 2017). It is comprised of CMC, hydroxyethyl cellulose (HEC), and hydroxpropyl cellulose (HPC) decorated BC (**Figure 12**; Kusano Sakko Inc, 2020). Their results show that the CMC-decorated BC (CM-BC), HEC-decorated BC (HE-BC), and HPC-decorated BC (HP-BC) are finer nanofibers compared with native BC (**Figure 12**). The average diameter size of these modified fibers is ranged from 20 to 50 nm, which is obviously smaller than that the native BC (Tajima et al., 2017). CM-BC and HE-BC, like BC, are hydrophilic, and can be well-dispersed in water. In comparison, HP-BC is amphipathic, and thus can be dispersed in both water and organic solvents (Tajima et al., 2017). Furthermore, HP-BC can be composited into polymethyl methacrylate resin (PMMA) with high dispersion. The composite PMMA resin maintains transparency when 1 wt % HP-BC was added, while the resin composed of 1 wt % CM-BC looks foggy (**Figure 12E**; Tajima et al., 2017). The mechanical properties of HP-BC-embedded PMMA resin are also remarkably improved, representing 15% enhancement in the tensile strength (Tajima et al., 2017). The commercial case suggests that BC can be prepared into diverse types by adding polymers, nanoparticles, and other components during fermentation, and subsequently the raw materials with different physiochemical properties can be further exploited for a boarder range of applications.

CONCLUSIONS AND PERSPECTIVE

In summary, BC is bacteria-secreted bottom-up cellulose nanofibers with high purity and high crystallinity. The synthesis efficiency of BC at a high yield is comparable to that of plant cellulose via photosynthesis procedure, and the land required

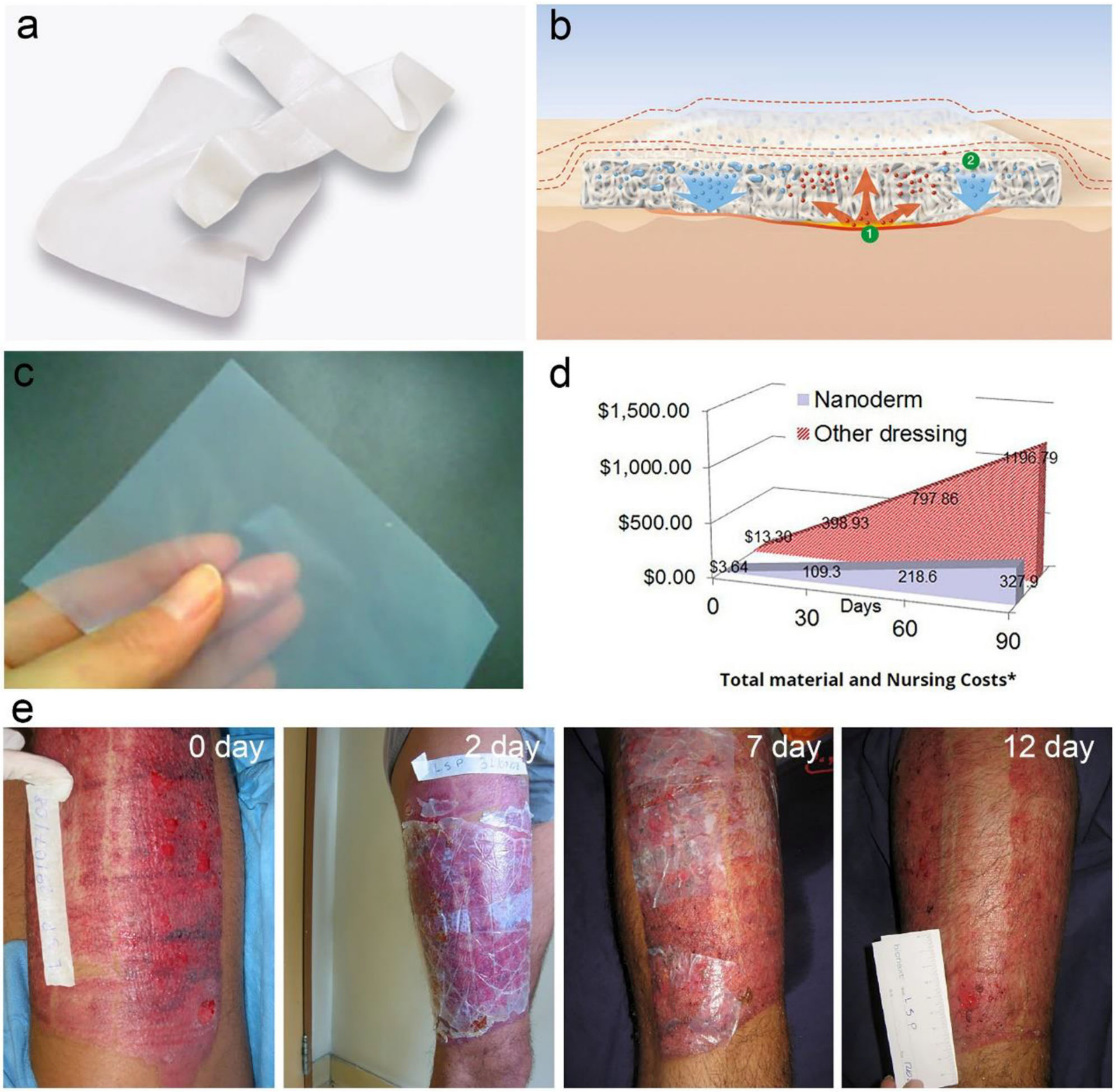

FIGURE 10 | BC-based wound dressing. **(a)** Suprasorb® X wet wound dressing composed of 1.5–4.3% BC and the other balance water. **(b)** Scheme shows Suprasorb® X wound dressing enables to absorb exudate from the wound (①) and transfer moisture to other areas with little exudate (②). Reproduced with permission from Lohmann and Rauscher International GmbH & Co., 2020, Suprasorb® X Lohmann Rauscher International (2020), and Suprasorb® X + PHMB Lohmann Rauscher International (2020). **(c)** Nanoderm™ dry wound dressing with flexible and semitransparent features. **(d)** Total material and nursing cost of Nanoderm™ wound dressing vs. regular wound dressing. Reproduced with permission from Axcelon Dermacare Inc (2020). **(e)** Nanoderm™ wound dressing applied to the skin donor site. The photographs from left to right are the initiated donor site, and 2, 7, and 12 days after treatment. Reproduced with permission from Axcelon Dermacare Inc (2020).

for the fermentation is also small than that for plant growth. Additionally, the agricultural and industrial wastes are used as nutrient sources for the fermentation, which not only reduces the cost but also alleviates the improper discard of the waste-induced environment pollutions. Structurally, BC has a unique structure with 3D reticulated network, and it is uncharged, which endows it more specific advantages such as outstanding mechanical properties, high water holding capability, excellent gas permeability, great suspension stability, low viscosity, and excellent tolerance to acid, salt and ethanol. It is also renewable, biocompatible and biodegradable. Moreover, BC with different morphologies and physiochemical properties can be produced

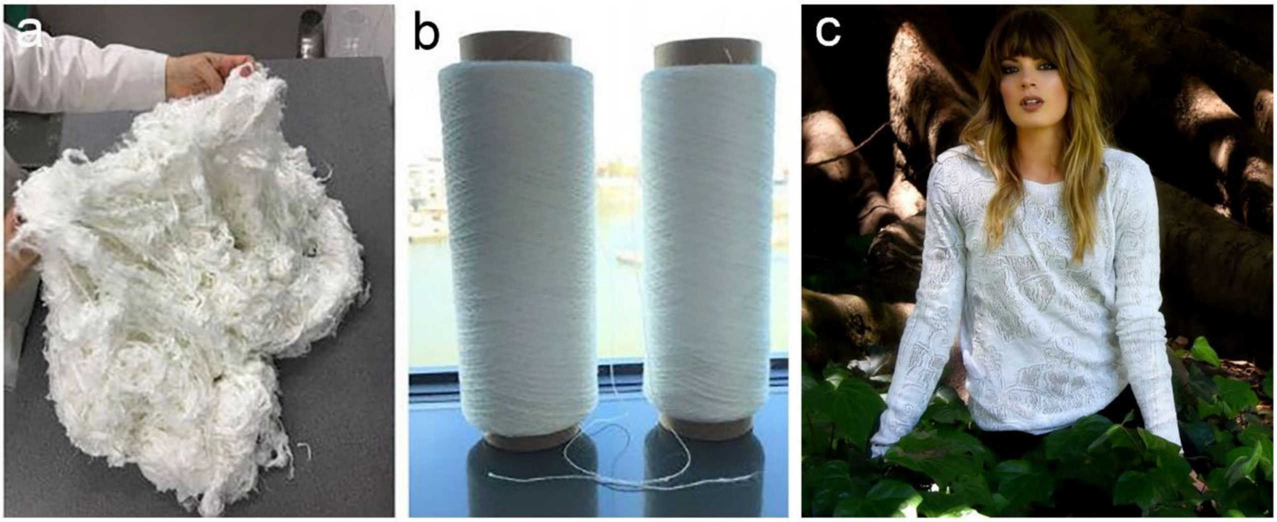

FIGURE 11 | Nanollose produced sustainable and tree-free viscose-rayon fiber, Nullarbor^{TM} fiber **(a)**, yarn **(b)**, and garment **(c)**. Reproduced with permission from Nanollose Ltd (2020).

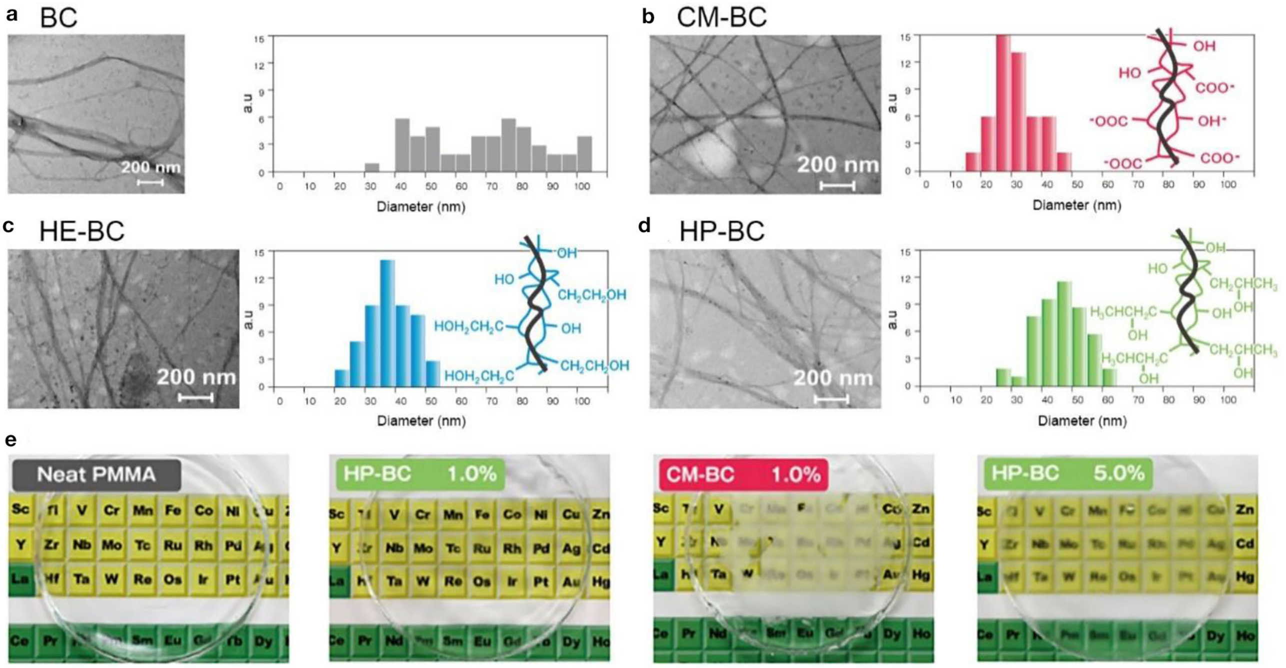

FIGURE 12 | Polymer-modified BC and their applications in composite resins. **(a)** native BC; **(b–d)** CM-BC **(b)**, HE-BC **(c)**, and HP-BC **(d)** that are produced by adding polymers during the fermentation. **(e)** PMMA resins composed of CM-BC (1.0 wt %) and HP-BC (1.0 and 5.0 wt %). Reproduced with permission from Kusano Sakko Inc (2020) and Tajima et al. (2017).

by easily adding polymers, nanoparticles and other components in the culture media. Therefore, BC is a sustainable and highly competitive alternative to plant-based cellulose nanofibers.

To date, BC has been industrially produced via both static and agitated fermentations. The commercial applications of BC have spread to diverse areas including foods, personal care products, household chemicals, biomedical areas, textiles and composite materials. In the future, BC will be applied in more and more areas. On the other hand, there are also several issues need improvement for industrial production and application development of BC. The static fermentation requires more labor and time, thus resulting in limited production capability. The production efficiency can be improved via several ways including isolation of high yield of BC-producing strains, development of new culture media and fermentation reactors, and utilization of automated equipment. The agitated fermentation can produce BC at large scale, but the non-cellulose mutation of bacteria reduces the yield of BC. Therefore, the production efficiency and the yield of BC are always needed to be improved. The cost of BC is higher than that of plant-derived cellulose nanofibers, and the industrial waste such as coconut water becomes inadequate and expensive along with the increase of marketing requirements. Therefore, new cost-effective nutrient sources such as beet molasses, liquid fermentation wastewater, and fruit juices can also be exploited for BC production. The current applications of BC are still limited. More efforts should be devoted into the exploitation of new usages of BC. The products under development announced by these companies should be well-developed. The industrial process of plant-based cellulose nanofibers is speeded up. There will be a competing relationship between BC and plant-based cellulose nanofibers in certain areas. Therefore, making good use of the advantages of BC will allow to maintain its competitiveness in the commercial market.

AUTHOR CONTRIBUTIONS

CZ designed and wrote the manuscript.

REFERENCES

Abeer, M. M., Mohd Amin, M. C., and Martin, C. (2014). A review of bacterial cellulose-based drug delivery systems: their biochemistry, current approaches and future prospects. *J. Pharm. Pharmacol.* 66, 1047–1061. doi: 10.1111/jphp.12234

Abitbol, T., Rivkin, A., Cao, Y., Nevo, Y., Abraham, E., Ben-Shalom, T., et al. (2016). Nanocellulose, a tiny fiber with huge applications. *Curr. Opin. Biotechnol.* 39, 76–88. doi: 10.1016/j.copbio.2016.01.002

Almeida, I. F., Pereira, T., Silva, N. H., Gomes, F. P., Silvestre, A. J., Freire, C. S., et al. (2014). Bacterial cellulose membranes as drug delivery systems: an *in vivo* skin compatibility study. *Eur. J. Pharm. Biopharm.* 86, 332–336. doi: 10.1016/j.ejpb.2013.08.008

Amnuaikit, T., Chusuit, T., Raknam, P., and Boonme, P. (2011). Effects of a cellulose mask synthesized by a bacterium on facial skin characteristics and user satisfaction. *Med. Devices* 4, 77–81. doi: 10.2147/MDER.S20935

Anderson, J. W., Baird, P., Davis, R. H. Jr. Ferreri, S., Knudtson, M., Koraym, A., et al. (2009). Health benefits of dietary fiber. *Nutr. Rev.* 67, 188–205. doi: 10.1111/j.1753-4887.2009.00189.x

Andrade, F. K., Silva, J. P., Carvalho, M., Castanheira, E. M. S., Soares, R., and Gama, M. (2011). Studies on the hemocompatibility of bacterial cellulose. *J. Biomed. Mater. Res. A* 98, 554–566. doi: 10.1002/jbm.a.33148

Andriani, D., Apriyana, A. Y., and Karina, M. (2020). The optimization of bacterial cellulose production and its applications: a review. *Cellulose* 27, 6747–6766. doi: 10.1007/s10570-020-03273-9

Anton-Sales, I., Beekmann, U., Laromaine, A., Roig, A., and Kralisch, D. (2019). Opportunities of bacterial cellulose to treat epithelial tissues. *Curr. Drug Targets* 20, 808–822. doi: 10.2174/1389450120666181129092144

Arena, M., Abbate, C., Fukushima, K., and Gennari, M. (2011). Degradation of poly (lactic acid) and nanocomposites by *Bacillus licheniformis*. *Environ. Sci. Pollut. Res. Int.* 18, 865–870. doi: 10.1007/s11356-011-0443-2

Axcelon Dermacare Inc (2020). Available online at: https://www.axcelondc.com/ (accessed August 20, 2020).

Aydin, Y. A., and Aksoy, N. D. (2014). Isolation and characterization of an efficient bacterial cellulose producer strain in agitated culture: *Gluconacetobacter hansenii* P2A. *Appl. Microbiol. Biotechnol.* 98, 1065–1075. doi: 10.1007/s00253-013-5296-9

Azeredo, H. M. C., Barud, H., Farinas, C. S., Vasconcellos, V. M., and Claro, A. M. (2019). Bacterial cellulose as a raw material for food and food packaging applications. *Front. Sustain. Food Syst.* 3:7. doi: 10.3389/fsufs.2019.00007

Azizi Samir, M. A., Alloin, F., and Dufresne, A. (2005). Review of recent research into cellulosic whiskers, their properties and their application in nanocomposite field. *Biomacromolecules* 6, 612–626. doi: 10.1021/bm0493685

Bianchet, R. T., Vieira Cubas, A. L., Machado, M. M., and Siegel Moecke, E. H. (2020). Applicability of bacterial cellulose in cosmetics-bibliometric review. *Biotechnol. Rep.* 27:e00502. doi: 10.1016/j.btre.2020.e00502

Brown, A. J. (1886). XLIII.-On an acetic ferment which forms cellulose. *J. Chem. Soc. Trans*. 49, 432–439. doi: 10.1039/CT8864900432

Buldum, G., Bismarck, A., and Mantalaris, A. (2018). Recombinant biosynthesis of bacterial cellulose in genetically modified *Escherichia coli*. *Bioprocess Biosyst. Eng.* 41, 265–279. doi: 10.1007/s00449-017-1864-1

Cao, Y., Lu, S., and Yang, Y. (2018). Production of bacterial cellulose from byproduct of citrus juice processing (citrus pulp) by *Gluconacetobacter hansenii*. *Cellulose* 25, 6977–6988. doi: 10.1007/s10570-018-2056-0

Carvalho, T., Guedes, G., Sousa, F. L., Freire, C. S. R., and Santos, H. A. (2019). Latest advances on bacterial cellulose-based materials for wound healing, delivery systems, and tissue engineering. *Biotechnol. J.* 14:e1900059. doi: 10.1002/biot.201900059

Chantereau, G., Sharma, M., Abednejad, A., Vilela, C., Costa, E. M., Veiga, M., et al. (2020). Bacterial nanocellulose membranes loaded with vitamin B-based ionic liquids for dermal care applications. *J. Mol. Liq.* 302:112547. doi: 10.1016/j.molliq.2020.112547

Chao, Y., Sugano, Y., and Shoda, M. (2001). Bacterial cellulose production under oxygen-enriched air at different fructose concentrations in a 50-liter, internal-loop airlift reactor. *Appl. Microbiol. Biotechnol.* 55, 673–679. doi: 10.1007/s002530000503

Chen, G., Wu, G., Alriksson, B., Chen, L., Wang, W., Jönsson, L. J., et al. (2018). Scale-up of production of bacterial nanocellulose using submerged cultivation. *J. Chem. Technol. Biotechnol.* 93, 3418–3427. doi: 10.1002/jctb.5699

Chen, H. H., Chen, L. C., Huang, H. C., and Lin, S. B. (2011). *In situ* modification of bacterial cellulose nanostructure by adding CMC during the growth of *Gluconacetobacter xylinus*. *Cellulose* 18, 1573–1583. doi: 10.1007/s10570-011-9594-z

Chen, W. S., Yu, H. P., Lee, S. Y., Wei, T., Li, J., and Fan, Z. J. (2018). Nanocellulose: a promising nanomaterial for advanced electrochemical energy storage. *Chem. Soc. Rev.* 47, 2837–2872. doi: 10.1039/c7cs00790f

Cheng, K. C., Catchmark, J. M., and Demirci, A. (2009). Effect of different additives on bacterial cellulose production by *Acetobacter xylinum* and analysis of material property. *Cellulose* 16, 1033–1045. doi: 10.1007/s10570-009-9346-5

Choi, S. M., and Shin, E. J. (2020). The nanofication and functionalization of bacterial cellulose and its applications. *Nanomaterials* 10:406. doi: 10.3390/nano10030406

Coelho, F., do Vale Braido, G. V., Cavicchioli, M., Mendes, L. S., Specian, S. S., Franchi, L. P., et al. (2019). Toxicity of therapeutic contact lenses based on bacterial cellulose with coatings to provide transparency. *Cont. Lens Anterior Eye* 42, 512–519. doi: 10.1016/j.clae.2019.03.006

CPKelco Inc (2020). Available online at: https://www.cpkelco.com/products/fermentation-derived-cellulose-fdc/ (accessed August 20, 2020).

Curvello, R., Raghuwanshi, V. S., and Garnier, G. (2019). Engineering nanocellulose hydrogels for biomedical applications. *Adv. Colloid Interface Sci.* 267, 47–61. doi: 10.1016/j.cis.2019.03.002

Czaja, W. K., Young, D. J., Kawecki, M., and Brown, R. M. (2007). The future prospects of microbial cellulose in biomedical applications. *Biomacromolecules* 8, 1–12. doi: 10.1021/bm060620d

Donini, Í. A. N., Salvi, D. T. B. D., Fukumoto, F. K., Lustri, W. R., Barud, H. S., Marchetto, R., et al. (2010). Biossíntese e recentes avanços na produção de celulose bacteriana. *Eclética Química* 35, 165–178. doi: 10.1590/S0100-46702010000400021

Dourado, F., Fontão, A., Leal, M., Cristina Rodrigues, A., and Gama, M. (2016a). "Chapter 12 - Process modeling and techno-economic evaluation of an industrial bacterial nanocellulose fermentation process," in *Bacterial Nanocellulose: From Biotechnology to Bio-economy*, eds M. Gama, F. Dourado, and S. Bielecki (Amsterdam: Elsevier), 199–214. doi: 10.1016/C2013-0-16061-8

Dourado, F., Leal, M., Martins, D., Fontão, A., Cristina Rodrigues, A., and Gama, M. (2016b). "Chapter 7 - Celluloses as food ingredients/additives: is there a room for BNC?" in *Bacterial Nanocellulose: From Biotechnology to Bio-economy,* eds M. Gama, F. Dourado, and S. Bielecki (Amsterdam: Elsevier), 123–133.

Drahushuk, A. T., Choy, C. O., Kumar, S., McReynolds, J. H., and Olson, J. R. (1997). Modulation of cytochrome P450 by 5,5'-bis-trifluoromethyl-2,2'-dichlorobiphenyl, a unique environmental contaminant. *Toxicology* 120, 197–205. doi: 10.1016/s0300-483x(97)00056-5

Fontana, J. D., Koop, H. S., Tiboni, M., Grzybowski, A., Pereira, A., Kruger, C. D., et al. (2017). "Chapter 7-New insights on bacterial cellulose," in *Food Biosynthesis-Handbook of Food Bioengineering,* eds A. M. Grumezescu and A. M. Holban (Amsterdam: Elsevier), 213–249. doi: 10.1016/B978-0-12-811372-1.00007-5

Gao, M., Li, J., Bao, Z., Hu, M., Nian, R., Feng, D., et al. (2019). A natural *in situ* fabrication method of functional bacterial cellulose using a microorganism. *Nat. Commun.* 10:437. doi: 10.1038/s41467-018-07879-3

Gatenholm, P., and Klemm, D. (2010). Bacterial nanocellulose as a renewable material for biomedical applications. *MRS Bull.* 35, 208–213. doi: 10.1557/mrs2010.653

Gorgieva, S. (2020). Bacterial cellulose as a versatile platform for research and development of biomedical materials. *Processes* 8:624. doi: 10.3390/pr8050624

Gorgieva, S., and Trcek, J. (2019). Bacterial cellulose: production, modification and perspectives in biomedical applications. *Nanomaterials* 9:1352. doi: 10.3390/nano9101352

Hainan Yeguo Foods Co., Ltd (2020). Available online at: http://www.yeguo.com (accessed August 20, 2020).

Hestrin, S., and Schramm, M. (1954). Synthesis of cellulose by *Acetobacter xylinum. II.* Preparation of freeze-dried cells capable of polymerizing glucose to cellulose. *Biochem. J.* 58, 345–352. doi: 10.1042/bj0580345

Hirai, A., Tsuji, M., Yamamoto, H., and Horii, F. (1998). *In situ* crystallization of bacterial cellulose III. Influences of different polymeric additives on the formation of microfibrils as revealed by transmission electron microscopy. *Cellulose* 5, 201–213. doi: 10.1023/A:1009233323237

Hori, R., and Wada, M. (2005). The thermal expansion of wood cellulose crystals. *Cellulose* 12, 479–484. doi: 10.1007/s10570-005-5967-5

Huang, Y., Zhu, C., Yang, J., Nie, Y., Chen, C., and Sun, D. (2014). Recent advances in bacterial cellulose. *Cellulose* 21, 1–30. doi: 10.1007/s10570-013-0088-z

Hussain, Z., Sajjad, W., Khan, T., and Wahid, F. (2019). Production of bacterial cellulose from industrial wastes: a review. *Cellulose* 26, 2895–2911. doi: 10.1007/s10570-019-02307-1

Iguchi, M., Yamanaka, S., and Budhiono, A. (2000). Bacterial cellulose-a masterpiece of nature's arts. *J. Mater. Sci.* 35, 261–270. doi: 10.1023/A:1004775229149

Im, W., Oh, K., Rajabi Abhari, A., Youn, H. J., and Lee, H. L. (2019). Recycling of isopropanol for cost-effective, environmentally friendly production of carboxymethylated cellulose nanofibrils. *Carbohydr. Polym.* 208, 365–371. doi: 10.1016/j.carbpol.2018.12.093

Islam, M. U., Ullah, M. W., Khan, S., Shah, N., and Park, J. K. (2017). Strategies for cost-effective and enhanced production of bacterial cellulose. *Int. J. Biol. Macromol.* 102 1166–1173. doi: 10.1016/j.ijbiomac.2017.04.110

Isogai, A., Saito, T., and Fukuzumi, H. (2011). TEMPO-oxidized cellulose nanofibers. *Nanoscale* 3, 71–85. doi: 10.1039/c0nr00583e

John McArthur Swazey, J., and Madison, N. (2010). *Methods of Improve the Compatibility and Efficiency of Powdered Versions of Microbirous Cellulose.* U.S. Patent No 2011/0,059,883 A1. Washington, DC: U.S. Patent and Trademark Office.

Jonas, R., and Farah, L. F. (1998). Production and application of microbial cellulose. *Polym. Degrad. Stabil.* 59, 101–106. doi: 10.1016/S0141-3910(97)00197-3

Jozala, A. F., de Lencastre-Novaes, L. C., Lopes, A. M., de Carvalho Santos-Ebinuma, V., Mazzola, P. G., Pessoa, A., et al. (2016). Bacterial nanocellulose production and application: a 10-year overview. *Appl. Microbiol. Biotechnol.* 100, 2063–2072. doi: 10.1007/s00253-015-7243-4

Julia, A., Andrea, C., Cláudio, G., Gloria, V., Emilia, S., and Leonie, S. (2019). Bacterial cellulose production using industrial fruit residues as subtract to industrial application. *Chem. Eng. Trans.* 74, 1165–1170. doi: 10.3303/CET1974195

Keshk, S. M. A. S. (2014). Bacterial cellulose production and its industrial applications. *J. Bioprocess. Biotechnol.* 4:1000150. doi: 10.4172/2155-9821.1000150

Keshk, S. M. A. S., and Sameshima, K. (2005). Evaluation of different carbon sources for bacterial cellulose production. *Afr. J. Biotechnol.* 4, 478–482. doi: 10.5897/AJB2005.000-3087

Kim, Y., Ullah, M. W., Ul-Islam, M., Khan, S., Jang, J. H., and Park, J. K. (2019). Self-assembly of bio-cellulose nanofibrils through intermediate phase in a cell-free enzyme system. *Biochem. Eng. J.* 142, 135–144. doi: 10.1016/j.bej.2018.11.017

Kimura, S., Chen, H. P., Saxena, I. M., Brown, R. M., and Itoh, T. (2001). Localization of c-di-GMP-binding protein with the linear terminal complexes of *Acetobacter xylinum*. *J. Bacteriol.* 183, 5668–5674. doi: 10.1128/JB.183.19.5668-5674.2001

Klemm, D., Cranston, E. D., Fischer, D., Gama, M., Kedzior, S. A., Kralisch, D., et al. (2018). Nanocellulose as a natural source for groundbreaking applications in materials science: Today's state. *Mater. Today* 21, 720–748. doi: 10.1016/j.mattod.2018.02.001

Klemm, D., Kramer, F., Moritz, S., Lindstrom, T., Ankerfors, M., Gray, D., et al. (2011). Nanocelluloses: a new family of nature-based materials. *Angew. Chem. Int. Ed. Engl.* 50, 5438–5466. doi: 10.1002/anie.2010 01273

Kongruang, S. (2008). Bacterial cellulose production by *Acetobacter xylinum* strains from agricultural waste products. *Appl. Biochem. Biotechnol.* 148, 45–256. doi: 10.1007/s12010-007-8119-6

Kose, R., Mitani, I., Kasai, W., and Kondo, T. (2011). Nanocellulose as a single nanofiber prepared from pellicle secreted by *Gluconacetobacter xylinus* using aqueous counter collision. *Biomacromolecules* 12, 716–720. doi: 10.1021/bm1013469

Krasteva, P. V., Bernal-Bayard, J., Travier, L., Martin, F. A., Kaminski, P. A., Karimova, G., et al. (2017). Insights into the structure and assembly of a bacterial cellulose secretion system. *Nat. Commun.* 8, 65. doi: 10.1038/s41467-017-01523-2

Krystynowicz, A., Czaja, W., Wiktorowska-Jezierska, A., Goncalves-Miskiewicz, M., Turkiewicz, M., and Bielecki, S. (2002). Factors affecting the yield and properties of bacterial cellulose. *J. Ind. Microbiol. Biotechnol.* 29, 189–195. doi: 10.1038/sj.jim.7000303

Kusano Sakko Inc (2020). Available online at: https://www.kusanosk.co.jp/lab/2016 (accessed August 20, 2020).

Li, Y., Tian, J., Tian, H., Chen, X., Ping, W., Tian, C., et al. (2016). Mutation-based selection and analysis of *Komagataeibacter hansenii* HDM1-3 for improvement in bacterial cellulose production. *J. Appl. Microbiol.* 121, 1323–1334. doi: 10.1111/jam.13244

Liu, W., Du, H. S., Zhang, M. M., Liu, K., Liu, H. Y., Xie, H. X., et al. (2020). Bacterial cellulose-based composite scaffolds for biomedical applications: a review. *Acs Sustain. Chem. Eng.* 8, 7536–7562. doi: 10.1021/acssuschemeng.0c00125

Lohmann and Rauscher International GmbH & Co. (2020). Available online at: https://www.lohmann-rauscher.com (accessed August 20, 2020).

Mariani, V., Gilles, S., Jakob, T., Thiel, M., Mueller, M. J., Ring, J., et al. (2007). Immunomodulatory mediators from pollen enhance the migratory capacity of dendritic cells and license them for Th2 attraction. *J. Immunol.* 178, 7623–7631. doi: 10.4049/jimmunol.178.12.7623

Mohammadkazemi, F., Azin, M., and Ashori, A. (2015). Production of bacterial cellulose using different carbon sources and culture media. *Carbohydr. Polym.* 117, 518–523. doi: 10.1016/j.carbpol.2014.10.008

Mokhena, T. C., and John, M. J. (2020). Cellulose nanomaterials: new generation materials for solving global issues. *Cellulose* 27, 1149–1194. doi: 10.1007/s10570-019-02889-w

Moniri, M., Moghaddam, A. B., Azizi, S., Rahim, R. A., Bin Ariff, A., Saad, W. Z., et al. (2017). Production and status of bacterial cellulose in biomedical engineering. *Nanomaterials* 7:257. doi: 10.3390/nano7090257

Moon, R. J., Martini, A., Nairn, J., Simonsen, J., and Youngblood, J. (2011). Cellulose nanomaterials review: structure, properties and nanocomposites. *Chem. Soc. Rev.* 40, 941–3994. doi: 10.1039/c0cs00108b

Morais, E. S., Silva, N., Sintra, T. E., Santos, S. A. O., Neves, B. M., Almeida, I. F., et al. (2019). Anti-inflammatory and antioxidant nanostructured cellulose membranes loaded with phenolic-based ionic liquids for cutaneous application. *Carbohydr. Polym.* 206, 87–197. doi: 10.1016/j.carbpol.2018.10.051

Nanollose Ltd (2020). Available online at: https://nanollose.com (accessed August 20, 2020).

Nishiyama, Y., Johnson, G. P., French, A. D., Forsyth, V. T., and Langan, P. (2008). Neutron crystallography, molecular dynamics, and quantum mechanics studies of the nature of hydrogen bonding in cellulose Iβ. *Biomacromolecules* 9, 3133–3140. doi: 10.1021/bm800726v

Noguchi, Y., Homma, I., and Watanabe, T. (2020). Properties of phosphorylated cellulose nanofiber dispersions under various conditions. *Cellulose* 27, 2029–2040. doi: 10.1007/s10570-019-02922-y

Numata, Y., Mazzarino, L., and Borsali, R. (2015). A slow-release system of bacterial cellulose gel and nanoparticles for hydrophobic active ingredients. *Int. J. Pharm.* 486, 217–225. doi: 10.1016/j.ijpharm.2015.03.068

O'Sullivan, A. C. (1997). Cellulose: the structure slowly unravels. *Cellulose* 4, 173–207. doi: 10.1023/A:1018431705579

Pacheco, G., de Mello, C. V., Chiari-Andreo, B. G., Isaac, V. L. B., Ribeiro, S. J. L., Pecoraro, E., et al. (2018). Bacterial cellulose skin masks-properties and sensory tests. *J. Cosmet. Dermatol.* 17, 840–847. doi: 10.1111/jocd.12441

Pang, M. J., Huang, Y. H., Meng, F. S., Zhuang, Y., Liu, H., Du, M. L., et al. (2020). Application of bacterial cellulose in skin and bone tissue engineering. *Eur. Polym. J.* 122, 109365. doi: 10.1016/j.eurpolymj.2019.109365

Perugini, P., Bleve, M., Cortinovis, F., and Colpani, A. (2018). Biocellulose masks as delivery systems: a novel methodological approach to assure quality and safety. *Cosmetics* 5:66. doi: 10.3390/cosmetics5040066

Petersen, N., and Gatenholm, P. (2011). Bacterial cellulose-based materials and medical devices: current state and perspectives. *Appl. Microbiol. Biotechnol.* 91, 1277–1286. doi: 10.1007/s00253-011-3432-y

Picheth, G. F., Pirich, C. L., Sierakowski, M. R., Woehl, M. A., Sakakibara, C. N., de Souza, C. F., et al. (2017). Bacterial cellulose in biomedical applications: a review. *Int. J. Biol. Macromol.* 104, 7–106. doi: 10.1016/j.ijbiomac.2017.05.171

Pogorelova, N., Rogachev, E., Digel, I., Chernigova, S., and Nardin, D. (2020). Bacterial cellulose nanocomposites: morphology and mechanical properties. *Materials* 13:2849. doi: 10.3390/ma13122849

Portela, R., Leal, C. R., Almeida, P. L., and Sobral, R. G. (2019). Bacterial cellulose: a versatile biopolymer for wound dressing applications. *Microb. Biotechnol.* 12, 586–610. doi: 10.1111/1751-7915.13392

Rajwade, J. M., Paknikar, K. M., and Kumbhar, J. V. (2015). Applications of bacterial cellulose and its composites in biomedicine. *Appl. Microbiol. Biotechnol.* 99, 2491–2511. doi: 10.1007/s00253-015-6426-3

Reiniati, I., Hrymak, A. N., and Margaritis, A. (2017). Recent developments in the production and applications of bacterial cellulose fibers and nanocrystals. *Crit. Rev. Biotechnol.* 37, 510–524. doi: 10.1080/07388551.2016.1189871

ResearchMoz and QYResearch (2017). Available online at: https://www.researchmoz.us/globalmicrobial-and-bacterial-cellulose-market-research-report-2017-report.html.

Rivas, B., Moldes, A. B., Dominguez, J. M., and Parajo, J. C. (2004). Development of culture media containing spent yeast cells of *Debaryomyces hansenii* and corn steep liquor for lactic acid production with *Lactobacillus rhamnosus*. *Int. J. Food Microbiol.* 97, 93–98. doi: 10.1016/j.ijfoodmicro.2004.05.006

Roman, M. (2015). Toxicity of cellulose nanocrystals: a review. *Ind. Biotechnol.* 11, 25–33. doi: 10.1089/ind.2014.0024

Romling, U., and Galperin, M. Y. (2015). Bacterial cellulose biosynthesis: diversity of operons, subunits, products, and functions. *Trends Microbiol.* 23, 545–557. doi: 10.1016/j.tim.2015.05.005

Ross, P., Mayer, R., and Benziman, M. (1991). Cellulose biosynthesis and function in bacteria. *Microbiol. Rev.* 55, 35–58.

Ruan, C., Zhu, Y., Zhou, X., Abidi, N., Hu, Y., and Catchmark, J. M. (2016). Effect of cellulose crystallinity on bacterial cellulose assembly. *Cellulose* 23, 3417–3427. doi: 10.1007/s10570-016-1065-0

Ruka, D. R., Simon, G. P., and Dean, K. (2014). Harvesting fibrils from bacterial cellulose pellicles and subsequent formation of biodegradable poly-3-hydroxybutyrate nanocomposites. *Cellulose* 21, 4299–4308. doi: 10.1007/s10570-014-0415-z

San-Ei Gen F.F.I., Inc (2020). Available online at: https://www.saneigenffi.co.jp/closeup/san.html (accessed August 20, 2020).

Sani, A., and Dahman, Y. (2010). Improvements in the production of bacterial synthesized biocellulose nanofibres using different culture methods. *J. Chem. Technol. Biotechnol.* 85, 151–164. doi: 10.1002/jctb.2300

Schumann, D. A., Wippermann, J., Klemm, D. O., Kramer, F., Koth, D., Kosmehl, H., et al. (2009). Artificial vascular implants from bacterial cellulose: preliminary results of small arterial substitutes. *Cellulose* 16, 877–885. doi: 10.1007/s10570-008-9264-y

Shi, Z., Zhang, Y., Phillips, G. O., and Yang, G. (2014). Utilization of bacterial cellulose in food. *Food Hydrocoll.* 35, 539–545. doi: 10.1016/j.foodhyd.2013.07.012

Sijabat, E. K., Nuruddin, A., Aditiawati, P., and Sunendar Purwasasmita, B. (2020). Optimization on the synthesis of bacterial nano cellulose (BNC) from banana peel waste for water filter membrane applications. *Mater. Res. Express* 7:055010. doi: 10.1088/2053-1591/ab8df7

Singhsa, P., Narain, R., and Manuspiya, H. (2018). Physical structure variations of bacterial cellulose produced by different *Komagataeibacter xylinus* strains and carbon sources in static and agitated conditions. *Cellulose* 25, 1571–1581. doi: 10.1007/s10570-018-1699-1

Son, H. J., Heo, M. S., Kim, Y. G., and Lee, S. J. (2001). Optimization of fermentation conditions for the production of bacterial cellulose by a newly isolated Acetobacter sp. A9 in shaking cultures. *Biotechnol. Appl. Biochem.* 33, 1–5. doi: 10.1042/ba20000065

Sulaeva, I., Henniges, U., Rosenau, T., and Potthast, A. (2015). Bacterial cellulose as a material for wound treatment: properties and modifications. *A review. Biotechnol. Adv.* 33, 1547–1571. doi: 10.1016/j.biotechadv.2015.07.009

Suprasorb® X + PHMB and Lohmann and Rauscher International (2020). Available online at: https://www.lohmann-rauscher.com/en/products/wound-care/modern-wound-care/suprasorb-x-phmb/ (accessed August 20, 2020).

Suprasorb® X and Lohmann and Rauscher International (2020). Available online at: https://www.lohmann-rauscher.com/en/products/wound-care/modern-wound-care/suprasorb-x/ (accessed August 20, 2020).

Swazey, J., Morrison, N., Yang, Z. F., Compton, J., and Nolan, T. (2013). *Microfibrous Cellulose Composition Comprising Fermentation Media and Surfactant*. U.S. Patent No 10,292,927 B2. Washington, DC: U.S. Patent and Trademark Office.

Swazey, J. M. (2014). *Surfactant Thickened Systems Comprising Microfibrous Cellulose and Methods of Making Same*. U.S. Patent No 8,772,359 B2. Washington, DC: U.S. Patent and Trademark Office.

Swazey, J. M., and Morrison, N. A. (2015a). *Liquid Detergents Comprising Microfibrous Cellulose and Methods of Making the Same*. U.S. Patent No 10,214,708 B2. Washington, DC: U.S. Patent and Trademark Office.

Swazey, J. M., and Morrison, N. A. (2015b). *Personal Care Products Comprising Microfibrous Cellulose and Methods of Making the Same*. U.S. Patent No 10,030,214 B2. Washington, DC: U.S. Patent and Trademark Office.

Tabuchi, M., Watanabe, K., Morinaga, Y., and Yoshinaga, F. (1998). Acetylation of bacterial cellulose: preparation of cellulose acetate having a high degree of polymerization. *Biosci. Biotechnol. Biochem.* 62, 1451–1454. doi: 10.1271/bbb.62.1451

Tahara, N., Tabuchi, M., Watanabe, K., Yano, H., Morinaga, Y., and Yoshinaga, F. (1997). Degree of polymerization of cellulose from *Acetobacter xylinum* BPR2001 decreased by cellulase produced by the strain. *Biosci. Biotechnol. Biochem.* 61, 1862–1865. doi: 10.1271/bbb.61.1862

Tajima, K., Kusumoto, R., Kose, R., Kono, H., Matsushima, T., Isono, T., et al. (2017). One-step production of amphiphilic nanofibrillated cellulose using a cellulose-producing bacterium. *Biomacromolecules* 18, 3432–3438. doi: 10.1021/acs.biomac.7b01100

Thomas, B., Raj, M. C., Athira, K. B., Rubiyah, M. H., Joy, J., Moores, A., et al. (2018). Nanocellulose, a versatile green platform: from biosources to materials and their applications. *Chem. Rev.* 118, 11575–11625. doi: 10.1021/acs.chemrev.7b00627

Thomas, S. (2008). A review of the physical, biological and clinical properties of a bacterial cellulose wound dressing. *J. Wound Care* 17, 349–352. doi: 10.12968/jowc.2008.17.8.30798

Tokoh, C., Takabe, K., Fujita, M., and Saiki, H. (1998). Cellulose synthesized by *Acetobacter xylinum* in the presence of acetyl glucomannan. *Cellulose* 5, 249–261. doi: 10.1023/A:1009211927183

Torres, F. G., Arroyo, J. J., and Troncoso, O. P. (2019). Bacterial cellulose nanocomposites: an all-nano type of material. *Mater. Sci. Eng. C. Mater. Biol. Appl.* 98, 1277–1293. doi: 10.1016/j.msec.2019.01.064

Torres, F. G., Commeaux, S., and Troncoso, O. P. (2012). Biocompatibility of bacterial cellulose based biomaterials. *J. Funct. Biomater.* 3, 864–878. doi: 10.3390/jfb3040864

Ul-Islam, M., Khan, S., Ullah, M. W., and Park., J. K. (2019). Comparative study of plant and bacterial cellulose pellicles regenerated from dissolved states. *Int. J. Biol. Macromol.* 137, 247–252. doi: 10.1016/j.ijbiomac.2019.06.232

Ul-Islam, M., Ullah, M. W., Khan, S., and Park, J. K. (2020). Production of bacterial cellulose from alternative cheap and waste resources: a step for cost reduction with positive environmental aspects. *Korean J. Chem. Eng.* 37, 925–937. doi: 10.1007/s11814-020-0524-3

Ullah, H., Santos, H. A., and Khan, T. (2016). Applications of bacterial cellulose in food, cosmetics and drug delivery. *Cellulose* 23, 2291–2314. doi: 10.1007/s10570-016-0986-y

Ullah, M. W., Ul-Islam, M., Khan, S., Kim, Y., and Park, J. K. (2015). Innovative production of bio-cellulose using a cell-free system derived from a single cell line. *Carbohydr. Polym.* 132, 286–294. doi: 10.1016/j.carbpol.2015.06.037

VanderHart, D. L., and Atalla, R. (1984). Studies of microstructure in native celluloses using solid-state carbon-13 NMR. *Macromolecules* 17, 1465–1472. doi: 10.1021/ma00138a009

Velásquez-Riaño, M., and Bojacá, V. (2017). Production of bacterial cellulose from alternative low-cost substrates. *Cellulose* 24, 2677–2698. doi: 10.1007/s10570-017-1309-7

Vogelnest, L. J. (2017). Skin as a marker of general feline health: cutaneous manifestations of systemic disease. *J. Feline Med. Surg.* 19, 948–960. doi: 10.1177/1098612X17723246

Watanabe, A., Morita, S., and Ozaki, Y. (2007). Temperature-dependent changes in hydrogen bonds in cellulose Iα studied by infrared spectroscopy in combination with perturbation-correlation moving-window two-dimensional correlation spectroscopy: comparison with cellulose Iβ. *Biomacromolecules* 8, 2969–2975. doi: 10.1021/bm700678u

Watanabe, K., Tabuchi, M., Morinaga, Y., and Yoshinaga, F. (1998). Structural features and properties of bacterial cellulose produced in agitated culture. *Cellulose* 5, 187–200. doi: 10.1023/A:1009272904582

Wei, R., and Zimmermann, W. (2017). Microbial enzymes for the recycling of recalcitrant petroleum-based plastics: how far are we? *Microb. Biotechnol.* 10, 1308–1322. doi: 10.1111/1751-7915.12710

Wu, J. M., and Liu, R. H. (2013). Cost-effective production of bacterial cellulose in static cultures using distillery wastewater. *J. Biosci. Bioeng.* 115, 284–290. doi: 10.1016/j.jbiosc.2012.09.014

Yamada, Y., Yukphan, P., Lan Vu, H. T., Muramatsu, Y., Ochaikul, D., Tanasupawat, S., et al. (2012). Description of *Komagataeibacter* gen. nov., with proposals of new combinations (Acetobacteraceae). *J. Gen. Appl. Microbiol.* 58, 397–404. doi: 10.2323/jgam.58.397

Yamamoto, H., Horii, F., and Hirai, A. (1996). *In situ* crystallization of bacterial cellulose II. Influences of different polymeric additives on the formation of celluloses Iα and Iβ at the early stage of incubation. *Cellulose* 3, 229–242. doi: 10.1007/BF02228804

Yamamoto, H., and Horn, F. (1994). *In situ* crystallization of bacterial cellulose I. Influences of polymeric additives, stirring and temperature on the formation celluloses Iα and Iβ as revealed by cross polarization/magic angle spinning (CP/MAS)13C NMR spectroscopy. *Cellulose* 1, 57–66. doi: 10.1007/BF00818798

Yamanaka, S., and Sugiyama, J. (2000). Structural modification of bacterial cellulose. *Cellulose* 7, 213–225. doi: 10.1023/A:1009208022957

Yamanaka, S., Watanabe, K., Kitamura, N., Iguchi, M., Mitsuhashi, S., Nishi, Y., et al. (1989). The structure and mechanical properties of sheets prepared from bacterial cellulose. *J. Mater. Sci.* 24, 3141–3145. doi: 10.1007/BF01139032

Yang, Y., Jia, J., Xing, J., Chen, J., and Lu, S. (2013). Isolation and characteristics analysis of a novel high bacterial cellulose producing strain *Gluconacetobacter intermedius* CIs26. *Carbohydr. Polym.* 92, 2012–2017. doi: 10.1016/j.carbpol.2012.11.065

Yuan, H., Chen, L., Hong, F. F., and Zhu, M. (2018). Evaluation of nanocellulose carriers produced by four different bacterial strains for laccase immobilization. *Carbohydr. Polym.* 196, 457–464. doi: 10.1016/j.carbpol.2018.05.055

Zhang, X. J., Wang, A. P., Shi, T. Y., Zhang, J., Xu, H., Wang, D. Q., et al. (2019). The psychosocial adaptation of patients with skin disease: a scoping review. *BMC Public Health* 19:1404. doi: 10.1186/s12889-019-7775-0

Zhong, C. (1996). *Method for Edible Fiber Product by Fermentation of Coconut Juice*.Chinese patent No: CN1066926C. Haikou: China National Intellectual Property Administration.

Zhong, C. (2008a).*Compressed Coconut and Method of Preparing the Same*. Chinese patent No: CN101278737A. Haikou: China National Intellectual Property Administration.

Zhong, C. (2008b). *Production of Edible Cellulose by Two-Step Method*. Chinese patent No: CN101265489A. Haikou: China National Intellectual Property Administration.

Zhong, C. (2009). *Gluconacetobacter oboediens Strain and Method for Breeding and Producing Bacteria cellulose Thereof*. Chinese patent No: CN101608167. Haikou: China National Intellectual Property Administration.

Zhong, C., Zhang, G. C., Liu, M., Zheng, X. T., Han, P. P., and Jia, S. R. (2013). Metabolic flux analysis of *Gluconacetobacter xylinus* for bacterial cellulose production. *Appl. Microbiol. Biotechnol.* 97, 6189–6199. doi: 10.1007/s00253-013-4908-8

Conflict of Interest: CZ is employed by company Hainan Yeguo Foods Co. Ltd., Hainan, China.

frontiers
in Bioengineering and Biotechnology

ORIGINAL RESEARCH
published: 28 January 2021
doi: 10.3389/fbioe.2021.606008

Refractive Index Change of Cellulose Nanocrystal-Based Electroactive Polyurethane by an Electric Field

*Jaehwan Kim**, Hyun-U Ko and Hyun Chan Kim*

Department of Mechanical Engineering, Creative Research Center for Nanocelluose Future Composites, Incheon, South Korea

A tunable optical lens can tune or reconfigure the lens material itself such that it can eliminate the moving part of the lens, which brings broad technological impacts. Many tunable optical lenses have been implemented using electroactive polymers that can change the shape of the lens. However, the refractive index (RI) change of electroactive polymers has not been well investigated. This paper investigated the RI change of CNC-based transparent and electroactive polyurethane (CPPU) in the presence of an actuating electric field. The prepared CPPU was electrically poled to enhance its electro-optical performance, and the poling conditions in terms of frequency and electric field were optimized. The poled CPPU was characterized using a Fourier transform infrared spectroscopy and a refractometer. To investigate the RI change in the presence of an actuating electric field, the poled CPPU was constrained between two electrodes with a fixed distance. The RI linearly increased as the actuating electric field increased. The RI change mechanism and the optimized poling conditions are illustrated. The tunable RI is a promising property for implementing a tunable optical lens.

Keywords: electroactive polymer actuator, cellulose nanocrystal, tunable lens, refractive index, polyurethane

Edited by:
Muhammad Wajid Ullah,
Huazhong University of Science and Technology, China

Reviewed by:
Jayaramudu Tippabattini,
University of Talca, Chile
Ajay Devidas Padsalgikar,
DSM, United States

****Correspondence:***
Jaehwan Kim
jaehwan@inha.ac.kr

Specialty section:
This article was submitted to Biomaterials, a section of the journal Frontiers in Bioengineering and Biotechnology

Received: *14 September 2020*
Accepted: *06 January 2021*
Published: *28 January 2021*

Citation:
Kim J, Ko H-U and Kim HC (2021) Refractive Index Change of Cellulose Nanocrystal-Based Electroactive Polyurethane by an Electric Field. Front. Bioeng. Biotechnol. 9:606008. doi: 10.3389/fbioe.2021.606008

INTRODUCTION

A tunable optical lens can change the focal distance and refractive index, optical angle, and optical intensity by tuning or reconfiguring the lens material itself (Choi et al., 2017; Ghilardi et al., 2019). **Figure 1** shows the concept of a tunable optical lens. A tunable optical lens can eliminate the moving part of a lens, which has a broad technological impact in the industry, military, and consumer products applications such as camera lenses, endoscopes, projectors, membrane optics, telescopes, spectroscopes, and flat-panel displays, etc.

There are two distinct ideas to implement a tunable optical lens by changing the shape of the lens and tuning the refractive index (RI) of the lens material. Shape change of lens materials has been studied in electroactive polymers (EAP) and soft actuator materials (Kim J. et al., 2019). The electrical response, lightweight, and high energy density of EAP make them suitable for biomimetic actuators, soft robots, and optical lenses (Mirfakhrai et al., 2007). There are many available EAPs for tunable optical lens applications such as thermo-responsive polymers (Kim J. et al., 2019), hydrogels (Jayaramudu et al., 2016, 2017), and dielectric elastomer (DE). DE, a kind of EAP, attracts much interest due to its impressive electroactive strain, mechanical robustness, and inexpensive and affordable high energy density, although large operation voltage over is its critical disadvantage (O'Halloran et al., 2008; Zurlo and Destrade, 2017). However, in realizing the tunable optical lens,

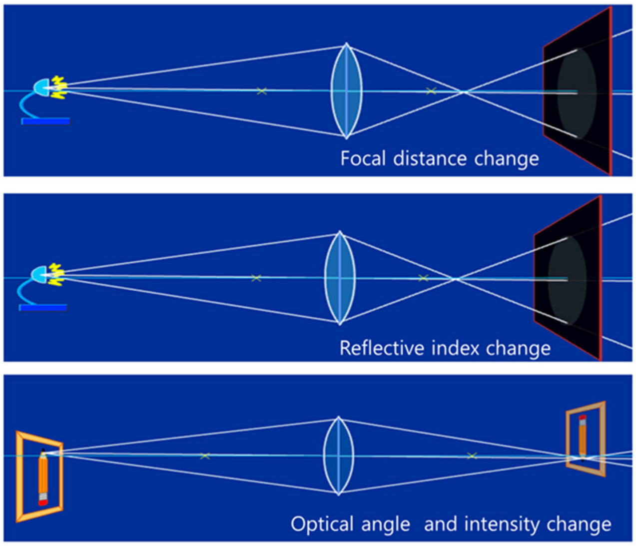

FIGURE 1 | Concepts of a tunable optical lens by focal distance change, refractive index change, and optical angle and intensity change (Choi et al., 2017, republished from IOP).

lens material's actuation performance against repetitive deformation and miniaturization should be carefully considered. Another consideration is the lens material should maintain its transparency from repeated light exposure and actuation. The dielectric property improvement of DE is critical to improving its actuation performance (Romasanta et al., 2015). The dielectric property of DE can be enhanced by blending high dielectric fillers or conductive fillers with dielectric elastomers with different mechanical and dielectric properties (Park et al., 2007; Gallone et al., 2010). However, the choice of dielectric fillers for DE in tunable optical lens research is limited because they should be transparent.

Cellulose nanocrystal (CNC) has been used as fillers of DE actuators and optoelectronics (Giese and Spengler, 2019; Wang et al., 2019). A new strategy was reported to achieve a transparent and reconfigurable actuator by using a DE actuator. Cellulose is a well known and abundant biopolymer globally, which consists of a crystal region and amorphous region. The crystal region, so-called cellulose nanocrystal (CNC), has remarkable advantages such as high mechanical specific strength, biocompatibility, nanoscale dimension, and sustainability (Habibi et al., 2010; Moon et al., 2011; Kim et al., 2015; Vanderfleet and Cranston, 2020; Wang et al., 2020). Typically CNC has lengths of 100–200 nm and cross-sections of 5–20 nm. CNC has been actively studied for many applications, including structural nanocomposites, optical films, and bio-composites. One fascinating property of CNC is its electrical and magnetic polarity (Pullawan et al., 2012). Due to its polarity, CNC can be the right candidate for improving its dielectric property of DE by blending it with polymeric materials without sacrificing polymers' optical transparency. The significance of biodegradable and transparent behaviors of CNC-polymer nanocomposites has been investigated in electronics, optics, and biomedical engineering (Siqueira et al., 2010). Recently, CNC-based transparent and electroactive polyurethane (CPPU) was reported, which is applicable for an actively tunable optical lens (Sadasivuni et al., 2016; Ko et al., 2017). CNC was used for high dielectric filler to improve the electromechanical behavior of CPPU. To achieve good transparency and a homogeneous distribution of CNC in polyurethane, CNC- Poly[di(ethylene glycol) adipate] (PDEGA) was used to play as a polyol. The fabricated CPPU exhibited high transparency (>90%) and 10% of electromechanical strain under 3 V/μm electric field. In this observation, the actuation mechanism was associated with the enhanced electrostatic force of the CPPU by the CNC dielectric filler.

However, a question remained on this actively tunable material. Can RI of CPPU actively change in the presence of an electric field? Recently some researchers reported that RI could be actively tuned by incorporating CNC or any filler materials in the presence of external stimuli. Self-assembled CNC three-layer films with the helicoidal and nematic-like organization of the CNCs were reported (De La Cruz et al., 2018). They exhibited high reflectivity tunable within the visible and near-infrared regions of the optical spectrum. A class of composite polymer films showed the refractive index change by simple mechanical forces (Sandrock et al., 2004). The films were comprised of 1,024 alternating layers of an elastomer and a glassy polymer. The elastomer component's layer thickness and thus, the effective RI of the composite can be varied by compressing the composite. The variable RI mechanism includes both changes in elastomer layer thickness and pressure dependence of the elastomer RI. A set of commercial (meth)acrylic resins was photopolymerized under identical irradiation conditions, and the evolution of their RI was reported that it linearly increased with conversion as long as the material was not in the glassy state (Aloui et al., 2018). This increase was related to a rise in the material density arising during polymerization.

This paper aims at investigating the RI change of CPPU in the presence of an electric field. The CPPU was prepared with different electrical poling conditions of field strength and frequency. Electrical poling is essential to align CNC, which improves the dielectric property of CPPU. Interaction of CNC in the poled CPPU was studied using a Fourier transform infrared spectroscopy (FTIR), and dielectric properties of CPPU were characterized using an LCR meter. RI of the poled CPPU was investigated using a refractometer and a laser displacement sensor. The electro-optical behavior of CPPU was investigated with three different actuation configurations.

MATERIALS AND METHODS

Materials

Micro cellulose, Avicel, was purchased from Sigma-Aldrich, St. Louis, Missouri, USA, and sulfuric acid (H_2SO_4) was purchased from JUNSEI chemical in Tokyo, Japan. PDEGA for the soft segment of CPPU and hexamethylene diisocyanate (HMDI) for the hard segment of CPPU were obtained from Sigma-Aldrich.

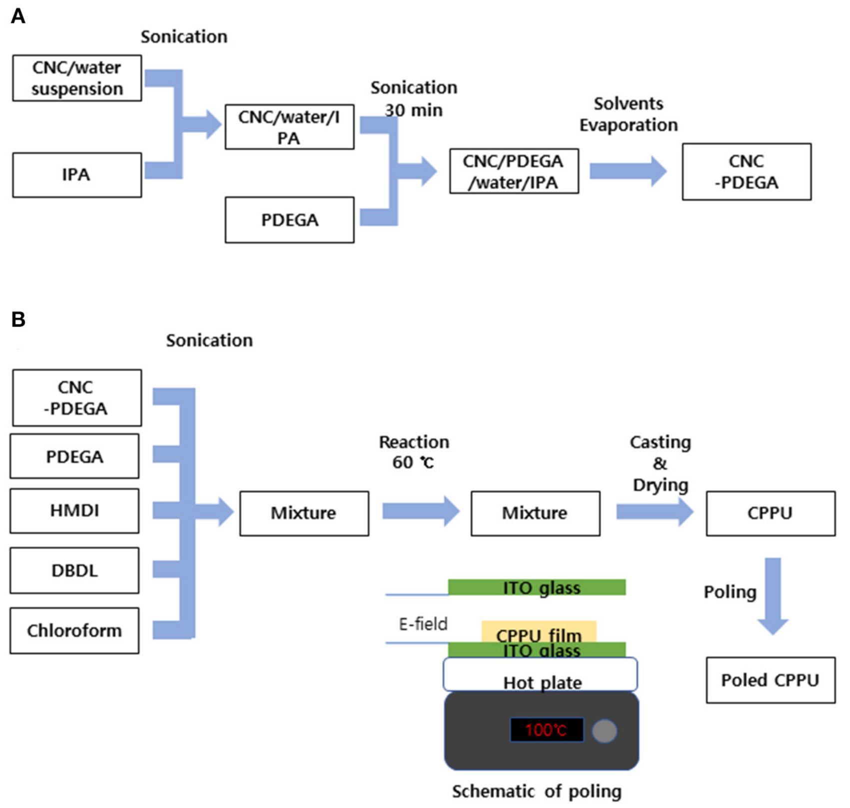

FIGURE 2 | Preparation process of CPPU: **(A)** CNC-PDEGA and **(B)** CPPU preparation and poling.

Dibutyltin dilaurate (DBDL) for catalysis of urethane reaction was also purchased from Sigma-Aldrich.

Fabrication of CPPU

Figure 2 shows the fabrication process of CPPU. CNC was isolated from micro cellulose using the previously reported acidic hydrolysis process (Kim et al., 2015). In 50 mL of 60 wt% H_2SO_4, Avicel was added and heated at 50°C, followed by stirring for 30 min until it turned to light brown suspension. The suspension was diluted with deionized (DI)-water and centrifuged until pH was changed to neutral. The CNC concentration was adjusted to 1 wt%.

The homogeneous distribution of CNC and PDEGA blend (CNC-PDEGA) was prepared before the urethane reaction. **Figure 2A** shows the process. The preparation process is following (Ko et al., 2017). At first, isopropyl alcohol (IPA) was mixed with CNC suspension at 10:1 ratio using an ultrasonic cleaner (FS30H, Fisher Scientific, Pittsburgh, Pennsylvania, USA) for a few seconds. Then the mixture was added into PDEGA and ran the ultrasonic cleaner for 30 min. The CNC concentration in CNC-PDEGA was varied by 0.001, 0.01, 0.05, and 0.05 wt%. The CNC/IPA/PDEGA solution was heated to removed water and IPA using an oven at 60°C for 48 h. The prepared CNC–PDEGA plays as a polyol in polyurethane. **Figure 2B** shows the CPPU preparation process. 1 g CNC-PDEGA and 1.25 g PDEGA were dissolved in 5 ml chloroform, and 0.125 g HMDI as an isocyanate salt and 0.1 g DBDL as catalysis for urethane were mixed in the solution. After mixing all chemicals, the solution was encapsulated and kept in the oven at 60°C to form a nucleophilic addition reaction for 5 h. After the reaction, the solution was cooled at room temperature to prevent bubbles generated by evaporating chloroform. The reacted solution was poured on a PDMS sheet and kept in the oven to evaporate the remained chloroform for 1 day. Finally, a solidified CPPU was obtained.

Electrical poling was conducted to enhance the electro-optical performance of CPPU. The prepared CPPU was loaded between two ITO glass electrodes with 5 mm gap. For effective poling, the prepared CPPU was heated at 100°C using a hotplate. The electrical poling signal was generated from a function generator (33220A, Agilent, Santa Clara, California, USA) and amplified using a high voltage amplifier (20/20, Trek, Lockport, New York, USA). Electrical poling field strength and frequency were changed to find an optimum poling condition. At last, a poled CPPU was prepared.

Characterizations

Interaction CPPU in the prepared CPPU was studied using an FTRI (VERTEX 80V, Bruker, Billerica, MA, USA). Dielectric properties were investigated using an LCR meter (Agilent 4284a) with a dielectric measurement fixture (16451b, Agilent, Santa Clara, California, USA). RI of the poled CPPU with various

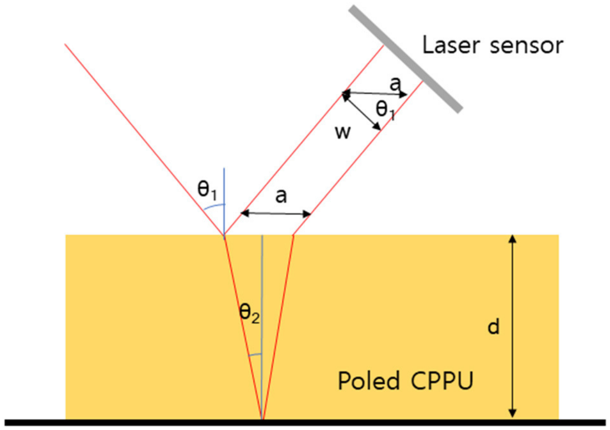

FIGURE 3 | Schematic of laser beam refractions at the surface and bottom of CPPU.

CNC concentration was investigated using a refractometer (DR-M2/1550, ATAGO, Tokyo, Japan). However, the reflectometer does not allow the measurement in the presence of an electric field. Thus, a laser displacement sensor (LK-G15, Keyence, Osaka, Japan) was used to measure the RI change under the electric field. **Figure 3** shows the schematic of the displacement sensor's laser light paths in CPPU how to calculate the RI. According to Snell's law, incidence angle θ_1 and refraction angle θ_2 have the following relation:

$$\frac{n_c}{n_{air}} \approx n_c = \frac{sin\theta_1}{sin\theta_2} \tag{1}$$

where n_c is the RI of CPPU, and θ_1 is 37.5°. The incidence angle θ_1 and refraction angle θ_2 also have the following relation with *d*, the CPPU thickness, and *w*, measured laser beam distance from the laser displacement sensor between the reflected beams at the bottom surface of CPPU.

$$2d \bullet tan\theta_2 = \frac{w}{\cos 37 \times 5^\circ} \tag{2}$$

$$\theta_2 = \tan^{-1}\left(\frac{w}{2d \bullet cos37 \times 5^\circ}\right) \tag{3}$$

From Equations (1)–(3), the RI of CPPU can be calculated as

$$n_c = \frac{\sin 37.5^\circ}{\sin\left(\tan^{-1}\left(\frac{w}{2d \bullet cos37 \times 5^\circ}\right)\right)} \tag{4}$$

The electro-optical behavior of the prepared CPPU was investigated using the experimental setup shown in **Figure 4A**. An electric signal was generated from the function generator and amplified using the high voltage amplifier. The electric field was applied to CPPU between two ITO glasses. Three different configurations of the ITO glass setup were used, as shown in **Figures 4B–D**. In the first setup shown in **Figure 4B** (configuration I), top ITO glass was located over CPPU with 5 mm gap to prevent contact between the CPPU and the top electrode. In the second setup shown in **Figure 4C** (configuration II), two ITO electrodes contacted the CPPU but no pillars, which allows the free deformation of CPPU in the presence of an electric field. The third setup is shown in **Figure 4D** (configuration III). Two ITO glasses contacted the CPPU with two pillars, and the distance between the two ITO glasses was fixed. The poled CPPU was cut into 5 × 5 mm^2. **Table 1** shows the test conditions for the electro-optical test. The electrical poling field was changed in 0–200 v/mm with 1–1,000 Hz. The measured RI values were verified by comparing them with the values found using a Mach Zehnder interferometer.

RESULTS AND DISCUSSION

Characteristics of CPPU With CNC Concentration

FTIR was carried out to investigate the chemical structure of poled CPPU with various CNC concentrations. **Figure 5A** shows FTIR spectra between 4,000 and 3,200 cm^{-1}, and **Supplementary Figure 1** represents decomposed FTIR spectra between 3,600 and 3,200 cm^{-1}. Different N-H peaks appeared at 3,321, 3,351, and 3,425 cm^{-1}, which correspond to ordered hydrogen-bonded N-H, disordered hydrogen-bonded N-H, and free N-H from urethane linkage, respectively (Pullawan et al., 2012). Peaks at 3,390 and 3,425 cm^{-1} correspond to hydrogen-bonded O-H peaks from CNC (Siqueira et al., 2010). A peak at 3,624 cm^{-1} responds to free O-H. As increasing the CNC concentration, the hydrogen-bonded O-H peak increased. Interestingly, disordered hydrogen-bonded N-H peak drastically improved, and ordered N-H peak and free N-H decreased as increasing the CNC concentration. The result might be due to wealthy OH groups in CNC act as hydrogen bonding sites to N-H groups, which are infiltrated between ordered urethane chains and played as an impurity for polyurethane crystal. Moreover, disordered hydrogen-bonded N-H peak shifted to higher wavenumber, 3,349 cm^{-1}, which might be due to reduced N-H bonding associated with the lower hydrogen bonding strength of N-HO than N-HN. The peak at 2,920 cm^{-1} shown in **Figure 5B** corresponds to the C-H stretching peak of alkane structure in polyurethane and CNC. The peak at 2,805 cm^{-1} is the amine peak of polyurethane. As the CNC concentration increasing, 2,948 and 2,867 cm^{-1} peaks corresponding to C-H groups from CNC increased. The FTIR results showed that CNC was well interacted with the amine group of polyurethane by hydrogen bonding, and urethane bonding was well-formed.

Figure 6 shows the dielectric properties of the poled CPPU with various CNC concentrations. Four polarizations typically govern dielectric properties as surficial, dipole, atomic, and electronic ones. Under GHz range, surficial and dipole polarizations are more dominant than others. The dielectric constant increased as increasing the CNC concentration up to 0.01 wt% and decreased after that (see **Figure 6A**). By the electrical poling, the dielectric constant increased due to the improved polarization. The dielectric constant at 50 kHz was over

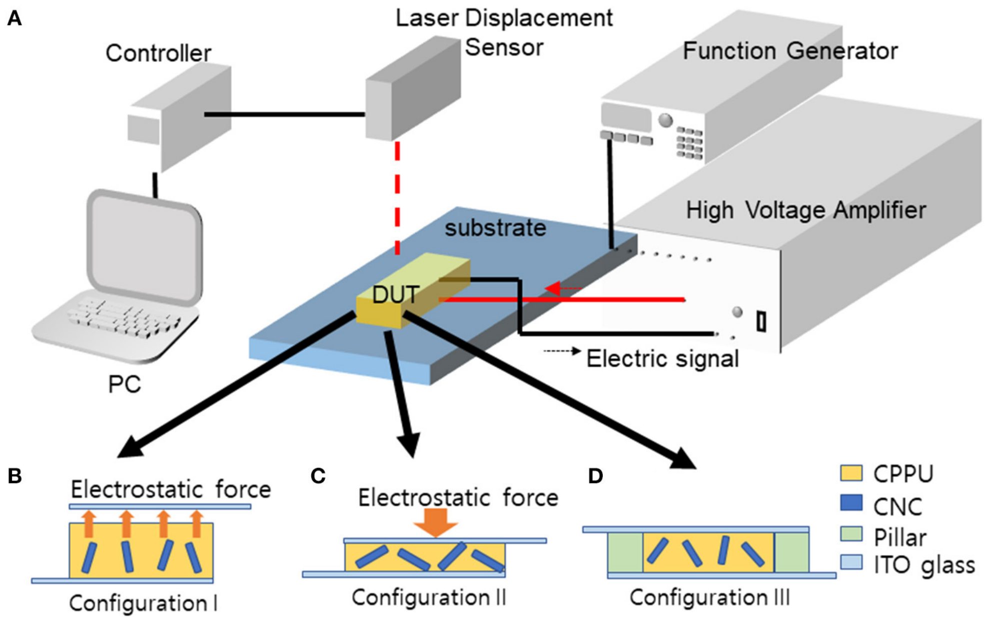

FIGURE 4 | **(A)** Experimental setup for electro-optic behavior and actuation test setup: **(B)** Configuration I, **(C)** Configuration II, **(D)** Configuration III.

TABLE 1 | Actuation and poling conditions for CPPU sample.

Sample	Actuation setup	Poling condition	
		Frequency (Hz)	Electric field (V/mm)
A	Configuration I	1	20
B	Configuration II	1	20
C	Configuration III	1	20
D	Configuration III	10	20
E	Configuration III	100	20
F	Configuration III	1,000	20
G	Configuration III	1	0
H	Configuration III	1	40
I	Configuration III	1	60
J	Configuration III	1	80
K	Configuration III	1	100
L	Configuration III	1	120
M	Configuration III	1	160
N	Configuration III	1	200

70% of the dielectric constant at 100 Hz. It indicates that the dipole polarization effect in the poled CPPU was more dominant than the surface polarization even at low frequency. Over 0.01 wt%, the rotation of polarized CNC might be limited due to the increased hydrogen bonds between CNC and polyurethane, as shown in the FTIR result. **Figure 6B** shows dielectric loss curves. As for increasing the CNC concentration, the dielectric loss decreased to 50 kHz, which increased after that. The dielectric loss curves can observe the threshold between surficial and dipole polarization. The dielectric loss result indicates that the surficial polarization effect decreased until 50 kHz. In other words, the dipole polarity was dominant over the point.

Supplementary Figure 2 shows the UV visible curves of the non-poled CPPU and the poled CPPU (Sample C). They delivered over 85% transparency.

The RI of the poled CPPU was investigated before testing the electro-optic behavior. The poling condition was 1 Hz AC with an electric field of 20 V/mm peak to peak, and the CNC concentration was 0.01 wt%. The RI value calculated using Equation (4) was 1.505; meanwhile, the refractometer measurement result was 1.489. It indicates that the RI computed using Equation (4) deviated 1% from the refractometer measurement, an acceptable error range. **Supplementary Figure 3** shows the RI of the poled CPPU measured using the refractometer. As increasing the CNC concentration in CNC-PDEGA from 0.001 to 0.05 wt%, the RI rose from 1.48 to 1.51. The RI change might be due to the well-known dielectric filler effect (Aloui et al., 2018). The CNC might be aligned along the electrical poling field.

Electro-Optical Behavior

RI change of the poled CPPU with 0.01 wt% CNC concentration was measured using the laser sensor for three configurations shown in **Figure 4** in the presence of an actuating electric field. **Figure 7** shows the measured RI changes in Configuration I and III. The non-contact electrode case (Configuration I), Sample A, did not show significant RI change as increasing the actuating electric field. It is due to the electrostatic force mitigation between the top electrode and the surface of the CPPU. **Supplementary Figure 4** shows the RI result of Configuration II (contact electrode without pillar case), Sample B. As increasing the actuating electric field, the RI slightly decreased, which might

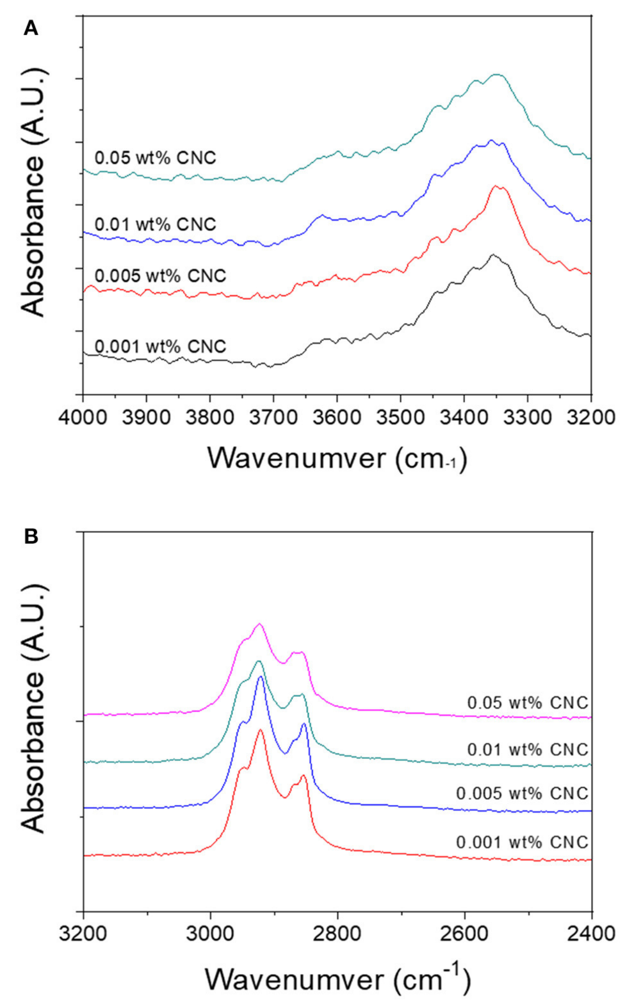

FIGURE 5 | FTIR spectra of poled CPPU with different CNC concentrations at two wavenumber regions: **(A)** 4,000–3,200 cm^{-1} and **(B)** 3,200–2,400 cm^{-1}.

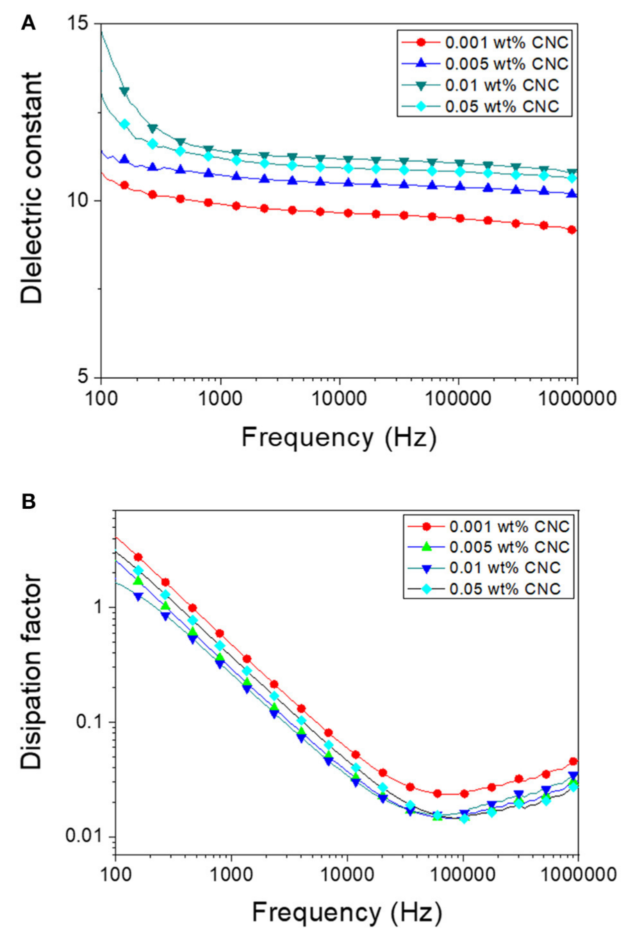

FIGURE 6 | Dielectric properties of poled CPPU with various CNC concentrations: **(A)** Dielectric constant and **(B)** Dissipation factor.

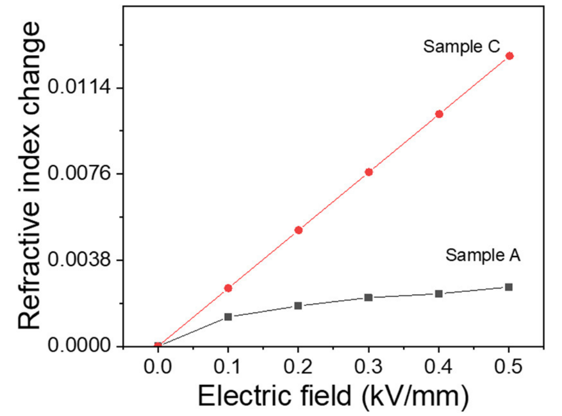

FIGURE 7 | Refractive index changes of configuration I and III with the actuating electric field.

be due to the compression of the poled CPPU by the electrostatic force. Initially, CNCs in the poled CPPU aligned along the poling electric field. When the poled CPPU is compressed, CNC could be rotated toward the perpendicular direction to the electric field, which results in the refractive index decrease (Kubo et al., 2007; Zhai et al., 2020). When the poled CPPU is elongated, CNC can be rotated back to the aligned initially and aligned along the electric field. Thus, the sample C (contact electrode with pillar case, Configuration III) was investigated to remove the electrostatic force (compression displacement) effect. In this test, displacement was not changed because of two fixed pillars. As **Figure 7** shows, the RI remarkably increased as increasing the actuating electric field. It is the opposite phenomenon with Configuration II (Sample B) due to the CNC alignment along the actuating electric field direction (Kim H. C. et al., 2019).

To optimized electro-optical properties, the effect of poling frequency and the poling electric field was investigated with the given conditions in **Table 1**. **Figure 8** shows the RI change results. When the poling frequency increased, the RI change was reduced, and over 100 Hz, the RI change was saturated. The frequency

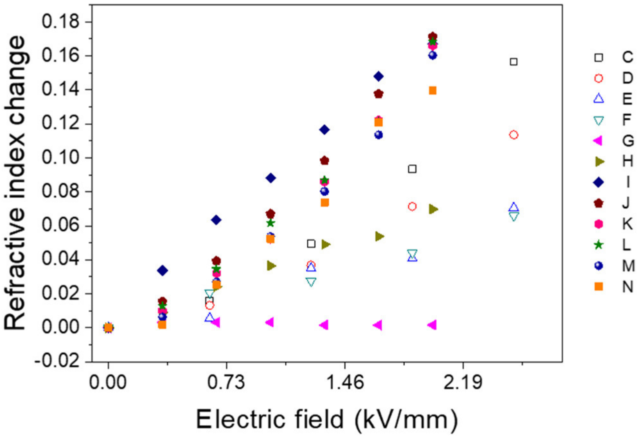

FIGURE 8 | Refractive index change of poled CPPU samples with various poling conditions.

dependence might be associated with the dielectrophoretic effect (Kadimi et al., 2014). The RI increased as increasing the poling electric field up to 60 V/mm and saturated after that. RI change saturation might be due to the optimized CNC alignment (Kubo et al., 2007).

The RI change was demonstrated using a Mach Zehnder interferometer, which compares the laser signal that passes through the poled CPPU with the original signal. **Supplementary Video 1** shows interference between two signals, demonstrating a refractive index change of the poled CPPU (Sample I).

The CNC-PDEGA solution can be synthesized for large volume production, and the CPPU can be fabricated by making a urethane bond between CNC-PDEGA and HMDI. After reacting them, the reacted CPPU can be molded for mass production of lens devices.

CONCLUSIONS

This paper investigated the refractive index change of CNC-based transparent and electroactive polyurethane (CPPU) in the presence of an actuating electric field. The prepared CPPU was electrically poled to enhance the electro-optical performance of CPPU. FTIR spectra showed CNC interacted with polyurethane by hydrogen bonding, and urethane bonding was well-formed. The increased CNC concentration increased the dielectric constant of the poled CPPU. Two electrodes were fixed with pillars that contacted the poled CPPU to eliminate the RI change caused by the deformation of CPPU. The RI linearly increased as the actuating electric field increased. Various electrical poling conditions were investigated to optimize the electro-optical behavior, and it was raised as decreasing the poling frequency. The RI change mechanism was associated with the CNC alignment by dielectrophoresis. The RI change increased as increasing the poling electric field up to 60 V/mm and saturated after that. It was due to CNC alignment was optimized at 60 V/mm poling electric field. The results proved that RI is tunable in the presence of the poling electric field, which is a promising property for implementing a tunable optical lens.

DATA AVAILABILITY STATEMENT

The raw data supporting the conclusions of this article will be made available by the authors, without undue reservation.

AUTHOR CONTRIBUTIONS

JK and H-UK: conceptualization, literature review, figures and graphs, and draft. H-UK: experiment. HK: data acquisition. JK: editing. All authors contributed to the article and approved the submitted version.

FUNDING

This research was supported by the Creative Research Initiatives Program through the National Research Foundation of Korea (NRF) funded by the Ministry of Science, Technology, and ICT (NRF-2015R1A3A2066301).

ACKNOWLEDGMENTS

The authors would like to acknowledge Dr. Yun, Sungryul of ETRI, for his effort on the video capture for the Mach Zehnder interferometer experiment.

SUPPLEMENTARY MATERIAL

The Supplementary Material for this article can be found online at: https://www.frontiersin.org/articles/10.3389/fbioe.2021.606008/full#supplementary-material

REFERENCES

Aloui, F., Lecamp, L., Lebaudy, P., and Burel, F. (2018). Refractive index evolution of various commercial acrylic resins during photopolymerization. *Express Polym. Lett.* 12, 966–971. doi: 10.3144/expresspolymlett.2018.83

Choi, S. H., Duzik, A. J., Kim, H.-J., Park, Y., Kim, J., Ko, H.-U, et al. (2017). Perspective and potential of smart optical materials. *Smart Mater. Struct.* 26:093001. doi: 10.1088/1361-665X/aa7c32

De La Cruz, J. A., Liu, Q., Senyuk, B., Frazier, A. W., and Peddireddy, K. (2018). Cellulose-based reflective liquid crystal films as optical filters and solar gain regulators. *ACS Photonics* 5, 2468–2477. doi: 10.1021/acsphotonics.8b00289

Gallone, G., Galantini, F., and Carpi, F. (2010). Perspectives for new dielectric elastomers with improved electromechanical actuation performance: composites versus blends. *Polym. Int.* 59, 400–406. doi: 10.1002/pi.2765

Ghilardi, M., Boys, H., Török, P., Busfield, J. J., and Carpi, F. (2019). Smart Lenses with electrically tuneable Astigmatism. *Sci. Rep.* 9, 1–10. doi: 10.1038/s41598-019-52168-8

Giese, M., and Spengler, M. (2019). Cellulose nanocrystals in nanoarchitectonics – towards photonic functional materials. *Mol. Syst. Des. Eng.* 4, 29–48. doi: 10.1039/C8ME00065D

Habibi, Y., Lucia, L. A., and Rojas, O. J. (2010). Cellulose nanocrystals: chemistry, self-assembly, and applications. *Chem. Rev.* 110, 3479–3500. doi: 10.1021/cr900339w

Jayaramudu, T., Ko, H.-U, Zhai, L., Li, Y., and Kim, J. (2017). Preparation and characterization of hydrogels from polyvinyl alcohol and cellulose and their electroactive behavior. *Soft Mater.* 15, 64–72. doi: 10.1080/1539445X.2016.1246458

Jayaramudu, T., Li, Y., Ko, H.-U, Shishir, M. I. R., and Kim, J. (2016). Poly(acrylic acid)-poly(vinyl alcohol) hydrogels for reconfigurable lens actuators. *Int. J. Precis. Engin. Manaf. Green Technol.* 3, 375–379. doi: 10.1007/s40684-016-0047-x

Kadimi, A., Benhamou, K., Ounaies, Z., Magnin, A., Dufresne, A., Kaddami, H., et al. (2014). Electric field alignment of nanofibrillated cellulose (NFC) in silicone oil: impact on electrical properties. *ACS Appl. Mater. Interf.* 6, 9418–9425. doi: 10.1021/am501808h

Kim, H. C., Kim, J. W., Zhai, L., and Kim, J. (2019). Strong and tough long cellulose fibers made by aligning cellulose nanofibers under magnetic and electric fields. *Cellulose* 26, 5821–5829. doi: 10.1007/s10570-019-02496-9

Kim, J., Kim, J. W., Kim, H. C., Zhai, L., Ko, H.-U, and Muthoka, R. M. (2019). Review of soft actuator materials. *Int. J. Precis. Engin. Manuf.* 20, 2221–2241. doi: 10.1007/s12541-019-00255-1

Kim, J.-H., Shim, B. S., Kim, H. S., Lee, Y.-J., Min, S. K., Jang, D., et al. (2015). Review of nanocellulose for sustainable future materials. *Int. J. Precis. Engin. Manaf. Green Technol.* 2, 197–213. doi: 10.1007/s40684-015-0024-9

Ko, H.-U, Kim, H. C., Kim, J. W., Zhai, L., Jayaramudu, T., and Kim, J. (2017). Fabrication and characterization of cellulose nanocrystal based transparent electroactive polyurethane. *Smart Mater. Struct.* 26:085012. doi: 10.1088/1361-665X/aa722d

Kubo, S., Diaz, A., Tang, Y., Mayer, T. S., Khoo, I. C., and Mallouk, T. E. (2007). Tunability of the refractive index of gold nanoparticle dispersions. *Nano Lett.* 7, 3418–3423. doi: 10.1021/nl071893x

Mirfakhrai, T., Madden, J. D. W., and Baughman, R. H. (2007). Polymer artificial muscles. *Mater. Today* 10, 30–38. doi: 10.1016/S1369-7021(07)70048-2

Moon, R. J., Martini, A., Nairn, J., Simonsen, J., and Youngblood, J. (2011). Cellulose nanomaterials review: structure, properties and nanocomposites. *Chem. Soc. Rev.* 40, 3941–3994. doi: 10.1039/c0cs00108b

O'Halloran, A., O'malley, F., and McHugh, P. A. (2008). Review on dielectric elastomer actuators, technology, applications, and challenges. *J. Appl. Phys.* 104:071101. doi: 10.1063/1.2981642

Park, I.-S., Kim, K. J., Nam, J.-D., Lee, J., and Yim, W. (2007). Mechanical, dielectric, and magnetic properties of the silicone elastomer with multi-walled carbon nanotubes as a nanofiller. *Polym. Eng. Sci.* 47, 1396–1405. doi: 10.1002/pen.20833

Pullawan, T., Wilkinson, A. N., and Eichhorn, S. J. (2012). Influence of magnetic field alignment of cellulose whiskers on the mechanics of all-cellulose nanocomposites. *Biomacromolecules* 13, 2528–2536. doi: 10.1021/bm300746r

Romasanta, L. J., Lopez-Manchado, M. A., and Verdejo, R. (2015). Increasing the performance of dielectric elastomer actuators: a review from the materials perspective. *Prog. Polym. Sci.* 51, 188–211. doi: 10.1016/j.progpolymsci.2015.08.002

Sadasivuni, K.K., Ponnamma, D., Ko, H.-U, Zhai, L., Kim, H.-C., and Kim, J. (2016). Electroactive and optically adaptive bionanocomposite for reconfigurable microlens. *J. Phys. Chem. B*, 120:4699–4705. doi: 10.1021/acs.jpcb.6b01370

Sandrock, M., Wiggins, M., Shirk, J. S., Tai, H., Ranade, A., Baer, E., et al. (2004). A widely tunable refractive index in a nanolayered photonic material. *Appl. Phys. Lett.* 84, 3621–3623. doi: 10.1063/1.1738513

Siqueira, G., Bras, J., and Dufresne, A. (2010). Cellulosic bionanocomposites: a review of preparation, properties and applications. *Polymers* 2, 728–765. doi: 10.3390/polym2040728

Vanderfleet, O.M., and Cranston, E.D. (2020). Production routes to tailor the performance of cellulose nanocrystals. *Nat. Rev. Mater.* doi: 10.1038/s41578-020-00239-y. [Epub ahead of print].

Wang, H., Zhu, J. J., Ma, Q., Agarwal, U. P., Gleisner, R., Reiner, R., et al. (2020). Pilot-scale production of cellulosic nanowhiskers with similar morphology to cellulose nanocrystals. *Front. Bioeng. Biotechnol.* 8:565084. doi: 10.3389/fbioe.2020.565084

Wang, J., Li, S., Gao, D., Xiong, J., and Lee, P. S. (2019). Reconfigurable and programmable origami dielectric elastomer actuators with 3D shape morphing and emissive architectures. *NPG Asia Mater.* 11:71. doi: 10.1038/s41427-019-0173-3

Zhai, L., Kim, H. C., Kim, J. W., and Kim, J. (2020). Alignment effect on the piezoelectric property of ultrathin cellulose nanofiber film. *ACS Appl. Bio Mater.* 3, 4329–4334. doi: 10.1021/acsabm.0c00364

Zurlo, G., and Destrade, M. (2017). Catastrophic thinning of dielectric elastomers. *Phys. Rev. Lett.* 118:078001. doi: 10.1103/PhysRevLett.118.078001

Conflict of Interest: The authors declare that the research was conducted in the absence of any commercial or financial relationships that could be construed as a potential conflict of interest.

frontiers
in Bioengineering and Biotechnology

ORIGINAL RESEARCH
published: 28 January 2021
doi: 10.3389/fbioe.2021.617097

Controllable Synthesis of Biocompatible Fluorescent Carbon Dots From Cellulose Hydrogel for the Specific Detection of Hg^{2+}

Hailong Huang, Hao Ge, Zhipeng Ren, Zhijian Huang, Min Xu and Xianghui Wang**

School of Physics and Electronic Science & Shanghai Key Laboratory of Magnetic Resonance, East China Normal University, Shanghai, China

Heavy metal ions overload can seriously harm human health. Simple and effective strategies for the specific detection of heavy metal ions are of great important. In this work, using different pretreatment methods, a series of carbon dots (CDs) with different particle sizes and doped with varying amounts of elements (O, N, S) were prepared based on the natural polymer, cellulose hydrogel. The CDs exhibit excellent fluorescence and biocompatibility. When the particle size decreased from 8.72 to 2.11 nm, the fluorescence quantum yield increased from 0.029 to 0.183. In addition, doping with elements (N) also effectively enhanced the fluorescent performance of the CDs. The fluorescence of the CDs, especially for the smallest, CD-4a, was significantly quenched in the presence of the heavy metal ion, Hg^{2+}. Thus, CD-4a may be used as a fluorescence sensor for the detection of Hg^{2+}. The fluorescence intensity of CD-4a exhibited a two-stage, concentration-dependent fluorescence response in the range 0.2–10 and 10–100 μmol/L Hg^{2+}, with each stage having different slopes; the detection limit was 0.2 μM. More importantly, even in the presence of interfering metal ions, the detection of Hg^{2+} using the CDs-4a remained stable. Therefore, these biocompatible CDs may serve as a promising candidate for the specific detection of Hg^{2+}.

Keywords: carbon dots, cellulose hydrogel, Hg^{2+} detection, fluorescent sensor, biocompatibility

Edited by:
Muhammad Wajid Ullah,
Huazhong University of Science and Technology, China

Reviewed by:
Rajendra Kumar Singh,
Institute of Tissue Regeneration Engineering (ITREN), South Korea
PaYaM ZarrinTaj,
Oklahoma State University, United States

****Correspondence:***
Min Xu
xumin@phy.ecnu.edu.cn
Xianghui Wang
xhwang@phy.ecnu.edu.cn

Specialty section:
This article was submitted to Biomaterials, a section of the journal Frontiers in Bioengineering and Biotechnology

Received: *14 October 2020*
Accepted: *04 January 2021*
Published: *28 January 2021*

Citation:
Huang H, Ge H, Ren Z, Huang Z, Xu M and Wang X (2021) Controllable Synthesis of Biocompatible Fluorescent Carbon Dots From Cellulose Hydrogel for the Specific Detection of Hg^{2+}. Front. Bioeng. Biotechnol. 9:617097. doi: 10.3389/fbioe.2021.617097

INTRODUCTION

With the development of industrialization, the pollution of the environment with heavy metal ions has become a serious concern all over the world. Heavy metal ions not only harm living organisms in water, but also affect the health of humans (Lu et al., 2018; Bolisetty et al., 2019; Sarma et al., 2019; Wu et al., 2019). The overloading of heavy metal ions such as Cu^{2+}, Fe^{3+}, Pb^{2+}, and Hg^{2+} is highly toxic to biological organisms and causes irreversible, dangerous oxidative stress and serious damage to the central nervous system leading to renal and neural problems (Ali and Khan, 2018; Kahlon et al., 2018; Cai et al., 2019; Kumar et al., 2020; Oliveira et al., 2020; Rossini-Oliva et al., 2020). During last few decades, many methods have been developed to detect heavy metal ions in water, such as inductively coupled plasma atomic emission spectroscopy (ICP-AES), X-ray absorption spectroscopy (XAS), atomic absorption spectroscopy and so on. These methods have been widely applied in the laboratory and have excellent limits of detection and provide accurate quantifications.

However, these methods do not meet the requirements for the simple and fast detection of metals in practical applications due to the complex sample preparation, high cost of instrumentation and complex analyses (Li et al., 2016; Bansod et al., 2017; Malik et al., 2019; Qi et al., 2020). Thus, an efficient, simple and sensitive method to detect and quantify heavy metal ions in aqueous media remains a challenge in environmental detection applications.

Carbon dots (CDs) are considered an ideal fluorescent material and have received significant attention as a result of their stable fluorescence, high optical absorptivity, good physicochemical stability, and biocompatibility; furthermore, they have been widely applied in medical diagnosis, bio-imaging, sensing, photocatalysis, optoelectronic devices and full-color displays (Sharma et al., 2017; Liu et al., 2019; Meng et al., 2019; Patel et al., 2019; Zhou et al., 2019). Recently, based on the fluorescence quenching effect caused by interactions between metal ions and the fluorophore functional groups, CDs have been demonstrated to be a promising fluorescent sensor for the detection of heavy metal ions, due to the unique dimensions and functional structure (Pang et al., 2017; Ansi and Renuka, 2019; Yarur et al., 2019; Yoo et al., 2019). Wang et al. (2015) used an acidic ionic liquid (SO_3H-IL) as a catalyst and an ionic liquid ([Bmim]Cl) as a solvent to prepare CDs from microcrystalline cellulose. The CDs exhibited excellent, selective detection of Hg^{2+} along with good water dispersibility and photostability. In the concentration range 6–80 μmol/L, it was demonstrated that the CDs were an effective fluorescent sensor for the selective quantification of Hg^{2+}, exhibiting a good linear relationship. Wang et al. (2019) also reported a simple hydrothermal method to synthesize nitrogen-doped CDs using an ethanolamine ionic liquid (1-carboxyethyl-3-methyl imidazole chloride) gel as a precursor. Due to the strong interactions between the metal ions and the surface groups and nitrogen atoms of the CDs, the CDs displayed significant heavy metal ion quenching ability for Hg^{2+} and Cu^{2+}, as well as sensitive detection properties. Wu et al. (2017) summarized the relationship between the fluorescence quenching effect and the precursors and methods used. They found that, the chemically doped element (O, N, S), particle size and solvatochromic effects effectively controlled not only the fluorescence performance and specific detection ability of the CDs, but also endowed the CDs with excellent heavy metal detection abilities. Their results may provide a theoretical basis from which to develop novel and improved fluorescence performance.

Although these studies (Sharma et al., 2017; Ansi and Renuka, 2019; Liu et al., 2019; Meng et al., 2019; Wang et al., 2019; Yarur et al., 2019; Zhou et al., 2019) have achieved significant progress in the development of biocompatible CDs for heavy metal ion detection, most require toxic precursors and reagents,

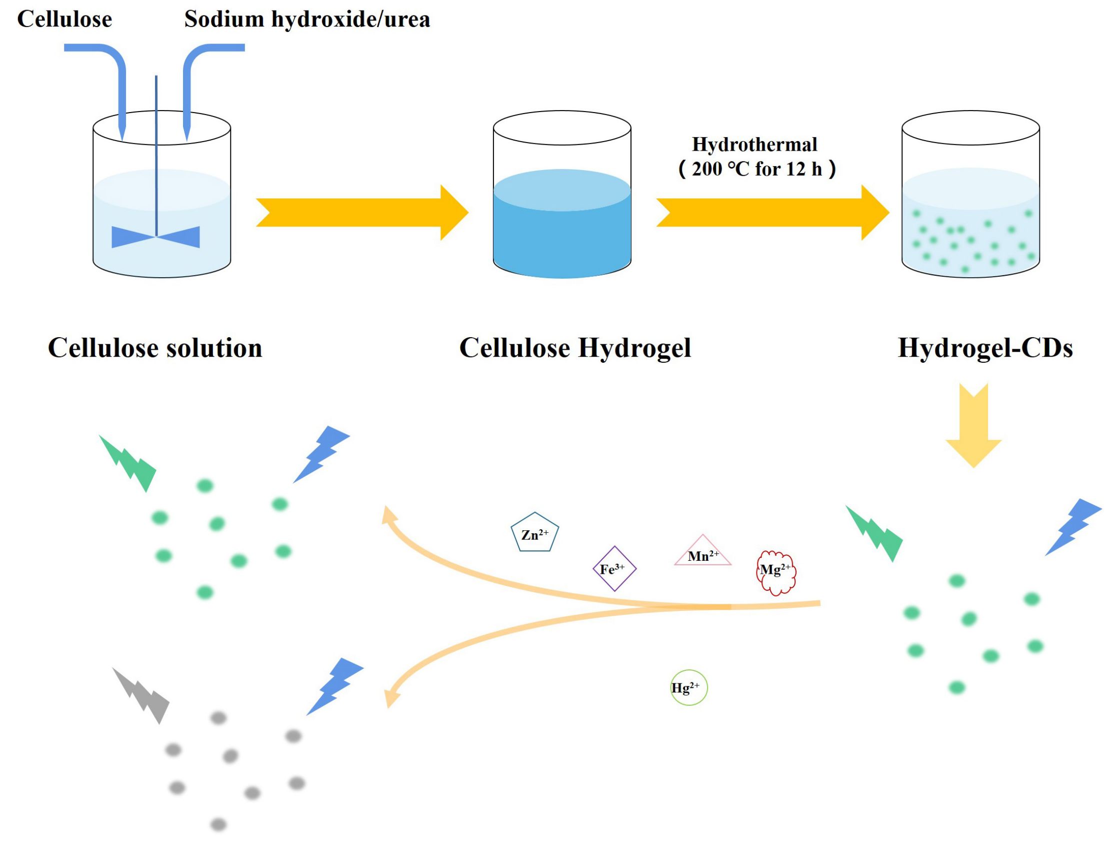

SCHEME 1 | Synthetic procedure and mechanism of the sensing of CDs.

TABLE 1 | Samples name of CDs with different treatment.

	Molecular weight cut-off (k)		
Pre-treatment	**<1.2**	**1.2–10**	**>10**
CDs from pure hydrogel without pre-treatment	CDs-1a	CDs-1b	CDs-1c
CDs from NaOH pre-treated hydrogel	CDs-2a	CDs-2b	CDs-2c
CDs from urea pre-treated hydrogel	CDs-3a	CDs-3b	CDs-3c
CDs from NaOH/urea pre-treated hydrogel	CDs-4a	CDs-4b	CDs-4c

and expensive or complex preparation methods, especially when modifying the functional groups of CDs. The simultaneous satisfaction of these requirements remains highly challenging. Therefore, the development of a simple and effective strategy to design biocompatible CDs with sensing properties specific to the detection of heavy metal ions is necessary.

Herein, we report a simple strategy to develop biocompatible CDs based on a low-cost and natural polymer, cellulose hydrogel *via* a hydrothermal reaction. The prepared CDs-4a exhibited excellent fluorescence performance and good biocompatibility due to the small particle size and the functional groups on the particle surface, which could be used for labeling in living cells. Based on complexion between the metal ions and the functional groups of CDs-4a, the CDs-4a demonstrated the highly sensitive and specific detection of Hg^{2+} (**Scheme 1**). The CDs-4a maintained an excellent detection ability even in a complex solution containing various heavy metal ions.

MATERIALS AND METHODS

Materials

Linter Cellulose ($M_w = 8 \times 10^4$) was provided by Hubei Chemical Fiber Group Co. Ltd. Epichlorohydrin (ECH), sodium hydroxide (NaOH), urea, copper sulfate ($CuSO_4$), mercury nitrate ($Hg(NO_3)_2$), silver nitrate ($AgNO_3$), manganese nitrate [$Mn(NO_3)_2$], chromium nitrate [$Cr(NO_3)_3$], lead nitrate [$Pb(NO_3)_2$], copper chloride ($CuCl_2$), ferric chloride ($FeCl_3$), calcium chloride ($CaCl_2$), nickel chloride ($NiCl_2$), cobalt chloride ($CoCl_2$), zinc chloride ($ZnCl_2$), and magnesium chloride ($MgCl_2$) were purchased from Sinopharm Group, Shanghai, China. All reagents were of analytical reagent grade, and all chemicals were used without further purification.

Preparation of CDs

Linter cellulose (4 g) was dissolved in a pre-cooled (−12°C) NaOH/urea aqueous solution (7/12 wt%, 100 g) to obtain the cellulose solution (Huang et al., 2016). Then, an amount of ECH (0.3 wt%) was added into the 4.5 g cellulose solution as crosslinking agent and stirred for 30 min at room temperature. Next, the homogeneous mixture was heated in the oven at 60°C for 4 h to obtain a uniform and transparent chemically crosslinked hydrogel. Finally, the hydrogel was soaked in deionized water for 48 h to completely remove the unreacted reagents from the pure cellulose hydrogel.

The pure cellulose hydrogel was placed in a hydrothermal reactor and heated at 200°C for 12 h. Then, the crude CDs formed were separated using high-speed centrifugation and

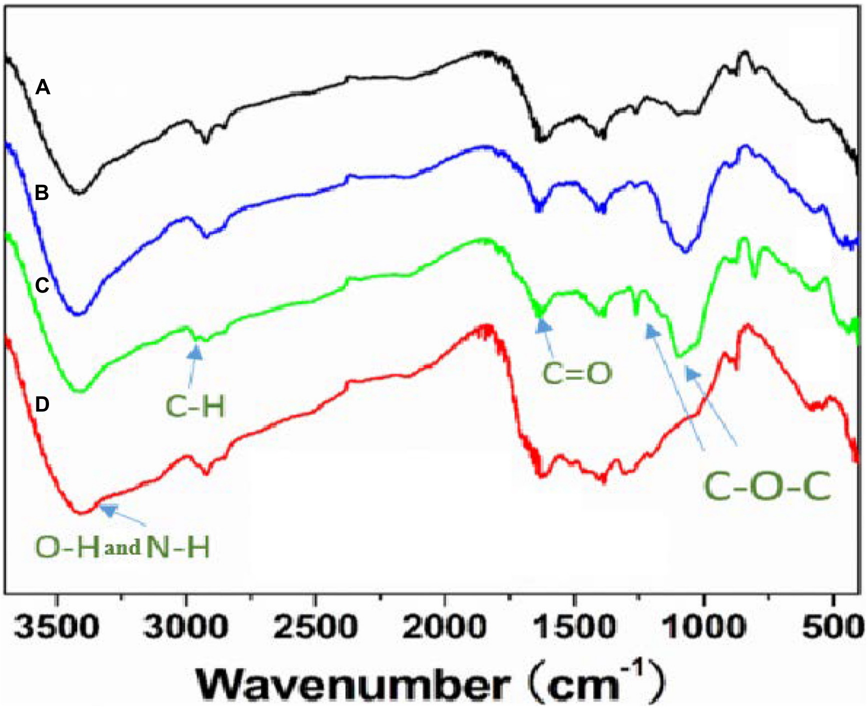

FIGURE 1 | FTIR spectra of different CDs samples prepared from differently pre-treated cellulose hydrogels: **(A)** CDs-4a; **(B)** CDs-3a; **(C)** CDs-2a; **(D)** Cellulose.

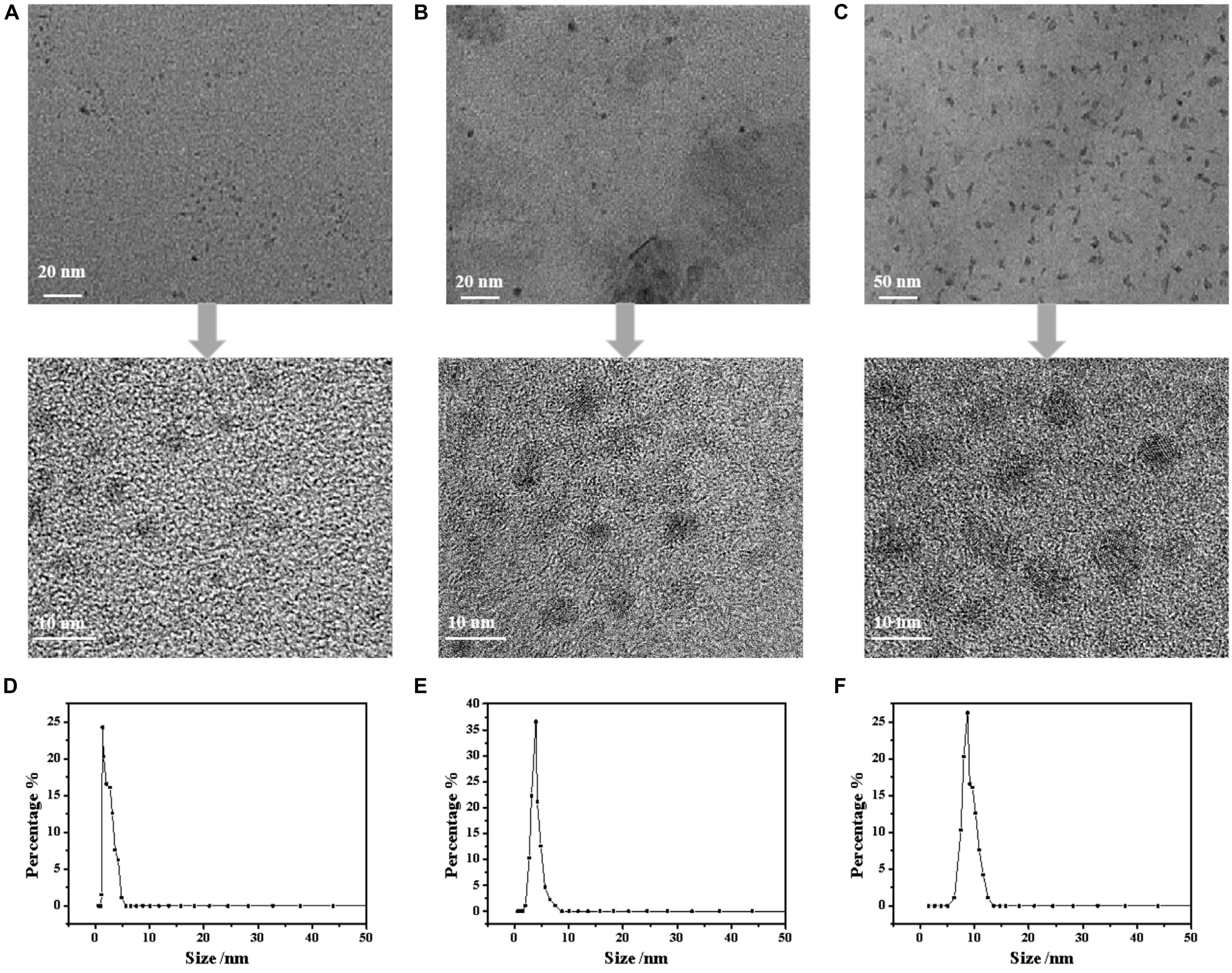

FIGURE 2 | The TEM images of CDs-4: **(A)** CDs-4a; **(B)** CDs-4b, and **(C)** CDs-4c. And the particle size of CDs-4: **(D)** CDs-4a; **(E)** CDs-4b, and **(F)** CDs-4c.

stored in ethyl alcohol. Next, the purified CDs were separated using dialysis bags with different molecular weight cut-off values (10 and 1.2 k); they were named CDs-a (<1.2 k), CDs-b (1.2–10 k), CDs-c (>10 k), respectively. In order to investigate the factors influencing hydrogel content, the pure cellulose hydrogel was pretreated with different methods before the hydrothermal reaction as described in the following. (1) The pure cellulose hydrogel was used directly without pretreatment. (2) The pure 4.5 g cellulose hydrogels were immersed in a 7 wt% NaOH solution for 48 h. (3) The pure 4.5 g cellulose hydrogels were immersed in a 12 wt% aqueous urea solution for 48 h. (4) The pure 4.5 g cellulose hydrogels were immersed in a (7/12%, wt%) aqueous NaOH–urea solution for 48 h. The corresponding CDs were named as shown in **Table 1**.

Characterization

Fourier transform infrared (FTIR) spectra of the CDs were obtained using a Nicolet-Nexus 870 spectrophotometer. The UV/vis absorption of the CDs was measured using a CARY-100 UV/Vis spectrometer. The fluorescence spectra of the CDs were measured using a Hitachi F-4500. The morphology of the CDs was observed using a transmission electron microscope (TEM) at room temperature using a JEM-2010 (Rajendra et al., 2020). X-ray photoelectron spectroscopy (XPS) spectra were recorded with ESCALAB 250XI (Thermo Fisher Scientific, United States). The relative fluorescence quantum yield (QY) of the CDs was determined using methods previously reported in the literature (Shi et al., 2016; Khan et al., 2017; Liu et al., 2018). A quinine sulfate–H_2SO_4 solution (n = 1.33, QY = 0.54) was used as a reference solution.

TABLE 2 | The fluorescence quantum yield of different CDs samples.

Sample	a	b	c
CDs-1	0.008	0.002	0.005
CDs-2	0.050	0.011	0.005
CDs-3	0.179	0.034	0.013
CDs-4	0.183	0.036	0.029

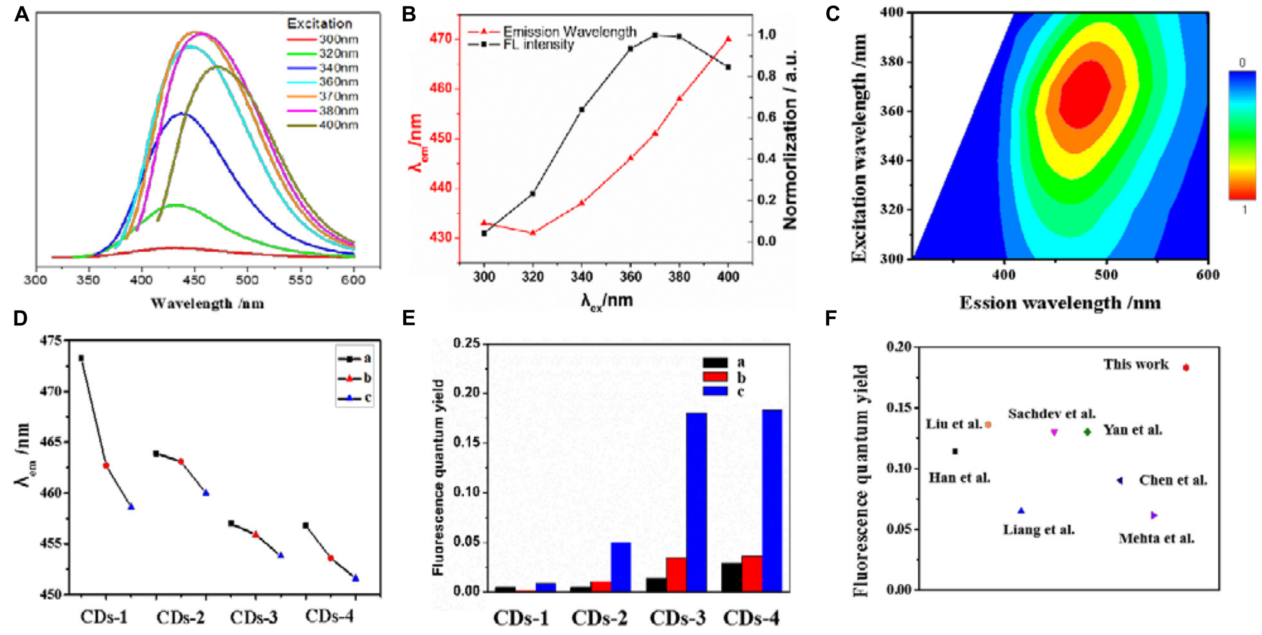

FIGURE 3 | The excitation-dependent PL behavior of the CDs-4a aqueous solution **(A,B)**. **(C)** 2D excitation-emission contour map of CDs-4a at different excitation wavelengths. The emission wavelength of different CDs samples with the same excitation wavelength at 370 nm **(D)**. The fluorescence quantum yield of different CDs samples **(E)**. Comparison of fluorescence quantum yield of CDs-4a with reported CDs in the literatures **(F)**.

The response of the CDs to metal stimuli was determined in a phosphate buffered saline (PBS) solution at pH 6.86. A 10 μmol/L aliquot of a solution containing different metal ions (Hg^{2+}, Ag^{+}, Mn^{2+}, Cr^{3+}, Ca^{2+}, Fe^{3+}, Ni^{2+}, Cu^{2+}, Co^{2+}, Zn^{2+}, Pb^{2+}, Mg^{2+}) was added into the CDs solution (50 μg/L). The fluorescence intensity at 450 nm was measured. Different metal ion solutions (10 μmol/L) were added into 3 mL of the CDs solution (50 μg/L), and the fluorescence intensity at emission wavelength of 450 nm was measured using fluorescence emission spectroscopy. Hg^{2+} solution with different concentration was added to the prepared CDs solution (50 μg/L), and the fluorescence intensity at emission wavelength of 450 nm was measured using fluorescence emission spectroscopy.

In vitro Cytotoxicity Assay

The influence of CDs-4a on the proliferation properties of an FL cell line was determined using a cell counting kit-8 (CCK-8) assay. The FL cell line was seeded in 96-well culture plates with a density of 1 × 10^4 cells/cm^2 in a medium containing 10% fetal bovine serum and 1% penicillin–streptomycin. After 13 h of standard incubation, the cells adhered and spread over the bottom of the plate. Subsequently, the old cell culture medium was removed, and the cells were rinsed in the PBS solution. Next, 200 μL of fresh media with varying concentrations of CDs was added for the continuous cell culture. At intervals of 24, 48, and 72 h later, the CCK-8 assay was performed in a dark environment to quantify the number of living cells. Fluorescence images of the trypsin digests cells labeled using CDs-4a with different particle sizes were obtained at an absorbance of 450 nm using the microplate reader (Gao et al., 2018; Malina et al., 2019; Ren et al., 2019).

RESULTS AND DISCUSSION

Preparation and Characterization of CDs

The FTIR spectra of the CDs are shown in **Figure 1**. The characteristic peak of the CDs at 3450 cm^{-1} relates to the stretching vibration of –OH and –NH. The peak at 2910 cm^{-1} is the stretching vibration of $-CH_3$. The characteristic peak at 1680 cm^{-1} corresponded to the stretching vibration of C=O, which resulted from C–OH oxidation during the hydrothermal reaction. This reaction is regarded as a luminescence emission source that can be used for fluorescence detection. It is worth noting that, compared with cellulose there was an obvious change of the characteristic peaks at 1230 cm^{-1} and 1100 cm^{-1} corresponding to the stretching vibrations of C–O–C, in the other types of CDs. This can be attributed to the ring-opening reaction of cellulose and its subsequent oxidation in the presence of NaOH or urea. The morphology of the NaOH/urea/cellulose CDs-4 was studied using TEM. As shown in **Figures 2A–C**, the CDs-4 particles were almost spherical in structure and exhibited no agglomeration or decomposition. In order to investigate the effect of particle size, the CDs-4 particles were separated into CDs-4a, CDs-4b, and CDs-4c using a dialysis bag with different molecular weight cut-off values; the higher the molecular weight, the bigger the particle size. **Figure 2D** shows the distribution of diameters for CDs-4a, CDs-4b, and CDs-4c were 2.11, 3.94, and 8.72 nm, respectively (**Table 1**).

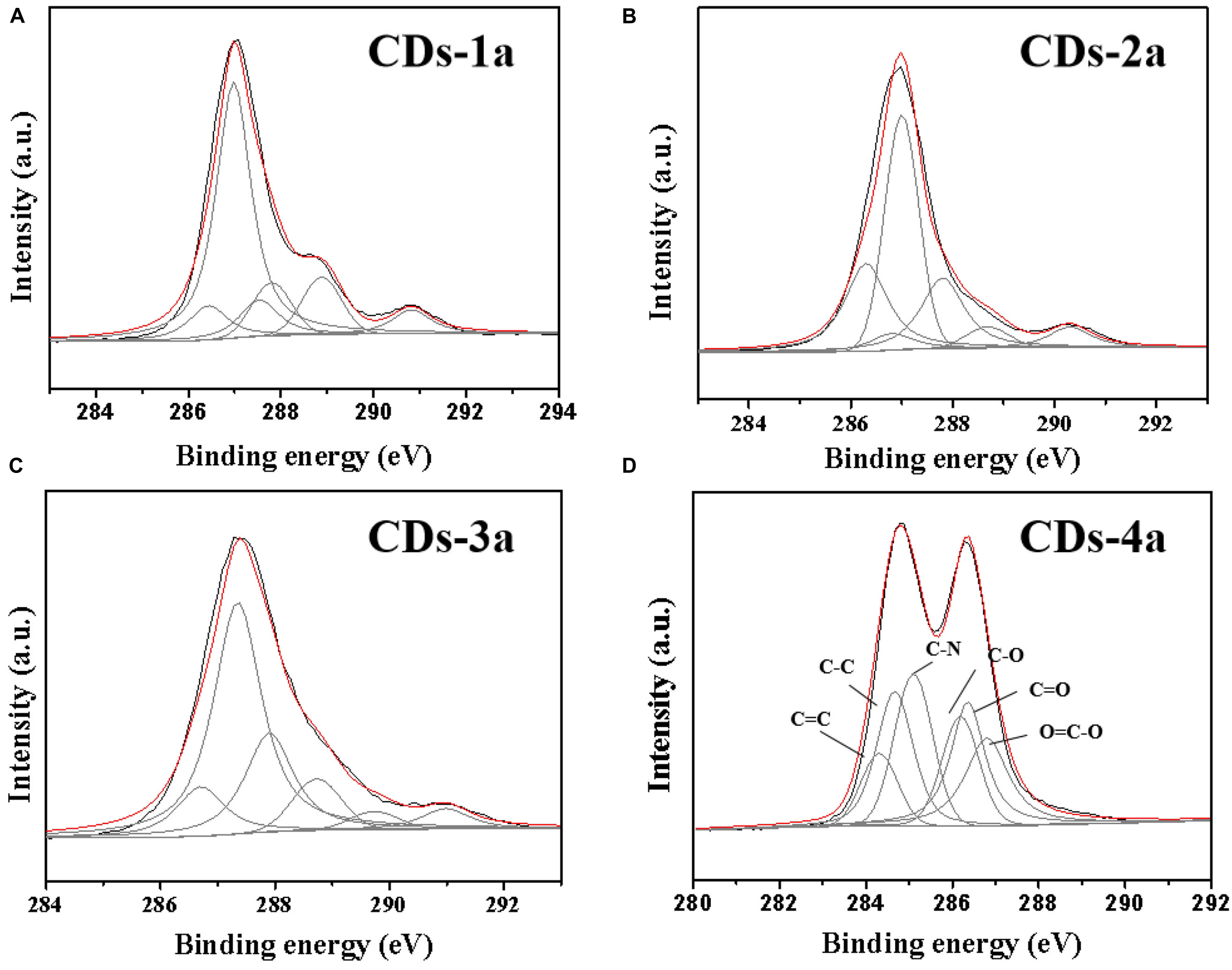

FIGURE 4 | The XPS spectra of CDs: **(A)** CDs-1a; **(B)** CDs-2a; **(C)** CDs-3a, and **(D)** CDs-4a.

TABLE 3 | The elements content and functional groups of different CDs samples.

Sample	C at%	N at%	O at%	C=C%	C=O%	C–N%
CDs-1a	82.74	1.06	16.19	8.69	15.92	6.76
CDs-2a	86.07	1.59	12.35	9.13	16.46	3.05
CDs-3a	74.31	6.97	18.72	12.29	20.99	17.63
CDs-4a	74.15	7.77	18.07	14.62	21.05	19.18

Fluorescence Properties of CDs

In order to investigate the fluorescence properties of CDs-4a, the excitation wavelength of CDs-4a was measured at wavelengths between 300 and 400 nm. As shown in **Figures 3A–C**, under the excitation wavelength of 370 nm, the fluorescence spectra of the CDs-4 exhibited a strong, single peak at 450 nm. Thus, an excitation wavelength of 370 nm was used for the following investigations. In addition, at the same excitation wavelength of 370 nm, it was found that the emission wavelength decreased as the particle size increased (**Figure 3D**). This results from the fact that the CDs particle size significantly affects the number of conjugated structures (Tao et al., 2017; Barman and Patra, 2018; Yan et al., 2019). Furthermore, the addition of NaOH or urea also affects the emission wavelength, leading to a blue shift. The maximum emission wavelengths of CDs-4a, CDs-4b, and CDs-4c were 450, 455, and 460 nm, respectively.

The relative fluorescence QY is an important factor in determining the fluorescence performance of fluorescent materials (Angshuman et al., 2016). Thus, the fluorescence QY of the different types of CDs was measured to evaluate the fluorescence properties. As shown in **Figure 3E** (**Table 2**), among all the types of CDs, CDs-1 exhibited the lowest QY. The introduction of NaOH or urea resulted in an obvious enhancement of the QY. Among all the samples, the CDs-4 exhibited the highest QY and the best fluorescence performance. Compared with most previously reported CDs, the QY of CDs-4a exhibits a higher performance of 0.183 (**Figure 3F**; Mehta et al., 2014; Sachdev and Gopinath, 2015; Chen et al., 2016; Liang et al., 2016; Yan et al., 2016; Liu et al., 2017; Han et al., 2018). This was a result of the effective promotion of the ring-opening and subsequent oxidation reaction of cellulose following the

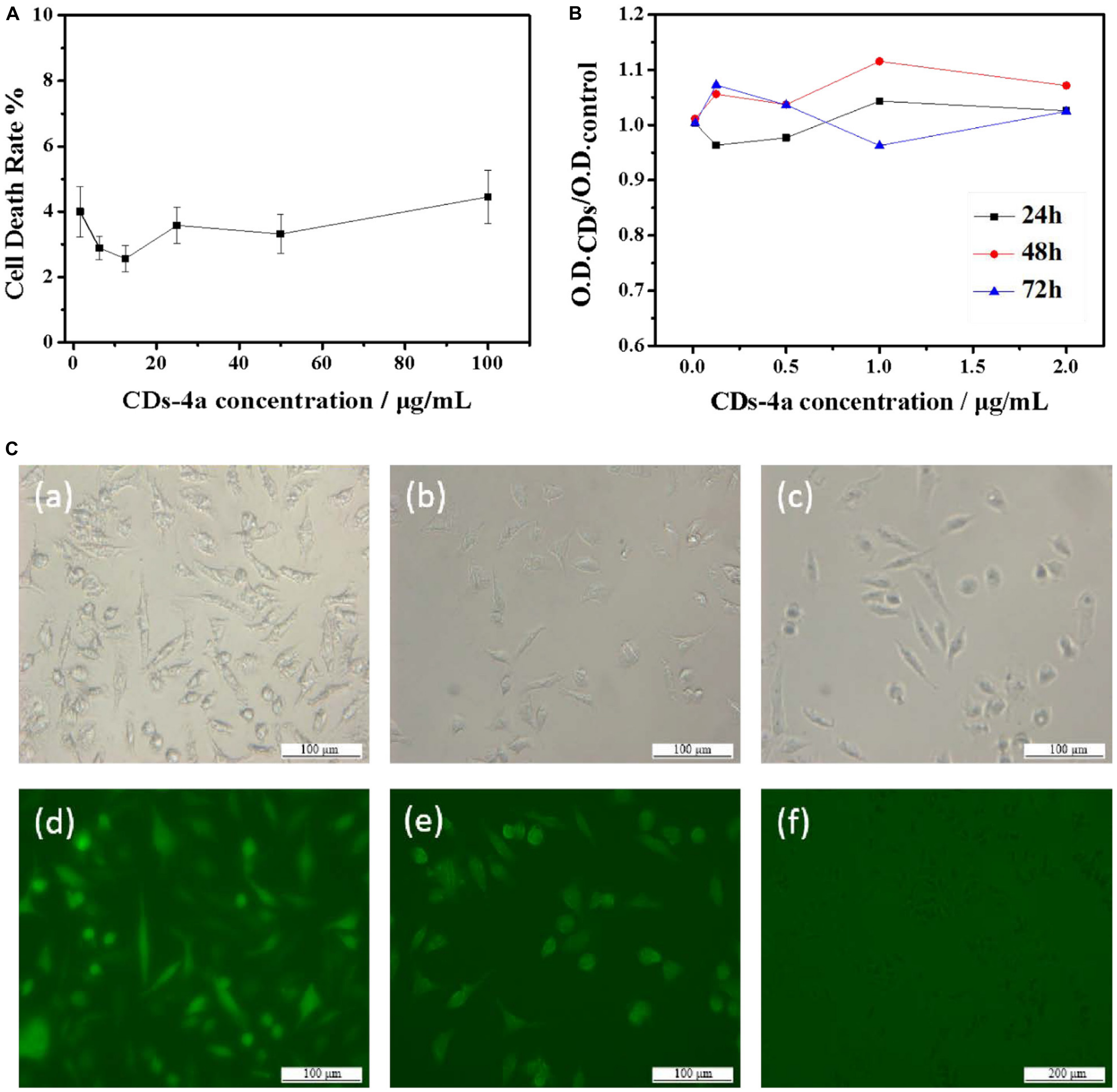

FIGURE 5 | (A) Curve of acute toxicity test of CDs-4a with different concentration. **(B)** Cytostasis curve of CDs-4a with different concentration in 24, 48, and 72 h. **(C)** The FL cells images of **(a)** CDs-4a, **(b)** CDs-4b, **(c)** CDs-4c under visible light and **(d)** CDs-4a, **(e)** CDs-4b, **(f)** CDs-4c under the UV excitation.

addition of NaOH or urea, which also provided increased doping of elements.

An XPS analysis of the CDs was performed (**Figure 4** and **Table 3**). It was found that, CDs-3a and CDs-4a contained a higher nitrogen content than that of CDs-1a and CDs-2a. This demonstrated that, the addition of urea increased the amount of nitrogen functional groups in the CDs during the hydrothermal reaction. Furthermore, the C1S spectrum indicated that the amount of C=C/C=O and C–N functional groups in CDs-3a and CDs-4a was substantially higher than that of CDs-1a and CDs-2a, and as such an effective auxochrome was produced that enhanced the relative fluorescence emission efficiency. Hence, in comparison with the other samples, the CDs-3a and CDs-4a exhibited the best relative fluorescence emission efficiency.

In addition, for CDs pretreated using the same method, the particle size significantly influenced the QY. With increasing particle size, the QY obviously decreased. For example, the QY of CDs-4a was 0.18, which was much higher than that of CDs-4b and CDs-4c. This may be attributed to the smaller particle size and corresponding high number of luminous groups on the surface. Due to their excellent relative fluorescence emission efficiency, the CDs-4a were regarded as the ideal candidate for use in the remainder of this study.

Biocompatibility of CDs-4

In terms of future applications, assessment of the potential cytotoxicity of the biocompatible CDs is extremely important. As such, the biocompatibility of the CDs-4a was evaluated using FL cells. As shown in **Figure 5A**, after 12 h incubation, the cell death

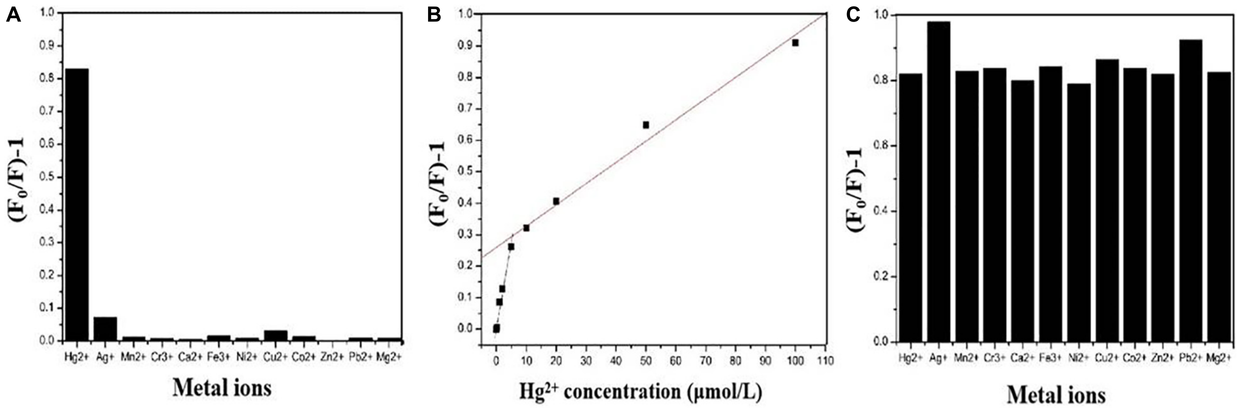

FIGURE 6 | Fluorescent response of CDs-4a in the presence of 10 μM of different metal ions **(A)**. Plots of the values of (F_0/F)-1 versus the concentration of Hg^{2+} **(B)**. Fluorescence response of CDs-4a in the presence of 10 μM Hg^{2+} and 10 μM another kind of metal ions **(C)**.

TABLE 4 | Detection limit and linear range of Hg^{2+} detectors.

Detection probes	Linear range (μ M)	Detection limit (μ M)	References
Hydrogel CDs	0.2–10, 10-100	0.2	This work
Eu^{3+}-CDs	5–250	2.2	Desai et al., 2018
N,S-CDs	1–75	0.5	Xu et al., 2018
N-CQDs	0–25	0.23	Zhang H. et al., 2020
TFIC MNPs	4–16	5.04	Wang et al., 2013
Polymer sensor	1–30	0.728	Li et al., 2012
NCDs	0.9–10	0.15	Zhang C. et al., 2020

rate remained below 5%, even at high CDs-4a concentrations of up to 100 μg/mL. Cytostatic curves of the CDs-4a were obtained at different concentrations. **Figure 5B** shows the cell viability following treatment with different concentrations of CDs for 24, 48, and 72 h. The exert concentration of CDs at different concentrations did not result in a significant decrease in cell viability after 72 h, which suggests good biocompatibility. This result is similar with the results of other biocompatible CDs from natural polymer biomaterials (Sharma et al., 2017; Zhou et al., 2017; Zhang et al., 2018; Meng et al., 2019; Zulfajri et al., 2020).

Figure 5C shows fluorescence images of trypsin digests cells labeled using different sized CDs-4. The brightest regions are the CDs-4a, indicating they can be clearly distinguished; therefore, the CDs-4a displayed the best fluorescence performance. As well as a high QY value, the CDs-4a have a small particle size meaning they are easily taken up by cells. These cytotoxicity results imply that the CDs-4a prepared from hydrogels have potential for use in the labeling of living cells.

Specific Detection of CDs-4a for Hg^{2+}

Figure 6A shows the fluorescence response performance of CDs-4a to different heavy metal ions. Compared with other metal ions, CDs-4a exhibited a specific response to Hg^{2+} ions. The addition of Hg^{2+} ions significantly quenched the fluorescence of CDs-4a, indicating promise for application in the selective detection of heavy metal ions. It could be attributed to the strong interactions between Hg^{2+} and functional groups of C=C/C=O and C–N of CDs-4a, which could effectively reduce the relative fluorescence strength. In order to evaluate the ability of the CDs-4a to detect Hg^{2+}, the fluorescence quenching intensity of the CDs-4a was measured at various Hg^{2+} ion concentrations and calculated using the Stern-Volmer equation:

$$\frac{F_0}{F} - 1 = \mathrm{K}\,[Q] \tag{1}$$

Where F_0 and F represent the fluorescence intensity of the fluorophore in the absence and presence of metal ions, respectively. K is the Stern-Volmer constant, and $[Q]$ is the metal ion concentration. As shown in **Figure 6B**, the fluorescence quenching intensity obviously increased when the metal ion concentration was increased from 0.2 to 100 μmol/L. A two-stage, concentration-dependent fluorescence response was observed. Both stages exhibited a good linear relationship between (F_0/F - 1) and concentration, ranging from 0.2 to 10 μmol/L (R^2 = 0.9948, K = 5.88 × 10^4) and from 10 to 100 μmol/L (R^2 = 0.9911, K = 6.66 × 10^3). The Stern-Volmer constant varies above and below a concentration of 10 μmol/L. In the low concentration stage, the slope is steep, and in the high concentration stage, the slope is less steep, which means that CDs-4a is more sensitive under lower concentration conditions. When the metal ion concentration was 0.2 μmol/L, the CDs-4a retained their Hg^{2+} detection ability and the fluorescence quenching intensity was maintain at approximately 0.1, which suggests a good sensitivity toward Hg^{2+} ions. Compared with most reports of Hg^{2+} ion detection, the CDs-4a displayed an excellent ability to detect Hg^{2+} ions (**Table 4**; Li et al., 2012; Wang et al., 2013; Desai et al., 2018; Xu et al., 2018; Zhang C. et al., 2020; Zhang H. et al., 2020). Based on the good linear relationship and low detection limit, the CDs-4a are able to specifically detect Hg^{2+} ions as well as quantify the concentration of Hg^{2+} ions.

During practical applications, interference from other metal ions that co-exist with Hg^{2+} ions in solution may affect the detection. To study the effect of these interfering ions, further experiments were performed. The ability of CDs-4a to detect Hg^{2+} ions in the presence of other, interfering metal ions was determined. **Figure 6C** shows the fluorescence quenching intensity measured in a solution of Hg^{2+} mixed with other ions, it was observed that the fluorescence quenching intensity of almost all the other ions was similar to that of the pure Hg^{2+} solution, only Ag^{+} and Pb^{2+} slightly increased the fluorescence quenching intensity. These results indicate the CDs-4a have the capacity to resist interference from other ions during the detection of Hg^{2+} ions, which is significant in practical applications.

CONCLUSION

In this work, a series of novel, biocompatible CDs were prepared from the natural polymer, cellulose hydrogel. Using an effective pretreatment method, the fluorescence performance was enhanced. Using dialysis bags with different molecular weight cut-off values, the CDs were separated into samples with different particle size. With the decrease of the particle size, the fluorescence QY of CDs increased. The CDs-4a exhibited good fluorescence during living cell labeling due to their small particle size and the presence of functional groups on the particle surface. More importantly, the CDs-4a exhibited specific detection of the heavy metal ion Hg^{2+} with high sensitivity. The LOD was as low as 0.2 μM and a two stage linear detection (0.2–10 and 10–100 μM) was observed. The CDs-4a also maintained an excellent detection ability, even in complex solutions containing interference metal ions, such as Fe^{3+}, Zn^{2+}, Mg^{2+}, and Ni^{2+}. We believe this work will provide novel insights into the development of high-performance multifunctional CDs based on a low-cost and natural polymer, cellulose hydrogel.

DATA AVAILABILITY STATEMENT

The original contributions presented in the study are included in the article/supplementary material, further inquiries can be directed to the corresponding authors.

AUTHOR CONTRIBUTIONS

MX and XW proposed the idea. HH and HG did the experiments. ZH helped the property evaluation of CDs. ZR helped the vitro cytotoxicity assay of CDs. All authors contributed to the article and approved the submitted version.

FUNDING

This work was supported by the National Key Research and Development Program of China (No. 2018YFC1602800).

REFERENCES

Ali, H., and Khan, E. (2018). Bioaccumulation of non-essential hazardous heavy metals and metalloids in freshwater fish. Risk to human health. *Environ. Chem. Lett.* 16, 903–917. doi: 10.1007/s10311-018-0734-7

Angshuman, R. C., Tanya, S., Sudip, K. G., and Sumanta, K. S. (2016). Carbon dots embedded magnetic Nanoparticles @Chitosan @Metal organic framework as a nanoprobe for pH sensitive targeted anticancer drug delivery. *ACS Appl. Mater. Interfaces* 8, 16573–16583. doi: 10.1021/acsami.6b03988

Ansi, V. A., and Renuka, N. K. (2019). Exfoliated graphitic carbon dots: application in heavy metal ion sensing. *J. Lumin.* 205, 467–474. doi: 10.1016/j.jlumin.2018.09.061

Bansod, B., Kumar, T., Thakur, R., Rana, S., and Singh, I. (2017). A review on various electrochemical techniques for heavy metal ions detection with different sensing platforms. *Biosens. Bioelectron.* 94, 443–455. doi: 10.1016/j.bios.2017.03.031

Barman, M. K., and Patra, A. (2018). Current status and prospects on chemical structure driven photoluminescence behaviour of carbon dots. *J. Photoch. Photobio. C.* 37, 1–22. doi: 10.1016/j.jphotochemrev.2018.08.001

Bolisetty, S., Peydayesh, M., and Mezzenga, R. (2019). Sustainable technologies for water purification from heavy metals: review and analysis. *Chem. Soc. Rev.* 48, 463–487. doi: 10.1039/c8cs00493e

Cai, L. M., Wang, Q. S., Luo, J., Chen, L. G., Zhu, R. L., Wang, S., et al. (2019). Heavy metal contamination and health risk assessment for children near a large Cu-smelter in central China. *Sci. Total Environ.* 650, 725–733. doi: 10.1016/j.scitotenv.2018.09.081

Chen, Y., Wu, Y., Weng, B., Wang, B., and Li, C. (2016). Facile synthesis of nitrogen and sulfur co-doped carbon dots and application for Fe (III) ions detection and cell imaging. *Sens. Actuators B Chem.* 223, 689–696. doi: 10.1016/j.snb.2015.09.081

Desai, M. L., Jha, S., Basu, H., Singhal, R. K., Sharma, P. K., and Kailasa, S. K. (2018). Microwave-assisted synthesis of water-soluble Eu3+ hybrid carbon dots with enhanced fluorescence for the sensing of Hg2+ ions and imaging of fungal cells. *New J. Chem.* 42, 6125–6133. doi: 10.1039/c7nj04835a

Gao, W., Song, H., Wang, X., Liu, X., Pang, X., Zhou, Y., et al. (2018). Carbon dots with red emission for sensing of Pt(2+), Au(3+), and Pd(2+) and their bioapplications in vitro and in vivo. *ACS Appl. Mater. Interfaces* 10, 1147–1154. doi: 10.1021/acsami.7b16991

Han, M., Zhu, S., Lu, S., Song, Y., Feng, T., Tao, S., et al. (2018). Recent progress on the photocatalysis of carbon dots: classification, mechanism and applications. *Nano Today* 19, 201–218. doi: 10.1016/j.nantod.2018.02.008

Huang, H., Wang, X., Ge, H., and Xu, M. (2016). Multifunctional magnetic cellulose surface-imprinted microspheres for highly selective adsorption of artesunate. *ACS Sustainable Chem. Eng.* 4, 3334–3343. doi: 10.1021/acssuschemeng.6b00386

Kahlon, S. K., Sharma, G., Julka, J. M., Kumar, A., Sharma, S., and Stadler, F. J. (2018). Impact of heavy metals and nanoparticles on aquatic biota. *Environ. Chem. Lett.* 16, 919–946. doi: 10.1007/s10311-018-0737-4

Khan, W. U., Wang, D., Zhang, W., Tang, Z., Ma, X., Ding, X., et al. (2017). High quantum yield green-emitting carbon dots for Fe(capital I, Ukrainiancapital I, Ukrainiancapital I, Ukrainian) detection, biocompatible fluorescent ink and cellular imaging. *Sci. Rep.* 7:14866. doi: 10.1038/s41598-017-15054-9

Kumar, A., Kumar, A. M., Cabral-Pinto, M. S., Chaturvedi, A. K., Shabnam, A. A., Subrahmanyam, G., et al. (2020). Lead toxicity: health hazards, influence on food chain, and sustainable remediation approaches. *Int. J. Environ. Res. Public Health.* 17:2179. doi: 10.3390/ijerph17072179

Li, J. F., Wu, Y. Z., Song, F. Y., Wei, G., Cheng, Y. X., and Zhu, C. J. (2012). A highly selective and sensitive polymer-based OFF–ON fluorescent sensor for Hg2+ detection incorporating salen and perylenyl moieties. *J. Mater. Chem.* 22, 478–482. doi: 10.1039/C1JM14037J

Li, Z., Chen, J., Guo, H., Fan, X., Wen, Z., Yeh, M. H., et al. (2016). Triboelectrification-enabled self-powered detection and removal of heavy metal ions in wastewater. *Adv. Mater.* 28, 2983–2991. doi: 10.1002/adma.201504356

Liang, Z., Kang, M., Payne, G. F., Wang, X., and Sun, R. (2016). Probing energy and electron transfer mechanisms in fluorescence quenching of biomass carbon quantum dots. *ACS Appl. Mater. Interfaces* 8, 17478–17488. doi: 10.1021/acsami.6b04826

Liu, H., Li, Z., Sun, Y., Geng, X., Hu, Y., Meng, H., et al. (2018). Synthesis of luminescent carbon dots with ultrahigh quantum yield and inherent folate receptor-positive cancer cell targetability. *Sci. Rep.* 8:1086. doi: 10.1038/s41598-018-19373

Liu, M. L., Chen, B. B., Li, C. M., and Huang, C. Z. (2019). Carbon dots: synthesis, formation mechanism, fluorescence origin and sensing applications. *Green Chem.* 21, 449–471. doi: 10.1039/c8gc02736f

Liu, W., Diao, H., Chang, H., Wang, H., Li, T., and Wei, W. (2017). Green synthesis of carbon dots from rose-heart radish and application for Fe3+ detection and cell imaging. *Sens. Actuators B Chem.* 241, 190–198. doi: 10.1016/j.snb.2016.10.068

Lu, Y., Liang, X., Niyungeko, C., Zhou, J., Xu, J., and Tian, G. (2018). A review of the identification and detection of heavy metal ions in the environment by voltammetry. *Talanta* 178, 324–338. doi: 10.1016/j.talanta.2017.08.033

Malik, L. A., Bashir, A., Qureashi, A., and Pandith, A. H. (2019). Detection and removal of heavy metal ions: a review. *Environ. Chem. Lett.* 17, 1495–1521. doi: 10.1007/s10311-019-00891-z

Malina, T., Poláková, K., Skopalík, J., Milotová, V., Holá, K., Havrdová, M., et al. (2019). Carbon dots for in vivo fluorescence imaging of adipose tissue-derived mesenchymal stromal cells. *Carbon* 152, 434–443. doi: 10.1016/j.carbon.2019.05.061

Mehta, V. N., Jha, S., Singhal, R. K., and Kailasa, S. K. (2014). Preparation of multicolor emitting carbon dots for HeLa cell imaging. *New J. Chem.* 38, 6152–6160. doi: 10.1039/C4NJ00840E

Meng, W., Bai, X., Wang, B., Liu, Z., Lu, S., and Yang, B. (2019). Biomass-derived carbon dots and their applications. *Energy Environ. Mater.* 2, 172–192. doi: 10.1002/eem2.12038

Oliveira, C. S., Segatto, A. L. A., Nogara, P. A., Piccoli, B. C., Loreto, E. L. S., Aschner, M., et al. (2020). Transcriptomic and proteomic tools in the study of hg toxicity: what is missing? *Front. Genet.* 11:425. doi: 10.3389/fgene.2020.00425

Pang, Y., Gao, H., Wu, S., and Li, X. (2017). Facile synthesis the nitrogen and sulfur co-doped carbon dots for selective fluorescence detection of heavy metal ions. *Mater. Lett.* 193, 236–239. doi: 10.1016/j.matlet.2017.01.149

Patel, K. D., Singh, R. K., and Kim, H. W. (2019). Carbon-based nanomaterials as an emerging platform for theranostics. *Mater. Horiz.* 6, 434–469. doi: 10.1039/C8MH00966J

Qi, Y., Ma, J., Chen, X., Xiu, F. R., Chen, Y., and Lu, Y. (2020). Practical aptamer-based assay of heavy metal mercury ion in contaminated environmental samples: convenience and sensitivity. *Anal. Bioanal. Chem.* 412, 439–448. doi: 10.1007/s00216-019-02253-8

Rajendra, K. S., Amal, G. K., Kapil, D. P., Nandin, M., Na-Hyun, L., Jonathan, C. K., et al. (2020). Label-free fluorescent mesoporous bioglass for drug delivery, optical triple-mode imaging, and photothermal/photodynamic synergistic cancer therapy. *ACS Appl. Bio. Mater.* 3, 2218–2229. doi: 10.1021/acsabm.0c00050

Ren, Z., Huang, H., Zhang, J., Qi, H., Xu, M., and Wang, X. (2019). Cellulose hydrogel is a novel carbon-source and doping-material-carrier to prepare fluorescent carbon dots for intracellular bioimaging. *SN Appl. Sci.* 2:17. doi: 10.1007/s42452-019-1794-4

Rossini-Oliva, S., Abreu, M. M., Santos, E. S., and Leidi, E. O. (2020). Soil–plant system and potential human health risk of Chinese cabbage and oregano growing in soils from Mn and Fe abandoned mines: microcosm assay. *Environ. Geochem. Health.* 42, 4073–4086. doi: 10.1007/s10653-020-00514-5

Sachdev, A., and Gopinath, P. (2015). Green synthesis of multifunctional carbon dots from coriander leaves and their potential application as antioxidants, sensors and bioimaging agents. *Analyst* 140, 4260–4269. doi: 10.1039/C5AN00454C

Sarma, G. K., Sen Gupta, S., and Bhattacharyya, K. G. (2019). Nanomaterials as versatile adsorbents for heavy metal ions in water: a review. *Environ. Sci. Pollut. Res. Int.* 26, 6245–6278. doi: 10.1007/s11356-018-04093-y

Sharma, V., Tiwari, P., and Mobin, S. M. (2017). Sustainable carbon-dots: recent advances in green carbon dots for sensing and bioimaging. *J. Mater. Chem B.* 5, 8904–8924. doi: 10.1039/c7tb02484c

Shi, L., Yang, J. H., Zeng, H. B., Chen, Y. M., Yang, S. C., Wu, C., et al. (2016). Carbon dots with high fluorescence quantum yield: the fluorescence originates from organic fluorophores. *Nanoscale* 8, 14374–14378. doi: 10.1039/c6nr00451b

Tao, S., Song, Y., Zhu, S., Shao, J., and Yang, B. (2017). A new type of polymer carbon dots with high quantum yield: from synthesis to investigation on fluorescence mechanism. *Polymer* 116, 472–478. doi: 10.1016/j.polymer.2017.02.039

Wang, B., Tan, H., Zhang, T., Duan, W., and Zhu, Y. (2019). Hydrothermal synthesis of N-doped carbon dots from an ethanolamine-ionic liquid gel to construct label-free multifunctional fluorescent probes for Hg2+, Cu2+ and S2O32-. *Analyst* 144, 3013–3022. doi: 10.1039/c9an00116f

Wang, C., Wang, C., Xu, P., Li, A., Chen, Y., and Zhuo, K. (2015). Synthesis of cellulose-derived carbon dots using acidic ionic liquid as a catalyst and its application for detection of Hg2+. *J. Mater. Sci.* 51, 861–867. doi: 10.1007/s10853-015-9410-5

Wang, W., Zhang, Y., Yang, Q. B., Sun, M. D., Fei, X. L., Song, Y., et al. (2013). Fluorescent and colorimetric magnetic microspheres as nanosensors for Hg2+ in aqueous solution prepared by a sol–gel grafting reaction and host-guest interaction. *Nanoscale* 5, 4958–4965. doi: 10.1039/C3NR00580A

Wu, Y., Pang, H., Liu, Y., Wang, X., Yu, S., Fu, D., et al. (2019). Environmental remediation of heavy metal ions by novel-nanomaterials: a review. *Environ. Pollut.* 246, 608–620. doi: 10.1016/j.envpol.2018.12.076

Wu, Z. L., Liu, Z. X., and Yuan, Y. H. (2017). Carbon dots: materials, synthesis, properties and approaches to long-wavelength and multicolor emission. *J. Mater. Chem. B.* 5, 3794–3809. doi: 10.1039/c7tb00363c

Xu, Y., Li, H., Wang, B., Liu, H., Zhao, L., Zhou, T. Y., et al. (2018). Microwave-assisted synthesis of carbon dots for "turn-on" fluorometric determination of Hg(II) via aggregation-induced emission. *Mikrochim. Acta* 185:252. doi: 10.1007/s00604-018-2781-y

Yan, F., Sun, Z., Zhang, H., Sun, X., Jiang, Y., and Bai, Z. (2019). The fluorescence mechanism of carbon dots, and methods for tuning their emission color: a review. *Mikrochim. Acta.* 186:583. doi: 10.1007/s00604-019-3688-y

Yan, Z., Zhang, Z., and Chen, J. (2016). Biomass-based carbon dots: synthesis and application in imatinib determination. *Sens. Actuators B Chem.* 225, 469–473. doi: 10.1016/j.snb.2015.10.107

Yarur, F., Macairan, J. R., and Naccache, R. (2019). Ratiometric detection of heavy metal ions using fluorescent carbon dots. *Environ. Sci.* 6, 1121–1130. doi: 10.1039/c8en01418c

Yoo, D., Park, Y., Cheon, B., and Park, M. H. (2019). Carbon dots as an effective fluorescent sensing platform for metal ion detection. *Nanoscale Res Lett.* 14:272. doi: 10.1186/s11671-019-3088-6

Zhang, C., Wu, S., Yu, Y., and Chen, F. (2020). Determination of thiourea based on the reversion of fluorescence quenching of nitrogen doped carbon dots by Hg2+. *Spectrochim. Acta Part A Mol. Biomol. Spectrosc.* 227:117666. doi: 10.1016/j.saa.2019.117666

Zhang, H., You, J., Wang, J., Dong, X., Guan, R., and Cao, D. (2020). Highly luminescent carbon dots as temperature sensors and "off-on" sensing of Hg2+ and biothiols. *Dyes Pigm.* 173:107950. doi: 10.1016/j.dyepig.2019.107950

Zhang, X., Jiang, M., Niu, N., Chen, Z., Li, S., Liu, S., et al. (2018). Natural-product-derived carbon dots: from natural products to functional materials. *ChemSusChem* 11, 11–24. doi: 10.1002/cssc.201701847

Zhou, Y., Desserre, A., Sharma, S. K., Li, S., Marksberry, M. H., Chusuei, C. C., et al. (2017). Gel-like carbon dots: characterization and their potential applications. *ChemPhysChem* 18, 890–897. doi: 10.1002/cphc.201700038

Zhou, Y., Mintz, K. J., Sharma, S. K., and Leblanc, R. M. (2019). Carbon dots: diverse preparation, application, and perspective in surface chemistry. *Langmuir* 35, 9115–9132. doi: 10.1021/acs.langmuir.9b00595

Zulfajri, M., Abdelhamid, H. N., Sudewi, S., Dayalan, S., Rasool, A., Habib, A., et al. (2020). Plant part-derived carbon dots for biosensing. *Biosensors* 10:68. doi: 10.3390/bios10060068

Conflict of Interest: The authors declare that the research was conducted in the absence of any commercial or financial relationships that could be construed as a potential conflict of interest.

frontiers
in Bioengineering and Biotechnology

ORIGINAL RESEARCH
published: 28 January 2021
doi: 10.3389/fbioe.2020.616467

Permeation of Silver Sulfadiazine Into TEMPO-Oxidized Bacterial Cellulose as an Antibacterial Agent

Shahia Khattak[1,2], *Xiao-Tong Qin*[1,2], *Fazli Wahid*[1,2], *Long-Hui Huang*[1,2], *Yan-Yan Xie*[1,2], *Shi-Ru Jia*[1,2] *and Cheng Zhong*[1,2]*

[1] State Key Laboratory of Food Nutrition & Safety, Tianjin University of Science & Technology, Tianjin, China, [2] Key Laboratory of Industrial Fermentation Microbiology, (Ministry of Education), Tianjin University of Science & Technology, Tianjin, China

Surface oxidation of bacterial cellulose (BC) was done with the TEMPO-mediated oxidation mechanism system. After that, TEMPO-oxidized bacterial cellulose (TOBC) was impregnated with silver sulfadiazine (AgSD) to prepare nanocomposite membranes. Fourier transform infrared spectroscopy (FTIR) was carried out to determine the existence of aldehyde groups on BC nanofibers and X-ray diffraction (XRD) demonstrated the degree of crystallinity. FESEM analysis revealed the impregnation of AgSD nanoparticles at TOBC nanocomposites with the average diameter size ranging from 11 nm to 17.5 nm. The sample $OBCS_3$ showed higher antibacterial activity against *Staphylococcus aureus*, *Pseudomonas aeruginosa*, and *Escherichia coli* by the disc diffusion method. The results showed AgSD content, dependent antibacterial activity against all tested bacteria, and degree of crystallinity increases with TOBC and AgSD. The main advantage of the applications of TEMPO-mediated oxidation to BC nanofibers is that the crystallinity of BC nanofibers is unchanged and increased after the oxidation. Also enhanced the reactivity of BC as it is one of the most promising method for cellulose fabrication and functionalization. We believe that the novel composite membrane could be a potential candidate for biomedical applications like wound dressing, BC scaffold, and tissue engineering.

Keywords: silver sulfadiazine, bacterial cellulose, TEMPO-oxidation, antibacterial activity, nanocomposites

Edited by:
Muhammad Wajid Ullah,
Huazhong University of Science and Technology, China

Reviewed by:
Mazhar Ul-Islam,
Dhofar University, Oman
Hengchong Shi,
Chinese Academy of Sciences, China

Correspondence:
Cheng Zhong
chzhong.tju@gmail.com

Specialty section:
This article was submitted to Biomaterials, a section of the journal Frontiers in Bioengineering and Biotechnology

Received: *12 October 2020*
Accepted: *16 December 2020*
Published: *28 January 2021*

Citation:
Khattak S, Qin X-T, Wahid F, Huang L-H, Xie Y-Y, Jia S-R and Zhong C (2021) Permeation of Silver Sulfadiazine Into TEMPO-Oxidized Bacterial Cellulose as an Antibacterial Agent. Front. Bioeng. Biotechnol. 8:616467. doi: 10.3389/fbioe.2020.616467

INTRODUCTION

Bacterial cellulose (BC) is one of the most promising biopolymers due to its environmentally friendly nature (Shao et al., 2017), which can be used for treatment of various bacterial infections after chemical modification (Zmejkoski et al., 2018). Bacterial infections being a chief health hazard necessitates antibacterial strategies, among which antibiotics are the most frequently used treatment (Percival et al., 2015; Qian et al., 2017). However, drug-resistant pathogens have forced researchers to explore novel antibacterial agents (Almeida et al., 2014; Ge et al., 2014). BC has several advantages over plant-derived cellulose, including high purity (Reiniati et al., 2017), high crystallinity, high elasticity (Wang et al., 2016), thermal stability, high degree of polymerization (Lin et al., 2013), excellent permeability, high porosity, water content, and high mechanical strength (Moniri et al., 2017). In spite of the several advantages, the significant drawback of the BC is that it lacks antibacterial property (Sulaeva et al., 2015). Modified BC is a splendid cure to all these failings of conventional antibiotics. Various treatments can be used to improve the properties of BC

(Fijałkowski et al., 2017). Such modification could improve/boost the properties of BC, for the applications in food industry as well as biomedical field (Habibi, 2014; Paximada et al., 2016). However, to obtain derivatives with innovative features, surface modification of BC (hydroxyl group on the surface of the BC) is an appealing strategy (Zmejkoski et al., 2018).

As the modification at C2 and C3, of the BC, usually leads to the decomposition of BC oligomers in case of using periodate oxidation (Saito and Isogai, 2004), so, in order to maintain the mechanical properties of BC, it is necessary to modify the hydroxyl group at the main surface only, i.e., selective oxidation (Lee et al., 2012). The commonly used method is the oxidation under alkaline conditions with TEMPO used in combination with NaBr/NaOCl (Saito and Isogai, 2004), because it binds the aldehydic (-CHO) and carboxylic (-COOH) functional groups obtained from the hydroxylic group present at the C6 position of BC. The surface modification with carboxylic groups promotes the decomposition of hydrogen bonds, which improve the accessibility of macromolecules and enhanced the reactivity (Okita et al., 2010). Also, the speed of reaction is high and is one of the most promising method for cellulose fabrication and functionalization (Isogai et al., 2011). TEMPO-mediated oxidation only increases the uniformity of accessibility of the reactive BC carboxylate (Lai et al., 2013). It did not induce antibacterial activity, which restricts/bounds the possibility of applications in the areas of biomedical applications. So, in order to solve this problem, some researchers have added Ag and Ag nanocomposites as an antibacterial agent (e.g., Ag, ZnO, and graphene oxide) in BC matrix (Fortunati et al., 2014; Liu et al., 2017; Khattak et al., 2019). Among them, Ag with sulfadiazine, i.e., AgSD, has been widely used as an antibacterial agent for topical treatment for decades (Atiyeh et al., 2007; Muangman et al., 2010). It also showed broader activity spectrum against *Pseudomonas aeruginosa*, *Escherichia coli*, and *Staphylococcus aureus* by disrupting the cell membrane (Hoffmann, 1984) and inhibiting the DNA replication (Aguzzi et al., 2014). Antibacterial activity develops by the degradation of AgSD into sulfadiazine and Ag ions (Fox and Modak, 1974; Fox, 1975). The Ag ion of the AgSD interrupts the triphosphate (ATP) synthesis (Liu et al., 2019), whereas sulfadiazine inhibits the synthesis of folic acid (Cook and Turner, 1975; Wei et al., 2011), because of the structural analog of p-aminobenzoic acid (PABA) (Baenziger and Struss, 1976) as shown in the example (**Figure 1A**). The chemical structure of AgSD is displayed in **Figure 1B**. Folic acid plays an essential role in the growth and reproduction of bacteria (Craig and Stitzel, 2004; Tacic et al., 2017). Folic acid synthesis and mode of action of sulfonamides (sulfadiazine) are schematically presented (**Figure 2**).

TEMPO oxidation enhances the reactivity of BC due to which the silver nanocomposites showed excellent antibacterial activity because the extensive surface morphology provides better contact with microorganisms (Tacic et al., 2017). Also, for the synthesis of silver nanoparticles, Ifuku et al. (2009) use the TEMPO-mediated oxidation system to prepare the TOBC pellicle as a reaction template. Recently, a conjugated highly porous antimicrobial dressing was developed by Mohseni et al. (2019), loaded with silver sulfadiazine, and its antibacterial activity and biocompatibility were evaluated. Silver-carboxylated nanocellulose was prepared from bagasse waste in treatment with ammonium persulfate using a facile and green photochemical approach (Caschera et al., 2020). In another study, the porous cellulose particles with solvent-releasing method, exhibiting high catalytic ability, were prepared and evaluated (Fujii et al., 2020). Garza-Cervantes and his co-workers synthesized a novel silver-containing biocomposite using green methodology (Garza-Cervantes et al., 2020). Wang and his co-workers developed an electroactive regenerated hydrogel with significant exhibited higher electrical conductivity (Wang et al., 2020). In another reported study, HEMA-based skin repair hydrogel was prepared with BC by polymerization (Di et al., 2017). Furthermore, thermally stable electrically conductive polyaniline-based BC biosensor nanotubes were prepared by Jasim et al. (2017). Sajjad and his co-workers also developed curcumin-based BC nanocomposites as wound dressing (Sajjad et al., 2020). Biopolymers like BC and chitosan were used to prepare scaffolds (Ul-Islam et al., 2019). Along with the above cited literature, silver nanoparticles have also been used in several applications incorporated with polymers like polyvinylpyrrolidone (PVP), polymethyl methacrylate (PMMA), zein, polyacrylonitrile (PAN), chitosan, 3D printing, and others as well (GhavamiNejad et al., 2015; Yang C. H. et al., 2016; Ullah et al., 2019). The commonly used modification methods include nanoparticle coating and metal oxide modification (Smith et al., 2017; Yao et al., 2018). Therefore, BC was considered to be an ideal matrix for these modifications (Martínez-Sanz et al., 2012; Yang et al., 2012; McCarthy et al., 2019). In the present study, TEMPO oxidation was used to introduce the carbonyl group (carboxylate) to BC, and it was further composited with AgSD particles. The main advantage of the TEMPO-mediated oxidation is the retained crystallinity of BC after oxidation and more reactivity while silver sulfadiazine (AgSD) makes it antibacterial. We believe that the composite membrane will find promising applications in the biomedical field like wound dressing, BC scaffolding, and tissue engineering.

MATERIALS AND METHODS

Materials

Silver sulfadiazine with molecular weight 357.14 g/mol was obtained from Meryer (Shanghai) Chemical Technology Co., Ltd. (Shanghai, China). Tryptone and yeast extract were obtained from Oxoid Ltd. (United Kingdom). Agar powder was purchased from Beijing Solarbio Science and Technology Co., Ltd. All other chemicals such as CH_3COOH, NaOH, and Na_2HPO_4 were of analytical grade.

Methods

Preparation of BC Membrane and Incubation Conditions

Microorganisms *Komagataeibacter xylinus* (*K. xylinus*) (CGMCC No. 2955) were evaluated/screened by our group (Zhong et al., 2013). BC films were prepared by the previously described method (Zhong et al., 2014; Yang X. N. et al., 2016). In brief, *K. xylinus* was cultured in a culture medium consisting of glucose (25.0 g/L), peptone (10 g/L), yeast extract (7.5 g/L), and disodium phosphate (10.0 g/L). The cultured medium pH

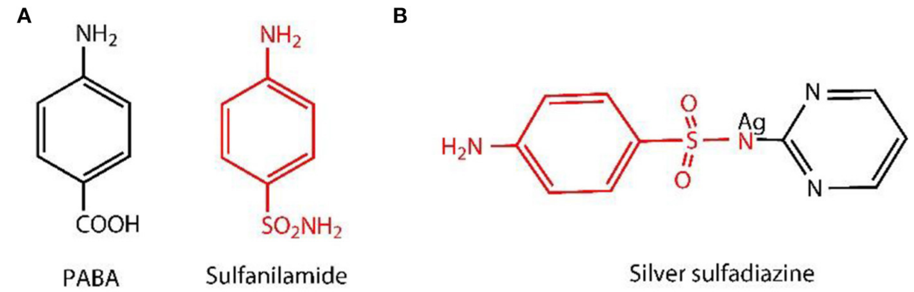

FIGURE 1 | Para-aminobenzoic acid (PABA) and structural analog of PABA (sulfanilamide) **(A)** and chemical structure of AgSD **(B)**.

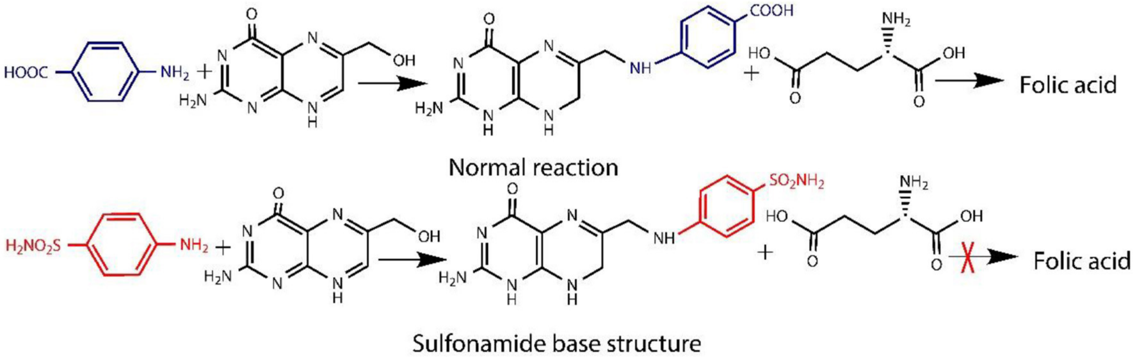

FIGURE 2 | Synthesis of Folic acid and sulfonamide action site.

was kept/adjusted to 6.0. The bacteria were inoculated into culture medium in a flask. The incubation was carried out at a temperature of 30°C and with a speed of 160 rpm for 24 h in a shaker. With a ratio of 8% (v/v), the cell suspension was inoculated into different culture medium and kept in incubation for 7 days at 30°C (Zhong et al., 2013). The BC membranes obtained were kept in alkaline solution (0.1 M NaOH) to remove the impurities. Membranes were washed with distilled water until neutral pH and stored for further use.

TEMPO-Mediated Oxidation of BC

BC was treated with a homogenizer (120 W) (Hualeda Instrument Co., Ltd, Beijing, China) until formation of the homogeneous slurry/pulp. In deionized water (100 ml), sample (1 g dry weight) of BC was suspended and stirred on a magnetic stirrer to form the homogeneous suspension of BC to properly oxidize it. In 20 ml of deionized water, sodium bromide (NaBr) (0.1 g) and TEMPO (0.016 g) were dissolved in order to form the TEMPO medium. This TEMPO-mediated solution was added to BC suspension with magnetic stirring. To initiate TEMPO-mediated oxidation, NaClO solution was added 10% (0.5 mmol/g) to the TEMPO-mediated BC suspension at room temperature. The pH of the solution was maintained between 10.5 and 11.0 with the addition of 0.5 mol/L NaOH solution. After 12 h, the oxidation was quenched by the addition of ethanol (C_2H_5OH) (5 ml). The oxidized BC was collected by centrifugation at 1000 rpm for 30 min, and with deionized water, it was washed thoroughly (Habibi et al., 2006; Okita et al., 2010). After washing, the precipitates of oxidized BC (TOBC) were stored at 4°C for further use (experiments).

Preparation of TOBC–AgSD Nanocomposites

The method of preparing TOBC–AgSD was described in literature with slight modification (Shao et al., 2016). To prepare the TOBC–AgSD composite, AgSD was dissolved in distilled water at room temperature and stirred with a magnetic stirrer the whole day and then sonicated for 90 min to form a homogeneous solution. AgSD was added into the TOBC dispersions and mixed for 1 h at magnetic stirring. The weight ratio of AgSD to TOBC was controlled to be 0.1 wt.%, 0.2 wt.%, and 0.3 wt.% (marked as $OBCS_1$, $OBCS_2$, and $OBCS_3$, respectively). Then, the mixture was treated by ultrasonication for 20 min. The weight of the TOBC (known) is kept constant. After the formation of AgSD–TOBC nanocomposites, samples were filtered and dried in the oven at 40–50°C.

Characterization

The FT-IR spectra of pure BC, TOBC, and TOBC–AgSD nanocomposites were measured using a Nicolet IS50 FT-IR spectrometer with a wavenumber ranging from 4000 to 400 cm^{-1}. XRD patterns of TOBC films and TOBC–AgSD nanocomposites were obtained using a Shimadzu XRD-6100 X-ray diffractometer at 40 kV with a scan range of 5–40° and a scan speed of 5°/min. The morphology of TOBC–AgSD nanocomposites was examined by FESEM. The elemental composition of AgSD was confirmed by EDS [energy-dispersive X-ray (EDX) analysis by EDAX].

Crystallinity Analysis

The degree of crystallinity (*CrI*) has been calculated by the reported method with slight modification (Pelegrini et al., 2019). Briefly, *CrI* is calculated from the ratio of the area of all crystalline peaks to the total area. XRD spectrum is used to calculate the *CrI*, by using software (Origin or Peak Fit) (Garvey et al., 2005). Gaussian functions in curve-fitting process are commonly used for the deconvolution of XRD spectra (Teeaar et al., 1987). Crystallinity can be calculated by using the equation.

$$\text{Crystallinity degree}(CRI) = \frac{Area\ of\ crystalline\ peaks}{Area\ of\ all\ peaks\ (\ crystalline\ +\ amorphous)} \times 100$$

Antibacterial Activity

The antibacterial activity of TOBC and TOBC–AgSD nanocomposites against *P. aeruginosa*, *E. coli*, and *S. aureus* was carried out by disk diffusion method. The disk diffusion method was performed in solid agar medium LB. TOBC (control) and AgSD–TOBC nanocomposites were cut into spherical shapes (10 mm diameter) and sterilized with an ultraviolet lamp for 30 min. The sterilized samples were then placed on solid agar carefully containing bacterial solution (1 ml) in 90-mm-diameter petri dishes. The plates (petri dishes) were incubated for 24 h in an incubator at 37°C. The diameter of the inhibition zones formed was measured and recorded using a Vernier caliper (Mohseni et al., 2019).

RESULTS AND DISCUSSION

Formation of TOBC–AgSD Nanocomposites

We used various concentrations of AgSD with TOBC to prepare TOBC–AgSD nanocomposites. Firstly, BC membranes, with the help of a homogenizer, were converted into BC slurry. Then, it was modified by the introduction of a carboxylic group under mild conditions using TEMPO-mediated oxidation. As the degree of oxidation increases, the hydrogen bonding between the TOBC matrix becomes stronger (Jia et al., 2019). The process is shown in **Figure 3**. Secondly, after oxidation, AgSD was mixed with TOBC slurry with different ratios. The proposed mechanism of the formation of TOBC–AgSD nanocomposites is shown in **Figure 4**.

EDX Analysis

EDX analysis was performed to quantitatively measure the content of Ag and sulfur in the nanofibers. It can be seen from **Figure 5** that $OBCS_1$ has lower Ag and S values than $OBCS_2$. The $OBCS_2$ has lower Ag and S values than Sample D, which means that Ag and S contents increase as the concentration of AgSD increases while keeping the content of the BC constant. Therefore, this is a direct control of the presence of Ag and S as active ingredients of the prepared nanofiber. In the EDX analysis, it was also observed that both Ag and S showed an upward trend in the EDX analysis.

FTIR

Fourier transform infrared spectroscopy (FTIR) analysis, was performed to assess the interaction between TOBC and AgSD. **Figure 6** shows the spectra of BC and TOBC, whereas **Figure 7** shows the spectra of TOBC–AgSD nanocomposites. In the case of BC and TOBC (**Figures 6A,B**), the FTIR spectrum obtained is

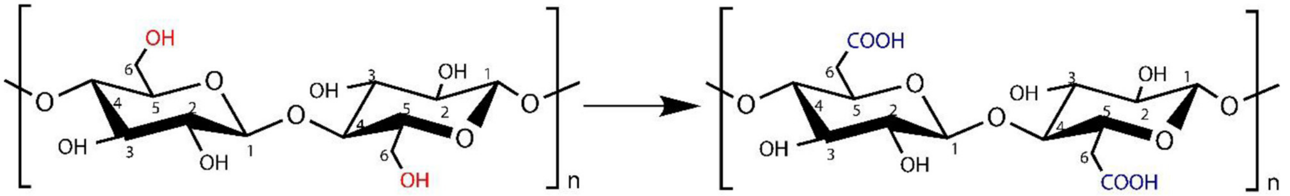

FIGURE 3 | Primary hydroxyls oxidation by TEMPO/NaBr/NaClO to C6 carboxylic group of cellulose.

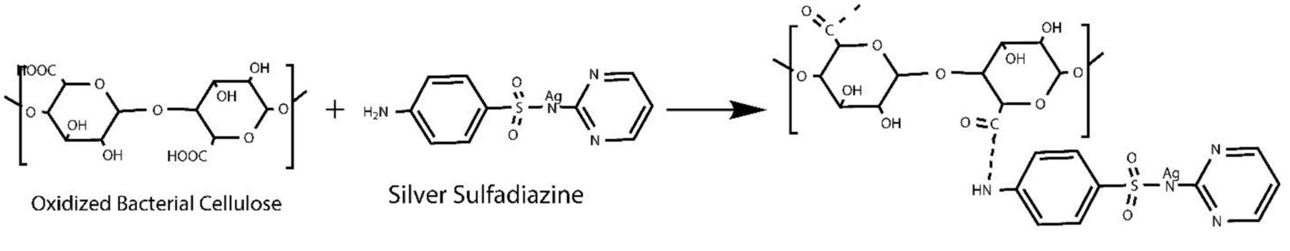

FIGURE 4 | Schematic representation of TOBC–AgSD nanocomposites.

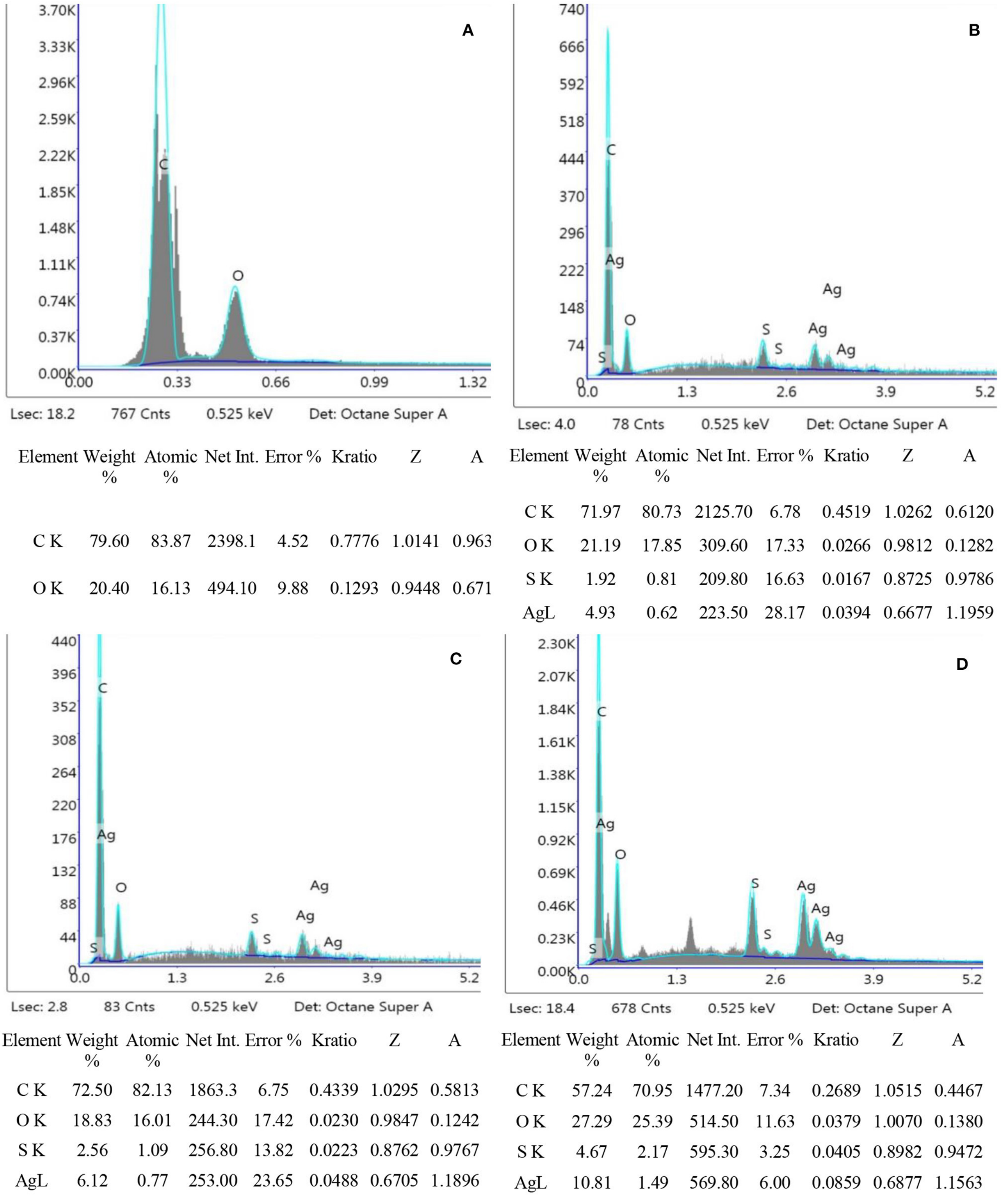

A

Element	Weight %	Atomic %	Net Int.	Error %	Kratio	Z	A
C K	79.60	83.87	2398.1	4.52	0.7776	1.0141	0.963
O K	20.40	16.13	494.10	9.88	0.1293	0.9448	0.671

B

Element	Weight %	Atomic %	Net Int.	Error %	Kratio	Z	A
C K	71.97	80.73	2125.70	6.78	0.4519	1.0262	0.6120
O K	21.19	17.85	309.60	17.33	0.0266	0.9812	0.1282
S K	1.92	0.81	209.80	16.63	0.0167	0.8725	0.9786
AgL	4.93	0.62	223.50	28.17	0.0394	0.6677	1.1959

C

Element	Weight %	Atomic %	Net Int.	Error %	Kratio	Z	A
C K	72.50	82.13	1863.3	6.75	0.4339	1.0295	0.5813
O K	18.83	16.01	244.30	17.42	0.0230	0.9847	0.1242
S K	2.56	1.09	256.80	13.82	0.0223	0.8762	0.9767
AgL	6.12	0.77	253.00	23.65	0.0488	0.6705	1.1896

D

Element	Weight %	Atomic %	Net Int.	Error %	Kratio	Z	A
C K	57.24	70.95	1477.20	7.34	0.2689	1.0515	0.4467
O K	27.29	25.39	514.50	11.63	0.0379	1.0070	0.1380
S K	4.67	2.17	595.30	3.25	0.0405	0.8982	0.9472
AgL	10.81	1.49	569.80	6.00	0.0859	0.6877	1.1563

FIGURE 5 | EDX analysis of TOBC **(A)**, $OBCS_1$ **(B)**, $OBCS_2$ **(C)**, and $OBCS_3$ **(D)**.

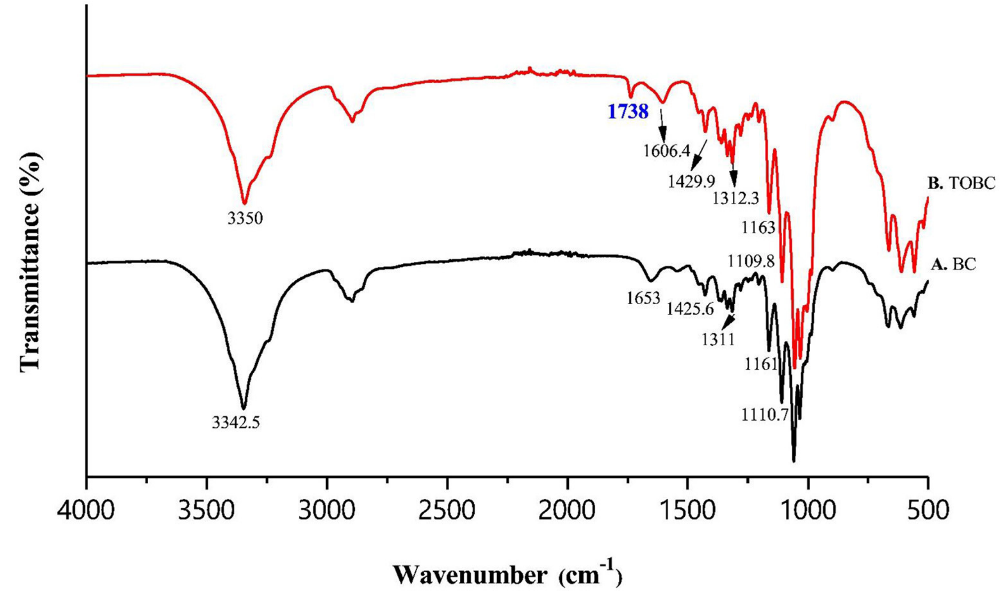

FIGURE 6 | FTIR spectra of BC **(A)** and TOBC **(B)**.

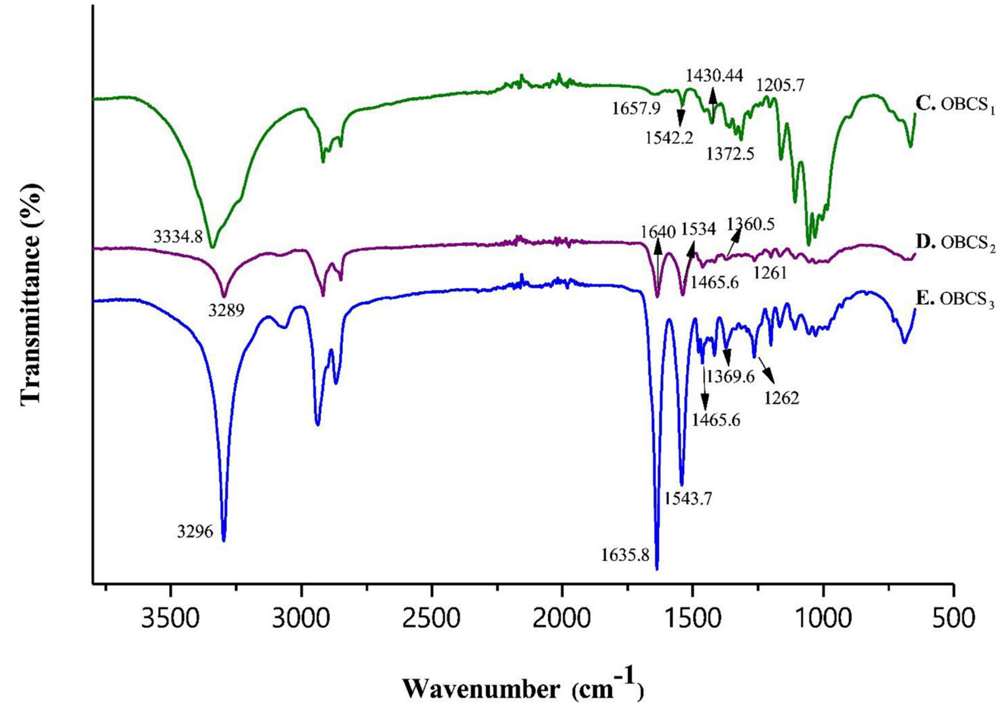

FIGURE 7 | FTIR analysis of TOBC nanocomposites with different loadings of AgSD.

typical and the dominant signals are at 3342.5–3,350 cm^{-1}, which corresponds to the intra hydrogen bonding and OH stretching (Feng et al., 2012; Wasim et al., 2020). The absorbance at 1,738 cm^{-1} (**Figure 6B**) appeared to correspond to the carboxylic (carbonyl) group (Luo et al., 2013). The peaks at 1,163 and 1,161 cm^{-1} represent C–O asymmetric stretching, whereas the peaks at 1110.7 and 1109.8 cm^{-1} (**Figures 6A,B**) correspond to the C–O–C pyranose ring skeletal vibration of BC (Park et al., 2013). The characteristic bands exhibited by AgSD–TOBC nanocomposites are shown in **Figure 7** (curves C, D, and E).

The bands that appeared at 1205.7 cm^{-1} (C), 1,261 cm^{-1} (D), and 1,262 cm^{-1} (E) were assigned to the asymmetric stretching of SO_2 bonds (Shao et al., 2016). The bands that appeared at 1542.2 cm^{-1} (C), 1,534 cm^{-1} (D), and 1543.7 cm^{-1} (E) can be assigned to pyrimidine skeletal vibrations due to silver (Ag^+) ions. The obtained results were similar to the reported study (Shao et al., 2016). Moreover, the bands present at 3334.8, 3,289, and 3,296 cm^{-1} were assigned to -NH_2 stretching bands. As the concentration of AgSD increases, the peak intensities in TOBC–AgSD nanocomposites in **Figure 7** (curves C, D & E) also increase. The sample (**Figure 7C**) with a high concentration of AgSD exhibits a significant peak at 1543.71 cm^{-1} due to the free N–H. Similar observations have previously been reported (Fajardo et al., 2013; Zepon et al., 2014; Liu et al., 2019). From the obtained results, it can be observed that the characteristic peaks of silver sulfadiazine are present and with an increase in the peak intensity in the FTIR spectra.

XRD Analysis

Figure 8 shows the XRD analysis of BC, TOBC, and TOBC–AgSD nanocomposites (**Figure 8**). Two broader peaks and one small (less obvious) peak at 2θ = 14.7°, 2θ = 17°, and 2θ = 22.8° (**Figure 8F**) were observed and attributed to the characteristic peaks (cellulose I_β crystal) of BC. TOBC also shows these characteristics peaks (**Figure 8B**), which confirms the crystalline nature of TOBC. The sharp peaks at 2θ = 10.2° (C), 9.7° (D), 8.5° and 9.9° (E), 2θ = 18.4° (C), 18.3° (D), and 18°(E), and numerous small peaks at 2θ = 37° and 38.4° (C, D, and E) show and confirmed the presence of AgSD (Ullah et al., 2019). Also, after the impregnation of TOBC with AgSD, crystallinity was increased, which means that the crystalline structure of TOBC was retained (Khamrai et al., 2017). Furthermore, an increase in the ratio of AgSD to TOBC increases peak intensity. BC exhibited a crystallinity of 88%, whereas TOBC exhibited 90%, which was higher than BC. It could be due to the fact that the carboxylate

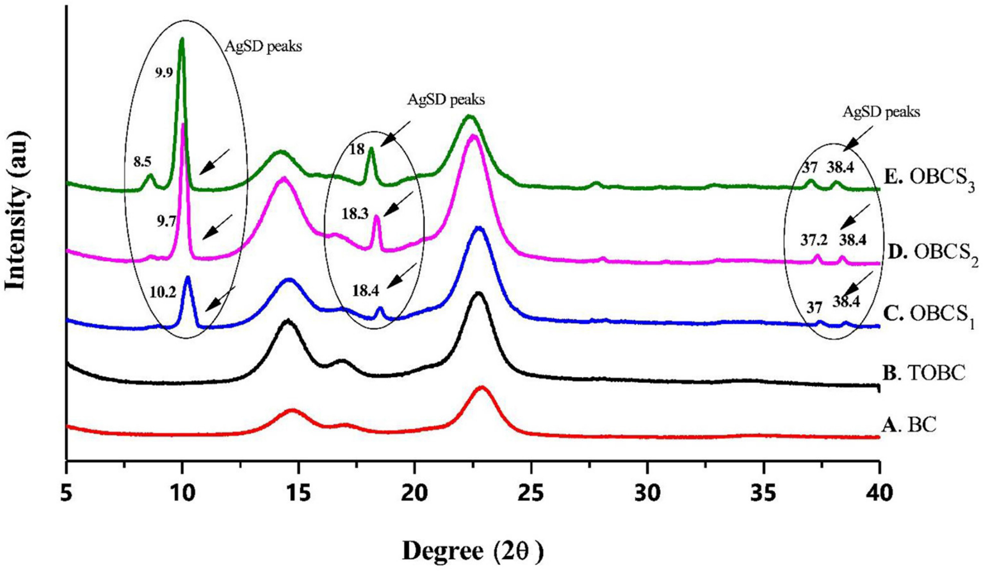

FIGURE 8 | XRD analysis of BC, TOBC, and TOBC–AgSD nanocomposites with different ratios of AgSD.

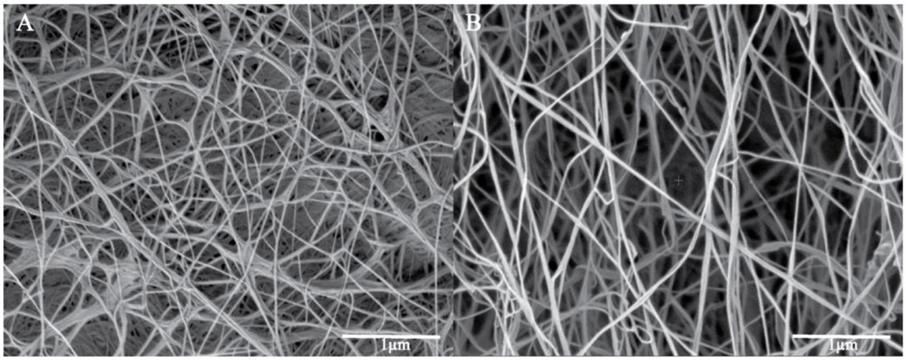

FIGURE 9 | FESEM images of original BC **(A)** and TOBC **(B)**.

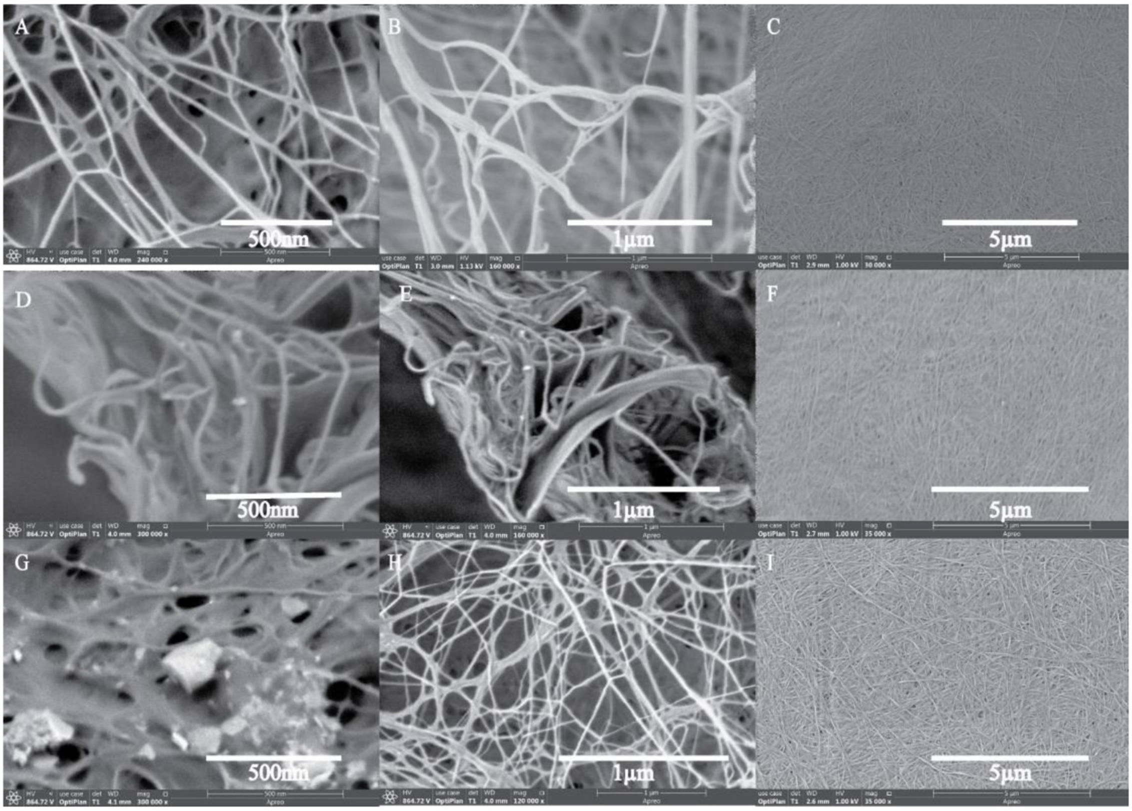

FIGURE 10 | FESEM images of TOBC–AgSD nanocomposites. OBCS$_1$ **(A–C)**, OBCS$_2$ **(D–F)**, and OBCS$_3$ **(G–I)** with different magnification.

generated in disordered regions combines with the hydroxyl groups to form inter-acetal linkages (Luo et al., 2013; Shao et al., 2016). The TOBC–AgSD nanocomposites showed crystallinities of 90, 92, and 93%, respectively.

FESEM Spectroscopy

Surface morphological studies of BC and TOBC (**Figure 9**) and TOBC–AgSD nanocomposites (**Figure 10**) were studied by FESEM. The results show that TEMPO oxidation did not change the morphology, i.e., the crystalline structure of BC is retained after the oxidation reaction, indicating the selective oxidation of the primary hydroxyl group on the surface of BC (Lu et al., 2014). TOBC and TOBC–AgSD nanocomposites exhibit a highly porous structure having interconnected pores, which is consistent with the other reported study (Shi et al., 2014). A denser network structure of AgSD particles with a significant dispersion in the TOBC matrix is shown in **Figures 10C,F,I**. An increase in the ratio of AgSD to TOBC results in the dense network structure, i.e., **Figure 10G**. However, for TOBC–AgSD nanocomposites with higher AgSD percentage (**Figures 10G,H**), larger AgSD particles accumulated in the matrix. This is because of the higher percentage of AgSD or loading of the AgSD, which leads to the overlapping with each other within the TOBC matrix. AgSd particles appear as white spots (**Figure 10**). In **Figure 11**, the average diameter graph of TOBC-AgSd nanofibers is displayed. The change in the diameter of nanofiber was observed with the addition of AgSD into the TOBC. The average of 50 nanofibers from each sample was selected and

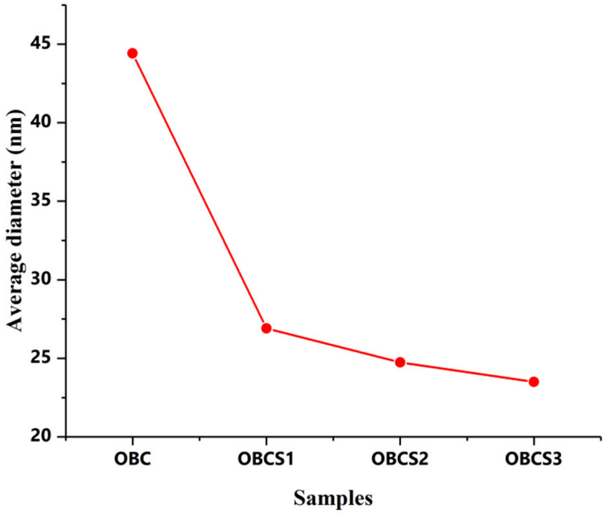

FIGURE 11 | Average diameter distribution of TOBC and AgSD–TOBC nanocomposites.

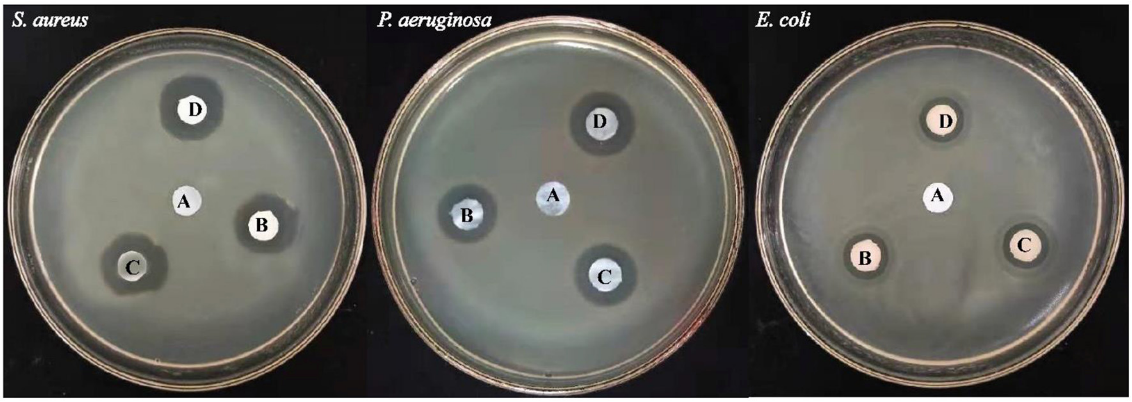

FIGURE 12 | Illustrating the inhibition zones for **(A)** TOBC, **(B)** OBCS$_1$, **(C)** OBCS$_2$, and **(D)** OBCS$_3$ by the disc diffusion method.

analyzed using ImageJ software. The average diameters of TOBC, OBCS$_1$, OBCS$_2$, and OBCS$_3$ nanocomposites were 44, 27, 24, and 23 nm. The diameter of the TOBC nanofiber was nearly unchanged by the TEMPO oxidation as BC fibers consist of 50–100 nm, whereas the average diameters of the AgSD particles were 11, 13, and 17 nm (Wu et al., 2018). Usually, with the addition of nanoparticles, there is an increase in the diameter of nanocomposites. However, in this case, the results were opposite. This could be due to the strong bonding between TOBC and AgSD nanoparticles as the sonicated AgSD particles were more uniform to permeate easily in the BC fibril network (Luan et al., 2012). Similar results were also observed with the previous reported study (Khan et al., 2019; Ullah et al., 2019).

Antibacterial Activity

E. coli, *P. aeruginosa* (both Gram-negative bacteria), and *S. aureus* (Gram-positive bacteria) were selected for antibacterial testing because they are usually the main cause of infection during the healing of infection (Jo et al., 2012; Fajardo et al., 2013). After 12 h, zone of inhibition was measured to check the antibacterial activity around the sample as shown in **Figure 12** using different concentrations of TOBC–AgSD. TOBC is used as a control, and no inhibition zone was observed around TOBC, which means that it does not possess any antibacterial activity against *P. aeruginosa*, *E. coli*, and *S. aureus*. On the other hand, due to the presence of AgSD, significant inhibition zone areas around other samples containing TOBC–AgSD confirmed their antibacterial properties as TOBC membrane is used as a matrix (**Table 1**). As the concentration of AgSD compound increases, there is an increase in the inhibition zone that is consistent with the reported literature (Mi et al., 2002). The zone of inhibition depends on the concentration of the AgSD. All samples exhibited excellent antibacterial efficacy, but the sample with 0.3% AgSD exhibited excellent antibacterial activity, which was also confirmed from the EDX and showed consistent results for the used bacteria. The amount of AgSD in the sample was found to increase and was very important. According to Laura et al. (2013), silver ion has major antibacterial activity against several bacteria, whereas sulfadiazine exhibits bacteriostatic properties.

TABLE 1 | The inhibition zones of TOBC–AgSD nanocomposites.

Samples	Inhibition zone (mm)		
	P. aeruginosa	***S. aureus***	***E. coli***
TOBC (control)	00	00	00
OBCS$_1$	19.11 ± 0.5	19.76 ± 0.4	12.29 ± 0.5
OBCS$_2$	19.49 ± 0.4	18.60 ± 0.6	13.36 ± 0.4
OBCS$_3$	21.25 ± 0.6	18.99 ± 0.5	13.81 ± 0.6

Perhaps, the difference in diameter in the zone of inhibition will be due to the difference of bacteria and their susceptibility to the prepared nanofibers. So, the results of this study are consistent with other studies especially on the bactericidal effects of AgSD (Fajardo et al., 2013).

This study clearly shows that TOBC–AgSD compounds have excellent antibacterial activity against Gram-negative and -positive bacteria; combined with all beneficial qualities, the prepared TOBC–AgSD compound is a good antibacterial material for wound dressings and also in other biomedical applications.

CONCLUSION

In summary, TOBC–AgSD nanocomposites were prepared by TEMPO-mediated oxidation. TEMPO oxidation enhances the reactivity of BC. Another advantage is retaining the structure of BC after the structure modification. TEMPO oxidation pertains to mechanical properties and reactivity to BC, while silver sulfadiazine (AgSD) makes it antibacterial. To check antibacterial activity, zone of inhibition test was performed against *P. aeruginosa*, *S. aureus*, and *E. coli*. OBCS$_3$ showed good antibacterial activity, which showed that AgSD concentrations by weight are an effective way to significantly increase antibacterial activity. In addition, the results obtained from FTIR and

XRD indicated that TEMPO oxidation retains the mechanical properties and reactivity of BC, while silver sulfadiazine (AgSD) makes it antibacterial. XRD results also showed that crystallinity increases with TEMPO oxidation of BC. The results also show the potential new antibacterial applications of AgSD–TOBC membranes. Altogether, our results suggest that it could be a promising candidate for biomedical applications especially in wound dressing, tissue engineering, and BC scaffold. However, human clinical trials and studies are required to use the potential medical/pharmaceutical interest of TOBC–AgSD nanocomposites.

DATA AVAILABILITY STATEMENT

The original contributions presented in the study are included in the article/supplementary material, further inquiries can be directed to the corresponding author.

AUTHOR CONTRIBUTIONS

CZ conceived the project, supervised the research, and wrote the manuscript. SK and X-TQ designed and performed the experiments, analyzed the results, wrote the manuscript, and prepared the figures. SK performed the characterization and wrote the manuscript. Y-YX and X-TQ assisted in analytical studies. CZ, S-RJ, and FW assisted in characterization analysis and manuscript writing. All authors read and approved the manuscript.

FUNDING

This work was supported by the National Natural Science Foundation of China (no. 21978219), the Natural Science Foundation of Tianjin (no. 19JCZDJC34700), and the Tianjin Science and Technology Support Program (no. 19PTSYJC00060).

REFERENCES

Aguzzi, C., Sandri, G., Bonferoni, C., Cerezo, P., Rossi, S., Ferrari, F., et al. (2014). Solid state characterisation of silver sulfadiazine loaded onmontmorillonite/chitosan nanocomposite for wound healing. *Coll. Surf. B* 113, 152–157. doi: 10.1016/j.colsurfb.2013.08.043

Almeida, I. F., Pereira, T., Silva, N. H. C. S., Gomes, F. P., Silvestre, A. J. D., Freire, C. S. R., et al. (2014). Bacterial cellulose membranes as drug delivery systems: an *in vivo* skin compatibility study. *Eur. J. Pharm. Biopharm*. 86, 332–336. doi: 10.1016/j.ejpb.2013.08.008

Atiyeh, B. S., Costagliola, M., Hayek, S. N., and Dibo, S. A. (2007). Effect of silver on burn wound infection control and healing: review of the literature. *Burns* 33,139–148. doi: 10.1016/j.burns.2006.06.010

Baenziger, N. C., and Struss, A. W. (1976). Crystal structure of 2-sulfanilamidopyrimidinesilver (I). *Inorg. Chem*. 15, 1807–1809. doi: 10.1021/ic50162a014

Caschera, D., Toro, R. G., Federici, F., Montanari, R., de Caro, T., Al-Shemy, M. T., et al. (2020). Green approach for the fabrication of silver-oxidized cellulose nanocomposite with antibacterial properties. *Cellulose* 27, 8059–8073. doi: 10.1007/s10570-020-03364-7

Cook, D. S., and Turner, M. F. (1975). Crystal and molecular structure of silver sulphadiazine (N 1-pyrimidin-2-ylsulphanilamide). *J. Chem. Soc. Perkin Trans*. 2, 1021–1025. doi: 10.1039/p29750001021

Craig, C. R., and Stitzel, R. E. (eds.). (2004). *Modern Pharmacology With Clinical Applications*. Philadelphia, PA: Lippincott Williams and Wilkins.

Di, Z., Shi, Z., Ullah, M. W., Li, S., and Yang, G. (2017). A transparent wound dressing based on bacterial cellulose whisker and poly (2-hydroxyethyl methacrylate). *Int. J. Biol. Macromol*. 105, 638–644. doi: 10.1016/j.ijbiomac.2017.07.075

Fajardo, A. R., Lopes, L. C., Caleare, A. O., Britta, E. A., Nakamura, C. V., and Rubira, A. F., et al. (2013). Silver sulfadiazine loaded chitosan/chondroitin sulfate films for apotential wound dressing application. *Mater. Sci. Eng. C* 33, 588–595. doi: 10.1016/j.msec.2012.09.025

Feng, Y., Zhang, X., Shen, Y., Yoshino, K., and Feng, W. (2012). A mechanically strong, flexible and conductive film based on bacterial cellulose/graphene nanocomposite. *Carbohydr. Polym*. 87, 644–649. doi: 10.1016/j.carbpol.2011.08.039

Fijałkowski, K., Zywicka, A., Drozd, R., Junka, A. F., Peitler, D., Kordas, M., et al. (2017). Increased water content in bacterial cellulose synthesized under rotating magnetic fields. *Electromagn. Biol. Med*. 36, 192–201. doi: 10.1080/15368378.2016.1243554

Fortunati, E., Rinaldi, S., Peltzer, M., Bloise, N., Visai, L., Armentano, I., et al. (2014). Nano-biocomposite films with modified cellulose nanocrystals and synthesized silver nanoparticles. *Carbohydr. Polym*. 101, 1122–1133. doi: 10.1016/j.carbpol.2013.10.055

Fox, C. L., and Modak, S. M. (1974). Mechanism of silver sulfadiazine action on burn wound infections. *Antimicrob. Agents Chemother*. 5, 582–588. doi: 10.1128/AAC.5.6.582

Fox, C. L. Jr. (1975). Silver sulfadiazine for control of burn wound infections. *Int. Surg. J*. 60:275.

Fujii, Y., Imagawa, K., Omura, T., Suzuki, T., and Minami, H. (2020). Preparation of cellulose/silver composite particles having a recyclable catalytic property. *ACS omega* 5, 1919–1926. doi: 10.1021/acsomega.9b03634

Garvey, C. J., Parker, I. H., and Simon, G. P. (2005). On the interpretation of X-ray diffraction powder patterns in terms of the nanostructure of cellulose I fibres. *Macromol. Chem. Phys*. 206, 1568–1575. doi: 10.1002/macp.200500008

Garza-Cervantes, J. A., Mendiola-Garza, G., de Melo, E. M., Dugmore, T. I., Matharu, A. S., and Morones-Ramirez, J. R. (2020). Antimicrobial activity of a silver-microfibrillated cellulose biocomposite against susceptible and resistant bacteria. *Sci. Rep*. 10, 1–7. doi: 10.1038/s41598-020-64127-9

Ge, Y., Li, S., Wang, S., and Moore, R. (eds.). (2014). *Nanomedicine: Principles and Perspectives*. New York, NY: Springer. doi: 10.1007/978-1-4614-2140-5

GhavamiNejad, A., Rajan Unnithan, A., Ramachandra Kurup Sasikala, A., Samarikhalaj, M., Thomas, R. G., Jeong, Y. Y., et al. (2015). Mussel-inspired electrospun nanofibers functionalized with size-controlled silver nanoparticles for wound dressing application. *ACS Appl. Mater. Interf*. 7, 12176–12183. doi: 10.1021/acsami.5b02542

Habibi, Y. (2014). Key advances in the chemical modification of nanocelluloses. *Chem. Soc. Rev*. 43, 1519–1542. doi: 10.1039/C3CS60204D

Habibi, Y., Chanzy, H., and Vignon, M. R. (2006). TEMPO-mediated surface oxidation of cellulose whiskers. *Cellulose* 13, 679–687. doi: 10.1007/s10570-006-9075-y

Hoffmann, S. (1984). Silver sulfadiazine: an antibacterial agent for topical use in burns. *Scand. J. Plast. Recons*. 18, 119–126. doi: 10.3109/02844318409057413

Ifuku, S., Tsuji, M., Morimoto, M., Saimoto, H., and Yano, H. (2009). Synthesis of silver nanoparticles templated by TEMPO-mediated oxidized bacterial cellulose nanofibers. *Biomacromolecules* 10, 2714–2717. doi: 10.1021/bm9006979

Isogai, A., Saito, T., and Fukuzumi, H. (2011). TEMPO-oxidized cellulose nanofibers. *Nanoscale* 3, 71–85. doi: 10.1039/C0NR00583E

Jasim, A., Ullah, M. W., Shi, Z., Lin, X., and Yang, G. (2017). Fabrication of bacterial cellulose/polyaniline/single-walled carbon nanotubes membrane for potential application as biosensor. *Carbohydr. Polym*. 163, 62–69. doi: 10.1016/j.carbpol.2017.01.056

Jia, Y., Zheng, M., Xu, Q., and Zhong, C. (2019). Rheological behaviors of Pickering emulsions stabilized by TEMPO-oxidized bacterial cellulose. *Carbohydr. Polym*. 215, 263–271. doi: 10.1016/j.carbpol.2019.03.073

Jo, E. R., Jung, P. M., Choi, J. I., and Lee, J. W. (2012). Radiation sensitivity of bacteria and virus in porcine xenoskin for dressing agent. *Radiat. Phys. Chem.* 81, 1259–1262. doi: 10.1016/j.radphyschem.2011.08.016

Khamrai, M., Banerjee, S. L., and Kundu, P. P. (2017). Modified bacterial cellulose based self-healable polyeloctrolyte film for wound dressing application. *Carbohydr. Polym.* 174, 580–590. doi: 10.1016/j.carbpol.2017.06.094

Khan, I., Saeed, K., and Khan, I. (2019). Nanoparticles: properties, applications and toxicities. *Arab. J. Chem.* 12, 908–931. doi: 10.1016/j.arabjc.2017.05.011

Khattak, S., Wahid, F., Liu, L. P., Jia, S. R., Chu, L. Q., Xie, Y. Y., et al. (2019). Applications of cellulose and chitin/chitosan derivatives and composites as antibacterial materials: current state and perspectives. *Appl. Microbiol. Biotechnol.* 103, 1989–2006. doi: 10.1007/s00253-018-09602-0

Lai, C., Zhang, S., Sheng, L., Liao, S., Xi, T., and Zhang, Z. (2013). TEMPO-mediated oxidation of bacterial cellulose in a bromide-free system. *Colloid and Polym. Bull.* 291, 2985–2992. doi: 10.1007/s00396-013-3033-7

Laura, C., Milena, S., Giovanna, B., Cristina, B. M., Giuseppina, S., and Giampiero, B. (2013). Characterization of silver sulfadiazine-loaded solid lipid nanoparticles by thermal analysis. *J. Therm. Anal. Calorim.* 111, 2149–2155. doi: 10.1007/s10973-012-2709-4

Lee, H. J., Chung, T. J., Kwon, H. J., Kim, H. J., and Tze, W. T. Y. (2012). Fabrication and evaluation of bacterial cellulose-polyaniline composites by interfacial polymerization. *Cellulose* 19, 1251–1258. doi: 10.1007/s10570-012-9705-5

Lin, S. P., Calvar, I. L., Catchmark, J. M., Liu, J. R., Demirci, A., and Cheng, K. C. (2013). Biosynthesis, production and applications of bacterial cellulose. *Cellulose* 20, 2191–2219. doi: 10.1007/s10570-013-9994-3

Liu, L. P., Yang, X. N., Ye, L., Xue, D. D., Liu, M., Jia, S. R., et al. (2017). Preparation and characterization of a photocatalytic antibacterial material: graphene oxide/TiO2/bacterial cellulose nanocomposite. *Carbohydr. Polym.* 174, 1078–1086. doi: 10.1016/j.carbpol.2017.07.042

Liu, X., Gan, H., Hu, C., Sun, W., Zhu, X., Meng, Z., et al. (2019). Silver sulfadiazine nanosuspension-loaded thermosensitive hydrogel as a topical antibacterial agent. *Int. J. Nanomed.* 14:289. doi: 10.2147/IJN.S187918

Lu, C., Chen, S. Y., Zheng, Y., Zheng, W. L., Xiang, C., and Wang, H. P. (2014). TEMPO-mediated oxidation of bacterial cellulose in buffer solution. *Mat. Sci. Forum* 789, 90–94. doi: 10.4028/www.scientific.net/MSF.789.90

Luan, J., Wu, J., Zheng, Y., Song, W., Wang, G., Guo, J., et al. (2012). Impregnation of silver sulfadiazine into bacterial cellulose for antimicrobial and biocompatible wound dressing. *Biomed. Mater.* 7:065006. doi: 10.1088/1748-6041/7/6/065006

Luo, H., Xiong, G., Hu, D., Ren, K., Yao, F., Zhu, Y., et al. (2013). Characterization of TEMPO-oxidized bacterial cellulose scaffolds for tissue engineering applications. *Mater. Chem. Phys.* 143, 373–379. doi: 10.1016/j.matchemphys.2013.09.012

Martínez-Sanz, M., Olsson, R. T., Lopez-Rubio, A., and Lagaron, J. M. (2012). Development of bacterial cellulose nanowhiskers reinforced EVOH composites by electrospinning. *J. Appl. Polym. Sci.* 124, 1398–1408. doi: 10.1002/app.35052

McCarthy, R. R., Ullah, M. W., Booth, P., Pei, E., and Yang, G. (2019). The use of bacterial polysaccharides in bioprinting. *Biotechnol. Adv.* 37:107448. doi: 10.1016/j.biotechadv.2019.107448

Mi, F. L., Wu, Y. B., Shyu, S. S., Schoung, J. Y., Huang, Y. B., Tsai, Y. H., et al. (2002). Control of wound infections using a bilayer chitosan wound dressing with sustainable antibiotic delivery. *J. Biomed. Mater. Res.* 59, 438–449. doi: 10.1002/jbm.1260

Mohseni, M., Shamloo, A., Aghababaie, Z., Afjoul, H., Abdi, S., Moravvej, H., et al. (2019). A comparative study of wound dressings loaded with silver sulfadiazine and silver nanoparticles: *in vitro* and *in vivo* evaluation. *Int. J. Pharm.* 564, 350–358. doi: 10.1016/j.ijpharm.2019.04.068

Moniri, M., Boroumand Moghaddam, A., Azizi, S., Abdul Rahim, R., Bin Ariff, A., Zuhainis Saad, W., et al. (2017). Production and status of bacterial cellulose in biomedical engineering. *Nanomaterials* 7:257. doi: 10.3390/nano7090257

Muangman, P., Pundee, C., Opasanon, S., and Muangman, S. (2010). A prospective, randomized trial of silver containing hydrofiber dressing versus 1% silver sulfadiazine for the treatment of partial thickness burns. *Int. Wound J.* 7, 271–276. doi: 10.1111/j.1742-481X.2010.00690.x

Okita, Y., Saito, T., and Isogai, A. (2010). Entire surface oxidation of various cellulose microfibrils by TEMPO-mediated oxidation. *Biomacromolecules* 11, 1696–1700. doi: 10.1021/bm100214b

Park, M., Cheng, J., Choi, J., Kim, J., and Hyun, J. (2013). Electromagnetic nanocomposite of bacterial cellulose using magnetite nanoclusters and polyaniline. *Colloids Surf. B* 102, 238–242. doi: 10.1016/j.colsurfb.2012.07.046

Paximada, P., Dimitrakopoulou, E. A., Tsouko, E., Koutinas, A. A., Fasseas, C., and Mandala, I. G. (2016). Structural modification of bacterial cellulose fibrils under ultrasonic irradiation. *Carbohydr. Polym.* 150, 5–12. doi: 10.1016/j.carbpol.2016.04.125

Pelegrini, B. L., Re, F., de Oliveira, M. M., Fernandes, T., de Oliveira, J. H., Oliveira Junior, A. G., et al. (2019). Cellulose nanocrystals as a sustainable raw material: cytotoxicity and applications on healthcare technology. *Macromol. Mater. Eng.* 304:1900092. doi: 10.1002/mame.201900092

Percival, S. L., McCarty, S. M., and Lipsky, B. (2015). Biofilms and wounds: an overview of the evidence. *Adv. Wound Care* 4, 373–381. doi: 10.1089/wound.2014.0557

Qian, W., Texter, J., and Yan, F. (2017). Frontiers in poly (ionic liquid) s: syntheses and applications. *Chem. Soc. Rev.* 46, 1124–1159. doi: 10.1039/C6CS00620E

Reiniati, I., Hrymak, A. N., and Margaritis, A. (2017). Kinetics of cell growth and crystalline nanocellulose production by Komagataeibacter xylinus. *Biochem. Eng. J.* 127, 21–31. doi: 10.1016/j.bej.2017.07.007

Saito, T., and Isogai, A. (2004). TEMPO-mediated oxidation of native cellulose. The effect of oxidation conditions on chemical and crystal structures of the water-insoluble fractions. *Biomacromolecules* 5, 1983–1989. doi: 10.1021/bm0497769

Sajjad, W., He, F., Ullah, M. W., Ikram, M., Shah, S. M., Khan, R., et al. (2020). Fabrication of bacterial cellulose-curcumin nanocomposite as a novel dressing for partial thickness skin burn. *Front. Bioeng. Biotechnol.* 8:553037. doi: 10.3389/fbioe.2020.553037

Shao, W., Liu, H., Wu, J., Wang, S., Liu, X., Huang, M., et al. (2016). Preparation, antibacterial activity and pH-responsive release behavior of silver sulfadiazine loaded bacterial cellulose for wound dressing applications. *J. Taiwan Inst. Chem. E* 63, 404–410. doi: 10.1016/j.jtice.2016.02.019

Shao, W., Wu, J., Liu, H., Ye, S., Jiang, L., and Liu, X. (2017). Novel bioactive surface functionalization of bacterial cellulose membrane. *Carbohydr. Polym.* 178, 270–276. doi: 10.1016/j.carbpol.2017.09.045

Shi, Z., Zhang, Y., Phillips, G. O., and Yang, G. (2014). Utilization of bacterial cellulose in food. *Food Hydrocoll.* 35, 539–545. doi: 10.1016/j.foodhyd.2013.07.012

Smith, C. J., Wagle, D. V., O'Neill, H. M., Evans, B. R., Baker, S. N., and Baker, G. A. (2017). Bacterial cellulose ionogels as chemosensory supports. *ACS Appl. Mater. Inter.* 9, 38042–38051. doi: 10.1021/acsami.7b12543

Sulaeva, I., Henniges, U., Rosenau, T., and Potthast, A. (2015). Bacterial cellulose as a material for wound treatment: properties and modifications. A review. *Biotechnol. Adv.* 33, 1547–1571. doi: 10.1016/j.biotechadv.2015.07.009

Tacic, A., Nikolic, V., Nikolic, L., and Savic, I. (2017). Antimicrobial sulfonamide drugs. *Adv. Technol.* 6, 58–71. doi: 10.5937/savteh1701058T

Teeaar, R., Serimaa, R., and Paakkarl, T. (1987). Crystallinity of cellulose, as determined by CP/MAS NMR and XRD methods. *Polym. Bull.* 17, 231–237. doi: 10.1007/BF00285355

Ul-Islam, M., Subhan, F., Islam, S. U., Khan, S., Shah, N., Manan, S., et al. (2019). Development of three-dimensional bacterial cellulose/chitosan scaffolds: analysis of cell-scaffold interaction for potential application in the diagnosis of ovarian cancer. *Int. J. Biol. Macromol.* 137, 1050–1059. doi: 10.1016/j.ijbiomac.2019.07.050

Ullah, S., Hashmi, M., Kharaghani, D., Khan, M. Q., Saito, Y., Yamamoto, T., et al. (2019). Antibacterial properties of *in situ* and surface functionalized impregnation of silver sulfadiazine in polyacrylonitrile nanofiber mats. *Int. J. Nanomed.* 14:2693. doi: 10.2147/IJN.S197665

Wang, L., Hu, S., Ullah, M. W., Li, X., Shi, Z., and Yang, G. (2020). Enhanced cell proliferation by electrical stimulation based on electroactive regenerated bacterial cellulose hydrogels. *Carbohydr. Polym.* 249:116829. doi: 10.1016/j.carbpol.2020.116829

Wang, S., Lu, A., and Zhang, L. (2016). Recent advances in regenerated cellulose materials. *Prog. Polym. Sci.* 53, 169–206. doi: 10.1016/j.progpolymsci.2015.07.003

Wasim, M., Mushtaq, M., Khan, S., and Salam, A. (2020). An overview of synthesized bacterial cellulose nanocomposites for biomedical applications. *Biomed. J. Sci. Tech. Res.* 27, 20653–20656. doi: 10.26717/BJSTR.2020.27.004483

Wei, B., Yang, G., and Hong, F. (2011). Preparation and evaluation of a kind of bacterial cellulose dry films with antibacterial properties. *Carbohydr. Polym.* 84, 533–538. doi: 10.1016/j.carbpol.2010.12.017

Wu, C. N., Fuh, S. C., Lin, S. P., Lin, Y. Y., Chen, H. Y., Liu, J. M., et al. (2018). TEMPO-oxidized bacterial cellulose pellicle with silver nanoparticles for wound dressing. *Biomacromolecules* 19, 544–554. doi: 10.1021/acs.biomac.7b01660

Yang, C. H., Wang, L. S., Chen, S. Y., Huang, M. C., Li, Y. H., Lin, Y. C., et al. (2016). Microfluidic assisted synthesis of silver nanoparticle–chitosan composite microparticles for antibacterial applications. *Int. J. Pharm.* 510, 493–500. doi: 10.1016/j.ijpharm.2016.01.010

Yang, G., Xie, J., Hong, F., Cao, Z., and Yang, X. (2012). Antimicrobial activity of silver nanoparticle impregnated bacterial cellulose membrane: effect of fermentation carbon sources of bacterial cellulose. *Carbohydr. Polym.* 87, 839–845. doi: 10.1016/j.carbpol.2011.08.079

Yang, X. N., Xue, D. D., Li, J. Y., Liu, M., Jia, S. R., Chu, L. Q., et al. (2016). Improvement of antimicrobial activity of graphene oxide/bacterial cellulose nanocomposites through the electrostatic modification. *Carbohydr. Polym.* 136, 1152–1160. doi: 10.1016/j.carbpol.2015.10.020

Yao, J., Ji, P., Wang, B., Wang, H., and Chen, S. (2018). Color-tunable luminescent macrofibers based on CdTe QDs-loaded bacterial cellulose nanofibers for pH and glucose sensing. *Sens. Actuators B Chem.* 254, 110–119. doi: 10.1016/j.snb.2017.07.071

Zepon, K. M., Petronilho, F., Soldi, V., Salmoria, G. V., and Kanis, L. A. (2014). Production and characterization of cornstarch/cellulose acetate/silver sulfadiazine extrudate matrices. *Mater. Sci. Eng. C* 44, 225–233. doi: 10.1016/j.msec.2014.08.011

Zhong, C., Li, F., Liu, M., Yang, X. N., Zhu, H. X., Jia, Y. Y., et al. (2014). Revealing differences in metabolic flux distributions between a mutant strain and its parent strain Gluconacetobacter xylinus CGMCC 2955. *PLoS ONE* 9:98772. doi: 10.1371/journal.pone.0098772

Zhong, C., Zhang, G. C., Liu, M., Zheng, X. T., Han, P. P., and Jia, S. R. (2013). Metabolic flux analysis of *Gluconacetobacter xylinus* for bacterial cellulose production. *Appl. Microbiol. Biot.* 97, 6189–6199. doi: 10.1007/s00253-013-4908-8

Zmejkoski, D., Spasojević, D., Orlovska, I., Kozyrovska, N., Soković, M., Glamočlija, J., et al. (2018). Bacterial cellulose-lignin composite hydrogel as a promising agent in chronic wound healing. *Int. J. Biol. Macromol.* 118, 494–503. doi: 10.1016/j.ijbiomac.2018.06.067

Conflict of Interest: The authors declare that the research was conducted in the absence of any commercial or financial relationships that could be construed as a potential conflict of interest.

frontiers
in Bioengineering and Biotechnology

ORIGINAL RESEARCH
published: 03 February 2021
doi: 10.3389/fbioe.2021.601988

Ex situ Synthesis and Characterization of High Strength Multipurpose Bacterial Cellulose-*Aloe vera* Hydrogels

Mazhar Ul-Islam*[1]*, Furqan Ahmad*[2]*, Atiya Fatima*[1]*, Nasrullah Shah*[3,4]*, Somayia Yasir*[1]*, Md. Wasi Ahmad*[1]*, Sehrish Manan*[5] *and Muhammad Wajid Ullah*[5]**

[1] Department of Chemical Engineering, College of Engineering, Dhofar University, Salalah, Oman, [2] Department of Mechanical and Mechatronics Engineering, College of Engineering, Dhofar University, Salalah, Oman, [3] Department of Chemistry, Abdul Wali Khan University Mardan, Mardan, Pakistan, [4] Department of Industrial and Manufacturing Systems Engineering, Kansas State University, Manhattan, KS, United States, [5] Department of Biomedical Engineering, Huazhong University of Science and Technology, Wuhan, China

OPEN ACCESS

Edited by:
Milana C. Vasudev,
University of Massachusetts Dartmouth, United States

Reviewed by:
Adil Denizli,
Hacettepe University, Turkey
Patricia Comeau,
University of Waterloo, Canada
Luismar Marques Porto,
Federal University of Santa Catarina, Brazil

****Correspondence:***
Muhammad Wajid Ullah
wajid_kundi@hust.edu.cn

Specialty section:
This article was submitted to Biomaterials, a section of the journal Frontiers in Bioengineering and Biotechnology

Received: *02 September 2020*
Accepted: *05 January 2021*
Published: *03 February 2021*

Citation:
Ul-Islam M, Ahmad F, Fatima A, Shah N, Yasir S, Ahmad MW, Manan S and Ullah MW (2021) Ex situ Synthesis and Characterization of High Strength Multipurpose Bacterial Cellulose-Aloe vera Hydrogels. Front. Bioeng. Biotechnol. 9:601988. doi: 10.3389/fbioe.2021.601988

The innate structural and functional properties of bacterial cellulose (BC) have been greatly improved by developing its composites with other materials for its applications in different fields. In the present study, BC-*Aloe vera* (BCA) gel composite with high tensile strength was *ex situ* developed and characterized for its potential applications in environmental and medical fields. FE-SEM micrographs showed the impregnation of *Aloe vera* gel into the fibril network of BC. The dry weight analysis showed the addition of 40 wt.% *Aloe vera* contents into the BC matrix. The addition of *Aloe vera* resulted in a 3-fold increase in the mechanical strength of BCA composite. The critical strain or stress concentration points were accurately identified in the composite using a three-dimensional digital image correlation (3D-DIC) system. The BCA composite retained water for an extended period of up to 70 h. The BCA composite effectively adsorbed Cu, Co, Fe, and Zn metals. Moreover, the BCA composite supported the adhesion and proliferation of MC3T3-E1 cells. The findings of this study suggest that the developed BCA composite could find multipurpose applications in different fields.

Keywords: composites, mechanical properties, adsorption, *Aloe vera*, bacterial cellulose, biocompatibility

INTRODUCTION

Bacterial cellulose is a natural polymer produced by a class of acetic acid bacteria (Khan et al., 2020; Skiba et al., 2020; Ul-Islam et al., 2020b) and cell-free systems (Ullah et al., 2015). Both the microbial and the cell-free systems utilize different sugar sources and produce β-1,4-glucan chains, which are protruded extracellularly through the pores (i.e., terminal complexes) present in the cellular membrane, and form high ordered structures (Kim et al., 2019). The exciting structural, physico-chemical, mechanical, thermal, and biological properties of BC enable it to find applications in biomedical (Curvello et al., 2019; Ul-Islam et al., 2019; Eslahi et al., 2020; Wang et al., 2020), pharmaceutical (Li et al., 2018), environment (Xiang et al., 2018; Shoukat et al., 2019), energy (Li et al., 2014; Bu et al., 2018), sensing (Jasim et al., 2017; Farooq et al., 2020), electronics (Khan et al., 2015a; Dhar et al., 2019; Ul-Islam et al., 2020a), and several other fields

(Aljohani et al., 2018; McCarthy et al., 2019a,b). For example, the presence of plentiful hydroxyl groups on its surface imparts hydrophilic nature to BC. Both the water holding and retention potential of BC are important from a medical perspective, especially in drug delivery (Li et al., 2018) and wound dressing (Di et al., 2017; Ciecholewska-Jusìko et al., 2020; Sajjad et al., 2020), where such properties are associated with the absorption of wound exudates and holding the drug for an extended time, thus greatly contributing to enhancing the therapeutic potential of BC. The free hydroxyl groups on the cellulose surface give rise to a binding module where the adsorption of the drug is driven through the formation of hydrogen bonding and van der Waals forces or through the electrostatic/aromatic interactions (Lombardo and Thielemans, 2019). Despite the broad-spectrum applications of BC in different fields, the lack of adhesion sites and low mechanical strength limit its direct use for different applications, thus necessitating the development of BC-based composites with other materials to impart such features to it.

Aloe vera represents one of the oldest plants known for its wound healing ability. The *Aloe vera* extract has been used in herbal and alternative medicine because of its antimicrobial, anti-inflammatory, and wound healing properties (Menda et al., 2014). Its gel mainly consists of water (99%) and mono- and polysaccharides (25% of dry weight). It contains 75 essential nutrients that play an important role in wound healing. The biocompatible feature of *Aloe vera* supports early epithelialization and develops a protective layer around the wound, thus leading to quick wound closure. Moreover, the moisturizing properties of *Aloe vera* gel accelerate cell proliferation, clot formation, and blood flow in the skin (Menda et al., 2014). The wound healing features of *Aloe vera* provide the base for the development of its composites with other biomaterials, including cellulose, chitosan, and alginate with optimized properties for biomedical applications (Pereira et al., 2013; Silva et al., 2013). Studies have reported that the addition of *Aloe vera* gel to the cellulose matrix increases its mechanical and biocompatible properties (Saibuatong and Phisalaphong, 2010; Godinho et al., 2016).

It has already been established that both the biocompatibility and mechanical properties of BC can be enhanced by developing its composites with appropriate materials (Khan et al., 2018). In the form of a hydrogel, BC contains only 1% cellulose, while approximately 99% is wet weight is comprised of water content; thus, any variation in water content leads to significant changes in its viscoelastic and electrochemical properties (Rebelo et al., 2018). The potential of different polymers like chitosan, gelatin, poly (vinyl alcohol), poly (3-hydroxybutyrate) as well as nanomaterials such as carbon nanotubes, zinc oxide, silver, TiO_2, and Au, and montmorillonite clays have already been evaluated for enhancing the mechanical and biological features of BC (Ul-Islam et al., 2015; Ullah et al., 2016). Similarly, the addition of water-soluble materials could prove to be imperative in wound healing properties of BC, where moisture content is an essential factor. In an early study, BC-based composites with different contents of *Aloe vera* gel (0 to 50%) were developed through the *in situ* synthesis strategy by adding the *Aloe vera* gel to the BC-producing culture medium. The results showed that the addition of up to 30% (v/v) *Aloe vera* gel contributed to improving the structural morphology and associated properties of BC/*Aloe vera* (BCA) composite, however, further addition of *Aloe vera* to the culture medium not only decreased the BC pellicle formation but also affected the morphology, crystallinity, mechanical features, and water holding capacity and vapor transmission (Saibuatong and Phisalaphong, 2010). In contrast, the *ex situ* added *Aloe vera* would only be accommodated among the empty spaces in the fibril network without disturbing the structural morphology, and in turn, would contribute to enhancing the mechanical strength and other properties of BCA composite.

In the present study, we *ex situ* synthesized BCA composite by immersing the BC sheets in *Aloe vera* gel. The tensile properties of the developed BC-*Aloe vera* composite were determined, for the first time, through the full-field deformation and strain investigation by using the 3D-DIC technique. We provided insights into the changes in the structure of BC concerning the critical strain during the synthesis of the composite. Such information could further lead to the optimization of the composite structure for tailored mechanical features. Moreover, the developed BCA composite was evaluated for its potential applications in the biomedical and environment fields through cytocompatibility and heavy metal absorption analyzes, respectively.

EXPERIMENTATION

Microbial Cell Culture

The BC-producing *Gluconacetobacter hansenii* PJK was cultured in a synthetic medium containing 10 g/L glucose, 7 g/L peptone, 10 g/L yeast extract, 0.2 g/L succinic acid, and 1.5 mL/L acetic acid. Additionally, 20 g/L agar was added to the synthetic medium for developing its solid cultures (Ul-Islam et al., 2014). The pH of the medium was adjusted to 5 by adding 0.1 N NaOH and autoclaved for 15 min at 121°C and 15 psi. The culture broth was prepared by inoculating few colonies of *G. hansenii* PJK grown on a solid culture plate into 100 mL of liquid broth in a 250 mL Erlenmeyer flask and incubated at 30°C under shaking at 200 rpm for 24 h.

Production of BC Sheets

Bacterial cellulose sheets were produced in sterilized rectangular containers with dimensions 20 cm × 10 cm × 10 cm under static condition. Briefly, the culture medium was inoculated with 5–10% (v/v) freshly prepared *G. hansenii* PJK pre-culture and incubated at 30°C for 7–10 days under static condition, which produced about 7 mm thick BC sheets. The BC sheets were harvested from the air-medium interface, thoroughly washed, and boiled in 0.3 N NaOH to kill any live bacterial cells embedded in the BC matrix. The cell debris and residual medium contents were removed *via* frequent washing until the pH of the medium became neutral. The BC sheets were then stored in distilled water at 4°C for further use.

Development of BCA

Aloe collenetteae Lavranos (*Aloe vera*) plant was collected from Salalah, Oman. The mature fresh leaves were picked and washed

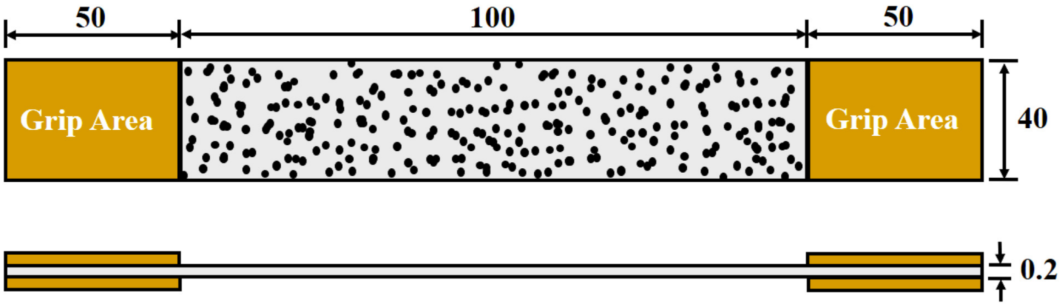

FIGURE 1 | Illustration of dimensions of BC or BCA sample for tensile testing measurement *via* the 3D-DIC system. All dimensions are in mm. A set of three samples of each BC and BCA composite were prepared for tensile testing measurement.

with distilled water. The thick epidermis of leaves was removed to collect the solid mucilaginous pulp, which was then grounded into a gel form and stored in a sterile container. Thereafter, BC and *Aloe vera* (BCA) hydrogel composite was *ex situ* developed at room temperature (i.e., 25°C) by dipping the 20 cm × 4 cm BC sheets in 300 mL *Aloe vera* gel for 2–3 days under shaking at 150 rpm in a beaker. The gel was adsorbed on the surface and impregnated into the BC matrix due to its porous geometry. The *Aloe vera* extract-loaded BC (BC-*Aloe vera*) membranes were refrigerated for further use. Both BC and BCA samples were air-dried and freeze-dried for desired characterization and use.

FE-SEM Analysis

The morphological features of the freeze-dried pristine BC and BCA composite were determined through FE-SEM analysis using a Hitachi S-4800 & EDX-350 (Horiba) FE-SEM (Tokyo, Japan). Briefly, the samples were fixed onto a brass holder and coated with osmium tetroxide (OsO_4) by a VD HPC-ISW osmium coater (Tokyo, Japan) for FE-SEM observation. FE-SEM analysis was conducted to observe the surface morphology and cross-sectional views of both pristine BC and BCA composite.

Mechanical Testing

Material Preparation

The samples were prepared by cutting the sections from the smooth part of air-dried BC and BCA composite sheets with dimensions of 200 mm × 40 mm × 0.2 mm (**Figure 1**). The white and black paints were used to create the speckled pattern on the surface of the samples to measure the full-field displacement and strain using the 3D-DIC system.

Tensile Test Setup

The tensile test was carried following a previously reported protocol (Abbassi and Ahmad, 2020; Jebri et al., 2020). Briefly, to compute the full-field strain, the 3D-DIC system was used, consisting of two high-resolution CCD cameras for image acquisition and a VIC-3D software for computing the DIC results. To correlate the two images, the first image of the object is taken as the reference, and it is correlated with the next image. The DIC system selects two subsets of pixels from the reference and deformed images having central point P and P^*, respectively. The system then calculates the displacement by taking the difference in the position of these two central points. An incandescent lamp is used to avoid the noise in the images. An Instron testing machine was used (Bluehill 3 software, the capacity of 100 kN) to measure the tensile properties of pristine BC and BCA composite. A constant loading rate of 1 mm/min was selected to perform all tests, and the tensile tests for pristine BC and BCA composite were performed in triplicate. A complete experimental setup used to perform the analysis of the tensile properties using the tensile testing machine and 3D-DIC system for the full-field strain shown in **Figure 2**.

Water Holding and Retention Analyses

The BC and BCA composites were tested for their water holding capacity (WHC) and water retention time (WRT). Briefly, the samples were cut into 5 cm × 3 cm rectangular pieces and freeze-dried at −80°C and 0.5 torr pressure for 48 h using the Uni-Freeze FD 8 model (DAIHAN Scientific). The freeze-dried sheets in a set of three samples were immersed in distilled water under static conditions at room temperature. By reaching the complete wet state (stabilized wet weight), the samples were analyzed for WRT by measuring their weights at various time intervals at ambient temperature until complete drying. The WHC was calculated by using the below equation:

$$WHC = \frac{\text{Mass of water removed during drying (g)}}{\text{Dry weight of BC sample (g)}}$$

Absorption and Desorption Studies

For heavy metal absorption analysis by the pristine BC and BCA composite hydrogels, different metal salts including $Zn(NO_3)_2$, $Cu(NO_3)_2$, $Co(NO_3)_2$, and $Fe(NO_3)_3$ were dissolved in deionized water at a concentration of 10 mg/L (10 ppm). Thereafter, 1 g each of freeze-dried BC and BCA composite was cut into small pieces and loaded into the flasks containing 250 mL of heavy metal solution. The samples were incubated overnight under stirring at 200 rpm at 25°C. For analysis, a 10 mL solution from each flask was taken and tested for residual metal ion concentrations using the atomic absorption spectrophotometer. For desorption studies, the harvested samples were placed in flasks containing 250 mL deionized water and stirred overnight at 200 rpm at 25°C. Finally, a 10 mL solution was taken from the flasks and analyzed for desorbed metal ion concentrations using the atomic

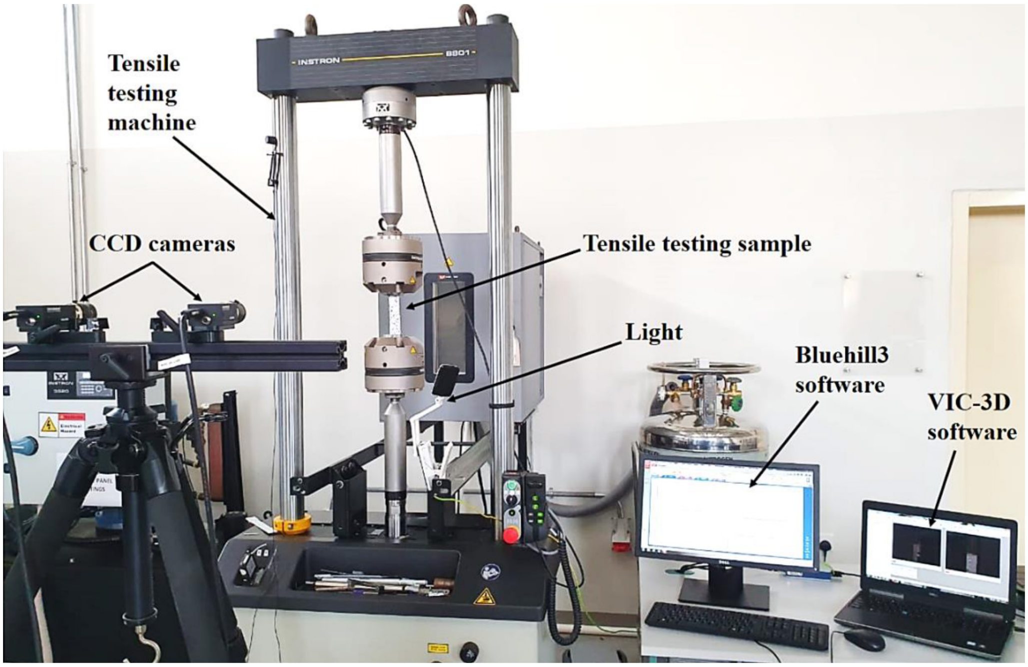

FIGURE 2 | The tensile test setup with a 3D-DIC system for the determination of mechanical properties of objects.

absorption spectrophotometer. The adsorption studies for both pristine BC and BCA composite were carried out in triplicate.

Cell Attachment and Proliferation Analysis

The cytocompatibility of pristine BC and BCA hydrogels was evaluated against osteoblast cells (MC3T3-E1 ATCC). Briefly, 10 mm diameter samples were sterilized by autoclaving at 121°C and 15 psi for 15 min and immersed in DMEM (Dulbecco's modified Eagle's medium) containing 10% FBS and 1% penicillin-G-streptomycin for 24 h. After pre-treatment, the samples were carefully placed in six-well plates. Thereafter, the cells were seeded on all samples at a density of 3×10^5 cells/well and incubated at 37°C and 5% CO_2 for 1 and 2 days. After incubation, the supernatant was discarded, and the samples were washed a few times with PBS and then fixed with 3% glutaraldehyde for 20 min. The cell adhesion on the hydrogel scaffolds was examined through FE-SEM analysis. The proliferation of MC3T3-E1 cells was determined in a 24-well plate through the ELISA method according to the manufacturer's instructions (Roche Molecular Biochemicals) (Haider et al., 2014; Ul-Islam et al., 2014). This method is based on the measurements of 5-Bromo-2-deoxyuridine (BrdU), which is up taken by the dividing cells during the DNA synthesis.

Statistical Analysis

All results are expressed as means ± SD for each experimental condition. Statistical analyses were performed using the two-tailed student's *t-test*. The difference between pristine BC and BCA composite was considered statistically significant at $^{*}p < 0.05$.

RESULTS AND DISCUSSION

Composite Synthesis and Characterization

The BC-based composites are commonly prepared through *in situ*, *ex situ*, and solution casting methods. Earlier reports of developing composites of BC with *Aloe vera* used the *in situ* strategy where *Aloe vera* gel was added to the culture medium of BC-producing microorganism. The added *Aloe vera* gel was entrapped among the growing cellulose fibrils (Saibuatong and Phisalaphong, 2010; Godinho et al., 2016), however, the *in situ* addition of *Aloe vera* above 30% (v/v) of the total volume of culture medium increased the viscosity of the medium, which consequently resulted in reduced BC production and altered morphology and mechanical features. The presence of high content of *Aloe vera* gel increased the viscosity of the medium and interrupted the oxygen supply to the growing microbial cells, thus leading to their retarded growth and ultimately resulted in low BC production with compromised features (Saibuatong and Phisalaphong, 2010). Keeping the high viscosity-induced retarded growth of bacterial cells during the *in situ* composite development strategy, we adopted the *ex situ* approach for the development of BC-*Aloe vera* composite hydrogel in the present study, where *Aloe vera* gel was impregnated into the matrix of the already produced BC. The degree of *Aloe vera* attachment to the surface and impregnation into the BC matrix

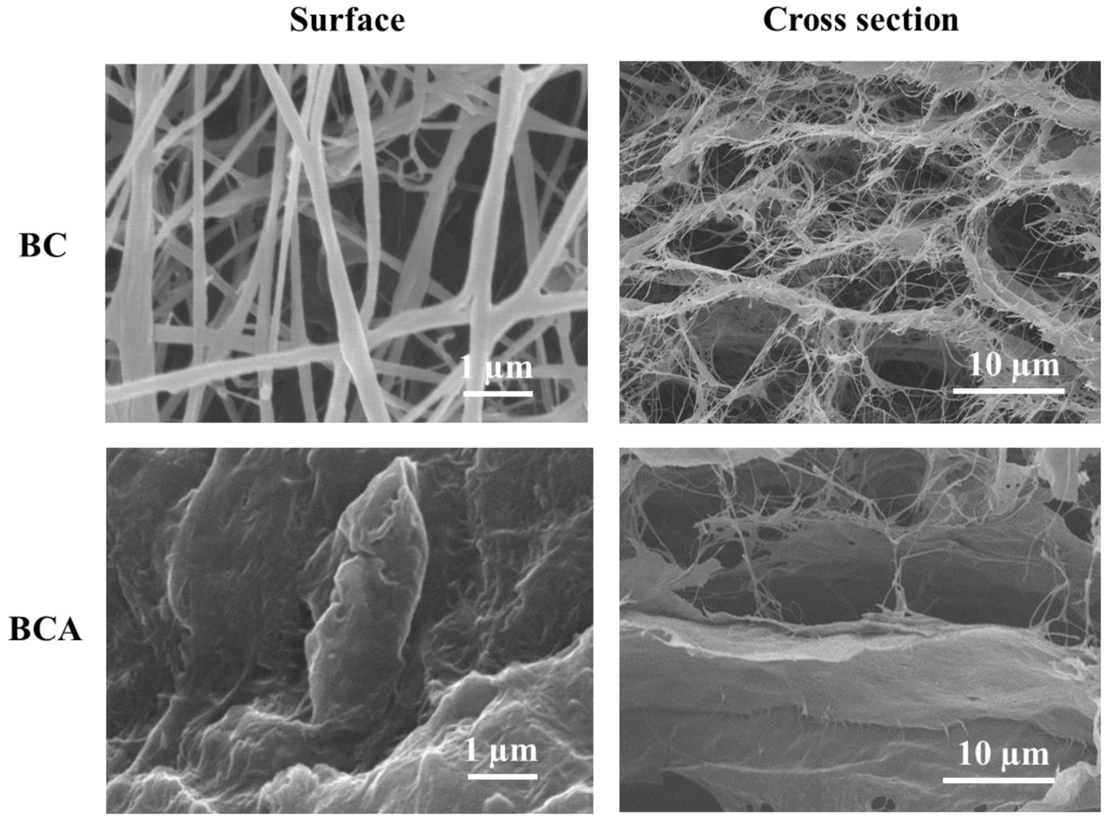

FIGURE 3 | Field-emission scanning electron micrographs of the surface and cross-sectional views of pristine BC and *ex situ* developed *Aloe vera*-loaded-BC composite (i.e., BCA) containing 40 wt.% *Aloe vera* gel.

and successful development of BCA composite was confirmed through FE-SEM microscopic observation of freeze-dried BC and BCA (**Figure 3**). The *ex situ* added *Aloe vera* gel was adsorbed not only on to the surface but also impregnated into the BC matrix. It was observed that the volume of *Aloe vera* gel did not change after 72 h immersion of BC pieces, indicating the saturation of accessible empty spaces in the fibrous network of BC. The *ex situ* addition of *Aloe vera* gel did not affect the fibrous morphology of BC as evident from the FE-SEM micrographs (**Figure 3**). Dry-weight analysis showed that the *Aloe vera* gel occupied 40% weight in the BCA composite.

The surface and cross-sectional views of the FE-SEM micrograph of pristine BC show a fibrous and porous network, indicating an ideal scenario for the impregnation of *Aloe vera* gel solution into its matrix. FE-SEM micrographs of both the surface and cross-sectional views of BCA composite shows the successful impregnation of *Aloe vera* into the BC matrix, where it got attached to the cellulose fibrils and covered the almost entire surface. The cross-sectional images also indicate the impregnation of *Aloe vera* gel among the layers of cellulose fibers and occupied the empty spaces in the matrix. This strong attachment could be attributed to the intermolecular hydrogen bonding between the hydroxyl groups on BC and amine and hydroxyl groups of *Aloe vera* (Saibuatong and Phisalaphong, 2010). Such strong interactions could contribute to enhancing the physico-mechanical properties of BCA composites.

Mechanical Strength of BCA Composite Hydrogel

For mechanical testing analysis, air-dried samples were used where the weak reversible hydrogen bonding among the cellulose fibrils is converted to strong irreversible hydrogen bonding upon the elimination of water content and leads to compact packing of the fibrils (Ul-Islam et al., 2013). The compact fibrils and strong hydrogen bonding restrict the mobility of polymer chain and enhance the toughness of BC and BC-based composites (Velmurugan and Mohan, 2009), which could offer more resistance to the applied external force and resist any structural changes in their structure. Therefore, it is expected that air-dried BC and BCA could offer high mechanical strength as compared to the freeze-dried samples.

The mechanical testing results shown in **Figure 4** indicate that BCA composite possessed better mechanical strength than pristine BC. The pristine BC and BCA composite showed a tensile strength of 54.3 and 142.4 MPa and Young's modulus of 0.45 and 1.4 GPa, respectively. These results show a 3-fold increase in the mechanical properties of BCA composite as compared

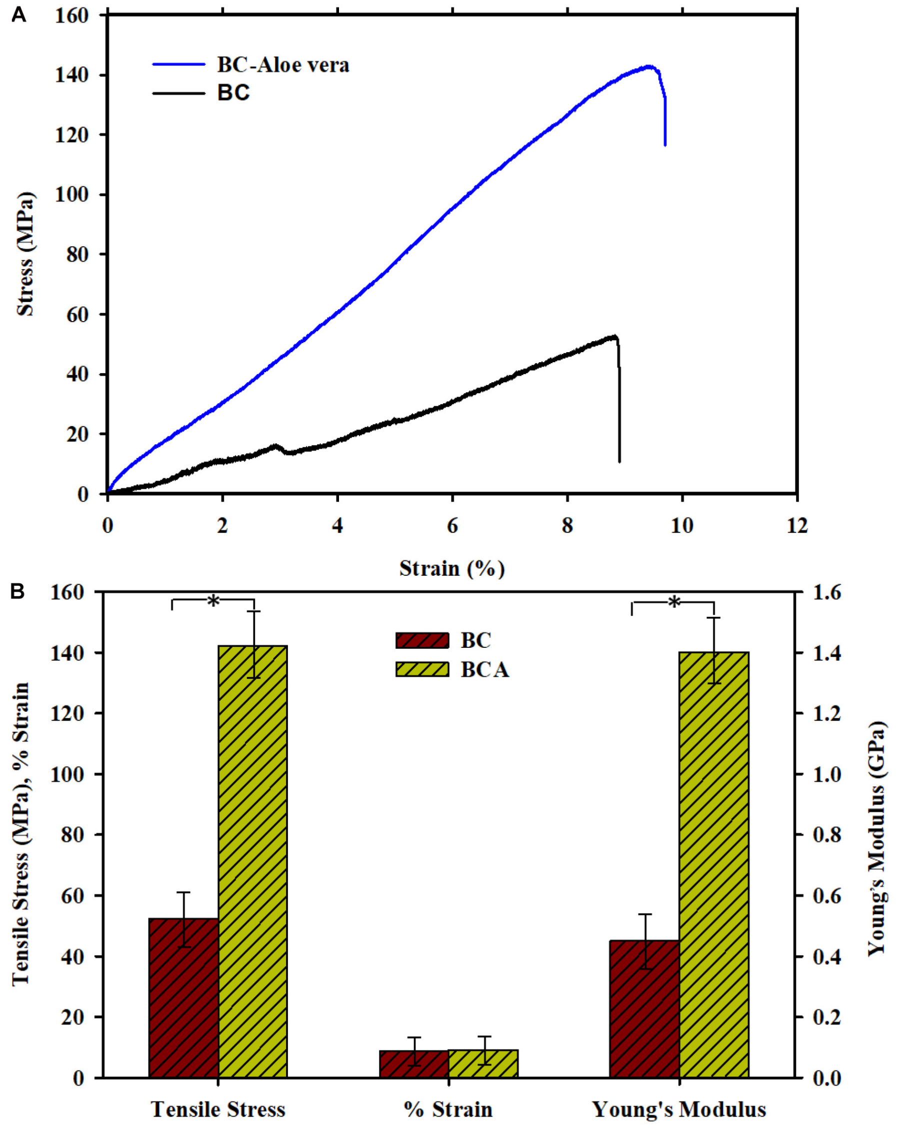

FIGURE 4 | Mechanical properties of pristine BC and *ex situ* developed *Aloe vera*-loaded-BC composite (i.e., BCA). **(A)** Stress-strain curve and **(B)** Tensile strength, % strain, and Young's modulus of BC and BCA composite. Asterisk (*) indicates a *P*-value of <0.05.

to the pristine BC. Moreover, the elasticity of BCA and BC hydrogels was found to be almost of the same strength. The increase in the mechanical features of BC, when composited with other materials, has been reported in several studies (Kim et al., 2010; Wang et al., 2018). In a study, the addition of 0 to 30% (v/v) *Aloe vera* gel resulted in a 1.6-fold increase in the tensile strength and elongation break of *in situ* prepared BCA composite, however, further addition of *Aloe vera* gel into the BC matrix resulted in reduced mechanical properties due to the disruption of BC fibril structure and arrangement during the *in situ* synthesis process (Saibuatong and Phisalaphong, 2010). The use of the *ex situ* composite synthesis strategy in the present study contributed to maintaining the undisturbed structural features of BC, which aided in enhancing its existing features and strengthening of fibrils upon the incorporation of *Aloe vera* gel. The maintenance of the original fibrous structure of BC upon the addition of *Aloe vera* gel could be the possible reason that even a high concentration (i.e., 40 wt.%) of *Aloe vera* gel in the BC matrix contributed to a 3-fold increase in the tensile strength.

The mechanical strength of the BCA composite was further determined through a 3D-DIC system *via* full-field deformation to provide insight into the BC structure with respect to the critical strain during the synthesis of the composite. The 3D-DIC is a modern but simple operational optical technique with a high level of precision in the field of engineering research. It is mainly used to obtain the full-field displacement and strain without any physical contact with the deforming object under any kind of loading. Although many researchers have used the 3D-DIC system for failure mechanism analysis of different structures and materials (Abbassi and Ahmad, 2020; Jebri et al., 2020), its application in BC research has been limited. In this study, the 3D-DIC system was used to locate the critical strain, and the fracture process zones for both pristine BC and BCA composite samples under tensile loading, and the results are shown in **Figure 5**. The image for pristine BC shows that the bottom left corner of the sample is under high strain (indicated by an arrow on the left side), and the sample deformed from the same location is shown on the right side (indicated by an arrow). From the deformed image of pristine BC, it is clear that further tensile loading will continue the deformation in the upward and horizontal direction from micro to large scale cracks. The results from the 3D-DIC system for the BCA sample, before and after the fracture, are also shown in **Figure 5**, indicating that the sample is comparatively under less strain (indicated by arrows). The respective deformed image from the same location in the BCA composite is shown on the right side (indicated by an arrow). It is clear from the left side of **Figure 5** that the samples initially failed from the bottom in the middle, indicating this point as the location of critical strain. The prediction of the 3D-DIC system was found accurate as the sample started to deform from the same location, indicating that

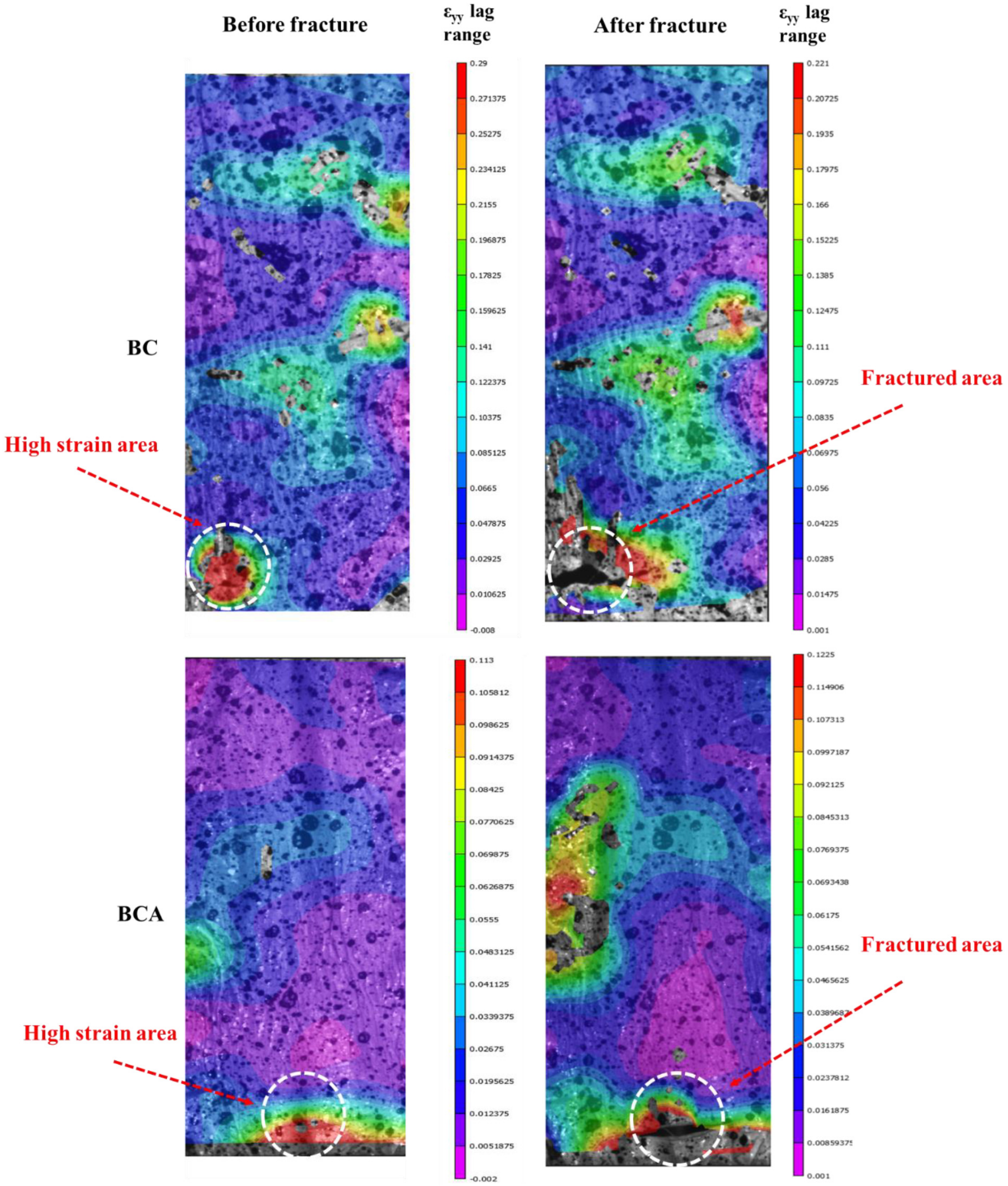

FIGURE 5 | Mechanical behavior of pristine BC and *ex situ* developed *Aloe vera*-loaded-BC composite (i.e., BCA) determined through the 3D-DIC system. The deformation of samples was determined before and after a fracture. The arrows indicate the high strain and fractured areas in both pristine BC and BCA composite.

it will continue to deform in the horizontal direction if a further tensile load is applied.

Absorption of Water and Heavy Metals by BCA Composite

The porous surface and hydrophilic nature of BC impart tremendous liquid and solid adsorption and water holding capabilities to BC. Several studies have reported that BC can hold water from a few to more than a hundred times its dry weight (Ul-Islam et al., 2013). The WHC of BC varies with its structural and processing features depending upon its surface area, pore size, and pore volume. The results for WHC of pristine BC and BCA composite are shown in **Figure 6A**. The results show that compared to the pristine BC holding 84 times more water than its dry weight, the BCA composite only held 73 times more water than its dry weight, indicating that the impregnation of *Aloe vera* gel to BC network reduced its WHC. The reduced WHC of BCA could be attributed to the reduction in the porosity of BC sheets and the unavailability of free hydroxyl groups in BC due to their interaction with those in the *Aloe vera* gel. Interestingly, the BCA composite retained water for a much longer time compared to the pristine BC, which could be attributed to the hydrophilic nature of *Aloe vera* gel. **Figure 6A** illustrates that pristine BC lost

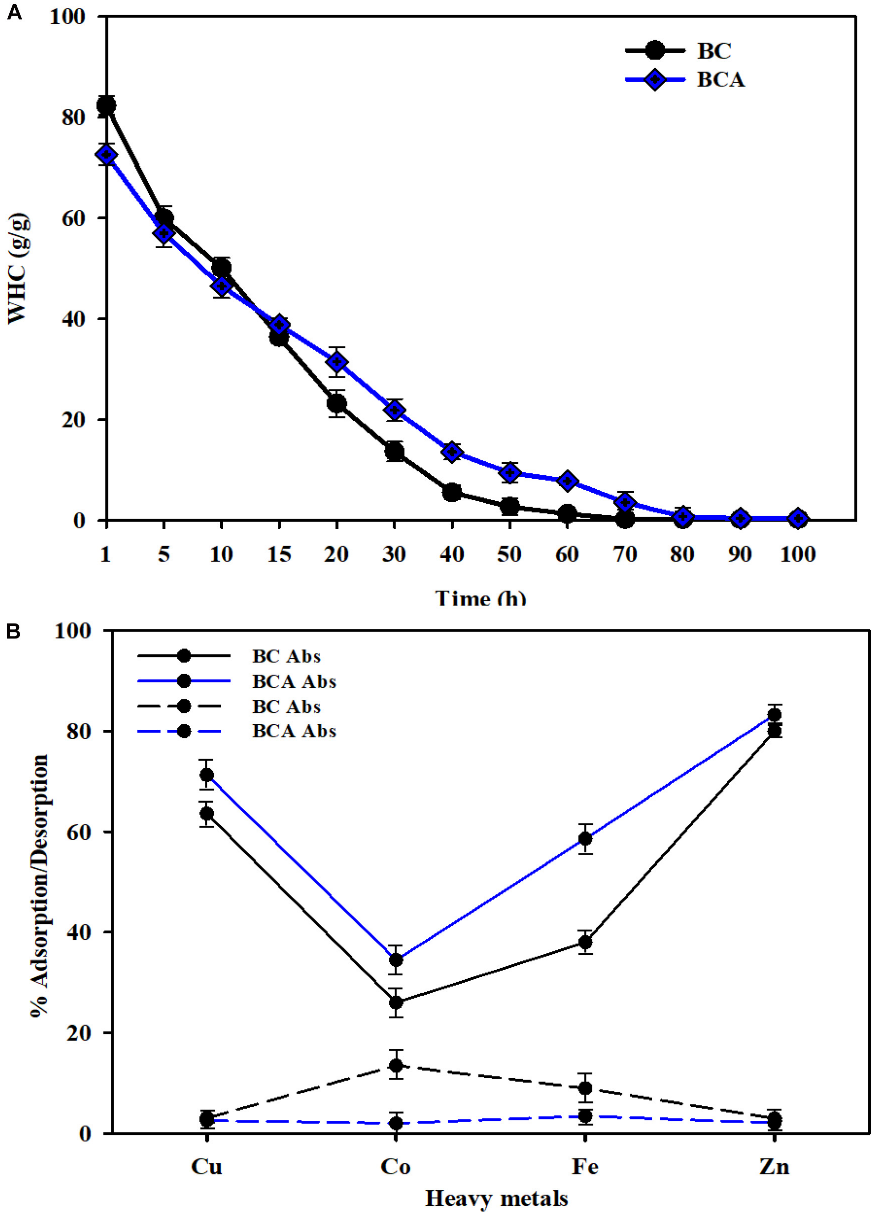

FIGURE 6 | Absorption analysis of pristine BC and *ex situ* developed *Aloe vera*-loaded-BC composite (i.e., BCA). **(A)** Water holding capacity **(B)** heavy metal absorption analysis for all samples was carried out at room temperature. Error bars indicate that the results are the mean from three independent experiments.

almost 90% of the water after 40 h, whereas BCA lost the same amount of water in 70 h. The slow WRT from BCA composite is an important feature for its application in drug delivery, chronic wound healing, and prolonged skin moisturizing to maintain a moist environment for cosmetic application (Khan et al., 2015b; Di et al., 2017).

The porous structure of BC plays an important role in absorbing heavy metals from aqueous solutions (Jin et al., 2017). To date, BC and other forms of cellulose have been extensively used in developing filters, where the primary aim is the absorption of unwanted and toxic materials from wastewater (Ul-Islam et al., 2016). Owing to its 3D nano-reticular microenvironment, BC could prove to be a better option for the absorption of heavy metals as compared to the crystalline cellulose (Chen et al., 2009). In the present study, the heavy metals absorption capabilities of both BC and BCA were evaluated against heavy metals, including Cu, Co, Fe, and Zn, and the results are shown in **Figure 6B**. The results show that both pristine BC and BCA composite effectively absorbed heavy metals from water, nevertheless, to different levels. The absorption ability of the BCA composite was better than pristine BC. Furthermore, the strength of the absorbed particles with cellulose fibrils was determined through desorption analysis, where an almost negligible desorption rate was observed with pristine BC and BCA composite. The BC-based composites with metal absorbing capabilities have already been reported where BC composite with poly (ethylene glycol) (BC-PEG) showed high potentials of Cu^{2+} and Pb^{2+} ions adsorption from aqueous solution (Chen et al., 2009). In another study (Chen et al., 2020) developed the composite of BC with attapulgite that

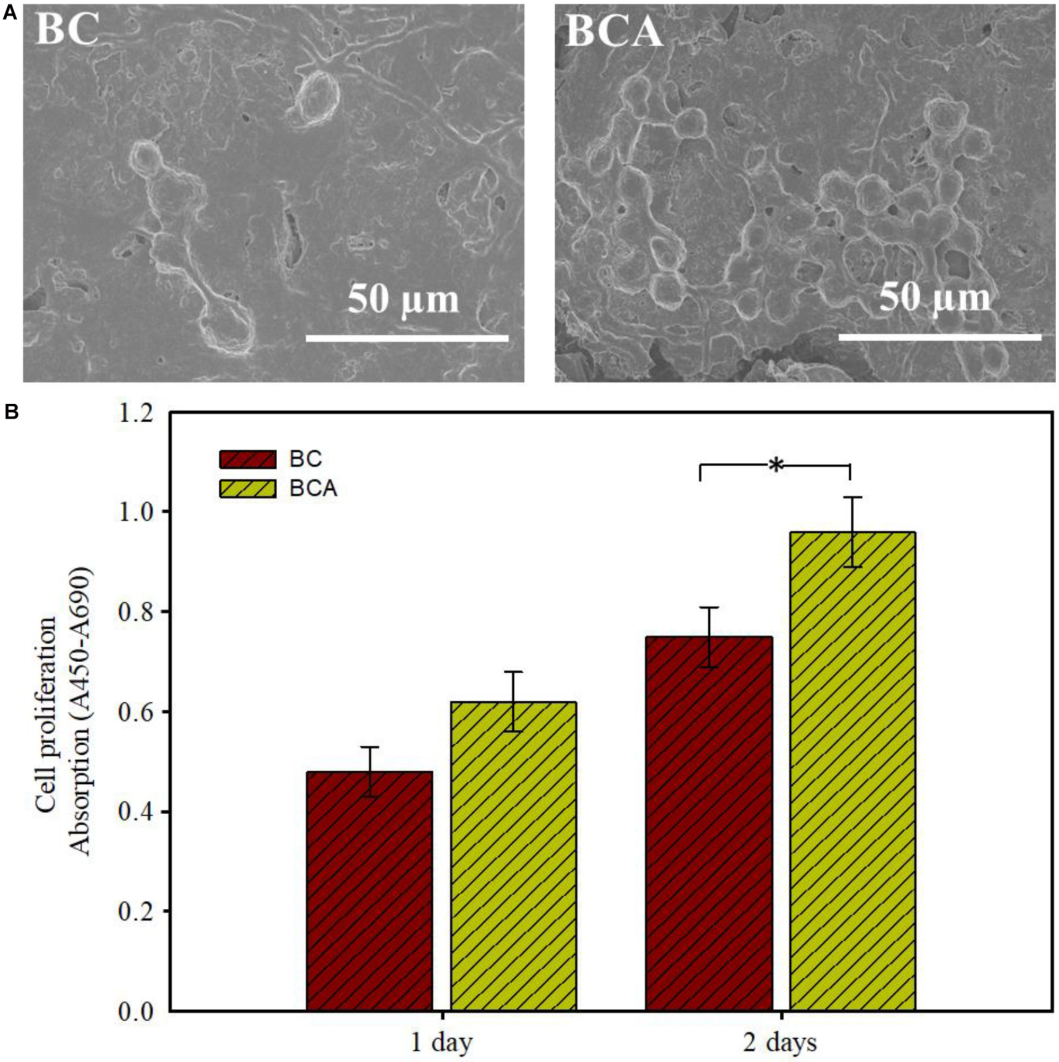

FIGURE 7 | Cytocompatibility analysis of pristine BC and *ex situ* developed *Aloe vera*-loaded-BC composite (i.e., BCA). **(A)** The adhesion and structural morphology of MC3T3-E1 cells on both samples was observed under FE-SEM. **(B)** The proliferation of MC3T3-E1 cells on the samples was determined by measuring the absorption after 1 and 2 days. The asterisk (*) indicates a *P*-value of <0.05.

effectively absorbed Pb^{2+}, Cu^{2+}, and Cr^{6+}, along with anionic organic dyes. Considering the structural features of BC, it can be concluded that this biopolymer could be utilized as a green material for developing composites for absorbing pollutants and toxic materials from wastewater, air, and other samples.

Cell Adhesion and Proliferation Analysis

To validate the feasibility of pristine BC and BCA composites in wound healing and related biomedical applications, it is important to observe their cell adhesion capabilities against animal cells. In the present study, the cytocompatible and non-toxic nature of pristine BC and BCA composite hydrogel was evaluated by determining their ability to support the adhesion and proliferation of MC3T3-E1, and the results are shown in **Figure 7**. The cell adhesion observed *via* FE-SEM revealed successful adhesion of MC3T3-E1 cells on both pristine BC and BCA composite (**Figure 7A**). Further, the MC3T3-E1 cells attained round morphology after 12 h on both BC and BCA composites displaying minor signs of their shape extension and formation of filopodia. Compared to the pristine BC, the MC3T3-E1 cells proliferated more effectively on BCA composite, indicating the improved cytocompatibility of BC upon impregnation of *Aloe vera* gel. The examination of cell proliferation illustrated appreciably high levels of BrdU absorption when cultured on both BC and BCA samples (**Figure 7B**). A significant increase in cell proliferation was observed on BCA composite as compared to the pristine BC after 1 and 2 days. These observations are in accordance with an earlier study (Godinho et al., 2016). Godinho et al. (2016) reported that BC-*Aloe vera* composite possess offered high cytocompatibility than pristine BC, where the viable animal cells fully covered the composite surface, indicating a strong adhesion and proliferation. The high level of cell adhesion capabilities of BCA composites could be attributed to the nitrogen-containing compounds in *Aloe vera* gel. Overall, the results of the current study show the potential of BCA composite with high mechanical strength as a remarkable scaffold for wound-healing applications.

CONCLUSION

A composite of BC with *Aloe vera* gel (BCA) was successfully developed through the *ex situ* composite synthesis strategy. The employed *ex situ* approach of impregnating *Aloe vera* gel into the BC matrix overcame the limitation associated with the *in situ* synthesis strategy and did not disturb the fibrous morphology, and contributed to enhancing the mechanical strength of BCA composite. The position of critical strain or stress concentration points were identified in the developed BCA composite by using the 3D-DIC system. The developed BCA composite demonstrated a high level of heavy metal absorption and supported the adhesion of animal cells, indicating its multipurpose applications in environmental and biomedical sectors, respectively. It can be concluded that the synthesized BCA composite with higher mechanical, cytocompatibility, and absorption properties could be used as a multipurpose material for applications in biomedical, environment, and other fields. Further, *in vivo* studies to evaluate the detailed biocompatibility for wound healing and tissue regeneration ability as well as drug loading capacity and release profile are warranted for practical tissue engineering applications of the developed BCA composite. Similarly, the utilization of BCA-composites as catalysts, adsorbents, and membrane filters and applying them to wastewaters, air, soil, and other samples wound further demonstrate their potential environmental applications.

DATA AVAILABILITY STATEMENT

The original contributions presented in the study are included in the article/supplementary material, further inquiries can be directed to the corresponding author.

AUTHOR CONTRIBUTIONS

FA, AF, and SY: methodology, investigation, and characterization. NS, MdA, SM: writing – original draft, writing – review, and editing. MU-I and MU: supervision, investigation, methodology, writing – review, and editing. All authors contributed to the article and approved the submitted version.

FUNDING

This research was supported by “The Research Council (TRC)” Oman through Block Research Funding Program (BFP/RGP/EBR/20/261) and China Postdoctoral Science Foundation (2016M602291).

REFERENCES

Abbassi, F., and Ahmad, F. (2020). Behavior analysis of concrete with recycled tire rubber as aggregate using 3D-digital image correlation. *J. Clean. Prod.* 274:123074. doi: 10.1016/j.jclepro.2020.123074

Aljohani, W., Ullah, M. W., Zhang, X., and Yang, G. (2018). Bioprinting and its applications in tissue engineering and regenerative medicine. *Int. J. Biol. Macromol.* 107, 261–275. doi: 10.1016/j.ijbiomac.2017.08.171

Bu, Y., Cao, M., Jiang, Y., Gao, L., Shi, Z., Xiao, X., et al. (2018). Ultra-thin bacterial cellulose/poly(ethylenedioxythiophene) nanofibers paper electrodes for all-solid-state flexible supercapacitors. *Electrochim. Acta* 271, 624–631. doi: 10.1016/j.electacta.2018.03.155

Chen, S., Zou, Y., Yan, Z., Shen, W., Shi, S., Zhang, X., et al. (2009). Carboxymethylated-bacterial cellulose for copper and lead ion removal. *J. Hazard. Mater.* 161, 1355–1359. doi: 10.1016/j.jhazmat.2008.04.098

Chen, X., Cui, J., Xu, X., Sun, B., Zhang, L., Dong, W., et al. (2020). Bacterial cellulose/attapulgite magnetic composites as an efficient adsorbent for heavy metal ions and dye treatment. *Carbohydr. Polym.* 229:115512. doi: 10.1016/j.carbpol.2019.115512

Ciecholewska-Jusìko, D., Żywicka, A., Junka, A., Drozd, R., Sobolewski, P., Migdał, P., et al. (2020). Superabsorbent crosslinked bacterial cellulose biomaterials for chronic wound dressings. *bioRxiv* [Preprint]. doi: 10.1101/2020.03.04.975003

Curvello, R., Raghuwanshi, V. S., and Garnier, G. (2019). Engineering nanocellulose hydrogels for biomedical applications. *Adv. Colloid Interface Sci.* 267, 47–61. doi: 10.1016/j.cis.2019.03.002

Dhar, P., Pratto, B., Gonçalves Cruz, A. J., and Bankar, S. (2019). Valorization of sugarcane straw to produce highly conductive bacterial cellulose / graphene nanocomposite films through in situ fermentation: kinetic analysis and property evaluation. *J. Clean. Prod.* 238:117859. doi: 10.1016/j.jclepro.2019.117859

Di, Z., Shi, Z., Ullah, M. W., Li, S., and Yang, G. (2017). A transparent wound dressing based on bacterial cellulose whisker and poly(2-hydroxyethyl methacrylate). *Int. J. Biol. Macromol.* 105, 638–644. doi: 10.1016/j.ijbiomac.2017.07.075

Eslahi, N., Mahmoodi, A., Mahmoudi, N., Zandi, N., and Simchi, A. (2020). Processing and properties of nanofibrous bacterial cellulose-containing polymer composites: a review of recent advances for biomedical applications. *Polym. Rev.* 60, 1–27. doi: 10.1080/15583724.2019.1663210

Farooq, U., Ullah, M. W., Yang, Q., Aziz, A., Xu, J., Zhou, L., et al. (2020). High-density phage particles immobilization in surface-modified bacterial cellulose for ultra-sensitive and selective electrochemical detection of Staphylococcus aureus. *Biosens. Bioelectron.* 157:112163. doi: 10.1016/j.bios.2020.112163

Godinho, J. F., Berti, F. V., Müller, D., Rambo, C. R., and Porto, L. M. (2016). Incorporation of Aloe vera extracts into nanocellulose during biosynthesis. *Cellulose* 23, 545–555. doi: 10.1007/s10570-015-0844-3

Haider, A., Gupta, K. C., and Kang, I. K. (2014). Morphological effects of HA on the cell compatibility of electrospun HA/PLGA composite nanofiber scaffolds. *Biomed. Res. Int.* 2014:308306. doi: 10.1155/2014/308306

Jasim, A., Ullah, M. W., Shi, Z., Lin, X., and Yang, G. (2017). Fabrication of bacterial cellulose/polyaniline/single-walled carbon nanotubes membrane for potential application as biosensor. *Carbohydr. Polym.* 163, 62–69. doi: 10.1016/j.carbpol.2017.01.056

Jebri, L., Abbassi, F., Demiral, M., Soula, M., and Ahmad, F. (2020). Experimental and numerical analysis of progressive damage and failure behavior of carbon Woven-PPS. *Compos. Struct.* 243:112234. doi: 10.1016/j.compstruct.2020.112234

Jin, X., Xiang, Z., Liu, Q., Chen, Y., and Lu, F. (2017). Polyethyleneimine-bacterial cellulose bioadsorbent for effective removal of copper and lead ions from aqueous solution. *Bioresour. Technol.* 244, 844–849. doi: 10.1016/j.biortech.2017.08.072

Khan, H., Kadam, A., and Dutt, D. (2020). Studies on bacterial cellulose produced by a novel strain of Lactobacillus genus. *Carbohydr. Polym.* 229:115513. doi: 10.1016/j.carbpol.2019.115513

Khan, S., Ul-Islam, M., Khattak, W. A., Ullah, M. W., and Park, J. K. (2015a). Bacterial cellulose-poly(3,4-ethylenedioxythiophene)-poly(styrenesulfonate) composites for optoelectronic applications. *Carbohydr. Polym.* 127, 86–93. doi: 10.1016/j.carbpol.2015.03.055

Khan, S., Ul-Islam, M., Ullah, M. W., Ikram, M., Subhan, F., Kim, Y., et al. (2015b). Engineered regenerated bacterial cellulose scaffolds for application in in vitro tissue regeneration. *RSC Adv.* 5, 84565–84573. doi: 10.1039/C5RA16985B

Khan, S., Ul-Islam, M., Ullah, M. W., Israr, M., Jang, J. H., and Park, J. K. (2018). Nano-gold assisted highly conducting and biocompatible bacterial cellulose-PEDOT:PSS films for biology-device interface applications. *Int. J. Biol. Macromol.* 107, 865–873. doi: 10.1016/j.ijbiomac.2017.09.064

Kim, J., Cai, Z., Lee, H. S., Choi, G. S., Lee, D. H., and Jo, C. (2010). Preparation and characterization of a Bacterial cellulose/Chitosan composite for potential biomedical application. *J. Polym. Res.* 18, 739–744. doi: 10.1007/s10965-010-9470-9

Kim, Y., Ullah, M. W., Ul-Islam, M., Khan, S., Jang, J. H., and Park, J. K. (2019). Self-assembly of bio-cellulose nanofibrils through intermediate phase in a cell-free enzyme system. *Biochem. Eng. J.* 142, 135–144. doi: 10.1016/j.bej.2018.11.017

Li, S., Huang, D., Zhang, B., Xu, X., Wang, M., Yang, G., et al. (2014). Flexible supercapacitors based on bacterial cellulose paper electrodes. *Adv. Energy Mater.* 4:1301655. doi: 10.1002/aenm.201301655

Li, S., Jasim, A., Zhao, W., Fu, L., Ullah, M. W., Shi, Z., et al. (2018). Fabrication of pH-electroactive bacterial Cellulose/Polyaniline hydrogel for the development of a controlled drug release system. *ES Mater. Manuf.* 1, 41–49. doi: 10.30919/esmm5f120

Lombardo, S., and Thielemans, W. (2019). Thermodynamics of adsorption on nanocellulose surfaces. *Cellulose* 26, 249–279. doi: 10.1007/s10570-018-02239-2

McCarthy, R. R., Ullah, M. W., Booth, P., Pei, E., and Yang, G. (2019a). The use of bacterial polysaccharides in bioprinting. *Biotechnol. Adv.* 37:107448. doi: 10.1016/j.biotechadv.2019.107448

McCarthy, R. R., Ullah, M. W., Pei, E., and Yang, G. (2019b). Antimicrobial Inks: the anti-infective applications of bioprinted bacterial polysaccharides. *Trends Biotechnol.* 37, 1153–1155. doi: 10.1016/j.tibtech.2019.05.004

Menda, J. P., Reddy, T., Deepika, R., Devi, P. M., and Sastry, T. P. (2014). Preparation and characterization of wound healing composites of chitosan, aloe vera and *Calendula officinalis*-a comparative study. *Am. J. Phytomedicine Clin. Ther.* 2, 61–76.

Pereira, R. F., Carvalho, A., Gil, M. H., Mendes, A., and Bártolo, P. J. (2013). Influence of Aloe vera on water absorption and enzymatic in vitro degradation of alginate hydrogel films. *Carbohydr. Polym.* 98, 311–320. doi: 10.1016/j.carbpol.2013.05.076

Rebelo, A. R., Archer, A. J., Chen, X., Liu, C., Yang, G., and Liu, Y. (2018). Dehydration of bacterial cellulose and the water content effects on its viscoelastic and electrochemical properties. *Sci. Technol. Adv. Mater.* 19, 203–211. doi: 10.1080/14686996.2018.1430981

Saibuatong, O. A., and Phisalaphong, M. (2010). Novo aloe vera-bacterial cellulose composite film from biosynthesis. *Carbohydr. Polym.* 79, 455–460. doi: 10.1016/j.carbpol.2009.08.039

Sajjad, W., He, F., Ullah, M. W., Ikram, M., Shah, S. M., Khan, R., et al. (2020). Fabrication of bacterial cellulose-curcumin nanocomposite as a novel dressing for partial thickness skin burn. *Front. Bioeng. Biotechnol.* 8:553037. doi: 10.3389/fbioe.2020.553037

Shoukat, A., Wahid, F., Khan, T., Siddique, M., Nasreen, S., Yang, G., et al. (2019). Titanium oxide-bacterial cellulose bioadsorbent for the removal of lead ions from aqueous solution. *Int. J. Biol. Macromol.* 129, 965–971. doi: 10.1016/j.ijbiomac.2019.02.032

Silva, S. S., Caridade, S. G., Mano, J. F., and Reis, R. L. (2013). Effect of crosslinking in chitosan/aloe vera-based membranes for biomedical applications. *Carbohydr. Polym.* 98, 581–588. doi: 10.1016/j.carbpol.2013.06.022

Skiba, E. A., Budaeva, V. V., Ovchinnikova, E. V., Gladysheva, E. K., Kashcheyeva, E. I., Pavlov, I. N., et al. (2020). A technology for pilot production of bacterial cellulose from oat hulls. *Chem. Eng. J.* 383:123128. doi: 10.1016/j.cej.2019.123128

Ul-Islam, M., Khan, S., Ullah, M. W., and Park, J. K. (2015). Bacterial cellulose composites: synthetic strategies and multiple applications in bio-medical and electro-conductive fields. *Biotechnol. J.* 10, 1847–1861. doi: 10.1002/biot.201500106

Ul-Islam, M., Khattak, W. A., Kang, M., Kim, S. M., Khan, T., and Park, J. K. (2013). Effect of post-synthetic processing conditions on structural variations and applications of bacterial cellulose. *Cellulose* 20, 253–263. doi: 10.1007/s10570-012-9799-9

Ul-Islam, M., Khattak, W. A., Ullah, M. W., Khan, S., and Park, J. K. (2014). Synthesis of regenerated bacterial cellulose-zinc oxide nanocomposite films for biomedical applications. *Cellulose* 21, 433–447. doi: 10.1007/s10570-013-0109-y

Ul-Islam, M., Subhan, F., Islam, S. U., Khan, S., Shah, N., Manan, S., et al. (2019). Development of three-dimensional bacterial cellulose/chitosan scaffolds: analysis of cell-scaffold interaction for potential application in the diagnosis of ovarian cancer. *Int. J. Biol. Macromol.* 137, 1050–1059. doi: 10.1016/j.ijbiomac.2019.07.050

Ul-Islam, M., Ullah, M. W., Khan, S., Kamal, T., Ul-Islam, S., Shah, N., et al. (2016). Recent advancement in cellulose based nanocomposite for addressing environmental challenges. *Recent. Pat. Nanotechnol.* 10, 169–180. doi: 10.2174/1872210510666160429144916

Ul-Islam, M., Ullah, M. W., Khan, S., and Park, J. K. (2020b). Production of bacterial cellulose from alternative cheap and waste resources: a step for cost reduction with positive environmental aspects. *Korean J. Chem. Eng.* 37, 925–937. doi: 10.1007/s11814-020-0524-3

Ul-Islam, M., Yasir, S., Mombasawala, L., Manan, S., and Wajid Ullah, M. (2020a). Bacterial cellulose: a versatile material for fabrication of conducting nanomaterials. *Curr. Nanosci.* 16. doi: 10.2174/1573413716999201005214832

Ullah, M. W., Ul-Islam, M., Khan, S., Kim, Y., Jang, J. H., and Park, J. K. (2016). In situ synthesis of a bio-cellulose/titanium dioxide nanocomposite by using a cell-free system. *RSC Adv.* 6, 22424–22435. doi: 10.1039/C5RA26704H

Ullah, M. W., Ul-Islam, M., Khan, S., Kim, Y., and Park, J. K. (2015). Innovative production of bio-cellulose using a cell-free system derived from a single cell line. *Carbohydr. Polym.* 132, 286–294. doi: 10.1016/j.carbpol.2015.06.037

Velmurugan, R., and Mohan, T. P. (2009). Epoxy-clay nanocomposites and hybrids: synthesis and characterization. *J. Reinf. Plast. Compos.* 28, 17–37. doi: 10.1177/0731684407081439

Wang, L., Hu, S., Ullah, M. W., Li, X., Shi, Z., and Yang, G. (2020). Enhanced cell proliferation by electrical stimulation based on electroactive regenerated bacterial cellulose hydrogels. *Carbohydr. Polym.* 249:116829. doi: 10.1016/j.carbpol.2020.116829

Wang, X., Xie, Y., Ge, H., Chen, L., Wang, J., Zhang, S., et al. (2018). Physical properties and antioxidant capacity of chitosan/epigallocatechin-3-gallate films reinforced with nano-bacterial cellulose. *Carbohydr. Polym.* 179, 207–220. doi: 10.1016/j.carbpol.2017.09.087

Xiang, Z., Chen, Y., Liu, Q., and Lu, F. (2018). A highly recyclable dip-catalyst produced from palladium nanoparticle-embedded bacterial cellulose and plant fibers. *Green Chem.* 20, 1085–1094. doi: 10.1039/c7gc02835k

Conflict of Interest: The authors declare that the research was conducted in the absence of any commercial or financial relationships that could be construed as a potential conflict of interest.

frontiers
in Bioengineering and Biotechnology

BRIEF RESEARCH REPORT
published: 05 February 2021
doi: 10.3389/fbioe.2021.608965

Lateral Gradient Ambidextrous Optical Reflection in Self-Organized Left-Handed Chiral Nematic Cellulose Nanocrystals Films

*Jiawei Tao, Jiaqi Li, Xiao Yu, Lihong Wei and Yan Xu**

State Key Laboratory of Inorganic Synthesis and Preparative Chemistry, Jilin University, Changchun, China

Artificial photonic materials displaying ordered reflected color patterns are desirable in the field of photonic technologies, however, it is challenging to realize. Here we present that self-assembly of cellulose nanocrystals (CNC) in a tilted cuvette leads to the formation of rainbow color CNC films. We show that the self-organized CNC films enable simultaneous reflection of left-handed circularly polarized (LCP) and right-handed circularly polarized (RCP) light with lateral gradient transmittance ratio (LCP/RCP: 8.7–0.9) and the maximum reflectance value up to *ca.* 72%. This unique ambidextrous optical reflection arises from left-handed chiral photonic architectures with lateral gradient photonic bandgaps and nematic-like defects at the film-substrate interface and between left-handed photonic bandgap layers acting as a half-wavelength retarder. We demonstrate that the tilted angle self-assembly method provides a feasible step toward color patterning of CNC-based photonic films capable of ambidextrous optical reflection.

Keywords: cellulose nanocrystals, tilted-angle self-assembly, gradient photonic bandgaps, circularly polarized light, ambidextrous reflection

Edited by:
Guang Yang,
Huazhong University of Science and Technology, China

Reviewed by:
PaYaM ZarrinTaj,
Oklahoma State University, United States
Dagang Liu,
Nanjing University of Information Science and Technology, China

****Correspondence:***
Yan Xu
yanxu@jlu.edu.cn

Specialty section:
This article was submitted to Biomaterials, a section of the journal Frontiers in Bioengineering and Biotechnology

Received: *22 September 2020*
Accepted: *20 January 2021*
Published: *05 February 2021*

Citation:
Tao J, Li J, Yu X, Wei L and Xu Y (2021) Lateral Gradient Ambidextrous Optical Reflection in Self-Organized Left-Handed Chiral Nematic Cellulose Nanocrystals Films. Front. Bioeng. Biotechnol. 9:608965. doi: 10.3389/fbioe.2021.608965

INTRODUCTION

Photonic crystals possessing periodic modulation of dielectric constants and photonic bandgaps (PBG) offer ways to manipulate light, which are of significance for applications including circular polarizers (Lv et al., 2019), photonic devices (Tao et al., 2020a), chiral catalysts (Cho et al., 2016), and biosensors (Lv et al., 2017). Chiral nematic materials are attractive as self-assembled one-dimensional photonic crystals displaying unique circular polarization ability. Structural coloration arising from light-matter interactions is common among many living organisms in nature (Zhao et al., 2012; Almeida et al., 2018). For example, helicoidal nanostructures of cellulose nanofibrils are responsible for the intense blue color found in many fruits and leaves (Vignolini et al., 2012). Similar phenomenon has been observed in some beetle cuticles. Of particular interests are the cuticle of beetle *Plusiotis resplendens* displaying optically ambidextrous reflection in a left-handed chiral nematic organization and the cuticle of beetle *Chrysina gloriosa* enabling strong polarization-insensitive reflection (Sharma et al., 2009). This effect originates from a nematic-like layer, which is sandwiched between two left-handed PBG layers, acting as a half-wavelength retarder (Caveney, 1971). These structure-endowed chiroptical activities have inspired the design and fabrication of artificial chiral photonic materials. In particular, cellulose nanocrystals (CNC) derived from natural cellulose self-assemble in colloidal dispersions into thermodynamically more stable left-handed helicoids that can be preserved upon drying. Evaporation-induced self-assembly on a planar surface is the common method used to fabricate photonic CNC films (Lagerwall et al., 2014; Tran et al., 2018; Tao and Xu, 2020). The left-handed chiral nematic structure of CNC has intrinsic ability to enable photonic bandgap-based reflection of left-handed circularly polarized (LCP) light, transmission of right-handed circularly polarized (RCP) light and RCP spontaneous luminescence (Klemm et al., 2011; Zheng et al., 2018; Tran et al., 2020). The wavelength of selective reflection follows the Eq. 1,

$$\lambda(\theta) = n_{avg} P sin\theta, \tag{1}$$

where n_{avg} is the average refractive index, P is the helical pitch and θ is the incident angle from nematic surface (Parker et al., 2018). Leveraging on CNC self-assembly thermodynamics vs. kinetics (Wang et al., 2016), quasinematic structures (Hiratani et al., 2017), nematic structures (Gan et al., 2019), microgap-embedded chiral photonic architectures (Fernandes et al., 2017), surface-textured chiral photonic architectures (Tran et al., 2018), and chiral nematic-nematic photonic architectures have been spontaneously organized, manifesting the wealth of CNC photonic materials (Tao et al., 2020b). Self-assembly of CNC in magnetic and electric fields narrow helical pitch and orientation polydispersity, which may facilitate the development of high efficiency circularly polarized luminescence materials (Frka-Petesic et al., 2017a,b). So far, chiral photonic CNC films with continuously varying PBG, to the best of our knowledge, has not been reported.

Here we report that self-assembly of CNC in a titled cuvette of stable colloidal dispersions produces chiral photonic CNC films that display rainbow colors and lateral gradient ambidextrous optical reflection. The CNC film features a photonic architecture formed with left-handed PBG layers and nematic-like layers at the film-substrate interface and embedded between PBG layers. It enables ambidextrous optical reflection showing lateral gradient transmittance values from the higher to the lower end of the cuvette. The ambidextrous chiroptical properties are owing to the half-wavelength retardation of nematic-like phases nucleated *in situ* and kinetically arrested. The transmittance values of the RCP light and LCP light are tilt angle-dependent, which appear most pronounced at 30°. Increasing the tilt angle weakens chiral nematic features and promotes unidirectional alignment of CNC. We demonstrate that tilted-angle self-assembly allows synergistic self-assembly and kinetic stabilization, providing a step toward self-organized chiral nematic-nematic films capable of color patterning, lateral gradient PBG and ambidextrous optical reflectivity.

MATERIALS AND METHODS

Materials

Cotton pulp board was purchased from Hebei Paper Group, China. Sulfuric acid was purchased from Beijing Chemical Company. Dialysis bags were purchased from Spectrum labs with 28 mm in diameter and molecular cut-off of 0.8–15 kDa. Left and right circular polarization filters were purchased from Jinan Photoelectric Technology Company with effective spectral range of 400–700 nm. All reagents were used as received without further purification.

Preparation of CNC Suspension

CNC was obtained from cotton pulp by acid hydrolysis using sulfuric acid (64%) and the acid/cotton pulp mass ratio was kept at 10:1. The hydrolysis reaction took place at 45°C for 90 min under vigorous stirring, and the reaction was terminated using deionized water. The solid product was centrifuged (8,000 r/min, 6 min) several times and dialyzed against deionized water until pH = 7. The suspension was diluted to desired concentrations for keeping.

Preparation of CNC-α Film

Two milliliter of CNC suspensions (4 wt%, pH = 7) without macroscopic phase separation was allowed to assemble in a tilted quartz cuvette (25°C) as illustrated in **Figure 1**. Changing the tilt angle (α) of the cuvette to base plane led to a range of iridescent rainbow color CNC films, denoted as CNC-α.

RESULTS AND DISCUSSION

CNC-30 film showed colors in order of red, orange, green and blue from the higher to the lower end of the cuvette against a black background when viewed in normal white light (**Figure 2A**). Notably, the portion of the film at the air-substrate interface at the higher end was colorless. The film colors dimmed when viewed through a 400–700 nm left-handed circular polarization (LCP) filter and intensified when viewed through a 400–700 nm right-handed circular polarization (RCP) filter (**Figures 2B,C**). It indicates that CNC-30 reflects simultaneously LCP and RCP light.

The self-assembly of CNC in the titled cuvette of stable dispersion experiences variation in kinetic factors including CNC concentration, assembly time and interfacial interactions that may lead to continuous change in the photonic properties. The CNC-30 film was laterally segmented into zones 1, 2, and 3 and individually examined using optical microscopy and UV-vis transmission spectroscopy. All spectra were recorded by facing the film-substrate side of films to incident beam (**Figure 2D**). The green-red reflection pattern of the zone 1 recorded in normal white light appeared a green-red stripped pattern or an intensified green-red pattern with a contrast variation when recorded through the LCP or RCP filter (**Figures 2E–G**). The corresponding transmission spectra showed simultaneous reflection of LCP and RCP light with the peak transmittance values of *ca.* 38 and 8% at 655 and 660 nm, respectively, consistent with the optical microscopy studies (**Figure 2H**, left vertical axis). The optical micrographs of the zone 2 displayed a blue-green pattern with a red tint under normal white light that appeared intensified or a green-red pattern with random blue and dark patches when recorded through the LCP or RCP filter (**Figures 2I–K**). The corresponding transmission spectra

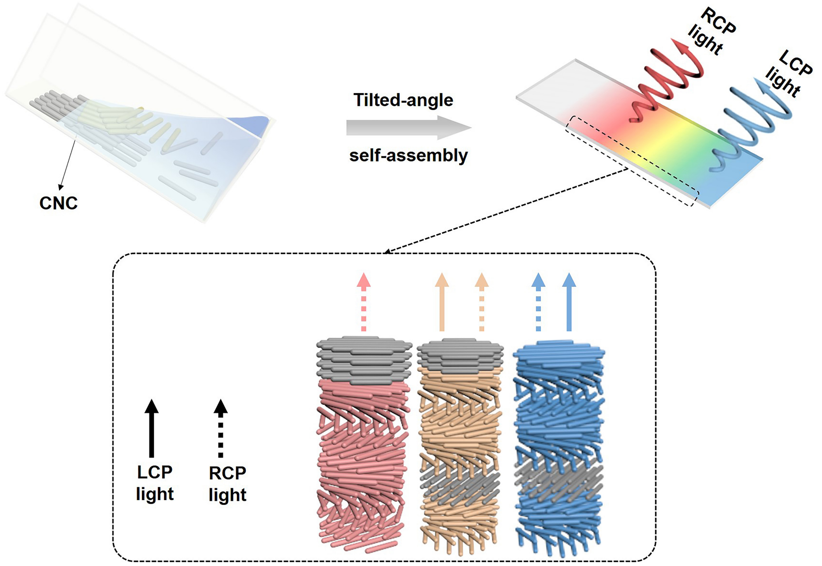

FIGURE 1 | Tilted-angle self-assembly leads to self-organized CNC films displaying rainbow colors and ambidextrous optical reflection. LCP light arises from selective reflection of incident light by left-handed chiral nematic structure. RCP light is due to *in situ* reversal of transmitted RCP light by embedded nematic-like layers that are found at the film-substrate interface as well as embedded between left-handed PBG layers. The nematic-like layer at the film-substrate interface above left-handed PBG layer causes *in situ* handedness reversal of LCP light to RCP light; the nematic-like layer embedded between two same left-handed PBG layers converts transmitted RCP light to LCP light, then reflected by the left-handed PBG layer below and converted further to RCP light as it propagates back through the nematic-like layer. Such mesostructural feature causes a total reflectance exceeding the 50% limit of a left-handed chiral nematic structure. Note: gray for nematic-like order; solid arrows for LCP light; dotted arrow for RCP light.

revealed simultaneous reflection of LCP and RCP light with the peak transmittance values of *ca.* 24 and 21% at 554 and 562 nm, respectively (**Figure 2L**, left vertical axis). The zone 3 displayed similar blue and yellow patterns with variations in color contrast recorded in normal white light or through the LCP or RCP filter (**Figures 2M–O**). The corresponding transmission spectra probed by the LCP or RCP filter revealed LCP or RCP light reflection band with the peak transmittance values of ca. 23 or 31% at 460 or 463 nm (**Figure 2P**, left vertical axis). We also examined zones 1, 2, 3 using circular dichroism (CD) spectroscopy (**Supplementary Figure 1**), the corresponding signals go from negative to positive, suggesting a change in chirality. Noteworthy are the ambidextrous optical reflections of CNC-30 with coincided band wavelengths of RCP and LCP light reflection and, more strikingly, a continuous change in the peak wavelength from the zone 1 to the zone 3. The reflection bands probed by normal white light coincided with the corresponding transmission bands in the peak wavelength and showed the peak reflectance values of ca. 64, 72, and 69%, exceeding exclusively the 50% limit of a single-handed chiral nematic phase (**Figures 2H,L,P**, right vertical axis; Michel and Dessaud, 2006). These results indicated that CNC-30 film was capable of reflecting circularly polarized light of both handedness with lateral gradient colors and chiral distribution.

We investigated the mesostructural features of the zones 1, 2, and 3 using scanning electron microscopy (SEM). High-magnification SEM images of the film cross-section revealed a chiral nematic-nematic bilayer architecture (**Figures 3A–C**), where the layer at the air-film interface contained primarily chiral nematic order with the helical pitches of P1 = 202 nm, P2 = 170 nm, and P3 = 142 nm (**Figures 3D–F**). The chiral nematic order was confirmed to be left-handed based on the Neville convention, while right-handed helicoids were not found (Majoinen et al., 2012). The helical pitch of the chiral nematic phase decreased from the zone 1 to the zone 3, consistent with the optical microscopy and transmission spectral studies (**Figure 2**). We attributed the decreasing helical pitches to the lateral increasing of local CNC concentration induced by tilt angle assembly (Dumanli et al., 2014). The layer formed at the film-substrate interface contained primarily unidirectionally aligned CNC with respective thickness of d1 = 3,938 nm, d2 = 3,521 nm and d3 = 2,971 nm. Nematic-like layers were also found between left-handed PBG layers and increased in number from the zone 1 to the zone 3, which resulted from reduction in fluidity and kinetically arrest of CNC.

When rotated around a plane perpendicular to the crossed polarizers in a transmission polarizing optical microscopy, the zone 1 showed birefringent patterns and a change in the transmitted intensity of some color appearances from minimum to maximum at a 45° rotation, confirming the presence of nematic-like phase (**Figures 3G,H**). These nematic-like layers may introduce a wavelength retardation L to the propagating light following the Eq. 2,

$$L = \Delta n d, \quad \Delta \mathrm{n} = n_e - n_o, \qquad (2)$$

where Δn is the net birefringence, n_e and n_o are the extraordinary and ordinary refractive indices of birefringent

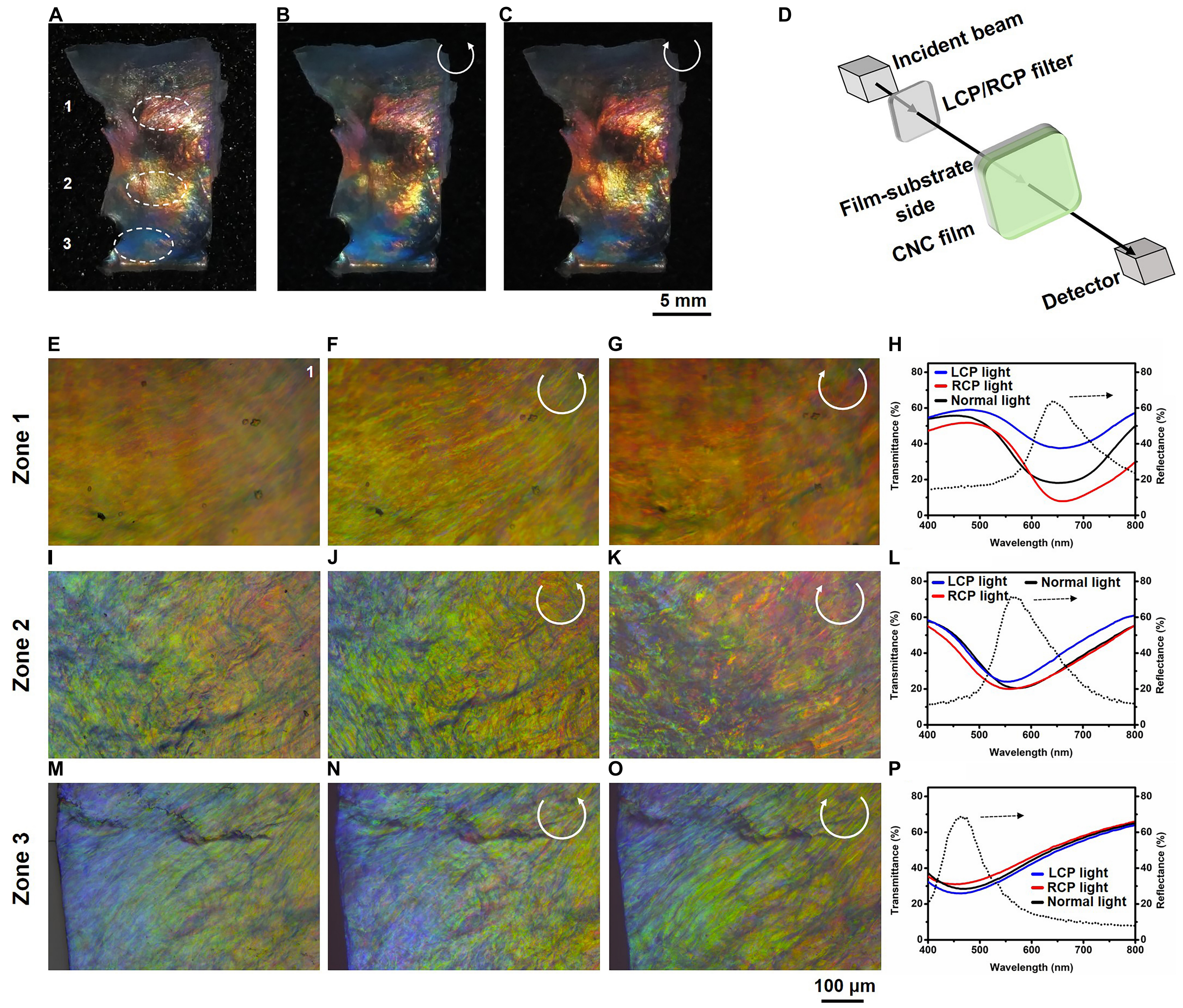

FIGURE 2 | (A–C) Photographs of CNC-30 viewed under normal light **(A)**, through the LCP filter **(B)** and through the RCP filter **(C)** showing lateral gradient color pattern. **(D)** Schematics illustrating the spectral measurement by exposing the film-substrate side to incident beam. Reflected optical micrographs of the zones 1, 2, 3 viewed under normal light **(E,I,M)**, through the LCP filter **(F,J,N),** and the RCP filter **(G,K,O)**, respectively. **(H,L,P)** The transmission spectra (left vertical axis) of the zones 1, 2 and 3 probed by normal light (solid black lines), through the LCP filter (solid blue lines) and the RCP filter (solid red lines) and reflection spectra (right vertical axis) probed by normal light (dotted black lines).

medium, respectively (Cruz et al., 2018), and d is the optical path length of the nematic-like layer that can be approximated to be the layer thickness. Significantly, half-wavelength retardation causes handedness reversal of propagating circularly polarized light. Taking the zone 1 for example, given that approximately d_1 = 3,938 nm and Δn = 0.08 (Krishnaiyer et al., 1968), transmitted RCP light at 630 nm would be half-wavelength retarded leading to LCP light reflection at the same wavelength. When the wavelength of the converted LCP light matches the PBG of subsequent chiral nematic layers, it is then reflected and undergoes further reversal into reflected RCP light as it propagates back through the nematic-like layer as evidenced by the transmission spectra probed by LCP or RCP light (see **Figures 2G,K,O**). Hence, these novel optical textures can be attributed to the synergy of left-handed chiral organizations with gradient changing helical pitches and nematic-like phases to light, the former leads to a rainbow pattern while the distribution of the latter results in the lateral gradient ambidextrous optical reflection.

We show that the rainbow color pattern and lateral gradient ambidextrous optical reflection are tilt angle-dependent. Taking CNC-60 for example, the film displayed colors in order of red, orange, yellow and blue under normal white light against a black background, and the color pattern remained literally unchanged when recorded through the LCP filter or RCP filter (**Figure 4A**). Selective reflection band emerged at the zone 4, next to the non-reflective region on the higher end of films, showed LCP and RCP light reflection bands with the peak transmittance values of 23 or

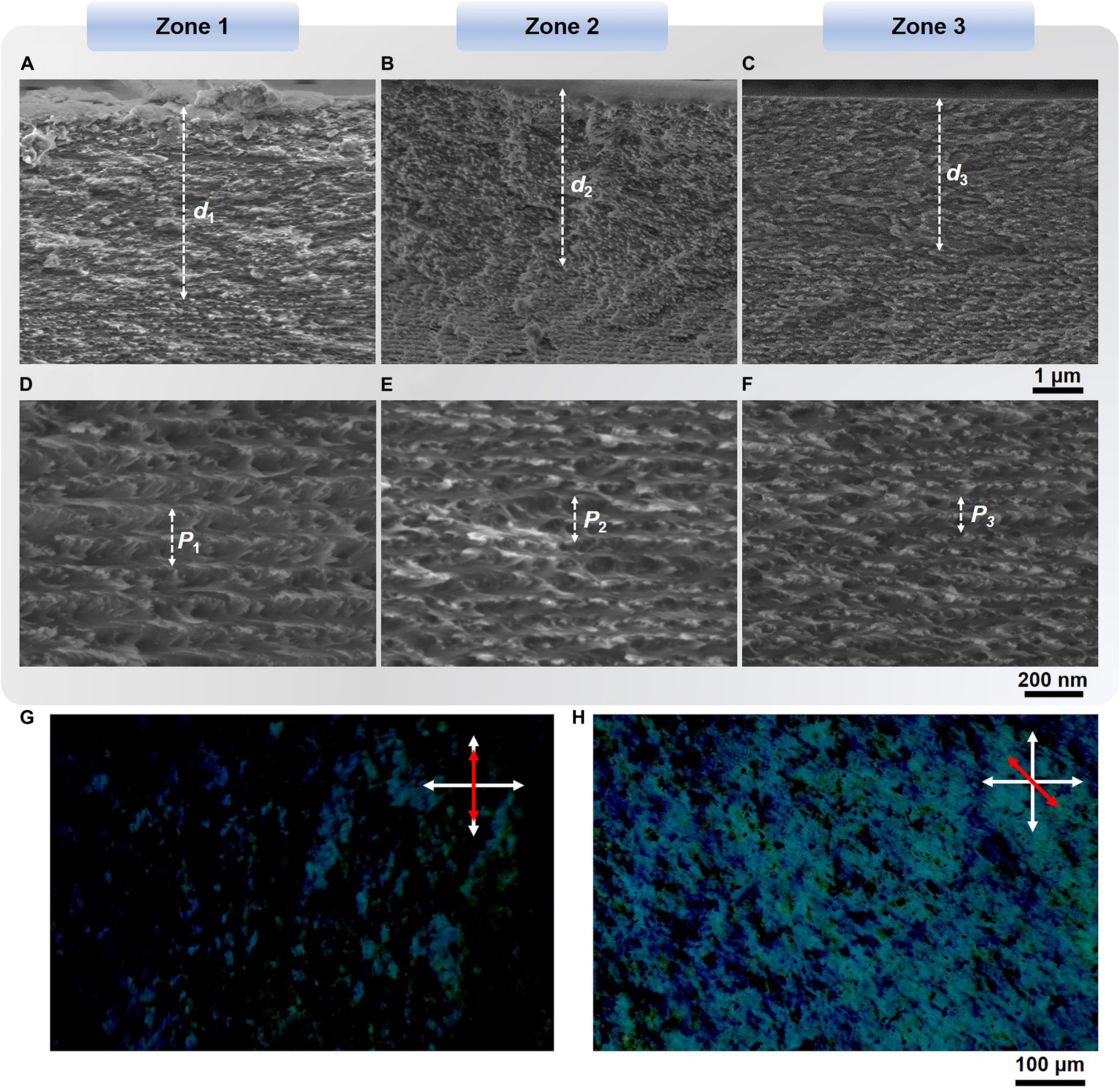

FIGURE 3 | (A–F) Cross-sectional SEM images of zones 1, 2, and 3 on CNC-30 show nematic-like layers at the film-substrate interface with the thickness of *ca*. d_1 = 3,938 nm, d_2 = 3,521 nm, and d_3 = 2,971 nm **(A–C)**. High magnification SEM images exhibit left-handed PBG layers with the helical pitches of P_1 = 202 nm, P_2 = 170 nm, and P_3 = 142 nm **(D–F)**. **(G,H)** Transmission polarized optical micrographs of CNC-60 show birefringent patterns with the transmitted intensity change from minimum **(G)** and to maximum at a 45° rotation **(H)**. The white double-headed arrows refer to cross-polarizers and red double-headed arrows represent the CNC director.

21% at 617 or 618 nm when probed through the LCP or RCP filter (**Figure 4B**). Nematic-like phase was found at the film-substrate interface as well as between left-handed PBG layers based on the SEM images (**Figures 4C,D**, highlighted by dotted white circles, the region above dotted white line). Notably, CNC-60 displayed larger non-reflective region at the cuvette higher end and closely matched transmittance values of the LCP and RCP light reflection compared with CNC-30. In other words, the transmittance ratio of LCP and RCP of CNC-60 was always close to 1.0, while for film CNC-30, the LCP/RCP ratio gradient decreased from 8.7 to 0.9 (**Figure 4E**).

In order to understand the CNC self-assembly in a tilted cuvette, two control films, CNC-0 and CNC-90, were fabricated in a CNC dispersion (4 wt%, 25°C, pH = 7) by evaporation-induced self-assembly method and by vertical deposition method (Gan et al., 2019), respectively. The CNC-0 film appeared red to the naked eyes under normal white light that intensified or dimmed when viewed through the LCP or RCP filter

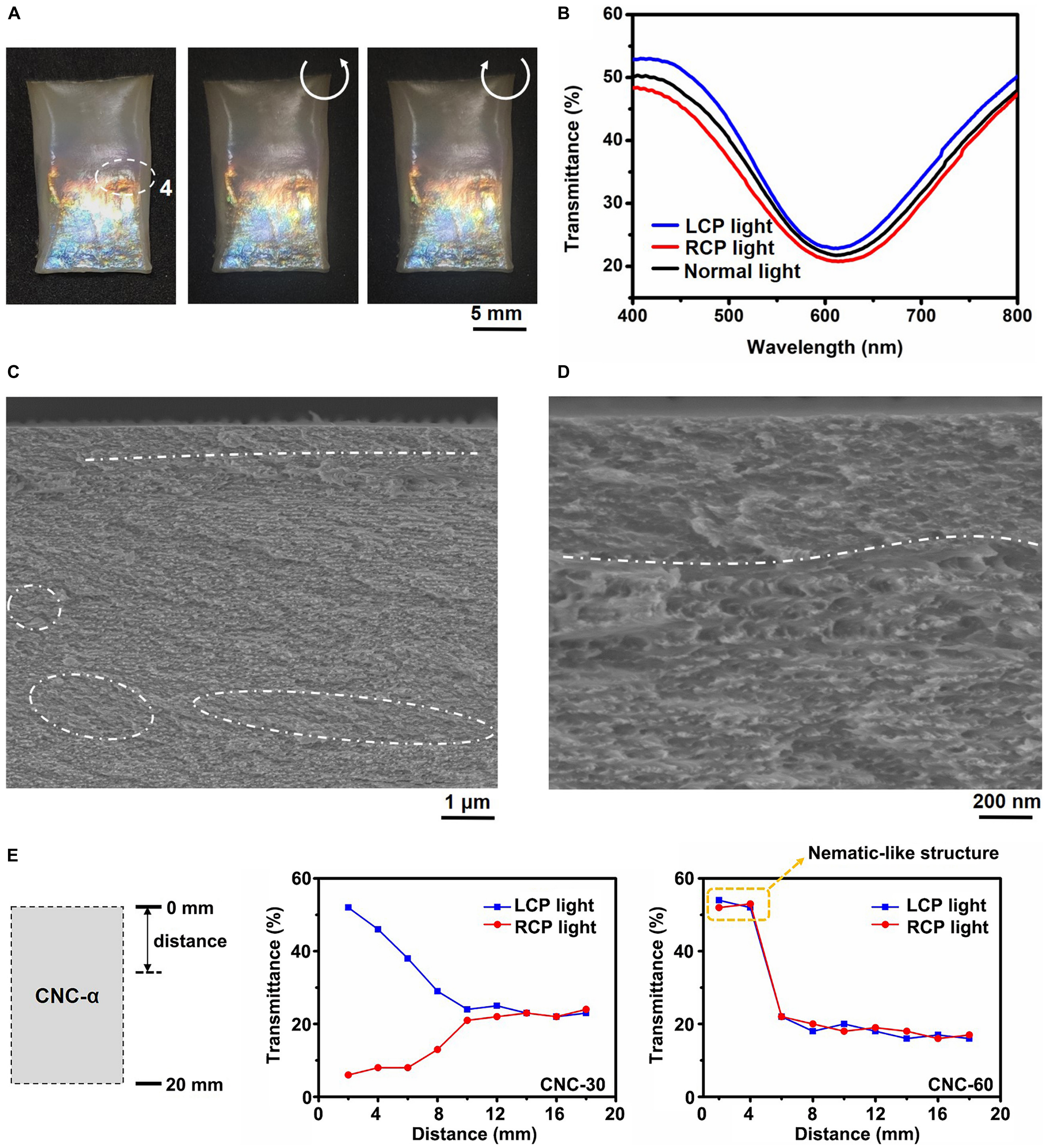

FIGURE 4 | (A–D) Photographs of CNC-60 viewed under normal white light (left), through the LCP filter (middle) and the RCP filter (right) **(A)**, the transmission spectra of CNC-60 probed by normal white light (solid black line), through the LCP filter (solid blue line) or the RCP filter (solid red line) **(B)**, SEM images show a chiral nematic-nematic architecture **(C)**, where the nematic-like layers (dotted white circles) are embedded between left-handed PBG layers and at the film-substrate interface (above dotted white lines) **(C,D)**. **(E)** Changes in the transmittance value of the LCP light (blue line) and RCP light (red line) in CNC-30 and CNC-60.

(**Supplementary Figure 2A**). One strong LCP or one weak RCP light reflection band (peak transmittance values of 27 and 82% at 644 nm) displayed on the transmission spectrum probed through the LCP or RCP filter (**Supplementary Figure 2B**). It indicates the presence of embedded nematic-like layer between the left-handed PBG layers, acting as a half-wavelength retarder, as evidenced by the SEM images (**Supplementary Figures 2C,D**). Vertical immersion of a quartz plate in a colloidal dispersion promotes unidirectional alignment leading to nematic-like CNC film, CNC-90, which is non-reflective in the visible light regime (**Supplementary Figure 3**). Taken together, CNC favored unidirectional nematic-like phases at the film-substrate interface along the direction of the tilt, which occupied a larger proportion when increasing the tilt angle. At the same time, the thermodynamically stable left-handed chiral nematic phases were weakened.

CONCLUSION

We have presented experimental evidences that tilt angle self-assembly produces chiral photonic CNC films displaying rainbow colors and lateral gradient ambidextrous optical reflection that can be tuned by a change in the tilt angle. We demonstrate how the circularly polarized light reflection of both handedness can be manipulated to produce chiral photonic CNC films with changing ambidextrous reflectivity and maximum reflectance values of *ca.* 72%. It allows lateral gradient change in assembly duration and local CNC concentrations and can be manipulated by a change in tilt angle. The formation of nematic-like phase at the film-substrate interface is owing to the combined effect of kinetic stabilization of transient phase and seeded growth. The self-organization of rainbow color CNC films in a tilted cuvette is demonstrated as a step toward synthetic construction of one-dimensional chiral photonic materials displaying optical patterning and ambidextrous reflection with lateral gradient chiroptical properties for photonic applications.

DATA AVAILABILITY STATEMENT

The original contributions presented in the study are included in the article/**Supplementary Material**, further inquiries can be directed to the corresponding author/s.

AUTHOR CONTRIBUTIONS

JT wrote this manuscript, designed, and carried out the whole experiments. JL and XY contributed to cellulose nanocrystals preparation and partial data collection. LW contributed to SEM imaging collection. YX supervised the work, contributed to data analysis, and manuscript revision. All authors discussed the results and contributed to the completion of the manuscript.

FUNDING

The work was funded by the NNSF China (Grant Nos. 21975095, 21671079, and 21373100), 111 project (Grant No. B17020), JLU International Co-advisorship Program (Grant No. 419020201362), JLU International Collaboration Program (Grant No. 45119031C015), and the State Key Laboratory of Inorganic Synthesis and Preparative Chemistry of JLU (Grant No. 1G3194101461).

SUPPLEMENTARY MATERIAL

The Supplementary Material for this article can be found online at: https://www.frontiersin.org/articles/10.3389/fbioe.2021.608965/full#supplementary-material

REFERENCES

Almeida, A. P., Canejo, J. P., Fernandes, S. N., Echeverria, C., Almeida, P. L., and Godinho, M. H. (2018). Cellulose-based biomimetics and their applications. *Adv. Materials* 30:1703655. doi: 10.1002/adma.201703655

Caveney, S. (1971). Cuticle Reflectivity and Optical Activity in Scarab Beetles: The Role of Uric Acid. *Proc. R. Soc. London Ser. B* 178, 205–225. doi: 10.1098/rspb.1971.0062

Cho, S., Li, Y., Seo, M., Seo, M., and Kumacheva, E. (2016). Nanofibrillar Stimulus-Responsive Cholesteric Microgels with Catalytic Properties. *Angew. Chem. Int. Ed.* 55, 14014–14018. doi: 10.1002/ange.201607406

Cruz, J. A., Liu, Q., Senyuk, B., Frazier, A. W., Peddireddy, K., and Smalyukh, I. I. (2018). Cellulose-Based Reflective Liquid Crystal Films as Optical Filters and Solar Gain Regulators. *ACS Photonics* 5, 2468–2477. doi: 10.1021/acsphotonics.8b00289

Dumanli, A. G., Kooij, H., Kamita, G., Reisner, E., Baumberg, J., Steiner, U., et al. (2014). Digital Color in Cellulose Nanocrystal Films. *ACS Appl. Mater. Interfaces* 15, 12302–12306. doi: 10.1021/am501995e

Fernandes, S. N., Almeida, P. L., Monge, N., Aguirre, L. E., Reis, D., de Oliveira, C. L., et al. (2017). Mind the microgap in iridescent cellulose nanocrystal films. *Adv. Mater.* 29:1603560. doi: 10.1002/adma.201603560

Frka-Petesic, B., Guidetti, G., Kamita, G., and Vignolini, S. (2017a). Controllingthe Photonic Properties of CholestericCelluloseNanocrystal Films with Magnets. *Adv. Mater.* 29:1701469. doi: 10.1002/adma.201701469

Frka-Petesic, B., Radavidson, H., Jean, B., and Heux, L. (2017b). Dynamically controlled iridescence of cholesteric cellulose nanocrystal suspensions using electric fields. *Adv. Mater.* 29:1606208. doi: 10.1002/adma.201606208

Gan, L., Feng, N., Liu, S., Zheng, S., Li, Z., and Huang, J. (2019). Assembly-Induced Emission of Cellulose Nanocrystals for Hiding Information. *Particle Particle Syst. Charac.* 36:1800412. doi: 10.1002/ppsc.201800412

Hiratani, T., Hamad, W. Y., and MacLachlan, M. J. (2017). Transparent depolarizing organic and inorganic films for optics and sensors. *Adv. Materials* 29:1606083. doi: 10.1002/adma.201606083

Klemm, D., Kramer, F., Moritz, S., Lindström, T., Ankerfors, M., Gray, D., et al. (2011). Nanocelluloses: a new family of nature-based materials. *Angewandte Chemie Int. Edit.* 50, 5438–5466. doi: 10.1002/anie.201001273

Krishnaiyer, K. R., Neelakantan, P., and Radhakrishnan, T. (1968). Birefringence of Native Cellulosic Fibers. I. Untreated Cotton and Ramie. *J. Polym. Sci., Part A* 6, 1747–1758. doi: 10.1002/pol.1968.160061005

Lagerwall, J., Schütz, C., Salajkova, M., Noh, J., Park, J., Scalia, G., et al. (2014). Cellulose Nanocrystal-Based Materials: from Liquid Crystal Self-Assembly and Glass Formation to Multifunctional Thin Films. *NPG Asia Materials* 6:e80. doi: 10.1038/am.2013.69

Lv, J., Ding, D., Yang, X., Hou, K., Miao, X., Wang, D., et al. (2019). Biomimetic Chiral Photonic Crystals. *Angew. Chem. Int. Ed.* 58, 7783–7787. doi: 10.1002/ange.201903264

Lv, J., Hou, K., Ding, D., Wang, D., Han, B., Gao, X., et al. (2017). Gold Nanowire Chiral Ultrathin Films with Ultrastrong and Broadband Optical Activity. *Angew. Chem. Int. Ed.* 56, 5055–5060. doi: 10.1002/anie.201701512

Majoinen, J., Kontturi, E., Ikkala, O., and Gray, D. G. (2012). SEM imaging of chiral nematic films cast from cellulose nanocrystal suspensions. *Cellulose* 19, 1599–1605. doi: 10.1007/s10570-012-9733-1

Michel, M., and Dessaud, N. (2006). Going Beyond the Reflectance Limit of Cholesteric Liquid Crystals. *Nat. Mater.* 5, 361–364. doi: 10.1038/nmat1619

Parker, R. M., Guidetti, G., Williams, C. A., Zhao, T., Narkevicius, A., Vignolini, S., et al. (2018). The Self-Assembly of Cellulose Nanocrystals: Hierarchical Design of Visual Appearance. *Adv. Mater.* 30, 1704477. doi: 10.1002/adma.201704477

Sharma, V., Crne, M., Park, J. O., and Srinivasarao, M. (2009). Structural origin of circularly polarized iridescence in jeweled beetles. *Science* 325, 449–451. doi: 10.1126/science.1172051

Tao, J., and Xu, Y. (2020). Cellulose Nanocrystals-based Chiroptical Materials. *Pap. Biomater.* 05, 14–30. doi: 10.12103/j.issn.2096-2355.2020.03.002

Tao, J., Li, B., Lu, Z., Liu, J., Su, L., Tang, Z., et al. (2020a). Endowing zeolite LTA superballs with multifold light manipulation ability. *Angew. Chem. Int. Ed.* 59, 19684–19690. doi: 10.1002/anie.202007064

Tao, J., Zou, C., Jiang, H., Li, M., Lu, D., Mann, S., et al. (2020b). Optically Ambidextrous Reflection and Luminescence in Self-organized Left-handed Chiral Nematic Cellulose Nanocrystal Films. *CCS Chem.* 2, 932–945. doi: 10.31635/ccschem.020.202000248

Tran, A., Boott, C. E., and MacLachlan, M. J. (2020). Understanding the Self-Assembly of Cellulose Nanocrystals—Toward Chiral Photonic Materials. *Adv. Materials* 2020:1905876. doi: 10.1002/adma.201905876

Tran, A., Hamad, W. Y., and MacLachlan, M. J. (2018). Fabrication of cellulose nanocrystal films through differential evaporation for patterned coatings. *ACS Appl. Nano Mater.* 1, 3098–3104. doi: 10.1021/acsanm.8b00947

Vignolini, S., Rudall, P. J., Rowland, A. V., Reed, A., Moyroud, E., Faden, R. B., et al. (2012). Pointillist structural color in Pollia fruit. *Proc. Natl. Acad. Sci.* 109, 15712–15715. doi: 10.1073/pnas.1210105109

Wang, P. X., Hamad, W. Y., and MacLachlan, M. J. (2016). Structure and transformation of tactoids in cellulose nanocrystal suspensions. *Nat. Communications* 7, 1–8. doi: 10.1038/ncomms11515

Zhao, Y. J., Xe, Z., Gu, H., Zhu, C., and Gu, Z. Z. (2012). Bio-Inspired Variable Structural Color Materials. *Chem. Soc. Rev.* 41, 3297–3317. doi: 10.1039/C2CS15267C

Zheng, H., Li, W., Li, W., Wang, X., Tang, Z. Y., Zhang, S. X. A., et al. (2018). Uncovering the Circular Polarization Potential of Chiral Photonic Cellulose Films for Photonic Applications. *Adv. Mater.* 30, 1705948. doi: 10.1002/adma.201705948

Conflict of Interest: The authors declare that the research was conducted in the absence of any commercial or financial relationships that could be construed as a potential conflict of interest.

frontiers
in Bioengineering and Biotechnology

ORIGINAL RESEARCH
published: 25 February 2021
doi: 10.3389/fbioe.2021.605924

Bioactive Cellulose Nanocrystal-Poly(ε-Caprolactone) Nanocomposites for Bone Tissue Engineering Applications

Jung Ki Hong[1], **Shelley L. Cooke**[2], **Abby R. Whittington**[1,2,3] **and Maren Roman**[1,4]*

[1] Macromolecules Innovation Institute, Virginia Tech, Blacksburg, VA, United States, [2] Department of Materials Science and Engineering, Virginia Tech, Blacksburg, VA, United States, [3] Department of Chemical Engineering, Virginia Tech, Blacksburg, VA, United States, [4] Department of Sustainable Biomaterials, Virginia Tech, Blacksburg, VA, United States

3D-printed bone scaffolds hold great promise for the individualized treatment of critical-size bone defects. Among the resorbable polymers available for use as 3D-printable scaffold materials, poly(ε-caprolactone) (PCL) has many benefits. However, its relatively low stiffness and lack of bioactivity limit its use in load-bearing bone scaffolds. This study tests the hypothesis that surface-oxidized cellulose nanocrystals (SO-CNCs), decorated with carboxyl groups, can act as multi-functional scaffold additives that (1) improve the mechanical properties of PCL and (2) induce biomineral formation upon PCL resorption. To this end, an *in vitro* biomineralization study was performed to assess the ability of SO-CNCs to induce the formation of calcium phosphate minerals. In addition, PCL nanocomposites containing different amounts of SO-CNCs (1, 2, 3, 5, and 10 wt%) were prepared using melt compounding extrusion and characterized in terms of Young's modulus, ultimate tensile strength, crystallinity, thermal transitions, and water contact angle. Neither sulfuric acid-hydrolyzed CNCs (SH-CNCs) nor SO-CNCs were toxic to MC3T3 preosteoblasts during a 24 h exposure at concentrations ranging from 0.25 to 3.0 mg/mL. SO-CNCs were more effective at inducing mineral formation than SH-CNCs in simulated body fluid (1x). An SO-CNC content of 10 wt% in the PCL matrix caused a more than 2-fold increase in Young's modulus (stiffness) and a more than 60% increase in ultimate tensile strength. The matrix glass transition and melting temperatures were not affected by the SO-CNCs but the crystallization temperature increased by about 5.5°C upon addition of 10 wt% SO-CNCs, the matrix crystallinity decreased from about 43 to about 40%, and the water contact angle decreased from 87 to 82.6°. The abilities of SO-CNCs to induce calcium phosphate mineral formation and increase the Young's modulus of PCL render them attractive for applications as multi-functional nanoscale additives in PCL-based bone scaffolds.

Keywords: cellulose nanocrystal, poly(ε-caprolactone), nanocomposite, biomineralization, bone scaffold

Edited by:
Muhammad Wajid Ullah,
Huazhong University of Science and Technology, China

Reviewed by:
Anuj Kumar,
Yeungnam University, South Korea
Fida Hussain,
Wuhan Technology and Business University, China

***Correspondence:**
Maren Roman
maren.roman@vt.edu

Specialty section:
This article was submitted to Biomaterials,
a section of the journal Frontiers in Bioengineering and Biotechnology

Received: *13 September 2020*
Accepted: *04 January 2021*
Published: *25 February 2021*

Citation:
Hong JK, Cooke SL, Whittington AR and Roman M (2021) Bioactive Cellulose Nanocrystal-Poly(ε-Caprolactone) Nanocomposites for Bone Tissue Engineering Applications.
Front. Bioeng. Biotechnol. 9:605924.
doi: 10.3389/fbioe.2021.605924

INTRODUCTION

Bone is one of a few organs in the body that have the ability to self-regenerate without scar tissue formation following injury. However, the self-healing capacity of bone is limited to smaller than critical-sized bone defects. Critical-sized defects typically need to be repaired with bone grafts, such as autografts, allografts, or xenografts, or with metal or ceramic implants. These approaches have several limitations including donor site morbidity, donor bone supply shortage, infection, corrosion, stress shielding, and secondary surgery.

Compared to ceramics and metals, bioresorbable polymers have several inherent benefits for bone scaffold applications, including 3D printability and biodegradability. However, their inferior strength, stiffness, and bioactivity present critical challenges that need to be addressed. A mechanical mismatch between the scaffold and surrounding bone tissue could result in bone resorption through a stress shielding effect or failure of the scaffolds at the defect sites (Liu et al., 2006; Sultana, 2013).

Bone is composed to 65% of mineral and 35% of an organic matrix. The mineral phase, primarily comprising hydroxyapatite (HA), $Ca_{10}(PO_4)_6(OH)_2$, plays important roles in both the mechanical strength of bone and mineral ion homeostasis. The surface layer of bone, called cortical bone, is dense (∼10% porosity) and provides most of the supportive and protective function of the skeletal system (Sikavitsas et al., 2001). Cortical bone has a tensile strength of 89–151 MPa and a Young's modulus of 6–17 GPa (Athanasiou et al., 2000). Cancellous bone, on the other hand, making up 20% of the total bone mass of the skeleton and found in the bone interior, has a sponge-like morphology (50–90% porosity) and mechanical properties up to 10 times inferior to those of cortical bone. Nevertheless, the mechanical properties of cancellous bone are as challenging to match as those of cortical bone when aiming for comparable scaffold porosity.

A polymer that has attracted considerable attention for bone scaffold applications is poly(ε-caprolactone) (PCL) (Porter et al., 2009; Ruckh et al., 2010; Perez et al., 2012). Among its advantages are a relatively low melting temperature, the ability to be slowly bioresorbed upon implantation, and its status with the U.S. Food and Drug Administration as approved for use in medical devices. The main drawbacks of PCL are its insufficient load-bearing properties and its lack of bioactivity in regards to biomineralization (i.e., HA formation).

Several studies have reported improvements in the properties of PCL-based bone scaffolds upon incorporation of nanoscale additives, including HA nanocrystals (Wutticharoenmongkol et al., 2006; Jing et al., 2015), nanosized calcium silicate (Wei et al., 2009), or carbon nanotubes (Pan et al., 2012). Observed improvements include enhanced mechanical properties (Wutticharoenmongkol et al., 2006; Pan et al., 2012; Jing et al., 2015) and superior biomineralization (Wei et al., 2009; Jing et al., 2015). The nucleation/growth of biominerals on surfaces has been shown to strongly depend on the chemical properties of the surface, impacting the supersaturation of the growth environment (Sato et al., 2001; Weiner and Dove, 2003; Colfen, 2010; Dey et al., 2010). Tanahashi and Matsuda (1997) examined the rate of apatite formation on self-assembled monolayers (SAMs) with different terminal functional groups in simulated body fluid (SBF). The most potent functional group for apatite formation was the negatively charged -PO_4H_2 followed by the -COOH group. Non-ionic groups, such as -$CONH_2$ and -OH, and a positively charged group (NH_2) showed weaker nucleating ability, and it was found that apatite formation was inhibited on CH_3-terminated SAMs (Tanahashi and Matsuda, 1997).

This study tests the hypothesis that cellulose nanocrystals (CNCs), functionalized through surface oxidation, can act as multi-functional PCL scaffold additives that (1) improve the mechanical properties of PCL and (2) induce biomineral formation upon PCL resorption. CNCs are elongated nanoparticles, derived from various cellulose sources, including wood, plant, tunicate, algae, or bacterial cellulose (Moon et al., 2011), that have garnered interest for a number of potential applications because of their unique characteristics, including excellent mechanical properties, reactive surface chemistry, biodegradability, biocompatibility, low ecotoxicological risk, and comparatively low cost (Fleming et al., 2000; Kovacs et al., 2010; Lin et al., 2012; Domingues et al., 2014). Over the past three decades, cellulose nanocrystals (CNCs) have drawn significant interest as nanofillers in polymer matrices (Dufresne, 2008; Habibi and Dufresne, 2008; Habibi et al., 2008; Chen et al., 2009). The specific objectives of this study were to determine whether surface oxidation of CNCs, resulting in the conversion of hydroxymethyl- to carboxyl groups, enhances their ability to induce biomineralization and whether surface-oxidized CNCs (SO-CNCs) improve the mechanical properties of PCL.

MATERIALS AND METHODS

Preparation of Sulfuric Acid-Hydrolyzed CNCs (SH-CNCs)

SH-CNCs were prepared from bleached, dissolving-grade softwood sulfite pulp (Temalpa 93A), kindly provided by Tembec, Inc. (Témiscaming, QC, CA). Milled (60 mesh, Thomas Wiley® Mini-Mill, Thomas Scientific) pulp was hydrolyzed for 60 min with 64 wt% sulfuric acid (96.2 wt%, Fischer Scientific) at 45.5°C and an acid-to-pulp ratio of 10 mL/g. After 60 min, the reaction mixture was diluted by addition of 2.5 L cold (∼4°C), deionized (DI) water (18.2 MΩ·cm, Millipore Direct-Q5 Ultrapure Water System) and the acid was removed by centrifugation at 4,500 rpm for 20 min at 4°C (IEC CENTRA GP8R Refrigerated Centrifuge, Thermo Electron Corporation) followed by discarding of the supernatant. The sediment was redispersed in DI water and centrifuged. This step was repeated three times. Then, the collected sediment was transferred to dialysis tubing (Spectra/Por 4, molecular weight cut off of 12–14 kDa) and dialyzed against DI water, exchanged daily, for 1 week to remove residual acid. After the dialysis, the SH-CNC suspension was sonicated (BRANSONIC® 3510) for 30 min and filtered through a poly(vinylidene fluoride) (PVDF) syringe filter (0.45 μm, Whatman, Ltd.). The final concentration of the obtained aqueous SH-CNC suspension was ∼1 wt%.

Preparation of Surface-Oxidized CNCs (SO-CNCs)

Surface oxidation of SH-CNCs (**Supplementary Figure 1**) was performed according to the method of Araki et al. (2001) with minor modifications, based on the method of Habibi et al. (2006). Briefly, 500 g of 1 wt% aqueous SH-CNC suspension, 0.5 g of (2,2,6,6-tetramethylpiperidin-1-yl)oxyl (TEMPO, free radical, 98%, Sigma-Aldrich), and 5 g of sodium bromide (99+%, extra pure, anhydrous, Acros Organics) were thoroughly mixed in a 1 L flask with a magnetic stir bar at room temperature. The reaction was started by gradual addition of 50 mL sodium hypochlorite solution (reagent grade, available chlorine 10–15%, Sigma-Aldrich) so that the pH of the reaction mixture remained in the range 10.2–10.5. The reaction was continued for 3 h under addition of sodium hydroxide (0.5 M) to maintain the pH. The reaction was quenched by addition of 5 mL of methanol and the mixture was transferred to dialysis tubing and dialyzed against DI water (refreshed daily) for 2 weeks. Finally, the obtained aqueous suspension of SO-CNCs was sonicated for 30 min and filtered through a 0.45 μm PVDF syringe filter. The concentration of both suspensions (SH-CNC and SO-CNC) was adjusted to 3 wt% with a rotary evaporator (Büchi Rotavapor R-200) using a water bath temperature of 40°C. The stock suspensions were stored in a refrigerator until used.

Conductometric Titration

The surface charge densities of SH-CNCs and SO-CNCs were determined by conductometric titration. The aqueous suspensions were placed over a small amount of ion-exchange resin (Rexyn®I-300 (H-OH), certified, research grade, Fisher Scientific) for 12 h and filtered through 1.0 μm PVDF syringe filters before the titration. The ion exchange resin-treated SH-CNCs and SO-CNCs are denoted SH-CNC-I and SO-CNC-I, respectively. Titrations of 45 mL of 0.20 wt% SH-CNC suspension were carried out after addition of 5 mL of 0.01 M potassium chloride to increase the ionic strength. Titrations of 40 mL of 0.20 wt% SO-CNC suspension were conducted after addition of 20 mL of 0.01 M hydrochloric acid. The electrical conductivity was recorded with a pH/conductivity meter (Mettler Toledo SevenMulti S47 pH/conductivity meter with an InLab 730 conductivity probe) every 30 s after addition of 100 μL aliquots of 0.01 M sodium hydroxide by micropipette. Reported values are means of duplicate measurements. The surface charge density (σ) was calculated with the following equation (Jiang et al., 2010):

$$\sigma = \frac{C_{NaOH} \times V_{NaOH}}{C_{CNC} \times \alpha_{CNC}}$$

where C_{NaOH} is the concentration of NaOH, V_{NaOH} is the volume of NaOH at the equivalence point, C_{CNC} is the concentration of the CNC suspension, α_{CNC} is the amount of CNC suspension titrated. For the SO-CNCs, V_{NaOH} was defined as V_2-V_1, where V_1 (1st equivalence point) is the volume of NaOH needed to neutralize excess HCl and the surface sulfate groups and V_2 (2nd equivalence point) is the volume of NaOH needed to neutralize the carboxyl groups, respectively.

Biomineralization of SH-CNCs and SO-CNCs *in vitro*

An *in vitro* biomineralization study was performed in SBF at 37°C. SBF with nearly identical ion concentrations to those of human blood plasma was carefully prepared as described in Kokubo and Takadama (2006), henceforth denoted corrected SBF (c-SBF). For CNC mineralization, 100 mL aliquots of 1 wt% aqueous suspensions of either SH-CNCs or SO-CNCs were placed in dialysis tubing and suspended in 3 L of SBF at 37°C for up to 800 h under stirring. The SBF was exchanged every 24 h. Samples of the mineralized CNCs (10 mL aliquots) were collected at different incubation time points and dialyzed against DI water for 48 h. The aqueous suspensions of mineralized SH-CNCs and SO-CNCs were stored at 4°C prior to analysis.

Inductively Coupled Plasma Atomic Emission Spectroscopy (ICP-AES)

ICP-AES (Spectro ARCOS, Spectro Analytical Instruments, Inc.) was used to analyze the concentrations of elements such as sulfur, phosphorus, and calcium before and after mineralization of the CNCs. Five milliliter of CNC suspensions (5 mg/mL) were treated with 25 mL of nitric acid (70%, TraceMetal Grade, Fisher Scientific) for 2 h at 60°C in an ultrasonic bath (40 kHz, 130 W). One milliliter of the thus digested suspension was added to 39 mL of DI water resulting in a final CNC concentration of 0.02 mg/mL in HNO_3. Reported values are means of three measurements.

SO-CNC/PCL Nanocomposites Fabrication

The SO-CNCs were suspended in acetonitrile (HPLC Grade, Fisher Scientific) by solvent exchange. The solvent exchange process was performed by addition of acetonitrile to the aqueous SO-CNC suspension. The mixture was centrifuged at 5,000 rpm (SORVALL LEGEND X1R Centrifuge, Thermo Scientific) for 20 min and fresh acetonitrile was added to the collected sediment. This step was followed by homogenization (Power Gen 500, Sawtooth 10 x 95 mm, Fisher Scientific) for 5 min and sonication for 30 min. This process was repeated three times. PCL (Mw = 70,000–90,000, Sigma Aldrich) was dissolved in dichloromethane (Fisher Scientific). The ratio of PCL to dichloromethane was 1:10 (w/v). The solvent-exchanged SO-CNC suspension was sonicated at 40°C for 30 min under stirring (300 rpm) and the PCL solution was slowly added before solvent casting into a glass petri dish. The cast film was allowed to dry at room temperature for 48 h, then placed in a vacuum oven at 40°C for 24 h. The solvent cast films were cut into small pellets, then thoroughly rinsed with DI water and dried in a vacuum oven at 40°C for 24 h. Finally, the pellets were extruded into a 3 mm (diameter) filament with a twin-screw extruder (HAAKE MiniLab II, ThermoFisher Scientific) at 80°C. SO-CNC/PCL nanocomposites were prepared with SO-CNC contents of 1, 2, 3, 5, and 10 wt%.

Atomic Force Microscopy (AFM)

AFM samples of SH-CNCs and SO-CNCs were prepared from 0.002 wt% aqueous suspensions. After 10 min sonication, 15 μL of each CNC suspension was spin coated at 4,000 rpm for 1 min with a spin coater (Laurell model WS-400B-6NPP/LITE) onto a freshly cleaved mica disc (diameter: 0.5 in., Ted Pella) mounted with epoxy adhesive resin onto a standard microscope slide. The spin coated CNC samples were dried overnight at 60°C under vacuum. AFM samples of the PCL nanocomposites were prepared by immersion of nanocomposite filaments in liquid N_2 followed by fracture of the filament in flow direction of the melt compounding extrusion process. Fresh fracture surfaces were imaged under ambient conditions in intermittent contact (AC) mode with an Asylum Research MFP3D-Bio atomic force microscope using standard silicon probes (Olympus OMCL-AC160TS, resonant frequency: ∼300 kHz, spring constant: ∼42 N/m, nominal tip radius: <10 nm). Images were recorded with a resolution of 512 points/scan and analyzed using IGOR pro software (RRID:SCR_000325) using identical parameters for the mask tool, flattening tool, z-scale, and phase range.

Cytotoxicity of SH-CNCs and SO-CNCs

Mouse preosteoblast (MC3T3, ATCC) cells were cultured in alpha minimum essential medium (α-MEM, Life Technologies) with 10% fetal bovine serum (FBS, Life Technologies) and 1% penicillin-streptomycin (Life Technologies). Aliquots of the SH-CNC and SO-CNC stock suspensions (30 mg/mL) were diluted with DI water to yield samples with four different concentrations: 1.67, 3.33, 6.67, and 20.00 mg/mL. The samples were filtered through 0.22 µm PVDF syringe filters and exposed to ultraviolet light for sterilization. One hundred fifty microliters of each sample was added to 850 µL of α-MEM containing 10,000 MC3T3 cells for cytotoxicity testing. After 24 h, 20 µL of trypan blue assay solution (0.4%, Life Technologies) was added. Live cells (clear) and dead cells (blue) were counted with an optical microscope (Fisher Scientific) and averaged with a hemacytometer. Experiments were carried out in triplicate and referenced against DI water (150 µL).

Tensile Tests

Tensile tests of SO-CNC/PCL nanocomposite filaments were performed with an MTS Sintech 10/GL Material Testing Workstation equipped with a 100 N load cell. A cross head speed of 10 mm/min was used at ambient conditions (in air at room temperature) was used. Reported values are means of quintuplicate measurements. Measurements with yield near the grips were excluded.

Thermal Analysis: DSC

DSC measurements were performed with a TA Instruments Q2000 differential scanning calorimeter that had been calibrated with indium and sapphire standards. Nitrogen, at a flow rate of 50 mL/min, was used as the purge gas. ∼5 mg of sample was placed in a standard aluminum DSC pan (TA Instrument). The DSC scans were done using a heating/cooling/heating/cooling protocol with a heating rate of 10°C/min and a temperature range of −75 to 100°C. Experiments were done in triplicate. The glass transition temperature (T_{g}), melting temperature (T_{m}), crystallization temperature (T_c), and enthalpy of fusion, ΔH_f, were measured with the TA Instruments' Universal Analysis 2000 software. The degree of matrix crystallinity, X_c, was calculated from ΔH_f with the following equation (Runt, 1980):

$$X_c = \frac{1}{(1-\omega_f)} \times \frac{\Delta H_{f_{sample}}}{\Delta H_{f_{PCL}}} \times 100\%$$

where ω_f is the weight fraction of the filler in the composite and $\Delta H_{f_{PCL}}$ is the heat of fusion of the matrix polymer at 100% crystallinity. The percentage of crystallinity was estimated using a value of 139.5 J/g for the heat of fusion of 100% crystalline PCL (Pitt et al., 1981).

In addition, the thermal degradation temperatures of SO-CNC (film form), pure PCL, and PCL with 10 wt% SO-CNCs were determined by thermogravimetric analysis (TGA, TA Instruments TGA Q500) (**Supplementary Figure 2**). Approximately 10–15 mg of sample was placed into a platinum TGA sample pan. Thermogravimetric (TG) and derivative TG (DTG) curves between ∼30 and 500°C were recorded with a heating rate of 10°C/min using air as sample purge gas.

Contact Angle Measurements

For contact angle measurements, SO-CNC/PCL nanocomposite films (∼5 mm in width, ∼2 mm in thickness) were prepared using a twin-screw extruder (HAAKE MiniLab II, ThermoFisher Scientific). Measurements were performed with an FTA 200 Dynamic Contact Angle Analyzer equipped with a motor-driven syringe. Droplets of approximately 1 µl of each DI water and SBF were carefully deposited onto the sample surface using a 250 µl syringe (Hamilton gastight®) with a stainless steel needle. Images were recorded within 2 s and the contact angle was analyzed with Drop Shape Analysis software (FTA32 Video 2.1). Reported values are means of three measurements.

Optical Light Microscopy

Thin slices of ∼50 µm thickness were microtomed off of the transverse surface (perpendicular to the flow direction) of the PCL nanocomposites using a sliding microtome (Model 860, American Optical Company). The microtomed slices were placed on regular microscopy cover glasses and heated to 300°C for 10 min using the TGA. After that, optical microscopy images were recorded with a Canon EOS 20D digital single-lens reflex camera (8.2 megapixels) mounted onto a Zeiss Axioskop 40 A POL microscope.

RESULTS

SH-CNCs are known to carry sulfate groups on their surface, in addition to primary and secondary hydroxyl groups. To study whether the presence of carboxyl groups enhances the ability of CNCs to induce biomineralization, SH-CNCs were modified by TEMPO-mediated oxidation to give SO-CNCs. The reaction converts some of the primary hydroxyl groups on the CNC surface to carboxyl groups (**Supplementary Figure 1**). The presences of carboxyl groups was confirmed by FTIR spectroscopy (**Supplementary Figure 3**). The surface charge densities of SH-CNC and SO-CNC, after treatment with ion exchange resin (denoted as SH-CNC-I and SO-CNC-I, respectively) for removal of residual electrolyte, were determined by conductometric titration (**Figure 1**). The titration curve of SH-CNC-I (**Figure 1A**) showed an initial decrease of conductivity, corresponding to the neutralization of partially dissociated sulfate groups, followed by an increase upon further NaOH addition, due to an excess of titrant. The amount of sulfate groups per mass of SH-CNC-I is calculated from the volume of NaOH at the equivalence point (V). The sulfate group density of SH-CNC-I was calculated to be 0.271 ± 0.002 mmol/g (compared to 0.316 ± 0.007 mmol/g for SH-CNC, see **Supplementary Figure 4** and **Supplementary Table 1**).

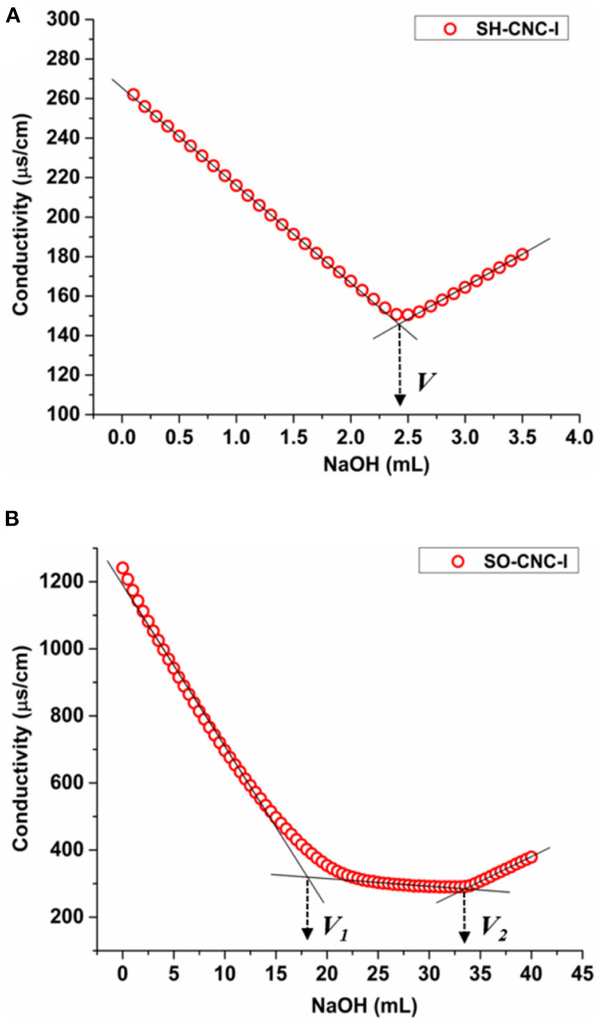

FIGURE 1 | Conductometric titration curves for **(A)** SH-CNC-I and **(B)** SO-CNC-I.

Titration curves of SO-CNC-I, on the other hand (**Figure 1B**), exhibited two equivalence points. The first equivalence point (V_1) corresponds to the neutralization of added HCl and any remaining sulfate groups. The second equivalence point (V_2) corresponds to the neutralization of the carboxyl groups. The number of carboxyl groups per mass of SO-CNC-I was estimated from the volume of the titrant between the two equivalence points. The obtained surface charge density of SO-CNC-I was 1.997 ± 0.142 mmol/g (compared to 1.840 ± 0.004 mmol/g for SO-CNC, **Supplementary Table 1**). Thus, the surface charge density of SO-CNC-I was about 7 times (6 times before ion exchange treatment) higher than that of SH-CNC-I.

The sulfur content of the CNCs before and after ion exchange treatment was measured by ICP AES. **Table 1** compares the sulfur contents of the CNC samples obtained by conductometric titration and ICP AES (see also **Supplementary Table 1**). As seen in the table, the values obtained by the two methods were in good agreement. Both, the surface oxidation and treatment with ion exchange resin, resulted in a decrease in the sulfur content of CNCs. According to the ICP AES data, surface oxidation caused a 21% reduction in the sulfur content (16% reduction after ion exchange resin treatment).

TABLE 1 | Sulfur content of CNCs before and after treatment with ion exchange resin measured by conductometric titration and ICP analysis.

	Sulfur content (mg/g)	
Sample	**Conductometric titration**	**ICP AES analysis**
SH-CNC	10.11 ± 0.22	10.83 ± 0.20
SH-CNC-I	8.67 ± 0.05	9.00 ± 0.21
SO-CNC	–	8.56 ± 0.21
SO-CNC-I	–	7.59 ± 0.08

The effect of the type of surface group, sulfate vs. carboxyl, on the *in vitro* mineralization of CNCs was evaluated by incubation of the CNCs in SBF (1x). **Figure 2** shows 3D AFM height images of CNCs before (0 h) and after incubation at 37°C for 400 h. Both CNCs appeared significantly larger after mineralization. The mean particle dimensions were determined from AFM height images. Before mineralization, SH-CNCs and SO-CNCs had a mean length of 121.5 ± 23.8 nm and a mean height of 3.86 ± 1.1 nm in accordance with the literature (Moon et al., 2011). The initial dimensions of SO-CNCs (mean length of 89.3 ± 22.7 nm and mean height of 2.23 ± 0.6 nm) were smaller, indicating an effect of the oxidation procedure on particle size. After 400 h of incubation in SBF, the size of CNCs was noticeably larger (**Figures 2B,D**) than before (**Figures 2A,C**). While the CNCs did not aggregate before incubation because of their negative surface charge (**Figures 2A,C**), mineralized CNCs exhibited some degree of aggregation (**Figures 2B,D**), possibly indicating a screening of their surface charge. Sonication was not performed during sample preparation for AFM analysis because it could affect the thickness of the mineral layer on the mineralized CNCs. For error minimization, only individual nanoparticles were used for height determination.

The extent of mineralization was quantified using height data because width and length data of CNCs have greater natural fluctuations. Moreover, as opposed to length and width measurements, AFM height measurements are not affected by tip broadening and therefore generally considered more accurate. The average height of the CNCs as a function of incubation time is shown in **Figure 3**. The initial mean height of SO-CNCs was smaller than that of SH-CNCs because of the effect of the oxidation process on particle size. For the SH-CNCs, the height was significantly increased from 0 h (3.9 ± 1.1 nm) to 10 h (4.5 ± 1.0 nm) and from 10 h to 40 h (5.1 ± 0.7 nm), but no statistical difference (Least Significant Difference (LSD) test at the 0.05 level) was observed from 20 h (5.1 ± 0.7 nm) to 800 h (5.4 ± 1.1 nm). For the SO-CNCs, the height was increased from 0 h (2.2 ± 0.6 nm) to 10 h (3.4 ± 0.7 nm) and from 20 h (3.6 ± 0.8 nm) to 30 h (4.8 ± 0.6 nm), but there was no statistically significant difference between 30 and 800 h

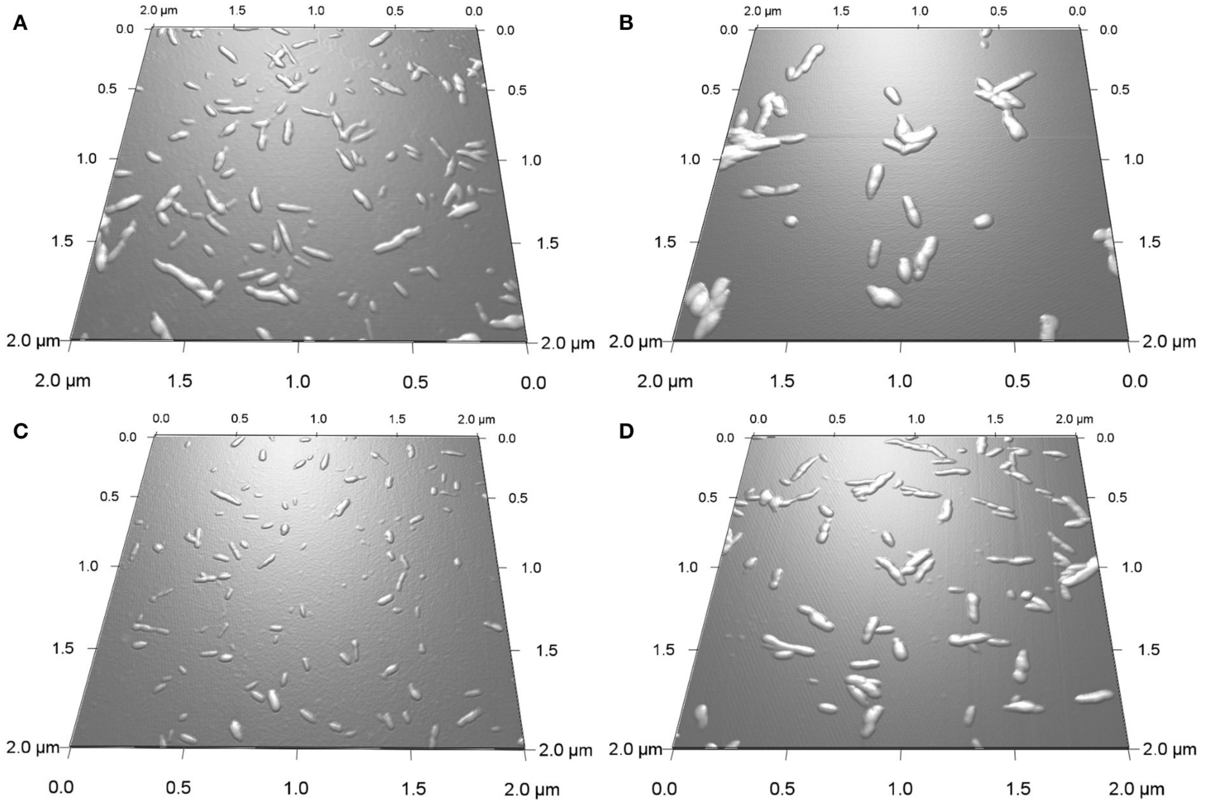

FIGURE 2 | 3D AFM height images of SH-CNCs **(A,B)** and SO-CNCs **(C,D)** before **(A,C)** and after **(B,D)** 400 h incubation in SBF at 37°C.

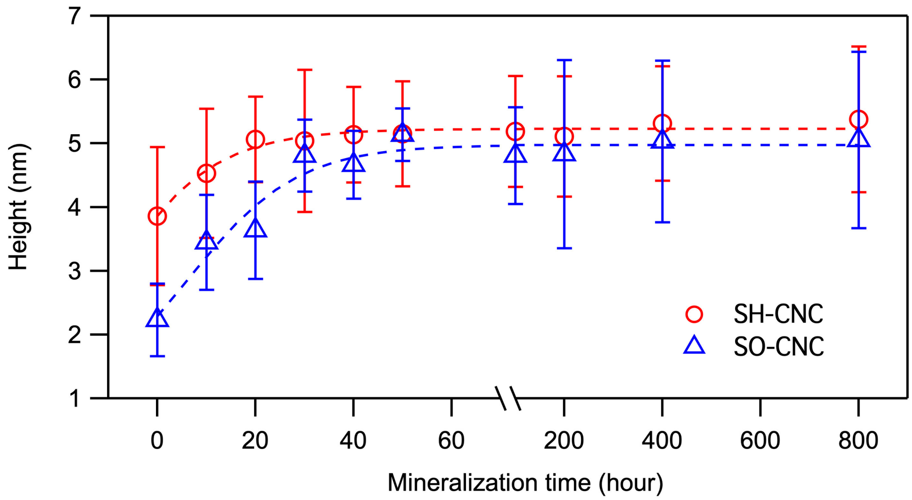

FIGURE 3 | Height changes of CNCs during the incubation in SBF at 37°C.

(5.1 ± 1.4 nm). Although a similar trend for the height change was observed for both CNCs, the total increase in height was greater for the SO-CNCs (2.3 times) than for the SH-CNCs (1.4 times). Considering the rod-like shape of CNCs, the height increase indicates that the SO-CNCs exhibited a thicker coating (~1.45 nm thickness) with certain minerals than the SH-CNCs (~0.75 nm thickness).

For the SH-CNCs, the height was significantly increased from 0 h (3.9 ± 1.1 nm) to 10 h (4.5 ± 1.0 nm) and from 10 to 40 h (5.1 ± 0.7 nm), but no statistical difference (Least Significant

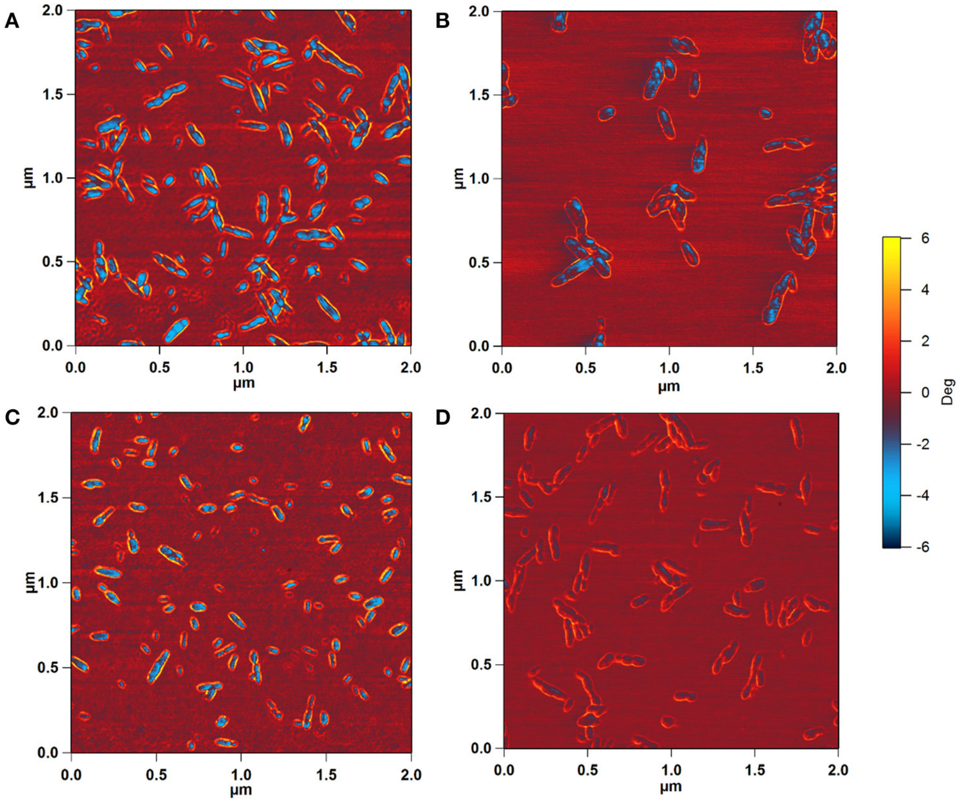

FIGURE 4 | AFM phase images of SH-CNCs **(A,B)** and SO-CNCs **(C,D)** before **(A,C)** and after **(B,D)** 400 h incubation in SBF at 37°C. Scan size: 2 μm x 2 μm.

Difference (LSD) test at the 0.05 level) was observed from 20 h (5.1 ± 0.7 nm) to 800 h (5.4 ± 1.1 nm). For the SO-CNCs, the height was increased from 0 h (2.2 ± 0.6 nm) to 10 h (3.4 ± 0.7 nm) and from 20 h (3.6 ± 0.8 nm) to 30 h (4.8 ± 0.6 nm), but there was no statistically significant difference between 30 and 800 h (5.1 ± 1.4 nm). Although a similar trend for the height change was observed for both CNCs, the total increase in height was greater for the SO-CNCs (2.3 times) than for the SH-CNCs (1.4 times).

To determine whether the observed height increase was due to aggregation of CNCs, the AFM phase images, collected together with the height images, were analyzed. AFM intermittent contact mode provides information about sample topography and surface properties, such as stiffness, viscoelasticity, or surface energy, by monitoring the phase shift (also known as phase lag) of the cantilever oscillation relative to the drive signal (Stark et al., 2001; Garcia et al., 2006, 2007) during a scan. The phase shift allows identification of regions of different tip-sample interactions through the amount of energy dissipated and thus visualization of different surface charge characteristics (Tamayo and Garcia, 1997; Cleveland et al., 1998; Czajkowsky et al., 1998). **Figure 4** shows the phase images corresponding to the height images in **Figure 2**. The phase shift of the substrate was about ±0.6°. For pristine SH-CNCs and SO-CNSs, the phase shift caused by the interactions between the CNCs and the AFM tip was 8.17° ± 1.11 (**Figure 4A**) and 7.88° ± 0.98 (**Figure 4C**), respectively, and there was no statistically significant difference (LSD test at the 0.05 level) between them. However, upon incubation in SBF, the phase shift was significantly reduced to 5.26° ± 0.81 (**Figure 4B**) in the case of SH-CNCs and 2.78° ± 0.73 in the case of SO-CNCs (**Figure 4D**). Furthermore, the decreases in phase shift for SH-CNCs and SO-CNCs of 2.91 ± 1.37° and 5.10 ± 1.22°, respectively, were statistically significantly different from one another.

The elemental composition of the surface deposit was analyzed by ICP AES. The elements that are of most interest for bone tissue engineering applications are calcium and phosphorus, making up half of the mass of the bone mineral HA. **Table 2** compares the calcium and phosphorus concentrations and Ca:P ratios measured for the two CNC samples with those obtained for a synthetic HA (≥97%, Sigma-Aldrich), having a composition of $Ca_{10}(PO_4)_6(OH)_2$ and a Ca:P ratio of 2.15 by atomic weight and 1.67 by atomic ratio. The Ca:P ratios obtained for the mineralized SH-CNCs and SO-CNCs differed substantially from the Ca:P ratio of the HA control. Specifically, the Ca:P ratios for the CNCs were significantly higher than that of the control. Attempts to detect and identify the calcium phosphate mineral on the surface of the CNCs by X-ray diffraction were unsuccessful (**Supplementary Figure 5**).

The toxicity of SH-CNCs and SO-CNCs to MC3T3 preosteoblasts was analyzed with a trypan blue viability assay (**Figure 5**). Suspensions of SH-CNCs and SO-CNCs in

TABLE 2 | ICP AES analysis of CNCs before and after mineralization.

Sample	Time (h)	Ca (mg/L)		P (mg/L)		Ca:P	
		Mean	STDEV	Mean	STDEV	Mean	STDEV
SH-CNC	0	<0.021	–	<0.015	0.001	–	–
	50	0.387	0.002	0.147	0.002	2.64	0.029
	800	0.292	0.001	0.035	0.001	8.25	0.327
SO-CNC	0	0.101	0.001	<0.015	–	–	–
	50	4.61	0.025	0.118	0.004	39.0	1.40
	800	1.99	0.017	0.060	0.005	33.4	2.82
HA	–	147.0	1.93	68.5	0.132	2.15	0.028
2% HNO_3	–	<0.021	–	<0.015	–	–	–

Samples were prepared in aqueous 2% HNO3, Data reported as mg/L, The "<" indicates concentrations less than the instrument detection limit. Time (h) indicates the incubation period at 37°C for the mineralization.

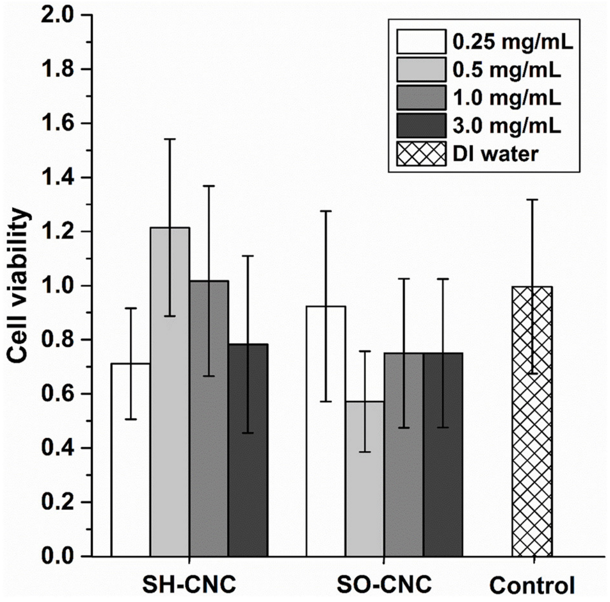

FIGURE 5 | Cytotoxicity of MC3T3 cells after 24 h exposure to SH-CNCs and SO-CNCs. Each data set mean value was normalized to the DI water control, data showed no significant difference in means (p < 0.05) compared to the control. Error bars represent one standard deviation.

DI water were added to MC3T3 cells in culture medium for final concentrations of 0.25, 0.5, 1.0, and 3.0 mg/mL. Dynamic light scattering analysis of SH-CNCs and SO-CNCs in culture medium (**Supplementary Figure 6** and **Supplementary Table 2**) indicated that SO-CNCs maintained a monomodal size distribution with a z-average ranging from 100 to 160 nm, depending on the concentration, whereas SH-CNCs exhibited a multi-modal size distribution with z-average values as large as 2 μm, indicating significant particle aggregation. There was no statistically significant difference in cell viability of MC3T3 cells exposed to SH-CNCs or SO-CNCs compared to cells exposed to pure DI water (control, **Figure 5**). Thus, both SH-CNCs and SO-CNCs were non-toxic to MC3T3 cells at concentrations of up to 3 mg/mL during 24 h of exposure.

Bone scaffolds for critical-sized defects need to have adequate mechanical properties. Here, the mechanical properties of SO-CNC/PCL nanocomposites were evaluated as a function of SO-CNC content. A general challenge in the development of polymer-based nanocomposites with naturally derived nanoparticles is achieving homogenous dispersion of the nanoparticles in the polymer matrix. Most naturally derived nanoparticles, such as polysaccharide-based nanoparticles, have hydrophilic groups (e.g., hydroxyl, carboxyl, and amino groups) whereas bioresorbable polymers are relatively hydrophobic. Inhomogeneous nanoparticle distribution can lead to undesirable properties and phase separation. Several methods have been reported for improving the dispersion of CNCs in polymer matrices. For example, CNCs were transferred from an aqueous to a non-aqueous system (e.g., organic media) prior to incorporation into the polymer matrix (Samir et al., 2004; Kvien et al., 2005; Marcovich et al., 2006; van den Berg et al., 2007) or chemically modified with hydrophobic functional groups (Grunert and Winter, 2002; Gousse et al., 2004), grafting-onto (Araki et al., 2001; Habibi and Dufresne, 2008), and grafting-from (Habibi et al., 2008) approaches to increase the compatibility.

In the present study, we aimed to prevent the aggregation of SO-CNCs in the PCL matrix with minimal use of harmful organic solvents through a simple four-step process including (a) solvent exchange of an aqueous SO-CNC suspension, (b) physical mixing, (c) solvent casting, and (d) melt compounding extrusion. First, the SO-CNCs were dispersed in CH_3CN by solvent exchange and the PCL pellets were dissolved in CH_2Cl_2 which is miscible with CH_3CN. After that, the dissolved PCL was slowly added to the SO-CNCs suspended in CH_3CN under stirring in ultrasonic bath. The SO-CNC/PCL nanocomposite filaments were prepared by solvent casting, followed by melt compounding extrusion using a twin-screw extruder.

The mechanical properties of the SO-CNC/PCL nanocomposite filaments were determined by tensile testing. **Figure 6** shows the tensile strength and Young's modulus as a function of SO-CNC content. Both, a decrease in ductility and pronounced mechanical reinforcement were observed in

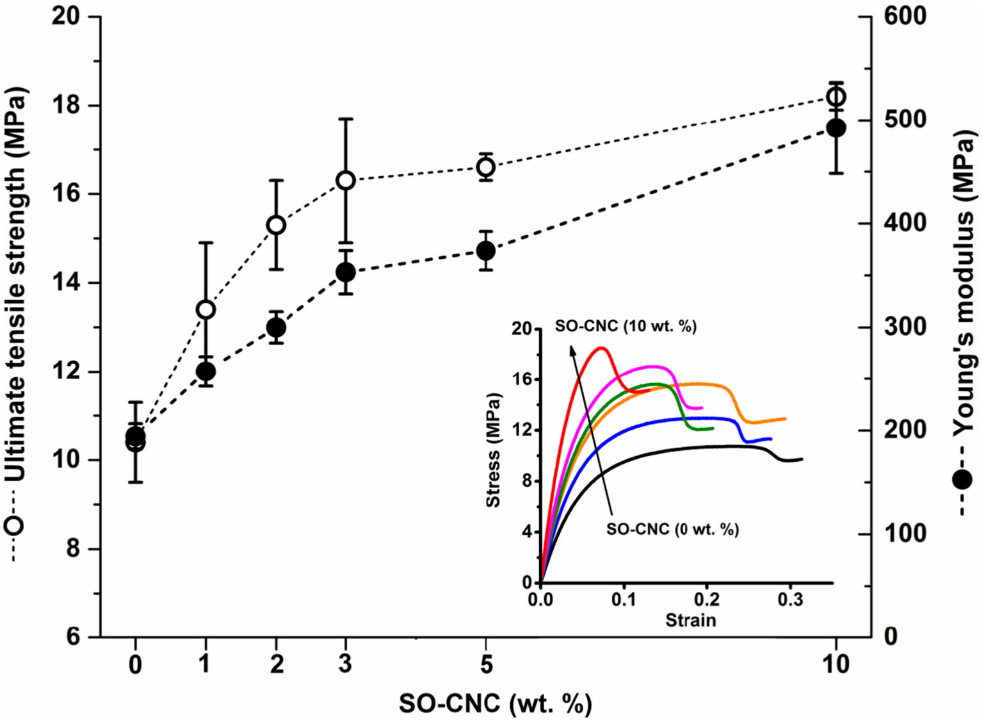

FIGURE 6 | Mechanical properties of SO-CNC/PCL nanocomposite filaments. Insert: Stress-strain curves of the nanocomposite filaments.

the stress-strain curves with increasing SO-CNC content. The maximum values of both strength (18.2 ± 0.3 MPa) and Young's modulus (492.5 ± 44.1 MPa) were obtained at 10 wt% loading of SO-CNCs. These mechanical properties are very similar to those of human cancellous bone [tibia, tension test, strength: 2.54 ± 1.18 MPa, Young's modulus: 483 MPa (Rohl et al., 1991)].

Attempts to assess the degree of dispersion of the SO-CNCs in the PCL matrix were moderately successful. **Supplementary Figure 7** shows optical microscopy images of the SO-CNC/PCL nanocomposites after heating to 300°C for 10 min. The high temperature results in thermal degradation of the SO-CNCs (**Supplementary Figure 2**), rendering them visible by discoloration. The discoloration was relatively uniform throughout the nanocomposites, although some larger dark patches indicated a certain degree of SO-CNC aggregation in the PCL matrix, which was more pronounced at higher SO-CNC contents. AFM phase images of the SO-CNC/PCL nanocomposites (**Supplementary Figure 8**) also confirmed an overall uniform distribution of SO-CNCs with regions of higher local concentration on a smaller scale and a more pronounced effect at higher SO-CNC contents.

The thermal properties of the nanocomposites were evaluated by DSC. The 1st heating cycle, from −75°C to 100°C, eliminated the thermal history during the nanocomposite fabrications. Identical DSC curves were observed for the 1st cooling and 2nd cooling cycles. The 2nd heating and cooling curves of pure PCL and PCL with 10 wt% SO-CNCs are shown in **Figure 7**. The thermal transitions are summarized in **Table 3**. The enthalpy of fusion, ΔH_f, was measured from the 2nd heating cycles (area under the melting peak) to calculate the percent crystallinity (X_c). The glass transition (T_g: ∼ −64°C) and melting (T_m: ∼56°C) temperatures were not influenced by the addition of SO-CNCs. However, the crystallization temperature (T_c) of the nanocomposites increased by about 4.5°C upon addition of 1 wt% SO-CNCs and by another ∼1°C upon increase of the

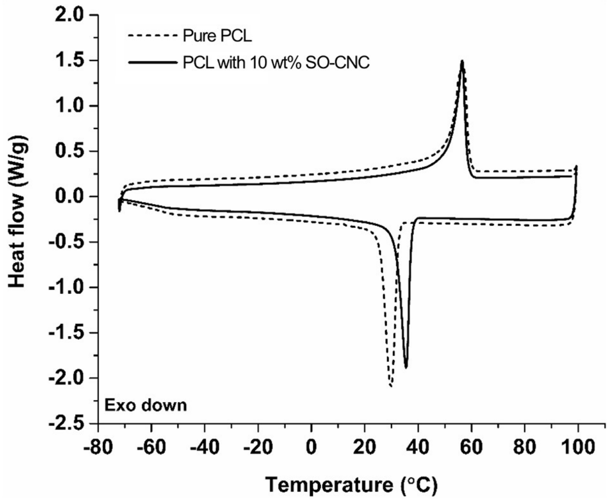

FIGURE 7 | DSC curves (2nd heating and 2nd cooling) of pure PCL and SO-CNC/PCL nanocomposite filament containing 10 wt% SO-CNC.

TABLE 3 | Summary of mechanical properties, thermal transitions, crystallinity, and contact angle measurements of the SO-CNC/PCL nanocomposites.

SO-CNC content (wt%)	Mechanical properties		Thermal transitions			Crystallinity	Contact angle	
	Ultimate strength (MPa)	Young's modulus (MPa)	T_g (°C)	T_c (°C)	T_m (°C)	X_c (%)	DI water (°)	SBF (°)
0	10.4 ± 0.9	194.3 ± 12.1	−64.6 ± 0.6	30.2 ± 0.3	56.0 ± 0.6	42.9 ± 0.7	87.0 ± 1.1	88.8 ± 0.9
1	13.4 ± 1.5	257.2 ± 14.4	−64.9 ± 0.8	34.6 ± 0.2	56.1 ± 0.1	42.5 ± 0.4	85.5 ± 0.9	88.7 ± 0.6
2	15.3 ± 1.0	299.9 ± 15.2	−64.7 ± 0.5	34.5 ± 0.1	56.2 ± 0.1	42.1 ± 0.6	–	–
3	16.3 ± 1.4	353.1 ± 20.9	−64.4 ± 0.9	35.5 ± 0.1	56.1 ± 0.1	40.5 ± 0.6	84.5 ± 1.2	85.4 ± 1.1
5	16.6 ± 0.3	373.8 ± 18.6	−64.6 ± 0.8	35.2 ± 0.3	56.4 ± 0.2	39.9 ± 0.9	83.6 ± 1.4	85.2 ± 0.7
10	18.2 ± 0.3	492.5 ± 44.1	−64.5 ± 0.4	35.7 ± 0.2	56.4 ± 0.4	39.7 ± 0.5	82.6 ± 1.9	82.6 ± 0.5

Tg, glass transition temperature; Tc, crystallization temperature; Tm, melting temperature.
Xc calculated from 1st heating cycle: 49.6 ± 0.6% (SO-CNC content: 0 wt%), 50.0 ± 1.0% (1 wt%), 50.6 ± 1.0% (2 wt%), 49.3 ± 0.6% (3 wt%), 49.0 ± 0.6% (5 wt%), and 48.9 ± 1.1% (10 wt%).

SO-CNC content to 10 wt%. The calculated ΔH_f gradually decreased from about 60 J/g (0 wt% SO-CNC) to about 50 J/g (10 wt% SO-CNC) and the crystallinity of the nanocomposites decreased from about 43% to about 40% with increasing SO-CNC content (from 0 to 10 wt%).

It is essential for implant materials to achieve an appropriate cellular response for tissue regeneration. The material surfaces will have direct contact with the biological environment and the resulting responses are critically important for successful implantation in tissue engineering applications. For bone scaffold materials, for example, the interactions between cell and material can promote preosteoblastic cell attachment, migration, proliferation, differentiation, and bioactivity (bone formation) (Wilson et al., 2005). It is commonly observed that hydrophilic surfaces provide a better environment for cell adhesion, but many bioresorbable polymers, including PCL, are relatively hydrophobic. The effect of the hydrophilic SO-CNCs on the PCL hydrophobicity was assessed by contact angle measurements. The average values obtained for DI water and SBF on SO-CNC/PCL nanocomposites are listed in **Table 3**. The contact angles of DI water and SBF decreased from 87.0 ± 1.1° and 88.8 ± 0.9° on pure PCL to 82.6 ± 1.9° and 82.6 ± 0.5° on the SO-CNC/PCL nanocomposite with 10 wt% SO-CNCs, respectively. This decrease in contact angle indicates an overall decrease in PCL hydrophobicity upon addition of the hydrophilic SO-CNCs.

DISCUSSION

The surface chemistry of SH-CNCs is dominated by sulfate half ester groups introduced during the cellulose hydrolysis with sulfuric acid. TEMPO-mediated oxidation of SH-CNCs, to produce SO-CNCs, selectively oxidizes the primary hydroxyl groups of cellulose. The obtained surface charge density of SO-CNC-I of 1.997 ± 0.142 mmol/g suggests that the reaction resulted in the conversion of approximately one third of the available surface hydroxyl groups, not carrying sulfate half-esters, to carboxyl groups. The 21% reduction in sulfur content upon surface oxidation indicates that SO-CNCs still contain about 80% of the initial sulfate groups. The high surface charge density of 1.997 ± 0.142 mmol/g signifies, however, that carboxyl groups are the primary functional group on SO-CNCs, accounting for 86–89% of the anionic surface groups.

Kokubo and Takadama (2006) reviewed correlations between apatite formation on the surface of various materials in SBF *in vitro* and their *in vivo* bioactivity. The researchers concluded that there is no correlation between apatite formation in SBF at non-natural concentration levels (e.g., 1.5x SBF) and its *in vivo* formation on a material. In contrast, results obtained using 1x SBF correlated well with *in vivo* bioactivity. This observation is crucial for the successful development of new bioactive bone scaffold materials on the basis of predictions from *in vitro* apatite formation on the material's surface. Although numerous studies using SBF with several-fold differences in concentration have reported *in vitro* HA formation with a Ca:P ratio of ∼1.67 on a bone scaffold material, it must be pointed out that the use of such fluids does not allow conclusions with regard to the ability of these materials to promote biomineralization *in vivo*.

In light of the observation of Kokubo and Takadama, the biomineralization experiments in this study were carried out with 1x SBF. Upon incubation in SBF, SO-CNCs exhibited a 64% greater height increase than SH-CNCs. The greater total height increase indicates that SO-CNCs build a thicker mineral coating (∼1.45 nm thickness) than the SH-CNCs (∼0.75 nm thickness) when exposed to calcium and phosphate ions. The thicker coating of SO-CNCs could be due to their higher surface charge density or the higher calcium affinity of the carboxyl group, compared to the sulfate group.

Prior to incubation in SBF, both SH-CNCs and SO-CNCs showed stronger interactions with the AFM tip compared to the mica substrate, as indicated by the greater phase shift. Upon incubation in SBF, the phase shift of both SH-CNCs and SO-CNCs was significantly reduced and SO-CNCs showed a statistically significantly greater decrease in phase shift relative to SH-CNCs. The mica substrate, which is mainly composed of SiO_2 (∼46%) and Al_2O_3 (∼33%), exhibited a very small phase shift, indicative of a hydrophobic surface (Boussu et al., 2005). The decrease in phase shift upon incubation in SBF signifies a decrease in the surface hydrophilicity of SH-CNCs and SO-CNCs, suggesting that the height increase was not caused by particle aggregation but by a buildup of a more hydrophobic mineral coating. The greater decrease observed with the SO-CNCs compared to the SH-CNCs could be due to a thicker mineral coating or a difference in mineral composition, resulting in a more hydrophobic composition on the SO-CNCs.

Analysis of the elemental composition of the mineral coating yielded much higher Ca:P ratios than expected for bone-like apatite or HA and an apparent absence of mineral diffraction peaks in X-ray diffractograms. The mechanism of HA formation is highly complex and still under investigation. Dey et al. (2010) demonstrated that the development of oriented apatite crystals is induced by the densification of amorphous calcium phosphate (ACP) at a templating surface, prior to which calcium phosphate prenucleation clusters (0.87 ± 0.2 nm in diameter) aggregate in equilibrium with ions in solution (SBF). In our study, the negatively charged CNCs, suspended in SBF, may have hindered the formation of prenucleation clusters by binding to and immobilizing SBF cations. The experimental setup in this study differed from those in other studies where the substrates were secured (commonly at the bottom) during the experiment. Consequently, the significantly higher Ca:P ratios in this study could be due to binding of calcium ions by the negatively charged surface groups of the CNCs suspended in the SBF.

Similar results have been reported by Zurick et al. (2013), who investigated the mineralization induction capabilities of the primary non-collagenous proteins bone sialoprotein (BSP), osteopontin (OPN), and the calcium binding subdomain of dentin sialophosphoprotein, dentin phosphoprotein (DPP). All minerals formed under the conditions used in this investigation had Ca:P ratios that were significantly larger than what has been found in native bone tissue. Proteins containing the carboxy-terminal fragment are highly negatively charged and have calcium chelating properties. The significantly larger Ca:P ratios observed (∼4–20) indicate a potential effect of the terminal carboxyl groups in mineralization process (Prasad et al., 2010; Zurick et al., 2013). One should, however, keep in mind that the mineralization of bone (or bone formation) only occurs if bone-forming cells (osteoblasts) and other biological factors are intimately involved and regulated properly in the body, which is a very complex process to mimic.

The greater bioactivity of SO-CNCs with respect to biomineralization in SBF, compared to SH-CNCs, combined with an equal lack of cytotoxicity, suggests that SO-CNCs are superior candidates for bone tissue engineering applications than SH-CNCs.

SO-CNCs proved highly effective as reinforcing nanofillers in PCL-based nanocomposites. An SO-CNC content of 10 wt% resulted in a more than 2-fold increase in Young's modulus (stiffness) and a more than 60% increase in ultimate tensile strength. The observed crystallinity decrease is in agreement with the literature. A decrease in the degree of crystallinity is commonly observed in the presence of particulates because particulates may act as nucleating agents and the filler-polymer interfaces provides heterogeneous nucleating sites (Hikosaka et al., 2006). The restricted mobility of polymer chains near the filler-polymer interface hinders the development of defect-free lamellar crystals and restricts the diffusion of polymer chains, thus affecting crystallization rate (Di Maio et al., 2004). The increase in crystallization temperature suggests that the SO-CNCs acted as nucleation sites for PCL crystallization and the decreased crystallinity in the SO-CNC/PCL nanocomposites, compared to pure PCL, could be a result of increased restriction of polymer mobility and diffusion near the SO-CNC surface, resulting in smaller PCL crystals with a greater number of lattice defects.

The decrease in hydrophobicity with increasing SO-CNC content, demonstrated by the decrease in DI water and SBF contact angle, indicates a greater biocompatibility and bioactivity of the SO-CNC/PCL nanocomposites, compared to pure PCL. The effect of SO-CNC filler content on the proliferation and differentiation of MC3T3 propsteoblasts on 3D printed scaffolds will be reported separately.

SUMMARY

This study assessed the ability of SO-CNCs, with a carboxylate-governed surface chemistry, to induce biomineralization and enhance the mechanical properties of PCL for use in bone scaffolds. SO-CNCs showed a greater ability than SH-CNCs, with a sulfate-governed surface chemistry, to induce the deposition of a calcium-phosphate layer on the CNC surface. Neither SH-CNCs nor SO-CNCs were toxic to MC3T3 preosteoblasts during a 24 h exposure at concentrations ranging from 0.25 to 3.0 mg/mL. SO-CNCs significantly increased the ultimate tensile strength and Young's modulus of PCL at filler contents of up to 10 wt%. The SO-CNCs had no effect on PCL glass transition and melting temperature but increased the crystallization temperature and hydrophilicity of the nanocomposites. The effectiveness of SO-CNCs to enhance the mechanical properties of PCL and induce the deposition of a calcium-phosphate layer on their surface makes them interesting multi-functional additives for resorbable polymer-based bone scaffolds.

DATA AVAILABILITY STATEMENT

The raw data supporting the conclusions of this article will be made available by the authors, without undue reservation.

AUTHOR CONTRIBUTIONS

JH carried out all experiments except the cell culture experiments and drafted the article. SC carried out the cell culture experiments and provided information on the experimental details for these experiments. AW supervised the cell culture experiments and provided feedback on the article draft. MR guided the research and revised the article draft to the submitted version. All authors contributed to the article and approved the submitted version.

FUNDING

This project was supported in part by the National Science Foundation under grant number DMR-0907567, the U.S. Department of Agriculture under grant numbers 2010-65504-20429, the Virginia Agricultural Experiment Station, the Hatch Multistate Program of the National Institute of Food and Agriculture of the U.S. Department of Agriculture, and the Institute for Critical Technology and Applied Science.

ACKNOWLEDGMENTS

The authors thank the Soil Testing Laboratory at Virginia Tech for performing the ICP AES analyses and Tembec, Inc., for donating the wood pulp sample.

SUPPLEMENTARY MATERIAL

The Supplementary Material for this article can be found online at: https://www.frontiersin.org/articles/10.3389/fbioe.2021.605924/full#supplementary-material

REFERENCES

Araki, J., Wada, M., and Kuga, S. (2001). Steric stabilization of a cellulose microcrystal suspension by poly(ethylene glycol) grafting. *Langmuir* 17, 21–27. doi: 10.1021/la001070m

Athanasiou, K. A., Zhu, C. F., Lanctot, D. R., Agrawal, C. M., and Wang, X. (2000). Fundamentals of biomechanics in tissue engineering of bone. *Tissue Eng.* 6, 361–381. doi: 10.1089/107632700418083

Boussu, K., Van der Bruggen, B., Volodin, A., Snauwaert, J., Van Haesendonck, C., and Vandecasteele, C. (2005). Roughness and hydrophobicity studies of nanofiltration membranes using different modes of AFM. *J. Colloid Interface Sci.* 286, 632–638. doi: 10.1016/j.jcis.2005.01.095

Chen, G. J., Dufresne, A., Huang, J., and Chang, P. R. (2009). A novel thermoformable bionanocomposite based on cellulose nanocrystal-graft-poly(epsilon-caprolactone). *Macromol. Mater. Eng.* 294, 59–67. doi: 10.1002/mame.200800261

Cleveland, J. P., Anczykowski, B., Schmid, A. E., and Elings, V. B. (1998). Energy dissipation in tapping-mode atomic force microscopy. *Appl. Phys. Lett.* 72, 2613–2615. doi: 10.1063/1.121434

Colfen, H. (2010). Biomineralization a crystal-clear view. *Nat. Mater.* 9, 960–961. doi: 10.1038/nmat2911

Czajkowsky, D. M., Allen, M. J., Elings, V., and Shao, Z. F. (1998). Direct visualization of surface charge in aqueous solution. *Ultramicroscopy* 74, 1–5. doi: 10.1016/S0304-3991(98)00024-2

Dey, A., Bomans, P. H. H., Muller, F. A., Will, J., Frederik, P. M., de With, G., et al. (2010). The role of prenucleation clusters in surface-induced calcium phosphate crystallization. *Nat. Mater.* 9, 1010–1014. doi: 10.1038/nmat2900

Di Maio, E., Iannace, S., Sorrentino, L., and Nicolais, L. (2004). Isothermal crystallization in PCL/clay nanocomposites investigated with thermal and rheometric methods. *Polymer* 45, 8893–8900. doi: 10.1016/j.polymer.2004.10.037

Domingues, R. M. A., Gomes, M. E., and Reis, R. L. (2014). The potential of cellulose nanocrystals in tissue engineering strategies. *Biomacromolecules* 15, 2327–2346. doi: 10.1021/bm500524s

Dufresne, A. (2008). Polysaccharide nano crystal reinforced nanocomposites. *Can. J. Chem. Rev. Can. Chim.* 86, 484–494. doi: 10.1139/v07-152

Fleming, K., Gray, D., Prasannan, S., and Matthews, S. (2000). Cellulose crystallites: a new and robust liquid crystalline medium for the measurement of residual dipolar couplings. *J. Am. Chem. Soc.* 122, 5224–5225. doi: 10.1021/ja000764e

Garcia, R., Gomez, C. J., Martinez, N. F., Patil, S., Dietz, C., and Magerle, R. (2006). Identification of nanoscale dissipation processes by dynamic atomic force microscopy. *Phys. Rev. Lett.* 97:016103. doi: 10.1103/PhysRevLett.97.016103

Garcia, R., Magerle, R., and Perez, R. (2007). Nanoscale compositional mapping with gentle forces. *Nat. Mater.* 6, 405–411. doi: 10.1038/nmat1925

Gousse, C., Chanzy, H., Cerrada, M. L., and Fleury, E. (2004). Surface silylation of cellulose microfibrils: preparation and rheological properties. *Polymer* 45, 1569–1575. doi: 10.1016/j.polymer.2003.12.028

Grunert, M., and Winter, W. T. (2002). Nanocomposites of cellulose acetate butyrate reinforced with cellulose nanocrystals. *J. Polym. Environ.* 10, 27–30. doi: 10.1023/A:1021065905986

Habibi, Y., Chanzy, H., and Vignon, M. R. (2006). TEMPO-mediated surface oxidation of cellulose whiskers. *Cellulose* 13, 679–687. doi: 10.1007/s10570-006-9075-y

Habibi, Y., and Dufresne, A. (2008). Highly filled bionanocomposites from functionalized polysaccharide nanocrystals. *Biomacromolecules* 9, 1974–1980. doi: 10.1021/bm8001717

Habibi, Y., Goffin, A. L., Schiltz, N., Duquesne, E., Dubois, P., and Dufresne, A. (2008). Bionanocomposites based on poly(epsilon-caprolactone)-grafted cellulose nanocrystals by ring-opening polymerization. *J. Mater. Chem.* 18, 5002–5010. doi: 10.1039/b809212e

Hikosaka, M. Y., Pulcinelli, S. H., Santilli, C. V., Dahmouche, K., and Craievich, A. F. (2006). Montmorillonite (MMT) effect on the structure of poly(oxyethylene) (PEO)-MMT nanocomposites and silica-PEO-MMT hybrid materials. *J. Non Cryst. Solids* 352, 3705–3710. doi: 10.1016/j.jnoncrysol.2006.02.124

Jiang, F., Esker, A. R., and Roman, M. (2010). Acid-catalyzed and solvolytic desulfation of H_2SO_4-hydrolyzed cellulose nanocrystals. *Langmuir* 26, 17919–17925. doi: 10.1021/la1028405

Jing, X., Jin, E., Mi, H.-Y., Li, W.-J., Peng, X.-F., and Turng, L.-S. (2015). Hierarchically decorated electrospun poly(epsilon-caprolactone)/nanohydroxyapatite composite nanofibers for bone tissue engineering. *J. Mater. Sci.* 50, 4174–4186. doi: 10.1007/s10853-015-8933-0

Kokubo, T., and Takadama, H. (2006). How useful is SBF in predicting *in vivo* bone bioactivity? *Biomaterials* 27, 2907–2915. doi: 10.1016/j.biomaterials.2006.01.017

Kovacs, T., Naish, V., O'Connor, B., Blaise, C., Gagné, F., Hall, L., et al. (2010). An Ecotoxicological characterization of nanocrystalline cellulose (NCC). *Nanotoxicology* 4, 255–270. doi: 10.3109/17435391003628713

Kvien, I., Tanem, B. S., and Oksman, K. (2005). Characterization of cellulose whiskers and their nanocomposites by atomic force and electron microscopy. *Biomacromolecules* 6, 3160–3165. doi: 10.1021/bm050479t

Lin, N., Huang, J., and Dufresne, A. (2012). Preparation, properties and applications of polysaccharide nanocrystals in advanced functional nanomaterials: a review. *Nanoscale* 4, 3274–3294. doi: 10.1039/c2nr30260h

Liu, H., Slamovich, E. B., and Webster, T. J. (2006). Increased osteoblast functions among nanophase titania/poly(lactide-co-glycolide) composites of the highest nanometer surface roughness. *J. Biomed. Mater. Res. Part A* 78A, 798–807. doi: 10.1002/jbm.a.30734

Marcovich, N. E., Auad, M. L., Bellesi, N. E., Nutt, S. R., and Aranguren, M. I. (2006). Cellulose micro/nanocrystals reinforced polyurethane. *J. Mater. Res.* 21, 870–881. doi: 10.1557/jmr.2006.0105

Moon, R. J., Martini, A., Nairn, J., Simonsen, J., and Youngblood, J. (2011). Cellulose nanomaterials review: structure, properties and nanocomposites. *Chem. Soc. Rev.* 40, 3941–3994. doi: 10.1039/c0cs00108b

Pan, L. L., Pei, X. B., He, R., Wan, Q. B., and Wang, J. (2012). Multiwall carbon nanotubes/polycaprolactone composites for bone tissue engineering application. *Colloids Surf. B. Biointerfaces* 93, 226–234. doi: 10.1016/j.colsurfb.2012.01.011

Perez, M. A. A., Guarino, V., Cirillo, V., and Ambrosio, L. (2012). *In vitro* mineralization and bone osteogenesis in poly(e-caprolactone)/gelatin nanofibers. *J. Biomed. Mater. Res. Part A* 100A, 3008–3019. doi: 10.1002/jbm.a.34233

Pitt, C. G., Chasalow, F. I., Hibionada, Y. M., Klimas, D. M., and Schindler, A. (1981). Aliphatic polyesters .1. The degradation of poly(epsilon-caprolactone) *in vivo*. *J. Appl. Polym. Sci.* 26, 3779–3787. doi: 10.1002/app.1981.070261124

Porter, J. R., Henson, A., and Popat, K. C. (2009). Biodegradable poly(epsilon-caprolactone) nanowires for bone tissue engineering applications. *Biomaterials* 30, 780–788. doi: 10.1016/j.biomaterials.2008.10.022

Prasad, M., Butler, W. T., and Qin, C. L. (2010). Dentin sialophosphoprotein in biomineralization. *Connect. Tissue Res.* 51, 404–417. doi: 10.3109/03008200903329789

Rohl, L., Larsen, E., Linde, F., Odgaard, A., and Jorgensen, J. (1991). Tensile and compressive properties of cancellous bone. *J. Biomech.* 24, 1143–1149. doi: 10.1016/0021-9290(91)90006-9

Ruckh, T. T., Kumar, K., Kipper, M. J., and Popat, K. C. (2010). Osteogenic differentiation of bone marrow stromal cells on poly(epsilon-caprolactone) nanofiber scaffolds. *Acta Biomater.* 6, 2949–2959. doi: 10.1016/j.actbio.2010.02.006

Runt, J. (1980). Polymers - crystal structure and morphology 9. Thermal analysis of polymers. *Methods Exp. Phys.* 16, 287–337. doi: 10.1016/S0076-695X(08)60760-7

Samir, M. A. S. A., Alloin, F., Sanchez, J. Y., El Kissi, N., and Dufresne, A. (2004). Preparation of cellulose whiskers reinforced nanocomposites from an organic medium suspension. *Macromolecules* 37, 1386–1393. doi: 10.1021/ma030532a

Sato, K., Kogure, T., Kumagai, Y., and Tanaka, J. (2001). Crystal orientation of hydroxyapatite induced by ordered carboxyl groups. *J. Colloid Interface Sci.* 240, 133–138. doi: 10.1006/jcis.2001.7617

Sikavitsas, V. I., Temenoff, J. S., and Mikos, A. G. (2001). Biomaterials and bone mechanotransduction. *Biomaterials* 22, 2581–2593. doi: 10.1016/S0142-9612(01)00002-3

Stark, M., Moller, C., Muller, D. J., and Guckenberger, R. (2001). From images to interactions: high-resolution phase imaging in tapping-mode atomic force microscopy. *Biophys. J.* 80, 3009–3018. doi: 10.1016/S0006-3495(01)76266-2

Sultana, N. (2013). *Biodegradable Polymer-Based Scaffolds for Bone Tissue Engineering*. New York, NY: Springer. doi: 10.1007/978-3-642-34802-0

Tamayo, J., and Garcia, R. (1997). Effects of elastic and inelastic interactions on phase contrast images in tapping-mode scanning force microscopy. *Appl. Phys. Lett.* 71, 2394–2396. doi: 10.1063/1.120039

Tanahashi, M., and Matsuda, T. (1997). Surface functional group dependence on apatite formation on self-assembled monolayers in a simulated body fluid. *J. Biomed. Mater. Res.* 34, 305–315. doi: 10.1002/(SICI)1097-4636(19970305)34:3<305::AID-JBM5>3.0.CO;2-O

van den Berg, O., Capadona, J. R., and Weder, C. (2007). Preparation of homogeneous dispersions of tunicate cellulose whiskers in organic solvents. *Biomacromolecules* 8, 1353–1357. doi: 10.1021/bm061104q

Wei, J., Heo, S. J., Li, C., Kim, D. H., Kim, S. E., Hyun, Y. T., et al. (2009). Preparation and characterization of bioactive calcium silicate and poly(epsilon-caprolactone) nanocomposite for bone tissue regeneration. *J. Biomed. Materials Res. Part A* 90A, 702–712. doi: 10.1002/jbm.a.32139

Weiner, S., and Dove, P. M. (2003). An overview of biomineralization processes and the problem of the vital effect. *Biomineralization* 54, 1–29. doi: 10.1515/9781501509346-006

Wilson, C. J., Clegg, R. E., Leavesley, D. I., and Pearcy, M. J. (2005). Mediation of biomaterial-cell interactions by adsorbed proteins: a review. *Tissue Eng.* 11, 1–18. doi: 10.1089/ten.2005.11.1

Wutticharoenmongkol, P., Sanchavanakit, N., Pavasant, P., and Supaphol, P. (2006). Preparation and characterization of novel bone scaffolds based on electrospun polycaprolactone fibers filled with nanoparticles. *Macromol. Biosci.* 6, 70–77. doi: 10.1002/mabi.200500150

Zurick, K. M., Qin, C. L., and Bernards, M. T. (2013). Mineralization induction effects of osteopontin, bone sialoprotein, and dentin phosphoprotein on a biomimetic collagen substrate. *J. Biomed. Mater. Res. Part A* 101, 1571–1581. doi: 10.1002/jbm.a.34462

Conflict of Interest: The authors declare that the research was conducted in the absence of any commercial or financial relationships that could be construed as a potential conflict of interest.

frontiers
in Bioengineering and Biotechnology

ORIGINAL RESEARCH
published: 17 March 2021
doi: 10.3389/fbioe.2021.605819

Controlling Cancer Cell Behavior by Improving the Stiffness of Gastric Tissue-Decellularized ECM Bioink With Cellulose Nanoparticles

Jisoo Kim[1], Jinah Jang[1,2,3,4] and Dong-Woo Cho[1,2,4]**

[1] School of Interdisciplinary Bioscience and Bioengineering, Pohang University of Science and Technology, Pohang, South Korea, [2] Department of Mechanical Engineering, Pohang University of Science and Technology, Pohang, South Korea, [3] Department of Convergence IT Engineering, Pohang University of Science and Technology, Pohang, South Korea, [4] Institute of Convergence Science, Yonsei University, Seoul, South Korea

A physiologically relevant tumor microenvironment is favorable for the progression and growth of gastric cancer cells. To simulate the tumor-specific conditions of *in vivo* environments, several biomaterials engineering studies have investigated three-dimensional (3D) cultures. However, the implementation of such cultures remains limited because of challenges in outlining the biochemical and biophysical characteristics of the gastric cancer microenvironment. In this study, we developed a 3D cell printing-based gastric cancer model, using a combination of gastric tissue-specific bioinks and cellulose nanoparticles (CN) to provide adequate stiffness to gastric cancer cells. To create a 3D gastric tissue-specific microenvironment, we developed a decellularization process for a gastric tissue-derived decellularized extracellular matrix (g-dECM) bioink, and investigated the effect of the g-dECM bioink on promoting the aggressiveness of gastric cancer cells using histological and genetic validation methods. We found that incorporating CN in the matrix improves its mechanical properties, which supports the progression of gastric cancer. These mechanical properties are distinguishing characteristics that can facilitate the development of an *in vitro* gastric cancer model. Further, the CN-supplemented g-dECM bioink was used to print a variety of free-standing 3D shapes, including gastric rugae. These results indicate that the proposed model can be used to develop a physiologically relevant gastric cancer system that can be used in future preclinical trials.

Keywords: 3D cell-printing, cellulose nanoparticles, tissue engineering, gastric-derived extracelluar matrix bioink, 3D gastric cancer model

Edited by:
Guang Yang,
Huazhong University of Science and Technology, China

Reviewed by:
Fatemeh Kabirian,
KU Leuven, Belgium
Giovanni Vozzi,
University of Pisa, Italy

****Correspondence:***
Jinah Jang
jinahjang@postech.ac.kr
Dong-Woo Cho
dwcho@postech.ac.kr

Specialty section:
This article was submitted to Biomaterials, a section of the journal Frontiers in Bioengineering and Biotechnology

Received: *13 September 2020*
Accepted: *10 February 2021*
Published: *17 March 2021*

Citation:
Kim J, Jang J and Cho D-W (2021) Controlling Cancer Cell Behavior by Improving the Stiffness of Gastric Tissue-Decellularized ECM Bioink With Cellulose Nanoparticles. Front. Bioeng. Biotechnol. 9:605819. doi: 10.3389/fbioe.2021.605819

INTRODUCTION

Gastric cancer is the fourth most common cancer, and the second most common cause of cancer-related death worldwide (Spolverato et al., 2015). In Western countries, more than 80% of patients that are diagnosed with advanced gastric cancer have poor prognosis. As a result, the 5-year survival rate for this disease is under 30% (Roukos, 2000). To date, surgical therapy is the only approach that completely eliminates local tumors; however, the opportunity to remove a patient's tumor is often lost, as diagnosis occurs too late (Spolverato et al., 2015). Patients with advanced stage gastric cancer receive chemotherapy as well as adjuvant or neoadjuvant therapy. Although this approach achieves improved therapeutic effects, survival rates remain unsatisfactory because of the tumors' high drug resistance (Yuan et al., 2017).

As the progression and growth of gastric cancer is influenced by the tumor microenvironment (da Cunha et al., 2016; Jang et al., 2018), establishing a physiologically relevant microenvironment is increasingly important in *in vitro* study. In particular, the extracellular matrix (ECM) surrounding cancerous growths regulates cellular functions such as migration and proliferation, through both cell–cell and cell–ECM interactions, which further affects cancer progression and aggressiveness (Crotti et al., 2017). Moreover, a decellularized tissue ECM (dECM) provides a tissue-specific microenvironment for the cells, and directs cellular behavior in cancerous growths (Hoshiba, 2019; Ferreira et al., 2020). Although several naturally-derived biomaterials such as collagen and Matrigel have been used for mimicking the cancer system (Jang et al., 2017), these purified materials find it difficult to recreate the substrata of their intrinsic environment (Tian et al., 2018). In this respect, development of biomaterials can provide cancer-specific microenvironmental components and compositions, which are essential in regulating *in vivo*-like cellular behaviors.

Recently, several studies have demonstrated that decellularized extracellular matrixes promote cancer cell behavior (Rijal and Li, 2017; Jin et al., 2019); a lung-derived decellularized ECM enabled the demonstration of cancer cell proliferation, with its morphological differences inducing the aggregation of cancer cells (Tian et al., 2018). Furthermore, through its control of the integrin-mediated pathway, ECM stiffness has a high potential to regulate the activation of cancer cell signaling (Seewaldt, 2014); with an increase in matrix stiffness, the promotion of integrin β1 clustering and the activation of β-catenin were observed, leading to an escalation of invasion and metastasis behaviors. Diverse attempts have been made to achieve sufficient mechanical strength for bioengineered matrixes, including increasing hydrogel concentration, or reinforcing the material by adding cellulose nanoparticles (CN), which are the most widespread natural material that have biocompatible characteristics (Jang et al., 2018; Athukoralalage et al., 2019). However, these approaches are yet to be studied in detail for the development of biochemically and biophysically related materials. Tissue-specific biomaterials and the regulation of matrix stiffness are crucial, as they can enable a more comprehensive assessment of gastric cancer cell responses by simulating the real microenvironment.

In this study, we introduce a mechanically reinforced bioink, consisting of gastric dECM (g-dECM) and CN, that models a biochemical microenvironment characteristic of gastric cancer. Moreover, CN enables the modulation of matrix stiffness, thereby achieving improved biophysical features. In addition, using a three-dimensional (3D) cell printing system, we fabricated 3D structures, including a mimic of a gastric ruga, using cell-laden bioink. Finally, we observed enhanced cancer-related characteristics such as cell aggregates, cellular interactions, and drug resistance in the developed bioink, compared with Matrigel and collagen.

MATERIALS AND METHODS

Decellularization of Gastric Tissue

Fresh porcine gastric tissue was obtained from a butcher shop (Pignara). Before starting the decellularization process, the mucosa layer was removed from the porcine gastric gland, cut into approximately 0.5-mm-thick slices, and washed with distilled water for 1 h to remove any remaining blood. The sliced tissues were then rinsed in a 25 mM 1 wt% sodium dodecyl sulfate (Thermo Fisher Scientific) solution for 24 h, and 25 mM 1% Triton X-100 solution (Sigma-Aldrich) for another 24 h, to remove residual cells. The tissues were subsequently treated in PBS for 24 h to wash the chemical detergents, and sterilized in 0.1 w/v% peracetic acid solution for 1 h. Following this, they were washed with PBS and distilled water for 30 min. Thereafter, decellularized gastric tissues were deep frozen at −80°C and lyophilized for 48 h. A g-dECM pre-gel solution was prepared by digesting 200 mg of the ground g-dECM powder in a solution of 0.5 M acetic acid (DUKSAN) supplemented with 20 mg of pepsin (Sigma-Aldrich), and stirring vigorously for 72 h. The biochemical characteristics of the g-dECM were evaluated using the remaining DNA, collagen, and glycosaminoglycan (GAGs), as described previously (Pati et al., 2014).

Before using the g-dECM bioink in experiments, the pH was adjusted to 7.4 by adding a 10 M NaOH solution, for thermal gelation. The g-dECM bioink and NaOH solution was preserved in ice during this pH adjustment process, to prevent gelation before use.

Preparation of Cellulose Nanoparticles

The aqueous suspensions of CN were prepared using a modified protocol from the literature (Kumar et al., 2017). In brief, acid hydrolysis was performed by stirring microcrystalline cellulose (MCC, Sigma-Aldrich) with a 64 wt% H_2SO_4 solution at 45°C for 60 min. This reaction was quenched with the addition of cold distilled water. The chilled solution was centrifuged several times, and dialyzed in distilled water, using snake skin (Thermo Fisher Scientific), to remove the acidic solution. The prepared aqueous suspensions of CN were stored at 4°C for further use.

Transmission Electron Microscopy

The morphology of the CN was examined by transmission electron microscopy (TEM, JEM-1011, Jeol). The aqueous suspensions of CN were diluted to 0.1 wt% and dropped onto the surface of a thin carbon film-coated copper grid. The sample was dried overnight, following which, TEM analysis was performed at an accelerating voltage of 100–120 kV.

Preparation of CN-Supplemented g-dECM Bioink

To prepare the CN-supplemented g-dECM bioink (CN-g-dECM bioink), CN solution was added to the 2% g-dECM bioink in a 1:40 ratio. The final concentration of the CN-supplemented bioink was varied in the range 0.01–0.5 wt% by adjusting the dilution of the aqueous CN solution prior to combination with g-dECM. This combination was mixed by applying over 70 cycles of gentle pipetting, to ensure the distribution of CN in g-dECM was uniform. In addition, to characterize the effect of CN on cellular behavior, we also created a g-dECM bioink control without CN (0% CN-g-dECM) for use in experiments.

Rheological Characterization

The rheological properties of the g-dECM bioink were characterized using a rheometer (DHR-2, TA Instruments) with a 20 mm-diameter plate. To determine its viscosity, a steady shear sweep analysis of the pre-gel bioink was performed at 15°C. Dynamic frequency sweep examinations were performed to analyze the material's frequency-dependent storage (G) and loss (G'') moduli at a 2% strain in the range 0.1–100 rad s^{-1} after incubation for 30 min at 37°C.

Rheological assessment of the CN-g-dECM bioink was performed similarly; dynamic frequency sweeps were conducted to measure the material's frequency-dependent storage (G) and loss (G'') moduli at a 2% strain in the range 0.1–100 rad s^{-1} after incubation for 30 min at 37°C, and treatment with 100×10^{-3} M calcium chloride ($CaCl_2$) solution.

2D/3D Cell Culture

Gastric cancer cell lines (AGS, SNU-1, and KATO3, Korean Cell Line Bank, South Korea) were cultured in RPMI 1640 (Gibco) supplemented with 10% FBS (Gibco) and 1% penicillin/streptomycin (Gibco). For the 3D cell culture, each cell line was encapsulated in g-dECM bioink, CN-g-dECM bioink, collagen, and Matrigel (Corning). The cell-printed g-dECM bioink, collagen, and Matrigel were fabricated and gelated by incubating at 37°C for 30 min. The cell-printed CN-g-dECM was crosslinked via treatment with 100×10^{-3} M $CaCl_2$ solution and then incubated with the printed structure at 37°C for 30 min. Every cell-laden hydrogel was refreshed with a cell culture medium every other day and harvested for further analysis.

Cell Viability Assay

Cell viability was evaluated by staining with Calcein AM and ethidium homodimer-1 solution (LIVE/DEAD Viability/cytotoxicity Kit, Thermo Fisher Scientific) following the instructions provided by the manufacturer.

Quantitative Polymerase Chain Reaction (qPCR)

The total RNA from collected hydrogels was isolated using the GeneJET RNA Purification Kit (Thermo Fisher Scientific) following the manufacturer's instructions. Complementary DNA (cDNA) was synthesized using the Maxima First Strand cDNA Synthesis Kit (Thermo Fisher Scientific) according to the manufacturer's instructions. Gene expressions were then analyzed with SYBR Green PCR Master Mix and StepOnePlus real-time PCR system (Applied Biosystems). The fold changes of the target genes were calculated using the $2^{-\Delta\Delta Ct}$ method by normalizing them with the housekeeping gene (GAPDH) expression. Coding sequences for GAPDH, matrix metalloproteinase-2 (MMP2), catenin beta-1 (β-catenin), and integrin beta-1 (integrin β1) were designed using the National Center for Biotechnology Information reference sequences (**Table 1**) and Primer Express software v3.0.1 (Thermo Fisher Scientific) for preparing primers.

Histological Analysis

To perform hematoxylin and eosin (H&E) staining, all cell-laden hydrogels were incubated in 10% buffered formalin solution for 30 min, washed three times with PBS, and fixed with paraffin. The hydrogels were subsequently sectioned to 30 μm slices using a Reichert-Jung 2035 microtome and placed on glass slides. The sections were immersed in xylene I and xylene II solution for 5 min each to remove the paraffin, then immersed in 100, 95, 80, and 75% ethanol solution, for 3 min each, and rinsed with distilled water for 5 min, for hydration. Then, sections were placed in hematoxylin solution for 10 min, washed with running tap water for 2 min, and placed in 1% acid alcohol solution for 5–30 s. To complete staining, the sections were immersed in eosin solution for 2 min, washed with running tap water for 1 min, and placed in ethanol solutions (70, 95, and 100%) for 2 min each, for dehydration. Finally, sections were immersed in xylene I and xylene II solution for 5 min each, and the glass slides were sealed with a coverslip, using Permount Mounting medium (Thermo Fisher Scientific). The H&E-stained samples were visualized with a microscope. The sizes of the cell aggregates in H&E images were measured using the analysis tools in ImageJ software version 1.47 (National Institute of Health, United States). The size of cell aggregates in an experimental group was subsequently calculated as the average size of the measurement from three different samples.

Immunostaining

To perform immunofluorescence staining experiments, all cell-laden hydrogels were fixed with 10% buffered formalin solution for 30 min, washed three times with PBS, and permeabilized with 0.1% Triton X-100 in PBS for 15 min. Next, hydrogels were stained with Alexa Fluor^{TM} 594 phalloidin and 4,6-diamidino-2 phenylindole (DAPI) (Thermo Fisher Scientific) and examined with a laser confocal microscope (Leica TCS SP5 II).

TABLE 1 | Primer sequences for qRT-PCR.

Target gene	Primer
GAPDH	CTCCTGCACCACCAACTGCT
	GGGCCATCCACAGTCTTCTG
MMP2	CGTCTGTCCCAGGATGACATC
	ATGTCAGGAGAGGCCCCATA
β-catenin	GATACCCAGCGCCGTACGT
	GACCCCCTCCACAAATTGC
Integrin β1	CAACACCAGCTAAGCTCAGGAA
	CTAAATGGGCTGGTGCAGTTC

Drug Resistance Testing

Gastric cancer cell-laden hydrogels were cultured in fresh media for 2 weeks. The media were supplemented with 5-Fluorouracil (5-FU, Sigma-Aldrich) after 3 days of culturing. Cell viability was determined using WST-8 [2-(2-methoxy-4-nitrophenyl)-3-(4-nitrophenyl)-5-(2,4-disulfophenyl)-2H-tetrazolium, monosodium salt] cell proliferation assays from an assay kit (Cell Counting Kit-8, Dojindo Molecular Technologies). The treatment responses for each culture condition were normalized to that of non-treated cultures. In addition, the IC_{50} value was calculated using GraphPad Prism 7 software.

3D Cell Printing Using the Gastric Cancer Cell-Laden g-dECM Bioink

To print the *in vitro* gastric cancer structures, we used a previously developed extrusion-based 3D cell-printing system named the Integrated Composite tissue/organ Building System (ICBS) (**Supplementary Figure S1**; Kim et al., 2017). The bioinks were prepared by encapsulating gastric cancer cell lines (cell concentration: 5×10^6 cells mL^{-1}) with 2% g-dECM pre-gel solution into each hydrogel. A grid pattern, rectangular shape, and gastric ruga shape were manufactured using the in-house developed 3D cell printing system with the 2% g-dECM bioink. The printing was performed at 15°C using a 300 μm nozzle, and the speed of the pushing motion was regulated in the range 20–70 kPa using the Nano Master SMP-III (Musashi Engineering, Ltd.). All printed structures were incubated at 37°C for 30 min and refreshed with a cell culture medium every other day.

Statistical Analysis

In this paper, statistical data is expressed as mean ± standard error. The Student's *t-test* was conducted to compare two different experimental groups, whereas one-way analysis of variance was performed to compare more than two different experimental groups. These procedures were followed by *post hoc* analysis using Tukey's multiple comparisons test. Values were considered significant at $^{*}p < 0.05$, $^{**}p < 0.01$.

RESULTS

Preparation and Characterization of the Gastric Decellularized Extracellular Matrix-Derived Bioink

We successfully developed processes for the preparation of g-dECM from native gastric tissue (**Figures 1A,B**). Our method for developing g-dECM removes cellular material from tissue while minimizing ECM loss and damage. This was validated through a DNA quantification assay, which determined that <37 ng/mg of dsDNA remained in the g-dECM, 2.7 ± 0.3% of the quantity in native tissue, whereas the collagen and GAG concentrations in the g-dECM were 173 ± 3% and 80 ± 3% of the contribution to the content of native tissue (**Figure 1B**). For effective decellularization, the quantity of cellular components should be less than 3% of the native tissue, and less than 50 ng/mg in the dECM (Pati et al., 2014). These results thus indicate that we effectively decellularized gastric tissue while preserving ECM components.

For cell culture, the pH of the g-dECM bioink is adjusted using NaOH (**Figure 1C**). When incubated at 37°C for 30 min, the pH-adjusted g-dECM bioink showed a hit-induced sol-to-gel transition in response to temperature changes. Before performing 3D cell culture, we measured the shear viscosity and storage/loss modulus of pH-adjusted g-dECM bioink to ensure its suitability for extrusion-based printing, and verify the shape retaining ability of printed structures. Both 1 and 2% g-dECM bioink showed a shear thinning behavior, wherein the viscosity of the bioink decreased as the shear rate increased (**Figure 1Di**). Such shear thinning behavior is vital for 3D cell-printing techniques, because it enables the dispersal of the bioink during printing. Further, after incubating at 37°C for 30 min, the storage modulus was higher than the loss modulus for both bioinks, indicating that they can retain their shape (**Figure 1Dii**), a critical factor for the fabrication of 3D cell-printed constructs (Pati et al., 2014). However, the 2% g-dECM demonstrated higher mechanical stability metrics than the 1% g-dECM bioink, suggesting that it is more suited to 3D cell culture.

To evaluate the toxicity of the developed g-dECM bioink—a fundamental aspect of developing biomaterials (Stoddart, 2011a,b)—we examined the cell viability of the g-dECM bioink with reference to that of collagen. In these experiments, we encapsulated 3D printed cell constructs using AGS, a gastric cancer cell line, in the pH-adjusted g-dECM bioink, and in collagen. Over 95% cell viability was observed with both groups on day 14 (**Figure 1E**), indicating that the g-dECM bioink is non-cytotoxic, given its similar response to the Type I collagen hydrogel.

3D Printing of Gastric Cancer Cells

3D cell printing is a promising tool for fabricating arbitrary shapes, and placing cells in designated locations simultaneously (Pati et al., 2014; Yi et al., 2019; Kim et al., 2020). To confirm its suitability for 3D cell printing, we measured the fidelity of shapes created using cell-laden g-dECM bioink (**Figure 2A**), demonstrating that it could print a pre-designed grid and rectangular patterns. Further, the gastric ruga pattern designed to mimic the shape of gastric tissue in the macro scale, was printed accurately. As it has been shown that the shear force during printing can damage the cells and reduce cell viability (Derby, 2012), we verified the cell viability after 3D cell printing. The viability of KATO-III in the printed structure was found to be sufficiently high (>95%) (**Figures 2B,C**) 1 and 7 days after cell printing, demonstrating that the developed bioink can be used not only for fabricating complex structures, but also for culturing various types of gastric cancer-related cells.

Response of Cellular Behavior Based on the Microenvironment

An *in vitro* aggregated cancer model that mimics the more realistic *in vivo* conditions (Adenis et al., 2020) has been demonstrated. In addition, *in vitro* cancer models that support tissue-specific function and cell aggregation using a decellularized

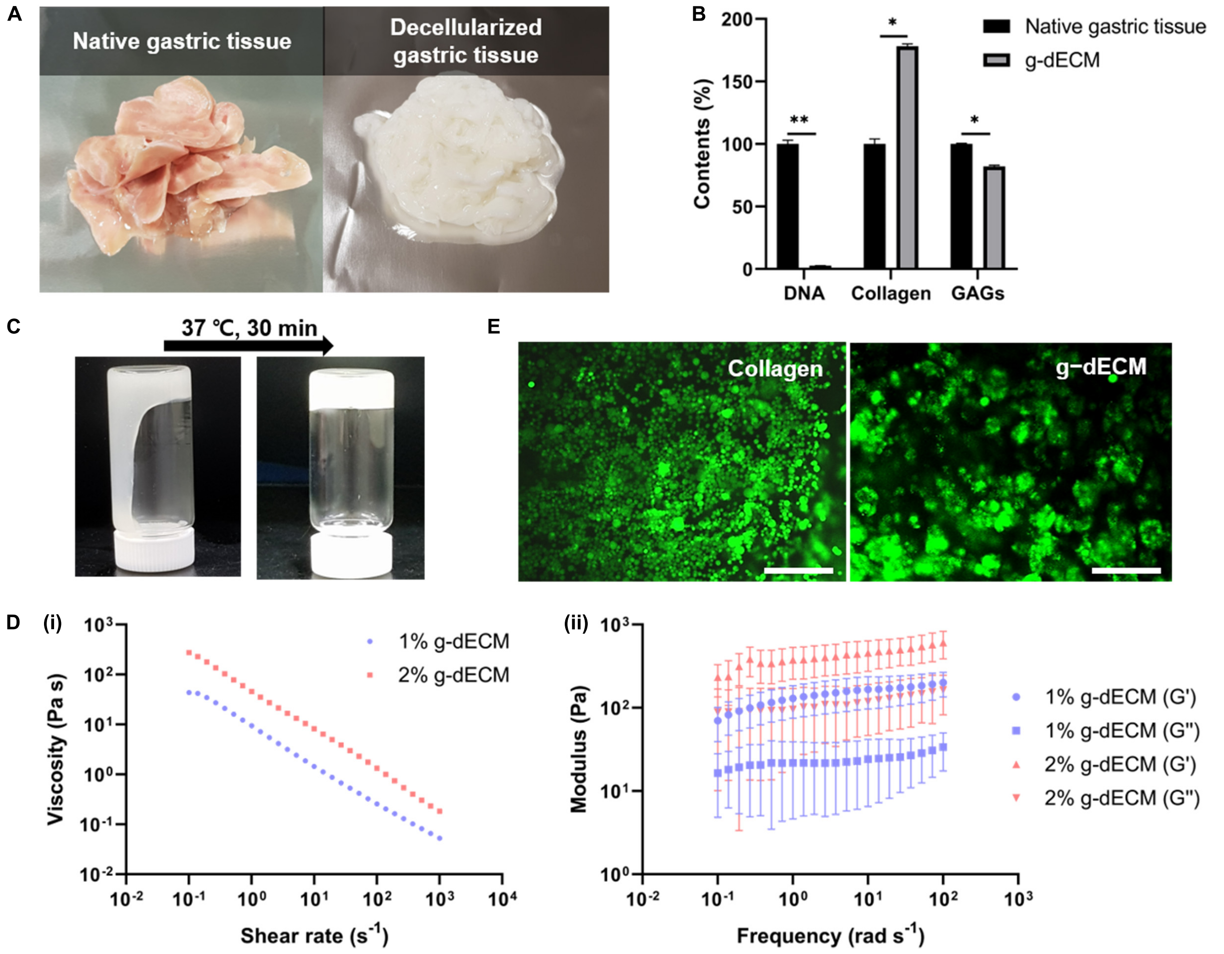

FIGURE 1 | Preparation and characterization of g-dECM bioink. **(A)** Optical micrographs of sliced native gastric tissue and decellularized gastric tissue (g-dECM). **(B)** Comparison of the amount of extracellular components (collagen, GAGs) and DNA in native tissue and g-dECM. **(C)** Sol-gel transition of the g-dECM bioink. **(D)** Rheological properties of g-dECM bioink: (i) viscosity at 15°C (ii) dynamic modulus at 37°C. **(E)** Live/dead evaluation of human gastric cancer cell-line (AGS) on day 14 (scale, 200 μm, $^*p < 0.05$, $^{**}p < 0.01$).

tissue ECM have also been reported (Rijal and Li, 2017; Tian et al., 2018). As the cellular function and drug resistance of cancers are related to cell aggregation (Jianmin et al., 2002; Zhang et al., 2010), we hypothesize that the g-dECM bioink can model the more aggressive characteristics of gastric cancer.

To verify this hypothesis, we examined the presentation of fundamental gastric cancer cell behaviors in the g-dECM bioink, using Matrigel and collagen as representative controls. Here, Matrigel, composed of basement membrane components from tumor cell/tissues (Benton et al., 2014), was selected as it is the most widely used material for modeling the cancer environment. Conversely, Type I collagen—a biomaterial obtained from natural ECM components—was selected as the negative control for cancer behavior, as it shows high biocompatibility and is widely used for developing tissue models (Che et al., 2006; Yip and Cho, 2013). To ensure all experiments were conducted in identical conditions to Matrigel, which has a protein concentration of approximately 10 mg/ml, the concentrations of the g-dECM and collagen were set at 1 w/v%. Histological analysis was performed to study the morphological behavior of the KATO-III gastric cancer cell line, which is derived from gastric signet ring cell carcinoma (Takeuchi et al., 2012). Interestingly, although signet ring cells were observed in all three groups, both H&E staining (**Figure 3A**) and confocal imaging (**Figure 3B**) indicate that cells only aggregate in the 1% g-dECM bioink. No cell aggregates were observed in either Matrigel or collagen, suggesting that the g-dECM bioink is more effective in inducing cancer cell aggregation.

The expression of the tissue remodeling marker (MMP2), the cell–cell interaction marker (β-catenin), and the cell–ECM interaction marker (integrin β1), which are involved in gastric cancer cell aggregation and are used to characterize the aggressiveness of cancer cells, were also investigated. We observed that the expression of MMP2, β-catenin, and integrin β1 was significantly higher with the 1% g-dECM bioink than with the Matrigel and collagen (**Figure 3C**). These results indicate that gastric cancer cells showed more aggressive characteristics in the g-dECM than in the other biomaterials.

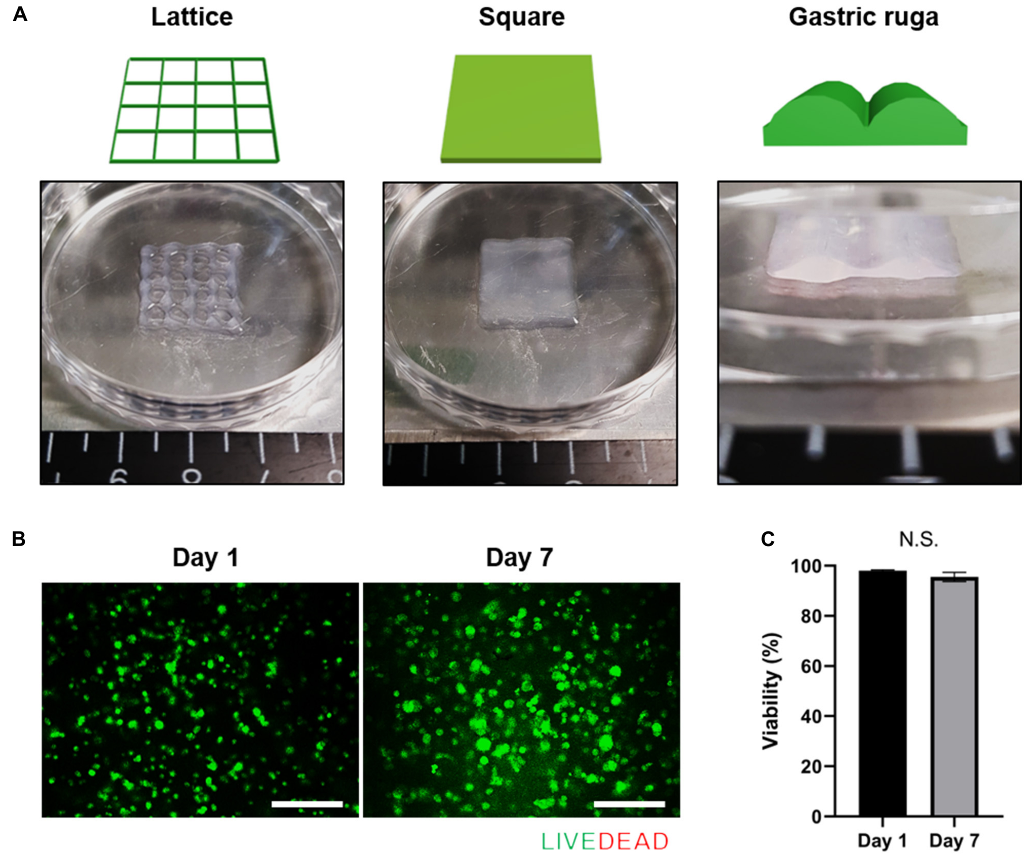

FIGURE 2 | Application of g-dECM bioink to 3D cell printing of a variety of constructs. **(A)**. Heterogeneous structures 3D cell printed in accordance with modeling. **(B)** Live/dead evaluation of the gastric cancer construct 1 and 7 days after culturing. **(C)** Viability of cells in construct 1 and 7 days after culturing (scale, 200 μm; N.S., no significance).

As cell adhesion molecules can play a crucial role in therapeutic resistance, we conducted drug tests by collating the response of cells in each biomaterial to 5-FU. Here, three different gastric cancer cell lines (SNU-1, KATO-III, and AGS) were encapsulated in each hydrogel, and cultured for 2 weeks. Then, 0–1,000 μM 5-FU was added for 2 days. As expected based on the increased expression of the marker genes, the IC_{50} values were higher in the 1% g-dECM group, with 6 and 2.7-fold increases noted for KATO-III, 1.8 and 1.3-fold increases noted for SNU-1, and 2.4 and 22.4-fold increases noted for AGS, in comparison to the values in Matrigel and collagen, respectively (**Figure 3D**). These figures indicate that culturing in the dECM bioink increased the drug resistance of gastric cancer cells. Thus, the proposed g-dECM bioink showed favorable feasibility for further applications in modeling gastric cancer.

Regulating Cancer Behavior Using the Stiffness of the g-dECM Bioink

Cancerous growths are usually observed in stiffer tissue environments than the environments of normal tissues. Hence, it has been surmised that cancer cellular behavior is regulated based on ECM stiffness (Gkretsi and Stylianopoulos, 2018; Kalli and Stylianopoulos, 2018). In a previous *in vitro* study, to modulate the cancer cells, ECM stiffness was controlled by changing the protein density or the degree of hydrogel crosslinking. These controls subsequently activated cancer cell behavior, such as enhancing the integrin–ECM adhesion of plaque mechanosensors (Gauthier and Roca-Cusachs, 2018). Thus, we hypothesize that behavior of gastric cancer cells can be upregulated by increasing the concentration of the g-dECM bioink.

To investigate this, we compared the behaviors of KATO-III and SNU-1 cells encapsulated in 1% g-dECM bioink with the behavior of the same gastric cell lines encapsulated in 2% g-dECM bioink. H&E staining showed that with both cell lines, the size of the cell aggregates were larger in the 2% g-dECM bioink than in the 1% g-dECM bioink (**Figures 4A,B**). From **Figure 1Dii**, under 1 $radS^{-1}$, the storage modulus of the 1% g-dECM was 129.8 ± 54.7 Pa, whereas the storage modulus of the 2% g-dECM ink was 376.6 ± 156.1 Pa under 1 $radS^{-1}$. This result thus indicates that the higher ECM stiffness caused the gastric cancer cells to form larger aggregates.

Further, we observed the expression of the cancer-related markers, MMP2, β-catenin, and integrin β1, which are associated with matrix stiffness and correlated with cancer cell invasion

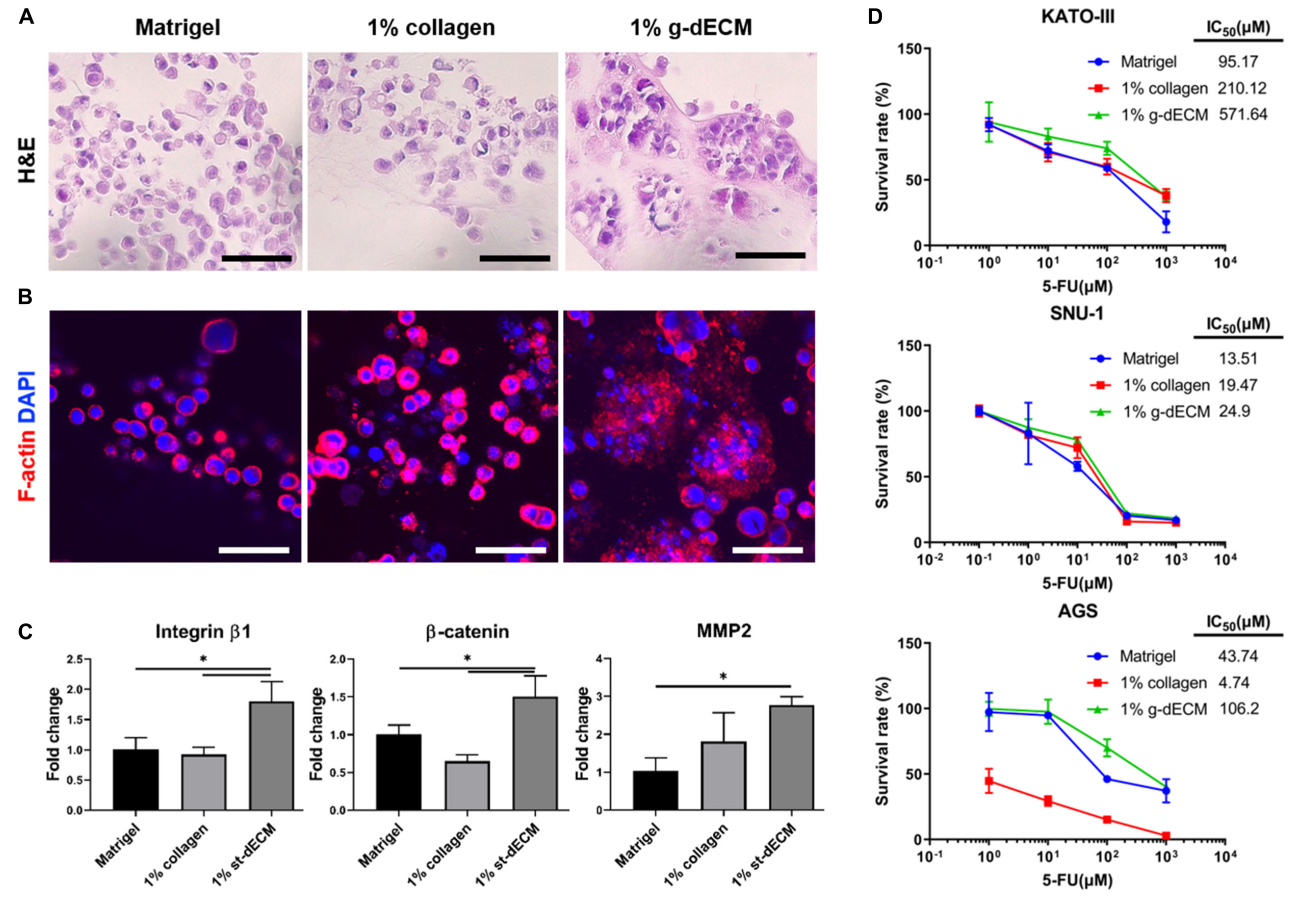

FIGURE 3 | Evaluation of cell aggregation and aggressiveness of gastric cancer cells 3D printed in different bioinks. **(A,B)** Histology of gastric cancer cell-line (KATO-III) grown in Matrigel, 1% collagen, and 1% g-dECM on day 14. **(A)** H%E stained images **(B)** Immunofluorescence images. **(C)** Comparative gene expression analyses of integrin β1, β-catenin, and MMP2 on day 14. **(D)** Response of gastric cancer cell-line (KATO–III, SNU-1, and AGS) proliferation in Matrigel, 1% collagen, and 1% g-dECM bioink to 5-FU treatment. (*n* = 3) (scale, 50 μm, **p* < 0.05).

and metastasis (Karamichos et al., 2007; You et al., 2015). As expected, the levels of MMP2, β-catenin, and integrin β1 were upregulated with increased g-dECM bioink stiffness (**Figure 4C**); in the 2% g-dECM bioink, KATO-III showed significantly higher expressions of all three markers, whereas SNU-1 showed a significantly higher expression of β-catenin, and more modest increases in MMP2 and integrin β1 expression. Thus, the g-dECM matrix stiffness regulates remodeling gene expression, demonstrating that control of the aggression of gastric cancer cells is feasible.

Effects of Cellulose Nanoparticles on Regulating the Mechanical Properties of g-dECM Bioink and Cellular Behavior

In the previous section, it was demonstrated that increasing the density of g-dECM bioink stimulated more aggressive gastric cancer behavior. However, the 2% g-dECM bioink formulation is the maximum concentration achievable. Hence, to enhance its mechanical properties and provide a more biophysically reliable gastric cancer environment, we investigated the use of a cross-linker in addition to the bioink. Cellulose has been identified as a promising biopolymer with remarkable biological properties such as biocompatibility, biodegradability, and low toxicity (Luo et al., 2019). Therefore, in this study we used CN to further increase the mechanical strength of the g-dECM bioink. CN particles were prepared following the methods previously described in the literature (Kumar et al., 2017). The diameters of the prepared particles were observed to be in the 50–100 nm range using TEM (**Figure 5A**). The final concentration of the prepared CN solution was approximately 20%. The concentration of the CN-g-dECM bioink was set in the range 0–0.5 w/v%, i.e., we compared the behavior of g-dECM without CN, to the behavior of g-dECM mixed with CN up to a concentration of 0.5 w/v%.

The stiffness of the 2% g-dECM bioink improved with increases to the concentration of added CN (**Figure 5B**). To investigate the effect of the CN on cellular behavior, KATO–III was encapsulated in each bioink formulation. Primary thermal crosslinking was subsequently conducted by incubating at 37°C for 30 min, followed by secondary crosslinking, conducted by treatment with 100×10^{-3} m $CaCl_2$. After culturing for 2 weeks,

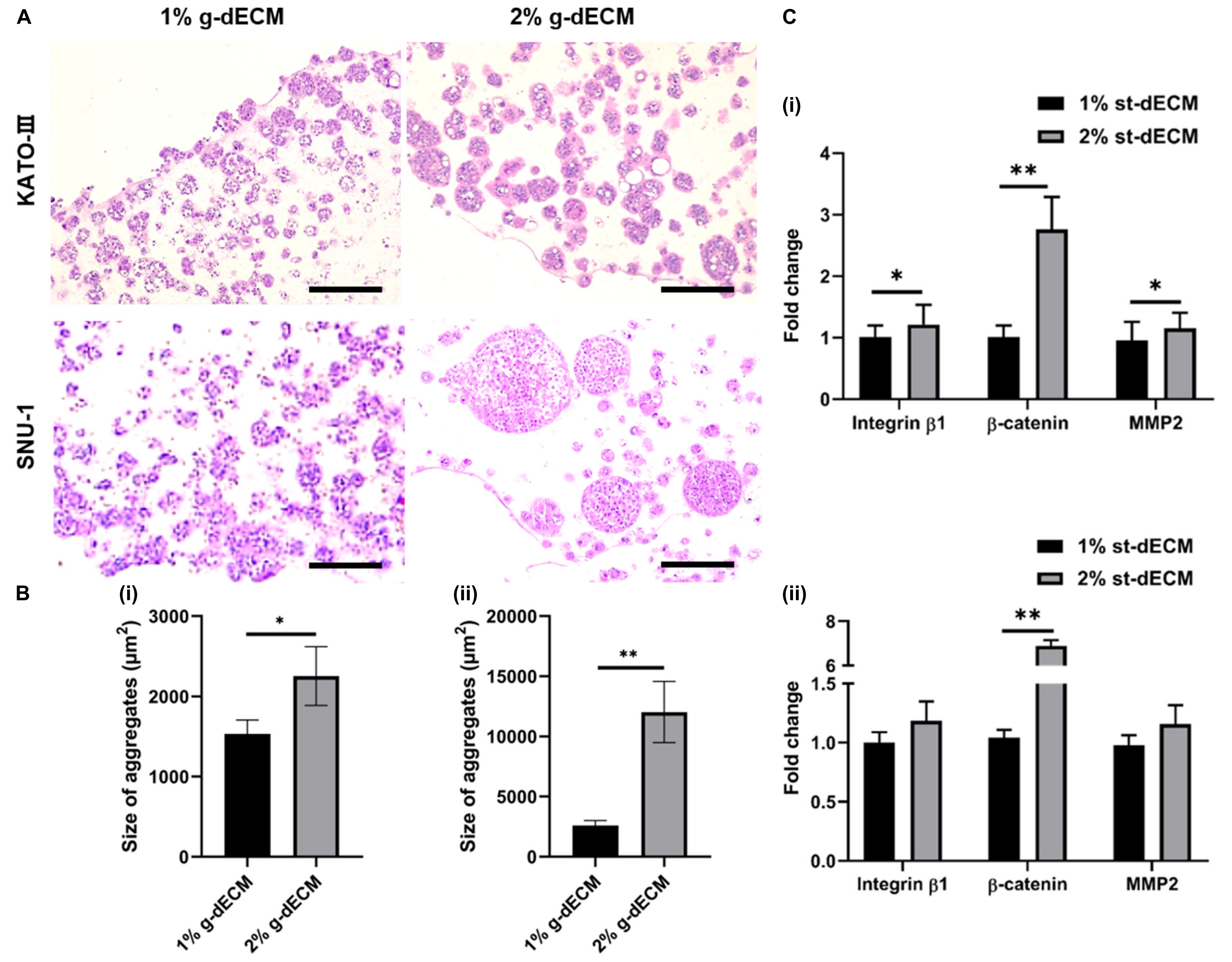

FIGURE 4 | Extracellular matrix density regulates gastric cancer cell aggressiveness. **(A)** H&E stained image of gastric cancer cell-lines (KATO-III and SNU-1) grown in 1 and 2% g-dECM bioink on day 14. **(B)** Quantification of the size of cell aggregates. **(C)** Comparative analyses of gene expression on day 14 (scale, 200 μm; $^{*}p < 0.05$, $^{**}p < 0.01$).

aggregated cells were observed in all groups through histological analysis (**Figure 5C**). The addition of the CN increased the size of aggregates from 2178.7 ± 210.7 μm^2 in the 0% CN-g-dECM group, to 3563.8 ± 583.3 μm^2, and 5666.5 ± 1440.1 μm^2 in the 0.01% CN-g-dECM, and 0.1% CN-g-dECM groups, respectively. In contrast, the size of cell aggregates in the 0.5% CN-g-dECM group decreased to 2095.1 ± 313.0 μm^2 (**Figure 5D**). These results indicate that adjusting the mechanical properties of the bioink using CN supplements can regulate cell aggregation. These observations were further corroborated using the expression of β-catenin and integrin β1, which are sensitive to stiffness (Samuel et al., 2011; Yeh et al., 2017). Up to a concentration of 0.1% CN in g-dECM bioink, where the largest aggregate sizes were observed, the levels of β-catenin and integrin β1 increased with an increase in the matrix stiffness. However, both gene expression and cell aggregate sizes were decreased in the 0.5% CN-g-dECM bioink (**Figure 5E**), suggesting an improper physical microenvironment for cell proliferation (Cavo et al., 2016). Thus, it can be surmised that an excessively high CN concentration results in an inordinately stiff cell environment that degrades cell properties.

These outcomes indicate that more aggressive cellular functions can be obtained by regulating the stiffness of the bioink using CN. Furthermore, an adequate biophysical environment for gastric cancer cells can be obtained by modulating the concentration of CN.

DISCUSSION

The behavior of gastric cancer cells is regulated by the surrounding environment (Ishimoto et al., 2014). Recognizing the importance of this variable, we developed a 3D cell printed gastric cancer model that uses a gastric specific bioink supplemented with cellulose nanoparticles to provide tissue-specific biochemical and biophysical stimulation of the

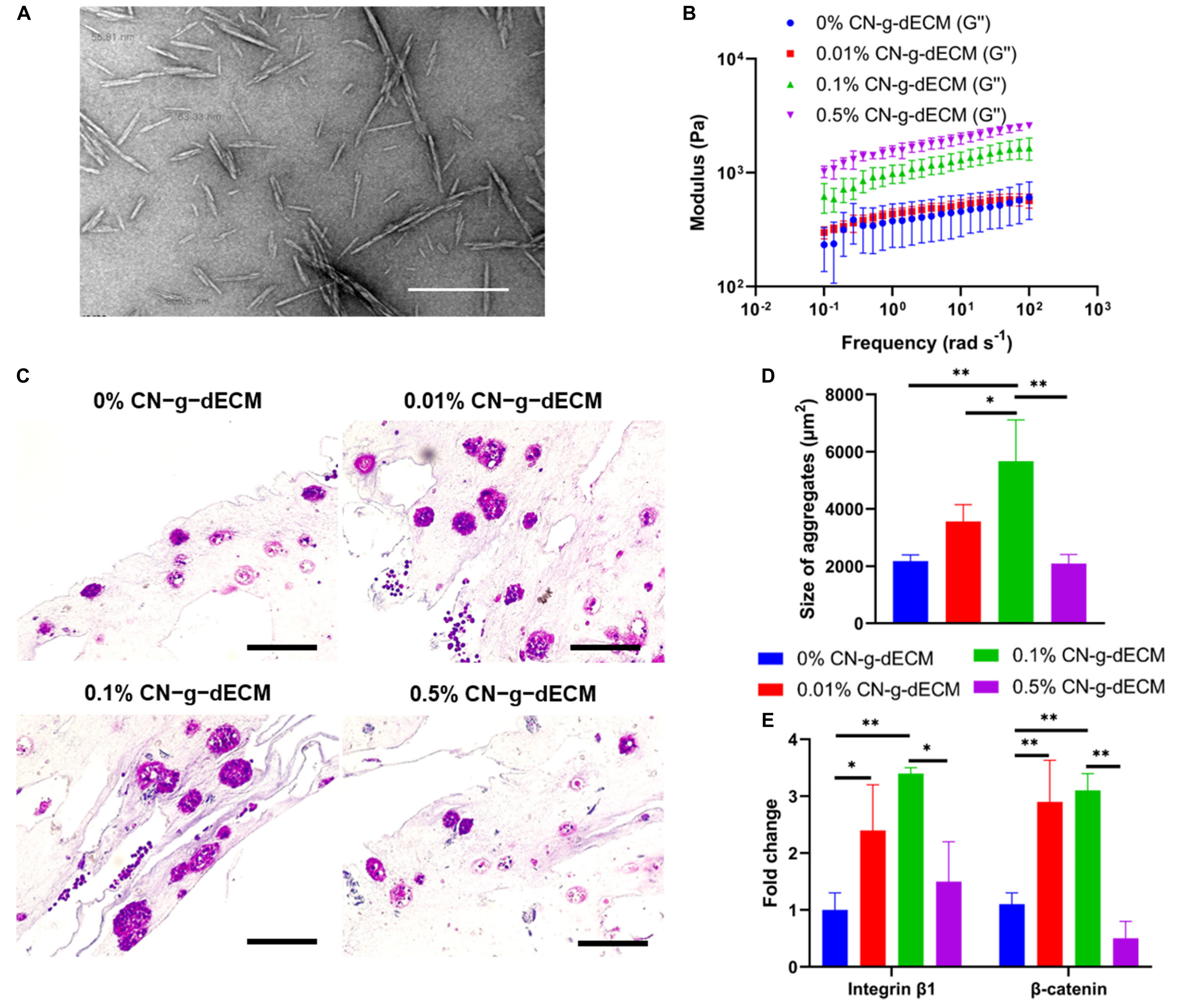

FIGURE 5 | Enhancement of extracellular matrix density using cellulose nanoparticles regulates the aggressive behavior of gastric cancer cells. **(A)** TEM image of cellulose nanoparticles. **(B)** Dynamic modulus of CN-g-dECM bioink at 37°C. **(C)** H&E stained image of gastric cancer tumor grown in CN-g-dECM bioink on day 14. **(D)** Quantification of the size of cell aggregates. **(E)** Comparative analyses of gene expression on day 14 (scale, 200 μm; *$p < 0.05$, **$p < 0.01$).

environment for cancer cells. In our study, we observed that gastric cancer cells in the g-dECM bioink were highly aggregated, in contrast to those in collagen and Matrigel at the same concentration to consider the features of natural ECM. Further, we observed that marker genes related to cancer aggressiveness—MMP2, β-catenin, and integrin β1—were expressed at higher levels in the g-dECM bioink. These results indicated that the g-dECM bioink affects cellular functions, such as matrix remodeling, cell–ECM interaction, and cell–cell interaction, which lead to cancer progression (Kaushik et al., 2019). In addition, because drug resistance is an intrinsic behavior of cancer and plays an important role in developing cancer models (Gottesman, 2002), and organ microenvironment may affect the response to chemotherapy (Khanna and Hunter, 2005), we verified that the therapeutic resistance of gastric cancer cells was increased in the g-dECM bioink. Our findings demonstrate the efficacy of the g-dECM bioink as a drug testing material, in mimicking *in vivo* conditions that showed high drug resistance. These observations are attributed to the fact that tissue-specific bioinks can provide a tissue-specific environment for cancer cells (Tian et al., 2018) that promote cancer cell progression.

In addition, as already demonstrated in previous studies, native gastric cancer tissues are stiff, and this matrix stiffness regulates the behavior of encapsulated gastric cancer cells (Song et al., 2013; da Cunha et al., 2016). To reconstruct this *in vitro*, in this study, two methods were chosen to influence the surrounding biophysical environment to regulate the cellular function. In the first method, we increased the ratio of g-dECM to acetic acid in the g-dECM bioink, to enhance its mechanical properties. As well as the enlargement of cell aggregates, we observed that increasing the concentration of g-dECM in the bioink upregulated β-catenin and integrin β1. This implies that the proposed g-dECM bioink can provide a biochemically and biophysically appropriate microenvironment for culturing gastric cancer cells. In the second method, we used CNs, which have superior mechanical strength and excellent biocompatibility (Luo et al., 2019), to enhance the stiffness of the g-dECM bioink. An increase in the modulus of the bioink induced larger cell aggregates and higher expression of β-catenin and integrin β1, which indicates that ECM stiffness of the prepared structure regulates cell–cell interaction and cell–ECM interaction. Moreover, we observed that the 0.1% CN-g-dECM bioink provided the most suitable stiffness for the gastric cancer cells. This indicates that, with its more aggressive characteristic, 0.1% CN-g-dECM can be used to provide a more reliable clinically applicable predictor, compared to previous methods relying on 2D and 3D culture in Matrigel and collagen.

In addition, the g-dECM bioink can be used to fabricate arbitrary 3D structures using automated 3D cell-printing techniques that enable the deposition of various cell-laden bioinks at appropriate positions (Pati et al., 2014). Hence, using the developed bioink, 3D cell-printing techniques could enable the fabrication of more complex gastric cancer systems with different types of cells, such as fibroblasts and endothelial cells, that can provide an alternative to animal models. This is important, as it is increasingly clear that owing to cross-species differences, animal models do not accurately predict the human body's response to drug testing. With their ability to mimic *in vivo* environments, and the automated model fabrication process, 3D cell-printed cancer models have become prominent candidates to replace animal models (Kang et al., 2020). Therefore, using our biochemically and biophysically improved bioink, we can fabricate more *in vivo* relevant gastric cancer systems in future studies.

CONCLUSION

In this study, we developed a CN-g-dECM bioink for 3D cell printing a gastric cancer model. With respect to clinical study, the developed bioink has the advantages of providing a biochemically and biophysically appropriate microenvironment for analyzing gastric cancer cells. Compared to commercially available hydrogels such as Matrigel and collagen, gastric cancer cells in this bioink showed more aggressive characteristics, as confirmed by morphological, drug testing, and genetical analyses. Moreover, the inclusion of CN in the g-dECM bioink allows the regulation of the size of cell aggregates, and the expression of MMP2, β-catenin, and integrin β1, by controlling the stiffness of the cancer microenvironment. Further, cell-laden bioink can be patterned in the appropriate position using 3D cell printing techniques, meaning that it can be applied for fabricating complex gastric cancer systems.

DATA AVAILABILITY STATEMENT

The datasets presented in this study can be found in online repositories. The names of the repository/repositories and accession number(s) can be found in the article/**Supplementary Material**.

AUTHOR CONTRIBUTIONS

JK, JJ, and D-WC conceived the initial idea and designed the experiments. JK performed the experiments. JK and JJ analyzed the data and drafted the manuscript. JJ and D-WC guided the work and revised the manuscript and worked on funding acquisition. All authors have read and approved the final manuscript.

FUNDING

This research was supported by the National Research Foundation of Korea (NRF) grant (NRF-2019R1A3A3005437) funded by the Korean government; Basic Science Research Program through the National Research Foundation of Korea (NRF) funded by the Ministry of Education (No. 2020R1A6A1A03047902).

ACKNOWLEDGMENTS

This research topic is dedicated to Prof. Lina Zhang on the occasion of her 80th birthday, in gratitude, esteem, and affection. We would like to thank the Experimental Teaching Center of Basic Medical Sciences, Wuhan University.

SUPPLEMENTARY MATERIAL

The Supplementary Material for this article can be found online at: https://www.frontiersin.org/articles/10.3389/fbioe.2021.605819/full#supplementary-material

REFERENCES

Adenis, L. L., Seksek, O., Juchaux, M., Deroulers, C., and Badoual, M. (2020). Modelling in vitro aggregation of cancer cells. *Biophys. J.* 118:459a. doi: 10.1016/j.bpj.2019.11.2555

Athukoralalage, S. S., Balu, R., Dutta, N. K., and Roy Choudhury, N. (2019). 3D bioprinted nanocellulose-based hydrogels for tissue engineering applications: a brief review. *Polymers* 11:898. doi: 10.3390/polym11050898

Benton, G., Arnaoutova, I., George, J., Kleinman, H. K., and Koblinski, J. (2014). Matrigel: from discovery and ECM mimicry to assays and models for cancer research. *Adv. Drug Deliv. Rev.* 79, 3–18. doi: 10.1016/j.addr.2014.06.005

Cavo, M., Fato, M., Peñuela, L., Beltrame, F., Raiteri, R., and Scaglione, S. (2016). Microenvironment complexity and matrix stiffness regulate breast cancer cell activity in a 3D in vitro model. *Sci. Rep.* 6:35367.

Che, Z. M., Jung, T. H., Choi, J. H., Yoon, D. J., Jeong, H. J., Lee, E. J., et al. (2006). Collagen-based co-culture for invasive study on cancer cells-fibroblasts interaction. *Biochem. Biophys. Res. Commun.* 346, 268–275. doi: 10.1016/j.bbrc.2006.05.111

Crotti, S., Piccoli, M., Rizzolio, F., Giordano, A., Nitti, D., and Agostini, M. (2017). Extracellular matrix and colorectal cancer: how surrounding microenvironment affects cancer cell behavior? *J. Cell. Physiol.* 232, 967–975. doi: 10.1002/jcp.25658

da Cunha, C. B., Klumpers, D. D., Koshy, S. T., Weaver, J. C., Chaudhuri, O., Seruca, R., et al. (2016). CD44 alternative splicing in gastric cancer cells is regulated by culture dimensionality and matrix stiffness. *Biomaterials* 98, 152–162. doi: 10.1016/j.biomaterials.2016.04.016

Derby, B. (2012). Printing and prototyping of tissues and scaffolds. *Science* 338, 921–926. doi: 10.1126/science.1226340

Ferreira, L. P., Gaspar, V. M., and Mano, J. F. (2020). Decellularized extracellular matrix for bioengineering physiomimetic 3D in vitro tumor models. *Trends Biotechnol.* 38, 1397–1414. doi: 10.1016/j.tibtech.2020.04.006

Gauthier, N. C., and Roca-Cusachs, P. (2018). Mechanosensing at integrin-mediated cell–matrix adhesions: from molecular to integrated mechanisms. *Curr. Opin. Cell Biol.* 50, 20–26. doi: 10.1016/j.ceb.2017.12.014

Gkretsi, V., and Stylianopoulos, T. (2018). Cell adhesion and matrix stiffness: coordinating cancer cell invasion and metastasis. *Front. Oncol.* 8:145. doi: 10.3389/fonc.2018.00145

Gottesman, M. M. (2002). Mechanisms of cancer drug resistance. *Annu. Rev. Med.* 53, 615–627.

Hoshiba, T. (2019). Decellularized extracellular matrix for cancer research. *Materials* 12:1311. doi: 10.3390/ma12081311

Ishimoto, T., Sawayama, H., Sugihara, H., and Baba, H. (2014). Interaction between gastric cancer stem cells and the tumor microenvironment. *J. Gastroenterol.* 49, 1111–1120. doi: 10.1007/s00535-014-0952-0

Jang, M., Koh, I., Lee, J. E., Lim, J. Y., Cheong, J.-H., and Kim, P. (2018). Increased extracellular matrix density disrupts E-cadherin/β-catenin complex in gastric cancer cells. *Biomaterials Sci.* 6, 2704–2713. doi: 10.1039/c8bm00843d

Jang, M., Koh, I., Lee, S. J., Cheong, J.-H., and Kim, P. (2017). Droplet-based microtumor model to assess cell-ECM interactions and drug resistance of gastric cancer cells. *Sci. Rep.* 7, 1–10.

Jianmin, Z., Hongfang, W., and Meifu, F. (2002). Resistance of multicellular aggregates to pharmorubicin observed in human hepatocarcinoma cells. *Braz. J. Med. Biol. Res.* 35, 255–260. doi: 10.1590/s0100-879x2002000200015

Jin, Q., Liu, G., Li, S., Yuan, H., Yun, Z., Zhang, W., et al. (2019). Decellularized breast matrix as bioactive microenvironment for in vitro three–dimensional cancer culture. *J. Cell. Physiol.* 234, 3425–3435. doi: 10.1002/jcp.26782

Kalli, M., and Stylianopoulos, T. (2018). Defining the role of solid stress and matrix stiffness in cancer cell proliferation and metastasis. *Front. Oncol.* 8:55. doi: 10.3389/fonc.2018.00055

Kang, Y., Datta, P., Shanmughapriya, S., and Ozbolat, I. T. (2020). 3D bioprinting of tumor models for cancer research. *ACS Appl. Bio Mater.* 3, 5552–5573. doi: 10.1021/acsabm.0c00791

Karamichos, D., Brown, R., and Mudera, V. (2007). Collagen stiffness regulates cellular contraction and matrix remodeling gene expression. *J. Biomed. Mater. Res. Part A* 83, 887–894. doi: 10.1002/jbm.a.31423

Kaushik, N., Kim, S., Suh, Y., and Lee, S.-J. (2019). Proinvasive extracellular matrix remodeling for tumor progression. *Arch. Pharm. Res.* 42, 40–47. doi: 10.1007/s12272-018-1097-0

Khanna, C., and Hunter, K. (2005). Modeling metastasis in vivo. *Carcinogenesis* 26, 513–523. doi: 10.1093/carcin/bgh261

Kim, B. S., Das, S., Jang, J., and Cho, D.-W. (2020). Decellularized extracellular matrix-based bioinks for engineering tissue-and organ-specific microenvironments. *Chem. Rev.* 120, 10608–10661. doi: 10.1021/acs.chemrev.9b00808

Kim, B. S., Lee, J.-S., Gao, G., and Cho, D.-W. (2017). Direct 3D cell-printing of human skin with functional transwell system. *Biofabrication* 9:025034. doi: 10.1088/1758-5090/aa71c8

Kumar, A., Lee, Y., Kim, D., Rao, K. M., Kim, J., Park, S., et al. (2017). Effect of crosslinking functionality on microstructure, mechanical properties, and in vitro cytocompatibility of cellulose nanocrystals reinforced poly (vinyl alcohol)/sodium alginate hybrid scaffolds. *Int. J. Biol. Macromol.* 95, 962–973. doi: 10.1016/j.ijbiomac.2016.10.085

Luo, H., Cha, R., Li, J., Hao, W., Zhang, Y., and Zhou, F. (2019). Advances in tissue engineering of nanocellulose-based scaffolds: a review. *Carbohydr. Polym.* 224:115144. doi: 10.1016/j.carbpol.2019.115144

Pati, F., Jang, J., Ha, D.-H., Kim, S. W., Rhie, J.-W., Shim, J.-H., et al. (2014). Printing three-dimensional tissue analogues with decellularized extracellular matrix bioink. *Nat. Commun.* 5, 1–11.

Rijal, G., and Li, W. (2017). A versatile 3D tissue matrix scaffold system for tumor modeling and drug screening. *Sci. Adv.* 3:e1700764. doi: 10.1126/sciadv.1700764

Roukos, D. (2000). Current status and future perspectives in gastric cancer management. *Cancer Treat. Rev.* 26, 243–255. doi: 10.1053/ctrv.2000.0164

Samuel, M. S., Lopez, J. I., Mcghee, E. J., Croft, D. R., Strachan, D., Timpson, P., et al. (2011). Actomyosin-mediated cellular tension drives increased tissue stiffness and β-catenin activation to induce epidermal hyperplasia and tumor growth. *Cancer Cell* 19, 776–791. doi: 10.1016/j.ccr.2011.05.008

Seewaldt, V. (2014). ECM stiffness paves the way for tumor cells. *Nat. Med.* 20, 332–333. doi: 10.1038/nm.3523

Song, W., Chen, C.-Y., Xu, J.-B., Ye, J.-N., Wang, L., Chen, C.-Q., et al. (2013). Pathological diagnosis is maybe non-essential for special gastric cancer: case reports and review. *World J. Gastroenterol. WJG* 19:3904. doi: 10.3748/wjg.v19.i24.3904

Spolverato, G., Ejaz, A., Kim, Y., Squires, M. H., Poultsides, G. A., Fields, R. C., et al. (2015). Use of endoscopic ultrasound in the preoperative staging of gastric cancer: a multi-institutional study of the US gastric cancer collaborative. *J. Am. Coll. Surg.* 220, 48–56. doi: 10.1016/j.jamcollsurg.2014.06.023

Stoddart, M. J. (2011a). "Cell viability assays: introduction," in *Mammalian Cell Viability*, ed. M. J. Stoddart (Berlin: Springer), 1–6. doi: 10.1007/978-1-61779-108-6_1

Stoddart, M. J. (2011b). *Mammalian Cell Viability: Methods and Protocols*. Berlin: Springer.

Takeuchi, T., Adachi, Y., and Nagayama, T. (2012). A WWOX-binding molecule, transmembrane protein 207, is related to the invasiveness of gastric signet-ring cell carcinoma. *Carcinogenesis* 33, 548–554. doi: 10.1093/carcin/bgs001

Tian, X., Werner, M. E., Roche, K. C., Hanson, A. D., Foote, H. P., Stephanie, K. Y., et al. (2018). Organ-specific metastases obtained by culturing colorectal cancer cells on tissue-specific decellularized scaffolds. *Nat. Biomed. Eng.* 2, 443–452. doi: 10.1038/s41551-018-0231-0

Yeh, Y.-C., Ling, J.-Y., Chen, W.-C., Lin, H.-H., and Tang, M.-J. (2017). Mechanotransduction of matrix stiffness in regulation of focal adhesion size and number: reciprocal regulation of caveolin-1 and β1 integrin. *Sci. Rep.* 7, 1–14.

Yi, H.-G., Jeong, Y. H., Kim, Y., Choi, Y.-J., Moon, H. E., Park, S. H., et al. (2019). A bioprinted human-glioblastoma-on-a-chip for the identification of patient-specific responses to chemoradiotherapy. *Nat. Biomed. Eng.* 3, 509–519. doi: 10.1038/s41551-019-0363-x

Yip, D., and Cho, C. H. (2013). A multicellular 3D heterospheroid model of liver tumor and stromal cells in collagen gel for anti-cancer drug testing. *Biochem. Biophys. Res. Commun.* 433, 327–332. doi: 10.1016/j.bbrc.2013.03.008

You, Y., Zheng, Q., Dong, Y., Wang, Y., Zhang, L., Xue, T., et al. (2015). Higher matrix stiffness upregulates osteopontin expression in hepatocellular carcinoma cells mediated by integrin β1/GSK3β/β-catenin signaling pathway. *PLoS One* 10:e0134243. doi: 10.1371/journal.pone.0134243

Yuan, R., Hou, Y., Sun, W., Yu, J., Liu, X., Niu, Y., et al. (2017). Natural products to prevent drug resistance in cancer chemotherapy: a review. *Ann. N.Y. Acad. Sci.* 1401, 19–27. doi: 10.1111/nyas.13387

Zhang, X., Xu, L.-H., and Yu, Q. (2010). Cell aggregation induces phosphorylation of PECAM-1 and Pyk2 and promotes tumor cell anchorage-independent growth. *Mol. Cancer* 9:7. doi: 10.1186/1476-4598-9-7

Conflict of Interest: The authors declare that the research was conducted in the absence of any commercial or financial relationships that could be construed as a potential conflict of interest.

frontiers
in Bioengineering and Biotechnology

REVIEW
published: 29 March 2021
doi: 10.3389/fbioe.2021.608826

Trends on the Cellulose-Based Textiles: Raw Materials and Technologies

Catarina Felgueiras[1], Nuno G. Azoia[2], Cidália Gonçalves[1], Miguel Gama[1] and Fernando Dourado[1]*

[1] *Centre of Biological Engineering, University of Minho, Braga, Portugal,* [2] *CeNTI–Centre for Nanotechnology and Smart Materials, Vila Nova de Famalicão, Portugal*

OPEN ACCESS

Edited by:
Muhammad Wajid Ullah,
Huazhong University of Science and Technology, China

Reviewed by:
Tairong Kuang,
Zhejiang University of Technology, China
Muhammad Asif,
Wuhan Institute of Technology, China

****Correspondence:***
Miguel Gama
fmgama@deb.uminho.pt

Specialty section:
This article was submitted to Biomaterials, a section of the journal Frontiers in Bioengineering and Biotechnology

Received: *21 September 2020*
Accepted: *25 February 2021*
Published: *29 March 2021*

Citation:
Felgueiras C, Azoia NG, Gonçalves C, Gama M and Dourado F (2021) Trends on the Cellulose-Based Textiles: Raw Materials and Technologies. Front. Bioeng. Biotechnol. 9:608826. doi: 10.3389/fbioe.2021.608826

There is an emerging environmental awareness and social concern regarding the environmental impact of the textile industry, highlighting the growing need for developing green and sustainable approaches throughout this industry's supply chain. Upstream, due to population growth and the rise in consumption of textile fibers, new sustainable raw materials and processes must be found. Cellulose presents unique structural features, being the most important and available renewable resource for textiles. The physical and chemical modification reactions yielding fibers are of high commercial importance today. Recently developed technologies allow the production of filaments with the strongest tensile performance without dissolution or any other harmful and complex chemical processes. Fibers without solvents are thus on the verge of commercialization. In this review, the technologies for the production of cellulose-based textiles, their surface modification and the recent trends on sustainable cellulose sources, such as bacterial nanocellulose, are discussed. The life cycle assessment of several cellulose fiber production methods is also discussed.

Keywords: bacterial nanocellulose, fiber, textile, sustainability, cellulose

INTRODUCTION

Mankind practices such as the excessive use of non-renewable sources of energy and raw materials, and the unlimited generation of waste in the vast majority of industrial processes, have wide impact on the environment sustainability (Akinsemolu, 2018). Such is the case with the escalating demand for textile products. The demand for textile fibers was 75.5 million tons in 2010 and is expected to increase to 133.5 million tons by 2030 (at a growth rate of 3.1%/year) (Häemmerle, 2011; Eichinger, 2012; Hummel et al., 2015). From the production of raw materials, to spinning, weaving fabrics and dyeing, substantial amounts of water and chemicals are required, including nutrients and pesticides for growing raw materials such as cotton. Downstream, consumers' use also bare a significant environmental footprint from the consumption of water, energy, and chemicals from washing, drying, and ironing (Sajn, 2019). In 2015, the United Nations set up an agenda aiming to achieve 17 Sustainable Development Goals (SDGs) by 2030, proposing several solutions to improve the economic and social development and providing the essentials to everyone without overwhelming nature (a concept understood as sustainability) (United Nations, 2015). The United

Nations Alliance for Sustainable Fashion emerged to ensure the achievement of the SDGs in the fashion industry, throughout the product value chain (United Nations, 2020)[1].

For a commercial competitive edge, lignocellulose-based materials need to have equal or better characteristics than those of fossil-based ones. Adding functionalities such as conductivity, magnetic properties, bioactivity, water repellency, self-cleaning surface effect, and flame retardance can further improve their competitiveness (Lundahl et al., 2017; Wei et al., 2020). While taking advantage of their nano-scalar dimension, spinning nanocelluloses without solvents provides the possibility of incorporating additives in the filament dope solution while avoiding the use of solvents which are environmentally damaging (Lundahl et al., 2017; Ewulonu et al., 2019; Gao et al., 2019).

The bio-based production of chemicals and microbial technology can also play a major role in this transition toward the future bioeconomy (Choi and Shin, 2020). Various microorganisms already play fundamental roles in our daily life and, if used intelligently, some significant problems associated with the production of green materials can be solved. Indeed, the vast diversity of microorganisms provides huge applications opportunities (Akinsemolu, 2018). The scientific research is still poor comparatively to what these bio-based knowledge areas can offer. In this review we also analyze the opportunities and challenges of using nanocelluloses, from microorganisms and plants, as sources of the most noble natural raw material for the textile industry, cellulose. Production methods used in the textile industry are discussed, such as the methods of Viscose, Lyocell, and Cellulose Acetate, as well as novel processes using Ionic Liquids and solvent-free fibers. Finally, the sustainability of textile fibers and their life cycle assessment (LCA) are analyzed.

TEXTILE FIBERS

Overview

Fibers are the starting point for all textile products that serve the everyday needs of society. Fibers of short length, called staple fibers, as is the case of most natural fibers, range between 3 and 20 cm in length. A filament is a fiber of indefinite length, being silk the only naturally produced. Most regenerated and synthetic fibers are manufactured as filaments. Distinct methods of drawing, spinning, and twisting, chosen according to the type of fiber, are used to form a continuous strand of yarn (Sinclair, 2015). The filament produced can be used as is, or can be cut into staple fibers. Artificial staple fibers, as the natural ones, must be transformed into yarns. At this stage is very common to blend different fibers, and blends with different combinations of natural and artificial fibers can be found in the market. The textile is then produced. Conventional textiles suit the common decorative or aesthetic usages. Technical textile products can be grouped into various categories, depending on their application, such as industrial, medical, packaging, sports, automotive, construction, aerospatial, geo-textiles, agro-textiles, and protective clothing. Each segment has a huge variety of products made from diversified fibers/raw materials using different manufacturing techniques and equipment (Keller and Giddings, 2020; Rasheed, 2020).

Textiles were produced domestically until the 17th century, mostly from vegetable sources using cotton, hemp, and flax but also from animal sources as wool and silk. Then, during the industrial revolution, the manufacture process was mechanized, providing totally new and faster processes (Texcoms, 2019). The fibers produced until the end of the 19th century were all natural (**Figure 1**). During the 1900s, the production of man-made fibers begun, more specifically regenerated cellulose fibers (RCF) by the Viscose method. This was not the first process for the making of artificial cellulose fibers to be industrialized, but soon became dominant. The synthetic fibers appeared in the textile market only by the 1940's, made from chemically synthesized polymers (Sinclair, 2015; Murthy, 2016).

Natural fibers, as animal (protein) and vegetable ones, compose up to 40% of the textile fibers manufactured annually in the world. Vegetable fiber (cellulose) is extracted from plants (Yu, 2014). The most abundant natural polymer on planet Earth is cellulose, representing over 30–40% of all terrestrial biomass, with a biosynthesis of 10^{11} tons annually (Levi et al., 2016; Kafy et al., 2017; Akhlaghi et al., 2020). Being biodegradable, renewable, biocompatible, and affordable polymer, cellulose has several other uses such as in paper, cellulose-based plastics, food additives, excipients, coatings, diapers, foams, textiles, and composites (Metsä, 2018; Kim et al., 2019; Havstad, 2020; Stora Enso, 2021). While generally synthesized by plants, it is also produced by some bacteria, fungi, and algae. In plants, cellulose is the main structural constituent of the primary cell wall (Brigham, 2018).

Cotton makes up around 90% of all natural fibers, being the most used one for the making of apparel, home furnishings, and industrial products. It is the main natural fiber crop (Yu, 2014). The use of cellulosic fibers is expected to grow from the current level of 3.7 kg per capita to 5.4 kg by 2030 (Häemmerle, 2011). Cotton fiber contains approximately 90% of cellulose, dried hemp has 40–50% and wood 40–55%, commonly found combined with other substances as lignin and hemicelluloses (Ansell and Mwaikambo, 2009; Wang J. et al., 2019). Additionally to cotton, flax, ramie, jute, kenaf, and sisal are widely used. Cultivation with cotton hybrids will expand and so, the harvest yield from 800 (2010) to 925 kg/ha (2030) will increase its production capacity. However, it will not make up for the disappearance of arable land and growing demand. It is estimated that only 3.1 kg of cotton per capita will be accessible in 2030 (Häemmerle, 2011). This cellulose gap provide new opportunities for man-made cellulosic fibers (MMCF). The gradual substitution of cotton by pulp-based fibers is also required from an environmental point of view. Nowadays, new natural fibers, mainly vegetable ones, are being utilized as kapok, pineapple, and apocynum (Yu, 2014).

Synthetic fibers have dominated the market since mid 1990s, overtaking cotton. These are made from organic synthetic high-molecular mass compounds and are produced synthetically from petroleum-based raw materials. They represented up to 63% of the global fiber production in 2019. The most used synthetic fiber was polyester, with a market share of around 52% of total

---

[1] https://unfashionalliance.org/

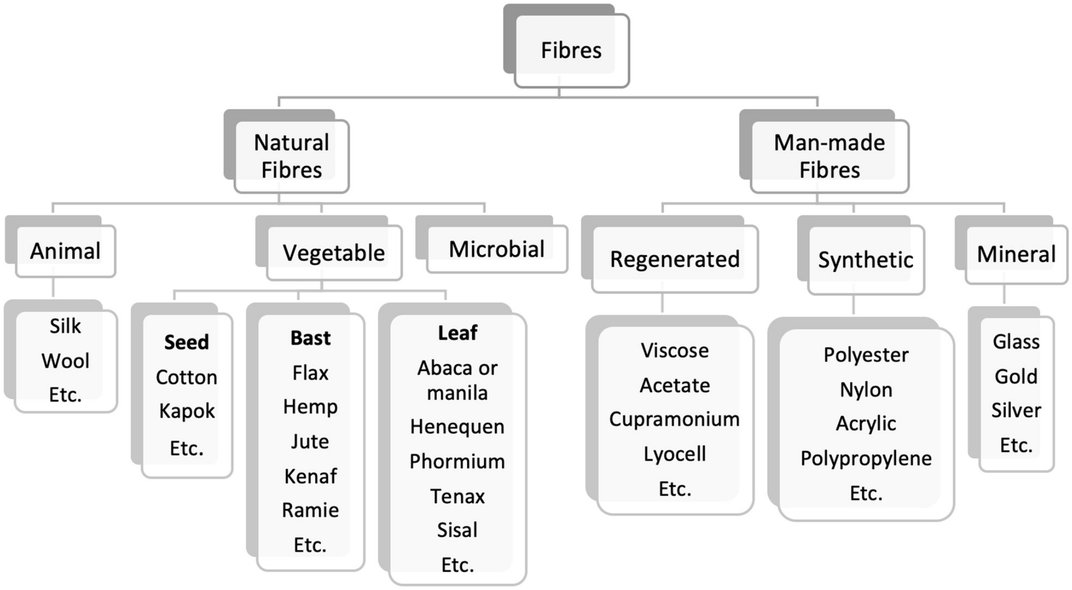

FIGURE 1 | Classification of main natural and man-made fibers [adapted from Murthy (2016), Sinclair (2015)].

global fiber manufacture. Cotton was second, with 23% (Textile Exchanges, 2020). Currently, fibers have a cost of 1.17 €/kg for cotton, 1.31 €/kg for Viscose, and 0.86 €/kg for polyester (Emerging Textiles, 2020)[2].

Novel Sources of Cellulose and Nanocelluloses

In recent years, several nanocelluloses (NC), from microbial and plant sources, have been tested as a source of textile fibers. The interest in NCs is essentially focused on taking advantage of their higher crystallinity, since they promote great mechanical resistance (Nunes, 2014). NC is not a single material type but rather a family of materials with very distinct features, mostly due to different sources and preparation methods (Clemons, 2016).

Bacterial Nanocellulose

An alternative to wood/plant cellulose is bacterial nanocellulose (BNC) (**Figure 2**), a homopolysaccharide extruded by Gram-negative species of the genera *Komagataeibacter*, *Acetobacter*, *Rhizobium*, *Agrobacterium*, *Pseudomonas*, *Salmonella*, *Alcaligenes*, and *Sarcina*, the only Gram-positive bacterial genus (Jonas and Farah, 1998; Dourado et al., 2016b). Different bacteria produce cellulose with distinct morphology, structure, properties, and yields (Wang J. et al., 2019). To obtain high yields of BNC, it is necessary to use the highest cellulose producer species, such as *Komagataeibacter xylinus* (Dourado et al., 2016b). In addition to using high BNC producers, other approaches toward improving the production of BNC include the use of advanced reactors, complex culture media or even the development of cell-free enzyme systems (Ul-Islam et al., 2020).

The BNC biosynthesis was first observed in kombucha, a fermented beverage produced by a symbiotic colony of bacteria and yeast, where a cellulose film is weaved on the culture media-air interface. It was first reported in Brown (1886), who identified a film with a structure chemically equivalent to that of plant cellulose. BNC consists of <100 nm ribbon-shaped fibrils, with 7–8 nm wide nanofibrils randomly aggregated into bundles, without lignin or hemicellulose (Gorgieva and Trček, 2019).

Bacterial nanocellulose has a chemical structure identical to that of plant cellulose. Linear homopolymer of glucose monomers are linked by β-(1→4) glycosidic linkage with the chemical formula (C6H10O5)*n*. Nevertheless, it has different macromolecular structure and properties (Ullah et al., 2019). The polymerization degrees are within 2000–6000 for BNC and 13,000–14,000 for plant cellulose, decreasing during pulping and purification. The unbranched chains of cellulose are held together through strong intra- and intermolecular hydrogen bonds to make the elementary fibers and the supramolecular structure (Choi and Shin, 2020; Fang et al., 2020). This structure possesses exclusive features, such as high mechanical strength, water-holding capacity, dimensional stability, crystallinity, biocompatibility, and biodegradability (Picheth et al., 2017). Given these features, numerous applications of BNC have been studied: in the biomedical field as a wound dressing, for tissue regeneration/substitution, drug delivery systems, biosensors and cancer diagnosis; in the textile and paper industries for fiber composites and coatings; in the food and cosmetic industries as an emulsifier and viscosifier (Klemm et al., 2005; Chawla et al., 2009; Müller et al., 2013; Nimeskern et al., 2013; Lee et al., 2014; Shi et al., 2014; Rajwade et al., 2015; Ul-Islam et al., 2019; Amorim et al., 2020; Anton-Sales et al., 2020; Cabañas-Romero et al., 2020; Farooq et al., 2020; Liu et al., 2020; Nanollose, 2020). The main application is still as a food item known as

---

[2] https://emergingtextiles.com/

FIGURE 2 | BNC membrane before **(A)** and after **(B)** purification.

nata de coco, mostly produced and consumed in Asian countries (Dourado et al., 2016a).

Bacterial nanocellulose can be produced through static or agitated cultures (Wang J. et al., 2019), most studies being carried out using the former (Zywicka et al., 2015). In this method, BNC is produced in containers filled with nutrients and incubated for 1–14 days, at 28–30°C and pH 4–7 (Wang J. et al., 2019). The efficiency of BNC production in stationary cultures is strongly connected with the air–liquid surface area (given that *Komagataeibacter* strains are mandatory aerobes), where it is produced as a hydrogel sheet containing around 99% of water (Wang J. et al., 2019).

To achieve industrial scale production, alternative fermentation technologies have been studied, using specific fermentation media and overproducing mutant strains include agitated and air-lift bioreactors, membrane reactors and horizontal bioreactors. The idea behind is that the agitated/shaking culture facilitates the oxygen delivery to bacteria during cultivation (Wang J. et al., 2019). Agitation and aeration leads to the formation of fibrous suspensions, which limits BNC applications and favors cellulose-negative mutants to control the population (limiting the cellulose yield), in addition to requiring high stirring power (as the viscosity of the suspension is too high) (Czaja et al., 2004; Huang et al., 2014; Rodrigues et al., 2019; Wang J. et al., 2019).

The textile fibers production amounts to 105.6 million tons per year, worldwide (Garside, 2019). The current BNC global production is far below this magnitude and confined to small scale production units (Dourado et al., 2016a; Phisalaphong et al., 2016; Piadozo, 2016). BNC's production costs are generally considered very high, preventing the scale of production from increasing to industrial levels. Indeed, *nata de coco* costs around 50–80$US, per kg (dry weight equivalent). The high cost of the fermentation medium has been pointed out as one main difficulty for the large-scale production of BNC. This may be overcome by using residues from the food industry as a low cost medium, which in addition to reducing the cost of production also helps to solve environmental problems related to waste disposal (Ul-Islam et al., 2020). However, according to other authors, the impact of the nutrients on the final cost is not so relevant, and the use of residues from the food industry may lead to more heavily charged wastewaters, hence more expensive to treat (Dourado et al., 2016a). Another big difficulty lies on the low BNC yield. In order to increase the yield of BNC produced, better strains are required, either isolated from nature or modified by genetic engineering techniques (Zhong, 2020). It must also be recognized that a comprehensive assessment of the very large scale industrialization potential of BNC remains to be accomplished, therefore its potential as a sustainable alternative for the textile industry cannot be fully ascertained at present (Choi and Shin, 2020).

Plant Nanocelluloses

The hydroxyl groups on one cellulose chain bond with the other to develop rigid and stable molecules, giving the plant stiffness and strength. The hydrogen bonding between cellulose chains makes it insoluble in water (Thomas et al., 2020). Fibrils are formed by joining cellulose molecules together. In turn, fibrils agglomerate into bundles, which the plant uses to form the cell wall combined with hemicelluloses and lignin (**Figure 3**; Lundahl, 2018). The cellulose fibrils morphology demonstrates a mesh-like structure (Thomas et al., 2020).

Nanocelluloses (NC) can be produced by top-down approaches, i.e., the dismantling of fibers by chemical, enzymatic, or mechanical methods in case of plant NC, or by bottom-up routes for BNC (Charreau et al., 2020). Plant NC is generally categorized in cellulose nanofibers (CNFs) and cellulose nanocrystals (CNCs) (Amorim et al., 2020). The final chemical and physical properties of NC depend directly on the source and manufacture conditions (Kargarzadeh et al., 2017). NCs have characteristics such as high strength and stiffness, low density, biodegradability, high surface area, and low thermal expansion, which led to much research and innovation during the last two decades. Both CNC and CNF have applications as composite materials, paper and board industry, adsorbent products, food and beverages, paints and coatings, adhesives, packaging, oil and gas, electronics, and medical, pharmaceutical, and cosmetic product (Charreau et al., 2020).

Different raw materials can be used to obtain NCs such as coconut husk fiber, mengkuang leaves (*Pandanus tectorius*), cotton, *Agave tequilana*, barley wastes, tomato peels, garlic straw residues, forest residues, corncob residue, *Gigantochloa scortechinni* bamboo culms, industrial waste cotton, cassava root bagasse and peelings, sugar palm fibers (*Arenga pinnata*), corn straw, and sago seed shells (Ventura-Cruz and Tecante, 2019). The raw material needs to be pre-treated to remove lignin and hemicellulose by milling, pulping and bleaching. CNCs, also named cellulose whiskers, nanowhiskers, or nanorods, are manufactured by transverse cleavage of cellulose using strong acids such as sulfuric and hydrochloric under defined conditions

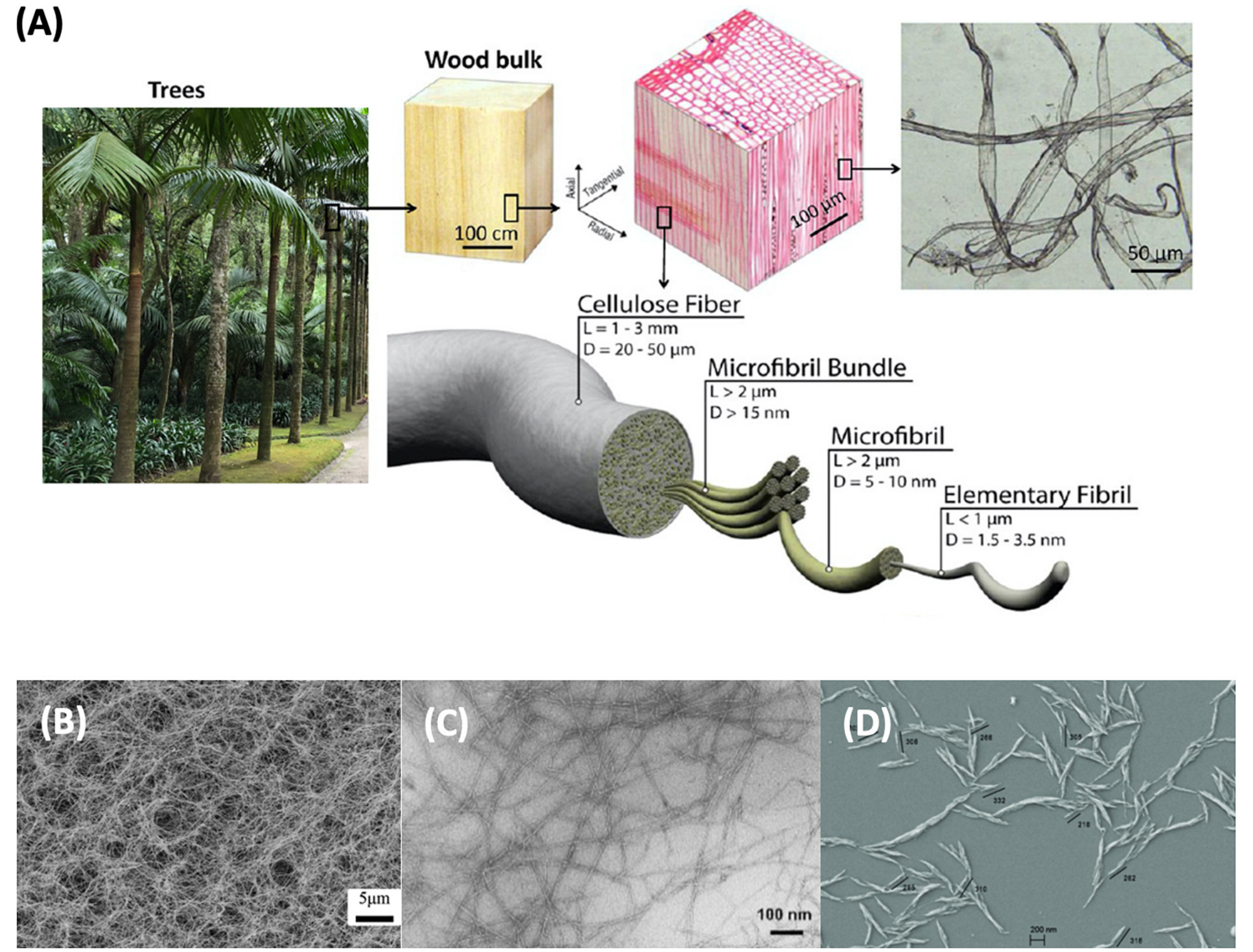

FIGURE 3 | (A) Hierarchical structure of wood fibers: Reprinted (adapted) with permission from Zhu et al. (2013). Copyright (2013) American Chemical Society. Comparison microscopic image of; **(B)** bacterial nanocellulose (Li et al., 2017): Published by The Royal Society of Chemistry, **(C)** nanofibrillated cellulose: Reprinted (adapted) with permission from Saito et al. (2007). Copyright (2007) American Chemical Society and, **(D)** nanocrystalline cellulose (Anžlovar et al., 2018).

of temperature, agitation, and time (Clemons, 2016; Charreau et al., 2020). CNC have a nanosized distribution: a diameter of 4–55 and 90–400 nm in length (Zinge and Kandasubramanian, 2020). After acid hydrolysis, CNC is obtained following washing, filtration/centrifugation, and dialysis, to take out the remaining acid (Charreau et al., 2020). Due to CNC higher crystalline structure, it has less flexibility than CNF (Zinge and Kandasubramanian, 2020). Currently, CNC is produced in commercial quantities of 2–260 ton/year (Charreau et al., 2020).

Cellulose nanofibers, also called cellulose nanofibrils or nanofibrillated cellulose, are obtained by mechanical disintegration (Amorim et al., 2020). CNF are cellulose structures of high aspect ratio bearing crystalline and amorphous regions. Although CNF isolation is associated with mechanical destructuring methods (pressure, cavitation, shear, and impact forces), the high energy consumption needed has led to the integration of pre-treatments to facilitate further fibrillation (Charreau et al., 2020). A common pre-treatment uses a 2,2,6,6-tetramethylpiperidine-1-oxy radical (TEMPO) catalyst to mediate the oxidation of native celluloses, that lowers the energy needed to fibrillate (Clemons, 2016). The product obtained is a translucent firm gel. CNF can be applied in absorbent materials, for the reinforcement of composites, as a rheology modifier agents and, mainly in papermaking, namely of paperboard, tissue, deodorant sheets, and cosmetics sheets. CNF is produced in commercial quantities of 24-560 ton/year (Charreau et al., 2020).

TECHNOLOGIES FOR THE PRODUCTION OF CELLULOSE TEXTILE FIBERS

Regenerated Cellulosic Fibers

Regenerated cellulose fibers are obtained by dissolving cellulose, pure or derivatized, from wood pulp or plant fibers. As the length of wood pulp fibers is too small for textile use, they need to be processed using continuous spinning and a regenerating technology (Navard, 2013). In the derivatization step the structure of the starting cellulose is changed, forming an intermediate compound such as sodium xanthate or acetate derivatives. Then these intermediate compounds are prepared and dissolved, along with the regeneration of the fiber (Woodings, 2001). The improvement of cellulose dissolution is a prevailing goal. The cellulose structure is transformed in different ways depending on the type of solvent and treatment conditions. Cellulose solvents can be divided into two groups: non-derivatizing–whereby the polymer is dissolved by intermolecular interactions; derivatizing–where the dissolution process is combined with the formation of unstable ether, ester or acetal derivatives. Both groups include aqueous and non-aqueous solvents (Heinze and Koschella, 2005). Presently, the most used industrial methods for dissolving cellulose pulp are the Viscose, Cuprammonium, and Lyocell methods.

Regenerated cellulose was the first man-made fiber utilized in the textile industry, in the beginning of its development, in the early twentieth century. These fibers have a smooth and lustrous silk-like aspect, combined with the outstanding water absorption capacity of cotton. In 1924 the generic name Rayon was accepted by the U.S. Department of Commerce and some industrial corporations to label RCF that include Viscose, Acetate, Lyocell, Modal, and Cupro (Chen, 2015; Textile Exchanges, 2020).

With an annual production volume of around 7.1 million tons in 2019, the global production volume of RCF has more than double since 1990. RCF have a market share of about 6.4% of the total fiber production volume and is expected to increase in the coming years. Viscose is the dominant RCF with a market share of around 79% of all RCF and a production volume of around 5.63 million tons in 2019. Acetate has a market share of around 13% of all RCF with a manufacture of roughly 0.95 million tons in 2019 but it is largely utilized for non-textile applications. Lyocell ranks third most utilized RCF after Viscose and Acetate in 2019. It had a market share of around 4.3% and a production volume of 0.3 million tons, being this fiber expected to grow faster than the others RCF. Using a production process quite similar to that of Viscose, Modal fibers had a market share of around 2.8% of the total RCF market in 2019 with a production of around 0.2 million tons. Cupro has a market share of less than 1% of the total RCF market. There is only one provider of Cupro, manufacturing 17,000 tons in 2019 (Textile Exchanges, 2020).

Regenerated cellulose fibers are being used in the most diverse materials, from sportswear to health care textiles, alone or combined with other natural or synthetic fibers, thanks to their characteristic properties as tensile strength and smoothness (Karthik and Rathinamoorthy, 2017).

Viscose Rayon

The Viscose process is the world's most widely used method for producing RCF. The first patent on the Viscose method was granted to Cross and Bevan in 1893. Over the past 100 years, this process underwent many alterations, although the basic chemistry is still the same, which allowed Viscose to become one of the most widely used regenerated fibers (Wilkes, 2001; Thakur et al., 2017).

The process, shown in **Figures 4**, **5**, consists in suspending the pulp in NaOH and, after steeping for a specified period of time, shredding and aging. The viscosity of the pulp depends on the aging time. The aged pulp is then treated using carbon disulfide (CS_2) to form the orange-colored cellulose xanthate. Lastly, this derivative is dissolved in NaOH with a lower concentration, the starting stage of Viscose formation (Shaikh et al., 2012). The polymer is finally precipitated in acid, for simultaneous neutralization and regeneration of the cellulose using a wet-spinning equipment. Then, several steps of washing and drawing yield a regenerated fiber of pure cellulose (Olsson and Westman, 2013; Chen, 2015). Currently, carbon disulfide can be reused up to 70%, the remaining being converted into sulfuric acid (H_2SO_4), which is also recovered (Rana et al., 2014).

Despite being made from wood, the fiber production by Viscose process is known to cause significant environmental problems due to the high usage of chemicals, such as sodium hydroxide, producing sodium sulfate as a by-product. The life cycle of the Viscose process encompasses other impacts, associated to how reagents are produced and recycled, as well as the consumption of energy, the use of fossil fuel and deforestation (Shen et al., 2010).

Recently, the company Nanollose announced the development of a Viscose making process using BNC. This method transforms BNC into Nullarbor^{TM} Tree-Free Viscose fibers using manufacturing equipment compatible with those currently used by the industry (Jinzarli et al., 2019; Nanollose, 2020)[3].

Lyocell Rayon

The direct dissolution of cellulose (without derivatization) has been the object of research for many years. This process may also ease the manufacture of regenerated cellulose by omitting several steps (Perepelkin, 2007; Olsson and Westman, 2013). The technology of direct dissolution of cellulose is a simpler process, reducing the use of chemicals by ten times in comparison to the Viscose process. Also, a direct solvent is easier to recycle, since no byproducts are formed, resulting in a more environmentally friendly process (Olsson and Westman, 2013). However, the Lyocell production costs are higher than the Viscose, due to the high cost of solvent and the use of high temperatures for cellulose dissolution (Alam and Christopher, 2017).

History of Lyocell

Lyocell is the first successful technology of cellulosic fibers by direct dissolution, resulting in fibers with exceptional properties, making it a serious competitor to the Viscose process, since it is more environmentally friendly (White, 2001; Peng et al., 2017). Lyocell fiber has higher tenacity (especially wet tenacity), higher modulus, lower shrinkage, better thermal stability, higher crystallinity, and greater degree of orientation, than Viscose (Edgar and Zhang, 2020). The Lyocell fiber market is estimated to grow from 760 million € in 2016 to over 1.35 billion € by 2024 (Pulidindi and Chakraborty, 2016).

A patent describing the process of cellulose dissolution using *N*-methylmorpholine-*N*-oxide (NMMO) solvent was filled by Mcorsley (1981), In 1992, in Mobile Alabama, United States, the

---

[3] https://nanollose.com/

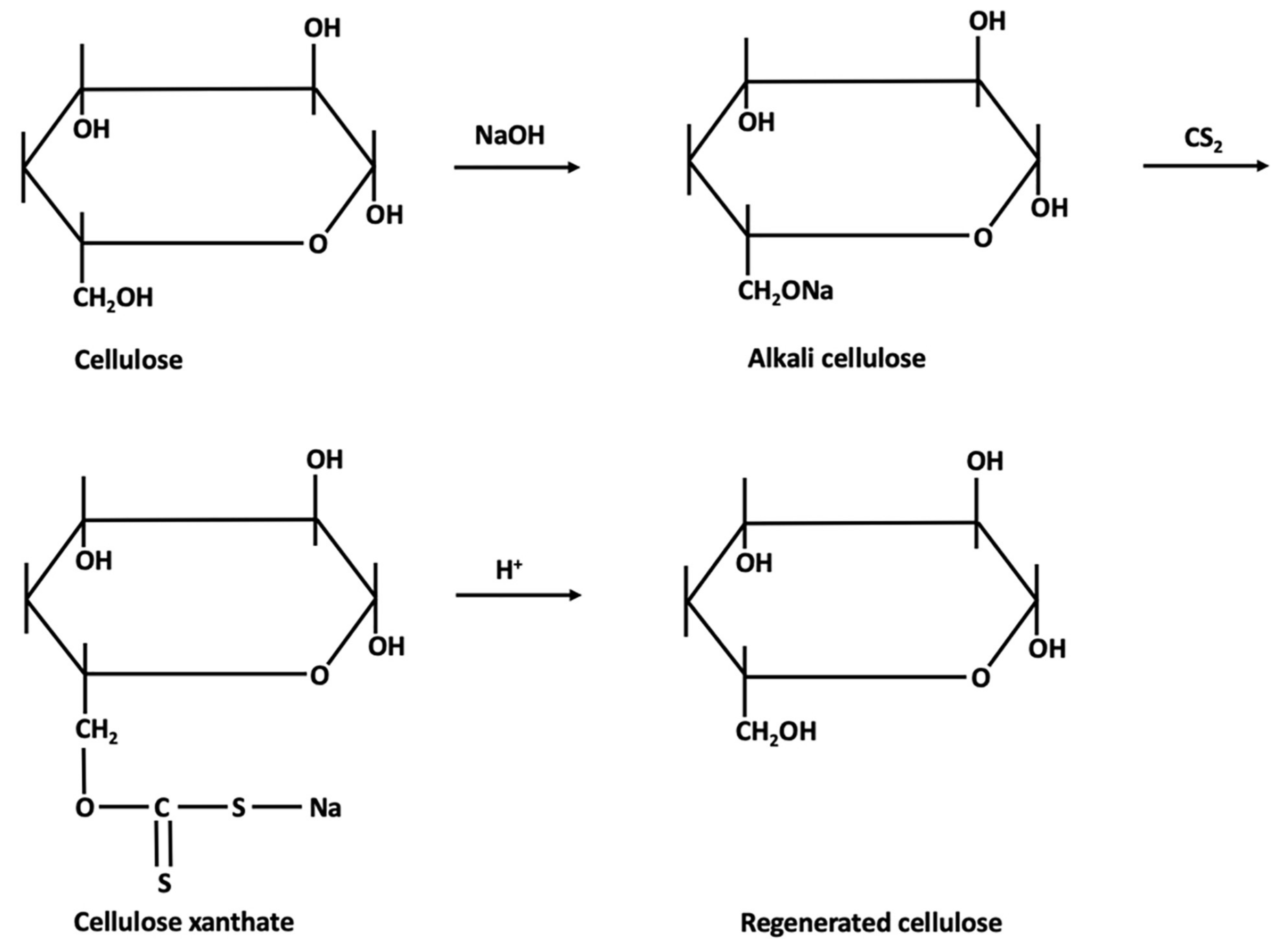

FIGURE 4 | Mechanism of Viscose fiber production [addapted from McKeen (2017), Rodgers and Waddell (2013)].

company Courtaulds, achieved the full commercial production with the trade name TENCEL® (Chen, 2015). Lenzing, an Austrian company, started the production of Lyocell fiber in 1990 with their first pilot plant. The full-scale production plant came into operation in 1997 and the fiber was called Lenzing Lyocell®. In 2004, Lenzing purchased the TENCEL® Group (Perepelkin, 2007). Today, Lenzing is the world's biggest Lyocell fiber producer (Rana et al., 2014). Other companies have emerged with new brand names for fibers obtained using this technology, as Alceru (TITK Rudolstadt), Newell (AkzoNobel), Acelon (Greencell), and Excel (Grasim) (Sayyed et al., 2019).

The solvent and phase diagram

N-methylmorpholine-*N*-oxide, commonly known as NMMO, is the most used of all non-derivatizing cellulose solvents, due to its capacity to directly dissolve high concentrations of cellulose, while preserving the chemical properties of the polymer. The possibility of recycling up to 99.7% of the solvent, makes the process economically viable and more environmentally friendly (White, 2001; Olsson and Westman, 2013).

N-methylmorpholine-*N*-oxide is completely soluble in water and very hygroscopic. The polarity of the N–O bond also results in a great ability to form hydrogen bonds. There are three types of NMMO: anhydrous NMMO, monohydrate NMMO ($NMMO{\cdot}H_2O$) with 13.3% (w/w) H_2O, and disesquihydrate NMMO ($NMMO{\cdot}2.5\ H_2O$) with 28% (w/w) H_2O (Wikandari et al., 2016). NMMO's oxygen can form two hydrogen bonds with hydroxyl groups from water or cellulose (**Figure 6**), the competition between water and cellulose for these hydrogen bonds, being the central feature of this dissolution process (Maia et al., 1981).

Since NMMO is thermally unstable, the dissolution of cellulose in NMMO at high temperatures is accomplished in well-controlled environment. NMMO degrades at temperatures higher than 120°C. Due to its reactivity, stabilizers should be added at the start of the dissolution process, most commonly propyl gallate (Rosenau et al., 2002).

The degradation of NMMO and following side reactions may include *N*-methylmorpholine, morpholine, and formaldehyde (Olsson and Westman, 2013). Some reactions are started by transition metal ions such as iron and copper and that's why these should not be used in this process (Klemm et al., 2005). Mechanical energy facilitates the rupture of cellulose-cellulose intermolecular bonds, favoring the interaction with

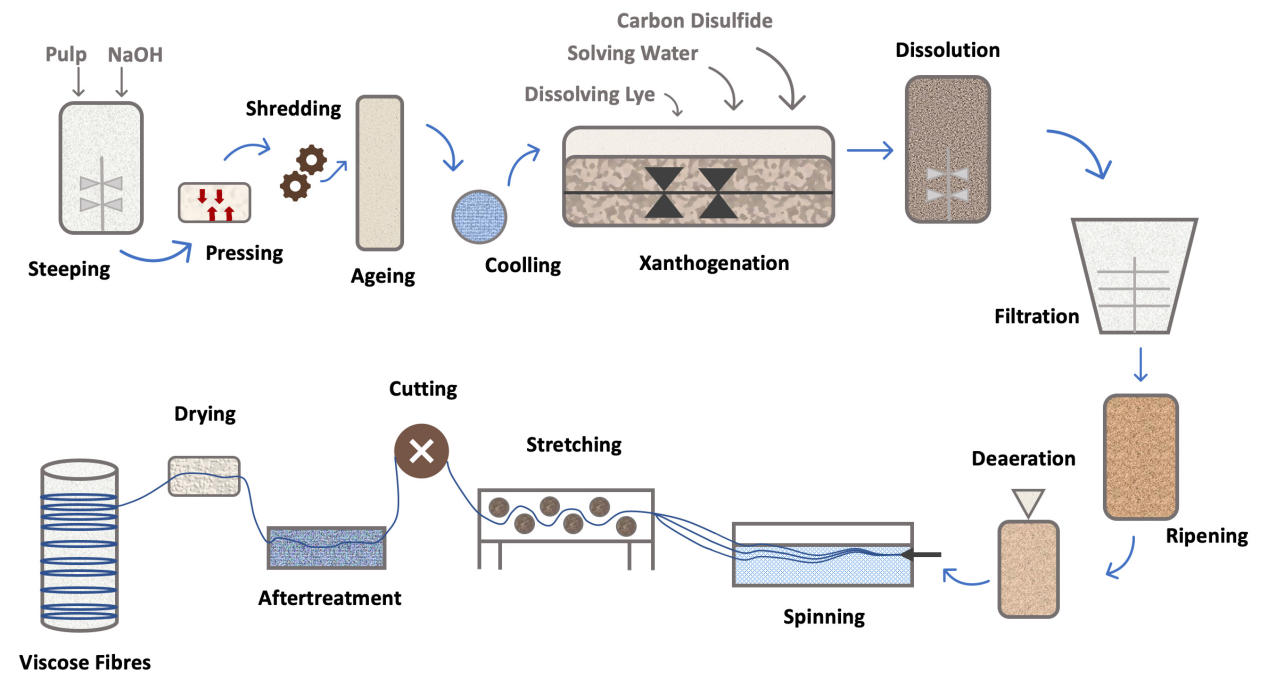

FIGURE 5 | Schematics of Viscose fiber production [addapted from Alagirusamy and Das (2015), Sayyed et al. (2019)].

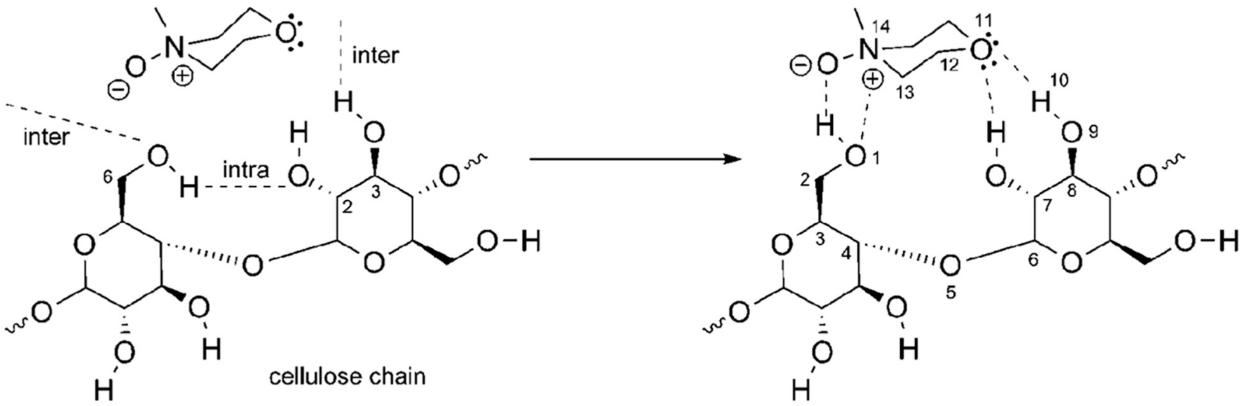

FIGURE 6 | *N*-methylmorpholine-*N*-oxide–cellulose dissolution mechanism: Reprinted with permission from Pinkert et al. (2010). Copyright (2010) American Chemical Society.

NMMO. Furthermore, the apparent viscosity decline with shear stress due to cellulose alignment, as anticipated for non-Newtonian polymer solutions. Cellulose concentration and degree of polymerization (DP) also influence the viscosity (Olsson and Westman, 2013).

The NMMO-water-cellulose phase diagram (**Figure 7**), shows the relative amounts of H_2O and NMMO required for cellulose dissolution to occur. NMMO–water mixtures are direct solvents for cellulose in its monohydrate state. With a higher amount of water, cellulose will not dissolve, since a competition for NMMO takes place between cellulose and water, the interaction with the latter being favored. Thus, NMMO only links with cellulose when there is shortage of water molecules (Biganska and Navard, 2003). The process (described in more detail in the next section) starts with using a high water content, to induce the swelling of the cellulose fibers. An homogeneous pulp is produced containing, e.g., 35% of H_2O, 9% cellulose, and 56% NMMO (point C in **Figure 7**). Then, the excess of water is removed under vacuum (point B). After further water removal, dissolution occurs at point A with a 14% cellulose, 10% H_2O, and 76% NMMO (Golova et al., 2010).

Dissolution process

The first industrial system used to dissolve cellulose with NMMO (**Figure 8**), involved the initial cellulose swelling. A cellulose pulp must first be milled into small particles to improve the

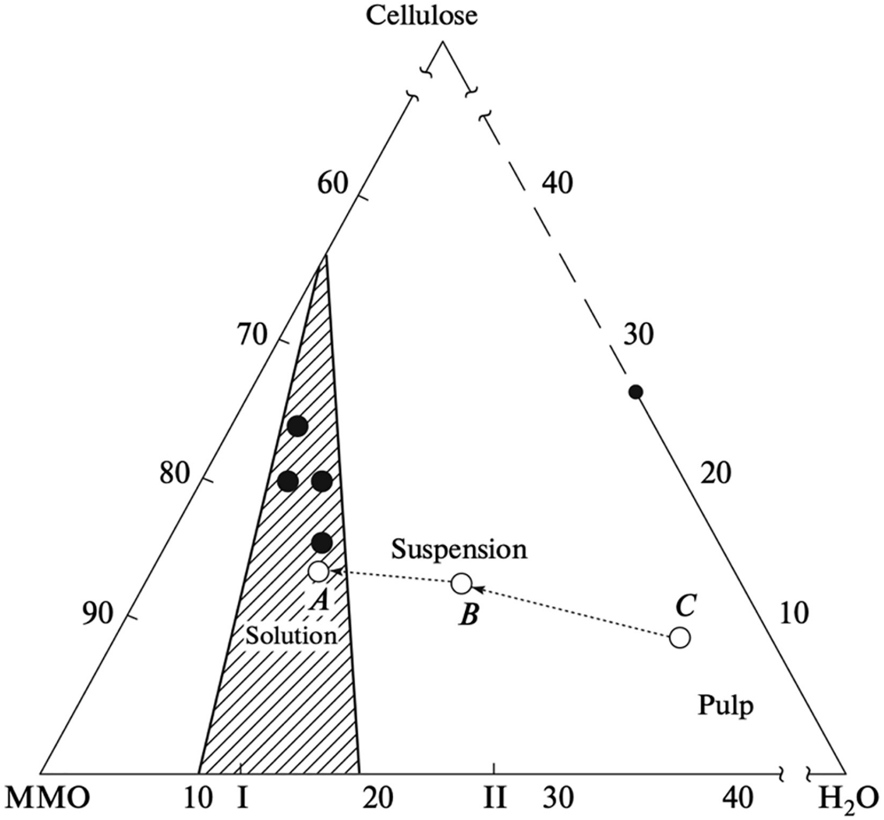

FIGURE 7 | Schematic phase diagram of the cellulose–MMO–H_2O system: (line CBA) variation in the composition of the system during cellulose dissolution via the traditional MMO process; (closed circles) composition of the system during cellulose dissolution via the solid-phase MMO process; (I) MMO monohydrate and (II) MMO 2.5-hydrate (Golova et al., 2013).

surface contact area with NMMO. Then it is mixed with NMMO containing 20–30% of water (Zhang S. et al., 2018). The amount of pulp fed to the mixer has to be quantified, to control the cellulose content. Mixing is done at 70–90°C, with high-speed refiners, to further break down the pulp, improving the solvent wetting. The resulting swollen pulp is then heated to 90–120°C, under vacuum, to remove excess water, yielding a clear dark amber-colored solution, to a final cellulose concentration within 10–18% (m/m) (White, 2001)The use of low pressure reduces the temperature required for water evaporation, so the NMMO does not undergo exothermic degradation (White, 2001). After dissolution, impurities such as undissolved pulp fibers are filtered. The mixture is then extruded and spun through an air gap into a spin bath with a polar liquid, like water or alcohol. These coagulation agents are miscible with NMMO, removing it from the cellulose solution (Biganska and Navard, 2011). This process is called dry-jet wet-spinning and consist of thousands of small holes through which the solution is extruded into fibers (White, 2001). Various other technologies are used in fiber spinning dope such as kettle-type dissolution, twin-screw extruder dissolution, vacuum mixed propulsive dissolution and vacuum membrane propulsive dissolution technology. The first one is intermittent, the others are continuous. Currently, the most used technology in industrial manufacturing is continuous vacuum film propulsive dissolution technology (Jiang et al., 2020).

To facilitate the cellulose dissolution process, various pre-treatment methods have been researched such as enzyme treatment, to enhance reactivity, microwave heating process to reduce crystallinity, mechanical blending technique, enzymatic peeling treatment, ball or vibration milling, steam explosion, and electron beam irradiation. However, industrially, most of the these are technically and economically non-viable (Sayyed et al., 2020). Pre-swelling at temperatures from 30 to 75°C lowers the pulp's crystallinity and forms a homogeneous solution with lower time and power consumption during the dissolution process. This makes Lyocell process more energy-efficient and sustainable (Sayyed et al., 2020).

The DP of cellulose pulp influence the mechanical strength of Lyocell fiber. The higher DP, the superior the mechanical strength; yet, a very high DP may result in a poorer solubility and an increase in the viscosity of spinning dope. The balance between DP and the solubility of dissolving pulp has a substantial impact on the spinning process and the mechanical properties of fiber (Jiang et al., 2020). Due to the difference in the DP between BNC and plant cellulose, the use of the same concentration may yield different results, given the large difference in viscosity. For example, a 6% (m/m) solution of BNC (DP 2000) has a viscosity

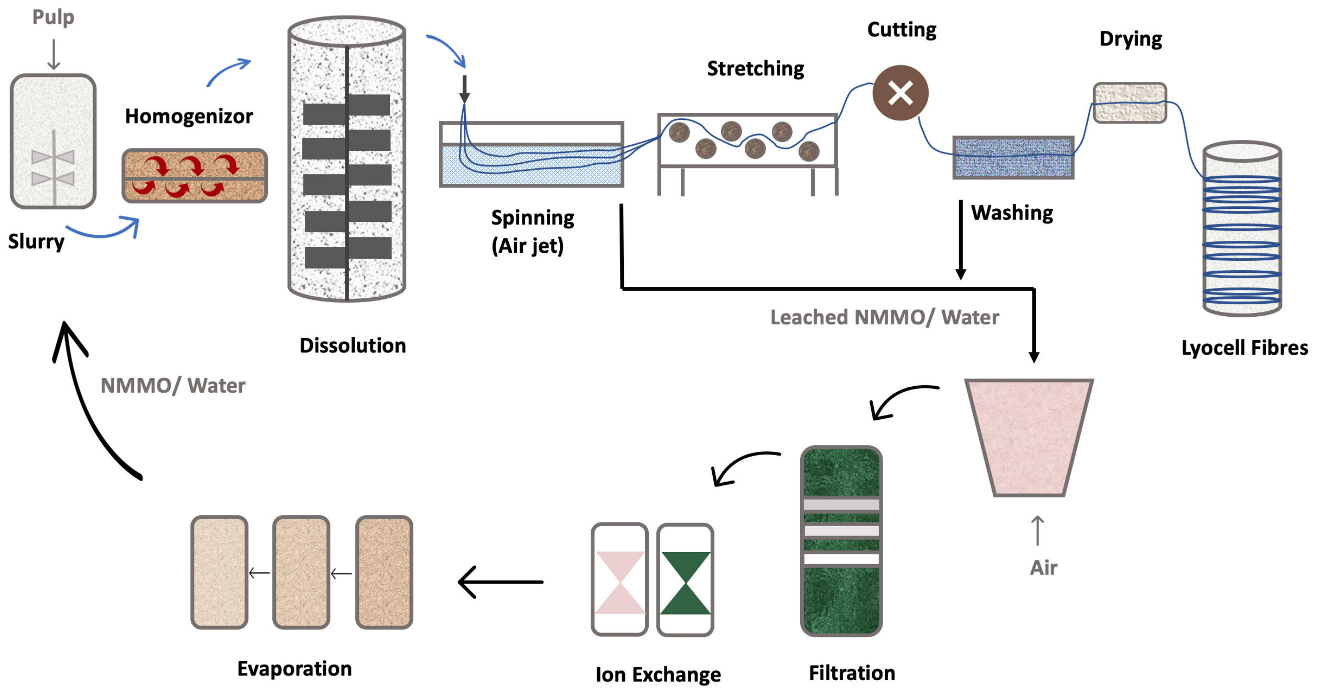

FIGURE 8 | NMMO based lyocell process [addapted from Jiang et al. (2020), Sayyed et al. (2019)].

10^3 Pa.s, which in the case of wood cellulose (DP of 600) is achieved only at 18% (m/m) (Makarov et al., 2019).

Bacterial nanocellulose Lyocell fibers have been produced by Gao et al. (2011). In their work, water was added to NMMO at 13.3% m/m and the mixture was heated at 90°C for 30 min. Then BNC powder was added (7% m/m) and the mixture was heated at 80°C for 12 h. The solution was extruded and BNC filaments were formed. The regenerated BNC fibers had a cellulose II crystalline structure, lower degree of crystallinity, smaller crystalline sizes, and better thermal stability than native BNC. This regenerated BNC fibers had a tensile strength of 0.5–1.5 cN/dtex and extension at break of 3–8% (Gao et al., 2011).

A different process for Lyocell fiber production, using the NMMO-water-cellulose solid-phase system at a concentration of cellulose under 25% (m/m), was developed at the All-Russian Scientific-Research Institute of Polymer Fibers (Golova et al., 1992; Golova, 1996). The method uses high-melting hydrate forms of NMMO, which better dissolves cellulose, substantially accelerating the process. The process starts with a solid-phase activation of cellulose by NMMO with a water content of 8% (m/m) or less. Cellulose dissolution occurs under triaxial compression, shearing, and forced plastic flow. Then, under temperature (105°C) and shear rate, the cellulose dissolves into a highly homogeneous and concentrated solution (Golova et al., 2013). This method has been successfully used with BNC fibers with a DP of ~1500 and a solid-phase activation of BNC and NMMO (water $<$ 10%); the mixture was heated at 120°C until a fluid solution was obtained (Makarov et al., 2019). The authors claim that the (mechanochemical) activation is mandatory for a homogeneous solutions to be obtained, as no swelling occurs. Concentrations of up to 8% of BNC were used, 6% being optimal. The fibers were spun by dry-jet wet-spinning into a water coagulation bath. The mechanical properties of the obtained fibers are shown in **Table 1**, along with other synthetic, natural and regenerated (man-made) cellulosic and organic synthetic fibers. The mechanical properties of Lyocell produced with BNC are similar with data for Viscose and Lyocell fibers (Makarov et al., 2019, 2020).

Nonetheless, the Lyocell process has some limitations related to NMMO's intrinsic properties. The N–O moiety blocks the application of redox-active agents, whereas the cyclic ether structure is susceptible to thermal runaway reactions, requiring stabilizers. The side reactions and considerable byproduct formation can cause the degradation of cellulose, a temporary or permanent discoloration of the spun fibers, a drop in product performance, a relevant decomposition of NMMO and higher consumption of stabilizers. So, alternative direct solvents for cellulose dissolution would be highly attractive for environmental and economic reasons (Rosenau et al., 2001; Hummel et al., 2015).

Cellulose Acetate

Although not so widely used, another method of producing fibers is available whereby cellulose acetate is obtained. Cellulose acetate is the acetate ester of cellulose. It was first manufactured at commercial scale by Celanese in 1923 (Sayyed et al., 2019) by reacting a cellulose pulp with acetic anhydride, to form acetate flakes (**Figure 9**). Then, these flakes are dissolved in a solvent and filtered to produce the spinning cellulose dope solution

TABLE 1 | Mechanical properties of different fibers.

	d (μm)	Young's Modulus (GPa)	Tensile Strength (MPa)	Elongation (%)	References
BNC Lyocell	10.3–15.4	8.6–10.1	420–495	5.5–6.5	Makarov et al., 2019
Ioncell	–	30	700–800	–	Sashina, 2019
Lyocell	9	22–31	472–624	6.8–13.7	Gindl et al., 2008; Manian et al., 2018
Viscose	10.5	9.3–11.6	220–340	8–23.5	Gindl et al., 2008; Manian et al., 2018
Cotton	10–27	8	600	7	Bunsell, 2018
Wool	15–40	2	170	35	Bunsell, 2018
Flax	15–20	65	650	1–3	Bunsell, 2018
Silk	12	8	400	25	Bunsell, 2018
Hemp	45	50	500	1–2	Bunsell, 2018
Jute	69	35	350	2.5	Bunsell, 2018
Polyamide 66 (Nylon 66)	20	<5	1000	20	Bunsell, 2018
Polyester (PET)	15	15	800	15	Bunsell, 2018
Kevlar 49	12	135	3000	4.5	Bunsell, 2018

(Ertas and Uyar, 2017). The cellulose dissolution with acetic acid and acetic anhydride is done in the presence of sulfuric acid. Partial hydrolysis of cellulose acetate in then performed in a controlled manner, to remove the sulfate and a sufficient number of acetate groups, to yield a product with wanted properties. The cellulose dope solution is then extruded through a spinneret and the yarns are produced by solvent evaporation. This process for producing acetate fiber is made using the dry-spinning method (Sayyed et al., 2019), and is mainly used to produce cigarette filters but also for drug delivery and nanofibers. These cellulose acetate fibers have limited use in the textile industry because of their poor strength, poor abrasion resistance and poor thermal retention (Watabe et al., 2018).

Ionic Liquids

Research on the use of Ionic liquids (ILs) for the direct dissolution of cellulose, first used in 2002, has shown promising results. A new class of next-generation RCF named Ioncell have recently been developed utilizing a novel IL solvent 1,5-diazabicyclo[4.3.0]non-5-enium acetate ([DBNH] [OAc]) (Michud et al., 2016). Ioncell fibers have been shown to exhibit better mechanical properties than all previously known ones, namely, their tensile strength reaches 0.7–0.8 GPa and elastic modulus of 30 GPa (Wanasekara et al., 2016; Sashina, 2019). Several garments have been produced and commercial production is expected by 2025 (Ioncell, 2020)[4]. The IL process is carried out using the Lyocell technology since the cellulose solution is spun according to the NMMO-based Lyocell method, in a dry-jet wet-spinning process where the filament go through an air gap and coagulate in a bath where the regenerated cellulosic fibers are formed (Sayyed et al., 2019).

Ionic liquids are liquids made-up of cations and anions, thus they can be designated as salts in the liquid state (Singh and Savoy, 2020). Overall, the dissolution process of cellulose in ILs is still not fully clarified (Hermanutz et al., 2019). The ILs ability to dissolve cellulose is due to small hydrogen bond accepting anions that can compete with the hydrogen bonding between the cellulose chains and cations that help increase the solubility (Andersson, 2018). ILs dissolves cellulose with no prior derivatization in concentrations of up to 300 g.L^{-1} and offer a potentially more environmentally friendly alternative to traditional processes (Hina et al., 2015; Wanasekara et al., 2016). These solvents are thermostable up to 300°C with a melting point up to 100°C. ILs practically do not have vapor pressure, and therefore do not pollute the atmosphere (Sashina, 2019). Due to their wide range of properties, they have been increasingly used in various fields of study such as biochemistry, engineering, physics, etc. as a green solvent. The properties of ILs can be modified depending on their application by altering the combination of cations and anions (Singh and Savoy, 2020).

Ionic liquids usually comprise imidazolium, pyridinium, or organic ammonium cations and anions such as chloride, bromide, or more complex structures such as hexafluorophosphate, trifluoromethyl sulfonate, bis(trifluoromethylsulfonyl)imide, and methylimidazolium chloride ([Amim]Cl) (Sayyed et al., 2019). ILs have been investigated either to dissolve or to create appropriate support for the functionalization of cellulose. For cellulose solubility, the counter anions with halide, such as the imidazolium type, have the best performance. One disadvantage with ILs with halide anions is their relatively high viscosities, which brings processing difficulties during dissolution (Isik et al., 2014). These ILs demonstrate good dissolution characteristics, allowing the production of cellulose dopes in concentration ranges that shows good spinnability (Sayyed et al., 2019). For industrial use, any IL selected for cellulose dissolution and processing has to match specific criteria for an economic process development: the IL should be easy to produce, recyclable in high amount (>99.5%), possess the lowest possible toxicity, should have literally no vapor pressure, a low melting point, a low propensity to side reactions and degeneration, have high dissolution capability for different pulp sources (Andersson, 2018; Hermanutz et al., 2019). To obtain concentrated cellulose solutions suitable for spinning, the researchers have tried to use ILs based on imidazolium, pyridinium and ammonium cations (Sashina, 2019). Currently, nearly thousand ionic liquids are described in the literature

---

[4] https://ioncell.fi/commercialization/

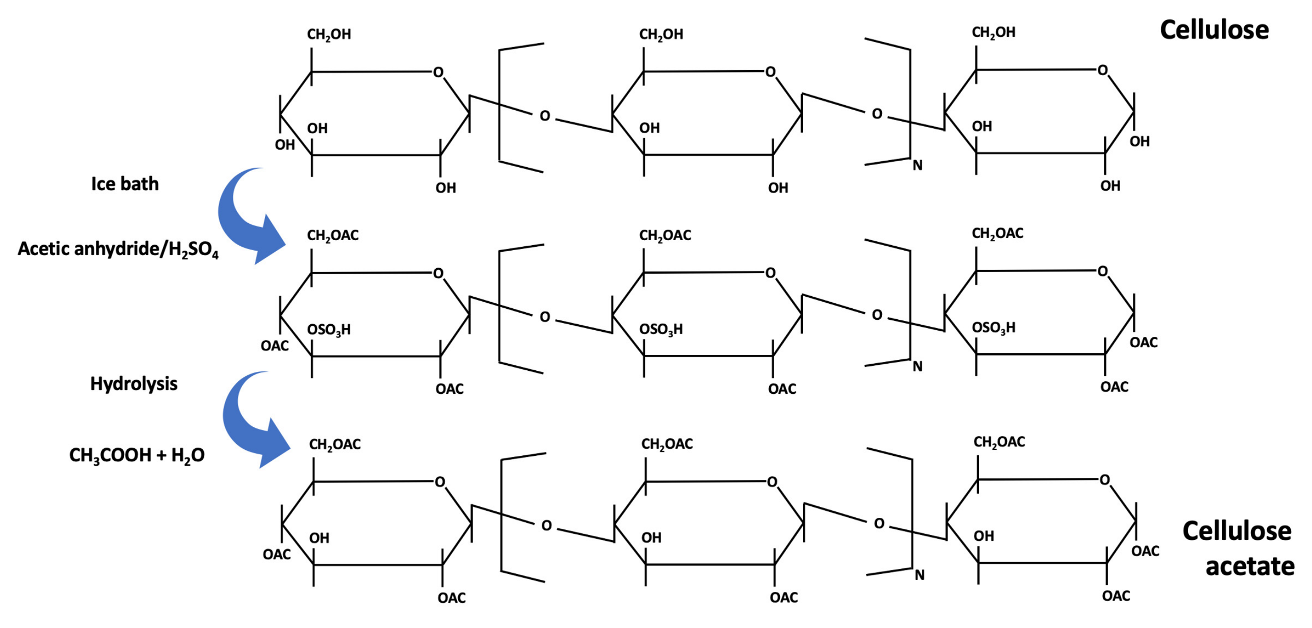

FIGURE 9 | Mechanism of the cellulose acetate preparation [addapted from Sayyed et al. (2019), Silva et al. (2017)].

(Meksi and Moussa, 2017; Wang H. et al., 2019; Zhang et al., 2019; Yang et al., 2020).

Filaments Without Solvents

Regenerated cellulose fibers have beneficial characteristics from both synthetic and natural fibers: they have uniform morphological, mechanical, and physical properties, as synthetic fibers. Also, they bear biodegradability, CO_2 neutrality, and low density of natural fibers. Still, their mechanical properties are lower than those of CNF (Hooshmand et al., 2015). To preserve the characteristics of CNF, several studies have been made to elaborate a system of filament production without solvents. Spinning CNF requires lower energy use and no harmful chemicals are used (Lundahl et al., 2017). Instead of dissolution, CNF are dispersed in water and spun into air or reusable organic solvents. This process was announced in 2011 and has since then progressed in the improvement of the fibers' mechanical properties and process scale-up (Iwamoto et al., 2011; Lundahl, 2018).

An isolated cellulose crystallite has a Young's modulus of up to 160 GPa and tensile strength of 6–7 GPa, exceeding those of carbon and Kevlar fiber in its longitudinal direction, while in the transverse direction a value of 8–57 GPa is observed (Wang et al., 2017). Thus, the mechanical performance of cellulose can be optimized when the crystallites are well aligned, a goal that can be accomplished by spinning (Lundahl, 2018). Wet and dry-spinning have to date been applied on CNF at laboratory scale, using a syringe pump, extruder, capillary rheometer, or 3D printer (Lundahl, 2018).

In the production of filaments, TEMPO oxidized CNF is used (Iwamoto et al., 2011) and extruded through a spinneret in a wet or dry-spinning process (**Figure 10**). In wet-spinning, a coagulation bath with acetone, water, ethanol, or $CaCl_2$ solution is used. The characteristics for the coagulants are miscibility with water, moderate polarity and hydrogen bonding ability (Iwamoto et al., 2011; Walther et al., 2011; Kim et al., 2019). The coagulant bath rapidly induces the generation of "a skin" on the surface of the CNF extrudate, stabilizing it against interfiber aggregation, to allow the formation of distinct macrofibers (Walther et al., 2011). In dry-spinning, the dope is pushed through the spinneret and the solvent is evaporated (Clemons, 2016). Independently of the spinning method, a high molecular alignment is induced in the drawing step, which is key to the high stiffness and strength of the fibers (Clemons, 2016).

Several parameters such as the spinning speed, inner diameter and length of needle, and drying temperature, affect the alignment of CNF and hydrogen bond formation between CFNs (Kim et al., 2019). In the first report of CNF filament production through a wet-spinning process, the influence of spinning rates (from 0.1 to 100 m/min) were studied. The highest speed rate resulted in filaments with better mechanical properties (Iwamoto et al., 2011). By using post drawing, more efficient alignment of the nanofibrils is achieved resulting in further improvement of the mechanical properties of the fibers (Walther et al., 2011). A wet-stretching process is used to induce high fibers orientation, improving their Young's Modulus from 8.2 to 33.7 GPa (Torres-Rendon et al., 2014). Various concentrations of CNF were tested, from 1 to 12%, being the higher ones processed through dry-spinning and the lowers by wet-spinning (Iwamoto et al., 2011; Hooshmand et al., 2015; Kim et al., 2019). In a study using a wet-spinning system 2% (m/m) CNF was considered the perfect solids content for achieving a high CNF alignment and filament strength, specifically, a Young Modulus of 37.5 GPa and Tensile Strength of 543.1 MPa (Kim et al., 2019). The mechanical properties of CNF filaments produced through the various processes are summarized in **Table 2**.

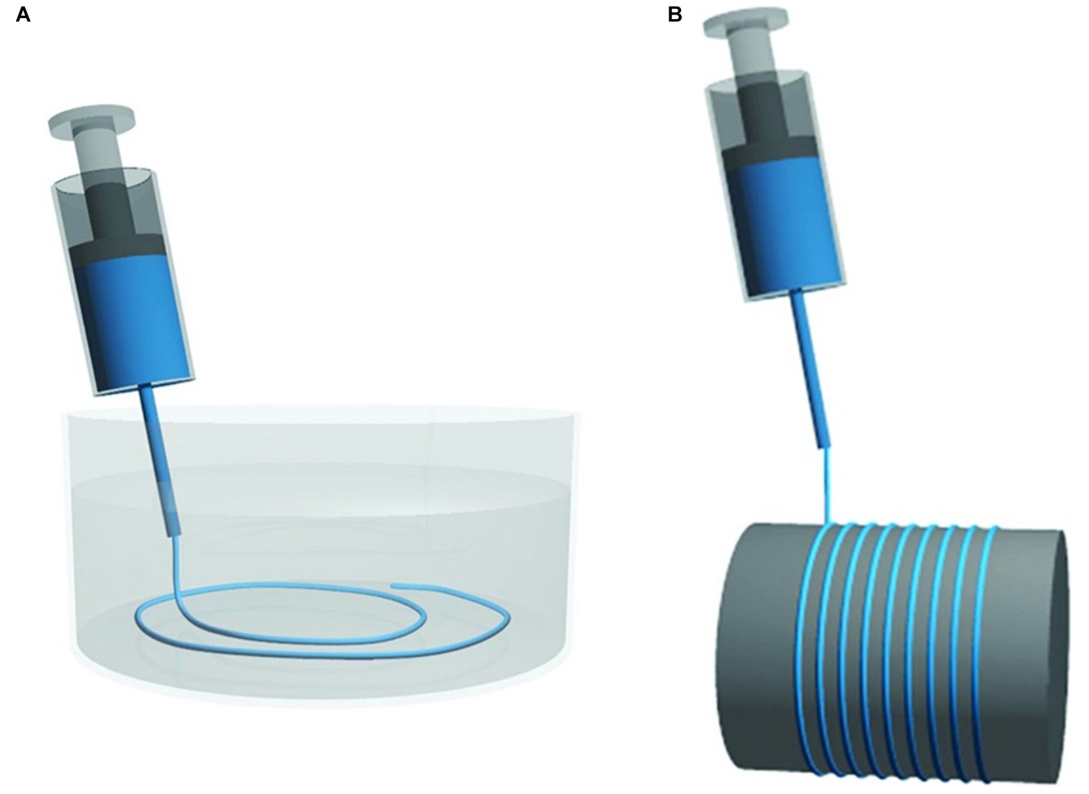

FIGURE 10 | Schematic illustrations of simplified systems for **(A)** wet-spinning and **(B)** dry-spinning. Reprinted (adapted) with permission from Lundahl (2018). Copyright (2018) American Chemical Society.

Flow focusing is another method for CNF filaments production, resulting in fibers with the strongest tensile performance, as compared to other methods (**Table 2**). The fibers are generated by aligning a CNF suspension in a double flow focusing channel through coagulation with acid, as shown in **Figure 11** (Mittal et al., 2018). The obtained filament has a Young's modulus of 86 GPa and tensile strength of 1570 MPa, superior to those known natural or synthetic fibers (Mittal et al., 2018). The specific strength of this CNF fibers also exceeds that of metals, alloys, and glass fibers.

TABLE 2 | Mechanical properties of different cellulose nanofiber filaments.

Spinning	Young's Modulus (GPa)	Tensile Strength (MPa)	Elongation (%)	References
Wet-spinning	23.6	321	2.2	Iwamoto et al., 2011
	22.5	275	–	Walther et al., 2011
	33.7	289	1.6	Torres-Rendon et al., 2014
	28.9	369.6	–	Geng et al., 2017
	23.9	383.3	6.6	Kafy et al., 2017
	37.5	543.1	3.7	Kim et al., 2019
Dry-spinning	12.6	222	3.6	Hooshmand et al., 2015
	6.5	100	–	Ghasemi et al., 2017
Flow focusing	86	1570	–	Mittal et al., 2018
BNC wet-spinning	16.4	248.6	3.8	Yao et al., 2017
BNC stretching	65.7	826	2.5	Wang et al., 2017

To our knowledge, the first and only company, to produce fibers without solvents, cellulose dissolution or any other harmful and complex chemical processes, is Spinnova Ltd. (Finland). The raw material is pulp from FSC certified wood. After mechanical pulping, the ground pulp passes through a single nozzle, where the fibers and fibrils rotate and align with the flow, providing a strong and elastic fiber network. The fiber is then spun and dried, suitable for spinning into yarn and then knitting or weaving into fabric (Salmela et al., 2016). The future goal is the recycling of the fibers for several times, minimizing the use of virgin materials. Spinnova fiber is now (2020) close to commercialization. The technology has been scaled up from a small pilot scale to an industrial pilot scale (Spinnova, 2020)[5].

Filaments based on aligned BNC nanofibers were prepared by wet-spinning and drawing procedures (Yao et al., 2017). This macrofibers showed Young's modulus of 16.4 GPa and tensile strength of 248.6 MPa using optimal process conditions (BNC 5.4 wt%; spinning rate 18.9 m/min), in which nanofibers displayed a high degree of alignment. The nanofiber suspension was prepared by TEMPO oxidation and then spun into an acetone coagulation bath (Yao et al., 2017). BNC Filaments without TEMPO oxidation were also produced. A super-strong and super-stiff cellulose

---

[5] https://spinnova.com/our-method/fibre/

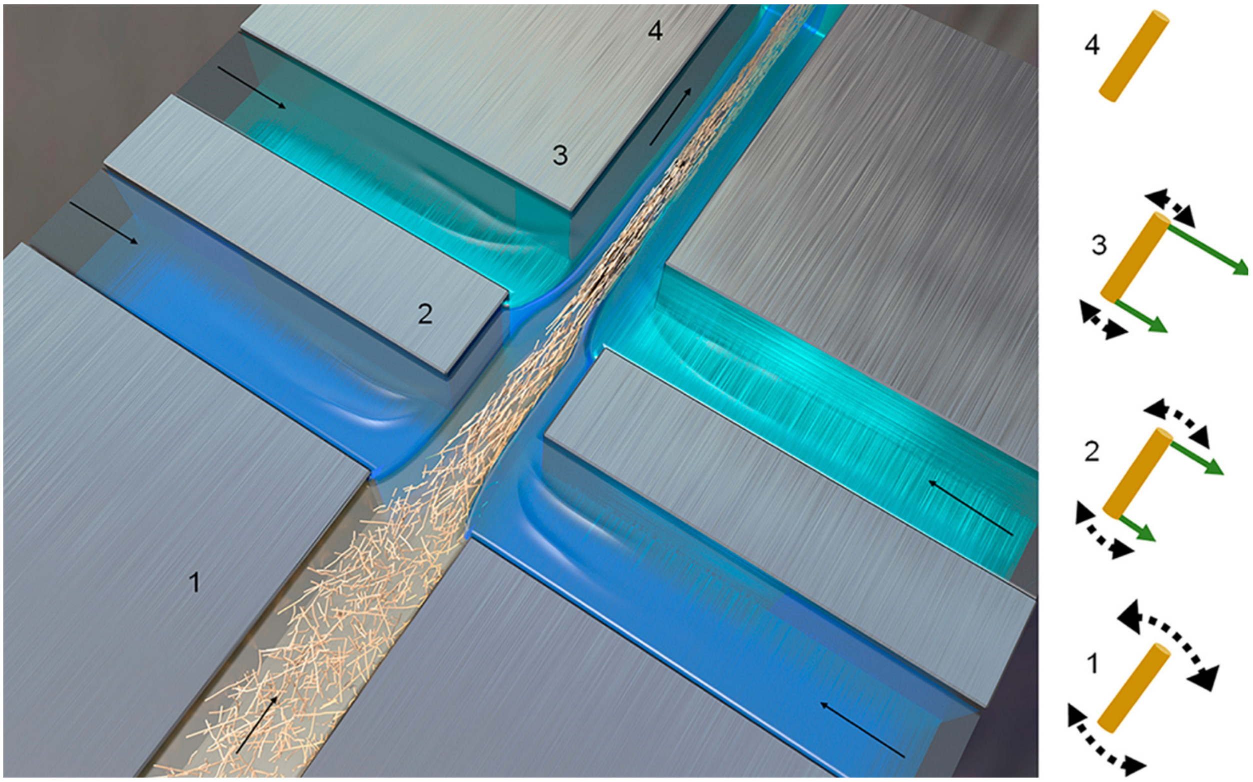

FIGURE 11 | Schematic of double flow-focusing channel used for CNF assembly (Mittal et al., 2018).

macrofibers was obtained from aligned ultralong BNC nanofibers via a facile and scalable wet-drawing and wet-twisting method (Wang et al., 2017). The macrofibers showed perfect integrity and well aligned structure, with a tensile strength of 826 MPa and Young's modulus of 65.7 GPa. BNC membranes were cut with a width of 7 mm and were wet-draw, becoming longer and thinner. From these, BNC macrofibers with diameters of around 300 μm were fabricated by wet-twisting and subsequently drying at 90°C for 12 h (Wang et al., 2017).

SUSTAINABILITY AND LIFE CYCLE ASSESSMENT

The rapid population growth and careless consumption of natural resources are causing serious global problems, such as air and water pollution and global warming. Fossil fuels exceeds 50% of the word's total energy sources and based on present water consumption, water resources are likely to decrease by 30% in 2050 (Kazan et al., 2020). In the last few decades, the environmental problems caused by humankind are reaching dangerous levels, being the search and adoption of more environmentally sustainable processes a mandatory paradigm change.

In this regard, environmental impact assessment gains a significant importance to rate the environmental effects of industrial activities. LCA can be used to evaluate a product, process or activity repercussions on the environment (Van Der Velden et al., 2014). "Cradle to gate" LCA studies take in account the raw materials and fuels used, as well all the processes involved until the product is delivered at the factory gate for further processing; "cradle to grave" involves, in addition to the later, post-manufacturing processes until the product (garment) end of life (Dibdiakova and Timmermann, 2014).

The global textile supply chain is complex, involving several stages (**Figure 12**). It is widely recognized that the textile industry is a major contributor to the environmental pollution and resource consumption. Among all, this industry is placed at fifth place in terms of the release of chemical oxygen demand (COD), implying large quantities of wastewater production and chemical consumption (Roos et al., 2018; Zhang Y. et al., 2018). Along COD, textile wastewaters may contain substances with a high biological oxygen demand (BOD), total suspended solids, oil and grease, sulfides, sulfates, phosphates, chromium, copper, and/or the salts of other heavy metals. The major part of the chemical substances used in textile manufacture are generated during wet processing (dyeing, washing, printing, and fabric finishing). Textile dyeing and finishing mills utilize 200 tons of water for every metric ton of textiles produced. The textile industry is a major energy-consuming industry with low efficiency in energy utilization. A large quantity of non-renewable energy sources is consumed in the form of electricity, not so much in the process of textile production (15–20%) but mostly in subsequent laundering processes during consumer use (75–80%) (Choudhury, 2014).

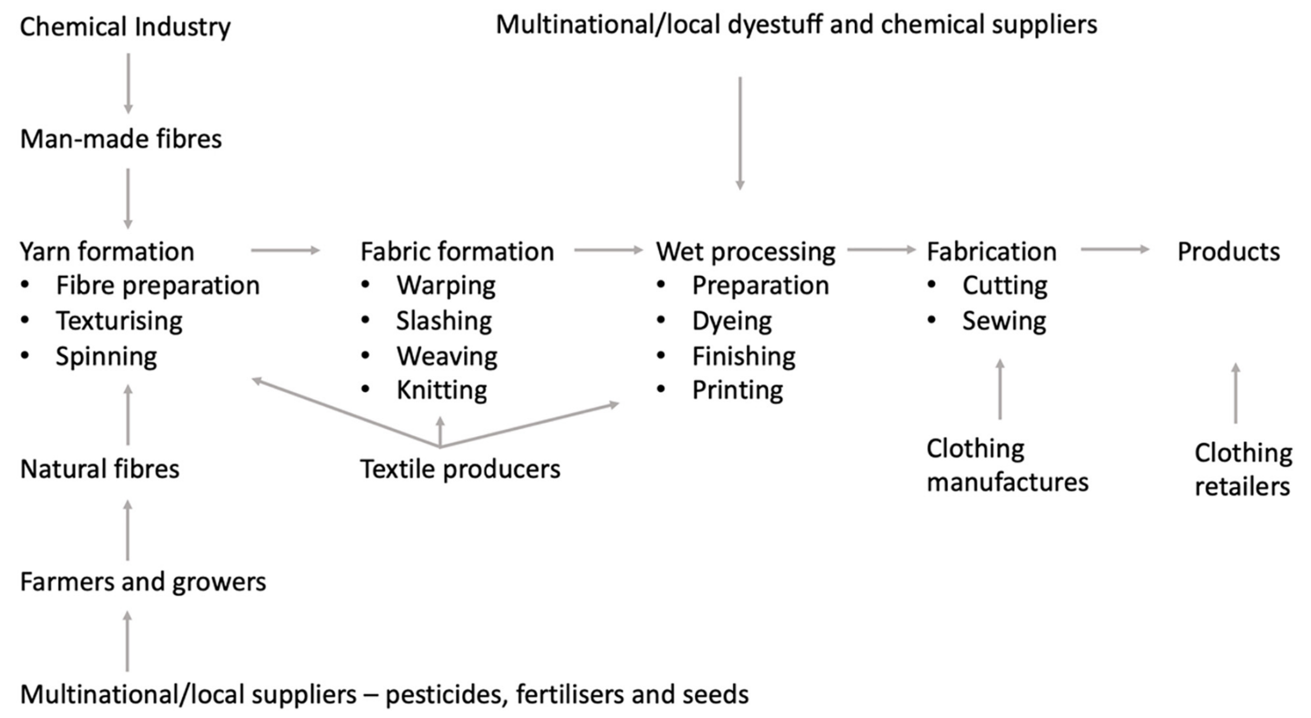

FIGURE 12 | The business involved in the textile and clothing supply chain [adapted from Choudhury (2014)].

TABLE 3 | LCA cradle-to-gate of different impact categories per 1000 kg of fiber (functional unit) produced under different methods.

Impact Category	Cotton Fiber	Tencel (lyocell)	Viscose Austria	Viscose Asia	Polyester
Water Use (m^3)	5730 [1]	263 [2]	445 [2]	319 [3]	125 [3]
Energy Demand (GJ)	55 [1]	65 [3]	70 [3]	106 [3]	96 [3]
Global Warming (kg CO_2-Equiv.)	2000 [1]	50 [3]	–250 [3]	3800 [3]	4100 [3]
Acidification (kg SO_2-Equiv.)	41 [1]	13 [3]	14 [3]	45 [3]	21 [3]
Eutrophication (kg phosphate-Equiv.)	22 [1]	1.9 [3]	1.2 [3]	2.3 [3]	1.2 [3]
Ozone Depletion ($\times 10^{-3}$ kg CFC11 Equiv.)	0.2 [1]	0.07 [3]	0.03 [3]	0.28 [3]	0.07 [3]
Land Use (ha/year)	1.07 [1]	0.22 [3]	0.69 [2]	0.35 [3]	0 [4]

[1] *Cotton Incorporated (2012).*
[2] *Taylor (2010).*
[3] *Shen and Patel (2010).*
[4] *Dibdiakova and Timmermann (2014).*

Although the entire process of textile production generates hazardous wastes, in this review we focus only on raw materials and fibers production. A cradle-to-gate LCA study, shown in **Table 3**, makes possible to evaluate the environmental impact of different fiber production processes (Dibdiakova and Timmermann, 2014). It is important to mention that, for a true comparative LCA, the same framework must be used for all stages of the life-cycle of a commercial product, process, or service (this means using the same criteria for a life cycle inventory of the required resources (energy and materials) across the value chain and determining the corresponding emissions to the environment). Data here collected was obtained from different sources and therefore a direct comparison of the impact categories is not straightforward.

Polyester, the most widely used synthetic fiber, has a lower water consumption than the other cellulose fibers, but has the highest impact on global warming from CO_2 emissions and also a high demand on energy (Zambrano et al., 2019). Cotton is the most used natural raw material in textile industry (Kazan et al., 2020). Nutrients and pesticides are used in raw material production to increase quantity and product quality and so, they pollute the groundwater and surface water. Up to 25% of global pesticide usage in agriculture corresponds to cotton production (Kazan et al., 2020). Although cotton has the advantage of being biodegradable, it has a significant water consumption, with an average global water footprint of 5730 m^3/ton in crops production and required water for processing (Cotton Incorporated, 2012). Some of the negative aspects of cotton production can be overcome by growing organic crops but it still has many negative environmental aspects compared to other fibers (Textile Exchanges, 2014; La Rosa and Grammatikos, 2019).

Regarding the processing stage, the Viscose process has different environmental impacts depending on where it is produced (Shen et al., 2010). The problems with these fibers are the chemicals used in the regeneration process and the need for large plantation areas for wood production. These plantation areas need to have a sustainable managing system, and preferably be certified, and, in the past, this was not always true.

Currently, the most environmentally friendly fibers on the market are produced by the Lyocell process (Shen et al., 2010). The solvent used is non-toxic and recyclable being the main challenge the sustainable sourcing of cellulose. Tencel, made of cellulose from sustainable eucalyptus plantations, which grows quickly and requires no irrigation or pesticides, is the best option on the market regarding its environmental impact. BNC may be the solution to Lyocell flaws as it can be produced anywhere without the use of forest resources. An attributional LCA was applied to a projected production of BNC, by static culture, following a cradle-to-gate approach which comprises the removal of natural resources and their conversion, the production of BNC, the utilities, the energy and equipment used, as well as the treatment and disposal of the waste produced by the BNC process chain. The results showed that water was the main resource used, most of which being returned back to fresh water after treatment. The BNC manufacture facility itself contributed little extent to the consumption of resources and environmental impact of the global life cycle. The materials production were accountable for most of natural resources utilized (water), and the emissions liberated to the environment, in this case released to fresh water (Forte et al., 2019).

CONCLUSION

Textile industry evolved over the years. Several types of fibers have been produced to fulfill people's needs and demands, polyester, cotton and Viscose being the most used. However, these fibers have environmental implications associated to raw material processing and transport, filament manufacture, product and byproducts disposal. Currently, the most environmentally friendly cellulose fibers on the market are produced by the Lyocell process. Current trends include the development of filaments without using solvents, the development of new solvents and new sources of fibers, which include different nanocelluloses, namely bacterial cellulose. This presents a superior outlook in terms of sustainability. However, the large scale production of this biotech cellulose is still to be demonstrated. Further research is still needed to scale up its production as their production cost.

Man-made cellulosic fibers are here to stay. Since its discovery, more than 100 years ago, they assume an important role in the textile industry. Along the history its commercialization faced one major problem: the price. These fibers are more expensive than cotton, and a lot more expensive than synthetics. But the world has changed. The population growth, and the increasing economic power in some underdeveloped economies are putting a tremendous pressure under some industries, especially those producing essential goods, like the textile industry for garment. To allow an increase in textile production, fibers production must increase also. Cotton cannot respond to this increase, because there is no arable land available, and nor the synthetics, presenting some major problems on recyclability, biodegradability, row material availability in the future and microplastics pollution. MMCF will have a very important role in the response of this need. And in the eternal quest for optimization, the MMCF will evolve along the entire value chain to minimize its environmental foot print, improving production methods and raw materials supply.

AUTHOR CONTRIBUTIONS

MG and FD: conceptualization. CF: writing. CF and CG: data analysis. CF, NA, CG, MG, and FD: writing-review and editing. All authors approved the manuscript.

FUNDING

This study was supported by the Portuguese Foundation for Science and Technology (FCT) under the scope of the strategic funding of UID/BIO/04469/2013 unit and COMPETE 2020 (POCI-01-0145-FEDER-006684) and BioTecNorte Operation (NORTE-01-0145-FEDER-000004) funded by the European Regional Development Fund under the scope of Norte2020–Programa Operacional Regional do Norte. Support from The Navigator Company through the I&D n° 21874, "Inpactus–Produtos e Tecnologias Inovadores a partir do Eucalipto," funded through the Fundo Europeu de Desenvolvimento Regional (FEDER) and the Programa Operacional Competitividade e Internacionalização (POCI) is acknowledged.

REFERENCES

Akhlaghi, M. A., Bagherpour, R., and Kalhori, H. (2020). Application of bacterial nanocellulose fibers as reinforcement in cement composites. *Construct. Build. Mater.* 241:118061. doi: 10.1016/j.conbuildmat.2020.118061

Akinsemolu, A. A. (2018). The role of microorganisms in achieving the sustainable development goals. *J. Clean. Prod.* 182, 139–155. doi: 10.1016/j.jclepro.2018.02.081

Alagirusamy, R., and Das, A. (2015). "Conversion of fibre to yarn: an overview," in *Textiles and Fashion: Materials, Design and Technology*, ed. R. Sinclair (Amsterdam: Elsevier Inc.), 159–189. doi: 10.1016/B978-1-84569-931-4.00008-8

Alam, M. N., and Christopher, L. P. (2017). A novel, cost-effective and eco-friendly method for preparation of textile fibers from cellulosic pulps. *Carbohydrate Pol.* 173, 253–258. doi: 10.1016/j.carbpol.2017.06.005

Amorim, J. D. P., de Souza, K. C., Duarte, C. R., da Silva, Duarte, I., de Assis Sales, et al. (2020). Plant and bacterial nanocellulose: production, properties and applications in medicine, food, cosmetics, electronics and engineering. a review. *Environ. Chem. Lett.* 18, 851–869. doi: 10.1007/s10311-020-00989-9

Andersson, E. (2018). *Dissolution and Fibre Spinning of Cellulose from an Ionic Liquid*. Lund: University: Lund.

Ansell, M. P., and Mwaikambo, L. Y. (2009). "The structure of cotton and other plant fibres," in *Handbook of Textile Fibre Structure*, Vol. 2, eds S. J. Eichhorn, J. W. S. Hearle, M. Jaffe, and T. Kikutani (Amsterdam: Elsevier Inc.), 62–94. doi: 10.1533/9781845697310.1.62

Anton-Sales, I., D'Antin, J. C., Fernández-Engroba, J., Charoenrook, V., Laromaine, A., Roig, A., et al. (2020). Bacterial nanocellulose as a corneal bandage material: a comparison with amniotic membrane. *Biomater. Sci.* 2020, 2921–2930. doi: 10.1039/d0bm00083c

Anžlovar, A., Kunaver, M., Krajnc, A., and Žagar, E. (2018). Nanocomposites of LLDPE and surface-modified cellulose nanocrystals prepared by melt processing. *Molecules* 23:1782. doi: 10.3390/molecules23071782

Biganska, O., and Navard, P. (2003). Phase diagram of a cellulose solvent: N-methylmorpholine-N-oxide-water mixtures. *Polymer* 44, 1035–1039. doi: 10.1016/S0032-3861(02)00902-3

Biganska, O., and Navard, P. (2011). "Dissolution, crystallisation and regeneration of cellulose in nmethylmorpholine N-oxyde," in *Proceedings of the MACRO-2004 International Conference on Polymers for Advanced Technologies*. Thiruvananthapuram: Society for Polymer Science.

Brigham, C. (2018). "Biopolymers: biodegradable alternatives to traditional plastics," in *Green Chemistry: an Inclusive Approach*, eds B. Török and T. Dransfield (Amsterdam: Elsevier Inc.), 753–770. doi: 10.1016/B978-0-12-809270-5.00027-3

Brown, A. J. (1886). XLIIL-On an Acetic Ferment which form Cellulose. *J. Chem. Soc.* 49, 432–439.

Bunsell, A. (2018). "Introduction to the science of fibers," in *Handbook of Properties of Textile and Technical Fibres*, 2nd Edn, ed. A. Bunsell (Amsterdam: Elsevier), 1–20. doi: 10.1016/B978-0-08-101272-7.00001-8

Cabañas-Romero, L. V., Valls, C., Valenzuela, S. V., Roncero, M. B., Pastor, F. I. J., Diaz, P., et al. (2020). Bacterial cellulose-chitosan paper with antimicrobial and antioxidant activities. *Biomacromolecules* 21, 1568–1577. doi: 10.1021/acs.biomac.0c00127

Charreau, H., Cavallo, E., and Foresti, M. L. (2020). Patents involving nanocellulose: analysis of their evolution since 2010. *Carbohydrate Pol.* 237:116039. doi: 10.1016/j.carbpol.2020.116039

Chawla, P. R., Bajaj, I. B., Survase, S. A., and Singhal, R. S. (2009). Microbial cellulose: fermentative production and applications. *Food Technol. Biotechnol.* 47, 107–124.

Chen, J. (2015). "Synthetic textile fibers: regenerated cellulose fibers," in *Textiles and Fashion: Materials, Design and Technology*, ed. R. Sinclair (Amsterdam: Elsevier), 79–95. doi: 10.1016/B978-1-84569-931-4.01001-1

Choi, S. M., and Shin, E. J. (2020). The nanofication and functionalization of bacterial cellulose and its applications. *Nanomaterials* 10:406. doi: 10.3390/nano10030406

Choudhury, R. (2014). "Environmental impacts of the textile industry and its assessment through life cycle assessment," in *Roadmap to Sustainable Textiles and Clothing*, ed. S. Muthu (Singapore: Springer), 41–61. doi: 10.1007/978-981-287-110-7

Clemons, C. (2016). Nanocellulose in spun continuous fibers: a review and future outlook. *J. Renew. Mater.* 4, 327–339. doi: 10.7569/JRM.2016.634112

Cotton Incorporated (2012). *Life Cycle Assessment of Cotton Fiber & Fabric*. North Carolina,NC: Cotton Incorporated.

Czaja, W., Romanovicz, D., and Brown, R. M. (2004). Structural investigations of microbial cellulose produced in stationary and agitated culture. *Cellulose* 11, 403–411. doi: 10.1023/b:cell.0000046412.11983.61

Dibdiakova, J., and Timmermann, V. (2014). *Life Cycle Assessment on Cotton and Viscose Fibres for Textile Production. Innovation Application of Regenerated Wood Cellulose Fibre*. Norway: Norwegian Forest and Landscape Institute

Dourado, F., Fontão, A., Leal, M., Cristina Rodrigues, A., and Gama, M. (2016a). "Process modeling and techno-economic evaluation of an industrial bacterial nanocellulose fermentation process," in *Bacterial Nanocellulose: From Biotechnology to Bio-Economy*, eds M. Gama, F. Dourado, and S. Bielecki (Amsterdam: Elsevier Inc.), 199–214. doi: 10.1016/B978-0-444-63458-0.00012-3

Dourado, F., Ryngajllo, M., Jedrzejczak-Krzepkowska, M., Bielecki, S., and Gama, M. (2016b). "Taxonomic review and microbial ecology in bacterial nanocellulose fermentation," in *Bacterial Nanocellulose from Biotechnology to Bio-economy*, eds M. Gama, F. Dourado, and S. Bielecki (Amsterdam: Elsevier), 1–17. doi: 10.1017/CBO9781107415324.004

Edgar, K. J., and Zhang, H. (2020). Antibacterial modification of lyocell fiber: a review. *Carbohydrate Pol.* 250:116932. doi: 10.1016/j.carbpol.2020.116932

Eichinger, D. (2012). A vision of the world of cellulosic fibers in 2020. *Lenzinger Ber* 90, 4–10.

Emerging Textiles (2020). *Price Reports - Emerging Textiles - Textile Market Information*. https://emergingtextiles.com/ (accessed August 4, 2020).

Ertas, Y., and Uyar, T. (2017). Fabrication of cellulose acetate/polybenzoxazine cross-linked electrospun nanofibrous membrane for water treatment. *Carbohydrate Pol.* 177, 378–387. doi: 10.1016/j.carbpol.2017.08.127

Ewulonu, C. M., Liu, X., Wu, M., and Yong, H. (2019). Lignin-Containing cellulose nanomaterials: a promising new nanomaterial for numerous applications. *J. Bioresources Bioprod.* 4, 3–10. doi: 10.21967/jbb.v4i1.186

Fang, Z., Li, B., Liu, Y., Zhu, J., Li, G., Hou, G., et al. (2020). Critical role of degree of polymerization of cellulose in super-strong nanocellulose films. *Matter* 2, 1000–1014. doi: 10.1016/j.matt.2020.01.016

Farooq, U., Ullah, M. W., Yang, Q., Aziz, A., Xu, J., Zhou, L., et al. (2020). High-density phage particles immobilization in surface-modified bacterial cellulose for ultra-sensitive and selective electrochemical detection of *Staphylococcus aureus*. *Biosensors Bioelectron.* 157:112163. doi: 10.1016/j.bios.2020.112163

Forte, A., Dourado, F., Gama, M., and Ferreira, E. (2019). "Life cycle assessment (cradle-to-gate) of bacterial cellulose production," in *Proceedings of the TSB2019 - The 31st Annual Meeting of the Thai Society for Biotechnology and International Conference*, (Patong), 146–146.

Gao, Q., Shen, X., and Lu, X. (2011). Regenerated bacterial cellulose fibers prepared by the NMMO·H 2O process. *Carbohydrate Pol.* 83, 1253–1256. doi: 10.1016/j.carbpol.2010.09.029

Gao, W., Inwood, J. P. W., and Fatehi, P. (2019). Sulfonation of Hydroxymethylated Lignin and Its Application. *J. Bioresources Bioprod.* 4, 80–88. doi: 10.21967/jbb.v4i2.228

Garside, M. (2019). *Chemical and Textile Fibers Production Worldwide 1975-2018*. Hamburg: Statista.

Geng, L., Chen, B., Peng, X., and Kuang, T. (2017). Strength and modulus improvement of wet-spun cellulose I filaments by sequential physical and chemical cross-linking. *Mater. Des.* 136, 45–53. doi: 10.1016/j.matdes.2017.09.054

Ghasemi, S., Tajvidi, M., Bousfield, D. W., Gardner, D. J., and Gramlich, W. M. (2017). Dry-spun neat cellulose nanofibril filaments: influence of drying temperature and nanofibril structure on filament properties. *Polymers* 9:392. doi: 10.3390/polym9090392

Gindl, W., Reifferscheid, M., Adusumalli, R. B., Weber, H., Röder, T., Sixta, H., et al. (2008). Anisotropy of the modulus of elasticity in regenerated cellulose fibres related to molecular orientation. *Polymer* 49, 792–799. doi: 10.1016/j.polymer.2007.12.016

Golova, L., Romanov, V., and Balashova, O. (1992). *Method for Producing a Solution for Spinning Fibers RF Patent 1645308*. Available online at: http://patents.su/3-1645308-sposob-polucheniya-rastvora-dlya-formovaniya-volokon.html (accessed 9 March, 2018)

Golova, L. K. (1996). Processing of cellulose via highly concentrated "Solid Solutions.". *Fibre Chem.* 28, 5–16. doi: 10.1007/BF01130691

Golova, L. K., Makarov, I. S., Matukhina, E. V., and Kulichikhin, V. G. (2010). Solutions of cellulose and its blends with synthetic polymers in N-methylmorpholine-N-oxide: preparation, phase state, structure, and properties. *Pol. Sci. Ser. A* 52, 1209–1219. doi: 10.1134/S0965545X10110155

Golova, L., Makarov, I., Kuznetsova, L., Plotnikova, E., and Kulichikhi, V. (2013). "Structure - properties interrelationships in multicomponent solutions based on cellulose and fibers spun therefrom," in *Cellulose - Fundamental Aspects*, (London: IntechOpen), doi: 10.5772/51688

Gorgieva, S., and Trček, J. (2019). Bacterial cellulose: production, modification and perspectives in biomedical applications. *Nanomaterials* 9:1352. doi: 10.3390/nano9101352

Häemmerle, F. M. (2011). The Cellulose Gap (the future of cellulose fibres). *Lenzinger Ber.* 89, 12–21.

Havstad, M. R. (2020). "Biodegradable plastics," in *Plastic Waste and Recycling* (1st Edn, ed. S. Pianavilla (Amsterdam: Elsevier), 97–129. doi: 10.1016/B978-0-12-817880-5.00005-0

Heinze, T., and Koschella, A. (2005). Solvents applied in the field of cellulose chemistry: a mini review. *Polímeros* 15, 84–90.

Hermanutz, F., Vocht, M. P., Panzier, N., and Buchmeiser, M. R. (2019). Processing of cellulose using ionic liquids. *Macromol. Mater. Eng.* 304:1800450. doi: 10.1002/mame.201800450

Hina, S., Zhang, Y., and Wang, H. (2015). Role of ionic liquids in dissolution and regeneration of cellulose. *Rev. Adv. Mater. Sci.* 40, 215–226.

Hooshmand, S., Aitomäki, Y., Norberg, N., Mathew, A. P., and Oksman, K. (2015). Dry-Spun single-filament fibers comprising solely cellulose nanofibers from bioresidue. *ACS Appl. Mater. Interfaces* 7, 13022–13028. doi: 10.1021/acsami.5b03091

Huang, Y., Zhu, C., Yang, J., Nie, Y., Chen, C., and Sun, D. (2014). Recent advances in bacterial cellulose. *Cellulose* 21, 1–30. doi: 10.1007/s10570-013-0088-z

Hummel, M., Michud, A., Tanttu, M., Asaadi, S., Ma, Y., Hauru, L. K. J., et al. (2015). "Ionic liquids for the production of man-made cellulosic fibers: opportunities and challenges," in *Cellulose Chemistry and Properties: Fibers, Nanocelluloses and Advanced Materials*, Vol. 271, ed. O. Rojas (Berlin: Springer New York LLC), 133–168. doi: 10.1007/12_2015_307

Ioncell (2020). *Ioncell Comercializaion*. Available online at: https://ioncell.fi/commercialization/ (accessed August 12, 2020).

Isik, M., Sardon, H., and Mecerreyes, D. (2014). Ionic liquids and cellulose: dissolution, chemical modification and preparation of new cellulosic materials. *Int. J. Mol. Sci.* 15, 11922–11940. doi: 10.3390/ijms150711922

Iwamoto, S., Isogai, A., and Iwata, T. (2011). Structure and mechanical properties of wet-spun fibers made from natural cellulose nanofibers. *Biomacromolecules* 12, 831–836. doi: 10.1021/bm101510r

Jiang, X., Bai, Y., Chen, X., and Liu, W. (2020). A review on raw materials, commercial production and properties of lyocell fiber. *J. Bioresources Bioprod.* 5, 16–25. doi: 10.1016/j.jobab.2020.03.002

Jinzarli, M. M., Cass, G. A., Moursounidis, J., and Best, W. M. (2019). *Methods for Producing a Viscose Dope from Microbial Cellulose (Patent No. WO/2019/109133) Applicant: Nanollose Limited.*

Jonas, R., and Farah, L. F. (1998). Production and application of microbial cellulose. *Pol. Degrad. Stab.* 59, 101–106. doi: 10.1016/S0141-3910(97)00197-3

Kafy, A., Kim, H. C., Zhai, L., Kim, J. W., Hai, L., Van, et al. (2017). Cellulose long fibers fabricated from cellulose nanofibers and its strong and tough characteristics. *Sci. Rep.* 7, 1–8. doi: 10.1038/s41598-017-17713-3

Kargarzadeh, H., Mariano, M., Huang, J., Lin, N., Ahmad, I., Dufresne, A., et al. (2017). Recent developments on nanocellulose reinforced polymer nanocomposites: a review. *Polymer* 132, 368–393. doi: 10.1016/j.polymer.2017.09.043

Karthik, T., and Rathinamoorthy, R. (2017). "Sustainable synthetic fibre production," in *Sustainable Fibres and Textiles*, ed. S. Muthu (Amsterdam: Elsevier Inc.), 191–240. doi: 10.1016/B978-0-08-102041-8.00008-1

Kazan, H., Akgul, D., and Kerc, A. (2020). Life cycle assessment of cotton woven shirts and alternative manufacturing techniques. *Clean Technol. Environ. Pol.* 22, 849–864. doi: 10.1007/s10098-020-01826-x

Keller, R., and Giddings, C. (2020). *Chromatography*. Chicago: Encyclopædia Britannica, Inc.

Kim, H. C., Kim, D., Lee, J. Y., Zhai, L., and Kim, J. (2019). Effect of wet spinning and stretching to enhance mechanical properties of cellulose nanofiber filament. *Int. J. Prec. Eng. Manufact. Green Technol.* 6, 567–575. doi: 10.1007/s40684-019-00070-z

Klemm, D., Heublein, B., Fink, H. P., and Bohn, A. (2005). Cellulose: fascinating biopolymer and sustainable raw material. *Angewandte Chemie - Int. Ed.* 44, 3358–3393. doi: 10.1002/anie.200460587

La Rosa, A. D., and Grammatikos, S. A. (2019). Comparative life cycle assessment of cotton and other natural fibers for textile applications. *Fibers* 7:101, doi: 10.3390/FIB7120101

Lee, K. Y., Buldum, G., Mantalaris, A., and Bismarck, A. (2014). More than meets the eye in bacterial cellulose: biosynthesis, bioprocessing, and applications in advanced fiber composites. *Macromol. Biosci.* 14, 10–32. doi: 10.1002/mabi.201300298

Levi, N., Khenkin, A. M., Hailegnaw, B., and Neumann, R. (2016). Depolymerization of cellulose in water catalyzed by phenylboronic acid derivatives. *ACS Sustainable Chem. Eng.* 4, 5799–5803. doi: 10.1021/acssuschemeng.6b01071

Li, G., Nandgaonkar, A. G., Habibi, Y., Krause, W. E., Wei, Q., and Lucia, L. A. (2017). An environmentally benign approach to achieving vectorial alignment and high microporosity in bacterial cellulose/chitosan scaffolds. *RSC Adv.* 7, 13678–13688. doi: 10.1039/c6ra26049g

Liu, W., Du, H., Zhang, M., Liu, K., Liu, H., Xie, H., et al. (2020). Bacterial cellulose-based composite scaffolds for biomedical applications: a review. *ACS Sustainable Chem. Eng.* 8, 7536–7562. doi: 10.1021/acssuschemeng.0c00125

Lundahl, M. J. (2018). Spinning of cellulose nanofibrils. *ACS Symposium Ser.* 1304, 153–169. doi: 10.1021/bk-2018-1304.ch008

Lundahl, M. J., Klar, V., Wang, L., Ago, M., and Rojas, O. J. (2017). Spinning of cellulose nanofibrils into filaments: a review. *Ind. Eng. Chem. Res.* 56, 8–19. doi: 10.1021/acs.iecr.6b04010

Maia, E., Peguy, A., and Pérez, S. (1981). Cellulose organic solvents. I. the structures of anhydrous N-methylmorpholine N-oxide and N-methylmorpholine N-oxide monohydrate. *Acta Crystallograph. Sec. B Struct. Crystallography Crystal Chem.* 37, 1858–1862. doi: 10.1107/s0567740881007413

Makarov, I. S., Golova, L. K., Vinogradov, M. I., Levin, I. S., Gromovykh, T. I., Arkharova, N. A., et al. (2019). Cellulose Fibers from Solutions of Bacterial Cellulose in N-Methylmorpholine N-Oxide. *Fibre Chem.* 51, 175–181. doi: 10.1007/s10692-019-10069-6

Makarov, I. S., Shambilova, G. K., Vinogradov, M. I., Zatonskih, P. V., Gromovykh, T. I., Lutsenko, S. V., et al. (2020). Films of bacterial cellulose prepared from solutions in N-Methylmorpholine-N-Oxide: structure and properties. *Processes* 8:171. doi: 10.3390/pr8020171

Manian, A. P., Pham, T., and Bechtold, T. (2018). "Regenerated cellulosic fibers," in *Handbook of Properties of Textile and Technical Fibres*, 2nd Edn, ed. A. Bunsell (Amsterdam: Elsevier), 329–343. doi: 10.1016/B978-0-08-101272-7.00010-9

McKeen, L. W. (2017). "Environmentally friendly polymers," in *Permeability Properties of Plastics and Elastomers*, 4th Edn, ed. L. McKeen (Amsterdam: Elsevier), 305–323. doi: 10.1016/b978-0-323-50859-9.00013-0

Mcorsley, C. (1981). *Process for Shaped Cellulose Article Prepared from Solution Containing Cellulose Dissolved in a Tertiary Amine N-oxide Solvent (Patent No. US 4246332)*. New York, NY: Akzona Incorporated.

Meksi, N., and Moussa, A. (2017). A review of progress in the ecological application of ionic liquids in textile processes. *J. Cleaner Prod.* 161, 105–126. doi: 10.1016/j.jclepro.2017.05.066

Metsä (2018). *Textile Fibre from Paper-grade pulp - MetsäSpring*. Helsinki: Metsä.

Michud, A., Tanttu, M., Asaadi, S., Ma, Y., Netti, E., Kääriainen, P., et al. (2016). Ioncell-F: ionic liquid-based cellulosic textile fibers as an alternative to viscose and Lyocell. *Textile Res. J.* 86, 543–552. doi: 10.1177/0040517515591774

Mittal, N., Ansari, F., Gowda Krishne, V., Brouzet, C., Chen, P., Larsson, P. T., et al. (2018). Multiscale control of nanocellulose assembly: transferring remarkable nanoscale fibril mechanics to macroscale fibers. *ACS Nano* 12, 6378–6388. doi: 10.1021/acsnano.8b01084

Müller, A., Ni, Z., Hessler, N., Wesarg, F., Müller, F. A., Kralisch, D., et al. (2013). The biopolymer bacterial nanocellulose as drug delivery system: investigation of drug loading and release using the model protein albumin. *J. Pharmaceutical Sci.* 102, 579–592. doi: 10.1002/jps.23385

Murthy, H. V. (2016). "Fibre characteristics," in *Introduction to Textile Fibres*, 1st Edn, ed. H. V. Murthy (Cambridge: Woodhead publishing india in textiles), 1–24. doi: 10.1201/b20597

Nanollose (2020). *Nanollose – Nanollose is a Leading Research and Development Company, Specialising in the Development of Plant-free Cellulose Technologies*. Australia: Nanollose.

Navard, P. (2013). The european polysaccharide network of excellence (EPNOE). *Carbohydr Polym.* 93:2.

Nimeskern, L., Martínez, Ávila, H., Sundberg, J., Gatenholm, P., Müller, R., et al. (2013). Mechanical evaluation of bacterial nanocellulose as an implant material for ear cartilage replacement. *J. Mechan. Behav. Biomed. Mater.* 22, 12–21. doi: 10.1016/j.jmbbm.2013.03.005

Nunes, T. F. G. (2014). *Produção, Caracterização e Aplicação de Nanofibras de Celulose*. Coimbra: University of Coimbra.

Olsson, C., and Westman, G. (2013). "Direct dissolution of cellulose: background, means and applications," in *Cellulose - Fundamental Aspects*, eds T. van de Ven and L. Godbout (London: Intech), doi: 10.5772/52144

Peng, H., Dai, G., Wang, S., and Xu, H. (2017). The evolution behavior and dissolution mechanism of cellulose in aqueous solvent. *J. Mol. Liquids* 241, 959–966. doi: 10.1016/j.molliq.2017.06.103

Perepelkin, K. E. (2007). Lyocell fibres based on direct dissolution of cellulose in N-methylmorpholine N-oxide: development and prospects. *Fibre Chem.* 39, 163–172. doi: 10.1007/s10692-007-0032-9

Phisalaphong, M., Tran, T. K., Taokaew, S., Budiraharjo, R., Febriana, G. G., Nguyen, D. N., et al. (2016). "Nata de coco industry in Vietnam, Thailand, and Indonesia," in *Bacterial Nanocellulose: From Biotechnology to Bio-Economy*, eds M. Gama, F. Dourado, and S. Bielecki (Amsterdam: Elsevier Inc.), 231–236. doi: 10.1016/B978-0-444-63458-0.00014-7

Piadozo, M. E. S. (2016). "Nata de coco industry in the philippines," in *Bacterial Nanocellulose: From Biotechnology to Bio-Economy*, eds M. Gama, F. Dourado, and S. Bielecki (Amsterdam: Elsevier Inc.), 215–229. doi: 10.1016/B978-0-444-63458-0.00013-5

Picheth, G. F., Pirich, C. L., Sierakowski, M. R., Woehl, M. A., Sakakibara, C. N., de Souza, C. F., et al. (2017). Bacterial cellulose in biomedical applications: a review. *Int. J. Biol. Macromol.* 104, 97–106. doi: 10.1016/j.ijbiomac.2017.05.171

Pinkert, A., Marsh, K. N., and Pang, S. (2010). Reflections on the solubility of cellulose. *Ind. Eng. Chem. Res.* 49, 11121–11130. doi: 10.1021/ie1006596

Pulidindi, K., and Chakraborty, S. (2016). *Lyocell Fiber Market Size - Industry Share Report 2017-2024*. Available online at: https://www.gminsights.com/industry-analysis/lyocell-fiber-market?utm_source=prnewswire.com&utm_medium=referral&utm_campaign=Paid_prnewswire (accessed July 20, 2020).

Rajwade, J. M., Paknikar, K. M., and Kumbhar, J. V. (2015). Applications of bacterial cellulose and its composites in biomedicine. *Appl. Microbiol. Biotechnol.* 99, 2491–2511. doi: 10.1007/s00253-015-6426-3

Rana, S., Pichandi, S., Parveen, S., and Fangueiro, R. (2014). "Biodegradation studies of textiles and clothing products," in *Roadmap to Sustainable Textiles and Clothing: Environmental and Social Aspects of Textiles and Clothing Supply Chain*, ed. S. Senthilkannan Muthu (Textile Science and Clothing Technology).

Rasheed, A. (2020). "Classification of technical textiles," in *Fibers for Technical Textiles*, eds S. Ahmad, A. Rasheed, and Y. Nawab (Cham: Springer), 49–64. doi: 10.1007/978-3-030-49224-3_3

Rodgers, B., and Waddell, W. (2013). "Tire engineering," in *The Science and Technology of Rubber*, 4th Edn, eds J. Mark, B. Erman, and M. Roland (Amsterdam: Elsevier Inc.), 653–695. doi: 10.1016/B978-0-12-394584-6.00014-5

Rodrigues, A. C., Fontão, A. I., Coelho, A., Leal, M., Soares, da Silva, F. A. G., et al. (2019). Response surface statistical optimization of bacterial nanocellulose fermentation in static culture using a low-cost medium. *New Biotechnol.* 49, 19–27. doi: 10.1016/j.nbt.2018.12.002

Roos, S., Holmquist, H., Jönsson, C., and Arvidsson, R. (2018). USEtox characterisation factors for textile chemicals based on a transparent data source selection strategy. *Int. J. Life Cycle Assess.* 23, 890–903. doi: 10.1007/s11367-017-1330-y

Rosenau, T., Potthast, A., Adorjan, I., Hofinger, A., Sixta, H., Firgo, H., et al. (2002). Cellulose solutions in N-methylmorpholine-N-oxide (NMMO) - degradation processes and stabilizers. *Cellulose* 9, 283–291. doi: 10.1023/A:1021127423041

Rosenau, T., Potthast, A., Sixta, H., and Kosma, P. (2001). The chemistry of side reactions and byproduct formation in the system NMMO/cellulose (Lyocell process). *Prog. Pol. Sci. (Oxford)* 26, 1763–1837. doi: 10.1016/S0079-6700(01)00023-5

Saito, T., Kimura, S., Nishiyama, Y., and Isogai, A. (2007). Cellulose nanofibers prepared by TEMPO-mediated oxidation of native cellulose. *Biomacromolecules* 8, 2485–2491. doi: 10.1021/bm0703970

Sajn, N. (2019). *Environmental Impact of Textile and Clothes Industry*. Available online at: http://www.europarl.europa.eu/RegData/etudes/BRIE/2019/633143/EPRS_BRI(2019)633143_EN.pdf (accessed August 5, 2020).

Salmela, J., Widmaier, T., Kuosmanen, P., Kiviluoma, P., Liukkonen, J., Koskinen, H., et al. (2016). *Method and apparatus for producing fibre yarn (Patent No. US 20160160400 A1)*. Acailable at: http://patft1.uspto.gov/netacgi/nph-Parser?Sect1=PTO1&Sect2=HITOFF&d=PALL&p=1&u=%2Fnetahtml%2FPTO%2Fsrchnum.htm&r=1&f=G&l=50&s1=9752257.PN.&OS=PN/9752257&RS=PN/9752257 (accessed August 5, 2020).

Sashina, E. (2019). Design of ionic solvents for production of man-made cellulose and silk fibers. *J. Textile Eng. Fash. Technol.* 5:15406. doi: 10.15406/jteft.2019.05.00188

Sayyed, A. J., Deshmukh, N. A., and Pinjari, D. V. (2019). A critical review of manufacturing processes used in regenerated cellulosic fibres: viscose, cellulose acetate, cuprammonium, LiCl/DMAc, ionic liquids, and NMMO based lyocell. *Cellulose* 26, 2913–2940. doi: 10.1007/s10570-019-02318-y

Sayyed, A. J., Gupta, D., Deshmukh, N. A., Mohite, L. V., and Pinjari, D. V. (2020). Influence of intensified cellulose dissolution process on spinning and properties of lyocell fibres. *Chem. Eng. Proc. Process Intensif.* 155:108063. doi: 10.1016/j.cep.2020.108063

Shaikh, T. N., Chaudhari, S. B., and Varma, A. (2012). Viscose rayon: a legendary development in the manmade textile. *Int. J. Eng. Res. Appl. (IJERA)* 2, 675–680.

Shen, L., and Patel, M. K. (2010). Life cycle assessment of man-made cellulose fibres. *Lenzinger Berichte* 88, 1–59.

Shen, L., Worrell, E., and Patel, M. K. (2010). Environmental impact assessment of man-made cellulose fibres. *Resource, Conserv. Recycl.* 55, 260–274. doi: 10.1016/j.resconrec.2010.10.001

Shi, Z., Zhang, Y., Phillips, G. O., and Yang, G. (2014). Utilization of bacterial cellulose in food. *Food Hydrocolloids* 35, 539–545. doi: 10.1016/j.foodhyd.2013.07.012

Silva, F., Morais Júnior, W., Silva, C., Vieira, A., Batista, A., Faria, A., et al. (2017). Preparation and characterization of cellulose triacetate as support for lecitase ultra immobilization. *Molecules* 22:1930. doi: 10.3390/molecules22111930

Sinclair, R. (2015). "Understanding textile fibres and their properties: what is a textile fibre?," in *Textiles and Fashion: Materials, Design and Technology*, 1st Edn, ed. R. Sinclair (Amsterdam: Elsevier Inc), 3–27. doi: 10.1016/B978-1-84569-931-4.00001-5

Singh, S. K., and Savoy, A. W. (2020). Ionic liquids synthesis and applications: an overview. *J. Mol. Liquids* 297:112038. doi: 10.1016/j.molliq.2019.112038

Spinnova (2020). *Fibre - Spinnova*. Available online at: https://spinnova.com/our-method/fibre/ (accessed August 26, 2020).

Stora Enso (2021). *A Sustainable Cellulose Foam*. Helsinki: Stora Enso.

Taylor, J. M. (2010). *Reducing the Textile Environmental Footprint with TENCEL®* . Stresa: 22nd International IFATCC Congress.

Texcoms (2019). *Textile Technology knowledge series Volume II: Vol. II*. Thennampalayam: Texcoms Textile Solution.

Textile Exchanges (2014). *The life cylce assessment of organic cotton fiber - a global average*. Available online at: https://textileexchange.org/wp-content/uploads/2017/06/TE-LCA_of_Organic_Cotton-Fiber-Summary_of-Findings.pdf (accessed July 7, 2020).

Textile Exchanges (2020). *Preferred Fiber & Materials Market Report 2020 Welcome to the 2020 Preferred Fiber & Materials Market Report*. Available online at: https://textileexchange.org/wp-content/uploads/2020/06/Textile-Exchange_Preferred-Fiber-Material-Market-Report_2020.pdf (accessed August 3, 2020).

Thakur, V. K., Thakur, M. K., and Kessler, M. R. (2017). "Handbook of composites from renewable materials," in *Handbook of Composites from Renewable Materials*, Vol. 1–8, eds V. K. Thakur, M. K. Thakur, and M. R. Kessler (Hoboken, NJ: Wiley), doi: 10.1002/9781119441632

Thomas, P., Duolikun, T., Rumjit, N. P., Moosavi, S., Lai, C. W., Bin Johan, M. R., et al. (2020). Comprehensive review on nanocellulose: recent developments, challenges and future prospects. *J. Mechan. Behav. Biomed. Mater.* 110:103884. doi: 10.1016/j.jmbbm.2020.103884

Torres-Rendon, J. G., Schacher, F. H., Ifuku, S., and Walther, A. (2014). Mechanical performance of macrofibers of cellulose and chitin nanofibrils aligned by wet-stretching: a critical comparison. *Biomacromolecules* 15, 2709–2717. doi: 10.1021/bm500566m

Ul-Islam, M., Subhan, F., Islam, S. U., Khan, S., Shah, N., Manan, S., et al. (2019). Development of three-dimensional bacterial cellulose/chitosan scaffolds: analysis of cell-scaffold interaction for potential application in the diagnosis of ovarian cancer. *Int. J. Biol. Macromol.* 137, 1050–1059. doi: 10.1016/j.ijbiomac.2019.07.050

Ul-Islam, M., Ullah, M. W., Khan, S., and Park, J. K. (2020). Production of bacterial cellulose from alternative cheap and waste resources: a step for cost reduction with positive environmental aspects. *Korean J. Chem. Eng.* 37, 925–937. doi: 10.1007/s11814-020-0524-3

Ullah, M. W., Manan, S., Kiprono, S. J., Ul-Islam, M., and Yang, G. (2019). "Synthesis, structure, and properties of bacterial cellulose," in *Nanocellulose*, eds J. Huang, A. Dufresne, and N. Lin (Weinheim: Wiley-VCH Verlag GmbH & Co), 81–113. doi: 10.1002/9783527807437.ch4

United Nations (2015). *Transforming Our World: the 2030 Agenda for Sustainable Development United Nations United Nations Transforming our World: the 2030 Agenda for Sustainable Development*. New York, NY: United Nations.

United Nations (2020). *The UN Alliance for Sustainable Fashion*. New York, NY: United Nations.

Van Der Velden, N. M., Patel, M. K., and Vogtländer, J. G. (2014). LCA benchmarking study on textiles made of cotton, polyester, nylon, acryl, or elastane. *Int. J. Life Cycle Assess.* 19, 331–356. doi: 10.1007/s11367-013-0626-9

Ventura-Cruz, S., and Tecante, A. (2019). Extraction and characterization of cellulose nanofibers from *Rose stems* (Rosa spp.). *Carbohydrate Pol.* 220, 53–59. doi: 10.1016/j.carbpol.2019.05.053

Walther, A., Timonen, J. V. I., Díez, I., Laukkanen, A., and Ikkala, O. (2011). Multifunctional high-performance biofibers based on wet-extrusion of renewable native cellulose nanofibrils. *Adv. Mater.* 23, 2924–2928. doi: 10.1002/adma.201100580

Wanasekara, N. D., Michud, A., Zhu, C., Rahatekar, S., Sixta, H., and Eichhorn, S. J. (2016). Deformation mechanisms in ionic liquid spun cellulose fibers. *Polymer* 99, 222–230. doi: 10.1016/j.polymer.2016.07.007

Wang, H., Hirth, K., Zhu, J., Ma, Q., Liu, C., and Zhu, J. Y. (2019). Dissolution of less-processed wood fibers without bleaching in an ionic liquid: effect of lignin condensation on wood component dissolution. *Int. J. Biol. Macromol.* 134, 740–748. doi: 10.1016/j.ijbiomac.2019.05.074

Wang, J., Tavakoli, J., and Tang, Y. (2019). Bacterial cellulose production, properties and applications with different culture methods – a review. *Carbohydrate Pol.* 219, 63–76. doi: 10.1016/j.carbpol.2019.05.008

Wang, S., Jiang, F., Xu, X., Kuang, Y., Fu, K., Hitz, E., et al. (2017). Super-Strong, super-stiff macrofibers with aligned, long bacterial cellulose nanofibers. *Adv. Mater.* 29, 1–8. doi: 10.1002/adma.201702498

Watabe, Y., Suzuki, Y., Koike, S., Shimamoto, S., and Kobayashi, Y. (2018). Cellulose acetate, a new candidate feed supplement for ruminant animals: in vitro evaluations. *J. Dairy Sci.* 101, 10929–10938. doi: 10.3168/jds.2018-14969

Wei, D. W., Wei, H., Gauthier, A. C., Song, J., Jin, Y., and Xiao, H. (2020). Superhydrophobic modification of cellulose and cotton textiles: methodologies and applications. *J. Bioresources Bioprod.* 5, 1–15. doi: 10.1016/j.jobab.2020.03.001

White, P. (2001). "Lyocell: the production process and market development," in *Regenerated Cellulose Fibres*, ed. C. Woodings (Amsterdam: Elsevier), 62–87. doi: 10.1533/9781855737587.62

Wikandari, R., Millati, R., and Taherzadeh, M. J. (2016). "Pretreatment of lignocelluloses with solvent N-Methylmorpholine N-oxide," in *Biomass Fractionation Technologies for a Lignocellulosic Feedstock Based Biorefinery*, ed. S. Mussatto (Amsterdam: Elsevier Inc.), 255–280. doi: 10.1016/B978-0-12-802323-5.00012-8

Wilkes, A. (2001). "The viscose process," in *Regenerated Cellulose Fibres*, ed. C. Woodings (Amsterdam: Elsevier), 37–61. doi: 10.1533/9781855737587.37

Woodings, C. (2001). "Regenerated cellulose fibres," in *Regenerated cellulose fibres*, ed. C. Woodings (Cambridge: Woodhead Publishing), 1–21. doi: 10.1533/9781855737587

Yang, J., Lu, X., Zhang, Y., Xu, J., Yang, Y., and Zhou, Q. (2020). A facile ionic liquid approach to prepare cellulose fiber with good mechanical properties directly from corn stalks. *Green Energy Environ.* 5, 223–231. doi: 10.1016/j.gee.2019.12.004

Yao, J., Chen, S., Chen, Y., Wang, B., Pei, Q., and Wang, H. (2017). Macrofibers with high mechanical performance based on aligned bacterial cellulose nanofibers. *ACS Appl. Mater. Interfaces* 9, 20330–20339. doi: 10.1021/acsami.6b14650

Yu, C. (2014). "Natural textile fibres: vegetable fibres," in *Textiles and Fashion: Materials, Design and Technology*, ed. R. Sinclair (Cambridge: Woodhead Publishing), 25–56.

Zambrano, M. C., Pawlak, J. J., Daystar, J., Ankeny, M., Cheng, J. J., and Venditti, R. A. (2019). Microfibers generated from the laundering of cotton, rayon and polyester based fabrics and their aquatic biodegradation. *Mar. Pollut. Bull.* 142, 394–407. doi: 10.1016/j.marpolbul.2019.02.062

Zhang, J., Kitayama, H., Gotoh, Y., Potthast, A., and Rosenau, T. (2019). Non-woven fabrics of fine regenerated cellulose fibers prepared from ionic-liquid solution via wet type solution blow spinning. *Carbohydrate Pol.* 226:115258. doi: 10.1016/j.carbpol.2019.115258

Zhang, S., Chen, C., Duan, C., Hu, H., Li, H., Li, J., et al. (2018). Regenerated cellulose by the lyocell process, a brief review of the process and properties. *BioResources* 13, 4577–4592.

Zhang, Y., Kang, H., Hou, H., Shao, S., Sun, X., Qin, C., et al. (2018). Improved design for textile production process based on life cycle assessment. *Clean Technol. Environ. Policy* 20, 1355–1365. doi: 10.1007/s10098-018-1572-9

Zhong, C. (2020). Industrial-Scale production and applications of bacterial cellulose. *Front. Bioeng. Biotechnol.* 8:605374. doi: 10.3389/fbioe.2020.605374

Zhu, H., Jia, Z., Chen, Y., Weadock, N., Wan, J., Vaaland, O., et al. (2013). Tin anode for sodium-ion batteries using natural wood fiber as a mechanical buffer and electrolyte reservoir. *Nano Lett.* 13, 3093–3100. doi: 10.1021/nl400998t

Zinge, C., and Kandasubramanian, B. (2020). Nanocellulose based biodegradable polymers. *Eur. Pol. J.* 133:109758. doi: 10.1016/j.eurpolymj.2020.109758

Zywicka, A., Peitler, D., Rakoczy, R., Konopacki, M., Kordas, M., and Fijałkowski, K. (2015). The effect of different agitation modes on bacterial cellulose synthesis. *Acta Sci. Pol. Zootechnica* 14, 137–150.

Conflict of Interest: The authors declare that the research was conducted in the absence of any commercial or financial relationships that could be construed as a potential conflict of interest.

frontiers
in Bioengineering and Biotechnology

ORIGINAL RESEARCH
published: 30 March 2021
doi: 10.3389/fbioe.2021.617328

Cellulose Based Photonic Materials Displaying Direction Modulated Photoluminescence

Molíria V. Santos[1,2]*, Fernando E. Maturi[1,2], Édison Pecoraro[1], Hernane S. Barud[3], Laís R. Lima[1], Rute A. S. Ferreira[2], Luís D. Carlos[2] and Sidney J. L. Ribeiro[1]*

[1] Institute of Chemistry, São Paulo State University (UNESP), Araraquara, Brazil, [2] Department of Physics, CICECO – Aveiro Institute of Materials, University of Aveiro, Aveiro, Portugal, [3] Biopolymers and Biomaterials Laboratory, University of Araraquara, Araraquara, Brazil

OPEN ACCESS

Edited by:
Muhammad Wajid Ullah,
Huazhong University of Science and Technology, China

Reviewed by:
Yan Qiao,
Institute of Chemistry (CAS), China
Adil Denizli,
Hacettepe University, Turkey

****Correspondence:***
Molíria V. Santos
moliria.santos@gmail.com
Sidney J. L. Ribeiro
sidney.jl.ribeiro@unesp.br

Specialty section:
This article was submitted to Biomaterials, a section of the journal Frontiers in Bioengineering and Biotechnology

Received: *26 October 2020*
Accepted: *08 March 2021*
Published: *30 March 2021*

Citation:
Santos MV, Maturi FE, Pecoraro É, Barud HS, Lima LR, Ferreira RAS, Carlos LD and Ribeiro SJL (2021) Cellulose Based Photonic Materials Displaying Direction Modulated Photoluminescence. Front. Bioeng. Biotechnol. 9:617328. doi: 10.3389/fbioe.2021.617328

Photonic materials featuring simultaneous iridescence and light emission are an attractive alternative for designing novel optical devices. The luminescence study of a new optical material that integrates light emission and iridescence through liquid crystal self-assembly of cellulose nanocrystal-template silica approach is herein presented. These materials containing Rhodamine 6G were obtained as freestanding composite films with a chiral nematic organization. The scanning electron microscopy confirms that the cellulose nanocrystal film structure comprises multi-domain Bragg reflectors and the optical properties of these films can be tuned through changes in the relative content of silica/cellulose nanocrystals. Moreover, the incorporation of the light-emitting compound allows a complementary control of the optical properties. Overall, such findings demonstrated that the photonic structure plays the role of direction-dependent inner-filter, causing selective suppression of the light emitted with angle-dependent detection.

Keywords: bacterial cellulose nanocrystals, chiral nematic liquid crystal, iridescence, photonic materials, luminescence, modulated light emission, rhodamine 6G

INTRODUCTION

In the past years, the use of photonic crystals for manipulating light has taken the development of optical devices to a whole new level (Abdollahramezani et al., 2020). The characteristic structural colors seen in such materials originate from the interaction of light with their periodic structure, such as diffraction, interference, scattering, or polarization (Liu et al., 2020). The structure-dependent color is more advantageous when compared to colors produced by pigments or dyes because it can be tuned by controlling the crystal morphology and it will not vanish over time (Boott et al., 2020; Xu et al., 2021). Despite most photonic crystals used in optoelectronics are obtained from synthetic materials, biomaterials are responsible for producing structural colors in different animals and plants (Tran et al., 2020).

Cellulose stands out among the myriad of biomaterials available because it is a renewable biopolymer and it is the most abundant raw material for the production of photonic crystals (Dumanli et al., 2014). The acid hydrolysis can be performed on different sources of cellulose [e.g., plants (Beck-Candanedo et al., 2005; Habibi et al., 2008; Siqueira et al., 2009), bacteria

(Roman and Winter, 2004), and tunicates (Favier et al., 1995)] by using sulfuric acid to obtain stable aqueous suspensions of needle-like cellulose nanocrystals (CNC) that selectively reflect polarized light (Eichhorn, 2011; Klemm et al., 2011). Above a certain critical concentration, CNC dispersed in water self-assembly into a lyotropic cholesteric liquid crystalline phase that can be preserved upon slow drying, resulting in iridescent films (Revol et al., 1992, 1998; Arrighi et al., 2002). The iridescence occurs because the CNC layers are stacked in a long-range assembly forming a helicoidal pitch (*P*) with a characteristic 360° degree rotation within the same length scale of the visible light (de Vries, 1951; Habibi et al., 2010; Mendoza-Galván et al., 2018), paving the way for the development of tunable filters (Driesen et al., 2007; Penninck et al., 2012), polarizing mirrors (Broer et al., 1995), reflective displays (Yang et al., 1994), and lasers (Kopp et al., 1998). However, CNC films are brittle materials and present poor mechanical properties, which is the main drawback of using pristine CNC (Niinivaara and Cranston, 2020).

Nevertheless, the self-assembly of CNC is still interesting because it can be used to produce freestanding inorganic films with chiral nematic structure by incorporating inorganic precursors into CNC suspensions, controlling the size and organization of template-driven structures, such as silica photonic crystals and organosilica films (Shopsowitz et al., 2012; Kelly et al., 2013, 2014; Habibi, 2014; Van Opdenbosch and Zollfrank, 2014; Hiratani et al., 2017). After the removal of CNC, mesoporous solid structures are achieved with high surface area and long helical twist range. Both helical pitch and porosity can be tailored by changing the relative content of silica precursors, tuning the chiral nematic structure (Shopsowitz et al., 2010; Shopsowitz et al., 2014). Furthermore, the modulation of light emission can be assessed by incorporating light-emitting compounds within the ordered structure of CNC, allowing applications such as anti-counterfeiting in documents, optical memories, and biochemical sensing (Chu et al., 2014a,b, 2015; Nguyen et al., 2014; Qu et al., 2016; Nguyen et al., 2017; Lin et al., 2018).

Recently, some of us have demonstrated a novel strategy to modulate the narrowband emission of trivalent lanthanide ions complexes by using CNC films for applications in sensors, lasers, and tunable filters (Santos et al., 2019). Herein, we report the preparation of luminescent iridescent films obtained by combining tetraethoxysilane (TEOS), a CNC suspension obtained from bacterial cellulose, and a light-emitting organic dye (Rhodamine 6G, Rh6G). The influence of the angle-dependent reflection of light on the emission properties was systematically studied and we evaluated the benefit of the simultaneous integration of light emission and photonic structure of the obtained CNC-based composite films.

MATERIALS AND METHODS

Production of Bacterial Cellulose Membranes

Bacterial cellulose (BC) was prepared according to a previously reported procedure (Barud et al., 2011; Tercjak et al., 2015). BC membranes were obtained from an isolated culture of *Gluconacetobacter xylinus* (American Type Culture Collection, ATCC 23769, 5 mL). The sterile culture medium (glucose, 50 g L^{-1}; yeast extracts, 4 g L^{-1}; anhydrous disodium phosphate, 2 g L^{-1}; heptahydrate magnesium sulfate, 0.8 g L^{-1}; and ethanol, 20 g L^{-1}) was kept at 28°C in plastic trays (30×50 cm^2). After 96 h, the obtained BC membranes (3 mm thick, 1 wt% cellulose and 99 wt% water) were washed several times with deionized water. An aqueous solution of NaOH (1 wt%, 70°C) was added until pH = 7.0 to remove the remaining bacteria. Dried BC membranes were obtained after drying at 80°C over Teflon® supports.

Preparation of Cellulose Nanocrystals

The preparation of CNC followed a previously reported method (Mendoza-Galván et al., 2018). Previously dried BC membranes (5 g) were milled using an IKA® A11 basic analytical mill and sieved with a stainless-steel sieve (mesh 35). The milled BC was hydrolyzed in sulfuric acid (Synth 98%, 88 mL, 64 wt% concentration) at 50°C for 0.5 h under vigorous stirring. The obtained suspension was diluted (1:10) in ultrapure cold water to stop the hydrolysis, and it was allowed to settle overnight. The clear top layer was decanted and the remaining cloudy layer was centrifuged at 6,000 rpm for 10 min (Jouan C3i—CR3i multifunction centrifuge). The supernatant was decanted and the resulting thick white suspension was washed three times with ultrapure water. The obtained suspension was dialyzed against ultrapure water (cellulose dialysis tubing, 12,000–14,000 MWCO) until constant pH = 2.4. The suspension was diluted to 3.0 wt% and dispersed using an ultrasound homogenizer (Sonics Vibra-Cell VC 505 500W 20 kHz) with a 6 mm diameter probe. The CNC suspension (3.0 wt%, 50 mL) was transferred to a 100 mL plastic tube and sonicated at 60% of the maximum power (300 W). Additionally, a prolonged sonication (energy input of 7,500 J g^{-1} of CNC) was performed in an ice bath to prevent desulfation caused by the heating generated during the process.

Preparation of Nanocrystalline CNC-Silica Composite Films

Different amounts (33 μL, 66 μL, 98 μL, 131 μL) of TEOS (Sigma-Aldrich 98%) were added to the obtained aqueous suspension of CNC (3.0 wt%, 4 mL) and the resulting mixtures were stirred at room temperature for 3 h, leading to homogeneous mixtures. Freestanding CNC/silica composites films were obtained by drying the solutions onto polystyrene Petri dishes (**Supplementary Figure S1**). Films were named according to the relative content of CNC/silica: 0% (CNC), 12.5 wt% (CS1), 25.0 wt% (CS2), 33.3 wt% (CS3), and 50.0 wt% (CS4).

Preparation of Nanocrystalline Photoluminescent CNC-Silica Composite Films

An ethanolic solution of Rh6G (200 μL, 10^{-4} mol L^{-1}) was added to the homogeneous mixture containing CNC and TEOS. The obtained mixtures were transferred to polystyrene Petri dishes, allowing its evaporation at room temperature until

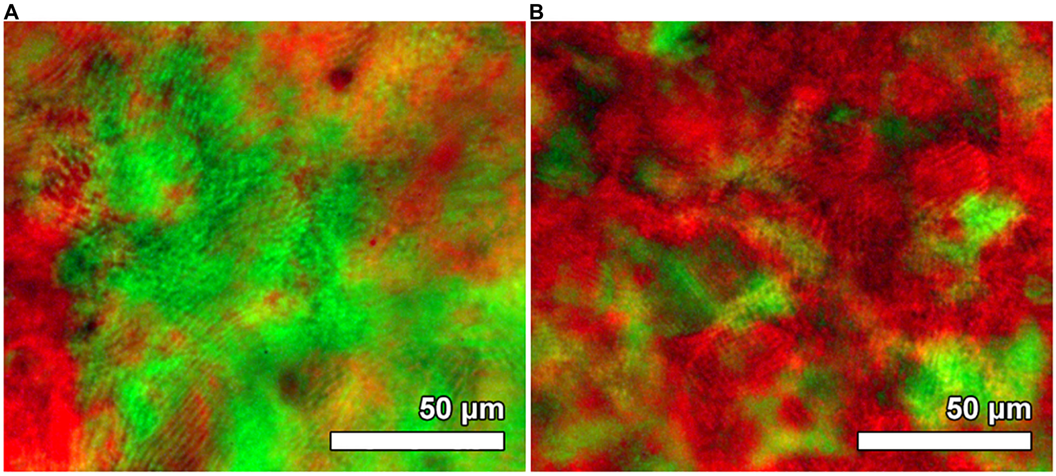

FIGURE 1 | POM image of sample CS1-Rh **(A)** and CS4-Rh **(B)** between crossed polarizers.

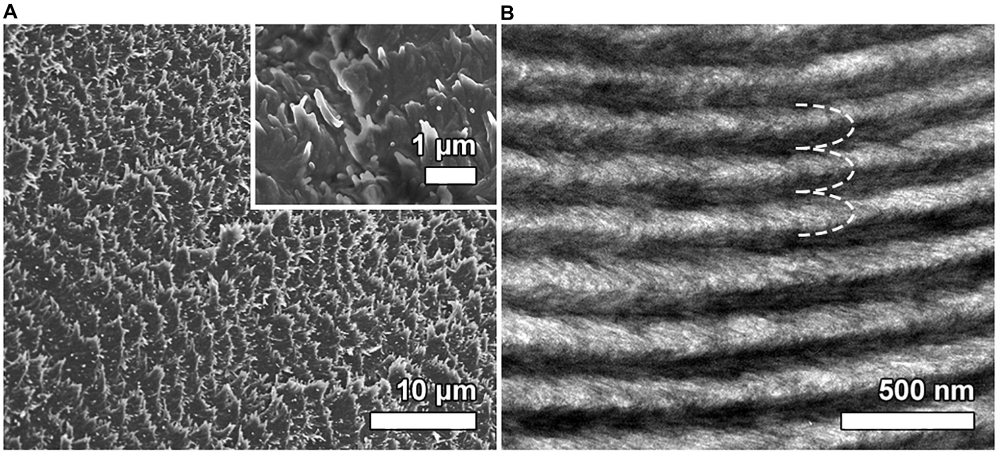

FIGURE 2 | SEM image of the surface view of the CS4-Rh sample **(A)**. The inset panel in A displays an SEM image with higher magnification highlighting the left-handed rotation of the chiral nematic organization. TEM image of an oblique cross-section of the CS4-Rh composite **(B)**. The dashed white line shows the arc-like appearance generated through the chiral nematic structure.

freestanding films were formed. The obtained composite films can be seen in **Supplementary Figure S2**.

Characterization of CNC and Composite Films

Thermogravimetric analysis (TGA) was performed using a Shimadzu TGA-50 system, in the temperature range from 25 to 800°C at a heating rate of 10°C min^{-1}, under a static atmosphere of air. Polarized optical microscopy (POM) images were obtained with an Olympus BX41 microscope, using crossed polarizers. Scanning Electronic Microscopy (SEM) images were registered with a Hitachi SU-70 electron microscope. The samples were attached to aluminum stubs using double-sided carbon adhesive tape or carbon glue. Pictures were obtained from the surface and cross-section areas. All the samples were sputter-coated with carbon through an EMITECH K950X Turbo Evaporator, at a single pulse, on an outgassing time of 30 s and an evaporating time of 2 s. Transmission electron microscopy (TEM) images were obtained by a Philips CM200 microscope with an accelerating potential of 100 keV. TEM samples were prepared using a method described by Giasson et al. (1988).

UV-Vis reflectance spectroscopy was carried out using a Perkin-Elmer Lambda 950 UV/Vis/NIR spectrophotometer and a Spectralon integrating sphere (Ø = 150 mm). The freestanding film surface was placed perpendicularly to the incident beam and the spectra were acquired as a function of the incident angle ($15° < \theta < 60°$) with 5° steps, as illustrated in **Supplementary Scheme 1**.

Photoluminescence

Excitation and emission spectra were recorded at room temperature with a modular double grating excitation

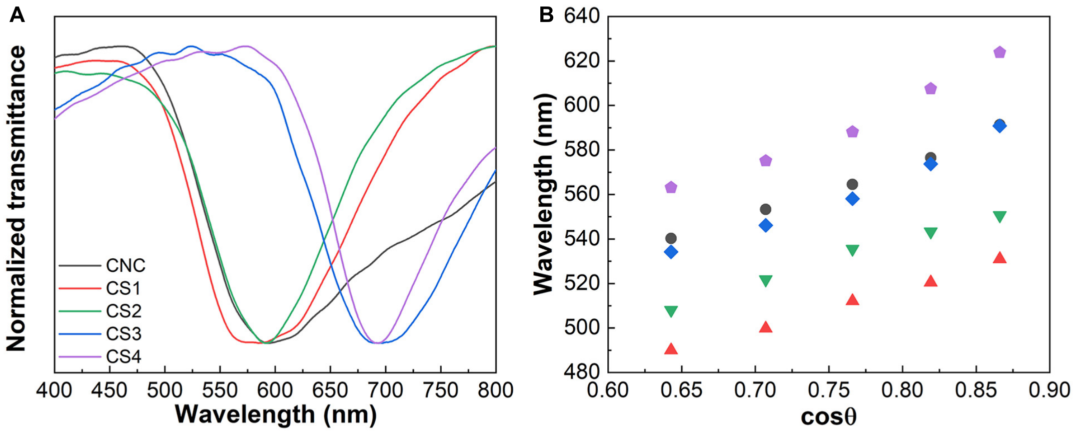

FIGURE 3 | Transmittance spectra of CNC, CS1, CS2, CS3, and CS4 samples **(A)**. Variation of the peak position of the reflectance spectra as a function of the cosθ for the same CNC/silica composites **(B)**.

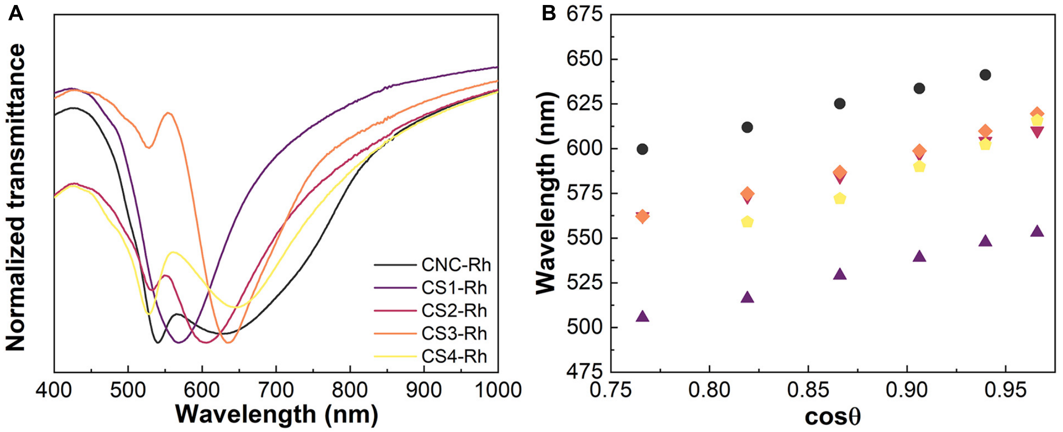

FIGURE 4 | Transmittance spectra of CNC, CS1-Rh, CS2-Rh, CS3-Rh, and CS4-Rh **(A)**. Variation of the peak position of the reflectance spectra as a function of the cosθ for the same CNC/silica composites doped with Rh6G **(B)**.

spectrofluorometer through a TRIAX 320 emission monochromator (Fluorolog-3, Horiba Scientific), coupled to an R928 Hamamatsu photomultiplier using the front face acquisition mode with a 450 W Xe arc lamp.

The angle-dependent emission spectra were recorded at room temperature as a function of the detection angle (0° < θ < –90° and 0° < θ < 90°) through a modular experimental setup, illustrated in **Supplementary Scheme 2**. The modular experimental setup consists of an Ocean Optics HR2000+ES USB spectrometer and a jacketed optical fiber (Ocean Optics) QP600-UV-Vis (core diameter of 600 mm and a total length of 1 m) to collect the emission signal. A diode laser (405 nm, CW mode, 5 mW, FWHM = 4 nm) was used as the excitation source. The laser beam was directed at an angle of 45° regarding the detection plane, and the optical fiber tip was aligned perpendicularly to the surface of the sample. At last, the sample holder was fixed at the center of the rotatory base with a goniometer and the tip of the fiber collected the emitted signal, allowing free rotation around it. The emission quantum yield (Φ) was measured at room temperature in a Quantaurus-QY Plus C13534 (Hamamatsu) system with a 150 W xenon lamp coupled to a monochromator, an integrating sphere, and two multichannel analyzers to record the emission intensity. For each sample, the reported Φ value is he average values of three measurements with an accuracy of 10%.

RESULTS AND DISCUSSION

The Rh6G doped CNC/silica composite films were obtained with 0, 8.5, 15.4, 20.7, and 35.2 wt% of silica (from TGA, **Supplementary Figure S3**) and named as CNC-Rh, CS1-Rh, CS2-Rh, CS3-Rh, and CS4-Rh, respectively. After a controlled drying, the chiral nematic phase was retained in the composites films, which display strong iridescence under non-polarized room light exposure (**Supplementary Figure S2**). POM images (**Figure 1**) of the composite films show a redshift of the color with increasing relative silica content while the overall texture remained essentially unchanged. The characteristic fingerprint lines of chiral nematic structures were observed orthogonally to the chiral nematic axis, with the shortest distance between lines equals half a pitch ($P/2$) of the cholesteric helix (Arrighi et al., 2002). The $P/2$ values obtained from **Figure 1** range from 2 to 3 μm, which are in good agreement with values reported for CNC films (Majoinen et al., 2012; Lagerwall et al., 2014).

Electron micrographs in **Figure 2** provided further confirmation of the preservation of chiral nematic organization after the incorporation of silica and Rh6G into the CNC structure. The top view of the surface of the CS4-Rh composite film (**Figure 2A**) shows a multilayered fan-like structure rotated in the counter-clockwise direction, indicating that nanocrystals present left-handed helicoids, as expected for chiral nematic helicoidal arrangements in a CNC-based structure (Wilts et al., 2017). The TEM image of a fractured cross-section of the film (**Figure 2B**) shows that the periodic structure is seen throughout the entire thickness of the film, in which each repeating layer gives rise to the arcing effect due to the 180° rotation of the chiral nematic direction (Arrighi et al., 2002; Majoinen et al., 2012; Zhanga et al., 2013).

Transmittance spectra of CNC/silica composite films (**Figure 3**) were obtained at a normal incident angle ($\theta = 0°$), where the Bragg diffraction peaks are seen in the visible part of the spectra between 550 and 700 nm. The transmittance spectra obtained for the Rh6G containing CNC/silica composites (**Figure 4**) present an additional absorption band peaking around 530 nm, which refers to the absorption of Rh6G (Martnez et al., 2005). These results are consistent with the formation of fluorescent J-type dimers due to the aggregation of Rh6G molecules when encapsulated into solid composite films (Martínez Martínez et al., 2005; Anedda et al., 2007), where the absorption band of the dye is shifted to lower energies by increasing the concentration of Rh6G (Lofaj et al., 2013).

Reflectance spectra were recorded as a function of the incident angle ($20° < \theta < 60°$, **Supplementary Figure S4**). **Figures 3B**, 4B display the variation of the peak position in the reflectance spectra as a function of the cosθ. The spectra show that Bragg diffraction is taking place, presenting a characteristic maximum wavelength (λ_0) which obeys the Vries' equation Eq. 1 (de Vries, 1951; Eichhorn, 2011):

$$\lambda_{\mathbf{0}} = \mathbf{n}_{ave}\mathbf{P}cos\theta \tag{1}$$

where θ is the incident angle between the normal surface of the sample and the incident ray, and n_{ave} is the average refractive index. In this case, the peaks observed in the reflectance spectra shift to shorter wavelengths as the viewing angle increases relatively to normal on the film. The specular reflectance spectra of the CS4-Rh composite (**Supplementary Figure S4B**) show a peak centered at 528 nm for $\theta > 50°$ due to the re-absorption process, i.e., part of the reflected light is absorbed by the dye molecules. Similar behavior was observed for all the samples containing Rh6G. It is possible to calculate l_0 through Vries' equation by using the values of P obtained from the chiral nematic structure. These values were determined from SEM images of cross-sectional views of the obtained composite films (**Supplementary Table S1**). The values of P depend on the relative amount of silica and at least two groups with similar values of P may be identified for lower and higher silica content. The pristine CNC presents a larger value of P than the values observed for samples with lower silica content, indicating that changes in P are caused by the formation of thicker nanocrystal walls after the incorporation of silica resulting from ionic interactions between negatively charged silica species and crystalline cellulose. This is supported by the band narrowing in the transmittance spectra of CNC/silica composites after the addition of silica (**Figure 4A**), which demonstrates an improvement of the chiral nematic organization and a better definition of P by increasing the silica content. The same behavior was observed for composites containing Rh6G, although the presence of Rh6G contributed to further increasing the values of P when compared to the composites without dye. Therefore, a complementary control of the optical properties is seen.

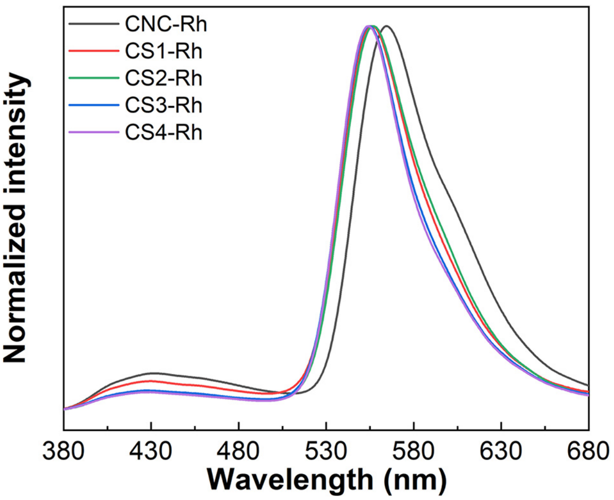

FIGURE 5 | Emission spectra of CNC/silica composite films doped with Rh6G under excitation at 348 nm.

TABLE 1 | Emission lifetime of CNC/silica composite films under excitation at 330 nm: the emission of cellulose (τ_1) and Rh6G (τ_2) was monitored at 430 and 560 nm, respectively.

Sample	τ_1 (ns)	τ_2 (ns)	Φ
CNC	6.83 ± 0.05	–	–
CNC-Rh	7.62 ± 0.06	3.74 ± 0.02	0.15 ± 0.01
CS1-Rh	9.47 ± 0.08	3.88 ± 0.02	0.40 ± 0.04
CS2-Rh	10.81 ± 0.09	4.21 ± 0.01	0.50 ± 0.05
CS3-Rh	12.76 ± 0.09	4.44 ± 0.01	0.65 ± 0.07
CS4-Rh	12.03 ± 0.11	4.23 ± 0.01	0.50 ± 0.05

Absolute quantum yield values under excitation at 528 nm: emission monitored at 567 and 556 nm for CNC-Rh and Rh6G containing CNC/silica samples, respectively.

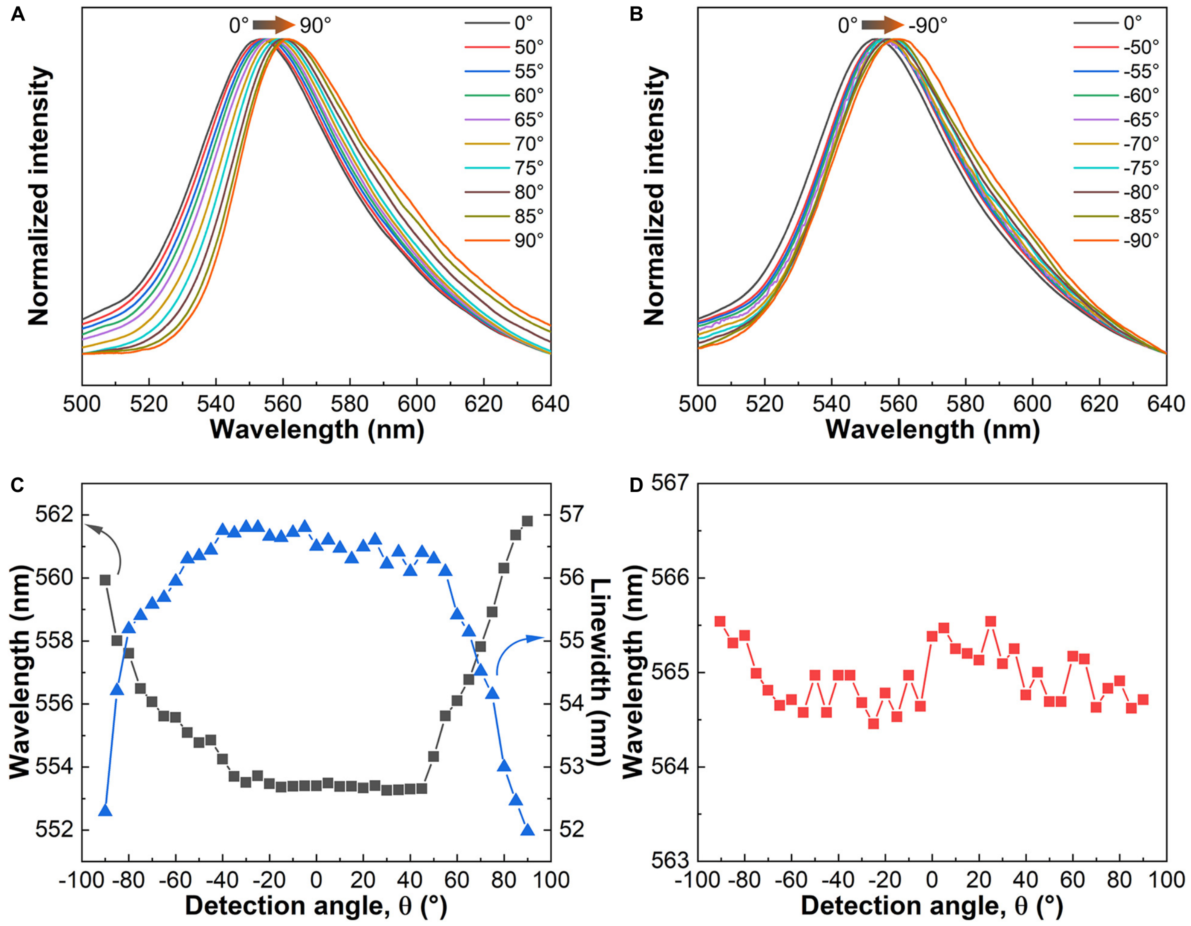

FIGURE 6 | Angle-dependent emission spectra of CS4-Rh under excitation at 348 nm: $-90° < \theta < 0°$ **(A)** and $0° < \theta < 90°$ **(B)**. Variation of the maximum wavelength (λ_0) and linewidth of the emission bands of the CS4-Rh composite as a function of the detection angle **(C)**. Variation of λ_0 of the emission bands of an Rh6G-containing cellulose membrane as a function of the detection angle **(D)**.

According to the analysis performed on the results presented in **Figure 2B**, there is a regular spacing corresponding to the $P/2$ value of 115 ± 3 nm for the CS4-Rh composite. This value is comparable to the one obtained for P, which can be calculated using the Vries' equation (P = 240 ± 12 nm). However, the texture is rich in parallel lines, with a distance of about 2–3 mm, suggesting that P is one order of magnitude larger than the Bragg reflection of visible light. Such intriguing superposed phenomena and apparent contradictions were discussed recently by Lagerwall et al. (2014). They proposed an explanation for the observation discussed above, taking into account the possible non-uniform drying at the surface and the core. During the drying process, the CNC concentration increases rapidly at the surface as the water evaporates leading to the helix development on the film plane, with P in the micrometer range. Nevertheless, in the core, the sample is still in a liquid crystalline state and the diffusion decreases drastically because the surface regime has been solidified. Hence, the increase in the core concentration is much slower than at the surface. In the core, the CNC concentration could increase further, yielding a sufficiently short pitch to produce a photonic bandgap in the visible wavelength range, as it is observed in the composite films.

The emission spectra of Rh6G-doped CNC/silica composites presented in **Figure 5** show that two emission bands can be seen under excitation at 345 nm. The first one corresponds to the emission of cellulose nanocrystals peaking around 430 nm (Li et al., 2009), confirmed by the emission spectrum of pristine CNC under excited at 348 nm (**Supplementary Figure S5**). The second one displays the characteristic emission of Rh6G, which is dependent on the relative dye content (Anedda et al., 2005). At lower concentrations, monomeric properties of Rh6G are observed, with an emission band centered around 550 nm (Bujdák, 2006; Carbonaro et al., 2009). The emission spectra in **Figure 5** display a band centered around 556 nm and a shoulder above 605 nm. Besides that, the emission spectrum of the sample without silica (CNC-Rh) showed a band centered at 565 nm and a shoulder above 610 nm. Bathochromic spectral shift related to the monomer can be attributed to the formation of fluorescent dimers (J-type). Usually, at relatively high concentrations of Rh6G, fluorescent (J-type) and non-fluorescent (H-type) dimers

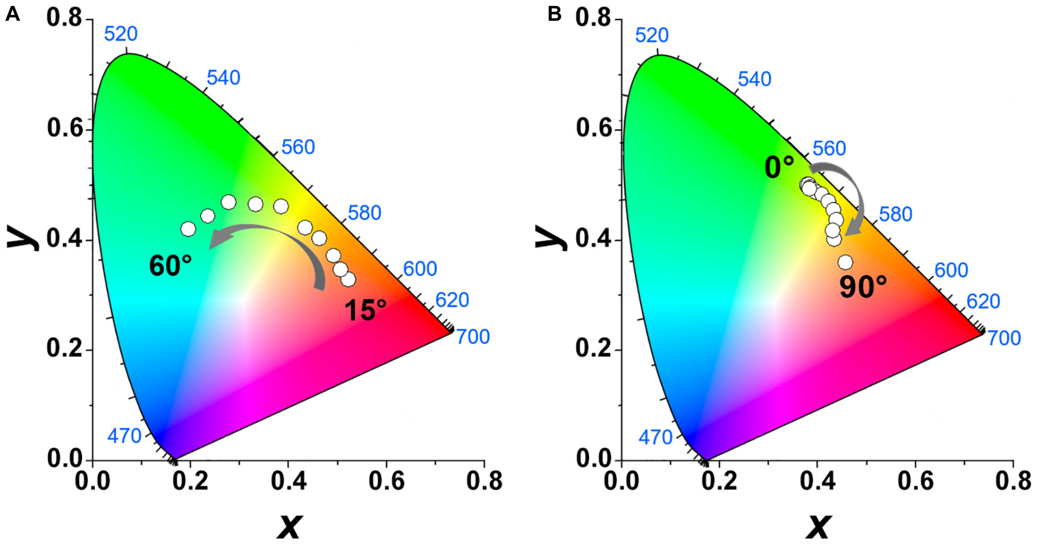

FIGURE 7 | Chromaticity diagram of reflection of the CS4-Rh composite film as a function of the detection angle (0° $< \theta <$ 60^{circ}, **A**). Chromaticity diagram of the emission of CS4-Rh composite film under excitation at 348 nm as a function of the detection angle (0° $< \theta <$ 90°, **B**).

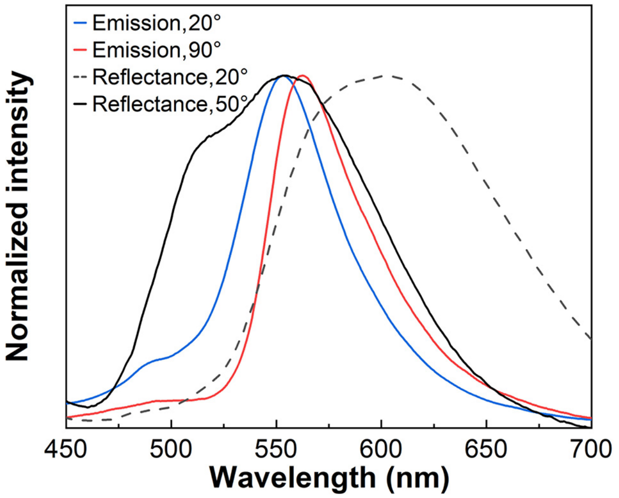

FIGURE 8 | Emission spectra of CS4-Rh at 20° and 90° detection angles under excitation at 348 nm. Reflectance spectra of the same sample at 20° and 50° detection angles.

are formed (Bujdák, 2006). Additionally, the dye aggregation leads to a concentration quenching of the luminescence of Rh6G (Martnez et al., 2005). The emission of J-type dimers is red-shifted in comparison to the monomer emission and the total emission spectra showed an overlap with emission spectra from the two molecular species. These results can also be attributed to changes in the chemical environment in their surroundings and the decrease in loading efficiency of Rh6G while the content of silica increases, which was observed in the transmittance spectra.

The emission lifetime and quantum yield values for CNC, CNC-Rh, and CS-Rh samples are shown in **Table 1**. The emission lifetime value of pristine CNC film is 6.83 ± 0.05 ns, which increases by increasing the relative content of silica due to the overlapping emission of cellulose and silica in the same wavelength range (Barud et al., 2008). The values obtained for Rh6G containing films are in good agreement with the literature (Martínez Martínez et al., 2005). The emission lifetime and quantum yield values of the composite film with higher silica content (CS4-Rh, emission monitored at 556 nm) are 4.23 ± 0.01 ns and 0.50 ± 0.05, respectively. The emission lifetime and quantum yield values obtained for the sample without silica (CNC-Rh, emission monitored at 567 nm) are 3.74 ± 0.02 ns and 0.15 ± 0.01, respectively. These results indicate that the addition of silica decreases the total amount of Rh6G dimers, since part of the dye molecules migrates to the SiO_2 phase, leading to a dilution effect.

The angle-dependent emission spectra presented in **Figure 6** were measured by varying the detection angle from 90° to −90°. The bandwidth of sample CS4-Rh decreases with a simultaneous redshift of λ_0 for $-90° \leq \theta \leq -40°$ and $40° \leq \theta \leq 90°$. **Figure 6C** shows the variation of λ_0 and the bandwidth with the detecting angle. These pronounced effects of the liquid crystal structure on the emission properties indicate potential photonic applications for these new materials. Results obtained for an Rh6G-doped achiral cellulose membrane are also shown (**Figure 6D**) to make clear that the photonic effects are indeed related to the unique liquid crystalline structure of CNC.

The color coordinate diagrams are seen in **Figure 7**. The shift observed for the emission color at different detection angles is a clear manifestation of the liquid crystal photonic properties of the host. **Figure 8** shows the emission spectra obtained for the sample CS4-Rh for detection angles of 20° and 90°. Reflectance spectra are also shown for incident angles of 20° and 50°. **Figure 8** intends to show that the general effect of the stopband is to blueshift the band emission compared to the one observed at 90°. It is possible to see in **Figures 7**, **8** that the observed emission spectra can be obtained from a convolution of Rh6G emission and the stopband due to the liquid crystal structure which changes with the detecting angle. The results obtained for the other samples are presented in **Supplementary Figure S6**. The same effect of the liquid crystalline structure on the emission spectra is observed. The values of *P* change by changing the silica content and the angular range where the redshift is seen in emission band changes as well. Therefore, the periodic structure with chiral nematic ordering leads to selective suppression of a range of the emitted wavelengths.

CONCLUSION

Freestanding luminescent and iridescent CNC-based silica composite films were obtained from bacterial cellulose and TEOS. The tuning of the helical pitch was achieved by adjusting the relative silica content, where the incorporation of luminescent Rhodamine 6G within the periodic chiral-nematic structure allowed the modulation of the emitted light by varying the detection angle. The combination of all these features into a single material offers a novel strategy to modulate the emission of luminescent species for applications in optical devices, such as sensors, lasers, or tunable filters.

DATA AVAILABILITY STATEMENT

The raw data supporting the conclusions of this article will be made available by the authors, without undue reservation.

AUTHOR CONTRIBUTIONS

HB, SR, and LC conceived the initial idea. ÉP and RF designed the experimental setup. MS, FM, and LL carried out the preparation of the materials and performed the experiments. MS and FM analyzed the data and wrote the manuscript. SR, HB, LC, and RF worked on funding acquisition. All authors have read and approved the final manuscript.

FUNDING

This work was supported by the Brazilian agencies CAPES and São Paulo Research Foundation, grants #2014/12424-2 and #2016/11591-8. Institute of Science and Technology-CNPq- Brazil was also acknowledged for financial support. Fundação para a Ciência e a Tecnologia, FEDER, COMPETE (UIDB/50011/2020 and 50011/2020) are acknowledged as well.

ACKNOWLEDGMENTS

M. C. Ferro from the University of Aveiro, Portugal, was acknowledged for her assistance in SEM analysis.

SUPPLEMENTARY MATERIAL

The Supplementary Material for this article can be found online at: https://www.frontiersin.org/articles/10.3389/fbioe.2021.617328/full#supplementary-material

REFERENCES

Abdollahramezani, S., Hemmatyar, O., Taghinejad, H., Krasnok, A., Kiarashinejad, Y., Zandehshahvar, M., et al. (2020). Tunable nanophotonics enabled by chalcogenide phase-change materials. *Nanophotonics* 9, 1189–1241. doi: 10.1515/nanoph-2020-0039

Anedda, A., Carbonaro, C. M., Clemente, F., Corpino, R., Grandi, S., Magistris, A., et al. (2005). Rhodamine 6G-SiO2 hybrids: a photoluminescence study. *J. Non Cryst. Solids* 351, 1850–1854. doi: 10.1016/j.jnoncrysol.2005.04.027

Anedda, A., Carbonaro, C. M., Corpino, R., Ricci, P. C., Grandi, S., and Mustarelli, P. C. (2007). Formation of fluorescent aggregates in rhodamine 6G doped silica glasses. *J. Non Cryst. Solids* 353, 481–485. doi: 10.1016/j.jnoncrysol.2006.10.014

Arrighi, V., Cowie, J. M. G., Vaqueiro, P., and Prior, K. A. (2002). Fine structure and optical properties of cholesteric films prepared from cellulose 4-methylphenyl urethane/ N-vinyl pyrrolidinone solutions. *Macromolecules* 35, 7354–7360. doi: 10.1021/ma012098n

Barud, H. S., Assunção, R. M. N., Martines, M. A. U., Dexpert-Ghys, J., Marques, R. F. C., Messaddeq, Y., et al. (2008). Bacterial cellulose–silica organic–inorganic hybrids. *J. Solgel Sci. Technol.* 46, 363–367. doi: 10.1007/s10971-007-1669-9

Barud, H. S., Regiani, T., Marques, R. F. C., Lustri, W. R., Messaddeq, Y., and Ribeiro, S. J. L. (2011). Antimicrobial bacterial cellulose-silver nanoparticles composite membranes. *J. Nanomater.* 2011:721631.

Beck-Candanedo, S., Roman, M., and Gray, D. G. (2005). Effect of reaction conditions on the properties and behavior of wood cellulose nanocrystal suspensions. *Biomacromolecules* 6, 1048–1054. doi: 10.1021/bm049300p

Boott, C. E., Tran, A., Hamad, W. Y., and MacLachlan, M. J. (2020). Cellulose nanocrystal elastomers with reversible visible color. *Angew. Chem. Int. Ed.* 59, 226–231. doi: 10.1002/anie.201911468

Broer, D. J., Lub, J., and Mol, G. N. (1995). Wide-band reflective polarizers from cholesteric polymer networks with a pitch gradient. *Nature* 378, 467–469. doi: 10.1038/378467a0

Bujdák, J. (2006). Effect of the layer charge of clay minerals on optical properties of organic dyes. a review. *Appl. Clay Sci.* 34, 58–73. doi: 10.1016/j.clay.2006.02.011

Carbonaro, C. M., Meinardi, F., Ricci, P. C., Salis, M., and Anedda, A. (2009). Light assisted dimer to monomer transformation in heavily doped rhodamine 6G-porous silica hybrids. *J. Phys. Chem. B* 113, 5111–5116. doi: 10.1021/jp810835j

Chu, G., Feng, J., Wang, Y., Zhang, X., Xu, Y., and Zhang, H. (2014a). Chiral nematic mesoporous films of ZrO 2:Eu 3+: new luminescent materials. *Dalton Trans.* 43, 15321–15327. doi: 10.1039/c4dt00662c

Chu, G., Wang, X., Chen, T., Xu, W., Wang, Y., Song, H., et al. (2015). Chiral electronic transitions of YVO 4:Eu 3+ nanoparticles in cellulose based photonic materials with circularly polarized excitation. *J Mater Chem C* 3, 3384–3390. doi: 10.1039/c4tc02913e

Chu, G., Xu, W., Qu, D., Wang, Y., Song, H., and Xu, Y. (2014b). Chiral nematic mesoporous films of Y 2 O 3:Eu 3+ with tunable optical properties and modulated photoluminescence. *J. Mater. Chem. C* 2, 9189–9195. doi: 10.1039/c4tc01482k

de Vries, H. (1951). Rotatory power and other optical properties of certain liquid crystals. *Acta Crystallogr.* 4, 219–226. doi: 10.1107/s0365110x51000751

Driesen, K., Moors, D., Beeckman, J., Neyts, K., Görller-Walrand, C., and Binnemans, K. (2007). Near-infrared luminescence emitted by an electrically switched liquid crystal cell. *J. Lumin.* 127, 611–615. doi: 10.1016/j.jlumin.2007.03.022

Dumanli, A. G., Van Der Kooij, H. M., Kamita, G., Reisner, E., Baumberg, J. J., Steiner, U., et al. (2014). Digital color in cellulose nanocrystal films. *ACS Appl. Mater. Interfaces* 6, 12302–12306.

Eichhorn, S. J. (2011). Cellulose nanowhiskers: promising materials for advanced applications. *Soft Matter* 7, 303–315. doi: 10.1039/c0sm00142b

Favier, V., Chanzy, H., and Cavaille, J. Y. (1995). Polymer nanocomposites reinforced by cellulose whiskers. *Macromolecules* 28, 6365–6367. doi: 10.1021/ma00122a053

Giasson, J., Revol, J.-F., Ritcey, A. M., and Gray, D. G. (1988). Electron microscopic evidence for cholesteric structure in films of cellulose and cellulose acetate. *Biopolymers* 27, 1999–2004. doi: 10.1002/bip.360271210

Habibi, Y. (2014). Key advances in the chemical modification of nanocelluloses. *Chem. Soc. Rev.* 43, 1519–1542. doi: 10.1039/c3cs60204d

Habibi, Y., Goffin, A., Schiltz, N., Duquesne, E., and Dufresne, A. (2008). Bionanocomposites based on poly (ε-caprolactone)-grafted cellulose nanocrystals by ring-opening polymerization. *J. Mater. Chem.* 18, 5002–5010. doi: 10.1039/b809212e

Habibi, Y., Lucia, L. A., and Rojas, O. J. (2010). Cellulose nanocrystals: chemistry, self-assembly, and applications. *Chem. Rev.* 110, 3479–3500. doi: 10.1021/cr900339w

Hiratani, T., Hamad, W. Y., and MacLachlan, M. J. (2017). Transparent depolarizing organic and inorganic films for optics and sensors. *Adv. Mater.* 29:1606083. doi: 10.1002/adma.201606083

Kelly, J. A., Giese, M., Shopsowitz, K. E., Hamad, W. Y., and MacLachlan, M. J. (2014). The development of chiral nematic mesoporous materials. *Acc. Chem. Res.* 47, 1088–1096. doi: 10.1021/ar400243m

Kelly, J. A., Shukaliak, A. M., Cheung, C. C. Y., Shopsowitz, K. E., Hamad, W. Y., and MacLachlan, M. J. (2013). Responsive photonic hydrogels based on nanocrystalline cellulose. *Angew. Chem. Int. Ed.* 52, 8912–8916. doi: 10.1002/anie.201302687

Klemm, D., Kramer, F., Moritz, S., Lindström, T., Ankerfors, M., Gray, D., et al. (2011). Nanocelluloses: a new family of nature-based materials. *Angew. Chem. Int. Ed.* 50, 5438–5466. doi: 10.1002/anie.201001273

Kopp, V. I., Fan, B., Vithana, H. K. M., and Genack, A. Z. (1998). Low-threshold lasing at the edge of a photonic stop band in cholesteric liquid crystals. *Opt. Lett.* 23, 1707–1709. doi: 10.1364/ol.23.001707

Lagerwall, J. P. F., Schütz, C., Salajkova, M., Noh, J., Park, J. H., Scalia, G., et al. (2014). Cellulose nanocrystal-based materials: from liquid crystal self-assembly and glass formation to multifunctional thin films. *NPG Asia Mater.* 6:e80. doi: 10.1038/am.2013.69

Li, X., Chen, S., Hu, W., Shi, S., Shen, W., Zhang, X., et al. (2009). In situ synthesis of CdS nanoparticles on bacterial cellulose nanofibers. *Carbohydr. Polym.* 76, 509–512. doi: 10.1016/j.carbpol.2008.11.014

Lin, P., Yan, Q., Wei, Z., Li, X., Wang, H., Huang, Z., et al. (2018). Electrically modulated optical properties of fluorescent chiral nematic liquid crystals. *Chem. Eng. J.* 341, 565–577. doi: 10.1016/j.cej.2018.02.007

Liu, C., Fan, Z., Tan, Y., Fan, F., and Xu, H. (2020). Tunable structural color patterns based on the visible light responsive dynamic diselenide metathesis. *Adv. Mater.* 32:1907569. doi: 10.1002/adma.201907569

Lofaj, M., Valent, I., and Bujdák, J. (2013). Mechanism of rhodamine 6G molecular aggregation in montmorillonite colloid. *Open Chem.* 11, 1606–1619. doi: 10.2478/s11532-013-0289-1

Majoinen, J., Kontturi, E., Ikkala, O., and Gray, D. G. (2012). SEM imaging of chiral nematic films cast from cellulose nanocrystal suspensions. *Cellulose* 19, 1599–1605. doi: 10.1007/s10570-012-9733-1

Martínez Martínez, V., López Arbeloa, F., Bañuelos Prieto, J., and López Arbeloa, I. (2005). Characterization of rhodamine 6G aggregates intercalated in solid thin films of laponite clay. 2 fluorescence spectroscopy. *J. Phys. Chem. B* 109, 7443–7450. doi: 10.1021/jp050440i

Martnez, V. M., Arbeloa, F. L., Prieto, J. B., Lpez, T. A., Arbeloa, I. L., and Spectroscopy, C. A. (2005). Characterization of rhodamine 6G aggregates intercalated in solid thin films of laponite clay . 1 . Absorption spectroscopy characterization of rhodamine 6G aggregates intercalated in solid thin films of laponite. *J. Phys. Chem. B* 109, 7443–7450. doi: 10.1021/jp050440i

Mendoza-Galván, A., Muñoz-Pineda, E., Ribeiro, S. J. L., Santos, M. V., Järrendahl, K., and Arwin, H. (2018). Mueller matrix spectroscopic ellipsometry study of chiral nanocrystalline cellulose films. *J. Opt.* 20:024001. doi: 10.1088/2040-8986/aa9e7d

Nguyen, T. D., Hamad, W. Y., and Maclachlan, M. J. (2014). CdS quantum dots encapsulated in chiral nematic mesoporous silica: new iridescent and luminescent materials. *Adv. Funct. Mater.* 24, 777–783. doi: 10.1002/adfm.201302521

Nguyen, T., Hamad, W. Y., and MacLachlan, M. J. (2017). Near-IR-Sensitive upconverting nanostructured photonic cellulose films. *Adv. Opt. Mater.* 5:1600514. doi: 10.1002/adom.201600514

Niinivaara, E., and Cranston, E. D. (2020). Bottom-up assembly of nanocellulose structures. *Carbohydr. Polym.* 247:116664. doi: 10.1016/j.carbpol.2020.116664

Penninck, L., Beeckman, J., De Visschere, P., and Neyts, K. (2012). Light emission from dye-doped cholesteric liquid crystals at oblique angles: simulation and experiment. *Phys. Rev. E Stat. Nonlin. Soft Matter Phys.* 85:041702.

Qu, D., Zhang, J., Chu, G., Jiang, H., Wu, C., and Xu, Y. (2016). Chiral fluorescent films of gold nanoclusters and photonic cellulose with modulated fluorescence emission. *J. Mater. Chem. C* 4, 1764–1768. doi: 10.1039/c5tc04163e

Revol, J. F., Bradford, H., Giasson, J., Marchessault, R. H., and Gray, D. G. (1992). Helicoidal self-ordering of cellulose microfibrils in aqueous suspension. *Int. J. Biol. Macromol.* 14, 170–172. doi: 10.1016/s0141-8130(05)80008-x

Revol, J.-F., Godbout, L., and Gray, D. G. (1998). Solid self-assembled films of cellulose with chiral nematic order and optically variable properties. *J. Pulp Paper Sci.* 24, 146–149.

Roman, M., and Winter, W. T. (2004). Effect of sulfate groups from sulfuric acid hydrolysis on the thermal degradation behavior of bacterial cellulose. *Biomacromolecules* 5, 1671–1677. doi: 10.1021/bm034519%2B

Santos, M. V., Maturi, F. E., Pecoraro, E., Ferreira, R. A. S., Carlos, L. D., and Ribeiro, S. J. L. (2019). "Photonic materials displaying direction modulated photoluminescence," in *In Proceedings of the 2019 SBFoton International Optics and Photonics Conference (SBFoton IOPC)*, (Sao Paulo: IEEE), 1–3. doi: 10.1016/j.optmat.2014.12.009

Shopsowitz, K. E., Kelly, J. A., Hamad, W. Y., and MacLachlan, M. J. (2014). Biopolymer templated glass with a twist: controlling the chirality, porosity, and photonic properties of silica with cellulose nanocrystals. *Adv. Funct. Mater.* 24, 327–338. doi: 10.1002/adfm.201301737

Shopsowitz, K. E., Qi, H., Hamad, W. Y., and MacLachlan, M. J. (2010). Free-standing mesoporous silica films with tunable chiral nematic structures. *Nature* 468, 422–426. doi: 10.1038/nature09540

Shopsowitz, K. E., Stahl, A., Hamad, W. Y., and MacLachlan, M. J. (2012). Hard templating of nanocrystalline titanium dioxide with chiral nematic ordering. *Angew. Chem. Int. Ed.* 51, 6886–6890. doi: 10.1002/anie.201201113

Siqueira, G., Bras, J., and Dufresne, A. (2009). Cellulose whiskers versus microfibrils: influence of the nature of the nanoparticle and its surface functionalization on the thermal and mechanical properties of nanocomposites. *Biomacromolecules* 10, 425–432. doi: 10.1021/bm801193d

Tercjak, A., Gutierrez, J., Barud, H. S., Domeneguetti, R. R., and Ribeiro, S. J. L. (2015). Nano- and macroscale structural and mechanical properties of in situ synthesized bacterial cellulose/PEO-b-PPO-b-PEO biocomposites. *ACS Appl. Mater. Interfaces* 7, 4142–4150. doi: 10.1021/am508273x

Tran, A., Boott, C. E., and MacLachlan, M. J. (2020). Understanding the self-assembly of cellulose Nanocrystals—toward chiral photonic materials. *Adv. Mater.* 32: 1905876. doi: 10.1002/adma.201905876

Van Opdenbosch, D., and Zollfrank, C. (2014). Cellulose-based biotemplated silica structuring. *Adv. Eng. Mater.* 16, 699–712. doi: 10.1002/adem.201400085

Wilts, B. D., Dumanli, A. G., Middleton, R., Vukusic, P., and Vignolini, S. (2017). Invited article: chiral optics of helicoidal cellulose nanocrystal films. *APL Photonics* 2:040801. doi: 10.1063/1.4978387

Xu, C., Huang, C., and Huang, H. (2021). Recent advances in structural color display of cellulose nanocrystal materials. *Appl. Mater. Today* 22:100912. doi: 10.1016/j.apmt.2020.100912

Yang, D., West, J. L., Chien, L., State, K., and Doane, J. W. (1994). Control of reflectivity and bistability in displays using cholesteric liquid-crystals. *J. Appl. Phys.* 2, 1331–1333. doi: 10.1063/1.358518

Zhanga, Y. P., Chodavarapua, V. P., Kirka, A. G., and Andrews, M. P. (2013). Structured color humidity indicator from reversible pitch tuning in self-assembled nanocrystalline cellulose films. *Sens. Actuators B Chem.* 176, 692–697. doi: 10.1016/j.snb.2012.09.100

Conflict of Interest: The authors declare that the research was conducted in the absence of any commercial or financial relationships that could be construed as a potential conflict of interest.

frontiers
in Bioengineering and Biotechnology

REVIEW
published: 07 May 2021
doi: 10.3389/fbioe.2021.616555

Perspective Applications and Associated Challenges of Using Nanocellulose in Treating Bone-Related Diseases

Suliman Khan[1†], Rabeea Siddique[1†], Ding Huanfei[2†], Muhammad Adnan Shereen[3], Ghulam Nabi[4], Qian Bai[1], Sehrish Manan[5], Mengzhou Xue[1], Muhammad Wajid Ullah[5]* and Hu Bowen[2]**

[1] Department of Cerebrovascular Diseases, The Second Affiliated Hospital of Zhengzhou University, Zhengzhou, China, [2] Department of Hepatobiliary and Pancreatic Surgery, The First Affiliated Hospital of Zhengzhou University, Zhengzhou, China, [3] State Key Laboratory of Virology, College of Life Sciences, Wuhan University, Wuhan, China, [4] Key Laboratory of Animal Physiology, Biochemistry and Molecular Biology of Hebei Province, College of Life Sciences, Hebei Normal University, Shijiazhuang, China, [5] Department of Biomedical Engineering, College of Life Science and Technology, Huazhong University of Science and Technology, Wuhan, China

Edited by:
Giovanni Vozzi,
University of Pisa, Italy

Reviewed by:
Rajendra Kumar Singh,
Institute of Tissue Regeneration Engineering (ITREN), South Korea
Hasan Uludag,
University of Alberta, Canada

***Correspondence:**
Mengzhou Xue
xuemengzhou@zzu.edu.cn
Hu Bowen
fcchubw@zzu.edu.cn
Muhammad Wajid Ullah
wajid_kundi@hust.edu.cn

† These authors have contributed equally to this work

Specialty section:
This article was submitted to Biomaterials, a section of the journal Frontiers in Bioengineering and Biotechnology

Received: 12 October 2020
Accepted: 09 April 2021
Published: 07 May 2021

Citation:
Khan S, Siddique R, Huanfei D, Shereen MA, Nabi G, Bai Q, Manan S, Xue M, Ullah MW and Bowen H (2021) Perspective Applications and Associated Challenges of Using Nanocellulose in Treating Bone-Related Diseases. Front. Bioeng. Biotechnol. 9:616555. doi: 10.3389/fbioe.2021.616555

Bone serves to maintain the shape of the human body due to its hard and solid nature. A loss or weakening of bone tissues, such as in case of traumatic injury, diseases (e.g., osteosarcoma), or old age, adversely affects the individual's quality of life. Although bone has the innate ability to remodel and regenerate in case of small damage or a crack, a loss of a large volume of bone in case of a traumatic injury requires the restoration of bone function by adopting different biophysical approaches and chemotherapies as well as a surgical reconstruction. Compared to the biophysical and chemotherapeutic approaches, which may cause complications and bear side effects, the surgical reconstruction involves the implantation of external materials such as ceramics, metals, and different other materials as bone substitutes. Compared to the synthetic substitutes, the use of biomaterials could be an ideal choice for bone regeneration owing to their renewability, non-toxicity, and non-immunogenicity. Among the different types of biomaterials, nanocellulose-based materials are receiving tremendous attention in the medical field during recent years, which are used for scaffolding as well as regeneration. Nanocellulose not only serves as the matrix for the deposition of bioceramics, metallic nanoparticles, polymers, and different other materials to develop bone substitutes but also serves as the drug carrier for treating osteosarcomas. This review describes the natural sources and production of nanocellulose and discusses its important properties to justify its suitability in developing scaffolds for bone and cartilage regeneration and serve as the matrix for reinforcement of different materials and as a drug carrier for treating osteosarcomas. It discusses the potential health risks, immunogenicity, and biodegradation of nanocellulose in the human body.

Keywords: nanocellulose, bone diseases, tissue engineering, biodegradation, medical applications

INTRODUCTION

Nanocellulose refers to the cellulosic materials with dimensions in the nanoscale range, which combines the important properties of cellulose with the features of nanomaterials (Mazhar et al., 2021). It is obtained from plants (de Amorim et al., 2020), produced by different microorganisms predominantly from acetic acid bacteria (Andriani et al., 2020; Khan et al., 2020b), algae (Liu et al., 2017), and animals (Bacakova et al., 2019), as well as synthesized enzymatically such as by the cell-free enzyme systems (Ullah et al., 2015; Kim et al., 2019). There exist different types of nanocellulose, including cellulose nanofibers (CNFs), cellulose nanocrystals (CNCs), and microorganisms-derived cellulose knows as bacterial nanocellulose (BNC) or bacterial cellulose (BC) (Klemm et al., 2018). The CNFs and CNCs are extracted from different plants through complex extraction procedures, involving physico-mechanical degradation and chemical de-structuring such as acid hydrolysis (Dufresne, 2013; Ullah et al., 2016c). BNC is chemically similar to plant-derived cellulose; nevertheless, it represents the purest form of cellulose, as unlike plant cellulose, it does not contain hemicellulose, lignin, and other minerals (Bacakova et al., 2019; Ul-Islam et al., 2019a).

Bacterial nanocellulose is the most prominent biopolymer synthesized by specific bacterial species through the fermentation of sugars and plant carbohydrates. It possesses unique structural, physico-chemical, mechanical, thermal, and biological features and is a Generally Recognized As Safe (GRAS) biological product (Yang et al., 2018; Zhong, 2020). It has been extensively used for various biomedical and other applications in the form of hydrogels, membranes, particles, and three-dimensional (3D) scaffolds, where its properties are tuned according to the target applications (Ul-Islam et al., 2015). Its innate features are modulated through the development of its composites with different materials like natural and synthetic polymers (Shah et al., 2013), nanomaterials (Ul-Islam et al., 2014; Khan et al., 2015; Ullah et al., 2016b), peptides (Curvello et al., 2019), ceramics (DeMello, 2012), clays (Ul-Islam et al., 2013a), plant extracts (Fatima et al., 2021; Ul-Islam et al., 2021a), and others (Mbituyimana et al., 2021). Similarly, its biological synthesis is regulated to produce BNC with controlled features in the form of mechanically and thermally stable hydrogels and form simple to complex 3D structures (Shi et al., 2016). Moreover, its structural features are modified through different pre- and post-synthesis processing approaches (Ul-Islam et al., 2013b). Although the harvesting procedures of BNC hydrogels from the production medium are simple, cost-effective, and time-efficient, the drying procedures such as air-drying, oven-drying, spray-drying, press-drying, critical point drying, and freeze-drying which ultimately determine the characteristic features of BNC, are time-consuming (Lin and Dufresne, 2014; Sharma and Bhardwaj, 2019), and may cause unwanted changes to the innate structure of BNC. For example, air-drying causes the loss of the 3D network structure of BNC due to strong shrinkage-mediated wrinkling, fiber aggregation, and superficial hornification and ultimately results in reduced porosity. On the other hand, critical point drying and freeze-drying, although gentle procedures and retain the original nanofibrous structure (Sharma and Bhardwaj, 2019), may result in complete drying and causes brittleness. BNC is a non-toxic biopolymer that has been found with no severe signs of inflammation and toxicity on the genetic and cellular levels, even in long-term application. Currently, more attention is given to developing BNC-based scaffolds for various medical applications. For instance, the development of BNC-based wound dressings is currently on the market, while some BNC implants are in the phase of clinical studies as a novel solution to yet unresolved complications in regenerative medicine (Klemm et al., 2018; Sharma and Bhardwaj, 2019; Zhong, 2020). Studies have shown that the BNC-based scaffolds play vital roles in the regeneration of bone and cartilage (Khan et al., 2020a), as the drug delivery systems (Pachuau, 2017; Li et al., 2018), biosensing platforms (Jasim et al., 2017; Farooq et al., 2020), diagnostic tools (Ul-Islam et al., 2019b), and several other areas (Islam et al., 2015; Derakhshanfar et al., 2018; McCarthy et al., 2019a,b, Wang et al., 2020a, 2021). The impregnation of nanomaterials to BNC and its use as the wound dressing biomaterial, broad-spectrum antimicrobial, surface disinfectant, and nanodrugs for the treatment of different diseases (Lin and Dufresne, 2014; Di et al., 2017; Wang et al., 2020b) could be an effective approach for addressing several clinical issues.

Bone and cartilage encounter different defects associated with diseases, injuries, and aging. Some of these defects are conventionally treated by using autografts, allografts, and xenografts; however, their general use is hindered by immune rejection. Similarly, osteosarcoma, the malignant bone-tumor accounting for 20% of primary bone cancers (Carina et al., 2019), is another class of bone diseases. The widespread application of currently used strategies for treating osteosarcoma such as surgery (e.g., amputations and bone reconstruction) combined with chemotherapy is limited by the low efficacy of different therapeutic options as well as some chemotherapeutic drugs cause adverse effects and lead to severe complications (Carina et al., 2019). To overcome the adverse effects of surgery and chemotherapy, various biophysical approaches such as sono- and photodynamic therapies, low-intensity pulsed ultrasound, high-intensity focused ultrasound, and hyperthermia have been developed (Sengupta and Balla, 2018; Carina et al., 2019). To date, the knowledge about the efficacy of biophysical therapies against osteosarcoma is limited, and there are only limited reports available about the usage of nanotechnology and nano-delivery systems for the treatment of osteosarcomas (Gu et al., 2013).

The applications of nanotechnology could be expanded toward the treatment of bone and cartilage defects. For example, nanoparticles possess unique properties such as low toxicity, biodegradability, selective tumor cell targeting, higher deposition and retention in tumor tissue, and prolonged blood circulation time (Panday et al., 2018; Zhang et al., 2018b). Although there are also unclear aspects of nanotechnology restricting its broad-spectrum applications, the inherent unique properties of nanomaterials could help in improving their therapeutic efficacy against osteosarcomas (Turnbull et al., 2018; Zhang et al., 2018b). In addition to different nanoparticles, nanocellulose could also be used to replace the affected bone, like in the form of bone substitutes, as a matrix for impregnation of nanomaterials, and as a drug carrier (Khan et al., 2019) for treating different bone-related diseases. For instance, bisphosphonate-modified nanocellulose (pNC) could be used as a bone substitute for bone regeneration. The pNC is a bioresponsive injectable bone material that suppresses the formation of osteoclasts and enhances the differentiation of osteoblasts. Considering the regulation of osteoclast/osteoblast activity, pNC has enormous potential for treating bone diseases (Nishiguchi and Taguchi, 2019). Although the mechanical strength of nanocellulose is quite low compared to that of the bone tissues, it can be improved, such as through crosslinking. In a study, mechanically stable CNCs-based scaffolds were developed through sulfuric acid hydrolysis crosslinking, which showed high compressive strength and porosity. The scaffolds demonstrated *in vivo* osteoinductivity and bone formation across the damaged site (Osorio et al., 2019a). Besides, nanocellulose could also be modified with anti-osteosarcoma metals or nanoparticles, for instance with selenium, strontium, and arsenic nanoparticles, where nanocellulose could not only function as a carrier for different drugs but also serve as a substitute for the damaged bone tissues (Khan et al., 2019; Luz et al., 2020). Both selenium and arsenic have been widely studied for their anticancer effects, where selenium has been found effective against osteosarcoma when doped with hydroxyapatite (Wang et al., 2016; Khan et al., 2019). Therefore, combining these metals with nanocellulose may further increase their utilization in treating bone diseases. Besides bone, nanocellulose could also be used as a substitute for the cartilage that is a smooth elastic tissue and covers the ends of long bones at the joints and nerves and is commonly present in the ear, nose, rib cage, intervertebral disks, and several other parts of the body. Cartilage is softer than bone but much stiffer than muscles and contains chondrocytes which produce a collagenous extracellular matrix. In a study, a highly porous hydrogel comprised of interpenetrating networks of sodium alginate and gelatin reinforced with cellulose nanocrystals was prepared. The composite hydrogel supported the adhesion, growth, penetration, and differentiation of mesenchymal stem cells (MSCs), thus could be used as a substitute for cartilage (Naseri et al., 2016). In another study, a mitogenic hydrogel ink comprised of alginate sulfate with nanocellulose was printed that supported the adhesion, spreading, and proliferation of chondrocyte and produced collagen II (Müller et al., 2017). The printed 3D scaffold could be used as a potential substitute for cartilage.

Literature survey shows that there exist few reviews on using different forms of nanocellulose for their tissue engineering and other biomedical applications. For example, a couple of reviews specifically discusses the tissue engineering applications of BC (Torgbo and Sukyai, 2018) and CNCs (Murizan et al., 2020), while others overview the use of different forms of nanocellulose for bone tissue engineering along with other biomedical applications (Bacakova et al., 2019; Luo et al., 2019; Pang et al., 2020; Subhedar et al., 2021). However, there is no comprehensive review discussing not only the tissue engineering applications but also the role of nanocellulose as a matrix for nanoparticles and drugs for treating osteosarcomas. Moreover, this review discusses the important structural, physiological, and biological features of nanocellulose from the perspective of developing scaffolds suitable for tissue engineering and carriers for drugs and nanoparticles for treating bone defects and cancers. Most importantly, it discusses the immunogenicity and complications associated with the introduction of nanocellulose to the human body.

NATURAL SOURCES OF NANOCELLULOSE

Plants

Plants represent the most abundant source of nanocellulose. It is extracted from different plant sources such as trees, roots, vegetables, grasses, shrubs and herbs, succulents, flowers, and different other plant-derived sources. Trees are the main source of nanocellulose, and it is mostly obtained from coniferous (*Pinus radiata*) (Powell et al., 2016) and leaved trees (birch) (Bacakova et al., 2019). Various other trees, for example, *Khaya senegalensis* (Adewuyi et al., 2018), *Banana pseudostem* (Faradilla et al., 2017), palm and balsa (Bacakova et al., 2019), citrus trees (Matharu et al., 2018), *Syzygium cumini* (Singla et al., 2017), and *Acacia mangium* (Jasmani and Adnan, 2017), are also good sources of nanocellulose. The nanocellulose extracted from coniferous and leaved trees is referred to as the softwood and hardwood-derived nanocellulose, respectively. Hibiscus and cotton are the shrub sources of nanocellulose (Poonguzhali et al., 2017). Various other plant sources of nanocellulose include the corn leaf, carrot, triticale straw, sisal (*Agave sisalana*), *Miscanthus giganteus* (grass), bamboo, pineapple leaf, rice husk, and soybean straw (Song et al., 2018).

Microorganisms

The microorganism-derived nanocellulose (i.e., BNC or BC) (Yuen et al., 2017) is mainly produced by the Gram-negative acetic acid bacteria belonging to genera *Gluconacetobacter*, *Acetobacter*, *Sarcina*, *Salmonella*, *Achromobacter*, *Agrobacterium*, *Alcaligenes*, *Rhodobacter*, *Azotobacter*, *Pseudomonas*, *Aerobacter*, and *Rhizobium*. Among the different BNC-producing bacterial genera, *Gluconacetobacter xylinum* and *Gluconacetobacter hansenii* are the most widely studied bacterial species (Ahrem et al., 2014; Ullah et al., 2017). Besides, *Gluconacetobacter kombuchae* and *Komagataeibacter medellinensis* (low pH-resistant strain) (Bacakova et al., 2019) are also known for high-quality BNC production. BNC is typically synthesized as pure cellulose by the BNC-producing bacteria, which, unlike the plant-derived cellulose, does not require intensive processing for removal of unwanted impurities or contaminants (Lin et al., 2013). To date, different strategies have been developed for increasing the yield and productivity, minimizing the production cost, and enhancing the structural features of BNC (Ullah et al., 2019c; Ul-Islam et al., 2021b). For example, the addition of yeast extract to the bacterial growth medium enhances bacterial growth, thus leading to high productivity and yield

(Saska et al., 2017; Kaminagakura et al., 2019). A study also reported enhanced BNC production through the symbiotic co-cultivation of *M. gisevii* with BNC-producing bacterium (Zharikov et al., 2018). The addition of different supplements to the growth medium not only improves the production but also enhances the structural features of BNC (Ul-Islam et al., 2017, 2020). Different reactors have also been designed for improving yield and productivity (Ullah et al., 2019c). Besides, extensive efforts have been made to explore low-cost substrates and utilize different wastes for cost-effective BNC production (Ul-Islam et al., 2017, 2020).

Cell-Free Enzyme System

Nanocellulose production by the cell-free enzyme systems represents a relatively new and previously uncharacterized approach. A cell-free enzyme system represents the state-of-the-art conversion of a substrate into the product through a series of enzymatic reactions, each catalyzed by specific enzymes and regulatory proteins (i.e., cofactors) (Khattak et al., 2014; Ullah et al., 2016a). Park and co-workers developed a *G. hansenii*-based cell-free enzyme system through a simple bead beating approach and demonstrated *in vitro* nanocellulose production (Ullah et al., 2015; Kim et al., 2019). The developed system contained all essential enzymes required for the synthesis of cellulose as characterized by the LC-MS/MS-LTQ Orbitrop and SDS-PAGE analyses. The system was further supplemented with external cofactors (i.e., ATP and NAD) to boost the nanocellulose-production (Ullah et al., 2015). The developed cell-free enzyme system effectively produced cellulose at a much higher yield (58%) as compared to the microbial cell system (i.e., 37%) under the same experimental conditions. Moreover, the synthesized cellulose demonstrated superior morphological structure, physiological features, and thermal and mechanical properties, as compared to the cellulose produced by the microbial cells (Ullah et al., 2016c). The cell-free enzyme system represents an *in vitro* and energy-efficient approach for nanocellulose synthesis that can be easily controlled, and the synthesized nanocellulose could be tuned for the desired structural features.

Algae

Cladophora and *Cystoseria myrica* are the major algal species that produce nanocellulose. *Cladophora*-derived nanocellulose is a potential biomedical material due to the presence of several useful materials in its structure, including endotoxins, glucans, and heavy metals (Liu et al., 2017). Its adsorption capacity for Congo-Red-dye (Ruan et al., 2018), hemocompatibility (Rocha et al., 2018), and suitability as the scaffold for cell adhesion and proliferation (Hua et al., 2016) have already been evaluated. Similarly, the *Cystoseria myrica*-derived nanocellulose together with Fe_3O_4 has been evaluated for the removal of mercury (Zarei et al., 2018).

Animals

Nanocellulose has also been obtained from some animals such as *Styela clava* and Halocynthia roretzi Drasche (tunicates from phylum Chordata) (Bacakova et al., 2019). *Styela clava*–derived nanocellulose has been used in wound dressings and other biomedical applications, including scaffolds-based tissue engineering and the development of absorbable hemostats and hemodialysis membranes and stitching fibers (Song et al., 2014, 2017). There are also various industrial and technological applications of nanocellulose from animals. For example, Halocynthia roretzi Drasche (composite)-derived nanocellulose together with TiO_2 nanoparticles was used for the removal of oil from wastewater (Zhan et al., 2018).

NANOCELLULOSE-RELATED HEALTH COMPLICATIONS IN HUMANS

Nanocellulose, mainly BNC, is applied in different forms to humans, such as skin substitute (Khan et al., 2018), wound dressing materials (Sajjad et al., 2020), synthetic blood vessels (Scherner et al., 2014), artificial cornea (Wang et al., 2010), bone and cartilage (Basu et al., 2018), synthetic heart valves (Mohammadi, 2011), gastrointestinal tract (Lamboni et al., 2019), tympanic membrane (Kim et al., 2013), dental implants (Jinga et al., 2014), neural implants (Yang et al., 2017), urinary conduit replacement (Huang et al., 2015), contact lenses (Cavicchioli et al., 2015), and several others, and therefore, it is necessary to identify the associated potential health risks (Endes et al., 2016). Several studies have reported brown lung, alveo-bronchiolitis, fibrosis, and granulomatous inflammation *in vivo* following the exposure to cellulose (Tátrai et al., 1995). Similarly, studies have reported the persistence of cellulose, both *in vitro* and *in vivo*, alveolitis, granulomata, and higher cellulose fiber durability in the lungs (Endes et al., 2016). A study has also reported the cytotoxicity of high doses of nanocellulose crystals (Yanamala et al., 2014). The high doses of cellulose can significantly increase the radical formation (Stefaniak et al., 2014) and generation of oxidative stress during long-term exposure, which can ultimately lead to serious consequences in the human body. Currently, few studies have investigated the genotoxic effects of nanocellulose in the human body, including potential for mutagenicity, formation of micronuclei, and measurement of DNA strand breaks (Endes et al., 2016). Although no studies have reported any effects on the formation of micronuclei or alteration in DNA quality after exposure to nanocellulose exposure (Kovacs et al., 2010; Catalán et al., 2015), a study by de Lima et al. (2012) found chromosomal aberration in the animal cells after exposure to nanocellulose. Surprisingly, the chronic exposure to nanocellulose *via* inhalation increased the susceptibility to cytotoxicity in males and was associated with higher inflammatory and oxidative stress. These biochemical alterations further cause significant genotoxicity (Shvedova et al., 2016), and the genotoxic effects are extremely detrimental to the male reproductive system (Farcas et al., 2016). However, a detailed long-term mechanistic toxicological assessment study to investigate the potential biological effects on human health is still lacking. These assessments are essential and are considered as the landmarks of nanotoxicological research strategies (Camarero-Espinosa et al., 2016).

ATTRACTIONS IN NANOCELLULOSE-BASED SCAFFOLDS TO SUBSTITUTE BONE TISSUES

As bone primarily maintains the shape of the body, the biological scaffolds serving as the bone substitute must demonstrate the desired mechanical strength and biocompatibility. Nanocellulose possesses unique structural, physico-chemical, mechanical, thermal, and biological features to meet the desired features of biological scaffolds. In addition, its 3D fibrous and porous structure and the presence of free hydroxyl (OH) groups on its surface provide an excellent platform for the development of biomaterials with tuned properties.

Abundance and Renewability

Nanocellulose is the most abundant and renewable material on Earth. As described earlier (see section "Natural Sources of Nanocellulose"), it is obtained from a variety of sources like plants, microorganisms, algae, and animals and synthesized enzymatically. The abundance, renewability, and easy availability, along with other properties, make nanocellulose an ideal choice for the development of biological scaffolds for applications in bone tissue engineering (**Table 1**).

Surface Chemistry

Nanocellulose has a high surface area and aspect ratio (length to diameter) and contains abundant OH groups. The cellulose chain is asymmetric, with one end having reducing functionality due to the presence of the OH group while the other end is non-reducing (Habibi et al., 2010; Islam et al., 2018). On average, each glucose monomer in cellulose contains three OH groups, which can be easily accessed for surface modification (Phanthong et al., 2018). For example, TEMPO-oxidation at the surface of nanocellulose creates a negative charge by replacing the OH groups with carboxylic (COOH) and aldehyde (CHO) groups, which allows the repulsion of nanofibrils and causes fibrillation (Saito et al., 2007; Isogai et al., 2011), thus greatly contributes to addressing the aggregation issue of cellulose fibrils. This aggregation issue could also be addressed by introducing the anionic sulfate groups onto the surface of nanocellulose that produces electrostatic repulsion among the fibers in the aqueous dispersion and yield stable CNCs (Eyley and Thielemans, 2014). It is worth mentioning here that not all OH groups are modified; a large number of reactive OH groups are preserved to allow the grafting or doping of other molecules to impart additional structural and functional characteristics to nanocellulose. A study reported the uptake of non-aggregated softwood pulp sheet-derived nanocellulose by different cells (Hosseinidoust et al., 2015), thus could be used as a carrier for nanodrugs.

Biocompatibility

Biocompatibility refers to the ability of a material to interact with living tissues without provoking the immunogenic response, inflammation, or allergy and remain non-toxic (Morais et al., 2010; Ul-Islam et al., 2015). According to Williams's definition, biocompatibility is "the ability of a material to perform with an appropriate host response in a specific application" (Williams, 2019). In general, all types of nanocelluloses are considered biocompatible materials in that these are non-toxic, non-immunogenic, non-inflammatory, non-allergic, and somehow supports the adhesion, proliferation, growth, migration, and differentiation of cells, either alone or in the form of composites with other materials (Eslahi et al., 2020). A study reported the use of bleached birch pulp-derived nanofibrillated cellulose for wound dressing, which effectively adhered and detached from the skin after completion of wound healing (Hakkarainen et al., 2016). Similarly, BNC is considered a moderate to highly biocompatible biomaterial due to its non-toxic nature and ability to support cell growth, proliferation, and infiltration owing to its highly porous and fibrous structure (Klemm et al., 2001; Schumann et al., 2009). An *in vivo* study demonstrated the subcutaneous implantation of BNC in rats up to 12 weeks that did not show any signs of immunogenicity, inflammation, or formation of exudates around the implant (Helenius et al., 2006). Although non-toxic, pristine BNC lacks cell adhesion sites and its biocompatibility is not up to the desired levels in some cases; thus, different strategies like a surface modification to introduce bioactive functional groups such as peptides antimicrobial peptides (Fürsatz et al., 2018) and formation of composites with compatible polymers like gelatin (Khan et al., 2018), chitosan (Ul-Islam et al., 2019b), collagen (Zhang et al., 2020; Li et al., 2021), and other materials, have been developed to achieve the desired biocompatibility for specific applications (Phanthong et al., 2018; Ullah et al., 2019b; **Table 1**).

Biodegradability/Bioresorbability

Biodegradation or bioresorbability is an important feature of nanocellulose for its application in bone tissue engineering (Ullah et al., 2019b). The nanocellulose-based scaffolds degrade both *in vitro* and *in vivo*; nevertheless, these sometimes require additional pre-treatment and modification, such as oxidation (Faradilla et al., 2017), and must degrade at a controlled rate of resorption for specific bone tissue engineering applications. Moreover, the degradation products of nanocellulose are also biologically safe due to their innate non-toxic nature; however, a careful selection of the reinforcement materials during the development of nanocellulose-based scaffolds must be ensured for the safety of the degradation products. A study reported that the architecture of biological scaffolds changes with the degradation, where the produced byproducts could interfere with other *in vivo* biological processes (Dorozhkin, 2013).

Compared to other forms of nanocellulose, BNC is rarely biodegradable due to its crystalline nature and compact fibrils arrangement. Moreover, human lacks the cellulose-degrading cellulase enzyme. The biodegradation of BNC has been enhanced through several methods. For example, Li et al. (2009) carried out the periodate oxidation of BNC, which led to its enhanced *in vitro* oxidation in water, phosphate buffer saline, and simulated body fluid. The periodate oxidation of BNC allows specific cleavage of C2–C3 of the glucopyranoside and produces two aldehyde molecules from a single glucose unit as well as the biodegradable and biocompatible 2,3-dialdehyde cellulose (DAC) (Fan et al., 2001; Li et al., 2009). The DAC is biodegradable at

TABLE 1 | Applications of BNC-based biomaterials in bone regeneration.

Reinforcement material	Synthesis method	Model system for analysis	Enhanced properties	References
HAp	Post-synthesis phosphorylation	Ca/P ratio	High Ca/P ratio	DeMello, 2012
	Loading of HAp to BNC	HAp loading	High loading of HAp in phosphorylated BNC	Wan et al., 2007
	Post-synthesis loading	Ca/P ratio, *in vivo* inflammatory tests	Ca/P ratio similar to natural bone and no *in vitro* inflammation	Saska et al., 2011
	Biomimetic synthesis	hBMSC	Enhanced cell adhesion and biological activity	Fang et al., 2009
	Post-synthesis loading	XPS analysis, ALP activity, osteoblast growth, and formation of bone nodule	Presence of Ca^{2+} and $PO_4{}^{2-}$, enhanced adhesion growth of osteoblast, and osteoconductivity on membranes	Tazi et al., 2012
HAp and magnetic nanoparticles		Ca/P ratio, crystallinity, magnetic field response, *in vitro* MC3T3-E1 cells	High porosity, decreased crystallinity and swelling, decreased saturation magnetization, and enhanced biocompatibility	Torgbo and Sukyai, 2019
HAp and graphene oxide	Wet chemical precipitation	ALP activity, growth of MG-63 and NIH-3T3 cells	Water uptake, *in vitro* degradation, cell adhesion and growth, and ALP activity	Ramani and Sastry, 2014
HAp and gelatin	Laser patterning	Porosity and *In vitro* C5.18 cells	Enhanced adhesion and proliferation of chondrogenic rat cells, high porosity	Jing et al., 2013
HAp and strontium	Oxidation of BNC, *ex situ* mineralization	*In vitro* cytotoxicity and hemocompatibility	Guided bone regeneration, *in vivo* biocompatibility, *in vitro* degradation, bioactivity, non-cytotoxicity, low inflammation, swelling, thermal stability, enhanced desorption	Luz et al., 2020
HAp or Col with and without OGP	Post-synthesis loading	CHO-K1 cells, CBMN assay, comet assay, XTT assay, and clonogenic assay	Cell adhesion and proliferation, and no mutagenic, genotoxic, or cytotoxic effects on the cells	Raquel Mantuaneli Scarel-Caminaga, 2014
HAp and poly (vinyl pyrrolidone)	Biomimetic mineralization	Ca/P ratio	Enhanced mineralization	Yin et al., 2011
Agarose, gelatin, HAp, and procyanidins	Post synthesis crosslinking	Mechanical strength, pore size distribution, *in vitro* hGMSCs, *in vitro* and *in vivo* bone formation	Porosity, mechanical strength, cell viability, *in vitro* bone formation in mice and *in vivo* bone repair in rabbit	Huang et al., 2017
GO, Hap, and β-glucan	Free radical polymerization and freeze-drying	Surface morphology, porosity, and mechanical strength, hydrophobicity, aqueous degradation, *in vitro* MC3T3-E1	High stability, hydrophobicity, aqueous degradation, spongy morphology, porosity, and mechanical strength, antibacterial activity, biocompatibility, hemocompatibility	Umar Aslam Khan et al., 2020
2-chloro-*N, N*-dimethyl ethylamine hydrochloride, glycidyl trimethyl ammonium chloride, and monochloro acetic acid sodium salt	Post-synthesis chemical reaction	*In vitro* EqMSCs	Enhanced *in vitro* adhesion, proliferation, and osteogenic differentiation of EqMSCs	Favi, 2014
Gelatin	Post-synthesis loading	Crystallinity index, mechanical strength, *in vitro* adhesion of NIH 3T3 cells	Crystallinity index, enhanced mechanical strength and thermal stability, improved *in vitro* cell adhesion	Cai and Kim, 2010
PVA and boron nitride	3D printing	Mechanical strength, swelling, *in vitro* osteoblast cell line	Decreased tensile strength and increased elongation strain, enhanced cell adhesion and viability, improved swelling	Aki et al., 2020
Plant-derived recombinant human osteopontin (p-rhOPN), and RGD-containing biomolecule	*In vitro* grafting	Quantification of p-rhOPN immobilization, *in vitro* mineralization, and *in vitro* hPDLSCs	Enhanced osteogenic differentiation of hPDLSCs, cytocompatibility, *in vitro* calcification	Klinthoopthamrong et al., 2020
Bone morphogenic protein (BMP-2)	Post-synthesis loading	*In vitro* mouse fibroblast-like C2C12 cells, *in vivo* bone formation	Differentiation of C2C12 cells into osteoblasts and *in vivo* formation of bone with high calcium content	Shi et al., 2012a,b
	3D scaffolds, ECM-mimicking	Low dose treatment of BMB-2, micro- and nano-porosity, *in vitro* C3H10T1/2 cells	Enhanced cell adhesion, growth, and infiltration, bone matrix secretion and maturation, biomineralization, osteoinduction	Dubey et al., 2020

(Continued)

TABLE 1 | Continued

Reinforcement material	Synthesis method	Model system for analysis	Enhanced properties	References
Collage and BMP-2	Malaprade and Schiff-base reactions, template method combined with reverse-phase suspension regeneration	Porosity, *in vitro* MC3T3-E1, ALP activity	Biocompatibility, 3D porous microspheres with multiple structures, thermal stability, increased crystallinity, osteoblast differentiation	Zhang et al., 2020
Otoliths and collagen	Post-synthesis loading	Histological examination	In vivo regeneration of bone tissue with higher osteoblast activity, degree of regularity, and osteo-reabsorption activity	Olyveira et al., 2011
Col1	Post-synthesis crosslinking	Tensile strength, elastic modulus, and morphology and proliferation of osteogenic cells	Decreased tensile strength and elastic modulus of BNC-Col1, a slight increase in strain at break, cell viability and proliferation, and maintenance of cell morphology on the scaffold	Saska et al., 2012
Paraffin wax particles	*In situ* loading of particles	MC3T3-E1 osteoprogenitor cells, confocal microscopy, and histology	Enhanced clustering of MC3T3-E1 osteoprogenitor cells in the porous composite	Zaborowska et al., 2010

An overview of different reinforcement materials, synthesis methods, model systems used for analysis, and enhanced properties of BNC and its composites.

physiological pH, both *in vitro* and *in vivo*, and produces 2,4-dihydroxybutyric acid and glycolic acid (Singh et al., 1982), where the former participates in the metabolism of L-homoserine in the liver while the latter is either excreted through urine or enters the Krebs's cycle (RoyChowdhury and Kumar, 2006). Similarly, a study by Yang et al. (2016) reported the development of carboxymethylated chitosan and hairy nanocrystalline cellulose-based biodegradable aerogels.

Immunogenicity

Immunogenicity refers to the potential of a substance, referred to as antigen, to provoke an immune response when it enters the body. Although nanocellulose is generally perceived as non-immunogenic, very little knowledge about the immunogenic impact of nanocellulose on the immune cells such as macrophages and dendritic cells is available. The evaluation of immunogenicity is particularly important when nanocellulose-based scaffolds are used for *in vivo* tissue engineering applications or when these come in direct contact with the blood. A very recent review provides the current-state of knowledge of the immunological aspects of nanocellulose against the immune cells (Čolić et al., 2020). A study reported that CNCs induce inflammation upon internalization by macrophages; nevertheless, this immunogenic response by the macrophages can be suppressed by introducing special functional groups on nanocellulose. For example, the introduction of carboxyl groups onto the surface of CNFs shifted the tolerogenic potential of dendritic cells toward the induction of regulatory $CD8^+$ T cells. On the other hand, the introduction of phosphonates onto the surface of CNFs enabled the dendritic cells to induce both the regulatory $CD8^+$ T cells and type I regulatory cells (Tomić et al., 2018). These and several other studies show that nanocellulose, especially CNCs, can potentially induce an immunogenic response; nevertheless, this response and its level are highly dependent on the source, preparation methods, morphology and size, agglomeration, presence of contaminants in nanocellulose as well as the type of interacting cells.

Hemocompatibility

Blood compatibility, known as hemocompatibility, refers to the ability of a biomaterial to interact with the blood without causing toxic effects. Hemocompatibility is an important property of biomaterials for the development of blood-contacting artificial organs, such as artificial heart valves (Mohammadi, 2011) and blood vessels (Scherner et al., 2014). The scaffold, which needs to be implanted into the human body, must be hemocompatible as non-hemocompatible scaffolds may cause toxic effects at the site of implantation such as inflammation, provoking an immune response, or infection. The nanocellulose-based scaffolds are generally hemocompatible (Andrade et al., 2011; Leitão et al., 2013) and allow proper osteoconduction, integration, and induction (Pang et al., 2020). The hemocompatible nature of BNC was first reported by Andrade et al. (2011), who determined the plasma recalcification time and whole blood clotting of RGD-modified BNC. The findings of this study showed the successful deposition of plasma protein and prevention of platelet adhesion both on pristine and RGD-modified BNC scaffolds, indicting the hemocompatible nature of BNC (Andrade et al., 2011). In another study, Leitão et al. (2013) evaluated hemocompatibility of BNC and polyvinyl alcohol (PVA) nanocomposite by determining the whole blood clotting time, plasma recalcification, Factor XII activation, platelet adhesion and activation, and hemolytic index. The findings of the study showed low activation of platelets and Factor XII, indicating the hemocompatible nature of BNC/PVA composite (Leitão et al., 2013). In a more recent study, Osorio et al. (2019b) compared the *in vitro* and *in vivo* hemocompatibility of 3D BNC scaffold with the 2D BNC architecture. The findings of the study showed antihemolytic and anti-thrombogenic effects and only a mild acute inflammatory response of BNC (Osorio et al., 2019b). The hemocompatible BNC-based scaffolds promote neo-vascularization, gaseous exchange, and diffusion of nutrients and minerals in the newly formed or regenerated bones (Seyednejad et al., 2012; Torgbo and Sukyai, 2018). A study showed that the oral administration of TEMPO-oxidized cellulose nanofibers in mice effectively reduced the concentrations of postprandial glucose-dependent insulinotropic-polypeptide, plasma insulin, triglycerides, and blood glucose, suggesting the occurrence of cellulose-induced significant biological and hemocompatible activities (Lin and Dufresne, 2014).

Mechanical Strength

The cellulose fibers containing strong hydrogen bonding networks and various OH groups offer unique surface properties (Dufresne, 2017; Klemm et al., 2018). The cellulose fibrils contain the crystalline (highly ordered regions) and amorphous (disordered regions) structures (Cheng et al., 2009). The chain molecules at the crystalline regions are packed in such ways that these significantly enhance the stiffness and strength of cellulose, while the amorphous regions confer flexibility (Klemm et al., 2018). Besides, the low density ($\sim$1.6 g/cm^3), lightweight, and other strength properties make nanofibers highly stiff of $\sim$220 GPa of elastic modulus (greater than Kevlar fiber) and high tensile strength of $\sim$10 GPa (greater than cast iron), and the strength ratio to weight is eight times greater than the stainless steel. The mechanical strength of nanocellulose is further enhanced by developing its composites with mechanically strong reinforcement materials such as ceramics, nanoparticles, and polymers. The nanocellulose-based composites possess excellent mechanical properties due to their transparent nature and lightweight (Abdul Khalil et al., 2012; Abitbol et al., 2016). For example, the soybean-derived nanocellulose impregnated with three different types of synthetic polymers showed excellent mechanical properties, including stiffness and tensile strength as compared to the pristine nanocellulose (Wang and Sain, 2007). In another study, Nogi et al. (2009) studied the fabrication of wood flour-derived nanocellulose-based transparent paper and found a high modulus (13 GPa) and strength (223 MPa) and minimal thermal expansion (8.5 ppm K^{-1}) of the optically transparent nanocellulose paper.

Porosity

Porosity is one of the most important properties of biomaterials, specifically for their applications in bone tissue engineering. A porous material promotes the effective release of biofactors such as cells, drugs, nanomaterials, proteins, and others from the scaffold. From the biomedical perspective, porosity is one of the most important features of nanocellulose as it allows the impregnation of different minerals, particles, ceramics, polymer solutions, and viable cells (Li et al., 2021).

Bacterial nanocellulose is porous in nature, and its level of porosity is largely dependent on its synthesis method, chemical composition of the medium, microbial strain, pre- and post-synthesis processing, and drying methods. The porous geometry of BNC provides an ideal environment for the impregnation of a variety of materials into its matrix, including solid particles of different shapes as well as liquid solutions (Shah et al., 2013). The innate porous nature of BNC could be advantageous from the perspective that it would prevent the invasion of microbial cells; however, the small pore size could be a limitation in that it may prevent the impregnation of large size particles and infiltration and migration of mammalian cells (Hutchens et al., 2006). The porous morphology of nanocellulose is also advantageous for the targeted drug delivery, as well as it serves as an efficient physical barrier against external infections (Kowalska-Ludwicka et al., 2013). Although the innate properties of BNC favor its application as a scaffold for bone, cartilage, and connective tissue formation, its small pore size prevents the infiltration of cells deep into its matrix, thus limiting its direct application. The pore size of BNC could be controlled at micro, nano, and mesoscales to meet the desired features for bone tissue engineering application. One such strategy is the introduction of various materials, called 'porogens' (Khan et al., 2016). Examples of porogens include different salts, paraffin particles, ice crystals, gelatin, and different sugars, which are added to the network structure of BNC as the space holders and subsequently removed, leaving behind pores of desired shape and size (Bäckdahl et al., 2008). The porogens should be adsorbed only physically and not chemically, whose removal should not alter the fibrous morphology of BNC. The porogens of the desired shape and size are selected according to the size of the cells and the end application of nanocellulose. In one study, Bäckdahl et al. (2008) used the potato starch and paraffin wax particles as the porogens for the development of interconnected BNC tubes. They achieved partial particle fusion through heat treatment of paraffin wax particles at specific temperatures. The developed BNC tubes supported the growth of smooth muscle cells inside the pores (Bäckdahl et al., 2008). In another study, gelatin was added as porogen to BNC to regenerate 3D microporous regenerated scaffolds. The developed scaffolds supported not only the adhesion and proliferation of cells but also their impregnation deep into the matrix of the scaffold, thus suggesting the development of 3D scaffolds. The developed porous scaffolds also showed considerable *in vivo* results in the mice model (Khan et al., 2018). In a study, a highly porous nanocomposite of BNC was developed through the incorporation of Fe_3O_4 and hydroxyapatite (BNC/Fe_3O_4/HAp) (Torgbo and Sukyai, 2019). The porosity of the nanocomposite was comparable to that of the trabecular/cancellous bone. Moreover, the BNC/Fe_3O_4/HAp nanocomposite demonstrated high mechanical strength and cytocompatibility, thus demonstrating its ability to promote bone tissue regeneration.

Electric Charge and Wettability

The electric charge and wettability, as well as the charge density of nanocellulose, play an important role in the biotechnological properties of biomaterials for their applications in tissue engineering. Nanocellulose can be desirably modulated by adding different chemical groups, and its structural properties could be tuned to meet the desired features of bone tissues. Generally, moderate wettability modulates the cell growth and adhesion or adsorption (Bacakova et al., 2011), while the charge density modulates the roughness and morphology of nanocellulose films (Ahola et al., 2008) and their interaction with the cells to improve the cell adhesion, growth, and susceptibility for transfection with DNA constructs (Liu et al., 2016).

APPLICATIONS

Nanocellulose as a Substitute for Bone and Cartilage Regeneration

The repairing of cartilage damage resulting from trauma or degeneration has been a serious clinical concern (Das et al., 2019). The available treatments for small cartilage defect repair include multiple drilling, abrasion arthroplasty, mosaicplasty, and autogenous and allogeneic chondrocyte transplantation (Cao et al., 2014). There are several limitations associated with the use of allografts, such as disease transmission, immune rejection, and slower remodeling. Likewise, autografts have limitations for their requirements of the patient to undergo many surgeries (Baldwin et al., 2019). The rise of tissue engineering that utilizes cells, biodegradable scaffolds, and growth factors provides a new avenue for the repair of articular cartilage (De Witte et al., 2018). In cartilage tissue engineering, scaffolds provide a 3D structure for cartilage cells and support cell adhesion and proliferation (De Witte et al., 2018; Kabir et al., 2020). The scaffolds are further supplemented with different growth factors or antimicrobial agents, which help in encountering microbial and other infections (Ul-Islam et al., 2014). The structure of a cartilage scaffold is required to mimic the native articular cartilage, which is an oriented structure associated with its mechanical function. The oriented ECM-derived scaffolds enhance the biomechanical property of tissue-engineered cartilage, while the oriented poly(lactide-co-glycolide) (PLGA) scaffolds efficiently promote cell migration, thus probably contributes to improving tissue regeneration. The physical and biochemical properties are crucial for the scaffolds during the entire cartilage repair process (Dorati et al., 2017; Kabir et al., 2020).

The scaffolds comprised of nanocellulose have a great efficacy for bone and cartilage regeneration and allows various types of cells to adhere and develop into the desired tissues and organs (**Figure 1**; Halib et al., 2017). A study reported that a membrane comprised of BNC and HAp was used to regenerate bone by significantly enhancing the adhesion and proliferation of osteoblastic cells with elevated bone nodules due to higher activity of phosphatase (Tazi et al., 2012). Studies have also reported the development of BNC and collagen composite. The developed scaffold supported the *in vitro* adhesion, growth, and migration of cells. Further, the developed scaffolds showed the regeneration of pig meniscus. The *in vitro* and *in vivo* studies show the potential use of BNC/collagen scaffolds in meniscus transplantation (Bodin et al., 2007) and artificial cartilage (Lopes et al., 2011) for treating articular joints. In a recent study, BNC was used to design an ear-shaped structure that could be utilized to develop a complete human ear with a specific size and shape (Nimeskern et al., 2013). *In vivo* evaluation of non-critical bone defects in rat tibiae on BNC membrane showed no inflammatory reactions with defects completely filled by the new bone tissues after 4 weeks (Saska et al., 2011). Similar results were obtained from studies on the bone regeneration effect of BNC membrane on rat skulls, which showed new bone formation on the margin and center of the bone defect after 8 weeks of the implant (Lee et al., 2017b). Another study conducted using healthy male beagle dogs showed healing of implant sites with no evidence of inflammatory reactions and implant failure (Lee et al., 2017a). The evaluation of BNC as a barrier membrane for guided bone regeneration on rat calvarial defect did not induce any inflammation and maintained adequate space for bone regeneration (Lee et al., 2015). Similarly, no foreign body reaction was observed when BNC was grafted to correct the nasal dorsum of rabbits, which showed a positive sign of BNC integration by fragmentation after 6 months (Amorim et al., 2009). Mineralized bone formation was observed both on the outer and inner surface of femoral cortical bone in dogs on day 14 of the implant (Yuan et al., 2006). In a study, BNC was used as a guided tissue regeneration membrane to repair maxillary canine periodontal defects in beagle dogs, which showed enhanced periodontal tissue regeneration and formation of new bone (Zhang et al., 2018a). It could be concluded from the above studies that the different nanocellulose-based scaffolds could be efficiently used in *in vivo* regeneration of different types of bones, including tibiae, skulls bones, calvarial defected bone, nasal dorsum bone, femoral cortical bone, tendon, and periodontal tissue regeneration through the formation of new bone (Jiang et al., 2020; Zhu et al., 2020). Typical bone regeneration by using BNC-based scaffold as the repair material is illustrated in **Figure 1**.

Nanocellulose as a Matrix for Doping of Minerals and Ceramics

In order to enhance the potency, accessibility, and stability of nanomaterials, such as HAp, silica, calcium carbonate ($CaCO_3$), calcium chloride ($CaCl_2$), and nanoclay, for their application in bone tissue engineering, these are impregnated into the fibrous network or blended with different types of nanocellulose whether these interact chemically with the free OH group or adsorb physically between the fibers. For this purpose, various strategies have been developed, such as *in situ* addition of nanomaterials to the culture medium (Shah et al., 2013), *ex situ* vigorous stirring of nanocellulose with the nanoparticles suspension (Zhang et al., 2015), and solvo (hydrothermal) approach where cation adsorption of cellulose is carried out (Shahmohammadi Jebel and Almasi, 2016). The addition of $CaCO_3$ to the bacterial growth culture helps the binding of nano metallic oxides to bind with BNC (Mohammadkazemi et al., 2016). Similarly, the soaking of BNC in an ethanol solution of silicon ethoxide enhanced the uptake of silica nanoparticles and the development of BNC-SiO_2 nanocomposite (Barud et al., 2008; Sai et al., 2013). To produce iron oxide containing BNC nanocomposite, the solvothermal technique was applied by autoclaving urea, BNC, and iron nitrate (Wan et al., 2015a,b). The solvothermal technique using ethanol or hot water was used to develop 30 nm sized CdS/BNC nanomaterials (Yang et al., 2012). To develop pure metallic nanoparticles and BNC/metal nanocomposites, two different approaches are used: either readymade metallic nanoparticles are mixed with BNC, or BNC itself is used as the reducing and capping agent for the generation of metallic nanoparticles from metallic salts. This approach has been effectively used for the production of Pd, Au, and Ag nanoparticles (Li et al., 2008;

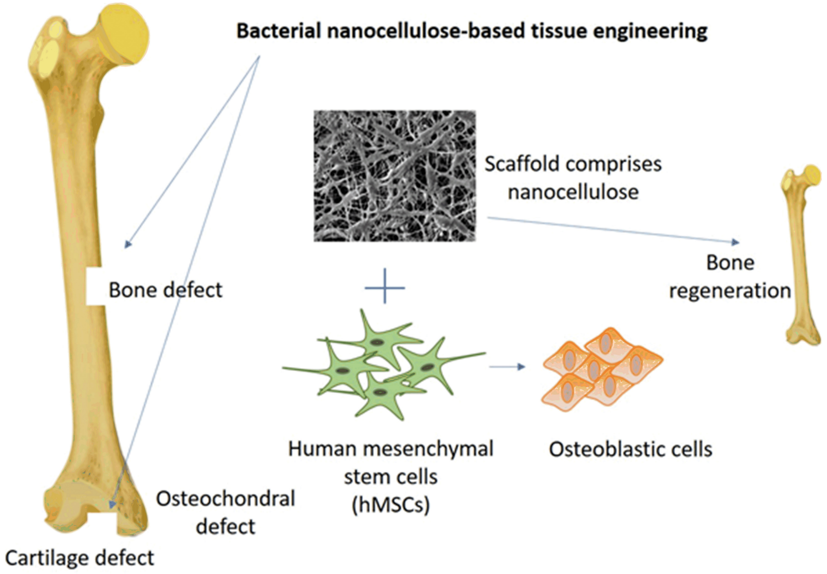

FIGURE 1 | Bone regeneration concept conducted by the synergistic effect of hMSCs cells and BNC-based scaffold. The scaffold allowed the differentiation of hMSCs into the osteoblasts.

Johnson et al., 2011). BNC can easily cause a reduction of silver or gold salt solutions at 55–100°C and produce BNC-capped silver and gold nanoparticles with enhanced availability and stability when exploited for variable applications. Although the *ex situ* impregnation of already prepared metallic nanoparticles into the BNC matrix can be achieved through simple stirring, the *in situ* uptake by the microbial cells requires chemical or physical treatment such as ultrasonic activation (Cai et al., 2011).

Hydroxyapatite, obtained from various sources, including eggshells and bones of animals or codfish, is considered as the efficient carrier for the nanodrugs due to its biocompatibility and hydrophilic nature and has been extensively used in bone tissue regeneration applications (Wang et al., 2011; Luo et al., 2014; Ramani and Sastry, 2014; Kong et al., 2016; Ullah et al., 2018, 2019a, 2020; **Table 1**). An earlier study reported the formation of calcium phosphate in the BNC matrix, which supported the adhesion and proliferation of osteoblast cells as well as the differentiation of mesenchymal stem cells into bone cells in the absence of external markers (Fang et al., 2009). A study by Zimmermann et al. (2011) reported the development of calcium-deficient HAp composite, which supported the adhesion of osteoprogenitor cells. Although the surface bioactivity of HAp causes the lack of biofunctionality of the implanted drug (Meagher et al., 2016), several studies have concluded that HAp takes the drug into the bloodstream instead of delivering it to the target site (Kundu et al., 2013; Sun et al., 2018). The drug released in the bloodstream can cause adverse effects and activate the immune cells, which eliminate the drug from the body prior to reaching the target site. Other limitations include low stability, high pH sensitivity, diverse chemical composition, and ionic surface, which may cause alteration in the drug composition or poor delivery of a drug (Huang et al., 2017; Veerla et al., 2019).

The mineralized tissues also contain $CaCO_3$ and $CaCl_2$. Earlier studies reported the deposition of $CaCO_3$ into the BNC matrix by using sodium carbonate and $CaCl_2$ as the reagents and in the presence of microwave irradiation (Stoica-Guzun et al., 2012, 2013). In another study, Saska et al. (2011) developed a BNC composite with $CaCl_2$ and sodium hydrogen phosphate that effectively regenerated a defect in rat tibial bone by completely regenerating the bone within 4 weeks of implantation and did not show any inflammation.

Nanocellulose as a Drug Carrier for Treating Bone-Related Diseases

Various novel approaches have been developed to treat bone-related diseases, among which the use of nanodrugs is receiving great attention due to their broad-spectrum antimicrobial and antitumor activities. For example, the $CaCO_3$, copper, silica, gold, magnesium-oxide, silver, and boron nanoparticles have been reported to effectively treat various bone-related diseases, such as multiple myeloma, rheumatoid arthritis, microbial infections, and osteoporosis (Bari et al., 2017; Hassani Besheli et al., 2017; Qadri et al., 2017; Gisbert-Garzarán et al., 2020; Cámara-Torres et al., 2021). In a study, the administration of gold nanoparticles in the ankle of rats effectively reduced collagen-induced arthritis and inhibited angiogenesis by blocking the key factors, such as vascular endothelial growth factor (VEGF), synovial fluid, and cell proliferation (Tsai et al., 2007). Besides the broad-spectrum therapeutic ability, nanodrugs have some limitations. For example, metallic nanoparticles might activate the immune system and immune responses and lead to the removal of nanodrug by the mononuclear phagocytic system, Kupffer cells, and phagocytic macrophages (Dong et al., 2012). The macrophage and phagocytosis removal of metallic nanoparticles could be avoided if their size is equal to or more than 100 nm and these are hydrophilic in character (Dong et al., 2012).

After injecting in humans, the nanodrugs are often taken up either by the Kupffer cells or hepatocytes. In Kupffer cells, the nanodrugs are degraded, while hepatocytes eliminate them through the hepatic biliary duct. For example, the PLGA nanoparticles can deliver the drugs; however, their retention time is very low in the bloodstream, and the drug is either eliminated by the Kupffer cells or hepatocytes due to their hydrophobic nature (Adjei et al., 2016). Even if the PLGA nanoparticles escape the Kupffer and hepatic cells and are delivered to the target site, these cause acidification in cells after degradation and give rise to the generation of reactive oxygen species (ROS) (Dos Reis et al., 2019). In a study, Yan et al. (2013) investigated the toxic effect of PLGA nanoparticles on the retinal pigment epithelium (RPE) cells and indicated that PLGA nanoparticles caused 20% apoptosis of RPE cells, and the apoptosis frequency reached 50% at higher concentration.

The free OH groups in BNC possess strong hydrogen bonding due to their hydrophilic nature; therefore, these serve as the ideal candidate for interaction with drugs and their controlled delivery (Pötzinger et al., 2017). The encapsulation of nanodrug in BNC can increase the size of nanoparticles and, due to the hydrophilic nature of cellulose, can skip the immune response. Various cell lines, such as HBMEC, bEnd, RAW 264, MCF-10A, MDA-MB-231, MDA-MB-468, KB, PC-3, and C6 were assessed for the cytotoxic effect of nanocellulose, where none of the cell lines were affected after 48 h (Pachuau, 2017). The fluorescein-5′-isothiocyanate technique was used to label the nanocellulose to elucidate the site-specific uptake that resulted in minimal imprecise cellular receive, indicating nanocellulose a useful candidate for drug delivery (Dong et al., 2012; Pachuau, 2017). The coating of BNC on tablets using the spray technique enhanced the mechanical properties of tablets with the prolonged drug release (Amin et al., 2012). In a similar study, berberine hydrochloride and berberine sulfate coated with BNC resulted in drug protection with increased drug release duration (Huang et al., 2013). The boding of cell-specific antigen and receptor with nanocellulose and nanodrugs can further enhance the cell-specific uptake ability of the drug (Tan et al., 2019). In a recent study, Li et al. (2018) reported the formation of a sandwiched structure of BNC with polyaniline that showed sustained drug release at varying pH and under electrical stimulation (Li et al., 2018). These studies demonstrate the potential use of different forms of nanocellulose and their composites as drug delivery systems for treating bone-related diseases.

CHALLENGES

Challenges Associated With Nanocellulose Production and Purification

Nanocellulose from plants and algae is not pure and contains impurities like unwanted toxic heavy metals, glucan, endotoxins, lignin, alkaloids, hemicelluloses, and pectin. Therefore, the plant and algal-derived nanocellulose require purification through chemical and physical approaches prior to their use for different applications (Sano et al., 2010; Picheth et al., 2017). The common methods used to extract nanocellulose from a cellulosic material contain several problems, such as the higher amount of acid wastewater generation for the acid hydrolysis, high energy utilization for the mechanical process, and elevated reaction duration for enzymatic hydrolysis (Phanthong et al., 2018; Skiba et al., 2020). As compared to the large-scale production of CNF and CNC, the BNC production is only limited to laboratory-scale due to the high cost of production medium and growth maintenance of BNC-producing microbial strains as well as the low yield (Ul-Islam et al., 2020). Regardless of the development of various bioreactors for BNC production, the highest productivity with aerosol bioreactor is only 0.38 g/(L/) (Lee et al., 2014). Although pristine nanocellulose is non-toxic and non-genotoxic, the chemically modified nanocellulose might cause complications when used for biomedical applications (Chinga-Carrasco, 2018). For example, an earlier study reported that the addition of the dialdehyde group to nanocellulose enhanced the gene expression of tumor necrosis factor α (TNF-α) and induced inflammation at the target site (Kollar et al., 2011). Moreover, the bacteria-derived nanocellulose might contain contamination of unwanted lipopolysaccharides, which may cause inflammation at the target site (Chinga-Carrasco, 2018).

In vivo Biodegradation of Nanocellulose

Cellulose has excellent mechanical and biocompatible properties; however, it is not degradable or degrades very slowly in animals due to a lack of cellulase enzyme (Lin and Dufresne, 2014); nevertheless, slow degradation of nanocellulose could be advantageous by favoring a continuous drug release, which could be further optimized (Patel et al., 2019). Furthermore, the innate features of nanocellulose such as hydration, swelling, and crystallinity may affect not only the degree of degradation but also the absorption and immune response (Lin and Dufresne, 2014). For example, in canine, cellulose, and cellulose derivatives, the rate of degradation depends mainly on the cellulose chemical derivation and crystalline form. The oxidized cellulose is more vulnerable to hydrolysis and, therefore, could be degraded by the human body (Luo et al., 2013). Mineral acids, such as phosphoric acid, sulfuric acid, and hydrochloric acid, hydrolyze the nanocellulose crystals (Endes et al., 2016). The composites of nanocellulose with metal oxide (Fe_2O_3, graphene oxide, ZnO, and TiO_2) have been utilized for improving the degradation rate (Shak et al., 2018). The degradation of nanocellulose could be enhanced by introducing *N*-acetylglucosamine residues and by incorporating cellulase enzymes, making it applicable for several medical purposes (Bacakova et al., 2019).

CONCLUSION AND PROSPECTS OF USING NANOCELLULOSE IN TREATING BONE-RELATED DISEASES

Over the past couple of decades, extensive efforts have been devoted to nanocellulose research. The nanocellulose research is primarily focused on exploring low-cost substrates, developing advanced and facile preparation strategies, and exploring new application areas. To date, different forms of nanocellulose, especially BNC, have been extensively explored for various biomedical applications, especially for developing tissue engineering scaffolds. Nanocellulose is not only suitable for the development of soft tissue scaffolds such as skin, neural, and other tissues, it can be effectively utilized for the development of hard tissues such as bone and cartilage when combined with other materials to impart it compatible compression and shape.

Advanced therapeutic strategies for treating bone diseases could be developed by using nanocellulose both as the scaffold and a matrix or carrier. Due to its high mechanical strength and biocompatible nature, nanocellulose could be used as a suitable biomaterial for scaffolding and bone regeneration and development. The deposition of metallic nanoparticles on nanocellulose would further impart antimicrobial activity to the scaffold. Nanocellulose could also be used as an immobilizer for macromolecules, such as DNA, protein, and enzymes. It can also be utilized to enhance the production of secondary metabolites in highly medicinal plants by activating the key genes. The loading of luminescent nanomaterial on nanocellulose could be a novel approach for its use as a fluorescent probe and for photoelectric and photothermal applications. Similarly, nanocellulose could serve as a matrix or carrier for the immobilization of drugs and nanoparticles for avoiding the immune response and for the controlled release of advanced therapeutic molecules and nanomaterials. For targeted delivery of therapeutic molecules/metallic components to treat bone diseases, there must be an appropriate nanocarrier that could be used to encapsulate the therapeutic entities in order to avoid the immune response and early elimination from the body. Certain nanocarriers that protect nanodrugs and deliver to a specific target site encounter several limitations; thus, an alternative approach is required. Nanocellulose could be a suitable nanocarrier for metallic nanoparticles to treat bone diseases. For example, nanocellulose biocompatible and works well as the stabilizing agent for metallic nanoparticles by preventing their agglomeration and maintaining their morphological stability. Nanocellulose can be implanted over metallic nanodrugs through chemical reduction or physical adsorption (electrostatic association). Furthermore, the attachment of osteoblastic antigen on the surface of nanocellulose can enhance the potency of targeted delivery of metallic nanodrugs and can become a novel approach to treat damaged bone or bone-related diseases. Similarly, a controlled drug release is an important phenomenon that gains high importance in cases where the timely release of drug is required. For instance, an anticancer drug bendamustine requires controlled release after oral delivery; therefore, nanocellulose can be helpful to regulate the drug release inside the body. Although nanocellulose is largely considered to be used for conventional FDA approved drugs, it can also be used for the delivery of more advanced therapeutic entities such as siRNAs. The siRNAs-based therapies are considered very effective; however, their poor stability in the biological environment is a serious concern. Therefore, nanocellulose-based materials can be used to provide protection from degradation and enhancing cellular uptake.

Although the above discussion justifies the importance and potential use of nanocellulose in treating bone-related diseases, further investigation on cell-scaffold interaction, *in vivo* degradation, and resorption of degradation products is required. Moreover, immunological analysis of nanocellulose-based scaffolds is required for a complete understanding of their effects on both innate and adaptive immunity. To this end, a detailed investigation on the identification of molecular mechanisms present in the immune system for recognition of nanocellulose and the activation of associated downstream signaling pathways will pave the way to rationally develop biologically safe nanocellulose-based scaffolds for clinical applications.

AUTHOR CONTRIBUTIONS

SK and RS wrote the original draft. SK, DH, MAS, GN, QB, SM, and MWU revised and modified the manuscript. MX, MWU, and HB supervised and edited the manuscript. All authors contributed to the article and approved the submitted version.

ACKNOWLEDGMENTS

The authors acknowledge the China Postdoctoral Science Foundation (grant nos. 2020M672291 and 2016M602291), the operating grant support from the National Natural Science Foundation of China (grant nos. 81870942, 81471174, and 81520108011), Key R&D and promotion projects (Science and Technology Project) from Henan Science and Technology Department, No: 212102310127, and Henan Middle-aged Youth Health Technology Innovation Talent Project, No: YXKC2020059.

REFERENCES

Abdul Khalil, H. P. S., Bhat, A. H., and Ireana Yusra, A. F. (2012). Green composites from sustainable cellulose nanofibrils: a review. *Carbohydr. Polym.* 87, 963–979. doi: 10.1016/j.carbpol.2011.08.078

Abitbol, T., Rivkin, A., Cao, Y., Nevo, Y., Abraham, E., Ben-Shalom, T., et al. (2016). Nanocellulose, a tiny fiber with huge applications. *Curr. Opin. Biotechnol.* 39, 76–88. doi: 10.1016/j.copbio.2016.01.002

Adewuyi, A., Otuechere, C. A., Adebayo, O. L., Anazodo, C., and Pereira, F. V. (2018). Renal toxicological evaluations of sulphonated nanocellulose from Khaya sengalensis seed in Wistar rats. *Chem. Biol. Interact.* 284, 56–68. doi: 10.1016/j.cbi.2018.02.015

Adjei, I. M., Sharma, B., Peetla, C., and Labhasetwar, V. (2016). Inhibition of bone loss with surface-modulated, drug-loaded nanoparticles in an intraosseous model of prostate cancer. *J. Control. Release* 232, 83–92. doi: 10.1016/j.jconrel.2016.04.019

Ahola, S., Salmi, J., Johansson, L. S., Laine, J., and Österberg, M. (2008). Model films from native cellulose nanofibrils. preparation, swelling, and surface interactions. *Biomacromolecules* 9, 1273–1282. doi: 10.1021/bm701317k

Ahrem, H., Pretzel, D., Endres, M., Conrad, D., Courseau, J., Müller, H., et al. (2014). Laser-structured bacterial nanocellulose hydrogels support ingrowth and differentiation of chondrocytes and show potential as cartilage implants. *Acta Biomater.* 10, 1341–1353. doi: 10.1016/j.actbio.2013.12.004

Aki, D., Ulag, S., Unal, S., Sengor, M., Ekren, N., Lin, C. C., et al. (2020). 3D printing of PVA/hexagonal boron nitride/bacterial cellulose composite scaffolds for bone tissue engineering. *Mater. Des.* 196:109094. doi: 10.1016/j.matdes.2020.109094

Amin, M. C. I. M., Abadi, A. G., Ahmad, N., Katas, H., and Jamal, J. A. (2012). Bacterial cellulose film coating as drug delivery system: physicochemical, thermal and drug release properties. *Sains Malaysiana* 41, 561–568.

Amorim, W. L., Costa, H. O., De Souza, F. C., De Castro, M. G., and Da Silva, L. (2009). Experimental study of the tissue reaction caused by the presence of cellulose produced. *Braz. J. Otorhinolaryngol.* 75, 200–207. doi: 10.1016/S1808-8694(15)30779-5

Andrade, F. K., Silva, J. P., Carvalho, M., Castanheira, E. M. S., Soares, R., and Gama, M. (2011). Studies on the hemocompatibility of bacterial cellulose. *J. Biomed. Mater. Res. Part A* 98A, 554–566. doi: 10.1002/jbm.a.33148

Andriani, D., Apriyana, A. Y., and Karina, M. (2020). The optimization of bacterial cellulose production and its applications: a review. *Cellulose* 27, 6747–6766. doi: 10.1007/s10570-020-03273-3279

Bacakova, L., Filova, E., Parizek, M., Ruml, T., and Svorcik, V. (2011). Modulation of cell adhesion, proliferation and differentiation on materials designed for body implants. *Biotechnol. Adv.* 29, 739–767. doi: 10.1016/j.biotechadv.2011.06.004

Bacakova, L., Pajorova, J., Bacakova, M., Skogberg, A., Kallio, P., Kolarova, K., et al. (2019). Versatile application of nanocellulose: from industry to skin tissue engineering and wound healing. *Nanomaterials* 9:164. doi: 10.3390/nano9020164

Bäckdahl, H., Esguerra, M., Delbro, D., Risberg, B., and Gatenholm, P. (2008). Engineering microporosity in bacterial cellulose scaffolds. *J. Tissue Eng. Regen. Med.* 2, 320–330. doi: 10.1002/term.97

Baldwin, P., Li, D. J., Auston, D. A., Mir, H. S., Yoon, R. S., and Koval, K. J. (2019). Autograft, allograft, and bone graft substitutes: clinical evidence and indications for use in the setting of orthopaedic trauma surgery. *J. Orthop. Trauma* 33, 203–213. doi: 10.1097/BOT.0000000000001420

Bari, A., Bloise, N., Fiorilli, S., Novajra, G., Vallet-Regí, M., Bruni, G., et al. (2017). Copper-containing mesoporous bioactive glass nanoparticles as multifunctional agent for bone regeneration. *Acta Biomater.* 55, 493–504. doi: 10.1016/j.actbio.2017.04.012

Barud, H. S., Assunção, R. M. N., Martines, M. A. U., Dexpert-Ghys, J., Marques, R. F. C., Messaddeq, Y., et al. (2008). Bacterial cellulose–silica organic–inorganic hybrids. *J. Sol-Gel Sci. Technol.* 46, 363–367. doi: 10.1007/s10971-007-1669-1669

Basu, P., Saha, N., Alexandrova, R., Andonova-Lilova, B., Georgieva, M., Miloshev, G., et al. (2018). Biocompatibility and biological efficiency of inorganic calcium filled bacterial cellulose based hydrogel scaffolds for bone bioengineering. *Int. J. Mol. Sci.* 19:3980. doi: 10.3390/ijms19123980

Bodin, A., Concaro, S., Brittberg, M., and Gatenholm, P. (2007). Bacterial cellulose as a potential meniscus implant. *J. Tissue Eng. Regen. Med.* 1, 406–408. doi: 10.1002/term.51

Cai, Z., Hou, C., Yang, G., and Kim, J. (2011). Bacterial cellulose as a template for the formation of polymer/nanoparticle nanocomposite. *J. Nanotechnol. Eng. Med.* 2:031006. doi: 10.1115/1.4004361

Cai, Z., and Kim, J. (2010). Preparation and characterization of novel bacterial cellulose/gelatin scaffold for tissue regeneration using bacterial cellulose hydrogel. *J. Nanotechnol. Eng. Med.* 1:021002. doi: 10.1115/1.4000858

Cámara-Torres, M., Duarte, S., Sinha, R., Egizabal, A., Álvarez, N., Bastianini, M., et al. (2021). 3D additive manufactured composite scaffolds with antibiotic-loaded lamellar fillers for bone infection prevention and tissue regeneration. *Bioact. Mater.* 6, 1073–1082. doi: 10.1016/j.bioactmat.2020.09.031

Camarero-Espinosa, S., Endes, C., Mueller, S., Petri-Fink, A., Rothen-Rutishauser, B., Weder, C., et al. (2016). Elucidating the potential biological impact of cellulose nanocrystals. *Fibers* 4:21. doi: 10.3390/fib4030021

Cao, Z., Dou, C., and Dong, S. (2014). Scaffolding biomaterials for cartilage regeneration. *J. Nanomater.* 2014, 1–8. doi: 10.1155/2014/489128

Carina, V., Costa, V., Sartori, M., Bellavia, D., Luca, A., De, et al. (2019). Adjuvant biophysical therapies in osteosarcoma. *Cancers (Basel)* 11:348. doi: 10.3390/cancers11030348

Catalán, J., Ilves, M., Järventaus, H., Hannukainen, K. S., Kontturi, E., Vanhala, E., et al. (2015). Genotoxic and immunotoxic effects of cellulose nanocrystals in vitro. *Environ. Mol. Mutagen.* 56, 171–182. doi: 10.1002/em.21913

Cavicchioli, M., Corso, C. T., Coelho, F., Mendes, L., Saska, S., Soares, C. P., et al. (2015). Characterization and cytotoxic, genotoxic and mutagenic evaluations of bacterial cellulose membranes incorporated with ciprofloxacin: a potential material for use as therapeutic contact lens. *World J. Pharm. Pharm. Sci.* 4, 1626–1647.

Cheng, Q., Wang, S., and Harper, D. P. (2009). Effects of process and source on elastic modulus of single cellulose fibrils evaluated by atomic force microscopy. *Compos. Part A Appl. Sci. Manuf.* 40, 583–588. doi: 10.1016/j.compositesa.2009.02.011

Chinga-Carrasco, G. (2018). Potential and limitations of nanocelluloses as components in biocomposite inks for three-dimensional bioprinting and for biomedical devices. *Biomacromolecules* 19, 701–711. doi: 10.1021/acs.biomac.8b00053

Čolić, M., Tomić, S., and Bekić, M. (2020). Immunological aspects of nanocellulose. *Immunol. Lett.* 222, 80–89. doi: 10.1016/j.imlet.2020.04.004

Curvello, R., Raghuwanshi, V. S., and Garnier, G. (2019). Engineering nanocellulose hydrogels for biomedical applications. *Adv. Colloid Interface Sci.* 267, 47–61. doi: 10.1016/j.cis.2019.03.002

Das, P., Singh, Y. P., Joardar, S. N., Biswas, B. K., Bhattacharya, R., Nandi, S. K., et al. (2019). Decellularized caprine conchal cartilage toward repair and regeneration of damaged cartilage. *ACS Appl. Bio Mater.* 5, 2037–2049. doi: 10.1021/acsabm.9b00078

de Amorim, J. D. P., de Souza, K. C., Duarte, C. R., da Silva, Duarte, I., de Assis Sales, et al. (2020). Plant and bacterial nanocellulose: production, properties and applications in medicine, food, cosmetics, electronics and engineering. a review. *Environ. Chem. Lett.* 18, 851–869. doi: 10.1007/s10311-020-00989-989

de Lima, R., Feitosa, L. O., Maruyama, C. R., Barga, M. A., Yamawaki, P. C., Vieira, I. J., et al. (2012). Evaluation of the genotoxicity of cellulose nanofibers. *Int. J. Nanomed.* 7, 3555–3565. doi: 10.2147/IJN.S30596

De Witte, T. M., Fratila-Apachitei, L. E., Zadpoor, A. A., and Peppas, N. A. (2018). Bone tissue engineering via growth factor delivery: from scaffolds to complex matrices. *Regen. Biomater.* 5, 197–211. doi: 10.1093/rb/rby013

DeMello, J. A. (2012). *Bacterial Cellulose Templates for Nano-Hydroxyapatite Fibre Synthesis*. Ph.D. Thesis, London: The University of Western Ontario.

Derakhshanfar, S., Mbeleck, R., Xu, K., Zhang, X., Zhong, W., and Xing, M. (2018). 3D bioprinting for biomedical devices and tissue engineering: a review of recent trends and advances. *Bioact. Mater.* 3, 144–156. doi: 10.1016/j.bioactmat.2017.11.008

Di, Z., Shi, Z., Ullah, M. W., Li, S., and Yang, G. (2017). A transparent wound dressing based on bacterial cellulose whisker and poly(2-hydroxyethyl methacrylate). *Int. J. Biol. Macromol.* 105, 638–644. doi: 10.1016/j.ijbiomac.2017.07.075

Dong, S., Hirani, A. A., Colacino, K. R., Lee, Y. W., and Roman, M. (2012). Cytotoxicity and cellular uptake of cellulose nanocrystals. *Nano Life* 2:1241006. doi: 10.1142/s1793984412410061

Dorati, R., DeTrizio, A., Modena, T., Conti, B., Benazzo, F., Gastaldi, G., et al. (2017). Biodegradable scaffolds for bone regeneration combined with drug-delivery systems in osteomyelitis therapy. *Pharmaceuticals* 10:96. doi: 10.3390/ph10040096

Dorozhkin, S. V. (2013). Calcium orthophosphate-based bioceramics. *Materials (Basel)* 6, 3840–3942. doi: 10.3390/ma6093840

Dos Reis, L. G., Lee, W. H., Svolos, M., Moir, L. M., Jaber, R., Windhab, N., et al. (2019). Nanotoxicologic effects of PLGA nanoparticles formulated with a cell-penetrating peptide: searching for a safe pDNA delivery system for the lungs. *Pharmaceutics* 11:12. doi: 10.3390/pharmaceutics11010012

Dubey, S., Mishra, R., Roy, P., and Singh, R. P. (2020). 3-D macro/microporous-nanofibrous bacterial cellulose scaffolds seeded with BMP-2 preconditioned mesenchymal stem cells exhibit remarkable potential for bone tissue engineering. *Int. J. Biol. Macromol.* 167, 934–946. doi: 10.1016/j.ijbiomac.2020.11.049

Dufresne, A. (2013). Nanocellulose: a new ageless bionanomaterial. *Mater. Today* 16, 220–227. doi: 10.1016/j.mattod.2013.06.004

Dufresne, A. (2017). *Nanocellulose: From Nature to High Performance Tailored Materials*, 2. Edn. Berlin: De gruyter. doi: 10.1515/9783110480412

Endes, C., Camarero-Espinosa, S., Mueller, S., Foster, E. J., Petri-Fink, A., Rothen-Rutishauser, B., et al. (2016). A critical review of the current knowledge regarding the biological impact of nanocellulose. *J. Nanobiotechnol.* 14:78. doi: 10.1186/s12951-016-0230-239

Eslahi, N., Mahmoodi, A., Mahmoudi, N., Zandi, N., and Simchi, A. (2020). Processing and properties of nanofibrous bacterial cellulose-containing polymer composites: a review of recent advances for biomedical applications. *Polym. Rev.* 60, 144–170. doi: 10.1080/15583724.2019.1663210

Eyley, S., and Thielemans, W. (2014). Surface modification of cellulose nanocrystals. *Nanoscale* 65, 45–55. doi: 10.1039/c4nr01756k

Fan, Q. G., Lewis, D. M., and Tapley, K. N. (2001). Characterization of cellulose aldehyde using fourier transform infrared spectroscopy. *J. Appl. Polym. Sci.* 82, 1195–1202. doi: 10.1002/app.1953

Fang, B., Wan, Y.-Z., Tang, T.-T., Gao, C., and Dai, K.-R. (2009). Proliferation and osteoblastic differentiation of human bone marrow stromal cells on hydroxyapatite/bacterial cellulose nanocomposite scaffolds. *Tissue Eng. Part A* 15, 1091–1098. doi: 10.1089/ten.tea.2008.0110

Faradilla, R. H. F., Lee, G., Arns, J. Y., Roberts, J., Martens, P., Stenzel, M. H., et al. (2017). Characteristics of a free-standing film from banana pseudostem nanocellulose generated from TEMPO-mediated oxidation. *Carbohydr. Polym*. 174, 1156–1163. doi: 10.1016/j.carbpol.2017.07.025

Farcas, M. T., Kisin, E. R., Menas, A. L., Gutkin, D. W., Star, A., Reiner, R. S., et al. (2016). Pulmonary exposure to cellulose nanocrystals caused deleterious effects to reproductive system in male mice. *J. Toxicol. Environ. Heal. - Part A Curr. Issues.* 79, 984–997. doi: 10.1080/15287394.2016.1211045

Farooq, U., Ullah, M. W., Yang, Q., Aziz, A., Xu, J., Zhou, L., et al. (2020). High-density phage particles immobilization in surface-modified bacterial cellulose for ultra-sensitive and selective electrochemical detection of Staphylococcus aureus. *Biosens. Bioelectron.* 157:112163. doi: 10.1016/j.bios.2020.112163

Fatima, A., Yasir, S., Khan, M. S., Manan, S., Ullah, M. W., and Ul-Islam, M. (2021). Plant extract-loaded bacterial cellulose composite membrane for potential biomedical applications. *J. Bioresour. Bioprod.* 6, 26–32. doi: 10.1016/j.jobab.2020.11.002

Favi, P. M. (2014). *Engineering Bacterial Cellulose Scaffold and its Biomimetic Composites for Bone and Cartilage Tissue Regeneration*. PhD disseration, Knoxville, TE: University of Tennessee.

Fürsatz, M., Skog, M., Sivlér, P., Palm, E., Aronsson, C., Skallberg, A., et al. (2018). Functionalization of bacterial cellulose wound dressings with the antimicrobial peptide ϵ-poly-L-Lysine. *Biomed. Mater.* 13:025014. doi: 10.1088/1748-605X/aa9486

Gisbert-Garzarán, M., Manzano, M., and Vallet-Regí, M. (2020). Mesoporous silica nanoparticles for the treatment of complex bone diseases: bone cancer, bone infection and osteoporosis. *Pharmaceutics* 12:83. doi: 10.3390/pharmaceutics12010083

Gu, W., Wu, C., Chen, J., and Xiao, Y. (2013). Nanotechnology in the targeted drug delivery for bone diseases and bone regeneration. *Int. J. Nanomed.* 8, 2305–2317. doi: 10.2147/IJN.S44393

Habibi, Y., Lucia, L. A., and Rojas, O. J. (2010). Cellulose nanocrystals: chemistry, self-assembly, and applications. *Chem. Rev.* 110, 3479–3500. doi: 10.1021/cr900339w

Hakkarainen, T., Koivuniemi, R., Kosonen, M., Escobedo-Lucea, C., Sanz-Garcia, A., Vuola, J., et al. (2016). Nanofibrillar cellulose wound dressing in skin graft donor site treatment. *J. Control. Release* 244(Pt B), 292–301. doi: 10.1016/j.jconrel.2016.07.053

Halib, N., Perrone, F., Cemazar, M., Dapas, B., Farra, R., Abrami, M., et al. (2017). Potential applications of nanocellulose-containing materials in the biomedical field. *Materials (Basel)* 10:977. doi: 10.3390/ma10080977

Hassani Besheli, N., Mottaghitalab, F., Eslami, M., Gholami, M., Kundu, S. C., Kaplan, D. L., et al. (2017). Sustainable release of vancomycin from silk fibroin nanoparticles for treating severe bone infection in rat tibia osteomyelitis model. *ACS Appl. Mater. Interfaces* 9, 5128–5138. doi: 10.1021/acsami.6b14912

Helenius, G., Bäckdahl, H., Bodin, A., Nannmark, U., Gatenholm, P., and Risberg, B. (2006). In vivo biocompatibility of bacterial cellulose. *J. Biomed. Mater. Res. - Part A* 76, 431–438. doi: 10.1002/jbm.a.30570

Hosseinidoust, Z., Alam, M. N., Sim, G., Tufenkji, N., and Van De Ven, T. G. M. (2015). Cellulose nanocrystals with tunable surface charge for nanomedicine. *Nanoscale* 7, 16647–16657. doi: 10.1039/c5nr02506k

Hua, K., Rocha, I., Zhang, P., Gustafsson, S., Ning, Y., Strømme, M., et al. (2016). Transition from bioinert to bioactive material by tailoring the biological cell response to carboxylated nanocellulose. *Biomacromolecules* 17, 1224–1233. doi: 10.1021/acs.biomac.6b00053

Huang, J. W., Lv, X. G., Li, Z., Song, L. J., Feng, C., Xie, M. K., et al. (2015). Urethral reconstruction with a 3D porous bacterial cellulose scaffold seeded with lingual keratinocytes in a rabbit model. *Biomed. Mater.* 10:055005. doi: 10.1088/1748-6041/10/5/055005

Huang, L., Chen, X., Nguyen, T. X., Tang, H., Zhang, L., and Yang, G. (2013). Nano-cellulose 3D-networks as controlled-release drug carriers. *J. Mater. Chem. B* 1, 2976–2984. doi: 10.1039/c3tb20149j

Huang, Y., Wang, J., Yang, F., Shao, Y., Zhang, X., and Dai, K. (2017). Modification and evaluation of micro-nano structured porous bacterial cellulose scaffold for bone tissue engineering. *Mater. Sci. Eng. C.* 75, 1034–1041. doi: 10.1016/j.msec.2017.02.174

Hutchens, S. A., Benson, R. S., Evans, B. R., O'Neill, H. M., and Rawn, C. J. (2006). Biomimetic synthesis of calcium-deficient hydroxyapatite in a natural hydrogel. *Biomaterials* 27, 4661–4670. doi: 10.1016/j.biomaterials.2006.04.032

Islam, M. S., Chen, L., Sisler, J., and Tam, K. C. (2018). Cellulose nanocrystal (CNC)-inorganic hybrid systems: synthesis, properties and applications. *J. Mater. Chem. B.* 6, 864–883. doi: 10.1039/c7tb03016a

Islam, M. U., Khan, S., Khattak, W. A., and Park, J. K. (2015). "Synthesis, chemistry, and medical application of bacterial cellulose nanocomposite," in *Eco-friendly Polymer Nanocomposites. Advanced Structured Materials*, Vol. 74, eds V. Thakur and M. Thakur (New Delhi: Springer).

Isogai, A., Saito, T., and Fukuzumi, H. (2011). TEMPO-oxidized cellulose nanofibers. *Nanoscale* 3, 71–85. doi: 10.1039/c0nr00583e

Jasim, A., Ullah, M. W., Shi, Z., Lin, X., and Yang, G. (2017). Fabrication of bacterial cellulose/polyaniline/single-walled carbon nanotubes membrane for potential application as biosensor. *Carbohydr. Polym.* 163, 62–69. doi: 10.1016/j.carbpol.2017.01.056

Jasmani, L., and Adnan, S. (2017). Preparation and characterization of nanocrystalline cellulose from *Acacia mangium* and its reinforcement potential. *Carbohydr. Polym*. 161, 166–171. doi: 10.1016/j.carbpol.2016.12.061

Jiang, X., Wu, S., Kuss, M., Kong, Y., Shi, W., Streubel, P. N., et al. (2020). 3D printing of multilayered scaffolds for rotator cuff tendon regeneration. *Bioact. Mater*. 5, 636–643. doi: 10.1016/j.bioactmat.2020.04.017

Jing, W., Chunxi, Y., Yizao, W., Honglin, L., Fang, H., Kerong, D., et al. (2013). Laser patterning of bacterial cellulose hydrogel and its modification with gelatin and hydroxyapatite for bone tissue engineering. *Soft Mater.* 11, 173–180. doi: 10.1080/1539445X.2011.611204

Jinga, S. I., Voicu, G., Stoica-Guzun, A., Stroescu, M., Grumezescu, A. M., and Bleotu, C. (2014). Biocellulose nanowhiskers cement composites for endodontic use. *Dig. J. Nanomater. Biostructures.* 9, 543–550.

Johnson, L., Thielemans, W., and Walsh, D. A. (2011). Synthesis of carbon-supported Pt nanoparticle electrocatalysts using nanocrystalline cellulose as reducing agent. *Green Chem.* 13, 1686–1693. doi: 10.1039/c0gc00881h

Kabir, W., Di Bella, C., Jo, I., Gould, D., and Choong, P. F. M. (2020). Human stem cell based tissue engineering for in vivo cartilage repair: a systematic review. *Tissue Eng. Part B Rev.* 27, 74–93. doi: 10.1089/ten.teb.2020.0155

Kaminagakura, K. L. N., Sue Sato, S., Sugino, P., Kataki, de Oliveira Veloso, L., dos Santos, D. C., et al. (2019). Nanoskin® to treat full thickness skin wounds. *J. Biomed. Mater. Res. - Part B Appl. Biomater.* 107, 724–732. doi: 10.1002/jbm.b.34166

Khan, A., Wang, B., and Ni, Y. (2020a). Chitosan-Nanocellulose composites for regenerative medicine applications. *Curr. Med. Chem.* 27, 4584–4592. doi: 10.2174/0929867327666200127152834

Khan, H., Kadam, A., and Dutt, D. (2020b). Studies on bacterial cellulose produced by a novel strain of *Lactobacillus genus*. *Carbohydr. Polym.* 229:115513. doi: 10.1016/j.carbpol.2019.115513

Khan, S., Ul-Islam, M., Ikram, M., Islam, S. U., Ullah, M. W., Israr, M., et al. (2018). Preparation and structural characterization of surface modified microporous bacterial cellulose scaffolds: a potential material for skin regeneration applications in vitro and in vivo. *Int. J. Biol. Macromol.* 117, 1200–1210. doi: 10.1016/j.ijbiomac.2018.06.044

Khan, S., Ul-Islam, M., Ikram, M., Ullah, M. W., Israr, M., Subhan, F., et al. (2016). Three-dimensionally microporous and highly biocompatible bacterial cellulose-gelatin composite scaffolds for tissue engineering applications. *RSC Adv.* 6, 110840–110849. doi: 10.1039/C6RA18847H

Khan, S., Ul-Islam, M., Khattak, W. A., Ullah, M. W., and Park, J. K. (2015). Bacterial cellulose-titanium dioxide nanocomposites: nanostructural characteristics, antibacterial mechanism, and biocompatibility. *Cellulose* 22, 565–579. doi: 10.1007/s10570-014-0528-524

Khan, S., Ullah, M. W., Siddique, R., Liu, Y., Ullah, I., Xue, M., et al. (2019). Catechins-modified selenium-doped hydroxyapatite nanomaterials for improved osteosarcoma therapy through generation of reactive oxygen species. *Front. Oncol.* 9:499. doi: 10.3389/fonc.2019.00499

Khattak, W. A., Ullah, M. W., Ul-Islam, M., Khan, S., Kim, M., Kim, Y., et al. (2014). Developmental strategies and regulation of cell-free enzyme system for ethanol production: a molecular prospective. *Appl. Microbiol. Biotechnol.* 98, 9561–9578. doi: 10.1007/s00253-014-6154-6150

Kim, J., Kim, S. W., Park, S., Lim, K. T., Seonwoo, H., Kim, Y., et al. (2013). Bacterial cellulose nanofibrillar patch as a wound healing platform of tympanic membrane perforation. *Adv. Healthc. Mater.* 2, 1525–1531. doi: 10.1002/adhm.201200368

Kim, Y., Ullah, M. W., Ul-Islam, M., Khan, S., Jang, J. H., and Park, J. K. (2019). Self-assembly of bio-cellulose nanofibrils through intermediate phase in a cell-free enzyme system. *Biochem. Eng. J.* 142, 135–144. doi: 10.1016/j.bej.2018.11.017

Klemm, D., Cranston, E. D., Fischer, D., Gama, M., Kedzior, S. A., Kralisch, D., et al. (2018). Nanocellulose as a natural source for groundbreaking applications in materials science: today's state. *Mater. Today* 21, 720–748. doi: 10.1016/j.mattod.2018.02.001

Klemm, D., Schumann, D., Udhardt, U., and Marsch, S. (2001). Bacterial synthesized cellulose - artificial blood vessels for microsurgery. *Prog. Polym. Sci.* 26, 1561–1603. doi: 10.1016/S0079-6700(01)00021-21

Klinthoopthamrong, N., Chaikiawkeaw, D., Phoolcharoen, W., Rattanapisit, K., Kaewpungsup, P., Pavasant, P., et al. (2020). Bacterial cellulose membrane conjugated with plant-derived osteopontin: preparation and its potential for bone tissue regeneration. *Int. J. Biol. Macromol.* 149, 51–59. doi: 10.1016/j.ijbiomac.2020.01.158

Kollar, P., Závalová, V., Hošek, J., Havelka, P., Sopuch, T., Karpíšek, M., et al. (2011). Cytotoxicity and effects on inflammatory response of modified types of cellulose in macrophage-like THP-1 cells. *Int. Immunopharmacol.* 11, 997–1001. doi: 10.1016/j.intimp.2011.02.016

Kong, L., Mu, Z., Yu, Y., Zhang, L., and Hu, J. (2016). Polyethyleneimine-stabilized hydroxyapatite nanoparticles modified with hyaluronic acid for targeted drug delivery. *RSC Adv.* 6, 101790–101799. doi: 10.1039/c6ra19351j

Kovacs, T., Naish, V., O'Connor, B., Blaise, C., Gagné, F., Hall, L., et al. (2010). An ecotoxicological characterization of nanocrystalline cellulose (NCC). *Nanotoxicology* 4, 255–270. doi: 10.3109/17435391003628713

Kowalska-Ludwicka, K., Cala, J., Grobelski, B., Sygut, D., Jesionek-Kupnicka, D., Kolodziejczyk, M., et al. (2013). Modified bacterial cellulose tubes for regeneration of damaged peripheral nerves. *Arch. Med. Sci.* 9, 527–534. doi: 10.5114/aoms.2013.33433

Kundu, B., Ghosh, D., Sinha, M. K., Sen, P. S., Balla, V. K., Das, N., et al. (2013). Doxorubicin-intercalated nano-hydroxyapatite drug-delivery system for liver cancer: an animal model. *Ceram. Int.* 39, 9557–9566. doi: 10.1016/j.ceramint.2013.05.074

Lamboni, L., Xu, C., Clasohm, J., Yang, J., Saumer, M., Schäfer, K. H., et al. (2019). Silk sericin-enhanced microstructured bacterial cellulose as tissue engineering scaffold towards prospective gut repair. *Mater. Sci. Eng. C* 102, 502–510. doi: 10.1016/j.msec.2019.04.043

Lee, K. Y., Buldum, G., Mantalaris, A., and Bismarck, A. (2014). More than meets the eye in bacterial cellulose: biosynthesis, bioprocessing, and applications in advanced fiber composites. *Macromol. Biosci.* 14, 10–32. doi: 10.1002/mabi.201300298

Li, Z., Friedrich, A., and Taubert, A. (2008). Gold microcrystal synthesis via reduction of HAuCl4 by cellulose in the ionic liquid 1-butyl-3-methyl imidazolium chloride. *J. Mater. Chem.* 18, 1008–1014. doi: 10.1039/b716135m

Lee, S. H., An, S. J., Lim, Y. M., and Huh, J. B. (2017a). The efficacy of electron beam irradiated bacterial cellulose membranes as compared with collagen membranes on guided bone regeneration in peri-implant bone defects. *Materials (Basel)* 10:1018. doi: 10.3390/ma10091018

Lee, Y. J., An, S. J., Bae, E., Bin, Gwon, H. J., Park, J. S., et al. (2017b). The effect of thickness of resorbable bacterial cellulose membrane on guided bone regeneration. *Materials (Basel)* 10:320. doi: 10.3390/ma10030320

Lee, S. H., Lim, Y. M., Jeong, S. I., An, S. J., Kang, S. S., Jeong, C. M., et al. (2015). The effect of bacterial cellulose membrane compared with collagen membrane on guided bone regeneration. *J. Adv. Prosthodont.* 7, 484–495. doi: 10.4047/jap.2015.7.6.484

Leitão, A. F., Gupta, S., Silva, J. P., Reviakine, I., and Gama, M. (2013). Hemocompatibility study of a bacterial cellulose/polyvinyl alcohol nanocomposite. *Colloids Surfaces B Biointerfaces* 111, 493–502. doi: 10.1016/j.colsurfb.2013.06.031

Li, J., Wan, Y., Li, L., Liang, H., and Wang, J. (2009). Preparation and characterization of 2,3-dialdehyde bacterial cellulose for potential biodegradable tissue engineering scaffolds. *Mater. Sci. Eng. C* 29, 1635–1642. doi: 10.1016/j.msec.2009.01.006

Li, S., Jasim, A., Zhao, W., Fu, L., Ullah, M. W., Shi, Z., et al. (2018). Fabrication of pH-electroactive bacterial cellulose/polyaniline hydrogel for the development of a controlled drug release system. *ES Mater. Manuf.* 1, 41–49. doi: 10.30919/esmm5f120

Li, Z., Du, T., Ruan, C., and Niu, X. (2021). Bioinspired mineralized collagen scaffolds for bone tissue engineering. *Bioact. Mater.* 6, 1491–1511. doi: 10.1016/j.bioactmat.2020.11.004

Lin, N., and Dufresne, A. (2014). Nanocellulose in biomedicine: current status and future prospect. *Eur. Polym. J.* 59, 302–325. doi: 10.1016/j.eurpolymj.2014.07.025

Lin, S. P., Loira Calvar, I., Catchmark, J. M., Liu, J. R., Demirci, A., and Cheng, K. C. (2013). Biosynthesis, production and applications of bacterial cellulose. *Cellulose* 20, 2191–2219. doi: 10.1007/s10570-013-9994-9993

Liu, J., Cheng, F., Grénman, H., Spoljaric, S., Seppälä, J., Eriksson, J. E., et al. (2016). Development of nanocellulose scaffolds with tunable structures to support 3D cell culture. *Carbohydr. Polym.* 148, 259–271. doi: 10.1016/j.carbpol.2016.04.064

Liu, J., Willför, S., and Mihranyan, A. (2017). On importance of impurities, potential leachables and extractables in algal nanocellulose for biomedical use. *Carbohydr. Polym.* 172, 11–19. doi: 10.1016/j.carbpol.2017.05.002

Lopes, J. L., Machado, J. M., Castanheira, L., Granja, P. L., Gama, F. M., Dourado, F., et al. (2011). Friction and wear behaviour of bacterial cellulose against articular cartilage. *Wear* 271, 2328–2333. doi: 10.1016/j.wear.2010.12.042

Luo, H., Cha, R., Li, J., Hao, W., Zhang, Y., and Zhou, F. (2019). Advances in tissue engineering of nanocellulose-based scaffolds: a review. *Carbohydr. Polym.* 224:115144. doi: 10.1016/j.carbpol.2019.115144

Luo, H., Xiong, G., Hu, D., Ren, K., Yao, F., Zhu, Y., et al. (2013). Characterization of TEMPO-oxidized bacterial cellulose scaffolds for tissue engineering applications. *Mater. Chem. Phys.* 143, 373–379. doi: 10.1016/j.matchemphys.2013.09.012

Luo, H., Zhang, J., Xiong, G., and Wan, Y. (2014). Evolution of morphology of bacterial cellulose scaffolds during early culture. *Carbohydr. Polym.* 111, 722–728. doi: 10.1016/j.carbpol.2014.04.097

Luz, E. P. C. G., das Chagas, B. S., de Almeida, N. T., de Fátima Borges, M., Andrade, F. K., Muniz, C. R., et al. (2020). Resorbable bacterial cellulose membranes with strontium release for guided bone regeneration. *Mater Sci Eng C Mater Biol Appl.* 116:111175. doi: 10.1016/j.msec.2020.111175

Matharu, A. S., de Melo, E. M., Remón, J., Wang, S., Abdulina, A., and Kontturi, E. (2018). Processing of citrus nanostructured cellulose: a rigorous design-of-experiment study of the hydrothermal microwave-assisted selective scissoring process. *ChemSusChem* 11, 1344–1353. doi: 10.1002/cssc.201702456

Mazhar, U.-I., Yasir, S., Mombasawala, L., Manan, S., and Wajid Ullah, M. (2021). Bacterial cellulose: a versatile material for fabrication of conducting nanomaterials. *Curr. Nanosci.* 16, doi: 10.2174/1573413716999201005214832

Mbituyimana, B., Mao, L., Hu, S., Ullah, M. W., Chen, K., Fu, L., et al. (2021). Bacterial cellulose/glycolic acid/glycerol composite membrane as a system to deliver glycolic acid for anti-aging treatment. *J. Bioresour. Bioprod.* doi: 10.1016/j.jobab.2021.02.003

McCarthy, R. R., Ullah, M. W., Booth, P., Pei, E., and Yang, G. (2019a). The use of bacterial polysaccharides in bioprinting. *Biotechnol. Adv.* 37:107448. doi: 10.1016/j.biotechadv.2019.107448

McCarthy, R. R., Ullah, M. W., Pei, E., and Yang, G. (2019b). Antimicrobial inks: the anti-infective applications of bioprinted bacterial polysaccharides. *Trends Biotechnol.* 37, 1153–1155. doi: 10.1016/j.tibtech.2019.05.004

Meagher, M. J., Weiss-Bilka, H. E., Best, M. E., Boerckel, J. D., Wagner, D. R., and Roeder, R. K. (2016). Acellular hydroxyapatite-collagen scaffolds support angiogenesis and osteogenic gene expression in an ectopic murine model:

effects of hydroxyapatite volume fraction. *J. Biomed. Mater. Res. - Part A*. 104, 2178–2188. doi: 10.1002/jbm.a.35760

Mohammadi, H. (2011). Nanocomposite biomaterial mimicking aortic heart valve leaflet mechanical behaviour. *Proc. Institution Mechan. Eng. Part H: J. Eng. Med.* 225, 718–722. doi: 10.1177/0954411911399826

Mohammadkazemi, F., Faria, M., and Cordeiro, N. (2016). In situ biosynthesis of bacterial nanocellulose-CaCO3 hybrid bionanocomposite: one-step process. *Mater. Sci. Eng. C* 65, 393–399. doi: 10.1016/j.msec.2016.04.069

Morais, J. M., Papadimitrakopoulos, F., and Burgess, D. J. (2010). Biomaterials/Tissue interactions: possible solutions to overcome foreign body response. *AAPS J.* 12, 188–196. doi: 10.1208/s12248-010-9175-9173

Müller, M., Öztürk, E., Arlov, Ø, Gatenholm, P., and Zenobi-Wong, M. (2017). Alginate sulfate–nanocellulose bioinks for cartilage bioprinting applications. *Ann. Biomed. Eng.* 45, 210–223. doi: 10.1007/s10439-016-1704-5

Murizan, N. I. S., Mustafa, N. S., Ngadiman, N. H. A., Yusof, N. M., and Idris, A. (2020). Review on nanocrystalline cellulose in bone tissue engineering applications. *Polymers (Basel)* 12, 1–22. doi: 10.3390/polym12122818

Naseri, N., Deepa, B., Mathew, A. P., Oksman, K., and Girandon, L. (2016). Nanocellulose-Based Interpenetrating Polymer Network (IPN) hydrogels for cartilage applications. *Biomacromolecules* 17, 3714–3723. doi: 10.1021/acs.biomac.6b01243

Nimeskern, L., Martínez Ávila, H., Sundberg, J., Gatenholm, P., Müller, R., and Stok, K. S. (2013). Mechanical evaluation of bacterial nanocellulose as an implant material for ear cartilage replacement. *J. Mech. Behav. Biomed. Mater.* 22, 12–21. doi: 10.1016/j.jmbbm.2013.03.005

Nishiguchi, A., and Taguchi, T. (2019). Osteoclast-Responsive, injectable bone of bisphosphonated-nanocellulose that regulates osteoclast/osteoblast activity for bone regeneration. *Biomacromolecules* 20, 1385–1393. doi: 10.1021/acs.biomac.8b01767

Nogi, M., Iwamoto, S., Nakagaito, A. N., and Yano, H. (2009). Optically transparent nanofiber paper. *Adv. Mater.* 21, 1595–1598. doi: 10.1002/adma.200803174

Olyveira, G., Valido, D. P., Costa, L. M. M., Gois, P. B. P., Xavier Filho, L., and Basmaji, P. (2011). First otoliths/collagen/bacterial cellulose nanocomposites as a potential scaffold for bone tissue regeneration. *J. Biomater. Nanobiotechnol.* 2, 239–243. doi: 10.4236/jbnb.2011.23030

Osorio, D. A., Lee, B. E. J., Kwiecien, J. M., Wang, X., Shahid, I., Hurley, A. L., et al. (2019a). Cross-linked cellulose nanocrystal aerogels as viable bone tissue scaffolds. *Acta Biomater.* 87, 152–165. doi: 10.1016/j.actbio.2019.01.049

Osorio, M., Cañas, A., Puerta, J., Díaz, L., Naranjo, T., Ortiz, I., et al. (2019b). Ex vivo and in vivo biocompatibility assessment (blood and tissue) of three-dimensional bacterial nanocellulose biomaterials for soft tissue implants. *Sci. Rep.* 9:10553. doi: 10.1038/s41598-019-46918-x

Pachuau, L. (2017). "Application of nanocellulose for controlled drug delivery," in *Nanocellulose and Nanohydrogel Matrices: Biotechnological and Biomedical Applications*, eds M. Jawaid and F. Mohammad (Hoboken, NJ: Wiley), doi: 10.1002/9783527803835.ch1

Panday, R., Poudel, A. J., Li, X., Adhikari, M., Ullah, M. W., and Yang, G. (2018). Amphiphilic core-shell nanoparticles: synthesis, biophysical properties, and applications. *Colloids Surfaces B Biointerfaces* 172, 68–81. doi: 10.1016/j.colsurfb.2018.08.019

Pang, M., Huang, Y., Meng, F., Zhuang, Y., Liu, H., Du, M., et al. (2020). Application of bacterial cellulose in skin and bone tissue engineering. *Eur. Polym. J.* 122:109365. doi: 10.1016/j.eurpolymj.2019.109365

Patel, D. K., Dutta, S. D., and Lim, K. T. (2019). Nanocellulose-based polymer hybrids and their emerging applications in biomedical engineering and water purification. *RSC Adv.* 9, 19143–19162. doi: 10.1039/c9ra03261d

Phanthong, P., Reubroycharoen, P., Hao, X., Xu, G., Abudula, A., and Guan, G. (2018). Nanocellulose: extraction and application. *Carbon Resour. Convers.* 1, 32–43. doi: 10.1016/j.crcon.2018.05.004

Picheth, G. F., Pirich, C. L., Sierakowski, M. R., Woehl, M. A., Sakakibara, C. N., de Souza, C. F., et al. (2017). Bacterial cellulose in biomedical applications: a review. *Int. J. Biol. Macromol.* 104, 97–106. doi: 10.1016/j.ijbiomac.2017.05.171

Poonguzhali, R., Basha, S. K., and Kumari, V. S. (2017). Synthesis and characterization of chitosan-PVP-nanocellulose composites for in-vitro wound dressing application. *Int. J. Biol. Macromol.* 105(Pt 1), 111–120. doi: 10.1016/j.ijbiomac.2017.07.006

Pötzinger, Y., Kralisch, D., and Fischer, D. (2017). Bacterial nanocellulose: the future of controlled drug delivery? *Ther. Deliv.* 8, 753–761. doi: 10.4155/tde-2017-2059

Powell, L. C., Khan, S., Chinga-Carrasco, G., Wright, C. J., Hill, K. E., and Thomas, D. W. (2016). An investigation of *Pseudomonas aeruginosa* biofilm growth on novel nanocellulose fibre dressings. *Carbohydr. Polym.* 137, 191–197. doi: 10.1016/j.carbpol.2015.10.024

Qadri, S., Haik, Y., Mensah-Brown, E., Bashir, G., Fernandez-Cabezudo, M. J., and al-Ramadi, B. K. (2017). Metallic nanoparticles to eradicate bacterial bone infection. *Nanomedicine* 13, 2241–2250. doi: 10.1016/j.nano.2017.05.013

Ramani, D., and Sastry, T. P. (2014). Bacterial cellulose-reinforced hydroxyapatite functionalized graphene oxide: a potential osteoinductive composite. *Cellulose* 21, 3585–3595. doi: 10.1007/s10570-014-0313-314

Raquel Mantuaneli, and Scarel-Caminaga. (2014). Nanocomposites based on bacterial cellulose in combination with osteogenic growth peptide for bone repair: cytotoxic, genotoxic and mutagenic evaluations. *J. Appl. Biol. Biotechnol.* 2, 001–008.

Rocha, I., Lindh, J., Hong, J., Strømme, M., Mihranyan, A., and Ferraz, N. (2018). Blood compatibility of sulfonated *Cladophora nanocellulose* beads. *Molecules* 23:601. doi: 10.3390/molecules23030601

RoyChowdhury, P., and Kumar, V. (2006). Fabrication and evaluation of porous 2,3-dialdehydecellulose membrane as a potential biodegradable tissue-engineering scaffold. *J. Biomed. Mater. Res. - Part A*. 76, 300–309. doi: 10.1002/jbm.a.30503

Ruan, C. Q., Strømme, M., and Lindh, J. (2018). Preparation of porous 2,3-dialdehyde cellulose beads crosslinked with chitosan and their application in adsorption of Congo red dye. *Carbohydr. Polym.* 181, 200–207. doi: 10.1016/j.carbpol.2017.10.072

Sai, H., Xing, L., Xiang, J., Cui, L., Jiao, J., Zhao, C., et al. (2013). Flexible aerogels based on an interpenetrating network of bacterial cellulose and silica by a non-supercritical drying process. *J. Mater. Chem. A*. 181, 200–207. doi: 10.1039/c3ta11198a

Saito, T., Kimura, S., Nishiyama, Y., and Isogai, A. (2007). Cellulose nanofibers prepared by TEMPO-mediated oxidation of native cellulose. *Biomacromolecules* 8, 2485–2491. doi: 10.1021/bm0703970

Sajjad, W., He, F., Ullah, M. W., Ikram, M., Shah, S. M., Khan, R., et al. (2020). Fabrication of bacterial cellulose-curcumin nanocomposite as a novel dressing for partial thickness skin burn. *Front. Bioeng. Biotechnol.* 8:553037. doi: 10.3389/fbioe.2020.553037

Sano, M. B., Rojas, A. D., Gatenholm, P., and Davalos, R. V. (2010). Electromagnetically controlled biological assembly of aligned bacterial cellulose nanofibers. *Ann. Biomed. Eng.* 38, 2475–2484. doi: 10.1007/s10439-010-9999-0

Saska, S., Barud, H. S., Gaspar, A. M. M., Marchetto, R., Ribeiro, S. J. L., and Messaddeq, Y. (2011). Bacterial cellulose-hydroxyapatite nanocomposites for bone regeneration. *Int. J. Biomater.* 2011, 1–8. doi: 10.1155/2011/175362

Saska, S., Teixeira, L. N., de Castro Raucci, L. M. S., Scarel-Caminaga, R. M., Franchi, L. P., dos Santos, R. A., et al. (2017). Nanocellulose-collagen-apatite composite associated with osteogenic growth peptide bone regeneration. *Int. J. Biol. Macromol.* 103, 467–476. doi: 10.1016/j.ijbiomac.2017.05.086

Saska, S., Teixeira, L. N., Tambasco, De Oliveira, P., Minarelli Gaspar, A. M., Lima Ribeiro, S. J., et al. (2012). Bacterial cellulose-collagen nanocomposite for bone tissue engineering. *J. Mater. Chem.* 22, 22102–22112. doi: 10.1039/c2jm33762b

Scherner, M., Reutter, S., Klemm, D., Sterner-Kock, A., Guschlbauer, M., Richter, T., et al. (2014). In vivo application of tissue-engineered blood vessels of bacterial cellulose as small arterial substitutes: proof of concept? *J. Surg. Res.* 189, 340–347. doi: 10.1016/j.jss.2014.02.011

Schumann, D. A., Wippermann, J., Klemm, D. O., Kramer, F., Koth, D., Kosmehl, H., et al. (2009). Artificial vascular implants from bacterial cellulose: preliminary results of small arterial substitutes. *Cellulose* 16, 877–885. doi: 10.1007/s10570-008-9264-y

Sengupta, S., and Balla, V. K. (2018). A review on the use of magnetic fields and ultrasound for non-invasive cancer treatment. *J. Adv. Res.* 14, 97–111. doi: 10.1016/j.jare.2018.06.003

Seyednejad, H., Gawlitta, D., Kuiper, R. V., De Bruin, A., Van Nostrum, C. F., Vermonden, T., et al. (2012). In vivo biocompatibility and biodegradation of 3D-printed porous scaffolds based on a hydroxyl-functionalized poly(ε-caprolactone). *Biomaterials* 33, 4309–4318. doi: 10.1016/j.biomaterials.2012.03.002

Shah, N., Ul-Islam, M., Khattak, W. A., and Park, J. K. (2013). Overview of bacterial cellulose composites: a multipurpose advanced material. *Carbohydr. Polym.* 98, 1585–1598. doi: 10.1016/j.carbpol.2013.08.018

Shahmohammadi Jebel, F., and Almasi, H. (2016). Morphological, physical, antimicrobial and release properties of ZnO nanoparticles-loaded bacterial cellulose films. *Carbohydr. Polym*. 149, 8–19. doi: 10.1016/j.carbpol.2016.04.089

Shak, K. P. Y., Pang, Y. L., and Mah, S. K. (2018). Nanocellulose: recent advances and its prospects in environmental remediation. *Beilstein J. Nanotechnol*. 9, 2479–2498. doi: 10.3762/bjnano.9.232

Sharma, C., and Bhardwaj, N. K. (2019). Bacterial nanocellulose: present status, biomedical applications and future perspectives. *Mater. Sci. Eng. C* 104:109963. doi: 10.1016/j.msec.2019.109963

Shi, Q., Li, Y., Sun, J., Zhang, H., Chen, L., Chen, B., et al. (2012a). The osteogenesis of bacterial cellulose scaffold loaded with bone morphogenetic protein-2. *Biomaterials* 33, 6644–6649. doi: 10.1016/j.biomaterials.2012.05.071

Shi, Z., Zang, S., Jiang, F., Huang, L., Lu, D., Ma, Y., et al. (2012b). In situ nano-assembly of bacterial cellulose–polyaniline composites. *RSC Adv.* 2, 1040–1046. doi: 10.1039/C1RA00719J

Shi, Z., Gao, X., Ullah, M. W., Li, S., Wang, Q., and Yang, G. (2016). Electroconductive natural polymer-based hydrogels. *Biomaterials* 111, 40–54. doi: 10.1016/j.biomaterials.2016.09.020

Shvedova, A. A., Kisin, E. R., Yanamala, N., Farcas, M. T., Menas, A. L., Williams, A., et al. (2016). Gender differences in murine pulmonary responses elicited by cellulose nanocrystals. *Part. Fibre Toxicol.* 13:28. doi: 10.1186/s12989-016-0140-x

Singh, M., Ray, A. R., and Vasudevan, P. (1982). Biodegradation studies on periodate oxidized cellulose. *Biomaterials* 3, 16–20. doi: 10.1016/0142-9612(82)90055-90052

Singla, R., Soni, S., Patial, V., Kulurkar, P. M., Kumari, A., Mahesh, S., et al. (2017). Cytocompatible anti-microbial dressings of *Syzygium cumini* cellulose nanocrystals decorated with silver nanoparticles accelerate acute and diabetic wound healing. *Sci. Rep*. 7:10457. doi: 10.1038/s41598-017-08897-8899

Skiba, E. A., Budaeva, V. V., Ovchinnikova, E. V., Gladysheva, E. K., Kashcheyeva, E. I., Pavlov, I. N., et al. (2020). A technology for pilot production of bacterial cellulose from oat hulls. *Chem. Eng. J.* 383:123128. doi: 10.1016/j.cej.2019.123128

Song, L., Li, Y., Xiong, Z., Pan, L., Luo, Q., Xu, X., et al. (2018). Water-Induced shape memory effect of nanocellulose papers from sisal cellulose nanofibers with graphene oxide. *Carbohydr. Polym*. 179, 110–117. doi: 10.1016/j.carbpol.2017.09.078

Song, S. H., Kim, J. E., Lee, Y. J., Kwak, M. H., Sung, G. Y., Kwon, S. H., et al. (2014). Cellulose film regenerated from *Styela clava* tunics have biodegradability, toxicity and biocompatibility in the skin of SD rats. *J. Mater. Sci. Mater. Med.* 25, 1519–1530. doi: 10.1007/s10856-014-5182-5188

Song, S. H., Seong, K. Y., Kim, J. E., Go, J., Koh, E. K., Sung, J. E., et al. (2017). Effects of different cellulose membranes regenerated from *Styela clava* tunics on wound healing. *Int. J. Mol. Med.* 39, 1173–1187. doi: 10.3892/ijmm.2017.2923

Stefaniak, A. B., Seehra, M. S., Fix, N. R., and Leonard, S. S. (2014). Lung biodurability and free radical production of cellulose nanomaterials. *Inhal. Toxicol*. 26, 733–749. doi: 10.3109/08958378.2014.948650

Stoica-Guzun, A., Stroescu, M., Jinga, S., Jipa, I., Dobre, T., and Dobre, L. (2012). Ultrasound influence upon calcium carbonate precipitation on bacterial cellulose membranes. *Ultrason. Sonochem.* 19, 909–915. doi: 10.1016/j.ultsonch.2011.12.002

Stoica-Guzun, A., Stroescu, M., Jinga, S. I., Jipa, I. M., and Dobre, T. (2013). Microwave assisted synthesis of bacterial cellulose-calcium carbonate composites. *Ind. Crops Prod*. 50, 414–422. doi: 10.1016/j.indcrop.2013.07.063

Subhedar, A., Bhadauria, S., Ahankari, S., and Kargarzadeh, H. (2021). Nanocellulose in biomedical and biosensing applications: a review. *Int. J. Biol. Macromol.* 166, 587–600. doi: 10.1016/j.ijbiomac.2020.10.217

Sun, W., Fan, J., Wang, S., Kang, Y., Du, J., and Peng, X. (2018). Biodegradable drug-loaded hydroxyapatite nanotherapeutic agent for targeted drug release in tumors. *ACS Appl. Mater. Interfaces* 10, 7832–7840. doi: 10.1021/acsami.7b19281

Tan, T. H., Lee, H. V., Dabdawb, W. A. Y., and Hamid, S. B. B. O. A. A. (2019). "Chapter 5 - a review of nanocellulose in the drug-delivery system," in *Materials for Biomedical Engineering*, eds A.-M. Holban and A. M. Grumezescu (Amsterdam: Elsevier), 131–164. doi: 10.1016/B978-0-12-816913-1.00005-2

Tátrai, F., Adamis, Z., Böhm, U., Merétey, K., and Ungváry, G. (1995). Role of cellulose in wood dust-induced fibrosing alveo-bronchiolitis in rat. *J. Appl. Toxicol*. 15, 45–48. doi: 10.1002/jat.2550150110

Tazi, N., Zhang, Z., Messaddeq, Y., Almeida-Lopes, L., Zanardi, L. M., Levinson, D., et al. (2012). Hydroxyapatite bioactivated bacterial cellulose promotes osteoblast growth and the formation of bone nodules. *AMB Express* 2:61. doi: 10.1186/2191-0855-2-61

Tomić, S., Ilić, N., Kokol, V., Gruden-Movsesijan, A., Mihajlović, D., Bekić, M., et al. (2018). Functionalization-dependent effects of cellulose nanofibrils on tolerogenic mechanisms of human dendritic cells. *Int. J. Nanomed.* 13, 6941–6960. doi: 10.2147/IJN.S183510

Torgbo, S., and Sukyai, P. (2018). Bacterial cellulose-based scaffold materials for bone tissue engineering. *Appl. Mater. Today* 11, 34–49. doi: 10.1016/j.apmt.2018.01.004

Torgbo, S., and Sukyai, P. (2019). Fabrication of microporous bacterial cellulose embedded with magnetite and hydroxyapatite nanocomposite scaffold for bone tissue engineering. *Mater. Chem. Phys*. 237:121868. doi: 10.1016/j.matchemphys.2019.121868

Tsai, C. Y., Shiau, A. L., Chen, S. Y., Chen, Y. H., Cheng, P. C., Chang, M. Y., et al. (2007). Amelioration of collagen-induced arthritis in rats by nanogold. *Arthritis Rheum.* 56, 544–554. doi: 10.1002/art.22401

Turnbull, G., Clarke, J., Picard, F., Riches, P., Jia, L., Han, F., et al. (2018). 3D bioactive composite scaffolds for bone tissue engineering. *Bioact. Mater.* 3, 278–314. doi: 10.1016/j.bioactmat.2017.10.001

Ul-Islam, M., Ahmad, F., Fatima, A., Shah, N., Yasir, S., Ahmad, M. W., et al. (2021a). Ex situ synthesis and characterization of high strength multipurpose bacterial cellulose-aloe vera hydrogels. *Front. Bioeng. Biotechnol.* 9:601988. doi: 10.3389/fbioe.2021.601988

Ul-Islam, M., Ullah, M. W., Khan, T., and Park, J. K. (2021b). "Bacterial cellulose: trends in synthesis, characterization, and applications," in *Handbook of Hydrocolloids*, eds G. O. Phillips and P. A. Williams (Amsterdam: Elsevier), 923–974. doi: 10.1016/B978-0-12-820104-6.00010-3

Ul-Islam, M., Khan, S., Ullah, M. W., and Park, J. K. (2015). Bacterial cellulose composites: synthetic strategies and multiple applications in bio-medical and electro-conductive fields. *Biotechnol. J.* 10, 1847–1861. doi: 10.1002/biot.201500106

Ul-Islam, M., Khan, S., Ullah, M. W., and Park, J. K. (2019a). Comparative study of plant and bacterial cellulose pellicles regenerated from dissolved states. *Int. J. Biol. Macromol.* 137, 247–252. doi: 10.1016/j.ijbiomac.2019.06.232

Ul-Islam, M., Subhan, F., Islam, S. U., Khan, S., Shah, N., Manan, S., et al. (2019b). Development of three-dimensional bacterial cellulose/chitosan scaffolds: analysis of cell-scaffold interaction for potential application in the diagnosis of ovarian cancer. *Int. J. Biol. Macromol.* 137, 1050–1059. doi: 10.1016/j.ijbiomac.2019.07.050

Ul-Islam, M., Khan, T., Khattak, W. A., and Park, J. K. (2013a). Bacterial cellulose-MMTs nanoreinforced composite films: novel wound dressing material with antibacterial properties. *Cellulose* 20, 589–596. doi: 10.1007/s10570-012-9849-9843

Ul-Islam, M., Khattak, W. A., Kang, M., Kim, S. M., Khan, T., and Park, J. K. (2013b). Effect of post-synthetic processing conditions on structural variations and applications of bacterial cellulose. *Cellulose* 20, 253–263. doi: 10.1007/s10570-012-9799-9799

Ul-Islam, M., Khattak, W. A., Ullah, M. W., Khan, S., and Park, J. K. (2014). Synthesis of regenerated bacterial cellulose-zinc oxide nanocomposite films for biomedical applications. *Cellulose* 21, 433–447. doi: 10.1007/s10570-013-0109-y

Ul-Islam, M., Ullah, M. W., Khan, S., and Park, J. K. (2020). Production of bacterial cellulose from alternative cheap and waste resources: a step for cost reduction with positive environmental aspects. *Korean J. Chem. Eng.* 37, 925–937. doi: 10.1007/s11814-020-0524-523

Ul-Islam, M., Ullah, M. W., Khan, S., Shah, N., and Park, J. K. (2017). Strategies for cost-effective and enhanced production of bacterial cellulose. *Int. J. Biol. Macromol.* 102, 1166–1173. doi: 10.1016/j.ijbiomac.2017.04.110

Ullah, I., Gloria, A., Zhang, W., Ullah, M. W., Wu, B., Li, W., et al. (2019a). Synthesis and characterization of sintered Sr/Fe-Modified hydroxyapatite bioceramics for bone tissue engineering applications. *ACS Biomater. Sci. Eng. Acsbiomater*. 6, 375–388. doi: 10.1021/acsbiomaterials.9b01666

Ullah, M. W., Fu, L., Lamboni, L., Shi, Z., and Yang, G. (2019b). "Current trends and biomedical applications of resorbable polymers," in *Materials for Biomedical Engineering*, (Amsterdam: Elsevier), 41–86. doi: 10.1016/B978-0-12-818415-8.00003-6

Ullah, M. W., Manan, S., Kiprono, S. J., Ul-Islam, M., and Yang, G. (2019c). "Synthesis, structure, and properties of bacterial cellulose," in *Nanocellulose*, eds J. Huang, A. Dufresne, and N. Lin (Hoboken, NJ: Wiley Online Library), doi: 10.1002/9783527807437.ch4

Ullah, I., Li, W., Lei, S., Zhang, Y., Zhang, W., Farooq, U., et al. (2018). Simultaneous co-substitution of Sr2+/Fe3+ in hydroxyapatite nanoparticles for potential biomedical applications. *Ceram. Int.* 44, 21338–21348. doi: 10.1016/j.ceramint.2018.08.187

Ullah, I., Zhang, W., Yang, L., Ullah, M. W., Atta, O. M., Khan, S., et al. (2020). Impact of structural features of Sr/Fe co-doped HAp on the osteoblast proliferation and osteogenic differentiation for its application as a bone substitute. *Mater. Sci. Eng. C* 110:110633. doi: 10.1016/j.msec.2020.110633

Ullah, M. W., Khattak, W. A., Ul-Islam, M., Khan, S., and Park, J. K. (2016a). Metabolic engineering of synthetic cell-free systems: strategies and applications. *Biochem. Eng. J.* 105, 391–405. doi: 10.1016/j.bej.2015.10.023

Ullah, M. W., Ul-Islam, M., Khan, S., Kim, Y., Jang, J. H., and Park, J. K. (2016b). In situ synthesis of a bio-cellulose/titanium dioxide nanocomposite by using a cell-free system. *RSC Adv.* 6, 22424–22435. doi: 10.1039/C5RA26704H

Ullah, M. W., Ul-Islam, M., Khan, S., Kim, Y., and Park, J. K. (2016c). Structural and physico-mechanical characterization of bio-cellulose produced by a cell-free system. *Carbohydr. Polym.* 136, 908–916. doi: 10.1016/j.carbpol.2015.10.010

Ullah, M. W., Ul Islam, M., Khan, S., Shah, N., and Park, J. K. (2017). Recent advancements in bioreactions of cellular and cell-free systems: a study of bacterial cellulose as a model. *Korean J. Chem. Eng.* 34, 1591–1599. doi: 10.1007/s11814-017-0121-122

Ullah, M. W., Ul-Islam, M., Khan, S., Kim, Y., and Park, J. K. (2015). Innovative production of bio-cellulose using a cell-free system derived from a single cell line. *Carbohydr. Polym.* 132, 286–294. doi: 10.1016/j.carbpol.2015.06.037

Umar Aslam, Khan, M., Haider, S., Haider, A., Rafiq Abdul, Kadir, M., et al. (2020). Development of porous, antibacterial and biocompatible GO/n-HAp/Bacterial Cellulose/ β-Glucan biocomposite scaffold for bone tissue engineering. *Arab. J. Chem.* 14:102924. doi: 10.1016/j.arabjc.2020.102924

Veerla, S. C., Kim, D. R., Kim, J., Sohn, H., and Yang, S. Y. (2019). Controlled nanoparticle synthesis of Ag/Fe co-doped hydroxyapatite system for cancer cell treatment. *Mater. Sci. Eng. C* 98, 311–323. doi: 10.1016/j.msec.2018.12.148

Wan, Y., Yang, Z., Xiong, G., Guo, R., Liu, Z., and Luo, H. (2015a). Anchoring Fe3O4 nanoparticles on three-dimensional carbon nanofibers toward flexible high-performance anodes for lithium-ion batteries. *J. Power Sources* 294, 414–419. doi: 10.1016/j.jpowsour.2015.06.057

Wan, Y., Yang, Z., Xiong, G., and Luo, H. (2015b). A general strategy of decorating 3D carbon nanofiber aerogels derived from bacterial cellulose with nano-Fe3O4 for high-performance flexible and binder-free lithium-ion battery anodes. *J. Mater. Chem. A* 3, 15386–15393. doi: 10.1039/c5ta03688g

Wan, Y. Z., Huang, Y., Yuan, C. D., Raman, S., Zhu, Y., Jiang, H. J., et al. (2007). Biomimetic synthesis of hydroxyapatite/bacterial cellulose nanocomposites for biomedical applications. *Mater. Sci. Eng. C* 27, 855–864. doi: 10.1016/j.msec.2006.10.002

Wang, B., and Sain, M. (2007). Isolation of nanofibers from soybean source and their reinforcing capability on synthetic polymers. *Compos. Sci. Technol.* 67, 2521–2527. doi: 10.1016/j.compscitech.2006.12.015

Wang, C., Huang, W., Zhou, Y., He, L., He, Z., Chen, Z., et al. (2020a). 3D printing of bone tissue engineering scaffolds. *Bioact. Mater*. 5, 82–91. doi: 10.1016/j.bioactmat.2020.01.004

Wang, L., Hu, S., Ullah, M. W., Li, X., Shi, Z., and Yang, G. (2020b). Enhanced cell proliferation by electrical stimulation based on electroactive regenerated bacterial cellulose hydrogels. *Carbohydr. Polym*. 249:116829. doi: 10.1016/j.carbpol.2020.116829

Wang, C., Lai, J., Li, K., Zhu, S., Lu, B., Liu, J., et al. (2021). Cryogenic 3D printing of dual-delivery scaffolds for improved bone regeneration with enhanced vascularization. *Bioact. Mater*. 6, 137–145. doi: 10.1016/j.bioactmat.2020.07.007

Wang, J., Gao, C., Zhang, Y., and Wan, Y. (2010). Preparation and in vitro characterization of BC/PVA hydrogel composite for its potential use as artificial cornea biomaterial. *Mater. Sci. Eng. C* 30, 214–218. doi: 10.1016/j.msec.2009.10.006

Wang, J., Wan, Y., Han, J., Lei, X., Yan, T., and Gao, C. (2011). Nanocomposite prepared by immobilising gelatin and hydroxyapatite on bacterial cellulose nanofibres. *Micro Nano Lett.* 6:133. doi: 10.1049/mnl.2010.0209

Wang, Y., Wang, J., Hao, H., Cai, M., Wang, S., Ma, J., et al. (2016). In vitro and in vivo mechanism of bone tumor inhibition by selenium-doped bone mineral nanoparticles. *ACS Nano* 10, 9927–9937. doi: 10.1021/acsnano.6b03835

Williams D. F. (2019). Biocompatibility in clinical practice: predictable and unpredictable outcomes. *Prog. Biomed. Eng.* 1:013001. doi: 10.1088/2516-1091/ab22cc

Yan, Y., Lin, H., Matsumoto, H., Bouzika, P., Miller, J., and Vavvas, D. (2013). Comparison of the toxicity of different drug delivery nanoparticles in RPE and photoreceptor cells. *Invest. Ophthalmol. Vis. Sci.* 54:1940.

Yanamala, N., Farcas, M. T., Hatfield, M. K., Kisin, E. R., Kagan, V. E., Geraci, C. L., et al. (2014). In vivo evaluation of the pulmonary toxicity of cellulose nanocrystals: a renewable and sustainable nanomaterial of the future. *ACS Sustainable Chem. Eng.* 2, 1691–1698. doi: 10.1021/sc500153k

Yang, H., Sheikhi, A., and Van De Ven, T. G. M. (2016). Reusable green aerogels from cross-linked hairy nanocrystalline cellulose and modified chitosan for dye removal. *Langmuir* 32, 11771–11779. doi: 10.1021/acs.langmuir.6b03084

Yang, J., Du, M., Wang, L., Li, S., Wang, G., Yang, X., et al. (2018). Bacterial cellulose as a supersoft neural interfacing substrate. *ACS Appl. Mater. Interfaces* 10, 33049–33059. doi: 10.1021/acsami.8b12083

Yang, J., Yang, X., Wang, L., Zhang, W., Yu, W., Wang, N., et al. (2017). Biomimetic nanofibers can construct effective tissue-engineered intervertebral discs for therapeutic implantation. *Nanoscale* 9, 13095–13103. doi: 10.1039/C7NR03944A

Yang, Z., Chen, S., Hu, W., Yin, N., Zhang, W., Xiang, C., et al. (2012). Flexible luminescent CdSe/bacterial cellulose nanocomoposite membranes. *Carbohydr. Polym*. 88, 173–178. doi: 10.1016/j.carbpol.2011.11.080

Yin, N., Chen, S., Ouyang, Y., Tang, L., Yang, J., and Wang, H. (2011). Biomimetic mineralization synthesis of hydroxyapatite bacterial cellulose nanocomposites. *Prog. Nat. Sci. Mater. Int.* 21, 472–477. doi: 10.1016/S1002-0071(12)60085-60089

Yuan, H., Van Blitterswijk, C. A., De Groot, K., and De Bruijn, J. D. (2006). A comparison of bone formation in biphasic calcium phosphate (BCP) and hydroxyapatite (HA) implanted in muscle and bone of dogs at different time periods. *J. Biomed. Mater. Res. - Part A.* 78, 139–147. doi: 10.1002/jbm.a.30707

Yuen, J. D., Walper, S. A., Melde, B. J., Daniele, M. A., and Stenger, D. A. (2017). Electrolyte-sensing transistor decals enabled by ultrathin microbial nanocellulose. *Sci. Rep.* 7:40867. doi: 10.1038/srep40867

Zaborowska, M., Bodin, A., Bäckdahl, H., Popp, J., Goldstein, A., and Gatenholm, P. (2010). Microporous bacterial cellulose as a potential scaffold for bone regeneration. *Acta Biomater*. 6, 2540–2547. doi: 10.1016/j.actbio.2010.01.004

Zarei, S., Niad, M., and Raanaei, H. (2018). The removal of mercury ion pollution by using Fe3O4-nanocellulose: synthesis, characterizations and DFT studies. *J. Hazard. Mater*. 344, 258–273. doi: 10.1016/j.jhazmat.2017.10.009

Zhan, H., Peng, N., Lei, X., Huang, Y., Li, D., Tao, R., et al. (2018). UV-induced self-cleanable TiO2/nanocellulose membrane for selective separation of oil/water emulsion. *Carbohydr. Polym*. 201, 464–470. doi: 10.1016/j.carbpol.2018.08.093

Zhang, G., Liao, Q., Zhang, Z., Liang, Q., Zhao, Y., Zheng, X., et al. (2015). Novel piezoelectric paper-based flexible nanogenerators composed of BaTiO3 nanoparticles and bacterial cellulose. *Adv. Sci*. 3:1500257. doi: 10.1002/advs.201500257

Zhang, H., Wang, J., Wang, K., and Xu, L. (2018a). A bilayered PLGA/multiwall carbon nanotubes/bacterial cellulose composite membrane for tissue regeneration of maxillary canine periodontal bone defects. *Mater. Lett.* 212, 118–121. doi: 10.1016/j.matlet.2017.10.058

Zhang, Y., Wang, F., Li, M., Yu, Z., Qi, R., Ding, J., et al. (2018b). Self-Stabilized hyaluronate nanogel for intracellular codelivery of doxorubicin and cisplatin to osteosarcoma. *Adv. Sci.* 5:1700821. doi: 10.1002/advs.201700821

Zhang, W., Wang, X., Li, X., Zhang, L., and Jiang, F. (2020). A 3D porous microsphere with multistage structure and component based on bacterial cellulose and collagen for bone tissue engineering. *Carbohydr. Polym.* 236:116043. doi: 10.1016/j.carbpol.2020.116043

Zharikov, A. N., Lubyansky, V. G., Gladysheva, E. K., Skiba, E. A., Budaeva, V. V., Semyonova, E. N., et al. (2018). Early morphological changes in tissues when replacing abdominal wall defects by bacterial nanocellulose in experimental trials. *J. Mater. Sci. Mater. Med.* 29:95. doi: 10.1007/s10856-018-6111-z

Zhong, C. (2020). Industrial-Scale production and applications of bacterial cellulose. *Front. Bioeng. Biotechnol.* 8:605374. doi: 10.3389/fbioe.2020.605374

Zhu, T., Cui, Y., Zhang, M., Zhao, D., Liu, G., and Ding, J. (2020). Engineered three-dimensional scaffolds for enhanced bone regeneration in osteonecrosis. *Bioact. Mater*. 5, 584–601. doi: 10.1016/j.bioactmat.2020.04.008

Zimmermann, K. A., LeBlanc, J. M., Sheets, K. T., Fox, R. W., and Gatenholm, P. (2011). Biomimetic design of a bacterial cellulose/hydroxyapatite nanocomposite for bone healing applications. *Mater. Sci. Eng. C* 31, 43–49. doi: 10.1016/J.MSEC.2009.10.007

Conflict of Interest: The authors declare that the research was conducted in the absence of any commercial or financial relationships that could be construed as a potential conflict of interest.

frontiers
in Bioengineering and Biotechnology

SYSTEMATIC REVIEW
published: 13 October 2021
doi: 10.3389/fbioe.2021.616753

Candidate Bioinks for Extrusion 3D Bioprinting—A Systematic Review of the Literature

Sam P. Tarassoli[1†], *Zita M. Jessop*[1,2†], *Thomas Jovic*[1,2], *Karl Hawkins*[3] and *Iain S. Whitaker*[1,2*]

[1] *Reconstructive Surgery & Regenerative Medicine Research Group (ReconRegen), Swansea University Medical School, Institute of Life Sciences, Swansea, United Kingdom,* [2] *The Welsh Centre for Burns & Plastic Surgery, Morriston Hospital, Swansea, United Kingdom,* [3] *Centre for NanoHealth, Swansea University Medical School, Institute of Life Sciences, Swansea, United Kingdom*

Purpose: Bioprinting is becoming an increasingly popular platform technology for engineering a variety of tissue types. Our aim was to identify biomaterials that have been found to be suitable for extrusion 3D bioprinting, outline their biomechanical properties and biocompatibility towards their application for bioprinting specific tissue types. This systematic review provides an in-depth overview of current biomaterials suitable for extrusion to aid bioink selection for specific research purposes and facilitate design of novel tailored bioinks.

Methods: A systematic search was performed on EMBASE, PubMed, Scopus and Web of Science databases according to the PRISMA guidelines. References of relevant articles, between December 2006 to January 2018, on candidate bioinks used in extrusion 3D bioprinting were reviewed by two independent investigators against standardised inclusion and exclusion criteria. Data was extracted on bioprinter brand and model, printing technique and specifications (speed and resolution), bioink material and class of mechanical assessment, cell type, viability, and target tissue. Also noted were authors, study design (*in vitro*/*in vivo*), study duration and year of publication.

Results: A total of 9,720 studies were identified, 123 of which met inclusion criteria, consisting of a total of 58 reports using natural biomaterials, 26 using synthetic biomaterials and 39 using a combination of biomaterials as bioinks. Alginate ($n = 50$) and PCL ($n = 33$) were the most commonly used bioinks, followed by gelatin ($n = 18$) and methacrylated gelatin (GelMA) ($n = 16$). Pneumatic extrusion bioprinting techniques were the most common ($n = 78$), followed by piston ($n = 28$). The majority of studies focus on the target tissue, most commonly bone and cartilage, and investigate only one bioink rather than assessing a range to identify those with the most promising printability and biocompatibility characteristics. The Bioscaffolder (GeSiM, Germany), 3D Discovery (regenHU, Switzerland), and Bioplotter (EnvisionTEC, Germany) were the most commonly used commercial bioprinters ($n = 35$ in total), but groups most often opted to create their own in-house devices ($n = 20$). Many studies also failed to specify whether the mechanical data reflected pre-, during or post-printing, pre- or post-crosslinking and with or without cells.

Edited by:
Muhammad Wajid Ullah,
Huazhong University of Science and Technology, China

Reviewed by:
Stephanie Michelle Willerth,
University of Victoria, Canada
Costas Adam Charitidis,
National Technical University of Athens, Greece

Correspondence:
Iain S. Whitaker
iainwhitaker@fastmail.fm
orcid.org/0000-0002-3922-2079

[†] *These authors share first authorship*

Specialty section:
This article was submitted to Biomaterials,
a section of the journal Frontiers in Bioengineering and Biotechnology

Received: *13 October 2020*
Accepted: *19 April 2021*
Published: *13 October 2021*

Citation:
Tarassoli SP, Jessop ZM, Jovic T, Hawkins K and Whitaker IS (2021) Candidate Bioinks for Extrusion 3D Bioprinting—A Systematic Review of the Literature. Front. Bioeng. Biotechnol. 9:616753. doi: 10.3389/fbioe.2021.616753

Conclusions: Despite the continued increase in the variety of biocompatible synthetic materials available, there has been a shift change towards using natural rather than synthetic bioinks for extrusion bioprinting, dominated by alginate either alone or in combination with other biomaterials. On qualitative analysis, no link was demonstrated between the type of bioink or extrusion technique and the target tissue, indicating that bioprinting research is in its infancy with no established tissue specific bioinks or bioprinting techniques. Further research is needed on side-by-side characterisation of bioinks with standardisation of the type and timing of biomechanical assessment.

Keywords: bioprinting, bioink, extrusion, systematic review, regenerative medicine

INTRODUCTION

Bioprinting is defined as the precise and accurate deposition of biomaterials simultaneously with cells, within a predesigned space using a computer-aided printer (Langer and Tirrell, 2004; Mironov, 2005). The process was first described in 1988 (Klebe, 1988) as "cytoscribing" which involved depositing coloured inks in three-dimensions (3D), inspired by the two-dimensional (2D) paper printers that preceded them. Since then, biological materials have been used and increasingly complex printing methods developed which have made significant contributions to this evolving field (Lee et al., 2010; Benwood et al., 2021). These printable biomaterials, known as bioinks, can mimic the extracellular matrix (ECM) environment to support cell adhesion, differentiation and proliferation. Bioinks differ from other inks used in additive manufacturing (or 3D printing) in that they must serve both biological and mechanical functions. As such, they are printed at much lower temperatures, are typically derived naturally and have mild cross-linking conditions to preserve the cells and prevent unwanted degradation of the biomolecules (Malda et al., 2013).

Several bioprinting technologies have been explored, from inkjet and stereolithography to laser-assisted (3). Extrusion based techniques, also known as fused deposition modelling or bioplotting, are the most commonly used and involve extrusion of a viscous material containing cells, as a continuous filament through a nozzle using either a pneumatic, piston, or screw forces (Landers et al., 2002; Jakab et al., 2008). After printing, the constructs can be solidified (i.e., gelled) layer-by-layer either physically or chemically, which makes this technique slower than others such as laser assisted or ink jet based (Landers et al., 2002; Smith et al., 2004; Jakab et al., 2008). However, the cost effectiveness (many are made from modifying commercially available 3D printers), simplicity and high cell viability makes extrusion bioprinting a popular choice for most research institutions and is the basis of the first commercial 3D bioprinter (Organovo Novogen MMX Bioprinter^{TM}) (Jürgen et al., 2016). The main limiting factors relate to achieving a high enough resolution to enable reproduction of native nano- and micro-architecture and maintaining post printing shape fidelity to enable bioprinting of complex macrostructures. The resolution itself will depend on the tissue type attempted to be recreated e.g., bundles and cell alignments for muscle bioprinting demanded a bioprinting resolution of $<50\,\mu m$ whereas some of the finest features of tissue microarchitectures required $\sim 10\,\mu m$ and mainly limited by the size of the individual cells themselves (Miri et al., 2019). These in turn depend on optimal material rheology and crosslinking ability (Jessop et al., 2017; Kyle et al., 2017).

The desirable characteristics of scaffolds for tissue engineering have been well-described (Hutmacher, 2000; Hollister, 2005; Al-Himdani et al., 2017), whereas those of bioinks are less well-defined (Kyle et al., 2017). The development and discovery of bioinks has had a staggered past with no natural research evolution (Tarassoli et al., 2018b). Initial studies used existing natural polymers (such as alginate or gelatin) for bioprinting rather than tailoring biomechanics to suit individual bioprinters (Boland et al., 2003; Jakab et al., 2004). These bioinks are still commonplace in modern bioprinting laboratory practise either alone or in combination with other biomaterials. More recent developments include smart polymers, consisting of synthetic materials with bioactive proteins to enable modification of biomechanical and biocompatibility properties, respectively (Galaev and Mattiasson, 1999). Their design allows for them to respond to specific stimuli (such as temperature, magnetism, ionic etc.) (Wei et al., 2017), but these are not necessarily optimised for extrusion bioprinting. Work has been carried out in the field of smart polymers in 3d bioprinting and cell therapy

---

Abbreviations: ABS, Acrylonitrile butadiene styrene; ADSC, Adipose Derived Stem Cell; ASSMC, Aortic sinus smooth muscle cells; BMPC, Bone marrow plasma cell; B-TCP, Beta tricalcium phosphate; CM, Compressive Modulus; ECM, Extracellular matrix; EM (Compressive), Elastic Modulus; EPC, Endothelial progenitor cell; HAMA, Hyaluronic Acid Methyacrylate; HAVIC, Human aortic valve interstitial cell; HDMEC, Human Brain Microvascular Endothelial cell; htMSC, Human turbinate mesenchymal stem cells; HUCPVC, Human Umbilical Cord Perivascular Cells; HUVEC, Human umbilical vein endothelial cell; MCS, Maximum Compressive Strength; MSC, Mesenchymal stem cell; P(AGE-co-G), Ally-functionalised poly(glycidol)s; PAEC, Porcine aorta endothelial cells; PBT, Polybutylene terephthalate; PCL, Polycaprolactone; PDLLA, Poly-DL-lactic acid; PEG-DA, Polyethylene glycol diacrylate; PEOT, Poly(ethylene oxide terephthalate); PEU, Poly ether urethane; PGS, Pyrolytic graphite sheet; pHMGCL, Phenyl magnesium chloride; PLGA, Poly-lactic-co-glycolic acid; PPF, Polypropylene fumarate; PU, Polyurethane; PUPEO, Polyurethane Polyethylene oxide; PVA, Polyvinyl acetate; RCS, Residual Compressive Stress; SM, Shear Storage Modulus; SEM, Shear Elastic Modulus; SVF, Stromal vascular fraction; TPU, Thermoplastic polyurethane; V, Viscosity.

and is becoming an emerging avenue for further research (Huang et al., 2019).

Bioinks are classified as natural or synthetic. Natural bioinks differ to synthetic bioinks in their ability to mimic the native cellular microenvironment, offering support to growing cells and thereby increasing the likelihood of cell adhesion and secretion of matrix. On the other hand, synthetic bioinks are easier to tailor for efficient printability (Gopinathan and Noh, 2018). Many features of bioinks, such as biodegradability, ability to functionalise and sterilise, will naturally overlap with those of conventional scaffolds used for tissue engineering applications (Al-Himdani et al., 2017). However, the requirement for "printability" of bioinks introduces a new array of design criteria, encompassing parameters such as viscosity, viscoelasticity, cell supportive ability and gelation kinetics, which require further characterisation (**Figure 1**) (Ersumo et al., 2016; Kyle et al., 2017). Ideally, the bioink should possess the biomechanical properties to allow easy extrusion at low shear forces during printing, whilst supporting cell growth and maintaining shape fidelity post-printing (Jessop et al., 2017). Other considerations include biocompatibility with the chosen cell type, allowing not only cell survival but promotion of cellular proliferation, differentiation and extracellular matrix secretion to promote formation of the target tissue (Kyle et al., 2017). Taken together these features can be defined as the "bio-printability" properties of bioinks. Such customisable technology means that properties required of candidate bioinks may not be equally weighted; resolution may be more important for one type of application and cell supportive ability might be more sought after for another (Malda et al., 2013). In addition, biological variation in the behaviour of even identical cell lines means that outcomes can differ independently of the bioink, adding to the complexity of research in this field (Hutmacher, 2000; Ersumo et al., 2016).

Advanced bioinks are now being designed to significantly improve printability and biocompatibility (Kyle et al., 2017). These can be achieved through careful control of various physical, chemical and biological properties. Biomechanical properties that can be assessed include rheology (viscosity, shear-thinning, viscoelasticity, and thixotropy), gelation kinetics, crosslinking and network architecture (Murphy et al., 2013; Jia et al., 2014; Blaeser et al., 2016). Biocompatibility can also be altered through biofunctionalisation which can affect cell function (cytocompatibility, cell adhesion, migration, proliferation, and differentiation) as well as biodegradation of materials (Skardal et al., 2012; Levato et al., 2014; Muller et al., 2015; Daly et al., 2016). The tunability of these scaffolds also serve the purpose of helping protecting cells (from stresses) and allowing them to achieve the highest degree of viability (Sharma et al., 2020).

The aim of this systematic review was to identify the types of bioinks that have been used to date for extrusion-based 3D bioprinting and analyse their biomechanical characteristics, biocompatibility and bioprinting parameters so that these may aid in decision making when selecting suitable bioinks for individual purposes as well as the design of novel tailored bioinks.

MATERIALS AND METHODS

Search Strategy

A systematic search for relevant articles was performed in accordance with the recommendations of the Preferred Reporting Items for Systematic Reviews and Meta-Analyses (PRISMA) guidelines (**Figure 2**) (Moher et al., 2015) to evaluate the types of biomaterials that have been used as bioinks for extrusion 3D bioprinting. Preclinical studies were identified through a systematic search across electronic databases Web of Science (Web of Science Core Collection, BIOSIS Citation index, KCI-Korean Journal Database, MEDLINE, SciELO Citation Index), PubMed, Scopus, OVID and Embase, from December 2006 to November 2017. Search terms included: "3d print" OR "3-dimensional print" OR "bioprint" OR "print" OR "additive manufacturing" OR "extrusion" OR "extrusion-based" OR "deposition" OR "pneumatic" OR "piston" OR "screw" AND ("bioink" OR "cell" OR "ink" OR "scaffold" OR "hydrogel").

Eligibility Criteria

The eligibility for including articles in this systematic review were as follows: (1) all studies included involved extrusion bioprinting; (2) either using animal or human cells; (3) both *in vitro* and *in vivo* studies; (4) English language articles only.

Exclusion Criteria

Studies were excluded if they met the following criteria: (1) no bioprinting component; (2) involved non-extrusion based bioprinting techniques; (3) contained no biomaterial component; (4) contained no cellular component; (5) were not available for viewing. Review articles and commentaries were also excluded.

Study Selection

Two reviewers (S.P.T. and Z.M.J.) independently reviewed the studies with differences resolved by the senior author (I.S.W.). The bibliographies of relevant articles were studied to identify further relevant publications (**Figure 3**). Titles were initially screened to exclude duplicates and further screened using the abstracts against inclusion and exclusion criteria. Finally, full text review of the remainder was performed to assess of eligibility.

Data Extraction and Main Outcomes

Data was extracted from the selected studies using a standardised format (Microsoft Office Excel 2016). The initial tabulated data collection included; bioink composition, biomechanics (compressive, elastic and shear storage moduli, viscosity or as stated in **Supplementary Table 1** as **MCS/CM/EM/RCS/SM**), crosslinking type, bioprinter type, type of extrusion technique (pneumatic, mechanical, piston, screw), printing parameters (resolution, speed), cell source, cell viability and target tissue. Also noted were study authors, study design (*in vitro*/*in vivo*) and year of publication.

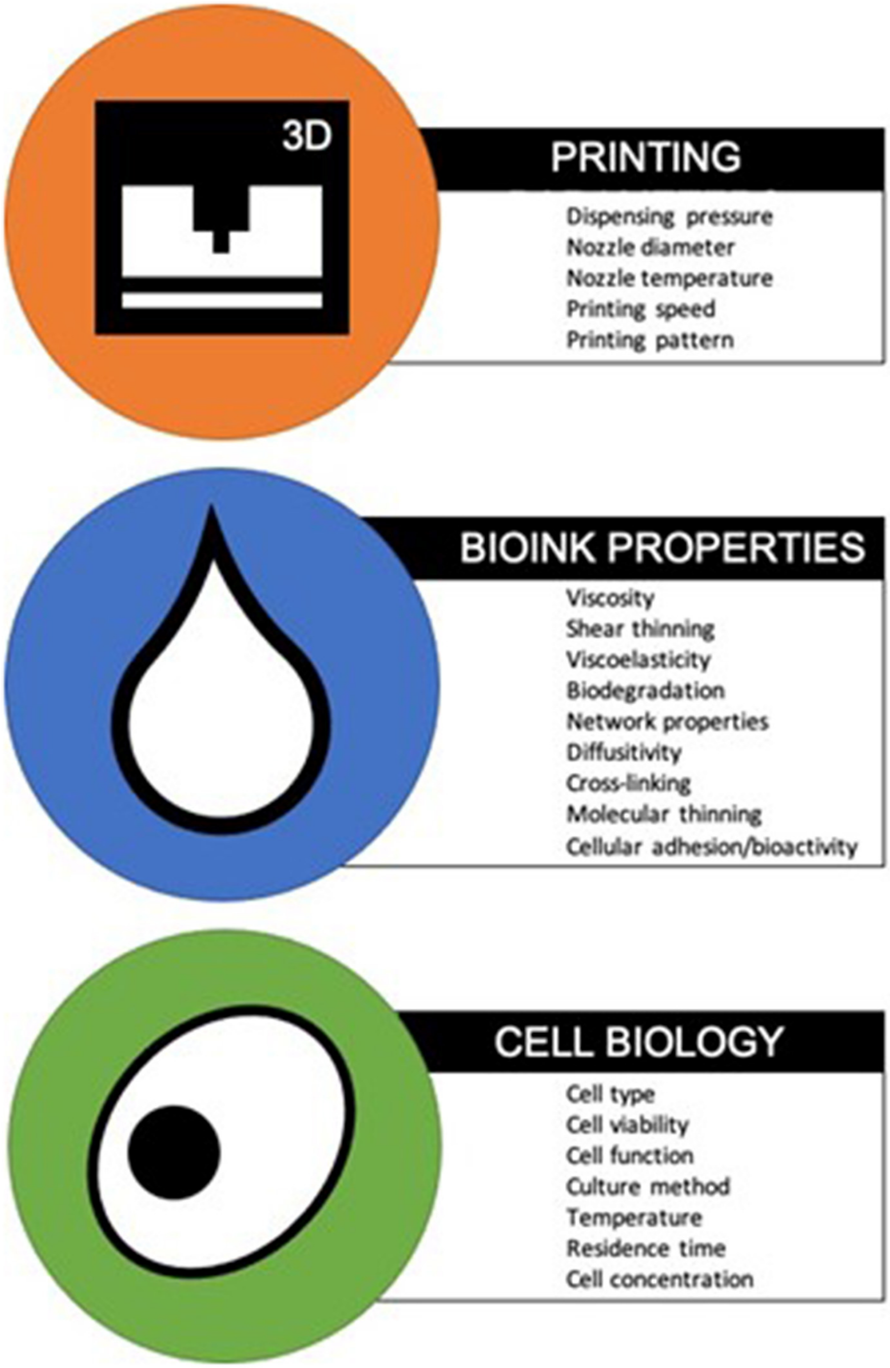

FIGURE 1 | 3D printer parameters, bioink properties, and cell characteristics for optimum bio-printability (Chang et al., 2008; Derby, 2012; Zhang and Cui, 2012; Kirchmajer et al., 2015).

RESULTS

Types of Bioinks Used for Extrusion Bioprinting

A total of 9,720 studies were identified, 123 of which met inclusion criteria, consisting of a total of 58 reports using natural biomaterials, 26 using synthetic biomaterials and 39 using a combination of biomaterials as bioinks. Alginate ($n = 53$) and PCL ($n = 30$) are the most common types of bioink, followed by gelatin ($n = 18$) and methacrylated gelatin (GelMA) ($n = 16$) (**Figure 3**).

Improvements in technology and biomaterial availability have resulted in an upward trend in the number of studies using bioinks for extrusion. There is a marked increase

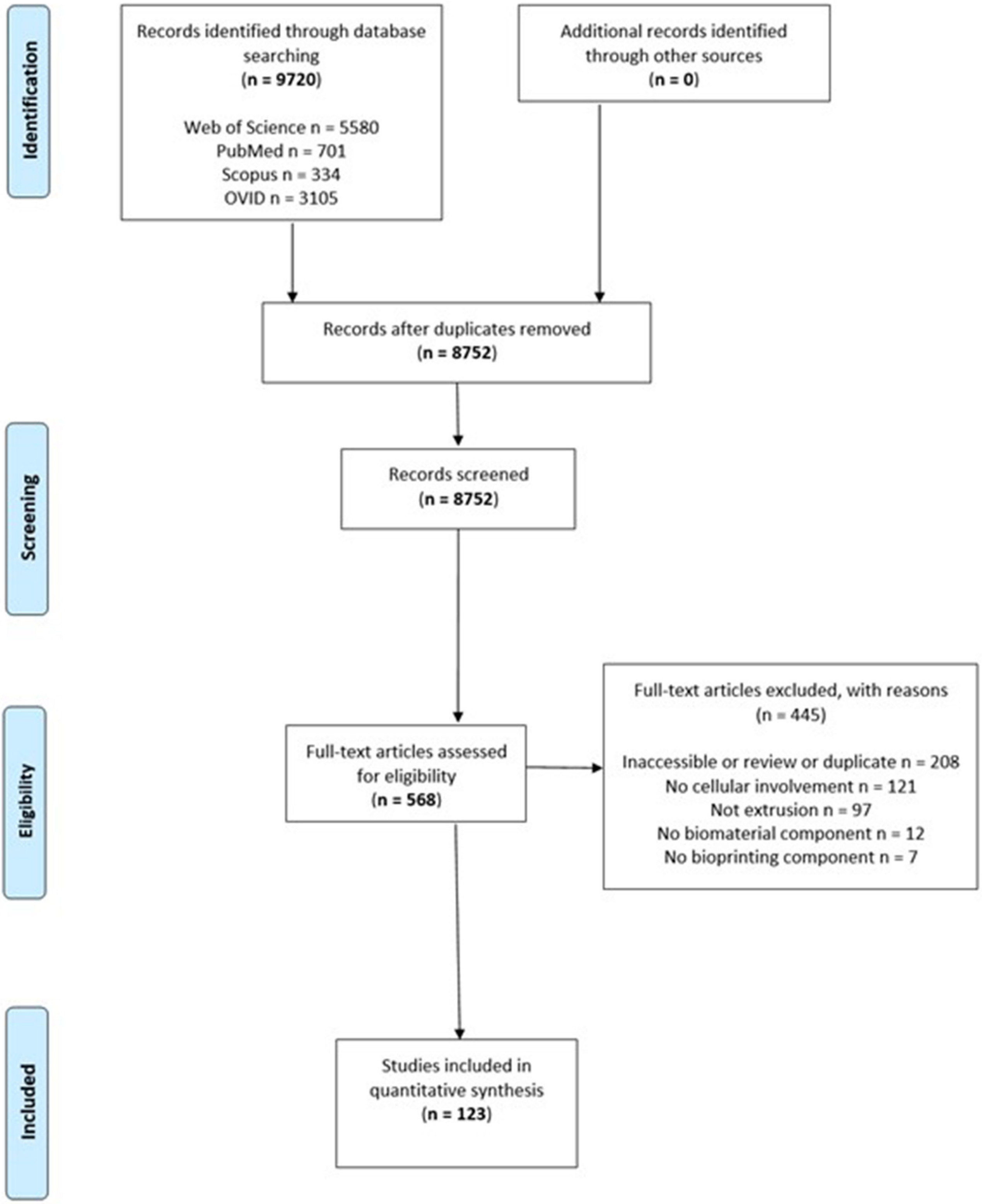

FIGURE 2 | Preferred Reporting Items for Systematic Reviews and Meta-Analyses flow chart of included studies.

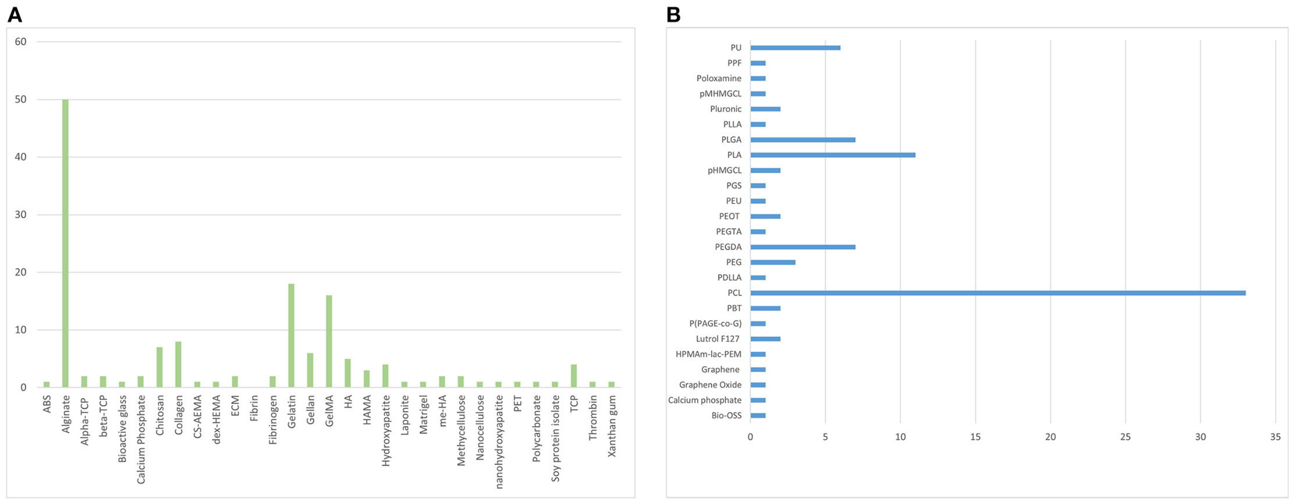

FIGURE 3 | The individual distribution frequency of natural **(A)** and synthetic **(B)** bioinks used in the analysed literature.

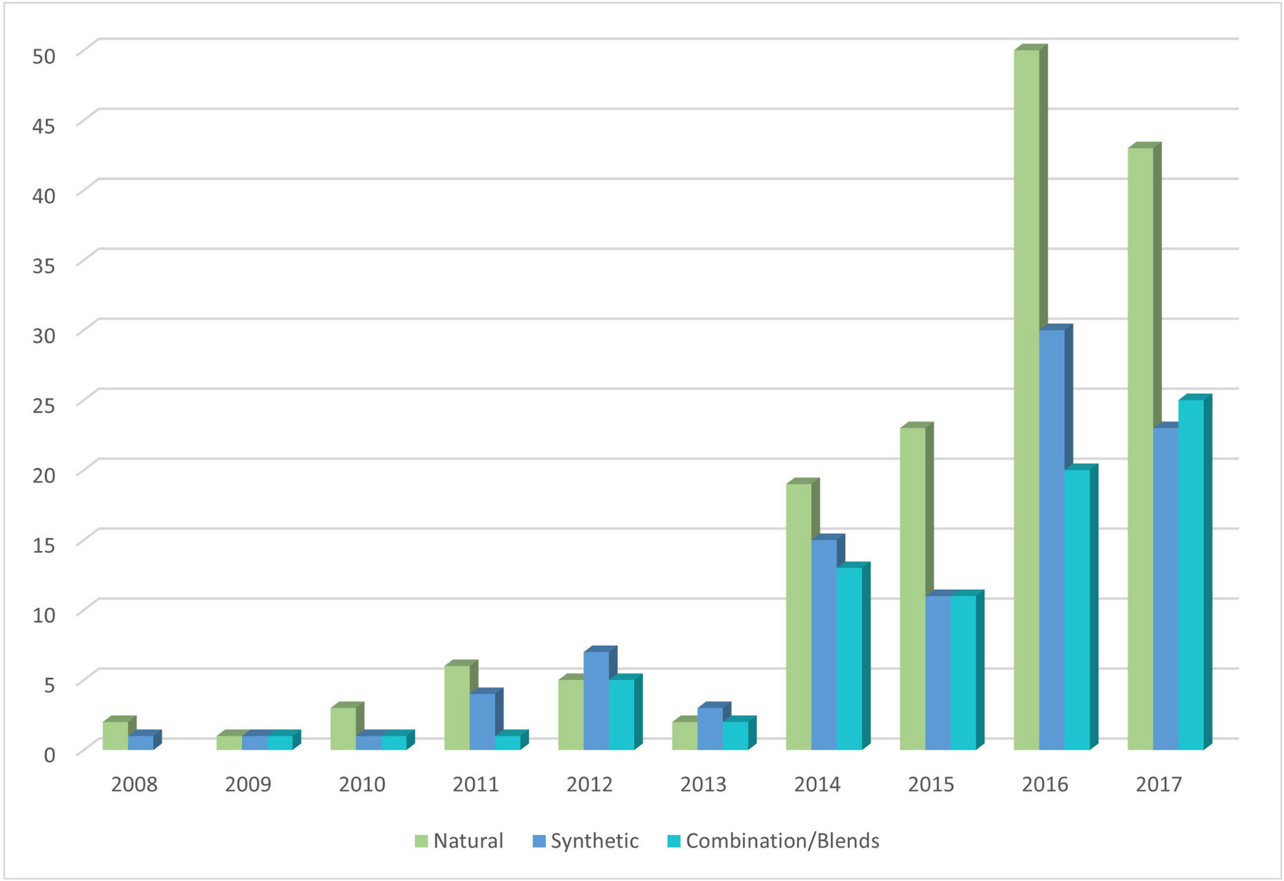

FIGURE 4 | Bioink type frequency in relation to the year of study.

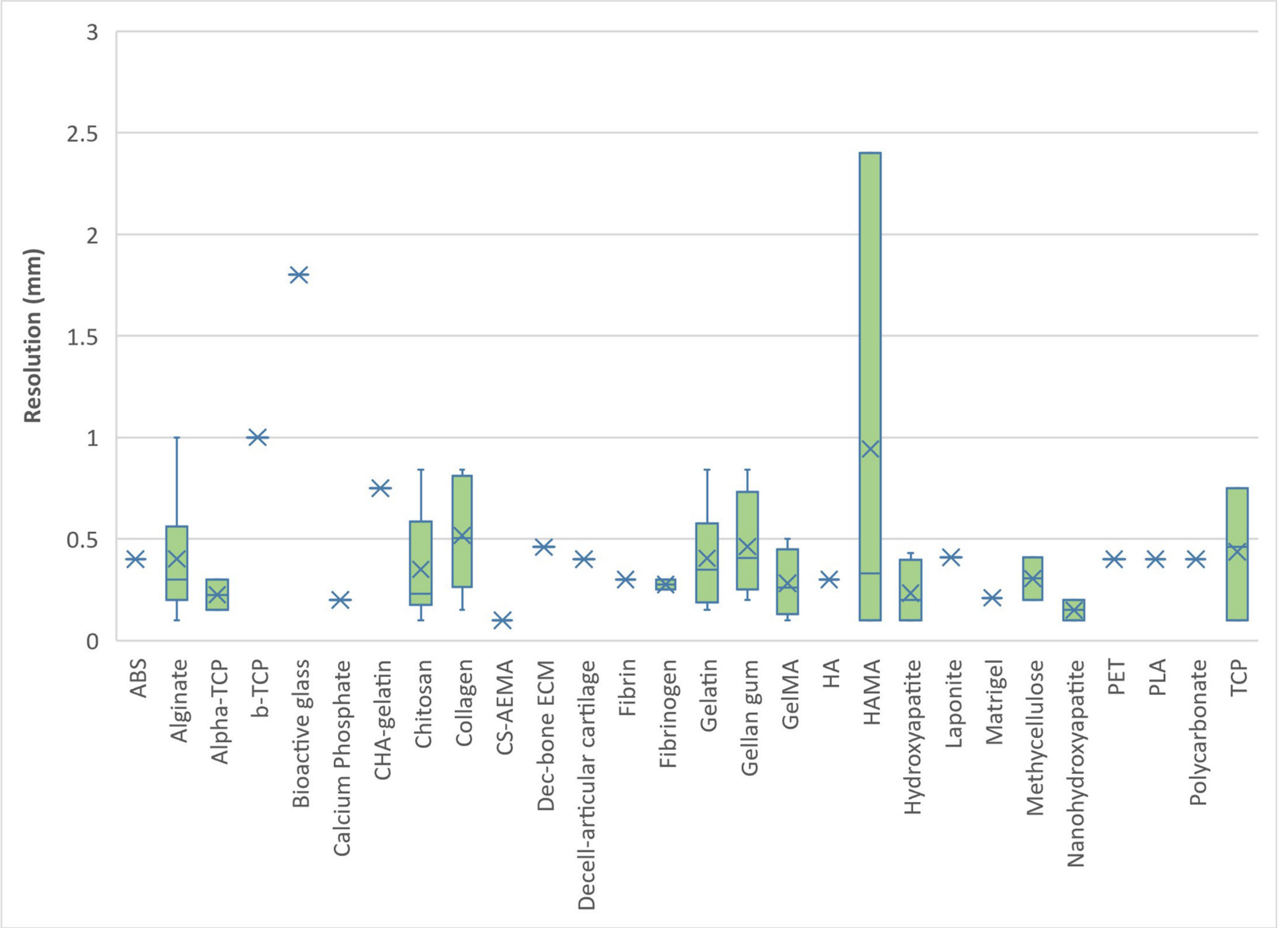

FIGURE 5 | Bioprinting resolution for natural-derived bioinks.

in the use of all three bioink types (natural, synthetic, and blend) published between 2013 and 2014 and to a lesser degree between 2015 and 2016 (**Figure 4**). There has been a disproportional increase in the amount of natural bioinks used in the literature compared to synthetic and blend bioinks suggesting increasing popularity in biomimetic approaches (**Figure 4**).

Pneumatic extrusion bioprinting techniques were the most common ($n = 78$), followed by piston ($n = 28$). Most studies have focused on bone and cartilage as the target tissue type, although bioprinting of solid organs e.g., liver/heart is gaining traction (**Supplementary Table 1**).

Most natural bioinks printed within 1.0 mm resolution. Alginate and HAMA were found to demonstrate the greatest range of printing resolution possible with natural bioinks (0.1–2.4 mm), followed closely by gelatin and collagen (**Figure 5**). Most synthetic bioinks printed within 0.5 mm resolution except for PCL, pHMGCL and PGLA which demonstrated the greatest range (0.1–1.7 mm) (**Figure 6**). The lowest resolution printed over all the bioinks (natural, synthetic, or blends) was with a synthetic material; HPMAm-lac-PEM at 0.025 mm.

From the 123 papers that were analysed, 36 (29%) were in-house printers and 87 (71%) were commercial variations. The analysis of the printing speed and resolution in relation to the bioprinter model used showed a broad scope and range (**Figures 7**, **8**). This is likely to reflect differences in researcher preferences and technical limitations of the different printers used: even the same bioprinter model has varying ranges in both speed and resolution. The 3D Discovery displayed the greatest range of bioprinter speed and resolution of all the models included in this review. However, this is also affected by the tissue type being printed; some cells can only be able to withstand certain printing resolutions and speeds. The lowest printed resolution was the Bioscaffolder at 0.025 mm and the quickest speed at 60 mm/s with the Printrbot (Printrbot, USA).

It was not possible to directly compare biomechanical properties of bioinks used in the literature due to the heterogeneity of mechanical tests used and timing of testing (i.e., pre or post printing, pre or post crosslinking, pre or post tissue maturation). Instead, the most common mechanical moduli used in studies for each tissue type was determined to provide an indication of the most useful biomechanical tests. The results

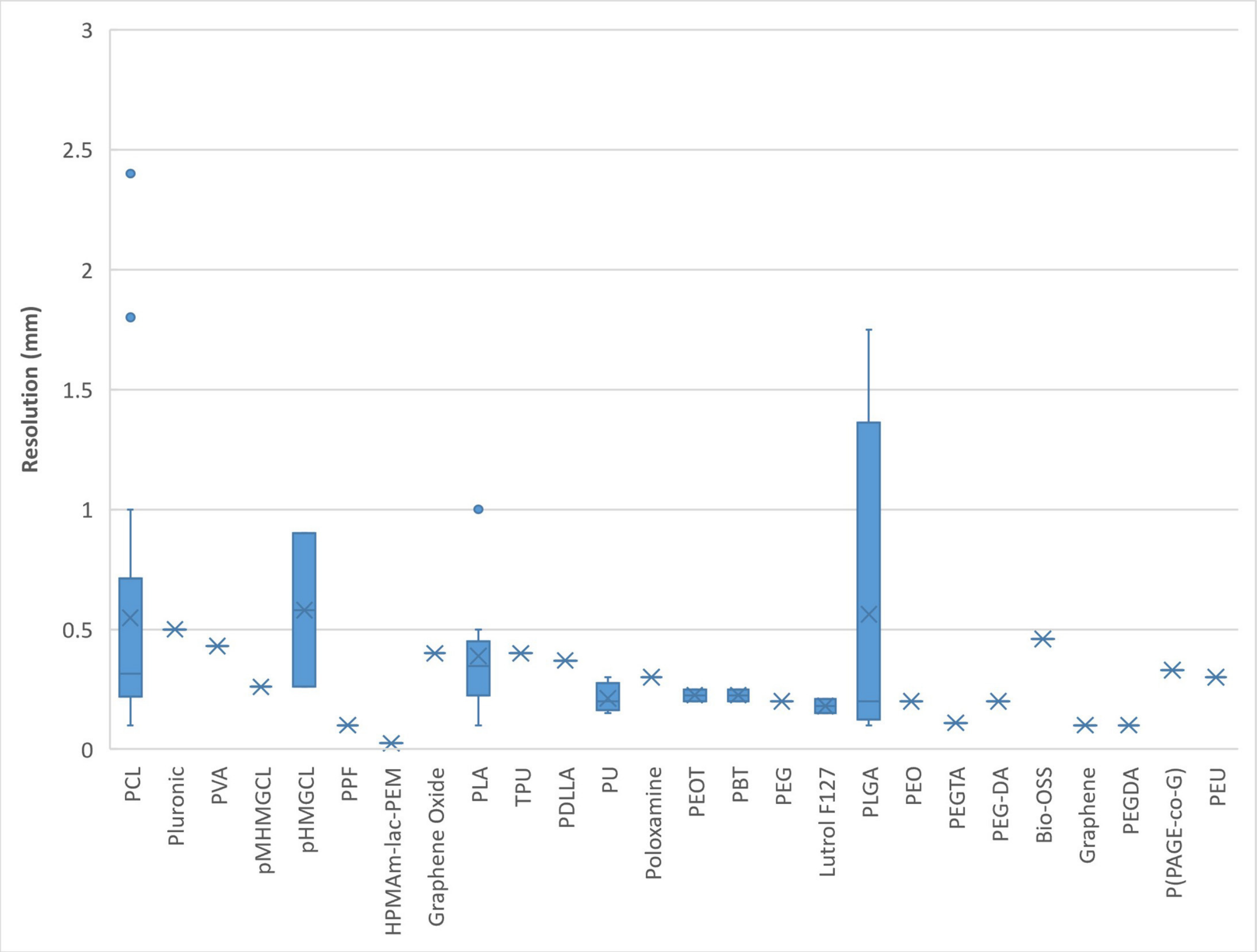

FIGURE 6 | Bioprinting resolution for synthetic-derived bioinks.

show that compressive modulus was the most frequently applied modulus overall and the most used for bone and cartilage tissues (**Figure 9**). Elastic modulus was more commonly applied than compressive modulus for a range of soft tissue, including muscle and vascular tissues. Hard tissues within the literature mostly referred to bone and bone derived tissue types (Nikolova and Chavali, 2019). Residual and maximum compressive stress were used least frequently.

DISCUSSION

Within the last 5 years, development of bioinks have mirrored the exponential growth of research in the 3D bioprinting field. The justification for this growth appears to be 2-fold: firstly the previous two decades have witnessed significant developments in printing technology and stereolithography, secondly, as this systematic review has illustrated, the efforts to engineer and combine novel bioinks have yielded a plethora of printable biomaterials for tissue engineering purposes (Tarassoli et al., 2018b). In line with the expansion of literature in the field of bioink materials and their combination in blends, there has been a call for comprehensive summaries in the field to facilitate the informed design, characterisation and development of further novel bioinks (Ersumo et al., 2016). This systematic review is the first to comprehensively identify the range of biomaterials suitable for extrusion 3D bioprinting, correlate approaches to the different target tissues and evaluate the scope of the methods used to quantify their mechanical properties.

There has been a clear shift towards the use of natural over synthetic scaffolds which may mirror the refinement of natural bioink extraction technology, increased availability and decreased cost. It suggests that research in the field is prioritising biomimicry over customisability. Although synthetic biomaterials were generally found to provide higher printing resolution and allowed tuning of rheological properties through blending (Gopinathan and Noh, 2018), natural bioinks have greater biocompatibility and biodegradability characteristics. Bioinks containing blended biomaterials provide the ability to augment the biological and mechanical properties of one material with another. However, our systematic review has demonstrated

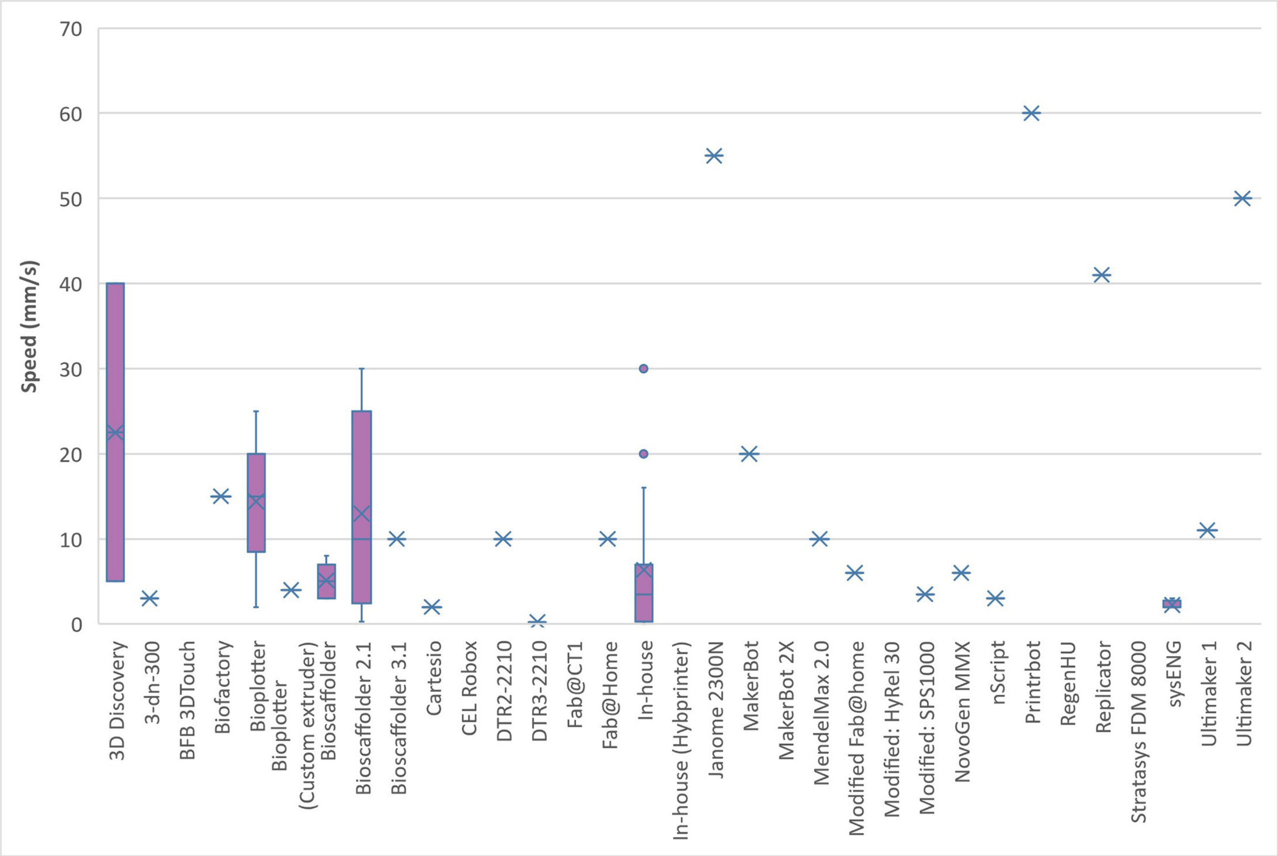

FIGURE 7 | Bioprinting speed for different models of commercial bioprinters.

that the percentage of published literature using pure bioinks (i.e., not blended or modified beyond the initial extraction/production stage) has more than tripled between 2012 and 2018 which could be attributed to the discovery of novel natural biomaterials with shear thinning properties to allow extrusion as well as improved extraction, chemical modification and crosslinking techniques, enabling individual properties to be maximised. Alginate was the most widely used natural material ($n = 50$), followed by gelatin ($n = 18$) and methacrylated gelatin (GelMA) ($n = 16$), whilst PCL was the most commonly used synthetic material ($n = 33$) for bioink composition. The rationale for alginate use was generally not specified in the included studies, though many did acknowledge that alginate was "the most abundant biomaterial in current bioprinting techniques" (Hill et al., 2006; Lee et al., 2013). Alginate has been widely used in the literature, as a matrix designed for cell encapsulation, due to its versatile, facile, and rapid crosslinking and ability to be mass-produced on a large scale at low cost (Purcell et al., 2009). Fifty litres of 2% alginate solution can be produced from 1 kg alginate, costing <£100 to purchase (SigmaAldrich, 2021a). Compared to alternative natural bioinks such as hyaluronic acid (£57 per gramme) (SigmaAldrich, 2021b). Chemical crosslinking enables gelation within seconds providing an ideal environment for cell storage, proliferation, and differentiation (Galateanu et al., 2012). PCL, on the other hand, has been used predominantly as a mechanically supportive bioink and can be blended with a matrix bioink to provide encapsulation as well as superior mechanical stability (Lee et al., 2013). This may explain why PCL was identified as a widely used bioink for cartilage and bone tissue engineering (Steffens et al., 2016; Stichler et al., 2017). Support bioinks tend to be synthetic polymers, like PCL, due to their thermosensitivity (and thus blendable) which provides controlled biodegradation/bioprintability (Kundu et al., 2015). This thermosensitivity can be taken advantage of by a modification of extrusion printing called "melt blending technology"; polymers that have good mechanical properties with moderate melt viscosity can be blended with other similar polymers in heated extruders (Jiao et al., 2019). PCL has also been found to be effective in both neural (Lee et al., 2017) and hepatic (Lee et al., 2016) tissue engineering, which require vastly different cell culture and bioprinting techniques. This versatility also justifies its popularity as a bioink in the literature. PCL bioprinting can also be combined with other techniques such as electrospinning (Lee et al., 2017) further illustrating its versatility in the field of bioengineering.

Our systematic review revealed that one of the major limitations of most extrusion bioprinting studies is opting for one or two specific bioinks with the goal of engineering a specific

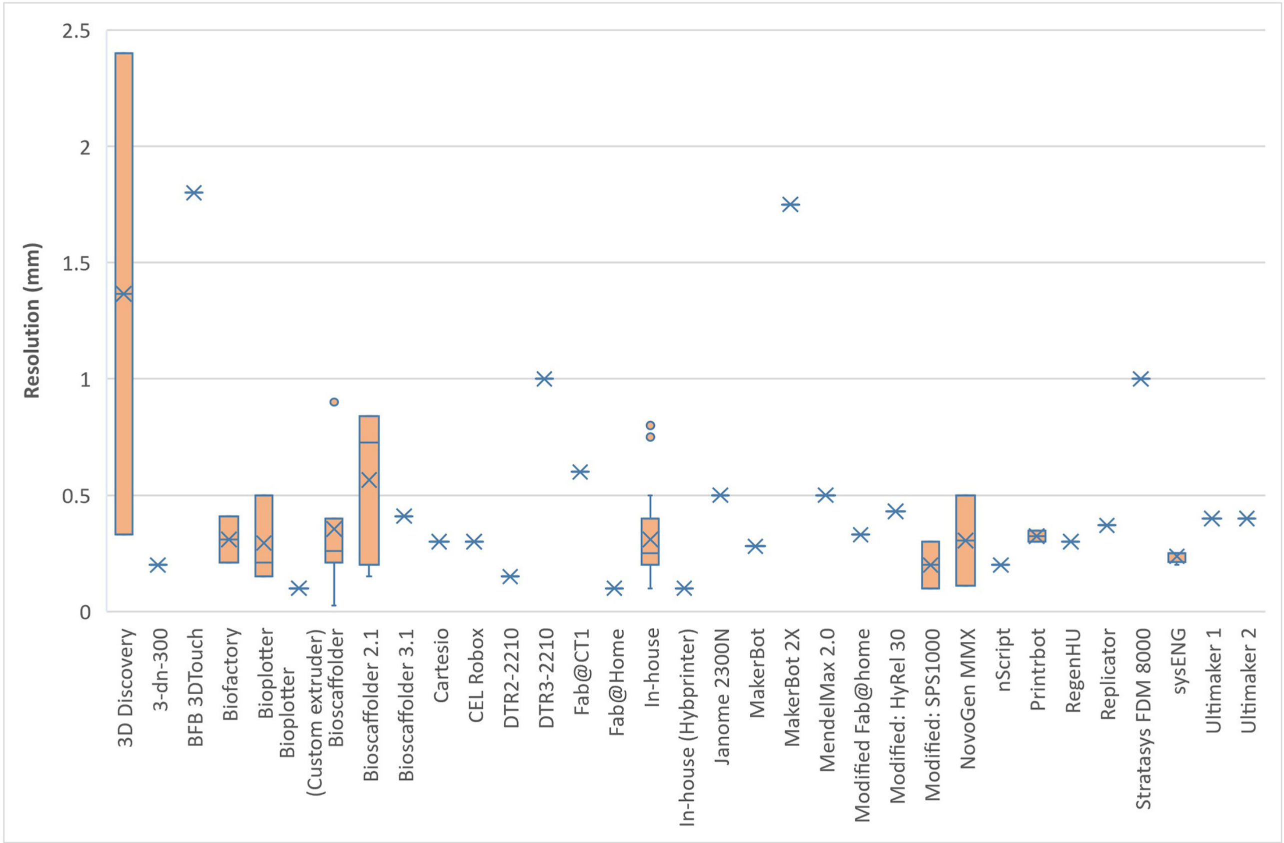

FIGURE 8 | Bioprinting resolution for different models of commercial bioprinters.

tissue type rather than side by side comparisons of bioinks to assess their overall properties and suitability. Akkineni's group (Akkineni A. et al., 2016; Akkineni A. R. et al., 2016) used alginate in 4 separate studies solely for engineering cartilage tissue. For the purposes of their studies, their specific aim was achieved, but it provides limited information on printability and biocompatibility of alginate bioinks overall. Similarly, Dubbin et al. (2017) and Fedorovich et al. (2008, 2009, 2011a,b) assessed synthetic-natural blends (PEGDA and Lutrol F127, respectively) for bone bioprinting using only certain cell types as well thus limiting the potential for full appraisal of those biomaterials. Mesenchymal stem cells appeared to be most commonly used cell source: a product of the dominance of bone and cartilage tissue engineering studies and the relative ease of obtaining mesenchymal stem cells over alternative stem cell sources.

The availability and cost effectiveness of bioprinters has improved significantly in the past few years (Tarassoli et al., 2018a) reflected in the range of bioprinters used in the studies we analysed (**Figures 7**, **8**). There is no "gold standard" bioprinter or extrusion technique and the increasing versatility and customisability of the printers provides a wider capacity for research. Pneumatic force was the most commonly used extrusion technique in those studies that identified the mode of extrusion (64% or 78 out of 123 studies) and suitable for both natural, synthetic and blend bioinks (Liu et al., 2017), followed by piston force technique ($n = 28$). The Bioscaffolder (GeSiM, Germany), 3D Discovery (regenHU, Switzerland) and Bioplotter (EnvisionTEC, Germany) were the most commonly used commercial bioprinters ($n = 35$), but interestingly groups most often opted to create their own in-house devices ($n = 20$). This is most likely due to the low cost of producing such a printer (much of the software and firmware used is open-source; Reid et al., 2016) and the associated potential limitless customisability. The printing speeds ranged from between 2 and 60 mm/s and printing resolutions ranged from 0.025–2.4 mm in the studies that had a full complement of printing information, with no discernible differences between commercial or in-house devices.

We found huge variability in the types of biomechanical tests used to characterise bioinks (Hu et al., 2019) thereby prohibiting direct comparisons of numerical values for moduli. Different approaches for characterising the mechanical properties of bioinks often reflected the target tissue type i.e., compressive tests were more commonly used to assess biomaterials applied to bone and cartilage tissue engineering whereas shear storage modulus was more commonly used to assess biomaterials for engineering soft tissues such as muscle (**Figure 10**). Many studies also failed to specify whether the mechanical data reflected pre-, during or post-printing, pre- or post-crosslinking and with or without cells

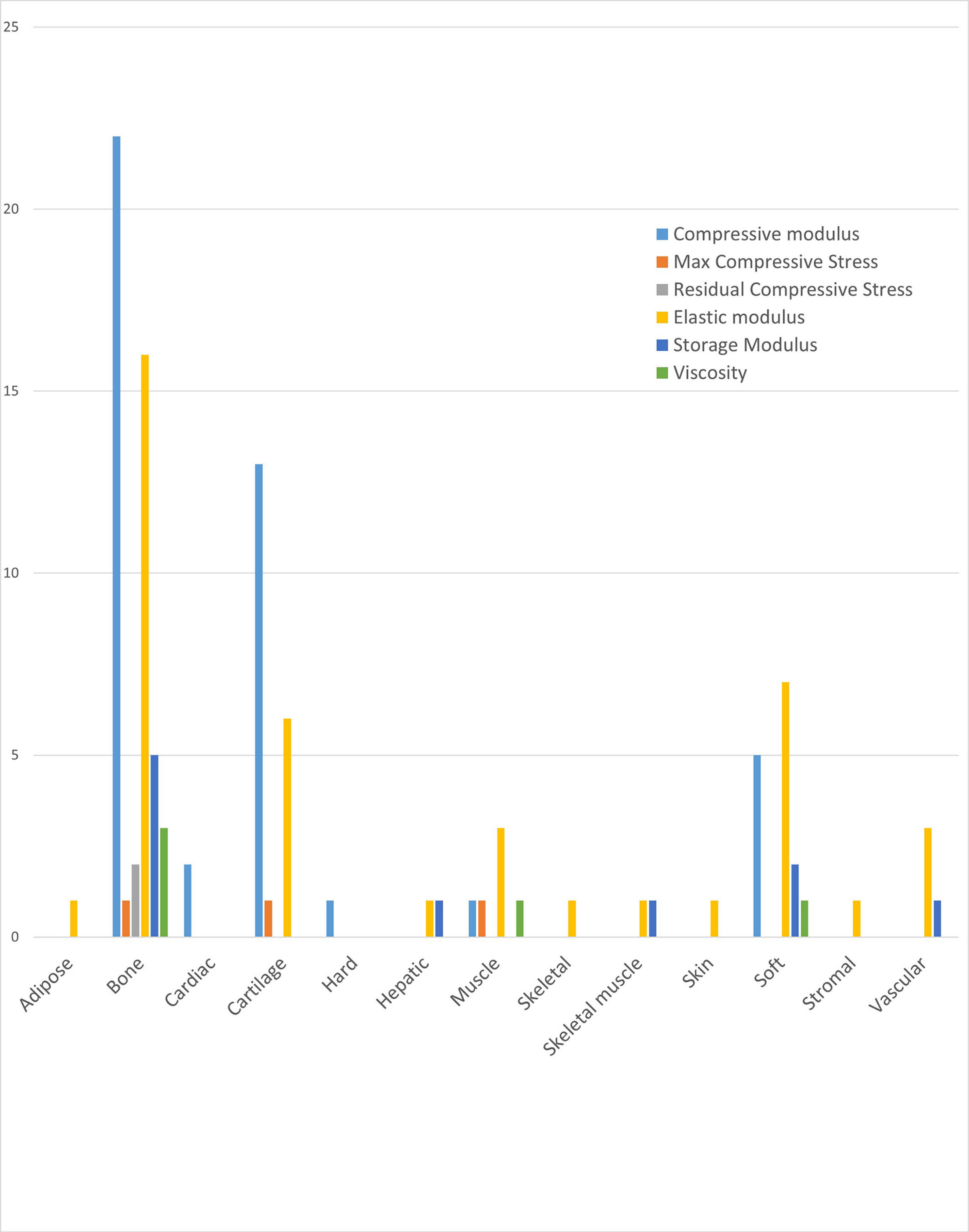

FIGURE 9 | Frequency and class of mechanical assessment for each tissue type.

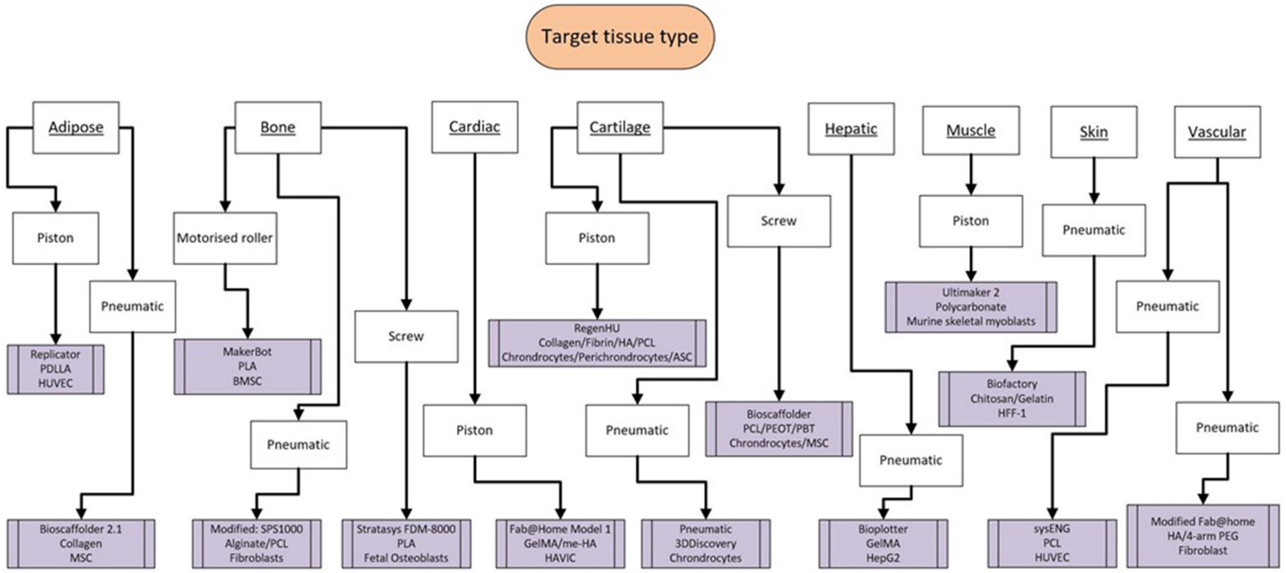

FIGURE 10 | Flowchart highlighting the scope of tissue type produced from the studies alongside the variability of bioprinter model, bioink, and cell source.

(154) (Hegewald et al., 2009; Zadpoor, 2017). It is recognised that biochemical makeup of a material inherently changes after cross-linking, incorporation of cells or secretion of extracellular matrix, which in turn alters its biomechanical properties (Hu et al., 2019) and this needs to be taken into account when characterising bioinks for extrusion. The biomechanical properties required for extrusion such as shear thinning to allow the material to flow with minimal stress to cells, are different to those post-crosslinking or following a period of cellular differentiation and matrix secretion, which should mirror mechanical properties of target tissue type (10, 15).

Emerging Future Trends From Recent Literature

A further search was carried out to include the literature from 2019 to 2021 using the PRISMA guidelines (Moher et al., 2015) and the same inclusion and exclusion criteria to allow us to establish the emerging recent trends in extrusion 3D bioprinting literature and compare and contrast this to our findings from the previous 12 years (2006–2018). A total of 104 papers met the inclusion criteria over the last 2 years, which is 85% of the total found from the inception of the technology to 2018. This demonstrates an exponential rise of research in the field. The reasons for this increase are multifactorial and likely due to the open-source nature of the technology (i.e., the feasibility of developing an in-house printer with easily available software), automation and customisability of laboratory-based tissue engineering research, combined with the increased availability of high-level work and increasing hubs of expertise in the field.

From analysis of the recent data (2019–2021), alginate continues to be the most widely used bioink accounting for 30% of the literature in pure or blended form. This, however, has reduced from 41% alginate use in literature published between 2006 and 2018 which may be attributed to the emergence of better manipulated synthetic bioinks such as PCL (Diaz-Gomez et al., 2020; Nulty et al., 2021) as well as novel natural bioinks such as nanocellulose (Markstedt et al., 2015; Kyle et al., 2018; Jessop et al., 2019). The most obvious trend that was found was the increase in the tissue type aimed to be recreated. It appears that there has been a shift from the soft tissue to hard and vascular derived tissue. Almost 50% of the studies were recreating bone or vessel tissue types. A hypothesis for this is the development and discovery of various growth factors (Dreyer et al., 2021) as well as more efficient cross-linking techniques to further the accuracy and precision of the printed construct (Benwood et al., 2021; Cooke and Rosenzweig, 2021; Huang et al., 2021).

The techniques of extrusion bioprinting has not changed dramatically in the last 2 years, but there is something to be said for more readily available commercial printers that are capable of high printing resolution and speeds; features that were only previously possible with industry produced equipment (Chang et al., 2021).

CONCLUSION

This systematic review provides a snapshot of the current natural and synthetic biomaterials that have been demonstrated to be suitable for extrusion bioprinting different tissue types. There is enormous breadth of bioink, bioprinter, and cell types as well as a range in biomechanical assessments. In part, this breadth can be attributed to the spectrum of tissue types the bioprinting process aims to replicate as well as an indicator that this research field is still in its infancy. There is increasing understanding that development of bioinks needs to address both biological properties, to support cell survival, proliferation, and differentiation, as well as biomechanical properties, to enable dispersion initially as a printed gel, and thereafter as a robust and durable solid tissue. Future research will need more transparency on the biomechanical properties required for different stages of the bioprinting process (pre-printing, shear thinning, post-crosslinking, and post-ECM formation) as well as head-to-head comparisons of different bioinks. The biomechanical suitability of the bioprinted tissue end-products will need to be assessed in the context of native tissue biomechanics and clinical end use application. Appropriate biomechanical methods that best assess *in vivo* stress requirements will need to be established to allow direct comparisons of bioink types. In addition, considering that the inclusion criteria for this systematic review meant that only studies involving cells in combination with biomaterials were included, it was surprising to find that more half of the studies analysed did not assess cell viability explicitly not to mention effects of proliferation or differentiation of bioinks on different cell types. There have been incremental developments in the field over the past 10 years, and the further refinement of bioprinting processes and bioink optimisation holds exciting potential for revolutionising tissue engineering approaches. It is difficult to speculate on what the landscape will be in several years of a decade, but the current frame within the literature is trending towards accuracy as well as precision (Bisht et al., 2021). The field of bioprinting will not be a "on size fits all" approach and unlikely to become a large-scale production of the technology, but rather a bespoke technology that will be produced depending on the patient's needs as well as the clinical application (Alcala-Orozco et al., 2021; Ji and Guvendiren, 2021).

DATA AVAILABILITY STATEMENT

The original contributions presented in the study are included in the article/**Supplementary Material**, further inquiries can be directed to the corresponding author/s.

AUTHOR CONTRIBUTIONS

ST: majority of writing and inception of review. ZJ: writing and inception of review. TJ: writing. KH: study design and draft work. IW: oversaw project. All authors contributed to the article and approved the submitted version.

FUNDING

This work was supported by Medical Research Council (MR/N002431/1).

SUPPLEMENTARY MATERIAL

The Supplementary Material for this article can be found online at: https://www.frontiersin.org/articles/10.3389/fbioe.2021.616753/full#supplementary-material

REFERENCES

Akkineni, A., Ahlfeld, T., Funk, A., Waske, A., Lode, A., and Gelinsky, M. (2016). Highly concentrated alginate-gellan gum composites for 3D plotting of complex tissue engineering scaffolds. *Polymers* 8:170. doi: 10.3390/polym8050170

Akkineni, A. R., Ahlfeld, T., Lode, A., and Gelinsky, M. (2016). A versatile method for combining different biopolymers in a core/shell fashion by 3D plotting to achieve mechanically robust constructs. *Biofabrication* 8:045001. doi: 10.1088/1758-5090/8/4/045001

Alcala-Orozco, C. R., Cui, X., Hooper, G. J., Lim, K. S., and Woodfield, T. B. F. (2021). Converging functionality: strategies for 3D hybrid-construct biofabrication and the role of composite biomaterials for skeletal regeneration. *Acta Biomater*. 3:8. doi: 10.1016/j.actbio.2021.03.008

Al-Himdani, S., Jessop, Z. M., Al-Sabah, A., Combellack, E., Ibrahim, A., Doak, S. H., et al. (2017). Tissue-engineered solutions in plastic and reconstructive surgery: principles and practice. *Front. Surg.* 4:4. doi: 10.3389/fsurg.2017.00004

Benwood, C., Chrenek, J., Kirsch, R. L., Masri, N. Z., Richards, H., Teetzen, K., et al. (2021). Natural biomaterials and their use as bioinks for printing tissues. *Bioengineering* 8:27. doi: 10.3390/bioengineering8020027

Bisht, B., Hope, A., Mukherjee, A., and Paul, M. K. (2021). Advances in the fabrication of scaffold and 3D printing of biomimetic bone graft. *Ann. Biomed. Eng.* 49, 1128–1150. doi: 10.1007/s10439-021-02752-9

Blaeser, A., Duarte Campos, D. F., Puster, U., Richtering, W., Stevens, M. M., and Fischer, H. (2016). Controlling shear stress in 3D bioprinting is a key factor to balance printing resolution and stem cell integrity. *Adv. Healthc. Mater*. 5, 326–333. doi: 10.1002/adhm.201500677

Boland, T., Mironov, V., Gutowska, A., Roth, E. A., and Markwald, R. R. (2003). Cell and organ printing 2: fusion of cell aggregates in three-dimensional gels. *Anat. Rec. A Discov. Mol. Cell. Evol. Biol*. 272, 497–502. doi: 10.1002/ar.a.10059

Chang, R., Nam, J., and Sun, W. (2008). Effects of dispensing pressure and nozzle diameter on cell survival from solid freeform fabrication-based direct cell writing. *Tissue Eng. Part A* 14, 41–48. doi: 10.1089/ten.2007.0004

Chang, Y. C., Mirhaidari, G., Kelly, J., and Breuer, C. (2021). Current challenges and solutions to tissue engineering of large-scale cardiac constructs. *Curr. Cardiol. Rep*. 23:47. doi: 10.1007/s11886-021-01474-7

Cooke, M. E., and Rosenzweig, D. H. (2021). The rheology of direct and suspended extrusion bioprinting. *APL Bioeng*. 5:011502. doi: 10.1063/5.0031475

Daly, A. C., Critchley, S. E., Rencsok, E. M., and Kelly, D. J. (2016). A comparison of different bioinks for 3D bioprinting of fibrocartilage and hyaline cartilage. *Biofabrication* 8:045002. doi: 10.1088/1758-5090/8/4/045002

Derby, B. (2012). Printing and prototyping of tissues and scaffolds. *Science* 338, 921–926. doi: 10.1126/science.1226340

Diaz-Gomez, L., Elizondo, M. E., Koons, G. L., Diba, M., Chim, L. K., Cosgriff-Hernandez, E., et al. (2020). Fiber engraving for bioink bioprinting within 3D printed tissue engineering scaffolds. *Bioprinting* 18:e00076. doi: 10.1016/j.bprint.2020.e00076

Dreyer, C. H., Jørgensen, N. R., Overgaard, S., Qin, L., and Ding, M. (2021). Vascular endothelial growth factor and mesenchymal stem cells revealed similar bone formation to allograft in a sheep model. *Biomed. Res. Int*. 2021:6676609. doi: 10.1155/2021/6676609

Dubbin, K., Tabet, A., and Heilshorn, S. C. (2017). Quantitative criteria to benchmark new and existing bio-inks for cell compatibility. *Biofabrication* 9:044102. doi: 10.1088/1758-5090/aa869f

Ersumo, N., Witherel, C. E., and Spiller, K. L. (2016). Differences in time-dependent mechanical properties between extruded and molded hydrogels. *Biofabrication* 8:035012. doi: 10.1088/1758-5090/8/3/035012

Fedorovich, N. E., De Wijn, J. R., Verbout, A. J., Alblas, J., and Dhert, W. J. (2008). Three-dimensional fiber deposition of cell-laden, viable, patterned constructs for bone tissue printing. *Tissue Eng. Part A* 14, 127–133. doi: 10.1089/ten.a.2007.0158

Fedorovich, N. E., Kuipers, E., Gawlitta, D., Dhert, W. J., and Alblas, J. (2011a). Scaffold porosity and oxygenation of printed hydrogel constructs affect functionality of embedded osteogenic progenitors. *Tissue Eng. Part A* 17, 2473–2486. doi: 10.1089/ten.tea.2011.0001

Fedorovich, N. E., Swennen, I., Girones, J., Moroni, L., van Blitterswijk, C. A., Schacht, E., et al. (2009). Evaluation of photocrosslinked Lutrol hydrogel for tissue printing applications. *Biomacromolecules* 10, 1689–1696. doi: 10.1021/bm801463q

Fedorovich, N. E., Wijnberg, H. M., Dhert, W. J., and Alblas, J. (2011b). Distinct tissue formation by heterogeneous printing of osteo- and endothelial progenitor cells. *Tissue Eng. Part A* 17, 2113–2121. doi: 10.1089/ten.tea.2011.0019

Galaev, I. Y., and Mattiasson, B. (1999). 'Smart' polymers and what they could do in biotechnology and medicine. *Trends Biotechnol.* 17, 335–340. doi: 10.1016/S0167-7799(99)01345-1

Galateanu, B., Dimonie, D., Vasile, E., Nae, S., Cimpean, A., and Costache, M. (2012). Layer-shaped alginate hydrogels enhance the biological performance of human adipose-derived stem cells. *BMC Biotechnol.* 12:35. doi: 10.1186/1472-6750-12-35

Gopinathan, J., and Noh, I. (2018). Recent trends in bioinks for 3D printing. *Biomater. Res.* 22:11. doi: 10.1186/s40824-018-0122-1

Hegewald, A. A., Knecht, S., Baumgartner, D., Gerber, H., Endres, M., Kaps, C., et al. (2009). Biomechanical testing of a polymer-based biomaterial for the restoration of spinal stability after nucleotomy. *J. Orthop. Surg. Res.* 4:25. doi: 10.1186/1749-799X-4-25

Hill, E., Boontheekul, T., and Mooney, D. J. (2006). Designing scaffolds to enhance transplanted myoblast survival and migration. *Tissue Eng.* 12, 1295–1304. doi: 10.1089/ten.2006.12.1295

Hollister, S. J. (2005). Porous scaffold design for tissue engineering. *Nat. Mater.* 4, 518–524. doi: 10.1038/nmat1421

Hu, J., Wang, J. H., Wang, R., Yu, X. B., Liu, Y., and Baur, D. A. (2019). Analysis of biomechanical behavior of 3D printed mandibular graft with porous scaffold structure designed by topological optimization. *3D Print. Med.* 5:5. doi: 10.1186/s41205-019-0042-2

Huang, H.-J., Tsai, Y.-L., Lin, S.-H., and Hsu, S.-H. (2019). Smart polymers for cell therapy and precision medicine. *J. Biomed. Sci.* 26:73. doi: 10.1186/s12929-019-0571-4

Huang, J., Huang, Z., Liang, Y., Yuan, W., Bian, L., Duan, L., et al. (2021). 3D printed gelatin/hydroxyapatite scaffolds for stem cell chondrogenic differentiation and articular cartilage repair. *Biomater. Sci.* 9, 2620–2630. doi: 10.1039/D0BM02103B

Hutmacher, D. W. (2000). Scaffolds in tissue engineering bone and cartilage. *Biomaterials* 21, 2529–2543. doi: 10.1016/S0142-9612(00)00121-6

Jakab, K., Neagu, A., Mironov, V., Markwald, R. R., and Forgacs, G. (2004). Engineering biological structures of prescribed shape using self-assembling multicellular systems. *Proc. Natl. Acad. Sci. U.S.A.* 101, 2864–2869. doi: 10.1073/pnas.0400164101

Jakab, K., Norotte, C., Damon, B., Marga, F., Neagu, A., Besch-Williford, C. L., et al. (2008). Tissue engineering by self-assembly of cells printed into topologically defined structures. *Tissue Eng. Part A* 14, 413–421. doi: 10.1089/tea.2007.0173

Jessop, Z. M., Al-Sabah, A., Gao, N., Kyle, S., Thomas, B., Badiei, N., et al. (2019). Printability of pulp derived crystal, fibril and blend nanocellulose-alginate bioinks for extrusion 3D bioprinting. *Biofabrication* 11:045006. doi: 10.1088/1758-5090/ab0631

Jessop, Z. M., Al-Sabah, A., Gardiner, M. D., Combellack, E., Hawkins, K., and Whitaker, I. S. (2017). 3D bioprinting for reconstructive surgery: principles, applications and challenges. *J. Plastic Reconstruct. Aesth. Surg.* 70, 1155–1170. doi: 10.1016/j.bjps.2017.06.001

Ji, S., and Guvendiren, M. (2021). Complex 3D bioprinting methods. *APL Bioeng.* 5:011508. doi: 10.1063/5.0034901

Jia, J., Richards, D. J., Pollard, S., Tan, Y., Rodriguez, J., Visconti, R. P., et al. (2014). Engineering alginate as bioink for bioprinting. *Acta Biomater.* 10, 4323–4331. doi: 10.1016/j.actbio.2014.06.034

Jiao, Z., Luo, B., Xiang, S., Ma, H., Yu, Y., and Yang, W. (2019). 3D printing of HA / PCL composite tissue engineering scaffolds. *Adv. Industr. Eng. Polymer Res.* 2, 196–202. doi: 10.1016/j.aiepr.2019.09.003

Jürgen, G., Thomas, B., Torsten, B., Jason, A. B., Dong-Woo, C., Paul, D. D., et al. (2016). Biofabrication: reappraising the definition of an evolving field. *Biofabrication* 8:013001. doi: 10.1088/1758-5090/8/1/013001

Kirchmajer, D. M., Gorkin Iii, R., and in het Panhuis, M. (2015). An overview of the suitability of hydrogel-forming polymers for extrusion-based 3D-printing. *J. Mater. Chem. B* 3, 4105–4117. doi: 10.1039/C5TB00393H

Klebe, R. J. (1988). Cytoscribing: a method for micropositioning cells and the construction of two- and three-dimensional synthetic tissues. *Exp. Cell Res.* 179, 362–373. doi: 10.1016/0014-4827(88)90275-3

Kundu, J., Shim, J. H., Jang, J., Kim, S. W., and Cho, D. W. (2015). An additive manufacturing-based PCL-alginate-chondrocyte bioprinted scaffold for cartilage tissue engineering. *J. Tissue Eng. Regen. Med.* 9, 1286–1297. doi: 10.1002/term.1682

Kyle, S., Jessop, Z. M., Al-Sabah, A., Hawkins, K., Lewis, A., Maffeis, T., et al. (2018). Characterization of pulp derived nanocellulose hydrogels using AVAP® technology. *Carbohydr. Polym.* 198, 270–280. doi: 10.1016/j.carbpol.2018.06.091

Kyle, S., Jessop, Z. M., Al-Sabah, A., and Whitaker, I. S. (2017). 'Printability' of candidate biomaterials for extrusion based 3D Printing: State-of-the-Art. *Adv. Healthcare Mater.* 6:1700264. doi: 10.1002/adhm.201700264

Landers, R., Hubner, U., Schmelzeisen, R., and Mulhaupt, R. (2002). Rapid prototyping of scaffolds derived from thermoreversible hydrogels and tailored for applications in tissue engineering. *Biomaterials* 23, 4437–4447. doi: 10.1016/S0142-9612(02)00139-4

Langer, R., and Tirrell, D. A. (2004). Designing materials for biology and medicine. *Nature* 428, 487–492. doi: 10.1038/nature02388

Lee, H., Ahn, S., Bonassar, L. J., Chun, W., and Kim, G. (2013). Cell-laden poly(ε-caprolactone)/alginate hybrid scaffolds fabricated by an aerosol cross-linking process for obtaining homogeneous cell distribution: fabrication, seeding efficiency, and cell proliferation and distribution. *Tissue Eng. Part C Methods* 19, 784–793. doi: 10.1089/ten.tec.2012.0651

Lee, J. W., Choi, Y. J., Yong, W. J., Pati, F., Shim, J. H., Kang, K. S., et al. (2016). Development of a 3D cell printed construct considering angiogenesis for liver tissue engineering. *Biofabrication* 8:015007. doi: 10.1088/1758-5090/8/1/015007

Lee, S. J., Nowicki, M., Harris, B., and Zhang, L. G. (2017). Fabrication of a highly aligned neural scaffold via a table top stereolithography 3D printing and electrospinning. *Tissue Eng. Part A* 23, 491–502. doi: 10.1089/ten.tea.2016.0353

Lee, W., Lee, V., Polio, S., Keegan, P., Lee, J. H., Fischer, K., et al. (2010). On-demand three-dimensional freeform fabrication of multi-layered hydrogel scaffold with fluidic channels. *Biotechnol. Bioeng.* 105, 1178–1186. doi: 10.1002/bit.22613

Levato, R., Visser, J., Planell, J. A., Engel, E., Malda, J., and Mateos-Timoneda, M. A. (2014). Biofabrication of tissue constructs by 3D bioprinting of cell-laden microcarriers. *Biofabrication* 6:035020. doi: 10.1088/1758-5082/6/3/035020

Liu, W., Heinrich, M. A., Zhou, Y., Akpek, A., Hu, N., Liu, X., et al. (2017). Extrusion bioprinting of shear-thinning gelatin methacryloyl bioinks. *Adv. Healthc. Mater.* 6. doi: 10.1002/adhm.201601451

Malda, J., Visser, J., Melchels, F. P., Jüngst, T., Hennink, W. E., Dhert, W. J. A., et al. (2013). 25th anniversary article: engineering hydrogels for biofabrication. *Adv. Mater.* 25, 5011–5028. doi: 10.1002/adma.201302042

Markstedt, K., Mantas, A., Tournier, I., Martinez Avila, H., Hagg, D., and Gatenholm, P. (2015). 3D bioprinting human chondrocytes with nanocellulose-alginate bioink for cartilage tissue engineering applications. *Biomacromolecules* 16, 1489–1496. doi: 10.1021/acs.biomac.5b00188

Miri, A. K., Mirzaee, I., Hassan, S., Mesbah Oskui, S., Nieto, D., Khademhosseini, A., et al. (2019). Effective bioprinting resolution in tissue model fabrication. *Lab Chip* 19, 2019–2037. doi: 10.1039/C8LC01037D

Mironov, V. (2005). The Second International Workshop on Bioprinting, Biopatterning and Bioassembly. *Expert Opin. Biol. Ther.* 5, 1111–1115. doi: 10.1517/14712598.5.8.1111

Moher, D., Shamseer, L., Clarke, M., Ghersi, D., Liberati, A., Petticrew, M., et al. (2015). Preferred reporting items for systematic review and meta-analysis protocols (PRISMA-P) 2015 statement. *Syst. Rev.* 4:1. doi: 10.1186/2046-4053-4-1

Muller, M., Becher, J., Schnabelrauch, M., and Zenobi-Wong, M. (2015). Nanostructured Pluronic hydrogels as bioinks for 3D bioprinting. *Biofabrication* 7:035006. doi: 10.1088/1758-5090/7/3/035006

Murphy, S. V., Skardal, A., and Atala, A. (2013). Evaluation of hydrogels for bio-printing applications. *J. Biomed. Mater. Res. Part A* 101A, 272–284. doi: 10.1002/jbm.a.34326

Nikolova, M. P., and Chavali, M. S. (2019). Recent advances in biomaterials for 3D scaffolds: a review. *Bioactive Mater*. 4, 271–292. doi: 10.1016/j.bioactmat.2019.10.005

Nulty, J., Freeman, F. E., Browe, D. C., Burdis, R., Ahern, D. P., Pitacco, P., et al. (2021). 3D Bioprinting of prevascularised implants for the repair of critically-sized bone defects. *Acta Biomater*. 3:3. doi: 10.1016/j.actbio.2021.03.003

Purcell, E. K., Singh, A., and Kipke, D. R. (2009). Alginate composition effects on a neural stem cell-seeded scaffold. *Tissue Eng. Part C Methods* 15, 541–550. doi: 10.1089/ten.tec.2008.0302

Reid, J. A., Mollica, P. A., Johnson, G. D., Ogle, R. C., Bruno, R. D., and Sachs, P. C. (2016). Accessible bioprinting: adaptation of a low-cost 3D-printer for precise cell placement and stem cell differentiation. *Biofabrication* 8:025017. doi: 10.1088/1758-5090/8/2/025017

Sharma, R., Smits, I. P. M., De La Vega, L., Lee, C., and Willerth, S. M. (2020). 3D bioprinting pluripotent stem cell derived neural tissues using a novel fibrin bioink containing drug releasing microspheres. *Front. Bioeng. Biotechnol.* 8:57. doi: 10.3389/fbioe.2020.00057

SigmaAldrich (2021a). *Sodium Alginate*. Darmstadt: ed Merck.

SigmaAldrich (2021b). *Hyaluronic Acid Sodium Salt From Streptococcus equi*. Darmstadt: ed Merck.

Skardal, A., Smith, L., Bharadwaj, S., Atala, A., Soker, S., and Zhang, Y. (2012). Tissue specific synthetic ECM hydrogels for 3-D *in vitro* maintenance of hepatocyte function. *Biomaterials* 33, 4565–4575. doi: 10.1016/j.biomaterials.2012.03.034

Smith, C. M., Stone, A. L., Parkhill, R. L., Stewart, R. L., Simpkins, M. W., Kachurin, A. M., et al. (2004). Three-dimensional bioassembly tool for generating viable tissue-engineered constructs. *Tissue Eng*. 10, 1566–1576. doi: 10.1089/1076327042500274

Steffens, D., Rezende, R. A., Santi, B., Pereira, F. D., Inforcatti Neto, P., da Silva, J. V., et al. (2016). 3D-printed PCL scaffolds for the cultivation of mesenchymal stem cells. *J. Appl. Biomater. Funct. Mater.* 14, e19–e25. doi: 10.5301/jabfm.5000252

Stichler, S., Bock, T., Paxton, N., Bertlein, S., Levato, R., Schill, V., et al. (2017). Double printing of hyaluronic acid/poly(glycidol) hybrid hydrogels with poly(epsilon-caprolactone) for MSC chondrogenesis. *Biofabrication* 9:044108. doi: 10.1088/1758-5090/aa8cb7

Tarassoli, S. P., Jessop, Z. M., Al-Sabah, A., Gao, N., Whitaker, S., Doak, S., et al. (2018a). Skin tissue engineering using 3D bioprinting: An evolving research field. *J. Plastic Reconstr. Aesth. Surg*. 71, 615–623. doi: 10.1016/j.bjps.2017.12.006

Tarassoli, S. P., Jessop, Z. M., Kyle, S., and Whitaker, I. S. (2018b). *3D Bioprinting for Reconstructive Surgery*. Cambridge, MA: Woodhead Publishing, 145–172.

Wei, M., Gao, Y., Li, X., and Serpe, M. J. (2017). Stimuli-responsive polymers and their applications. *Polym. Chem*. 8, 127–143. doi: 10.1039/C6PY01585A

Zadpoor, A. A. (2017). Biomaterials and tissue biomechanics: a match made in heaven?. *Materials* 10:528. doi: 10.3390/ma10050528

Zhang, Z., and Cui, H. (2012). Biodegradability and biocompatibility study of poly(chitosan-g-lactic acid) scaffolds. *Molecules* 17, 3243–3258. doi: 10.3390/molecules17033243

Conflict of Interest: The authors declare that the research was conducted in the absence of any commercial or financial relationships that could be construed as a potential conflict of interest.

Advantages of publishing in Frontiers

OPEN ACCESS
Articles are free to read
for greatest visibility
and readership

FAST PUBLICATION
Around 90 days
from submission
to decision

HIGH QUALITY PEER-REVIEW
Rigorous, collaborative,
and constructive
peer-review

TRANSPARENT PEER-REVIEW
Editors and reviewers
acknowledged by name
on published articles

Frontiers
Avenue du Tribunal-Fédéral 34
1005 Lausanne | Switzerland

Visit us: www.frontiersin.org
Contact us: frontiersin.org/about/contact

REPRODUCIBILITY OF RESEARCH
Support open data
and methods to enhance
research reproducibility

DIGITAL PUBLISHING
Articles designed
for optimal readership
across devices

FOLLOW US
@frontiersin

IMPACT METRICS
Advanced article metrics
track visibility across
digital media

EXTENSIVE PROMOTION
Marketing
and promotion
of impactful research

LOOP RESEARCH NETWORK
Our network
increases your
article's readership